A Micromechanics-Based Continuum Damage Mechanics Approach to the Mechanical Behaviour of Brittle Matrix Composites.

by

Chia Yan Hon, Julian

Submitted to the University of Glasgow

for the degree of

Doctor of Philosophy

in

Mechanical Engineering

Abstract

The thesis describes the development of a new continuum damage mechanics (hereafter, CDM) model for the deformation and failure of brittle matrix composites reinforced with continuous fibres. The CDM model is valid over sizes scales large compared to the spacing of the fibres and the dimensions of the damage. The composite is allowed to sustain damage in the form of matrix micro-cracking, shear delamination, tensile delamination and fibre failure. The constitutive equations are developed by decomposing the composite compliance into terms attributable to the fibre and matrix, and modelling the competing failure modes by intersecting failure surfaces based on maximum stress theory. The fibres are treated as being weakly bonded to the matrix so that the fibres only transmit axial loads, and fail in tension. The matrix is modelled as isotropic linear elastic and is treated as transversely-isotropic after damage has initiated. The effect of multiple matrix cracking on the stiffness was determined from experimental data, while failure was modelled by a rapid decay in the load bearing capacity. Although the model is motivated largely to proportional loading, matrix unloading and damage closure has been modelled by damage elasticity. During compression, the matrix stiffness is identical to the undamaged state with the exception that the fibres are assumed not to transmit compressive loads. The model was implemented computationally through a FORTRAN subroutine interfaced with the ABAQUS/Standard finite element solver.

The CDM model was validated by comparing experimental and computational results of test specimens with unidirectional and balanced 0°-90° woven fibres of a brittle matrix composite, fabricated from polyester fibres in a polyester matrix. This composite system exhibits low elastic mismatch between fibres and matrix, and has similar non-dimensionalised stress–strain response to a SiC/SiC composite proposed for the exhaust diffuser unit of the Rolls-Royce EJ200 aero-engine. Test specimens reinforced with aligned and misaligned fibres have been uniaxially tensioned to the tensile axis to produce a range of damage mechanisms and failure processes. To demonstrate the ability of the model to analyse engineering structures, a range of idealised parts from the exhaust diffuser unit of the Rolls-Royce EJ200 aero-engine were tested and analysed in bending. The sub-structural specimens included a simple rectangular bar, a bar with a thickened cross-section, and a T-shaped component. These

sub-structures showed the full range of damage mechanisms, which often occurs simultaneously in engineering structures made from brittle matrix composites.

The behaviour of the fibre-matrix interface is central to the behaviour of fibre reinforced composites. It is argued that a full range of interfacial properties can be modelled by treating the interface as imperfect such can be formalised as an infinite periodic array of cracks. Interfacial elements were developed to model the properties of an imperfect interface. The result support the simplification used to represent the fibres as simple axial load bearing components in the CDM model, and gave insight into the behaviour of imperfectly bonded interfaces.

Acknowledgements

I wish to formally express my sincere gratitude to the following persons and organisations for their help and support to complete this thesis.

My deepest gratitude goes to Professor John W. Hancock, my academic supervisor. You have taught me invaluable skills concerning research and personal management. I am especially indebted to you for the encouragement, guidance, support and grace in making this thesis come to past, recommendation to the Committee of Vice-Chancellors and Principles (CVCP) of the Universities of the United Kingdom to receive the Overseas Research Student (ORS) Award, recommendation to the University of Glasgow to receive the Mechanical Engineering Departmental Scholarship, and provision of a pleasant work environment in the department.

I would like to acknowledge and thank Professor Mike Cowling for supporting my application for the ORS and Departmental Scholarship; Dr. David V. Philips for advice on finite element modelling techniques; Dr. Ronald D. Thomson for advice on continuum mechanics; Dr Bill Broughton for advice on composite testing; Dr. Neil L. McCartney for correspondence on composite modelling; Mr Ian Peden for technical work on the acoustic emission detection system; Dr. Ian Watson for technical resources for the acoustic emission detection system; Mr. Jamie Cunningham for advice on thermodynamics; Mr Alexander Tory for making the mechanical test rigs and fabrication jigs for the experimental work on composites and sharing an office with me; Mr Alan Birkbeck, Mr George Falconor, Mr John Davidson and Mr Brian Robb for shaping the composite specimens; Panagiotis Tsouchnikas, Christos Kastritseas, Lubrano Andrea, Niall MacLeod for assisting in the fabrication and analysis of the composite specimens; Mr Kenny Stevenson, Ms Yassamine Mather, Walter Robinson for computing support; Ms Fiona Downie, Ms Careen Fraser, Ms Pauline Kyriacou, Ms Elaine McNamara, Ms Jane Livingstone for administrative support in the department; Ms Marion Richardson for administrative support in the engineering faculty; Bostjan Bezensek, Anuradha Banerjee, Kirsteen Lowe and Moshiur Rahman for being supportive colleagues in the fracture mechanics group; Dr Paul Molly, Ms Margaret Smith, Dr Maureen Joan Perry and Dr Muhammad Shahid for being supportive colleagues in the department; Dr Seat Han Cheng, Dr Wu Jia Jang, Dr Yeo Chiew Beng

Allen, Dr Chong Boon Keat and Dr Mark Müller for being supportive colleagues and friends within and outwith the engineering faculty.

I would also like to thank my brothers and sisters in Glasgow Chinese Christian Church (GCCC), St. Silas Church, and Faith Assembly of God Church (Singapore) for their encouragement and support. Thanks also go to GCCC for the accommodation and sustenance during my stay in Glasgow and allowing the youths in Refiner's Fire to be a special part of my life. Also, I would like to thank Matty Chan Yiu Tung for being my flatmate and Deacon Paul Watson for his Scottish friendship.

My special and heartfelt appreciation goes to my dad, David, and mum, Irene, for their unfailing love to see me complete the thesis. Also to my brother Michael, sister-in-law Stella, sisters Angela and Caroline, nephew John, niece Grace, grandma Cheong Foong Yin, uncle Chia Weng Kok & family for their encouragement during my research. I would also like to remember my late grandpa Chin Koon Seng and late uncle Chia Weng Fatt for their kind influence on my life. Finally, I would like to specially thank my Saviour and Lord, Jesus Christ, for grace, hope, faith and love during this thesis.

Nomenclature

Stresses, Strains and Elasticity

C_{ijkl}	Stiffness tensor of a material
$\mathbf{e}_1, \mathbf{e}_2, \mathbf{e}_3$	Unit vectors of three mutally perpendicular co-ordinate axis x_1, x_2, and x_3.
ε_{ij}	Strain tensor
n	
ε	Resultant strain vector
ε_n	Normal strain vector
ε_s	Shear strain vector
$\widetilde{\varepsilon}$	Mean strain
$\widetilde{\varepsilon}\delta_{ij}$	Hydrostratic strain tensor
ε_v	Volumetric or dilatational strain
e_{ij}	Deviatoric strain tensor
E	Young's modulus
F_i	Body force
G	Shear modulus
$\mathbf{G}$	Transformation matrix for the stress and strain tensor
$\mathbf{H}$	Transformation matrix for engineering strain
γ	Engieering shear strain
$\gamma_1, \gamma_2, \gamma_3$	Principal engineering shear strain
Ω	Complementary energy denisty or the complementary energy per unit volume
l_{ij}	Direction cosine between the co-ordinate axes x_i'and x_j
I_1, I_2, I_3	Invariants of stress tensor σ_{ij}
I_1', I_2', I_3'	Invariants of strain tensor ε_{ij}
J_1, J_2, J_3	Invariants of the deviatoric stress tensor s_{ij}
J_1', J_2', J_3'	Invariants of the deviatoric strain tensor e_{ij}
$\mathbf{n}$	Unit normal of a plane in a continuous body.
n_i, n_j	Direction cosines between $\mathbf{n}$ and $\mathbf{e}_1, \mathbf{e}_2, \mathbf{e}_3$.
$\mathbf{n}^{(1)}, \mathbf{n}^{(2)}, \mathbf{n}^{(3)}$	Principal directions
ν	Poisson's ratio
σ_{ij}	Cauchy's stress tensor.
σ_n	Normal stress vector
σ_s	Shear stress vector
σ	Principal stress
$\widetilde{\sigma}$	Mean stress
$\widetilde{\sigma}\delta_{ij}$	Hydrostratic stress tensor
s_{ij}	Deviatoric stress tensor

s	Principal deviatoric stress tensor
S_{ijkl}	Compliance tensor of material
$\vartheta_1, \vartheta_2, \vartheta_3$	Principal shear strain
$\overset{n}{\mathbf{T}}, \overset{n}{T}_i$	Cauchy's stress (or traction) vector.
u_i	Displacement vector
W	Strain energy density or the strain energy per unit volume
δW	Rate of change of the strain energy density W

Damage Mechanics

Ψ	Kachanov (1958) scaler damage variable
ω	Robotnov (1968) scaler damage variable
Ω	Murakami & Ohno (1981) second-order damage tensor
$\boldsymbol{D}$	Cordebois & Sidoroff (1981) second-order damage tensor
D_{ijkl}	Lemaitre & Chaboche (1978) fourth-order damage tensor
ω_o	Void area density in a plane
A	Net area
A_n	Apparent area
$\overline{\sigma}$	Net stress or effective stress
s	Entropy density
S	Entropy
ξ_α	Internal state variables (where $\alpha = 1 \ldots, n$)
u	Internal energy density
ρ	Density
r	Body heating and radiation
$\mathbf{q}$	Heat flow vector
T	Absolute temperature
Γ	Internal entropy production
ψ	Helmholtz free energy denisty
η	Gibb's free energy density
γ	Internal entropy production per unit mass

Composites Terminology

α	ratio of $E_m V_m$ over $E_f V_f$
ε_{mu}	ultimate failure strain of matrix
ε_{fu}	ultimate failure strain of fibres
γ	applied shear strain
γ_m	fracture work to form a matrix crack surface
γ_{db}	energy used to debond fibres bridging a unit area of matrix crack

σ_b	fibre bundle stress
σ_{bu}	ultimate failure stress of fibre bundle
σ_c	composite stress
σ_{cu}	ultimate failure stress of composite
σ_f	fibre stress
σ_{fu}	ultimate failure stress of fibres
$\overline{\sigma}_{fu}$	mean ultimate failure stress of fibres
σ'_f	fibre stress when matrix cracks
σ_b	fibre bundle stress
σ_{bu}	ultimate failure stress of fibre bundle
σ_m	matrix stress
σ_{mc}	matrix crack initiation stress
$\sigma_{mc(sat)}$	matrix crack saturation stress
σ_{ms}	matrix softening stress
σ_{mu}	ultimate failure stress of matrix
${}^{o}\sigma_m$	radial stress in matrix with respect to fibre axis
σ_{sd}	shear delamination stress of composite
σ_{td}	tensile delamination stress of composite
σ_∞	far field stress
τ	interfacial shear stress
ΔU_f	change in fibre strain energy per unit area
ΔU_m	change in matrix strain energy per unit area
ΔW	work done to create a steady state matrix crack per unit area
Δw or dl	additional displacement of fibres during matrix cracking
a	crack length
a_o	transient crack length
E_c	Young's modulus of composite
E_f	Young's modulus of fibres
E_m	Young's modulus of matrix
E_{Voigt}	Young's modulus of a composite by Voigt
E_{Ruess}	Young's modulus of a composite by Ruess
G_c	Shear modulus of composite
G_f	Shear modulus of fibres
G_m	Shear modulus of matrix
G_{Voigt}	Shear modulus of a composite by Voigt
G_{Ruess}	Shear modulus of a composite by Ruess
G_I	fracture energy release rate of matrix per unit area
G_{II}	debond energy release rate of fibre-matrix interface per unit area
L	fibre length
K^c	effective stress intensity factor of composite

K^m	effective stress intensity factor of matrix
K_{IC}^c	critical stress intensity factor of composite
K_{IC}^m	critical stress intensity factor of matrix
m	Weibull modulus
p_f	probability density failure function
P_f	probability of failure
P_s	probability of survival
r_o	fibre radius
p	closure pressure at matrix crack surface
R	centre-to centre separation distance of fibres
T	closure traction by bridging fibres
u	displacement at crack surface
U_c	matrix crack surface energy per unit area
U_s	energy dissipate due to frictional sliding per unit area
V_f	volume fraction of fibres
$V_{f\,\mathrm{crit}}$	critical fibre volume fraction at which multiple matrix crack forms
V_m	volume fraction of matrix
x'	critical load transfer distance
$\bar{x}'$	mean load transfer distance
X	normalised distance at crack surface

Computational Model

σ	- stress
ε	- strain
S	- compliance
C	- stiffness
E	- Young's modulus
G	- shear modulus
ν	- Poisson's ratio
T	- transformation
d	- an increment of
V	- volume fraction
A	- area fraction
$\{\ \}$	- 3 x 1 vector
$[\ ]$	- 3 x 3 matrix
$\|\ \|$	- magnitude of

Subscripts

c	- composite
f	- fibre
m	- matrix
mc	- matrix cracking
mc(sat)	- matrix crack saturation
ms	- matrix softening
td	- tensile delamination
sd	- shear delamination
u	- ultimate failure

Superscripts

n	- current increment
n-1	- previous increment
c	- composite position system
f	- fibre position system
m	- matrix principal stress position system

List Of Figures

List Of Tables

Contents

CHAPTER 1

Introduction

1.1 An Overview of the Development of Brittle Matrix Composites

The development of low density, high strength, tough materials with good corrosion resistance is a primary aim in many engineering applications. Ceramics show many of these properties. However, their use is limited by low toughness, typically of the order of 1 $\mathrm{MPa}\sqrt{\mathrm{m}}$. Nevertheless, since the 1980s, interest in ceramics has increased following the discovery that toughness could be improved by grain refinement or by composite technologies. Marshall & Ritter (1987) and Evans (1990) have reviewed these approaches. Grain refinement has improved toughness by a factor of two. The modification of grain shape to an elongated microstructure also results in further enhancement of toughness. However, the most important contributor to toughness enhancement in this field is the creation of microstructures using second phases, such as zirconia additives, which cause stress-induced phase transformations at the wake of crack tips: a process termed *transformation toughening* (Marshall (1986), Heuer (1987)). Toughness values of up to $20\,\mathrm{MPa}\sqrt{\mathrm{m}}$ have been reported. The mechanics of transformation toughening are described by McMeeking & Evans (1982) and Budiansky *et al* (1983). However, greater levels of toughening in ceramics have been achieved through composite technologies, in which high strength ductile fibres are incorporated into a ceramic matrix. Toughness values in excess of $30\,\mathrm{MPa}\sqrt{\mathrm{m}}$ have been reported. The micro-mechanics and computational modelling of such brittle matrix composite materials is the subject of this thesis.

Lewis (1995) has given a historical overview of the development of ceramic composites. The development of tough ceramics using embedded fibrous reinforcements followed the successes of fibre reinforced plastics during the 1950-60s. Fibre reinforced plastic materials are capable of tensile strengths approaching 1GPa and toughnesses equivalent to metals, and densities approximately half that of aluminium and one-sixth that of steel. A primary motivation for developing ceramic composites is the need for better high-temperature structural materials for aero-engine

applications and high Mach number airframe components. Superalloys are already approaching their limit as operation temperatures approach melting points. An early success was the British work on tough carbon fibre-reinforced glasses by Tinklepaugh (1965), Sambell et al (1972) and Levitt (1972). The key development in understanding the toughening mechanisms was provided by Cook & Gordon (1964), Aveston, Cooper & Kelly (1971), hereafter ACK, and Hale & Kelly (1972), who demonstrated the significance of weak fibre-matrix interfaces. In the work of ACK and Hale & Kelly (1972), interfacial shear strength of the order of a few MPa was shown sufficient to achieve improved toughness levels.

Despite these early results, the control of interfacial strength in ceramic fibre-ceramic matrix composites was difficult to achieve. The high processing temperatures and the reactivity of most ceramics often resulted in well-bonded interfaces. Significant advances only started with the introduction of a high strength-toughness Nicalon™ SiC-fibre reinforced glass ceramic composite in the early 80s by Prewo and Brennan (1980, 1982) and Brennan & Prewo (1982) at the United Technology Research Centre (UTRC). Generally known as Compglas™, the weak interface contributing to improved toughness was achieved by using Nb_2O_5 as the nucleating agent for a lithium aluminium silicate (LAS) glass-ceramic matrix. This resulted in the formation of a weak carbon interfacial layer. First, carbon from the fibre reacts with Nb to form a NbC layer. As the reaction saturates, the formation of a weak carbon layer within the carbide layer occurs because further diffusion of carbon into the glass ceramic is prevented. The formation of the carbon layer is illustrated in Fig 1.1-1. Following these developments, Rice (1981a,b, 1984) and Rice et al (1982), Jamet et al (1984), Brender et al (1990) at the National Research Laboratory (NRL) demonstrated that ceramic fibres with chemical-vapour-deposition (CVD) coatings of BN could provide the necessary weak interface in many ceramic matrix composites. When there is reactivity between BN and the matrix ceramic, a bi-layer BN/SiC coating is introduced. To date, the carbon, BN or BN/SiC interfaces have produced the best composite strength and toughness.

1.2 Benefits and Applications

A recent review of the benefits and applications of ceramic composites has been presented by Richlen (1995). The basis of his review was the need for improved

energy efficiency, productivity and competitiveness in the United States. Following proposals by the National Critical Technologies Panel in the United States on advanced materials, both ceramic and composite systems were identified as crucial technologies. A forecast by the US Department of Energy estimated a potential annual energy saving of 1.2×10^{18} Joules if ceramic composites were used. This would result in increased cost-competitiveness of industrial products and a decrease of national dependence on imported energy sources resulting in reduced emissions and improved environmental health.

The sectors most likely to benefit from ceramic composite technology were identified as: industrial, aerospace/defence and biomedical sectors. In the industrial sector, potential applications include heat management systems, power generation, processing, separation systems and structural applications. The potential economic impact was estimated at US$400 billion. In the aerospace/defence sector, the potential applications include propulsion systems, thermal protectors and structural components, while, in the biomedical sector, applications such as re-constructive surgery and implants were recommended. A table of the potential applications is given in Tables 1.1 to 1.3.

The application of ceramic composites in gas turbine engines has attracted particular attention. The market includes electrical power generation and aero-propulsion engine systems. In electrical power generating turbines, ceramic composites are strategic choices for rotors, stators, combustion chamber liners, cross fire tubes, combustor to turbine transition piece, turbine shrouds and blade tip seals, first-stage nozzles and buckets, and regenerators. Their use allows higher operation inlet temperature, which results in increased thermodynamic energy conversion efficiency and reduced fuel consumption. Because of the higher operation temperature range, areas of incomplete combustion are eliminated. More discharge air from the compressor is freed for combustion, hence reducing undesirable emissions of carbon monoxide and unburned hydrocarbons into the atmosphere. The increased volume of air also acts as a heat sink to reduce flame temperatures such that oxidation of nitrogen proceeds too slowly to produce NO_x gases. A potential reduction of NO_x emissions by 272×10^6 kg/yr has been estimated. Between 2000 to 2009, the utility industry in US projects an additional capacity requirement of 135×10^6 KW. If mature ceramic composite technology were successfully implemented into gas turbine power

generators, a potential electrical capacity of 530 x 10^9 KWh/yr could be generated. In aero-propulsion engines, the other advantage is improved thrust-to-weight ratios. Ceramic composites will offer the potential for higher fracture toughness, higher strength and thermal stability at lower densities than metallic counterparts.

Aerospace/Defence Applications	Specific CFCC Components
Propulsion Engine Systems	
Gas Turbine Engines, Rocket Engines, Aircraft Engines, and Vehicles	Rotors, airfoils, guide vanes, blades, tip seals, disks, augmenters, compressors, stators
Combustor	Combustor plates, combustor linings
Engine Exhaust	Nozzle components, flaps
Thermal Protection	Fasteners, aero-brakes, ablators, insulators
Structural Components	
Aerospace Structures	Missiles, radomes, aircraft structures, modified signature structures

Table 1.2-2. Recommended Aerospace/Defense Applications for Ceramic Composite (adapted from Richlen, 1995).

Type of Applications	Specific CFCC Components
Re-constructive Surgery and Implants	Dental implants
	Jaw bone reconstruction
	Bone and joint surgery Bone plates Long bones

Table 1.2-3. Recommended Biomedical Applications for Ceramic Composites (adapted from Richlen, 1995).

CFCC Product Area/Typical Examples	Likely Industrial Markets
Heat Management Systems	
Waste incineration systems Handling equipment, furnace intemals, clean-up	Conventional MSW/RDF facilities, advanced toxic or hazardous waste facilities; with/without energy recovery
Heat recovery equipment intemals Air preheaters, recuperators	Any indirect heating uses; energy intensive industrial processes (aluminium remelters, steel reheaters, glass melters)
Burners and combustors Radiant tube bumers	Potentially any indirect-fired, high temperature and/or controlled atmosphere heating/melting/heat treating use
Burners and combustors Catathermal combustors	Low NO_x clean fuel heating applications, including - gas turbine combustors, industrial process heat
Burners and combustors Low temperature radiant combustors	Low NO_x clean fuel heating applications, including small scale (space heating) and large scale (industrial processes)
Refractories and related products Furnace linings, crucibles	High temperature industrial heating/ milting/heat treating processes (primary retrofit applications)
Power Generation	
Stationary engines Combustors/liners, wear parts	Primary high temperature gas turbines (especially combustors); possibly adiabatic diesels, S-1 engines
Fusion reactor	Long-term program; potential power source for electric utility industry after 2040
Processing	
Process equipment Reformers, reactors, high pressure heat exchangers, burners, pyrolysis tubes	Chemical process industry; petroleum refining; corrosives handling and storage
Separation Systems	
Separation/filtration systems Filters, substrates, centrifuges	Gas turbine, combined cycle, and IGCC configurations; diesel exhaust particle traps; molten metal filters; sewage treatment
Structural Applications	
Structural components Beams, panels, decking, containers	Possible niche uses for ENU shielding, corrosive/abrasive environments, fire or missile protection, infrastructure repair

Table 1.2-1 Recommended Industrial Applications for Ceramic Composites (adapted from Richlen, 1995).

1.3 Problems

Although ceramic composite materials are potentially useful and economical, their use in engineering components and structures is slow due to the lack of efficient

and reliable methods for material analysis during the early design stages. One of the key factors is due to a lack of confidence in current failure criteria. Hinton & Soden (1998) have reported this finding following the observations of current commercial design practices in fibre-reinforced polymer composites in which fabrication and mechanical testing are commonplace. In the less mature field of fibre reinforced ceramic composites, the "make and test" approach is also commonly practised. Nonetheless, it is realised that the traditional approach is clearly inefficient, and a computational approach to design and analyses must be considered.

The computational modelling of brittle matrix composites is however not an easy task. This is because the mechanical properties of the composite material are highly anisotropic and non-linear. This is due to the fibre architecture, mismatches in modulus and thermo-expansion coefficient of the fibres and matrix, and damage in the fibre, matrix and fibre-matrix interface.

A literature review of fibre-reinforced composites has identified two different approaches to modelling anisotropy and non-linearity. In the first approach, a macroscopic viewpoint is taken in which the composite is treated as single material and deformation and failure is modelled at a composite level. The fibre direction establishes the axes of anisotropy and classical anisotropic elastic equations are used to model deformation (Hull & Clyne (1996) and Jones (1999)). Failure is predicted with interactive failure criteria such as the quadratic polynomial curve fits proposed by Tsai-Hill (Tsai, 1968) and Hoffman (1967) or non-interactive failure criteria such as the maximum stress or maximum strain criteria (Hull & Clyne (1996) and Jones (1999)). Non-linear and anisotropic effects due to damage are considered by using continuum damage mechanics (Lemaitre, 1996) based on the framework of the thermodynamics of irreversible processes (Lubliner, 1972). Examples of macro-damage model include Talreja (1985), which allowed crack formations normal or parallel to the fibre reinforcement direction. In the Gerard & Baste (1994) model, active and passive cracks were considered normal to the maximum principal stress direction of the composite and Matzenmiller *et al* (1995) have considered fibre breakage or buckling failures. From a design perspective, the advantage of the macro approach is that the analysis is simplified, so that the number of parameters required to model the composite is few. However, its disadvantage is that no distinction is made between the matrix and fibre phases. As such, local effects such as fibre-matrix

interaction and stress-redistribution caused by damage in the matrix or fibres are not considered. Consequently, the specific contribution of the fibre and matrix to the deformation and failure of the composite is not understood.

In the second approach, a micro-mechanical viewpoint is taken. In such approaches, the matrix and fibres are treated separately in local analyses which are linked to describe the composite behaviour. The advantages over the macro-models are that any damage or failure in the matrix or fibres is identified, and the deformation of the matrix and fibres are specifically accounted for. In the linear elastic regime, an example of a micro approach is the linear elastic micro-mechanics theory of composites described in Hull & Clyne (1996) and Jones (1999). In the damage regime, the use of micro-mechanics with continuum damage mechanics is found in the work of Voyiadjis & Kattan (1993) and Burr *et al* (1995, 1997) and Hild *et al* (1996). In the approach by Voyiadjis & Kattan (1993), micro-mechanics was integrated into continuum damage mechanics by modelling damage, stress and strain at a constituent level. The advantages of the approach are that tensile, compressive and shear damage in the matrix and fibres can be considered. However, the approach does not explain the mechanistic principles of the damage processes. To overcome this limitation, Burr *et al* (1995) and Hild *et al* (1996) have introduced a mechanistic continuum damage model which models matrix cracking and fibre breakage Burr *et al* (1997).

Advances in the micro-mechanical approach to model damage in continuum damage mechanics are significant, however further developments are still required to extend their use for the design and analysis of structural composites. An area for development is to provide an ability to model delamination. This is important because the stress to show delamination is significantly lower than the stress to initiate matrix cracking or fibre breakage. This ability has not been developed in the damage models that have been reviewed. Recently, McCartney (1998, 1999) has introduced crack models to predict the tensile delamination stress of glass-reinforced plastic cross-ply laminates. This is based on the micro-mechanics of transverse cracks propagating parallel to the fibre reinforcement direction when loaded normal to the fibre direction. The treatment however does not consider shear delamination nor cracking in the matrix or the fibres. To date a computational model capable of modelling matrix cracking, fibre breakage, and tensile and shear delamination in brittle matrix composites has yet to be developed.

1.4 Scope

The novel work of this thesis is concerned with developing a damage mechanics approach by which damage such as matrix cracking, fibre breakage and tensile and shear delamination in brittle matrix composites can be comprehensively modelled and studied computationally. The specific application is intended for analysing fibre-reinforced ceramic composite structures.

In order to establish such a damage model, the preliminary theories of stress, strain, elasticity and continuum damage mechanics are reviewed in Chapter 2. This is followed by reviews of mechanical theories on deformation and strength of brittle matrix composites in Chapter 3. The development of a computational model requires physical bases for damage modelling and experimental data for benchmarking and validation. This necessitates mechanical testing which typically involves high manufacturing costs and long manufacturing times. For these reasons, a polymer material system that has similar characteristics to a ceramic composite has been used. Chapter 4 introduces the polymer material systems and configurations that are tested in tension and shear. In Chapter 5, the mechanical testing of the polymer system formed into simplified sub-structures replicating components in the exhaust unit of an aero-engine are tested. The development of a computational model using a finite element method first requires an understanding of the advantages and disadvantages of current finite element modelling techniques. These are briefly reviewed and discussed in Chapter 6. In Chapter 7, the damage mechanics approach for modelling damage in finite element theory is presented. This includes a description of the concepts and explanation of the FORTRAN algorithm that implements the damage model, and benchmarking of the damage model for simple stress-state. In Chapter 8, the damage model is applied to analyse misaligned composites in tension and the engineering sub-structures of Chapter 5. Significantly, this chapter serves to demonstrate the capabilities and limitations of the model. Because the behaviour of fibre-matrix interfaces is not well understood, a damage model using imperfect interfacial spring was developed to analyse imperfect interfaces. This is applied to interfaces that are elastic and is presented in Chapter 9. Finally, in Chapter 10, the conclusion of the thesis and a brief discussion on future work are presented.

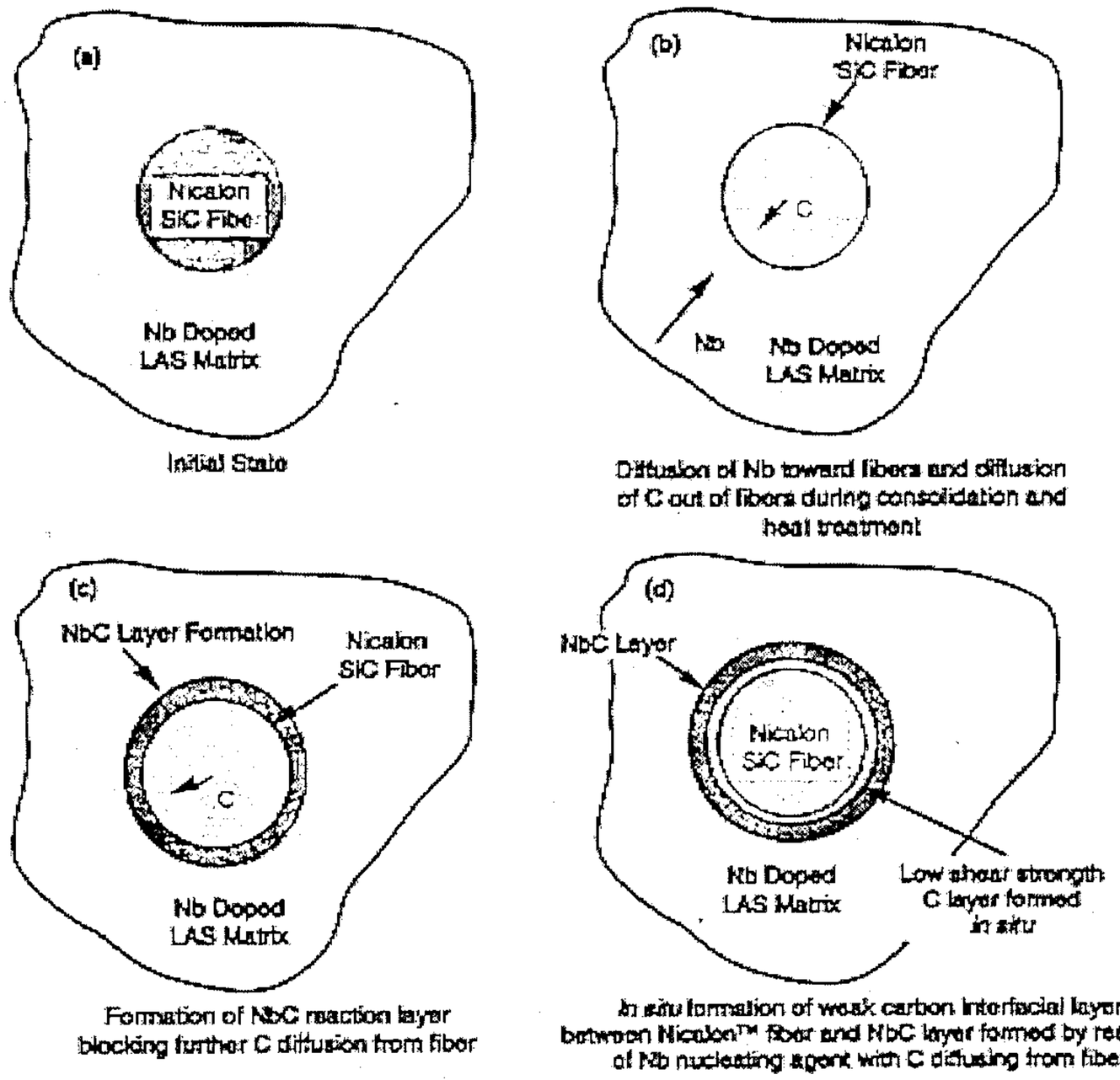

Fig. 1.1-1 Schematic diagram of *in situ* formation of the weak carbon debond layer in Compglass™, which leads to increased composite toughness (adapted from Lewis, 1995).

CHAPTER 2

Modelling Preliminaries

2.1 Introduction

The concepts of *stress*, *strain* and *stress-strain relations* form the basis of any discussion of the mechanical behaviour of engineering materials. This chapter establishes these fundamental concepts and introduces the basic notation that will be used in the thesis. The chapter concludes with a review of *continuum damage mechanics theories* by introducing the concept of damage as a tensor, the state potential relating damage with stress-strain relations, and the evolution law of damage.

2.2 Stress and Equilibrium

The concept of stress is a mathematical characterisation of the average internal force intensities in a material element that is large compared to micro-structural dimensions. The dimensions of the element must also be small compared to the size of the global specimen so that stress gradients across the element are negligible. Consider such an element in a continuous body under load. The element in Fig 2.2-1 is sectioned into parts I and II by a plane Δp_n having an area ΔA with direction defined by the unit normal $\mathbf{n}$. Let $\mathbf{P}_n$ be the resultant force acting across the area ΔA from I to II with an equal and opposite resultant force $-\mathbf{P}_n$ acting from II to I when in equilibrium. In the limit as ΔA approaches zero, the resultant internal force intensity in the element is given as:

$$\overset{n}{\mathbf{T}} = \lim_{\Delta A \to 0} \frac{\mathbf{P}_n}{\Delta A} \tag{2.2.1}$$

This is commonly known as *Cauchy's stress (or traction) vector* and is independent of the element size but dependent on the orientation of the element plane Δp_n.

To describe the stress-state at a point, the stress vectors $\overset{1}{\mathbf{T}}, \overset{2}{\mathbf{T}}, \overset{3}{\mathbf{T}}$ on three mutually perpendicular planes are defined for the resultant stress vector $\overset{n}{\mathbf{T}}$ using the Cartesian system of axes x_1, x_2, x_3 illustrated in Fig 2.2-2:

$$\overset{n}{\mathbf{T}} = \overset{1}{\mathbf{T}} n_1 + \overset{2}{\mathbf{T}} n_2 + \overset{3}{\mathbf{T}} n_3 \qquad (2.2.2)$$

The unit normal **n** defining the plane Δp_n written in component form is:

$$\mathbf{n} = (n_1, n_2, n_3) \qquad (2.2.3)$$

and has direction cosines n_1, n_2 and n_3 given by:

$$\begin{aligned} n_1 &= \cos(\mathbf{e}_1, \mathbf{n}) \\ n_2 &= \cos(\mathbf{e}_2, \mathbf{n}) \\ n_3 &= \cos(\mathbf{e}_3, \mathbf{n}) \end{aligned} \qquad (2.2.4)$$

Here $\mathbf{e}_1$, $\mathbf{e}_2$ and $\mathbf{e}_3$ are the unit vectors for the three mutually perpendicular co-ordinate axis x_1, x_2, and x_3.

All stress vectors consist of a stress component normal to the plane Δp_n and two shear stress components parallel to the plane. These stress components are represented by the symbol σ_{ij}. The combination of suffices $i=j$ represents normal stress components and the combination $i \neq j$ represents shear stress components. The suffix i indicates the positive directions of the three orthogonal axis x_i while suffix j indicates the direction of the force component on the plane (see Fig 2.2-3). In general, the three orthogonal stress vectors $\overset{1}{\mathbf{T}}, \overset{2}{\mathbf{T}}, \overset{3}{\mathbf{T}}$ can be expressed as:

$$\overset{i}{\mathbf{T}} = \sigma_{ij} \mathbf{e}_j \qquad (2.2.5)$$

where
$$\sigma_{ij} = \begin{bmatrix} \overset{1}{\mathbf{T}} \\ \overset{2}{\mathbf{T}} \\ \overset{3}{\mathbf{T}} \end{bmatrix} = \begin{bmatrix} \sigma_{11} & \sigma_{12} & \sigma_{13} \\ \sigma_{21} & \sigma_{22} & \sigma_{23} \\ \sigma_{31} & \sigma_{32} & \sigma_{33} \end{bmatrix} = \begin{bmatrix} \sigma_{xx} & \sigma_{xy} & \sigma_{xz} \\ \sigma_{yx} & \sigma_{yy} & \sigma_{yz} \\ \sigma_{zx} & \sigma_{zy} & \sigma_{zz} \end{bmatrix} \qquad (2.2.6)$$

This alludes to the concept of stress as a second-order tensor in which σ_{ij} is recognised as *Cauchy's stress tensor*. Substituting eqn(2.2.5) into eqn(2.2.2), the expression for the resultant stress vector $\overset{n}{\mathbf{T}}$ can be rewritten in tensor notation as:

$$T_i = \sigma_{ji} n_j = \sigma_{ij} n_j \qquad (2.2.7)$$

where the stress tensor σ_{ij} is symmetric, i.e. $\sigma_{ij} = \sigma_{ji}$. The stress tensor σ_{ij} defined with respect to the x_i co-ordinate system can be expressed as σ_{ij}' for a new x_i' co-ordinate system. This is given as:

$$\sigma_{ij}' = l_{ik} l_{jl} \sigma_{kl} \qquad (2.2.8)$$

where l_{ik}, l_{jl} are the direction cosines with respect to the primed and unprimed co-ordinate axes.

In Fig 2.2-4, the definitions of a normal and shear stress vector σ_n and σ_s are shown. The magnitude of the normal stress vector is given by:

$$\sigma_n = \overset{n}{\mathbf{T}} \bullet \mathbf{n} = \overset{n}{T}_i \, n_i \qquad (2.2.9)$$

where • denotes dot-product of two vectors. Substituting eqn (2.2.7) into eqn (2.2.9) gives the resultant normal stress vector in terms of the stress tensor as:

$$\sigma_n = \sigma_{ij} n_i n_j \qquad (2.2.10)$$

The magnitude of the resultant shear stress vector is:

$$\sigma_s^2 = \left(\overset{n}{\mathbf{T}}\right)^2 - \sigma_n^2 \qquad (2.2.11)$$

where $\left(\overset{n}{\mathbf{T}}\right)^2$ is obtained from (2.2.7) as:

$$\left(\overset{n}{\mathbf{T}}\right)^2 = \overset{n}{\mathbf{T}} \bullet \overset{n}{\mathbf{T}} = \overset{n}{T}_i \overset{n}{T}_i = \left(\sigma_{ij} n_j\right)\left(\sigma_{ik} n_k\right) = \sigma_{ij}\sigma_{ik} n_j n_k \qquad (2.2.12)$$

Mathematically, it is possible for the resultant stress vector $\overset{n}{\mathbf{T}}$ to consist only of normal stress vector components σ_n such that there are no shear stress vectors (σ_s=0). The direction parallel to the plane normal **n** is called *principal direction* while the plane Δp_n is called the *principal plane* at the point. The normal stress vector σ_n is then called the *principal stress vector* at that point and the following definition develops (see Fig 2.2-5):

$$\overset{n}{\mathbf{T}} = \sigma_n = \sigma \mathbf{n} \qquad (2.2.13)$$

or in component form:

$$\overset{n}{T}_i = \sigma n_i \qquad (2.2.14)$$

where σ is the *principal stress vector* consisting of only three normal stress components. Substituting eqn (2.2.7) into eqn (2.2.14) leads to:

$$\left(\sigma_{ij} - \sigma\delta_{ij}\right) n_j = 0 \qquad (2.2.15)$$

where δ_{ij} is the Kronecker delta ($\delta_{ij} = 1$ if i = j and $\delta_{ij} = 0$ if i ≠ j). By allowing the determinants of the coefficients to vanish, i.e.

$$\left|\sigma_{ij} - \sigma\,\delta_{ij}\right| = 0 \qquad (2.2.16)$$

a *characteristic equation* of cubic nature is derived, which upon solving yields three possible magnitudes for the principal stress tensor σ. Commonly recognised as the *Hamilton-Cayley equation*, the characteristic equation written in terms of principal stresses is:

$$\sigma^3 - I_1 \sigma^2 + I_2 \sigma - I_3 = 0 \qquad (2.2.17)$$

in which (I_1,I_2,I_3) are *invariants of stress tensor*. The invariants have the same values regardless of the orientation of the axes. The invariants can be expressed in terms of the stress tensor σ_{ij} or the principal stress tensor σ_1, σ_2, σ_3 as:

$$I_1 = \sigma_{11} + \sigma_{22} + \sigma_{33} = \sigma_{xx} + \sigma_{yy} + \sigma_{zz} = \sigma_1 + \sigma_2 + \sigma_3 \qquad (2.2.18)$$

$$\begin{aligned} I_2 &= \begin{vmatrix} \sigma_{22} & \sigma_{23} \\ \sigma_{32} & \sigma_{33} \end{vmatrix} + \begin{vmatrix} \sigma_{11} & \sigma_{13} \\ \sigma_{31} & \sigma_{33} \end{vmatrix} + \begin{vmatrix} \sigma_{11} & \sigma_{22} \\ \sigma_{31} & \sigma_{23} \end{vmatrix} \\ &= \begin{vmatrix} \sigma_{yy} & \sigma_{yz} \\ \sigma_{zy} & \sigma_{zz} \end{vmatrix} + \begin{vmatrix} \sigma_{xx} & \sigma_{xz} \\ \sigma_{zx} & \sigma_{zz} \end{vmatrix} + \begin{vmatrix} \sigma_{xx} & \sigma_{yy} \\ \sigma_{zx} & \sigma_{yz} \end{vmatrix} \\ &= \sigma_1\sigma_2 + \sigma_2\sigma_3 + \sigma_3\sigma_1 \end{aligned} \qquad (2.2.19)$$

$$I_3 = \begin{vmatrix} \sigma_{11} & \sigma_{12} & \sigma_{13} \\ \sigma_{21} & \sigma_{22} & \sigma_{23} \\ \sigma_{31} & \sigma_{32} & \sigma_{33} \end{vmatrix} = \begin{vmatrix} \sigma_{xx} & \sigma_{xy} & \sigma_{xz} \\ \sigma_{yx} & \sigma_{yy} & \sigma_{yz} \\ \sigma_{zx} & \sigma_{zy} & \sigma_{zz} \end{vmatrix} = \sigma_1\sigma_2\sigma_3 \qquad (2.2.20)$$

Substituting σ_1, σ_2 and σ_3 into eqn (2.2.15), respectively, and using the identity

$$n_1^2 + n_2^2 + n_3^2 = 1 \qquad (2.2.21)$$

the *principal directions* at the point are determined. For each value of σ, the components of these principal direction vectors are:

$$\begin{aligned} \mathbf{n}^{(1)} &= \left(n_1^{(1)}, n_2^{(1)}, n_3^{(1)}\right) \quad for\ \sigma = \sigma_1 \\ \mathbf{n}^{(2)} &= \left(n_1^{(2)}, n_2^{(2)}, n_3^{(2)}\right) \quad for\ \sigma = \sigma_2 \\ \mathbf{n}^{(3)} &= \left(n_1^{(3)}, n_2^{(3)}, n_3^{(3)}\right) \quad for\ \sigma = \sigma_3 \end{aligned} \qquad (2.2.22)$$

The absolute nature of the stress invariants (I_1,I_2,I_3) simplifies the description of stress at a point. As such, alternative forms have also been introduced and are described by Chen & Saleeb (1994).

When the principal axes are rotated to bisect the angle between principal planes, the stress vector σ_s assumes stationary values. These stresses are called *principal shear stresses* and have values of $\frac{1}{2}|\sigma_1-\sigma_2|$, $\frac{1}{2}|\sigma_2-\sigma_3|$ and $\frac{1}{2}|\sigma_1-\sigma_3|$. The largest value of the principal shear stresses is commonly termed the *maximum shear stress* (τ_{max}). The planes on which the principal shear stresses occur are however not pure shear planes.

This is because the normal stress vector defined in eqn (2.2.10) expressed in terms of the principal stress co-ordinate system is:

$$\sigma_n = \sigma_1 n_1^2 + \sigma_2 n_2^2 + \sigma_3 n_3^2 \qquad (2.2.23)$$

Instead, a state of pure shear is defined when the stress tensor at a point is devoid of all normal components, i.e.

$$I_1 = \sigma_{11} + \sigma_{22} + \sigma_{33} = \sigma_{xx} + \sigma_{yy} + \sigma_{zz} = \sigma_1 + \sigma_2 + \sigma_3 = \sigma_{ii} = 0 \qquad (2.2.24)$$

This is shown in Fig 2.2-6.

To model the stress-state of a material, it is sometime useful to decompose the stress tensor σ_{ij} into a *hydrostatic stress* component $\tilde{\sigma}\delta_{ij}$ to describes volume changes and a *deviatoric stress* component s_{ij} to describe shape changes, i.e:

$$\sigma_{ij} = s_{ij} + \tilde{\sigma}\delta_{ij} \qquad (2.2.25)$$

Here, $\tilde{\sigma}$ is the mean stress such that:

$$\tilde{\sigma} = \tfrac{1}{3}\sigma_{kk} = \tfrac{1}{3}\left(\sigma_x + \sigma_y + \sigma_z\right) = \tfrac{1}{3}I_1 \qquad (2.2.26)$$

and the hydrostatic stress tensor $\tilde{\sigma}\delta_{ij}$ is shown to be an invariant. The deviatoric stress tensor s_{ij} determined from eqn (2.2.25 & 26) is:

$$s_{ij} = \begin{bmatrix} s_{11} & s_{12} & s_{13} \\ s_{12} & s_{22} & s_{23} \\ s_{13} & s_{23} & s_{33} \end{bmatrix} = \begin{bmatrix} \dfrac{2s_{11} - s_{22} - s_{33}}{3} & s_{12} & s_{13} \\ s_{12} & \dfrac{2s_{22} - s_{33} - s_{11}}{3} & s_{23} \\ s_{13} & s_{23} & \dfrac{2s_{33} - s_{11} - s_{22}}{3} \end{bmatrix} \qquad (2.2.27)$$

or, in terms of principal stress is,

$$s_{ij} = \begin{bmatrix} \dfrac{2s_1 - s_2 - s_3}{3} & 0 & 0 \\ 0 & \dfrac{2s_2 - s_3 - s_1}{3} & 0 \\ 0 & 0 & \dfrac{2s_3 - s_1 - s_2}{3} \end{bmatrix} \qquad (2.2.28)$$

and is recognised as a state of pure shear. As for the principal stress tensor σ, a cubic characteristic equation in principal deviatoric stress space is obtainable, i.e.

$$\left| s_{ij} - s\,\delta_{ij} \right| = 0 \qquad (2.2.29)$$

or
$$s^3 - J_1 s^2 + J_2 s - J_3 = 0 \qquad (2.2.30)$$

such that s is the principal deviatoric stress tensor and J_1, J_2, J_3 are the deviatoric stress invariants:

$$J_1 = s_{ii} = s_{11} + s_{22} + s_{33} = s_1 + s_2 + s_3 = 0 \qquad (2.2.31)$$

$$
\begin{aligned}
J_2 &= \tfrac{1}{2}\, s_{ij} s_{ji} = \tfrac{1}{2}\left(s_1^2 + s_2^2 + s_3^2\right) \\
&= \tfrac{1}{2}\left(s_{11}^2 + s_{22}^2 + s_{33}^2 + 2\sigma_{12}^2 + 2\sigma_{23}^2 + 2\sigma_{31}^2\right) \\
&= -s_{11}s_{22} - s_{22}s_{33} - s_{33}s_{11} + \sigma_{12}^2 + \sigma_{23}^2 + \sigma_{31}^2 = -\left(s_1 s_2 + s_2 s_3 + s_3 s_1\right) \\
&= \tfrac{1}{6}\left[\left(s_{11} - s_{22}\right)^2 + \left(s_{22} - s_{33}\right)^2 + \left(s_{33} - s_{11}\right)^2\right] + \sigma_{12}^2 + \sigma_{23}^2 + \sigma_{31}^2 \\
&= \tfrac{1}{6}\left[\left(\sigma_x - \sigma_y\right)^2 + \left(\sigma_y - \sigma_z\right)^2 + \left(\sigma_z - \sigma_x\right)^2\right] + \tau_{xy}^2 + \tau_{yz}^2 + \tau_{zx}^2 \\
&= \tfrac{1}{6}\left[\left(\sigma_1 - \sigma_2\right)^2 + \left(\sigma_2 - \sigma_3\right)^2 + \left(\sigma_3 - \sigma_1\right)^2\right]
\end{aligned}
\tag{2.2.32}
$$

$$
J_3 = \tfrac{1}{3}\, s_{ij}\, s_{jk}\, s_{ki} = \begin{vmatrix} s_x & \tau_{xy} & \tau_{xz} \\ \tau_{yx} & s_y & \tau_{yz} \\ \tau_{zx} & \tau_{zy} & s_z \end{vmatrix} = \tfrac{1}{3}\left(s_1^3 + s_2^3 + s_3^3\right) = s_1 s_2 s_3 \tag{2.2.33}
$$

or in terms of the hydrostatic stress invariants (I_1, I_2, I_3),

$$
\begin{aligned}
J_1 &= 0 \\
J_2 &= \tfrac{1}{3}\left(I_1^2 - 3I_2\right) \\
J_3 &= \tfrac{1}{27}\left(2I_1^3 - 9I_1 I_2 + 27I_3\right)
\end{aligned}
\tag{2.2.34}
$$

Finally, for any continuous body of volume V with surface area A, equilibrium condition is satisfied if:

$$
\sigma_{ij,j} + F_i = 0 \tag{2.2.35}
$$

Here F_i represents the body forces and the comma indicates differential notation, i.e. σ_{ij} is differentiated with respect to $j = (1,2,3$ or $x, y, z)$.

2.3 Strain and Compatibility

Forces when applied to a body cause stresses; they also cause deformation via *rigid-body-motion* and *strain*. In rigid-body-motion, the relative distances or angles between points in a body are unchanged. Examples include translation and rotation. However, when a body is strained, the relative distances or angles between points in the body are changed and a new geometry is formed. Examples include extension, compression and distortion.

Extension and compression are causes of *normal* or *direct strain* ε, which is defined as the unit change in length in the direction of the original length. Consider a one-dimensional problem where two points A and B in a stress free body are separated by a length dx as shown in Fig 2.3-1. When stressed, the points A, B are displaced to A', B' such that the displacement of A to A' is u and the displacement of B to B' is

$u + \frac{\partial u}{\partial x} dx$. If the displacements u and $u + \frac{\partial u}{\partial x} dx$ are not equal, then direct strain in the x axes has occurred and is given as:

$$\varepsilon_x = \frac{\left(u + \frac{\partial u}{\partial x} dx\right) - u}{dx} = \frac{\frac{\partial u}{\partial x} dx}{dx} = \frac{\partial u}{\partial x} \qquad (2.3.1)$$

When the direct strain is positive, then extension is indicated, else a negative direct strain indicates compression. In two-dimensional problems, the number of direct strain components is increased to two. To show this, consider an element *ABCD* in a state of plane strain described in the Cartesian axes x, y and z such that:

$$u = u(x, y) \qquad v = v(x, y) \qquad w = 0 \qquad (2.3.2)$$

Here, u, v and w are the displacements in the respective x, y and z axes. When stressed, the element undergoes translation and strain and it's new position is described by *A'B'C'D'* as shown in Fig 2.3-2. Now if the displacements of *A* to *A'* are u and v, and the displacements of *B* to *B'* are $u + \frac{\partial u}{\partial x} dx$ and $v + \frac{\partial v}{\partial x} dx$, it follows that:

$$(A'B')^2 = [dx(1 + \varepsilon_x)]^2 = \left(dx + \frac{\partial u}{\partial x} dx\right)^2 + \left(\frac{\partial v}{\partial x} dx\right)^2 \qquad (2.3.3)$$

so that

$$\varepsilon_x{}^2 + 2\varepsilon_x + 1 = 1 + 2\frac{\partial u}{\partial x} + \left(\frac{\partial u}{\partial x}\right)^2 + \left(\frac{\partial v}{\partial x}\right)^2 \qquad (2.3.4)$$

If the distance and displacements of the points *A* and *B* are infinitesimal, then the higher order terms in eqn (2.3.4) can be ignored and the direct strain with respect to the x axis is:

$$\varepsilon_x = \frac{\partial u}{\partial x} \qquad (2.3.5)$$

which is identical to eqn (2.3.1). Similarly, if the displacements of *D* to *D'* are $u + \frac{\partial u}{\partial y} dy$ and $v + \frac{\partial v}{\partial y} dy$, and infinitesimal strain is assumed, the direct strain component with respect to the y axes is:

$$\varepsilon_y = \frac{\partial v}{\partial y} \qquad (2.3.6)$$

In the case of distortion, the angles between points of a body are changed and *shear strain* γ is induced. Like shear stress, shear strain is associated with two orthogonal directions and is defined as the change in the original right angle between two axes measured in radians. Shear strain is positive if the right angle between the positive directions of the co-ordinate axes x, y, z decreases. Referring to Fig 2.3-2, shear strain γ_{xy} in the x-y plane is:

$$\gamma_{xy} = \frac{\pi}{2} - \beta = \theta - \lambda \tag{2.3.7}$$

where the negative λ indicates that counter-clockwise angles of rotation with respect to the *y* axis are defined as positive. It follows that:

$$\theta = \frac{\frac{\partial v}{\partial x} dx}{dx + \frac{\partial u}{\partial x} dx} \tag{2.3.8}$$

when strain is infinitesimal since for small angles $\tan\theta = \theta$. Neglecting $\frac{\partial u}{\partial x}$ as being small compared to 1, eqn (2.3.8) reduces to

$$\theta = \frac{\partial v}{\partial x} \tag{2.3.9}$$

and similarly,

$$\lambda = -\frac{\partial u}{\partial y} \tag{2.3.10}$$

Substituting eqn (2.3.9 & 10) into (2.3.7), the definition of shear strain γ_{xy} in terms of the in plane displacements *u* and *v* is:

$$\gamma_{xy} = \frac{\partial u}{\partial y} + \frac{\partial v}{\partial x} \tag{2.3.11}$$

and is called the *engineering shear strain.*

The definitions of direct strain and engineering shear strain for the two-dimensional case when extended to a three-dimensional case require the displacements to be:

$$u = u(x, y, z) \qquad v = v(x, y, z) \qquad w = w(x, y, z) \tag{2.3.12}$$

Explicitly, the components of strain are:

$$\varepsilon_{ij} = \begin{bmatrix} \varepsilon_x & \gamma_{xy} & \gamma_{xz} \\ \gamma_{yx} & \varepsilon_y & \gamma_{yz} \\ \gamma_{zx} & \gamma_{zy} & \varepsilon_z \end{bmatrix} = \begin{bmatrix} \frac{\partial u}{\partial x} & \left(\frac{\partial u}{\partial y} + \frac{\partial v}{\partial x}\right) & \left(\frac{\partial u}{\partial z} + \frac{\partial w}{\partial x}\right) \\ \left(\frac{\partial u}{\partial y} + \frac{\partial v}{\partial x}\right) & \frac{\partial v}{\partial y} & \left(\frac{\partial v}{\partial z} + \frac{\partial w}{\partial y}\right) \\ \left(\frac{\partial u}{\partial z} + \frac{\partial w}{\partial x}\right) & \left(\frac{\partial v}{\partial z} + \frac{\partial w}{\partial y}\right) & \frac{\partial w}{\partial z} \end{bmatrix} \tag{2.3.13}$$

where the suffix *i* denotes the Cartesian directions *x*, *y*, *z* and the suffix *j* indicates the direction of strain.

The description of strain in eqn (2.3.13) however does not represent strain as a second-order tensor, though it properties are symmetric. This is because it does not satisfy the transformation properties of a tensor, as described for the stress tensor in

eqn (2.2.8). To establish a strain tensor to describe the strain-state at a point, consider the case of two points A_o and A in a body with initial positions of $\left(x_1^o, x_2^o, x_3^o\right)$ and $\left(x_1, x_2, x_3\right)$ as shown in Fig 2.3-3. When the body is strained, the displacement of point A_o to A_o', i.e. $\left(x_1^o + u_1^o,\ x_2^o + u_2^o,\ x_3^o + u_2^o\right)$, is $u_i^o\left(x_1^o, x_2^o, x_3^o\right)$. Similarly, the displacement of point A to A' at position $\left(x_1 + u_1,\ x_2 + u_2,\ x_3 + u_2\right)$ is $u_i\left(x_1, x_2, x_3\right)$. By expanding u_i into a Taylor series around A_o, the displacement vector u_i becomes

$$u_i = u_i^o + \frac{\partial u_i}{\partial x_j}\left(x_j - x_j^o\right) + \frac{1}{2!}\frac{\partial^2 u}{\partial x_j \partial x_k}\left(x_j - x_j^o\right)\left(x_k - x_k^o\right) + \ldots \qquad (2.3.14)$$

and assuming infinitesimal strain, the expression further simplifies to

$$u_i = u_i^o + \frac{\partial u_i}{\partial x_j}\left(x_j - x_j^o\right) = u_i^o + \frac{\partial u_i}{\partial x_j} dx_j \qquad (2.3.15)$$

The gradient of the vector u_i, i.e. $\partial u_i / \partial x_j$, is itself a second-order tensor and may be decomposed into symmetric and anti-symmetric parts. As such, eqn (2.3.15) can be rewritten as:

$$u_i = u_i^o + \frac{1}{2}\left(\frac{\partial u_i}{\partial x_j} + \frac{\partial u_j}{\partial x_i}\right) dx_j + \frac{1}{2}\left(\frac{\partial u_i}{\partial x_j} - \frac{\partial u_j}{\partial x_i}\right) dx_j \qquad (2.3.16)$$

or
$$u_i = u_i^o + \varepsilon_{ij}\, dx_j + \omega_{ij}\, dx_j \qquad (2.3.17)$$

in which
$$\varepsilon_{ij} = \frac{1}{2}\left(\frac{\partial u_i}{\partial x_j} + \frac{\partial u_j}{\partial x_i}\right) \qquad (2.3.18)$$

and
$$\omega_{ij} = \frac{1}{2}\left(\frac{\partial u_i}{\partial x_j} - \frac{\partial u_j}{\partial x_i}\right) \qquad (2.3.19)$$

The former symbol, ε_{ij}, is the symmetric part of the second-order tensor $\partial u_i / \partial x_j$ and is itself a symmetric second-order tensor. It is called the *strain tensor* and its components are:

$$\varepsilon_{ij} = \begin{bmatrix} \varepsilon_{11} & \varepsilon_{12} & \varepsilon_{13} \\ \varepsilon_{21} & \varepsilon_{22} & \varepsilon_{23} \\ \varepsilon_{31} & \varepsilon_{32} & \varepsilon_{33} \end{bmatrix} = \begin{bmatrix} \dfrac{\partial u_1}{\partial x_1} & \dfrac{1}{2}\left(\dfrac{\partial u_1}{\partial x_2} + \dfrac{\partial u_2}{\partial x_1}\right) & \dfrac{1}{2}\left(\dfrac{\partial u_1}{\partial x_3} + \dfrac{\partial u_3}{\partial x_1}\right) \\ \dfrac{1}{2}\left(\dfrac{\partial u_1}{\partial x_2} + \dfrac{\partial u_2}{\partial x_1}\right) & \dfrac{\partial u_2}{\partial x_2} & \dfrac{1}{2}\left(\dfrac{\partial u_2}{\partial x_3} + \dfrac{\partial u_3}{\partial x_2}\right) \\ \dfrac{1}{2}\left(\dfrac{\partial u_1}{\partial x_3} + \dfrac{\partial u_3}{\partial x_1}\right) & \dfrac{1}{2}\left(\dfrac{\partial u_2}{\partial x_3} + \dfrac{\partial u_3}{\partial x_2}\right) & \dfrac{\partial u_3}{\partial x_3} \end{bmatrix} = \begin{bmatrix} \varepsilon_{xx} & \dfrac{\gamma_{xy}}{2} & \dfrac{\gamma_{xz}}{2} \\ \dfrac{\gamma_{yx}}{2} & \varepsilon_{yy} & \dfrac{\gamma_{yz}}{2} \\ \dfrac{\gamma_{zx}}{2} & \dfrac{\gamma_{zy}}{2} & \varepsilon_{zz} \end{bmatrix} \qquad (2.3.20)$$

The latter symbol, ω_{ij}, is the anti-symmetric part of $\partial u_i / \partial x_j$. It is called the *rotation tensor* and its components are:

$$\omega_{ij} = \begin{bmatrix} \omega_{11} & \omega_{12} & \omega_{13} \\ \omega_{21} & \omega_{22} & \omega_{23} \\ \omega_{31} & \omega_{32} & \omega_{33} \end{bmatrix} = \begin{bmatrix} 0 & \frac{1}{2}\left(\frac{\partial u_1}{\partial x_2} - \frac{\partial u_2}{\partial x_1}\right) & \frac{1}{2}\left(\frac{\partial u_1}{\partial x_3} - \frac{\partial u_3}{\partial x_1}\right) \\ \frac{1}{2}\left(\frac{\partial u_1}{\partial x_2} - \frac{\partial u_2}{\partial x_1}\right) & 0 & \frac{1}{2}\left(\frac{\partial u_2}{\partial x_3} - \frac{\partial u_3}{\partial x_2}\right) \\ \frac{1}{2}\left(\frac{\partial u_1}{\partial x_3} - \frac{\partial u_3}{\partial x_1}\right) & \frac{1}{2}\left(\frac{\partial u_2}{\partial x_3} - \frac{\partial u_3}{\partial x_2}\right) & 0 \end{bmatrix} \qquad (2.3.21)$$

Like the stress tensor, the relationship between the strain tensor ε_{ij} in the x_i co-ordinate system and in the x_i' co-ordinate system is given as:

$$\varepsilon'_{ij} = l_{ik} l_{jl} \varepsilon_{kl} \qquad (2.3.22)$$

where l_{ik}, l_{jl} are the direction cosines with respect to the primed and unprimed co-ordinate axes.

At a vector level, the state of strain at a point (as is in the definition of stress) with unit normal **n** having components (n_1, n_2, n_3) is defined as:

$$\overset{n}{\varepsilon} = \varepsilon^{1} \mathbf{n}_1 + \varepsilon^{2} \mathbf{n}_2 + \varepsilon^{3} \mathbf{n}_3 = \overset{n}{\varepsilon}_i = \varepsilon_{ji} n_j = \varepsilon_{ij} n_j \qquad (2.3.23)$$

Here, $\overset{n}{\varepsilon}$ is the resultant strain vector with three mutually perpendicular components $\overset{1}{\varepsilon}, \overset{2}{\varepsilon}$ and $\overset{3}{\varepsilon}$ in the direction of the co-ordinate axes x_1, x_2 and x_3. Alternatively, the resultant strain vector may be decomposed into it normal and shear components, as shown in Fig 2.3-4. The magnitude of the *normal strain vector* is given by:

$$\varepsilon_n = \overset{n}{\varepsilon} \bullet \mathbf{n} = \overset{n}{\varepsilon}_i n_i = \varepsilon_{ij} n_i n_j \qquad (2.3.24)$$

For a unit vector **s** having components (s_1,s_2,s_3) normal to direction **n**, the magnitude of the *shear strain vector* is given by:

$$\varepsilon_s = \overset{n}{\varepsilon} \bullet s = \overset{n}{\varepsilon}_i s_i = \varepsilon_{ij} n_j s_i \qquad (2.3.25)$$

When the resultant strain vector $\overset{n}{\varepsilon}$ is in the direction of the unit normal **n**, i.e. the shear strain vector has zero magnitude, a state of *principal strain* occurs. The direction at which this occurs is the *principal strain direction* or *axis* and is shown in Fig 2.3-5. Thus,

$$\overset{n}{\varepsilon} = \varepsilon_n = \varepsilon \mathbf{n} \qquad (2.3.26)$$

or in component form:

$$\overset{n}{\varepsilon}_i = \varepsilon n_i \tag{2.3.27}$$

where ε is the *principal strains* consisting of only three normal strain components. Substituting eqn (2.3.23) into eqn (2.3.27) leads to:

$$\left(\varepsilon_{ij} - \varepsilon\delta_{ij}\right) n_j = 0 \tag{2.3.28}$$

where δ_{ij} is the Kronecker delta. By allowing the determinants of the coefficients to vanish, i.e.

$$\left|\varepsilon_{ij} - \varepsilon\delta_{ij}\right| = 0 \tag{2.3.29}$$

a *characteristic equation* of a cubic nature, as is for principal stress (see eqn 2.2.17), is derived. Solution to the cubic equation yields three possible magnitudes for the *principal strain tensor* ε. The characteristic equation is given by:

$$\varepsilon^3 - I_1'\varepsilon^2 + I_2'\varepsilon - I_3' = 0 \tag{2.3.30}$$

where the strain invariants I_1', I_2' and I_3' are given by:

$$I_1' = \varepsilon_{11} + \varepsilon_{22} + \varepsilon_{33} = \varepsilon_{xx} + \varepsilon_{yy} + \varepsilon_{zz} = \varepsilon_1 + \varepsilon_2 + \varepsilon_3 \tag{2.3.31}$$

$$\begin{aligned} I_2' &= \begin{vmatrix} \varepsilon_{22} & \varepsilon_{23} \\ \varepsilon_{32} & \varepsilon_{33} \end{vmatrix} + \begin{vmatrix} \varepsilon_{11} & \varepsilon_{13} \\ \varepsilon_{31} & \varepsilon_{33} \end{vmatrix} + \begin{vmatrix} \varepsilon_{11} & \varepsilon_{22} \\ \varepsilon_{31} & \varepsilon_{23} \end{vmatrix} \\ &= \begin{vmatrix} \varepsilon_{yy} & \varepsilon_{yz} \\ \varepsilon_{zy} & \varepsilon_{zz} \end{vmatrix} + \begin{vmatrix} \varepsilon_{xx} & \varepsilon_{xz} \\ \varepsilon_{zx} & \varepsilon_{zz} \end{vmatrix} + \begin{vmatrix} \varepsilon_{xx} & \varepsilon_{yy} \\ \varepsilon_{zx} & \varepsilon_{yz} \end{vmatrix} \\ &= \varepsilon_1\varepsilon_2 + \varepsilon_2\varepsilon_3 + \varepsilon_3\varepsilon_1 \end{aligned} \tag{2.3.32}$$

$$I_3' = \begin{vmatrix} \varepsilon_{11} & \varepsilon_{12} & \varepsilon_{13} \\ \varepsilon_{21} & \varepsilon_{22} & \varepsilon_{23} \\ \varepsilon_{31} & \varepsilon_{32} & \varepsilon_{33} \end{vmatrix} = \begin{vmatrix} \varepsilon_{xx} & \varepsilon_{xy} & \varepsilon_{xz} \\ \varepsilon_{yx} & \varepsilon_{yy} & \varepsilon_{yz} \\ \varepsilon_{zx} & \varepsilon_{zy} & \varepsilon_{zz} \end{vmatrix} = \varepsilon_1\varepsilon_2\varepsilon_3 \tag{2.3.33}$$

By substituting ε_1, ε_2 and ε_3 into eqn (2.3.28), the principal directions $\mathbf{n}^{(1)}$, $\mathbf{n}^{(2)}$ and $\mathbf{n}^{(3)}$ is obtained.

When the principal axes are rotated such that the strain vector ε_s assumes stationary values, *principal shear strains* are determined. Magnitudes of the tensorial principal shear strains are:

$$\begin{aligned} \vartheta_1 &= \tfrac{1}{2}\left|\varepsilon_2 - \varepsilon_3\right| \\ \vartheta_2 &= \tfrac{1}{2}\left|\varepsilon_1 - \varepsilon_3\right| \\ \vartheta_3 &= \tfrac{1}{2}\left|\varepsilon_1 - \varepsilon_2\right| \end{aligned} \tag{2.3.34}$$

while the magnitude of the *engineering principal shear strains* are:

$$\begin{aligned}\gamma_1 &= |\varepsilon_2 - \varepsilon_3| \\ \gamma_2 &= |\varepsilon_1 - \varepsilon_3| \\ \gamma_3 &= |\varepsilon_1 - \varepsilon_2|\end{aligned} \tag{2.3.35}$$

The largest value of the principal shear strains is the *maximum shear strain*. Hence for $\varepsilon_1 > \varepsilon_2 > \varepsilon_3$, the maximum shear strain is given as:

$$\gamma_{\max} = 2\vartheta_{\max} = |\varepsilon_1 - \varepsilon_3| \tag{2.3.36}$$

Like the stress tensor (see eqn (2.2.25)), the strain tensor is comprised of a *spherical* part that describes volumetric changes and a *deviatoric* part that describes shape changes (distortion), i.e.

$$\varepsilon_{ij} = e_{ij} + \bar{\varepsilon}\delta_{ij} \tag{2.3.37}$$

Here $\bar{\varepsilon} = \frac{1}{3}\varepsilon_{kk} = \frac{1}{3}(\varepsilon_x + \varepsilon_y + \varepsilon_z) = \frac{1}{3}I_1'$ is the *mean* or *hydrostatic strain* while, e_{ij}, the *deviatoric strain tensor* is the difference between the strain tensor ε_{ij} and the spherical strain tensor $\bar{\varepsilon}\delta_{ij}$, i.e.

$$e_{ij} = \begin{bmatrix} e_{11} & e_{12} & e_{13} \\ e_{12} & e_{22} & e_{23} \\ e_{13} & e_{23} & e_{33} \end{bmatrix} = \begin{bmatrix} \frac{2\varepsilon_{11} - \varepsilon_{22} - \varepsilon_{33}}{3} & \varepsilon_{12} & \varepsilon_{13} \\ \varepsilon_{12} & \frac{2\varepsilon_{22} - \varepsilon_{33} - \varepsilon_{11}}{3} & \varepsilon_{23} \\ \varepsilon_{13} & \varepsilon_{23} & \frac{2\varepsilon_{33} - \varepsilon_{11} - \varepsilon_{22}}{3} \end{bmatrix} \tag{2.3.38}$$

or, in terms of principal strains,

$$e_{ij} = \begin{bmatrix} \frac{2\varepsilon_1 - \varepsilon_2 - \varepsilon_3}{3} & 0 & 0 \\ 0 & \frac{2\varepsilon_2 - \varepsilon_3 - \varepsilon_1}{3} & 0 \\ 0 & 0 & \frac{2\varepsilon_3 - \varepsilon_1 - \varepsilon_2}{3} \end{bmatrix} \tag{2.3.39}$$

Importantly, the strain deviator e_{ij} represents a pure shear state ($\varepsilon_{kk} = 0$). Seen from eqn (2.3.22), this also implies that e_{ij} and ε_{ij} have similar principal axes.

The invariants for the strain deviator tensor e_{ij} are analogous to those of the stress deviator tensor s_{ij}. Solving for:

$$|e_{ij} - e\delta_{ij}| = 0 \tag{2.3.40}$$

a cubic expression for the principal values of the deviator strain tensor is obtained:

$$e^3 - J_1'e^2 + J_2'e - J_3' = 0 \tag{2.3.41}$$

where the invariants of the deviatoric strain tensor are given as:

$$J_1' = e_{ii} = e_{11} + e_{22} + e_{33} = e_1 + e_2 + e_3 = 0 \tag{2.3.42}$$

$$\begin{aligned}
J_2' &= \tfrac{1}{2} s_{ij} s_{ji} = \tfrac{1}{2}\left(e_1^2 + e_2^2 + e_3^2\right) \\
&= \tfrac{1}{2}\left(e_{11}^2 + e_{22}^2 + e_{33}^2 + 2e_{12}^2 + 2e_{23}^2 + 2e_{31}^2\right) \\
&= -e_{11}e_{22} - e_{22}e_{33} - e_{33}e_{11} + \varepsilon_{12}^2 + \varepsilon_{23}^2 + \varepsilon_{31}^2 = -(e_1 e_2 + e_2 e_3 + e_3 e_1) \\
&= \tfrac{1}{6}\left[(e_{11} - e_{22})^2 + (e_{22} - e_{33})^2 + (e_{33} - e_{11})^2\right] + \varepsilon_{12}^2 + \varepsilon_{23}^2 + \varepsilon_{31}^2 \\
&= \tfrac{1}{6}\left[(\varepsilon_x - \varepsilon_y)^2 + (\varepsilon_y - \varepsilon_z)^2 + (\varepsilon_z - \varepsilon_x)^2\right] + \varepsilon_{xy}^2 + \varepsilon_{yz}^2 + \varepsilon_{zx}^2 \\
&= \tfrac{1}{6}\left[(\varepsilon_1 - \varepsilon_2)^2 + (\varepsilon_2 - \varepsilon_3)^2 + (\varepsilon_3 - \varepsilon_1)^2\right]
\end{aligned} \tag{2.3.43}$$

$$J_3' = \tfrac{1}{3} e_{ij} e_{jk} e_{ki} = \begin{vmatrix} e_x & e_{xy} & e_{xz} \\ e_{yx} & e_y & e_{yz} \\ e_{zx} & e_{zy} & e_z \end{vmatrix} = \tfrac{1}{3}(e_1^3 + e_2^3 + e_3^3) = e_1 e_2 e_3 \tag{2.3.44}$$

or in terms of the spherical strain invariants (I_1',I_2',I_3'),

$$\begin{aligned}
J_1' &= 0 \\
J_2' &= \tfrac{1}{3}(I_1'^2 - 3I_2') \\
J_3' &= \tfrac{1}{27}(2I_1'^3 - 9I_1' I_2' + 27I_3')
\end{aligned} \tag{2.3.45}$$

The *volumetric* or *dilatational strain* ε_v is defined as the relative change in volume (volume change per unit volume) between the strained and the unstrain state. Consider a unit cube with edge normal parallel to the principal strain axes 1,2 and 3. When strained, the axes remains orthogonal and has new edges $(1+\varepsilon_1)$, $(1+\varepsilon_2)$ and $(1+\varepsilon_3)$. Therefore, ε_v is given by:

$$\varepsilon_v = \frac{\Delta V}{V} = (1+\varepsilon_1)(1+\varepsilon_2)(1+\varepsilon_3) - 1 \tag{2.3.46}$$

and for small strain, the above reduces to:

$$\varepsilon_v = \frac{\Delta V}{V} = \varepsilon_1 + \varepsilon_2 + \varepsilon_3 = J_1' = \varepsilon_{kk} \tag{2.3.47}$$

That is, the spherical strain tensor is proportional to volumetric changes.

In the definition of strain given in eqn (2.3.20), the state of strain at a point is completely described through the definition of the displacements vectors u_i. However, it is apparent that the converse is untrue since there are six equations to three unknown functions of u_i. To ensure a single-valued continuous displacement function u_i, *compatibility conditions* are imposed on the strain tensor ε_{ij}, which gives:

$$\varepsilon_{ij,kl} + \varepsilon_{kl,ij} - \varepsilon_{ik,jl} - \varepsilon_{jl,ik} = 0 \tag{2.3.48}$$

or, explicitly,

$$\frac{\partial^2 \varepsilon_x}{\partial y^2} + \frac{\partial^2 \varepsilon_y}{\partial x^2} = \frac{\partial^2 \varepsilon_{xy}}{\partial x \partial y}$$
$$\frac{\partial^2 \varepsilon_y}{\partial z^2} + \frac{\partial^2 \varepsilon_z}{\partial y^2} = \frac{\partial^2 \varepsilon_{yz}}{\partial y \partial z} \qquad (2.3.49)$$
$$\frac{\partial^2 \varepsilon_z}{\partial x^2} + \frac{\partial^2 \varepsilon_x}{\partial z^2} = \frac{\partial^2 \varepsilon_{zx}}{\partial z \partial x}$$

$$\frac{\partial}{\partial x}\left(-\frac{\partial \varepsilon_{yz}}{\partial x} + \frac{\partial \varepsilon_{zx}}{\partial y} + \frac{\partial \varepsilon_{xy}}{\partial z}\right) = \frac{\partial^2 \varepsilon_x}{\partial y \partial z}$$
$$\frac{\partial}{\partial y}\left(-\frac{\partial \varepsilon_{zx}}{\partial x} + \frac{\partial \varepsilon_{xy}}{\partial y} + \frac{\partial \varepsilon_{yz}}{\partial z}\right) = \frac{\partial^2 \varepsilon_y}{\partial z \partial x} \qquad (2.3.50)$$
$$\frac{\partial}{\partial z}\left(-\frac{\partial \varepsilon_{xy}}{\partial x} + \frac{\partial \varepsilon_{yz}}{\partial y} + \frac{\partial \varepsilon_{zx}}{\partial z}\right) = \frac{\partial^2 \varepsilon_z}{\partial x \partial y}$$

2.4 Elastic Stress-Strain Relations

To establish a general formulation for solving the mechanics of a continuous body, it is necessary to define the governing relations between the state of stress and strain. In the case of a general linear elastic material, the stress-strain relation is given by *Hooke's law* in which:

$$\sigma_{ij} = C_{ijkl}\varepsilon_{kl} \qquad (2.4.1)$$

or conversely,
$$\varepsilon_{ij} = S_{ijkl}\sigma_{kl} \qquad (2.4.2)$$

Here, the constants C_{ijkl} and S_{ijkl} are the *stiffness* and *compliance* of a linear elastic material and are fourth-order tensors composed of 3^4 (= 81) components called elastic constants. Owing to the symmetric properties of both the stress and strain tensors,

$$C_{ijkl} = C_{ijlk} = C_{jikl} = C_{jilk} \qquad (2.4.3)$$

$$S_{ijkl} = S_{ijlk} = S_{jikl} = S_{jilk} \qquad (2.4.4)$$

and an inherent material symmetry $C_{(ij)(kl)} = C_{(kl)(ij)}$, the total number of independent elastic constants are reduced from 81 to 36 and 36 to 21, respectively. Using a *contracted notation* in which:

$$\begin{aligned} &\sigma_{11} = \sigma_1,\ \sigma_{22} = \sigma_2,\ \sigma_{33} = \sigma_3,\ \sigma_{12} = \tau_{12} = \sigma_4,\ \sigma_{13} = \tau_{13} = \sigma_5,\ \sigma_{23} = \tau_{23} = \sigma_6 \\ &\varepsilon_{11} = \varepsilon_1,\ \varepsilon_{22} = \varepsilon_2,\ \varepsilon_{33} = \varepsilon_3,\ \varepsilon_{12} = \tfrac{1}{2}\gamma_{12} = \varepsilon_4,\ \varepsilon_{13} = \tfrac{1}{2}\gamma_{13} = \varepsilon_5,\ \varepsilon_{23} = \tfrac{1}{2}\gamma_{23} = \varepsilon_6 \end{aligned} \qquad (2.4.5)$$

where γ_{ij} and τ_{ij} (where $i \neq j$) represent engineering shear strains and stresses, the constitutive relations of a general linear elastic material, i.e. a material which does not exhibit material symmetry (*anisotropic*), are defined as:

$$\begin{Bmatrix}\sigma_1\\ \sigma_2\\ \sigma_3\\ \sigma_4\\ \sigma_5\\ \sigma_6\end{Bmatrix}=\begin{bmatrix}C_{11} & C_{12} & C_{13} & 2C_{14} & 2C_{15} & 2C_{16}\\ & C_{22} & C_{23} & 2C_{24} & 2C_{25} & 2C_{26}\\ & & C_{33} & 2C_{34} & 2C_{35} & 2C_{36}\\ & & & 2C_{44} & 2C_{45} & 2C_{46}\\ \textit{symmetric} & & & & 2C_{55} & 2C_{56}\\ & & & & & 2C_{66}\end{bmatrix}\begin{Bmatrix}\varepsilon_1\\ \varepsilon_2\\ \varepsilon_3\\ \varepsilon_4\\ \varepsilon_5\\ \varepsilon_6\end{Bmatrix} \tag{2.4.6}$$

and

$$\begin{Bmatrix}\varepsilon_1\\ \varepsilon_2\\ \varepsilon_3\\ \varepsilon_4\\ \varepsilon_5\\ \varepsilon_6\end{Bmatrix}=\begin{bmatrix}S_{11} & S_{12} & S_{13} & S_{14}/2 & S_{15}/2 & S_{16}/2\\ & S_{22} & S_{23} & S_{24}/2 & S_{25}/2 & S_{26}/2\\ & & S_{33} & S_{34}/2 & S_{35}/2 & S_{36}/2\\ & & & S_{44}/2 & S_{45}/2 & S_{46}/2\\ \textit{symmetric} & & & & S_{55}/2 & S_{56}/2\\ & & & & & S_{66}/2\end{bmatrix}\begin{Bmatrix}\sigma_1\\ \sigma_2\\ \sigma_3\\ \sigma_4\\ \sigma_5\\ \sigma_6\end{Bmatrix} \tag{2.4.7}$$

, or, in terms of the engineering definitions:

$$\begin{Bmatrix}\sigma_1\\ \sigma_2\\ \sigma_3\\ \tau_{23}\\ \tau_{13}\\ \tau_{12}\end{Bmatrix}=\begin{bmatrix}C_{11} & C_{12} & C_{13} & C_{14} & C_{15} & C_{16}\\ & C_{22} & C_{23} & C_{24} & C_{25} & C_{26}\\ & & C_{33} & C_{34} & C_{35} & C_{36}\\ & & & C_{44} & C_{45} & C_{46}\\ \textit{symmetric} & & & & C_{55} & C_{56}\\ & & & & & C_{66}\end{bmatrix}\begin{Bmatrix}\varepsilon_1\\ \varepsilon_2\\ \varepsilon_3\\ \gamma_{23}\\ \gamma_{13}\\ \gamma_{12}\end{Bmatrix} \tag{2.4.8}$$

and

$$\begin{Bmatrix}\varepsilon_1\\ \varepsilon_2\\ \varepsilon_3\\ \gamma_{23}\\ \gamma_{13}\\ \gamma_{12}\end{Bmatrix}=\begin{bmatrix}S_{11} & S_{12} & S_{13} & S_{14} & S_{15} & S_{16}\\ & S_{22} & S_{23} & S_{24} & S_{25} & S_{26}\\ & & S_{33} & S_{34} & S_{35} & S_{36}\\ & & & S_{44} & S_{45} & S_{46}\\ \textit{symmetric} & & & & S_{55} & S_{56}\\ & & & & & S_{66}\end{bmatrix}\begin{Bmatrix}\sigma_1\\ \sigma_2\\ \sigma_3\\ \tau_{23}\\ \tau_{13}\\ \tau_{12}\end{Bmatrix} \tag{2.4.9}$$

Such materials are also termed *triclinic*.

If the body posseses some material symmetry, the corresponding stiffness and compliance can be determined through a group of orthogonal linear co-ordinate transformations or *transformation laws*. This is obtained by considering the transformation law governing a first order tensor:

$$r'_i = l_{ij}\, r_j = \begin{pmatrix} l_{11} & l_{12} & l_{13}\\ l_{21} & l_{22} & l_{23}\\ l_{31} & l_{32} & l_{33}\end{pmatrix} r_j \tag{2.4.10}$$

where l_{ij} represents direction such that in general $l_{ij} \neq l_{ji}$ and have properties:

$$\begin{aligned} l_{11}^2 + l_{12}^2 + l_{13}^2 = 1 \quad &, \quad l_{11}l_{21} + l_{12}l_{22} + l_{13}l_{23} = 0\\ l_{21}^2 + l_{22}^2 + l_{23}^2 = 1 \quad &, \quad l_{11}l_{31} + l_{12}l_{32} + l_{13}l_{33} = 0\\ l_{31}^2 + l_{32}^2 + l_{33}^2 = 1 \quad &, \quad l_{21}l_{31} + l_{22}l_{32} + l_{23}l_{33} = 0 \end{aligned} \tag{2.4.11}$$

due to orthogonality, $l_{ij}^{-1} = l_{ij}^{T}$. This implies that the transformation laws given in eqn (2.2.8) and eqn (2.3.22), for engineering stresses and strains expressed in contracted notation (see eqn (2.4.5)) become:

$$\begin{Bmatrix}\sigma'_1\\ \sigma'_2\\ \sigma'_3\\ \tau'_{23}\\ \tau'_{13}\\ \tau'_{12}\end{Bmatrix}=(\mathbf{G})\begin{Bmatrix}\sigma_1\\ \sigma_2\\ \sigma_3\\ \tau_{23}\\ \tau_{13}\\ \tau_{12}\end{Bmatrix},\quad \begin{Bmatrix}\sigma_1\\ \sigma_2\\ \sigma_3\\ \tau_{23}\\ \tau_{13}\\ \tau_{12}\end{Bmatrix}=(\mathbf{G})^{-1}\begin{Bmatrix}\sigma'_1\\ \sigma'_2\\ \sigma'_3\\ \tau'_{23}\\ \tau'_{13}\\ \tau'_{12}\end{Bmatrix}\quad \begin{Bmatrix}\varepsilon'_1\\ \varepsilon'_2\\ \varepsilon'_3\\ \gamma'_{23}\\ \gamma'_{13}\\ \gamma'_{12}\end{Bmatrix}=(\mathbf{H})\begin{Bmatrix}\varepsilon_1\\ \varepsilon_2\\ \varepsilon_3\\ \gamma_{23}\\ \gamma_{13}\\ \gamma_{12}\end{Bmatrix},\quad \begin{Bmatrix}\varepsilon_1\\ \varepsilon_2\\ \varepsilon_3\\ \gamma_{23}\\ \gamma_{13}\\ \gamma_{12}\end{Bmatrix}=(\mathbf{H})^{-1}\begin{Bmatrix}\varepsilon'_1\\ \varepsilon'_2\\ \varepsilon'_3\\ \gamma'_{23}\\ \gamma'_{13}\\ \gamma'_{12}\end{Bmatrix} \tag{2.4.12}$$

where

$$(\mathbf{G})=\begin{pmatrix} l_{11}^2 & l_{12}^2 & l_{13}^2 & 2\,l_{12}l_{13} & 2\,l_{11}l_{13} & 2\,l_{11}l_{12}\\ l_{21}^2 & l_{22}^2 & l_{23}^2 & 2\,l_{22}l_{23} & 2\,l_{21}l_{23} & 2\,l_{22}l_{21}\\ l_{31}^2 & l_{32}^2 & l_{33}^2 & 2\,l_{32}l_{33} & 2\,l_{31}l_{33} & 2\,l_{31}l_{32}\\ l_{21}l_{31} & l_{22}l_{32} & l_{23}l_{33} & l_{22}l_{33}+l_{23}l_{32} & l_{21}l_{33}+l_{23}l_{31} & l_{21}l_{32}+l_{22}l_{31}\\ l_{11}l_{31} & l_{12}l_{32} & l_{13}l_{33} & l_{12}l_{33}+l_{13}l_{32} & l_{11}l_{33}+l_{13}l_{31} & l_{11}l_{32}+l_{12}l_{31}\\ l_{11}l_{21} & l_{12}l_{22} & l_{13}l_{23} & l_{12}l_{23}+l_{13}l_{22} & l_{11}l_{23}+l_{13}l_{21} & l_{11}l_{22}+l_{12}l_{21}\end{pmatrix} \tag{2.4.13}$$

$$(\mathbf{H})=\begin{pmatrix} l_{11}^2 & l_{12}^2 & l_{13}^2 & l_{12}l_{13} & l_{13}l_{11} & l_{11}l_{12}\\ l_{21}^2 & l_{22}^2 & l_{23}^2 & l_{22}l_{23} & l_{23}l_{21} & l_{21}l_{22}\\ l_{31}^2 & l_{32}^2 & l_{33}^2 & l_{32}l_{33} & l_{33}l_{21} & l_{31}l_{32}\\ 2\,l_{21}l_{31} & 2\,l_{22}l_{32} & 2\,l_{23}l_{33} & l_{22}l_{33}+l_{23}l_{32} & l_{21}l_{33}+l_{23}l_{31} & l_{21}l_{32}+l_{22}l_{31}\\ 2\,l_{11}l_{31} & 2\,l_{12}l_{32} & 2\,l_{13}l_{33} & l_{12}l_{33}+l_{13}l_{32} & l_{11}l_{33}+l_{13}l_{31} & l_{11}l_{32}+l_{12}l_{31}\\ 2\,l_{11}l_{21} & 2\,l_{12}l_{22} & 2\,l_{13}l_{23} & l_{12}l_{23}+l_{13}l_{22} & l_{11}l_{23}+l_{13}l_{21} & l_{11}l_{22}+l_{12}l_{21}\end{pmatrix} \tag{2.4.14}$$

$$(\mathbf{G})^{-1}=\begin{pmatrix} l_{11}^2 & l_{21}^2 & l_{31}^2 & 2\,l_{21}l_{31} & 2\,l_{11}l_{31} & 2\,l_{11}l_{21}\\ l_{12}^2 & l_{22}^2 & l_{32}^2 & 2\,l_{22}l_{32} & 2\,l_{12}l_{32} & 2\,l_{22}l_{12}\\ l_{13}^2 & l_{23}^2 & l_{33}^2 & 2\,l_{23}l_{33} & 2\,l_{13}l_{33} & 2\,l_{13}l_{23}\\ l_{12}l_{13} & l_{22}l_{23} & l_{32}l_{33} & l_{22}l_{33}+l_{32}l_{23} & l_{12}l_{33}+l_{32}l_{13} & l_{12}l_{23}+l_{22}l_{13}\\ l_{11}l_{13} & l_{21}l_{23} & l_{31}l_{33} & l_{21}l_{33}+l_{31}l_{23} & l_{11}l_{33}+l_{31}l_{13} & l_{11}l_{23}+l_{21}l_{13}\\ l_{11}l_{12} & l_{21}l_{22} & l_{31}l_{23} & l_{21}l_{31}+l_{31}l_{22} & l_{11}l_{32}+l_{31}l_{12} & l_{11}l_{22}+l_{21}l_{12}\end{pmatrix} \tag{2.4.15}$$

$$(\mathbf{H})^{-1}=\begin{pmatrix} l_{11}^2 & l_{21}^2 & l_{31}^2 & l_{21}l_{31} & l_{11}l_{31} & l_{11}l_{21}\\ l_{12}^2 & l_{22}^2 & l_{32}^2 & l_{22}l_{23} & l_{12}l_{32} & l_{12}l_{22}\\ l_{13}^2 & l_{23}^2 & l_{33}^2 & l_{23}l_{33} & l_{13}l_{33} & l_{13}l_{23}\\ 2\,l_{21}l_{31} & 2\,l_{22}l_{32} & 2\,l_{23}l_{33} & l_{22}l_{33}+l_{23}l_{32} & l_{21}l_{33}+l_{23}l_{31} & l_{21}l_{32}+l_{22}l_{31}\\ 2\,l_{11}l_{13} & 2\,l_{21}l_{23} & 2\,l_{31}l_{33} & l_{21}l_{33}+l_{31}l_{23} & l_{11}l_{33}+l_{31}l_{13} & l_{11}l_{23}+l_{21}l_{13}\\ 2\,l_{11}l_{12} & 2\,l_{21}l_{22} & 2\,l_{31}l_{32} & l_{21}l_{31}+l_{31}l_{22} & l_{11}l_{32}+l_{31}l_{12} & l_{11}l_{22}+l_{21}l_{12}\end{pmatrix} \tag{2.4.16}$$

Thus, the transformation law of the stiffness and compliance of a linear elastic material given in tensor notation are obtained as:

$$C'_{ijkl}=l_{im}l_{jn}l_{ko}l_{lp}C_{mnop} \tag{2.4.17}$$

$$S'_{ijkl}=l_{im}l_{jn}l_{ko}l_{lp}S_{mnop} \tag{2.4.18}$$

or in contracted notation:

$$\begin{aligned}&\{\sigma'\}=(\mathbf{G})\{\sigma\}=(\mathbf{G})[\mathbf{C}]\{\varepsilon\}=(\mathbf{G})[\mathbf{C}](\mathbf{H})^{-1}\{\varepsilon'\}\\ \Rightarrow\ &[\mathbf{C}']=(\mathbf{G})[\mathbf{C}](\mathbf{H})^{-1}\end{aligned} \tag{2.4.19}$$

and
$$\{\varepsilon'\} = (\mathbf{H})\{\varepsilon\} = (\mathbf{H})[\mathbf{S}]\{\sigma\} = (\mathbf{H})[\mathbf{S}](\mathbf{G})^{-1}\{\sigma'\}$$
$$\Rightarrow [\mathbf{S}'] = (\mathbf{H})[\mathbf{S}](\mathbf{G})^{-1} \tag{2.4.20}$$

Therefore, if the anisotropic body contains a plane of elastic symmetry, for example the plane *x*-*y*, the direction cosines in eqn (2.4.10) becomes:

$$l_{ij} = \begin{pmatrix} 1 & 0 & 0 \\ 0 & 1 & 0 \\ 0 & 0 & -1 \end{pmatrix} \tag{2.4.21}$$

Substituting for eqn (2.4.13 to 16 & 19 to 20), the plane of elastic symmetry requires that:

$$\begin{aligned} &C_{14}=0 \quad C_{15}=0 \quad C_{24}=0 \quad C_{25}=0 \\ &C_{34}=0 \quad C_{35}=0 \quad C_{46}=0 \quad C_{56}=0 \\ &S_{14}=0 \quad S_{15}=0 \quad S_{24}=0 \quad S_{25}=0 \\ &S_{34}=0 \quad S_{35}=0 \quad S_{46}=0 \quad S_{56}=0 \end{aligned} \tag{2.4.22}$$

Thus, the number of independent elastic constants is reduced from 21 to 13, which gives the constitutive relations for a *monoclinic* material as:

$$\begin{Bmatrix} \sigma_1 \\ \sigma_2 \\ \sigma_3 \\ \tau_{23} \\ \tau_{13} \\ \tau_{12} \end{Bmatrix} = \begin{bmatrix} C_{11} & C_{12} & C_{13} & 0 & 0 & C_{16} \\ C_{12} & C_{22} & C_{23} & 0 & 0 & C_{26} \\ C_{13} & C_{23} & C_{33} & 0 & 0 & C_{36} \\ 0 & 0 & 0 & C_{44} & C_{45} & 0 \\ 0 & 0 & 0 & C_{45} & C_{55} & 0 \\ C_{16} & C_{26} & C_{36} & 0 & 0 & C_{66} \end{bmatrix} \begin{Bmatrix} \varepsilon_1 \\ \varepsilon_2 \\ \varepsilon_3 \\ \gamma_{23} \\ \gamma_{13} \\ \gamma_{12} \end{Bmatrix} \tag{2.4.23}$$

and
$$\begin{Bmatrix} \varepsilon_1 \\ \varepsilon_2 \\ \varepsilon_3 \\ \gamma_{23} \\ \gamma_{13} \\ \gamma_{12} \end{Bmatrix} = \begin{bmatrix} S_{11} & S_{12} & S_{13} & 0 & 0 & S_{16} \\ S_{12} & S_{22} & S_{23} & 0 & 0 & S_{26} \\ S_{13} & S_{23} & S_{33} & 0 & 0 & S_{36} \\ 0 & 0 & 0 & S_{44} & S_{45} & 0 \\ 0 & 0 & 0 & S_{45} & S_{55} & 0 \\ S_{16} & S_{26} & S_{36} & 0 & 0 & S_{66} \end{bmatrix} \begin{Bmatrix} \sigma_1 \\ \sigma_2 \\ \sigma_3 \\ \tau_{23} \\ \tau_{13} \\ \tau_{12} \end{Bmatrix} \tag{2.4.24}$$

Similarly, if elastic symmetry occurs at plane *x*-*z*, the elastic constants of the anisotropic material must satisfy:

$$\begin{aligned} &C_{14}=0 \quad C_{16}=0 \quad C_{24}=0 \quad C_{26}=0 \\ &C_{34}=0 \quad C_{36}=0 \quad C_{46}=0 \quad C_{56}=0 \\ &S_{14}=0 \quad S_{16}=0 \quad S_{24}=0 \quad S_{16}=0 \\ &S_{34}=0 \quad S_{36}=0 \quad S_{46}=0 \quad S_{56}=0 \end{aligned} \tag{2.4.25}$$

For elastic symmetry at plane *y*-*z*, requirements of the elastic constants are:

$$\begin{aligned} &C_{15}=0 \quad C_{16}=0 \quad C_{25}=0 \quad C_{26}=0 \\ &C_{35}=0 \quad C_{36}=0 \quad C_{45}=0 \quad C_{46}=0 \\ &S_{15}=0 \quad S_{16}=0 \quad S_{25}=0 \quad S_{16}=0 \\ &S_{35}=0 \quad S_{36}=0 \quad S_{45}=0 \quad S_{46}=0 \end{aligned} \tag{2.4.26}$$

From eqn (2.4.22, 25 & 26), it is seen that when an anisotropic material has two mutually orthogonal planes of elastic symmetry, elastic symmetry invariably exists relative to a third orthogonal plane, i.e. the material possesses three orthogonal planes of symmetry. Such materials are termed *orthotropic*. This implies that the elastic constants must satisfy:

$$\begin{array}{llll} C_{14}=0 & C_{15}=0 & C_{16}=0 & C_{24}=0 \\ C_{25}=0 & C_{26}=0 & C_{34}=0 & C_{35}=0 \\ C_{36}=0 & C_{45}=0 & C_{46}=0 & C_{56}=0 \\ S_{14}=0 & S_{15}=0 & S_{16}=0 & S_{24}=0 \\ S_{25}=0 & S_{26}=0 & S_{34}=0 & S_{35}=0 \\ S_{36}=0 & S_{45}=0 & S_{46}=0 & S_{56}=0 \end{array} \tag{2.4.27}$$

which reduces the total number of independent elastic constants from 13 to 9. The constitutive relations for an orthotropic material are then defined as:

$$\begin{Bmatrix} \sigma_1 \\ \sigma_2 \\ \sigma_3 \\ \tau_{23} \\ \tau_{13} \\ \tau_{12} \end{Bmatrix} = \begin{bmatrix} C_{11} & C_{12} & C_{13} & 0 & 0 & 0 \\ C_{12} & C_{22} & C_{23} & 0 & 0 & 0 \\ C_{13} & C_{23} & C_{33} & 0 & 0 & 0 \\ 0 & 0 & 0 & C_{44} & 0 & 0 \\ 0 & 0 & 0 & 0 & C_{55} & 0 \\ 0 & 0 & 0 & 0 & 0 & C_{66} \end{bmatrix} \begin{Bmatrix} \varepsilon_1 \\ \varepsilon_2 \\ \varepsilon_3 \\ \gamma_{23} \\ \gamma_{13} \\ \gamma_{12} \end{Bmatrix} \tag{2.4.28}$$

and

$$\begin{Bmatrix} \varepsilon_1 \\ \varepsilon_2 \\ \varepsilon_3 \\ \gamma_{23} \\ \gamma_{13} \\ \gamma_{12} \end{Bmatrix} = \begin{bmatrix} S_{11} & S_{12} & S_{13} & 0 & 0 & 0 \\ S_{12} & S_{22} & S_{23} & 0 & 0 & 0 \\ S_{13} & S_{23} & S_{33} & 0 & 0 & 0 \\ 0 & 0 & 0 & S_{44} & 0 & 0 \\ 0 & 0 & 0 & 0 & S_{55} & 0 \\ 0 & 0 & 0 & 0 & 0 & S_{66} \end{bmatrix} \begin{Bmatrix} \sigma_1 \\ \sigma_2 \\ \sigma_3 \\ \tau_{23} \\ \tau_{13} \\ \tau_{12} \end{Bmatrix} \tag{2.4.29}$$

In such materials, the normal strains are a function of only normal stresses while the shear strains are only a function of the shear stresses on the same plane.

When a material exhibits a rotational elastic symmetry about one of the co-ordinate axes, i.e. contains a symmetric plane in which the properties are invariant, the material is termed *transversely isotropic*. If the rotational symmetry occurs about the z-axis, the stiffness and compliance is derived from an orthotropic material by imposing the additional requirement that eqn (2.4.13-20) must also satisfy for any rotational transformation l_{ij} of the form:

$$l_{ij} = \begin{pmatrix} \cos\theta & \sin\theta & 0 \\ -\sin\theta & \cos\theta & 0 \\ 0 & 0 & 1 \end{pmatrix} \tag{2.4.30}$$

in which θ represents the angle of rotation about the axis of elastic symmetry (z-axis). This requirement reduces the number of independent elastic constants from 9 to only 5, giving the constitutive relations as:

$$\begin{Bmatrix}\sigma_1\\ \sigma_2\\ \sigma_3\\ \tau_{23}\\ \tau_{13}\\ \tau_{12}\end{Bmatrix} = \begin{bmatrix}C_{11} & C_{12} & C_{12} & 0 & 0 & 0\\ C_{12} & C_{22} & C_{23} & 0 & 0 & 0\\ C_{12} & C_{23} & C_{22} & 0 & 0 & 0\\ 0 & 0 & 0 & C_{55} & 0 & 0\\ 0 & 0 & 0 & 0 & C_{55} & 0\\ 0 & 0 & 0 & 0 & 0 & \frac{1}{2}(C_{11}-C_{12})\end{bmatrix}\begin{Bmatrix}\varepsilon_1\\ \varepsilon_2\\ \varepsilon_3\\ \gamma_{23}\\ \gamma_{13}\\ \gamma_{12}\end{Bmatrix} \tag{2.4.31}$$

and

$$\begin{Bmatrix}\varepsilon_1\\ \varepsilon_2\\ \varepsilon_3\\ \gamma_{23}\\ \gamma_{13}\\ \gamma_{12}\end{Bmatrix} = \begin{bmatrix}S_{11} & S_{12} & S_{12} & 0 & 0 & 0\\ S_{12} & S_{22} & S_{23} & 0 & 0 & 0\\ S_{12} & S_{23} & S_{22} & 0 & 0 & 0\\ 0 & 0 & 0 & S_{55} & 0 & 0\\ 0 & 0 & 0 & 0 & S_{55} & 0\\ 0 & 0 & 0 & 0 & 0 & 2(S_{22}-S_{12})\end{bmatrix}\begin{Bmatrix}\sigma_1\\ \sigma_2\\ \sigma_3\\ \tau_{23}\\ \tau_{13}\\ \tau_{12}\end{Bmatrix} \tag{2.4.32}$$

Finally, if the elastic properties are independent of direction, i.e. *isotropic*, the number of independent elastic constants is reduced to two and the constitutive relations become:

$$\begin{Bmatrix}\sigma_1\\ \sigma_2\\ \sigma_3\\ \tau_{23}\\ \tau_{13}\\ \tau_{12}\end{Bmatrix} = \begin{bmatrix}C_{11} & C_{12} & C_{12} & 0 & 0 & 0\\ C_{12} & C_{11} & C_{12} & 0 & 0 & 0\\ C_{12} & C_{12} & C_{11} & 0 & 0 & 0\\ 0 & 0 & 0 & \frac{1}{2}(C_{11}-C_{12}) & 0 & 0\\ 0 & 0 & 0 & 0 & \frac{1}{2}(C_{11}-C_{12}) & 0\\ 0 & 0 & 0 & 0 & 0 & \frac{1}{2}(C_{11}-C_{12})\end{bmatrix}\begin{Bmatrix}\varepsilon_1\\ \varepsilon_2\\ \varepsilon_3\\ \gamma_{23}\\ \gamma_{13}\\ \gamma_{12}\end{Bmatrix} \tag{2.4.33}$$

and

$$\begin{Bmatrix}\varepsilon_1\\ \varepsilon_2\\ \varepsilon_3\\ \gamma_{23}\\ \gamma_{13}\\ \gamma_{12}\end{Bmatrix} = \begin{bmatrix}S_{11} & S_{12} & S_{12} & 0 & 0 & 0\\ S_{12} & S_{11} & S_{12} & 0 & 0 & 0\\ S_{12} & S_{12} & S_{11} & 0 & 0 & 0\\ 0 & 0 & 0 & 2(S_{11}-S_{12}) & 0 & 0\\ 0 & 0 & 0 & 0 & 2(S_{11}-S_{12}) & 0\\ 0 & 0 & 0 & 0 & 0 & 2(S_{11}-S_{12})\end{bmatrix}\begin{Bmatrix}\sigma_1\\ \sigma_2\\ \sigma_3\\ \tau_{23}\\ \tau_{13}\\ \tau_{12}\end{Bmatrix} \tag{2.4.34}$$

For these constitutive relations to be useful in engineering practice, it is necessary that the independent elastic constants be related to mechanical properties determined through experimental tests, i.e. *engineering constants*. Consider a *uniaxial tension test* such that the applied stress $\sigma = \sigma_i$ (where i = 1 or 2 or 3) while all other stresses are zero. The resistance to elastic strain in the x_i-direction represented by *Young's modulus*, E_i, is defined as:

$$E_i = \frac{\sigma_i}{\varepsilon_i} \tag{2.4.35}$$

Poisson's ratio, ν_{ij}, defined as the ratio between the transverse strain ε_j in the x_j direction and the axial strain ε_i due to the applied stress in the x_i direction, is:

$$\nu_{ij} = -\frac{\varepsilon_j}{\varepsilon_i} \tag{2.4.36}$$

In *simple shear*, the applied stress $\tau = \sigma_i$ (where $i = 4$ or 5 or 6) and all other stresses are zero. The resistance to shear deformation defined through the *shear modulus* or *modulus of rigidity*, G_i, is given by:

$$G_i = \frac{\sigma_i}{\gamma_i} = \frac{\sigma_i}{2\varepsilon_i} \tag{2.4.37}$$

Having defined the above engineering constants, the strain–stress relations for an orthotropic material (see eqn (2.4.29)) in terms of engineering shear strains are:

$$\begin{Bmatrix} \varepsilon_1 \\ \varepsilon_2 \\ \varepsilon_3 \\ \gamma_4 \\ \gamma_5 \\ \gamma_6 \end{Bmatrix} = \begin{bmatrix} 1/E_1 & -\nu_{21}/E_2 & -\nu_{31}/E_3 & 0 & 0 & 0 \\ -\nu_{12}/E_1 & 1/E_2 & -\nu_{32}/E_3 & 0 & 0 & 0 \\ -\nu_{13}/E_1 & -\nu_{23}/E_2 & 1/E_3 & 0 & 0 & 0 \\ 0 & 0 & 0 & 1/G_{12} & 0 & 0 \\ 0 & 0 & 0 & 0 & 1/G_{13} & 0 \\ 0 & 0 & 0 & 0 & 0 & 1/G_{23} \end{bmatrix} \begin{Bmatrix} \sigma_1 \\ \sigma_2 \\ \sigma_3 \\ \sigma_4 \\ \sigma_5 \\ \sigma_6 \end{Bmatrix} \tag{2.4.38}$$

Because of the inherent material symmetry in linear elastic materials, i.e. $S_{ij} = S_{ji}$, it also implies that:

$$\frac{\nu_{ij}}{E_i} = \frac{\nu_{ji}}{E_j} \tag{2.4.39}$$

that is, for an orthotropic elastic material $\nu_{12} \neq \nu_{21}$ when $E_1 \neq E_2$. Relations between the stiffness and compliance is defined by:

$$[C_{ij}] = [S_{ij}]^{-1} = \frac{[co\ S_{ij}]^T}{|S_{ij}|} \tag{2.4.40}$$

in which the stiffness matrix $[C_{ij}]$ is the *adjoint* of $[S_{ij}]$, $[co\ S_{ij}]^T$ is the transpose of the cofactor matrix of $[S_{ij}]$ and $|S_{ij}|$ is the determinant of the matrix $[S_{ij}]$, or explicitly for an orthotropic material:

$$C_{ij} = \begin{bmatrix} \frac{(S_{22}S_{33}-S_{23}^2)}{D} & \frac{(S_{13}S_{23}-S_{12}S_{33})}{D} & \frac{(S_{12}S_{23}-S_{13}S_{22})}{D} & 0 & 0 & 0 \\ \frac{(S_{31}S_{32}-S_{12}S_{33})}{D} & \frac{(S_{33}S_{11}-S_{13}^2)/D}{D} & \frac{(S_{12}S_{13}-S_{23}S_{11})}{D} & 0 & 0 & 0 \\ \frac{(S_{21}S_{32}-S_{31}S_{22})}{D} & \frac{(S_{21}S_{31}-S_{32}S_{11})/D}{D} & \frac{(S_{11}S_{22}-S_{12}^2)}{D} & 0 & 0 & 0 \\ 0 & 0 & 0 & \frac{1}{S_{44}} & 0 & 0 \\ 0 & 0 & 0 & 0 & \frac{1}{S_{55}} & 0 \\ 0 & 0 & 0 & 0 & 0 & \frac{1}{S_{66}} \end{bmatrix} \tag{2.4.41}$$

where $D = S_{11}S_{22}S_{33} - S_{11}S_{23}^2 - S_{22}S_{13}^2 - S_{33}S_{12}^2 + 2S_{12}S_{23}S_{31}$. Substituting for the components of the compliance matrix in eqn (2.4.38), the corresponding stress-strain relations of an orthotropic elastic material is:

$$\begin{Bmatrix} \sigma_1 \\ \sigma_2 \\ \sigma_3 \\ \sigma_4 \\ \sigma_5 \\ \sigma_6 \end{Bmatrix} = \begin{bmatrix} \frac{E_1(1-\nu_{23}\nu_{32})}{\Psi} & \frac{E_1(\nu_{21}-\nu_{31}\nu_{23})}{\Psi} & \frac{E_1(\nu_{31}-\nu_{21}\nu_{32})}{\Psi} & 0 & 0 & 0 \\ \frac{E_2(\nu_{12}-\nu_{13}\nu_{32})}{\Psi} & \frac{E_2(1-\nu_{31}\nu_{12})}{\Psi} & \frac{E_2(\nu_{32}-\nu_{12}\nu_{31})}{\Psi} & 0 & 0 & 0 \\ \frac{E_3(\nu_{13}-\nu_{13}\nu_{32})}{\Psi} & \frac{E_3(\nu_{23}-\nu_{21}\nu_{13})}{\Psi} & \frac{E_3(1-\nu_{12}\nu_{21})}{\Psi} & 0 & 0 & 0 \\ 0 & 0 & 0 & \frac{1}{G_{23}} & 0 & 0 \\ 0 & 0 & 0 & 0 & \frac{1}{G_{13}} & 0 \\ 0 & 0 & 0 & 0 & 0 & \frac{1}{G_{12}} \end{bmatrix} \begin{Bmatrix} \varepsilon_1 \\ \varepsilon_2 \\ \varepsilon_3 \\ \gamma_4 \\ \gamma_5 \\ \gamma_6 \end{Bmatrix} \tag{2.4.42}$$

where $\Psi = 1-\nu_{12}\nu_{21}-\nu_{23}\nu_{32}-\nu_{31}\nu_{13}-2\nu_{21}\nu_{32}\nu_{13}$. If $\varepsilon_{ij}(i \neq j)$ is used instead of $\gamma_{ij}(i \neq j)$, a factor of 2 must be included before C_{44}, C_{55} and C_{66} to satisfy the condition of $\varepsilon_{ij} = \frac{1}{2}\gamma_{ij}$.

For a transversely isotropic material, e.g. having a rotational symmetry about the z-axis, the engineering definition of the strain-stress relations in eqn (2.4.32) become:

$$\begin{Bmatrix} \varepsilon_1 \\ \varepsilon_2 \\ \varepsilon_3 \\ \gamma_{23} \\ \gamma_{13} \\ \gamma_{12} \end{Bmatrix} = \begin{bmatrix} 1/E & -\nu/E & -\nu'/E' & 0 & 0 & 0 \\ -\nu/E & 1/E & -\nu'/E' & 0 & 0 & 0 \\ -\nu'/E' & -\nu'/E' & 1/E' & 0 & 0 & 0 \\ 0 & 0 & 0 & 1/G' & 0 & 0 \\ 0 & 0 & 0 & 0 & 1/G' & 0 \\ 0 & 0 & 0 & 0 & 0 & 1/G' \end{bmatrix} \begin{Bmatrix} \sigma_1 \\ \sigma_2 \\ \sigma_3 \\ \tau_{23} \\ \tau_{13} \\ \tau_{12} \end{Bmatrix} \tag{2.4.43}$$

where the unprimed engineering constants indicates material properties in the plane of isotropy while the primed engineering constants are material properties normal to the plane. Eqn (2.4.41) is reduced to:

$$C_{ij} = \begin{bmatrix} \frac{(S_{22}^2 - S_{23}^2)}{H} & \frac{(S_{12}S_{23} - S_{12}S_{22})}{H} & \frac{(S_{12}S_{23} - S_{12}S_{22})}{H} & 0 & 0 & 0 \\ \frac{(S_{12}S_{23} - S_{12}S_{22})}{H} & \frac{(S_{22}S_{11} - S_{12}^2)}{H} & \frac{(S_{12}^2 - S_{23}S_{11})}{H} & 0 & 0 & 0 \\ \frac{(S_{12}S_{23} - S_{12}S_{22})}{H} & \frac{(S_{12}^2 - S_{23}S_{11})}{H} & \frac{(S_{22}S_{11} - S_{12}^2)}{H} & 0 & 0 & 0 \\ 0 & 0 & 0 & \frac{1}{2(S_{22} - S_{23})} & 0 & 0 \\ 0 & 0 & 0 & 0 & \frac{1}{S_{66}} & 0 \\ 0 & 0 & 0 & 0 & 0 & \frac{1}{S_{66}} \end{bmatrix} \tag{2.4.44}$$

where $H = S_{11}S_{22}^2 - S_{11}S_{23}^2 - 2S_{22}S_{12}^2 + 2S_{23}S_{12}^2$ and the corresponding stress-strain relations for transversely isotropic materials is:

$$\begin{Bmatrix} \sigma_1 \\ \sigma_2 \\ \sigma_3 \\ \tau_{23} \\ \tau_{13} \\ \tau_{12} \end{Bmatrix} = \begin{bmatrix} \frac{(1-\nu^2)}{\Lambda E^2} & \frac{\nu'(\nu+1)}{\Lambda E^2 E'} & \frac{\nu'(\nu+1)}{\Lambda E^2 E'} & 0 & 0 & 0 \\ \frac{\nu'(\nu+1)}{\Lambda E^2 E'} & \frac{1}{\Lambda E'}\left(\frac{1}{E} - \frac{\nu'^2}{E'}\right) & \frac{1}{\Lambda E'}\left(\frac{\nu'^2}{E'} + \frac{\nu'}{E}\right) & 0 & 0 & 0 \\ \frac{\nu'(\nu+1)}{\Lambda E^2 E'} & \frac{1}{\Lambda E'}\left(\frac{\nu'^2}{E'} + \frac{\nu'}{E}\right) & \frac{1}{\Lambda E'}\left(\frac{1}{E} - \frac{\nu'^2}{E'}\right) & 0 & 0 & 0 \\ 0 & 0 & 0 & \frac{1}{G} & 0 & 0 \\ 0 & 0 & 0 & 0 & \frac{1}{G'} & 0 \\ 0 & 0 & 0 & 0 & 0 & \frac{1}{G'} \end{bmatrix} \begin{Bmatrix} \varepsilon_1 \\ \varepsilon_2 \\ \varepsilon_3 \\ \gamma_{23} \\ \gamma_{13} \\ \gamma_{12} \end{Bmatrix} \tag{2.4.45}$$

where $\Lambda = \frac{1-\nu^2}{E'E^2} - \frac{2\nu'^2(1+\nu)}{E'^2 E}$ and $G = \frac{E}{2(1+\nu)}$.

For isotropic elastic materials, Young's modulus and Poisson's ratio are independent of direction. Therefore, the constitutive relations are simply:

$$\begin{Bmatrix} \varepsilon_1 \\ \varepsilon_2 \\ \varepsilon_3 \\ \gamma_{23} \\ \gamma_{13} \\ \gamma_{12} \end{Bmatrix} = \begin{bmatrix} 1/E & -\nu/E & -\nu/E & 0 & 0 & 0 \\ -\nu/E & 1/E & -\nu/E & 0 & 0 & 0 \\ -\nu/E & -\nu/E & 1/E & 0 & 0 & 0 \\ 0 & 0 & 0 & 1/G & 0 & 0 \\ 0 & 0 & 0 & 0 & 1/G & 0 \\ 0 & 0 & 0 & 0 & 0 & 1/G \end{bmatrix} \begin{Bmatrix} \sigma_1 \\ \sigma_2 \\ \sigma_3 \\ \tau_{23} \\ \tau_{13} \\ \tau_{12} \end{Bmatrix} \tag{2.4.46}$$

and

$$\begin{Bmatrix} \sigma_1 \\ \sigma_2 \\ \sigma_3 \\ \tau_{23} \\ \tau_{13} \\ \tau_{12} \end{Bmatrix} = \frac{E}{(1+\nu)(1-2\nu)} \begin{bmatrix} (1-\nu) & \nu & \nu & 0 & 0 & 0 \\ \nu & (1-\nu) & \nu & 0 & 0 & 0 \\ \nu & \nu & (1-\nu) & 0 & 0 & 0 \\ 0 & 0 & 0 & \frac{(1-2\nu)}{2} & 0 & 0 \\ 0 & 0 & 0 & 0 & \frac{(1-2\nu)}{2} & 0 \\ 0 & 0 & 0 & 0 & 0 & \frac{(1-2\nu)}{2} \end{bmatrix} \begin{Bmatrix} \varepsilon_1 \\ \varepsilon_2 \\ \varepsilon_3 \\ \gamma_{23} \\ \gamma_{13} \\ \gamma_{12} \end{Bmatrix} \tag{2.4.47}$$

Alternatively, the constitutive relations expressed in tensor notation are:

$$\sigma_{ij} = \frac{E}{(1+\nu)}\varepsilon_{ij} + \frac{\nu E}{(1+\nu)(1-2\nu)}\varepsilon_{kk}\,\delta_{ij} \qquad (2.4.48)$$

and

$$\varepsilon_{ij} = \frac{(1+\nu)}{E}\sigma_{ij} + \frac{\nu}{E}\sigma_{kk}\,\delta_{ij} \qquad (2.4.49)$$

For isotropic linear elastic materials, the principal directions of the stress and strain tensor coincide. Also, the engineering constants E and G must be positive, i.e. $E > 0$ and $G > 0$, and values of Poisson's ratio must satisfy:

$$-1 \le \nu \le 0.5 \qquad (2.4.50)$$

Most materials in practice have positive values of Poisson's ratio. If $\nu = 0.5$, it implies that the material is *elastically incompressible* and the shear modulus $G = E/3$.

When reduced to two dimensional plane stress condition (e.g. $\sigma_3 = \tau_{23} = \tau_{13} = 0$), the constitutive relations for isotropic linear elastic materials are:

$$\begin{Bmatrix}\varepsilon_1\\ \varepsilon_2\\ \gamma_{12}\end{Bmatrix} = \frac{1}{E}\begin{bmatrix}1 & -\nu & 0\\ -\nu & 1 & 0\\ 0 & 0 & 2(1+\nu)\end{bmatrix}\begin{Bmatrix}\sigma_1\\ \sigma_2\\ \tau_{12}\end{Bmatrix} \qquad (2.4.51)$$

and

$$\begin{Bmatrix}\sigma_1\\ \sigma_2\\ \tau_{12}\end{Bmatrix} = \frac{E}{(1-\nu^2)}\begin{bmatrix}1 & \nu & 0\\ \nu & 1 & 0\\ 0 & 0 & \dfrac{(1-\nu)}{2}\end{bmatrix}\begin{Bmatrix}\varepsilon_1\\ \varepsilon_2\\ \gamma_{12}\end{Bmatrix} \qquad (2.4.52)$$

where the strain normal to the stress plane with zero stress is:

$$\varepsilon_3 = \frac{-\nu}{E}(\sigma_1+\sigma_2) = \frac{-\nu}{1-\nu}(\varepsilon_1+\varepsilon_2) \qquad (2.4.53)$$

In two dimensional plane strain conditions (e.g. $\varepsilon_3 = \gamma_{23} = \gamma_{13} = 0$), the constitutive relations are simply:

$$\begin{Bmatrix}\varepsilon_1\\ \varepsilon_2\\ \gamma_{12}\end{Bmatrix} = \frac{(1+\nu)}{E}\begin{bmatrix}1-\nu & -\nu & 0\\ -\nu & 1-\nu & 0\\ 0 & 0 & 2\end{bmatrix}\begin{Bmatrix}\sigma_1\\ \sigma_2\\ \tau_{12}\end{Bmatrix} \qquad (2.4.54)$$

and

$$\begin{Bmatrix}\sigma_1\\ \sigma_2\\ \tau_{12}\end{Bmatrix} = \frac{E}{(1+\nu)(1-2\nu)}\begin{bmatrix}1-\nu & \nu & 0\\ \nu & 1-\nu & 0\\ 0 & 0 & \dfrac{(1-2\nu)}{2}\end{bmatrix}\begin{Bmatrix}\varepsilon_1\\ \varepsilon_2\\ \gamma_{12}\end{Bmatrix} \qquad (2.4.55)$$

such that the stress components $\tau_{23} = \tau_{13} = 0$ while the stress component normal to the plane where $\varepsilon_3 = 0$ is given by:

$$\sigma_3 = \nu(\sigma_1+\sigma_2) \qquad (2.4.56)$$

2.5 Continuum Damage Mechanics

The mechanical properties and behaviour of materials are dependent on atomic bonding and microstructure. In metals and crystalline ceramics, the crystal structure is usually imperfect due to the presence of voids, microcracks and crystal defects. These imperfections induce local stress and strain concentrations, which nucleate new defects. Consequently, irreversible changes, which can be regarded as *damage*, modify mechanical properties such as strength, stiffness and fracture toughness and lead to final failure.

The effective use of materials demands ways of modelling damage and its effects on mechanical properties. Kachanov (1958) and Rabotnov (1968) have pioneered phenomenological approaches using a continuous internal state variable to characterise damage. By incorporating the damage state variable into constitutive theories, such as elasticity (Cordebios & Sidoroff, 1981; Krajcinovic & Fonseka (1981), Krajcinovic (1983)) and plasticity (Lemaitre, 1984; Marquis & Lemaitre, 1988; Ju, 1989), an ability to analyse damaged material behaviour has been established. In the past four decades, these approaches have matured into a distinct field known as *continuum damage mechanics*, which is supported within a framework of the thermodynamics of irreversible processes with internal variables (Lubliner, 1972). A range of damage models have been proposed and these are reviewed in Sect. 1.3.

In the following sections, the theory of continuum damage mechanics is reviewed. Central to the theory is the concept of an *internal state variable* such as damage which defines the damage condition of the material; the *thermodynamic principles* and *state potential* which relates the internal state variables; and the evolutionary laws of the internal state variables. Following Krajcinovic & Fonseka (1981), the term *damage* limits the discussion to defects such as cracks or voids while defects such as dislocations are treated separately through the theory of plasticity. To satisfy continuity, damage at a point x implies a representative volume element V around x, which is large enough to include damage, and yet sufficiently small for the state of stress, strain and damage distribution to be homogenised. Further, damage is assumed to be time-independent and isothermal. The arguments presented are generally set within the framework of small deformation elasticity theory.

2.5.1 The Damage State Variables

Chaboche (1987) suggest that: *"The first step in developing a damage theory concerns the definition of the damage variable"*. This involves establishing the *tensor nature* of the damage state variable and identifying suitable measures to quantify damage.

The mathematical properties of damage variables have undergone significant developments. Initially, Kachanov (1958) introduced a scalar variable ψ to represent creep damage, such that $\psi = 1$ specified the initial undamaged state and $\psi = 0$ the final ruptured state. The physical meaning of ψ is interpreted as the ratio of the load-carrying capacity of the net area A_n and the apparent area A (Murakami, 1987):

$$\psi = A_n / A \tag{2.5.1.1}$$

Subsequently, Rabotnov (1968) introduced a scalar damage variable:

$$\omega = 1 - \psi \tag{2.5.1.2}$$

in which ω is interpreted as the area fraction in the apparent area A which does not bear load due to damage. As such, the *net stress* or *effective stress* $\overline{\sigma}$ due to damage is:

$$\overline{\sigma} = \frac{\sigma}{\psi} = \frac{\sigma}{1-\omega} \tag{2.5.1.3}$$

which shows that stress in a damaged material is magnified due to the reduction in net area.

The scalar variable introduced by Kachanov (1958) and Rabotnov (1968) assumes that damage is isotropic. Hayhurst (1972), however, showed that the orientation of microcrack planes in high temperature creep cavitation occurs normal to the direction of maximum principal stress, i.e. damage is anisotropic. Subsequently, Hayhurst & Leckie (1973) and Leckie & Hayhurst (1974) refined the Kachanov (1958) and Rabotnov (1968) approach by applying a scalar variable to selected component of the principal stress tensor.

At the same time, Davison and Stevens (1973) introduced a vector damage variable to represent spall in elastic bodies. This approach was further advanced by Krajcinovic & Fonseka (1981) and Krajcinovic (1985) to include damage by both cleavage and slip modes, and, the effects of active (open) and passive (closed) cracks, in brittle materials. In general, the damage vector ω is defined locally by the void area density ω_o in a plane defined by a normal $\mathbf{e}_1$:

$$\omega = \omega_o \mathbf{e}_1 \qquad (2.5.1.4)$$

where (1, 2, 3) is the principal damage (void) co-ordinate system corresponding to the principal stress co-ordinate system with $\sigma_1 > \sigma_2 > \sigma_3$.

A second-order tensor damage variable has been introduced by Murakami & Ohno (1981) and Murakami (1983). The second-order damage tensor Ω is symmetric and has principal components as in Cauchy's stress tensor. In its principal axes, damage is defined as:

$$\Omega = \sum_{i=3}^{3} \Omega_i \boldsymbol{n}_i \otimes \boldsymbol{n}_i \qquad (2.5.1.5)$$

where Ω_i and $\boldsymbol{n}_i$ are the principal values and principal directions of the damage tensor Ω and the symbol $\otimes$ denotes cross product. The components of the damage tensor Ω_i are interpreted as the void area density in the plane perpendicular to the principal direction $\boldsymbol{n}_i$ of the damage.

Cordebois & Sidoroff (1981) also introduced a second-order damage tensor $\boldsymbol{D}$ based on the concept of *net stress* or *effective stress* $\bar{\sigma}$, given in (2.5.1.3). In terms of the principal stress co-ordinate system, the effective principal stress tensor is:

$$\bar{\sigma}_i = \frac{\sigma_i}{1 - D_i} \qquad (2.5.1.6)$$

where the damage tensor $\boldsymbol{D}$ in principal stress space is defined as:

$$\boldsymbol{D} = \begin{bmatrix} D_1 & 0 & 0 \\ 0 & D_2 & 0 \\ 0 & 0 & D_2 \end{bmatrix} \qquad (2.5.1.7)$$

To obtain an explicit description of the components of the damage tensor, an equivalence of strain energy hypothesis was adopted. The hypothesis assumes "*the elastic energy for a damaged material is equivalent in form to that of the undamaged (effective) material except that the stress is replaced by the effective stress in the energy formulation.*" (Voyiadjis & Kattan, 1999). Corresponding to the effective stress tensor (2.5.1.6), an effective strain $\bar{\varepsilon}_i$ tensor is introduced:

$$\bar{\varepsilon}_i = (1 - D_i)\varepsilon_i \qquad (2.5.1.8)$$

where ε_i is the apparent strain tensor of the damage material. Limiting discussion to uni-axial tension, Cordebois & Sidoroff (1981) provide explicit expressions for the

components of the damage tensor $\boldsymbol{D}$ using the effective stress, effective strain concepts and Hooke's law. These are:

$$\begin{aligned} \overline{E} &= E(1-D_1)^2 \\ \overline{\nu} &= \nu(1-D_1)/(1-D_2) \end{aligned} \qquad (2.5.1.9)$$

where, E and ν denotes Young's modulus and Poisson's ratio, while $\overline{E}$ and $\overline{\nu}$ are the corresponding effective properties measured from experiment. An important difference between the approach of Cordebois & Sidoroff (1981) and Murakami & Ohno (1981) approach is that the former characterised the damage state by the change of elastic constants, which is easy to obtain, while the latter characterises damage through measured cavities area in crystal structure, which is experimentally difficult.

A fourth-order damage tensor was introduced by Lemaitre & Chaboche (1978) and Chaboche (1979, 1981), which characterised the damage tensor using changes in the elastic constants. To derive a fourth-order damage tensor, an equivalent strain hypothesis (Lemaitre, 1971) was adopted, which states: "*Any strain constitutive equation for a damaged material may be derived in the same way as for a virgin (effective) material except that the usual stress is replaced by the effective stress.*" For a one-dimensional problem, the following relations are derived:

$$\varepsilon = = \frac{\overline{\sigma}}{E} = \frac{\sigma}{E(1-D)} = \frac{\sigma}{\overline{E}} \qquad (2.5.1.10)$$

$$D = 1 - \frac{\overline{E}}{E}, \qquad \overline{\sigma} = \frac{\sigma}{1-D} = \frac{E\sigma}{\overline{E}} \qquad (2.5.1.11)$$

A discussion of the advantages of using a fourth-order damage tensor compared to other forms of tensor representation is given by Krajcinovic & Mastilovic (1995). To compare the different tensorial representations of damage, a dilute concentration model was adopted to model planar and monoclinic distribution of cracks. Comparing the computed effective compliance with exact solutions Krajcinovic & Mastilovic (1995) concluded that:

- The scalar representation of damage is limited to isotropy and ceases to be viable for any other case.
- Second-order damage tensors are applicable to isotropic and transversely anisotropic cases and provide a reasonably close fit (5% to 10% error) for other distributions.

- Both fourth-order and higher-order damage tensors give identical predictions to exact solutions. Thus computations using tensors of order higher than the order of four are unnecessary.

The debate on the appropriate tensorial nature of a damage variable is now narrowed to the second- and fourth-order tensors. The advantage of a second-order damage tensor is its simplicity. It is simple to manipulate and is familiar to mechanicians and engineers. These views are however subjective and may still be contentious since implementing changes in the components of a fourth-order damage tensor are easy to do in contracted-tensor notation. In addition, simple algebraic relations for manipulating fourth-order tensor are well established and are widely available.

The major advantages of the fourth-order damage tensor is that, it is described using affined mechanical properties such as Young's modulus which are readily measurable. The concept is consistent with the thermodynamic framework (Chaboche, 1981), independent of size effects (Krajcinovic and Basista, 1991) and insensitive to stress concentration, crack distribution and crack interactions. This is because Young's modulus is directly related to the nature of atomic bonds and damage distribution. Moreover, Young's modulus is widely used in micro-mechanical and continuum theory, which facilitates its implementation in computational algorithms. Unlike its other counterparts, it can be implemented directly to construct an effective compliance or effective stiffness tensor and is computationally efficient. In comparison to the approach of Cordebois & Sidoroff (1981), the fourth-order damage tensor has the ability to consider all forms of anisotropy.

The different ways to quantify damage experimentally have been identified by Murakami (1983), Chaboche (1987) and Lemaitre (1992). Excluding measurements of changes in damage area and elastic modulus, other measures include density, micro-hardness, electrical resistance, cyclic plasticity response, ultrasonic wave propagation, tertiary creep response and acoustic emission.

Micro-mechanics has been used by Burr et al (1997) to model matrix cracking in brittle matrix composites. Damage by matrix cracking can be described by considering an elementary cell of size $2L$ x $2W$ containing a crack size of $2a$ as shown in Fig 2.5.1-1. The matrix in the elementary cell is isotropic elastic and has a Young's modulus E,

and the effective Young's modulus $\overline{E}$ of the cell normal to the circular crack is approximated as:

$$\frac{\overline{E}}{E} = \frac{1}{1 + 2\frac{\pi a^2}{4LW}} \qquad (2.5.1.12)$$

in which $\pi a^2 / 4LW$ is the crack density. Comparing with the damage relationship of Lamaitre & Chaboche (1978) given in (2.5.1.11), the micro-mechanical description of damage variable defining matrix cracking is given by:

$$D = \frac{2\frac{\pi a^2}{4LW}}{1 + 2\frac{\pi a^2}{4LW}} \qquad (2.5.1.13)$$

2.5.2 The State Potential

The *state potential* is a scalar energetic descriptor of the physical (state) processes within a body. Essentially, the state potential defines the *state laws* governing the relationships of the state variables. This is derived using the framework of the thermodynamics of irreversible processes with internal variables, which originates from Coleman & Noll (1963). Following Lubliner (1972, 1990), a review of the thermodynamic principles and the state potentials is now given.

The local thermodynamic state of a body can be assumed to be a unique function of the strain tensor ε_{ij}, the entropy density s and a set of internal state variables ξ_α (where α = 1.., n) which represents phenomenological events such as matrix cracking, creep, etc…). In addition, the internal state variables ξ_α may be a tensor of any order. Since internal energy is a descriptor of thermodynamic states, it follows that the *internal energy density* or the *internal energy potential u* can be written as:

$$u = u\left(\varepsilon_{ij},\, s,\, \xi_\alpha\right) \qquad (2.5.2.1)$$

in which its time derivative, defined as partial derivative of its functions, is:

$$\dot{u} = \frac{\partial u}{\partial \varepsilon_{ij}}\dot{\varepsilon}_{ij} + \frac{\partial u}{\partial s}\dot{s} + \frac{\partial u}{\partial \xi_\alpha}\dot{\xi}_\alpha \qquad (2.5.2.2)$$

An expression for the rate of change in internal energy density can also be obtained using the first law of thermodynamics. In the absence of changes in kinetic or potential energy, the change of internal energy density in a body should be equal to the sum of mechanical and heat energies, i.e.:

$$\dot{u} = \sigma_{ij}\dot{\varepsilon}_{ij} - \nabla \dot{q} \qquad (2.5.2.3)$$

Here, σ_{ij} is the Cauchy's stress tensor, $\dot{q}$ is the specific heat flux out a body, and ∇ is the gradient operator.

The second law of thermodynamics states that the entropy (which is a measure of disorder) of an isolated system increases in all real processes (spontaneous or irreversible). If this is true during the deformation of a body, then the Clausius-Duhem inequality for a irreversible process, which describes the second law of thermodynamics, must be satisfied, i.e.:

$$\dot{s} + \nabla\left(\frac{\dot{q}}{T}\right) \geq 0 \qquad (2.5.2.4)$$

Here, T denotes the absolute temperature. Substituting eqn (2.5.2.3) into (2.5.2.4), it can be shown that

$$\left(T - \frac{\partial u}{\partial s}\right)\dot{s} + \left(\sigma_{ij} - \frac{\partial u}{\partial \varepsilon_{ij}}\right)\dot{\varepsilon}_{ij} - \frac{\partial u}{\partial \xi}\dot{\xi} - \dot{q}\frac{\nabla T}{T} \geq 0 \qquad (2.5.2.5)$$

Because the strain rate tensor $\dot{\varepsilon}_{ij}$ and entropy density rate $\dot{s}$ is arbitrary in a given thermodynamic state, their coefficients must vanish, giving:

$$T = \frac{\partial u}{\partial s} \qquad (2.5.2.6)$$

$$\sigma_{ij} = \rho\frac{\partial u}{\partial \varepsilon_{ij}} \qquad (2.5.2.7)$$

and

$$-\left(\frac{\partial u}{\partial \xi}\dot{\xi}_{\alpha} + \dot{q}\frac{\nabla T}{T}\right) \geq 0 \qquad (2.5.2.8)$$

For an isothermal body, eqn (2.5.2.8) reduces to:

$$-\frac{\partial u}{\partial \xi}\dot{\xi}_{\alpha} \geq 0 \qquad (2.5.2.9)$$

Using the Legendre transformation of the internal energy, two other state potentials may be derived. The first is the *Helmholtz free energy density* ψ:

$$\psi = u - T\,s = \psi\left(\varepsilon_{ij}, T, \xi_{\alpha}\right) \qquad (2.5.2.10)$$

with the properties

$$s = -\frac{\partial \psi}{\partial T} \qquad (2.5.2.11)$$

$$\sigma_{ij} = \frac{\partial \psi}{\partial \varepsilon_{ij}} = \sigma_{ij}\left(\varepsilon_{ij}, T, \xi_{\alpha}\right) \qquad (2.5.2.12)$$

and

$$-\frac{\partial \psi}{\partial \xi_{\alpha}}\dot{\xi}_{\alpha} \geq 0 \qquad (2.5.2.13)$$

The second is the *Gibbs free energy density* (or free enthalpy, or complementary free energy) η:

$$\eta = \sigma_{ij}\varepsilon_{ij} - \psi = \eta\left(\sigma_{ij}, T, \xi_\alpha\right) \tag{2.5.2.14}$$

with the properties

$$s = \frac{\partial \eta}{\partial T} \tag{2.5.2.15}$$

$$\sigma_{ij} = \frac{\partial \eta}{\partial \varepsilon_{ij}} = \varepsilon_{ij}\left(\sigma, T, \xi_\alpha\right) \tag{2.5.2.16}$$

and

$$-\frac{\partial \eta}{\partial \xi_\alpha}\dot{\xi}_\alpha \leq 0 \tag{2.5.2.17}$$

Essentially, any set of eqns (2.5.2.6-7), (2.5.2.11-12) and (2.5.2.15-16) are sufficient to define the thermo-mechanical constitutive relations for a material. Furthermore, any one of the eqns. (2.5.2.9), (2.5.2.13) and (2.5.2.17) is sufficient to describe the state law of the phenomenological events. The physical interpretation of the equation states that the phenomenological events reduce the internal energy and the Helmholtz free energy of a body while the Gibbs free energy is increased. Also, if the thermodynamic force Y (or energy release rate) associated with the phenomenological events is:

$$Y = -\frac{\partial u}{\partial \xi_\alpha} = -\frac{\partial \psi}{\partial \xi_\alpha} = -\frac{\partial \eta}{\partial \xi_\alpha} \tag{2.5.2.18}$$

then the evolution of the phenomenological events $\dot{\xi}_\alpha$ must be a non-negative function.

2.5.3 Evolution Laws for the Damage State Variable

To model the damaged stress-state of a body the evolution law of the damage variable must be defined. In cases where damage is isotropic, Lemaitre (1996) has postulated that the damage evolution law can be derived from a *damage potential* F_D which is a scalar continuous and convex function of the damage energy release rate Y. Assuming that normality condition is satisfied during damage, the evolution law of the damage variable can be given as:

$$\dot{D} = \frac{\partial F_D}{\partial Y}\dot{\lambda} \tag{2.5.3.1}$$

in which the symbol $\dot{\lambda}$ is a multiplier that takes account of the damage strain rate.

Alternatively, experiments can also be used to derive the evolution of damage. This is achieved by measuring the damage development as a function of applied strain, i.e. $D = D(\varepsilon)$. Lemaitre (1984) first showed this for metals by performing a repetition of unloading-reloading tension tests followed by measuring the elastic moduli of the specimen. Substituting into eqn (2.5.1.11), a plot of the damage as a function of strain is obtained in which the evolution of damage is derived. This procedure is shown in Fig 2.5.3-1. In comparison with micro-mechanics approaches, the experimental approach is simpler. Also, it is more accurate because the Young's moduli measured directly relate the nature of atomic bonds and the damage accumulated in the material. The stress-state of a material during damage is achieved by incorporating the experimental damage into the damage stress-strain relation, such as in eqn (2.5.1.10).

In cases where damage is anisotropic, the theory that evolution of damage can be derived from a scalar damage potential is inappropriate. This is because the evolution of damage with respect to each direction is different. A typical example of this is found in uni-directional fibre reinforced brittle matrix composites when loaded in tension. Depending on the fibre orientation, Evans (1990) has shown that the composite can suffer from matrix cracking or delamination. In matrix cracking, the composite exhibits gradual cracking, however in delamination, unstable cracking occurs and the composite fails catastrophically. As such, the evolution of damage is different. To derive the evolution of matrix cracking in ceramic composites, Burr, Hild and Leckie (1995, 1997) have used the experimental approach determined by Lemaitre (1984) to measure the effective Young's moduli of the composite. McCafferty (1994) has used an experimental-analytical approach to determine the effective tangent moduli of the matrix during matrix cracking of a ceramic composite. Chia & Hancock (2000, 2002) have extended the experimental-analytical approach by McCafferty (1994) to model matrix cracking evolution whereas the evolution of delamination was mathematically modelled with an exponential decaying function, as elaborated in Chapter 7.

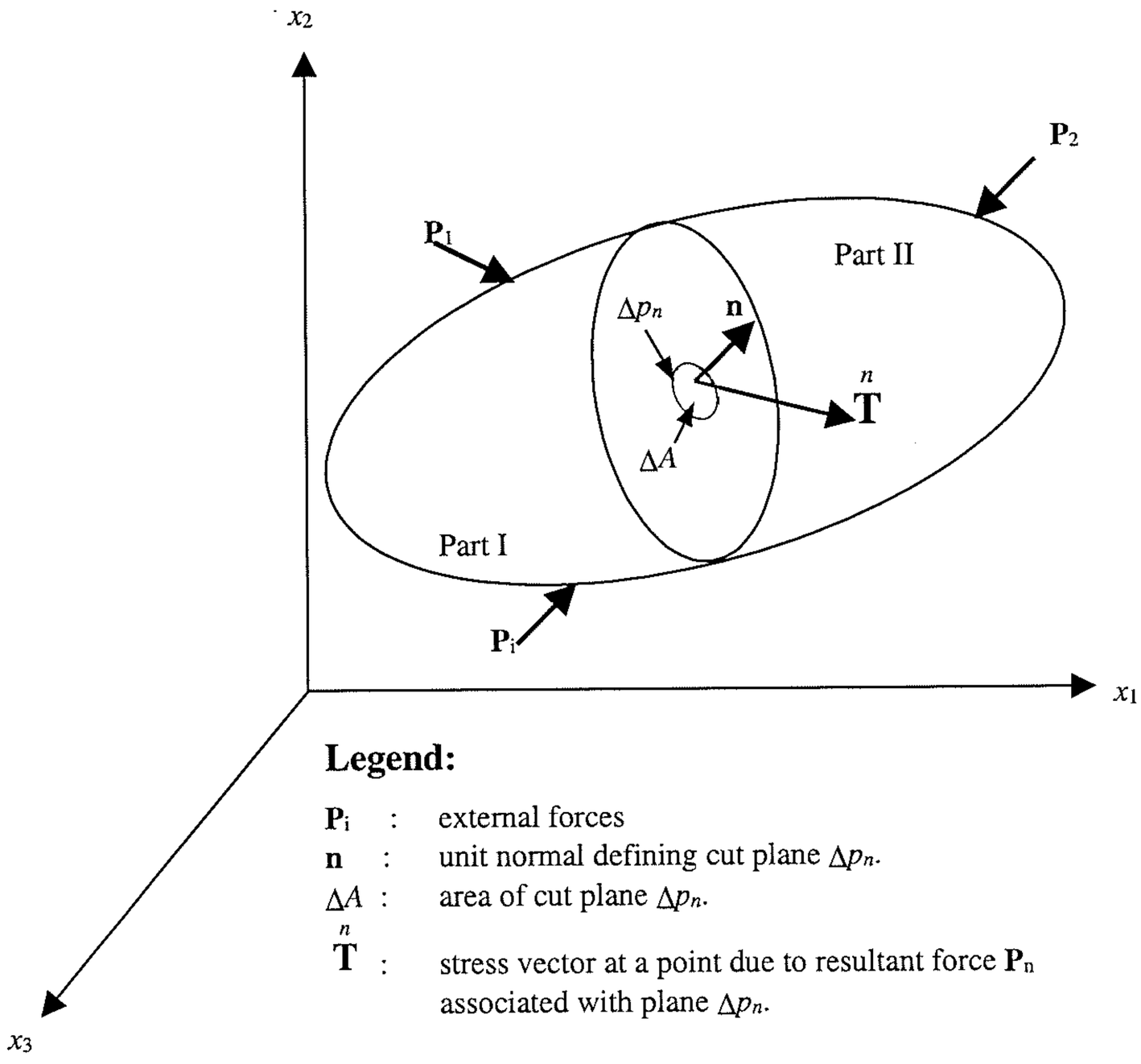

Fig. 2.2-1 Illustration of forces and Cauchy's stress vector in a loaded continuum.

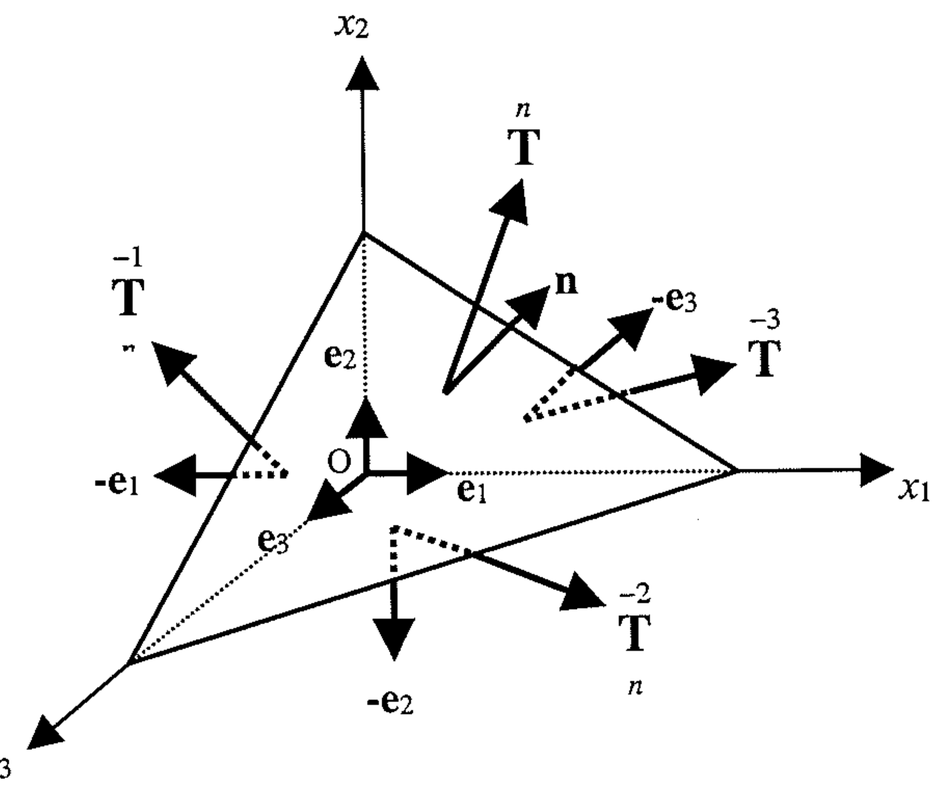

Fig. 2.2-2 Relationship between the stress vector on the arbitrary plane **n** and the three stress vector acting on the orthogonal planes defined by base vector $\mathbf{e}_1$, $\mathbf{e}_2$, $\mathbf{e}_3$.

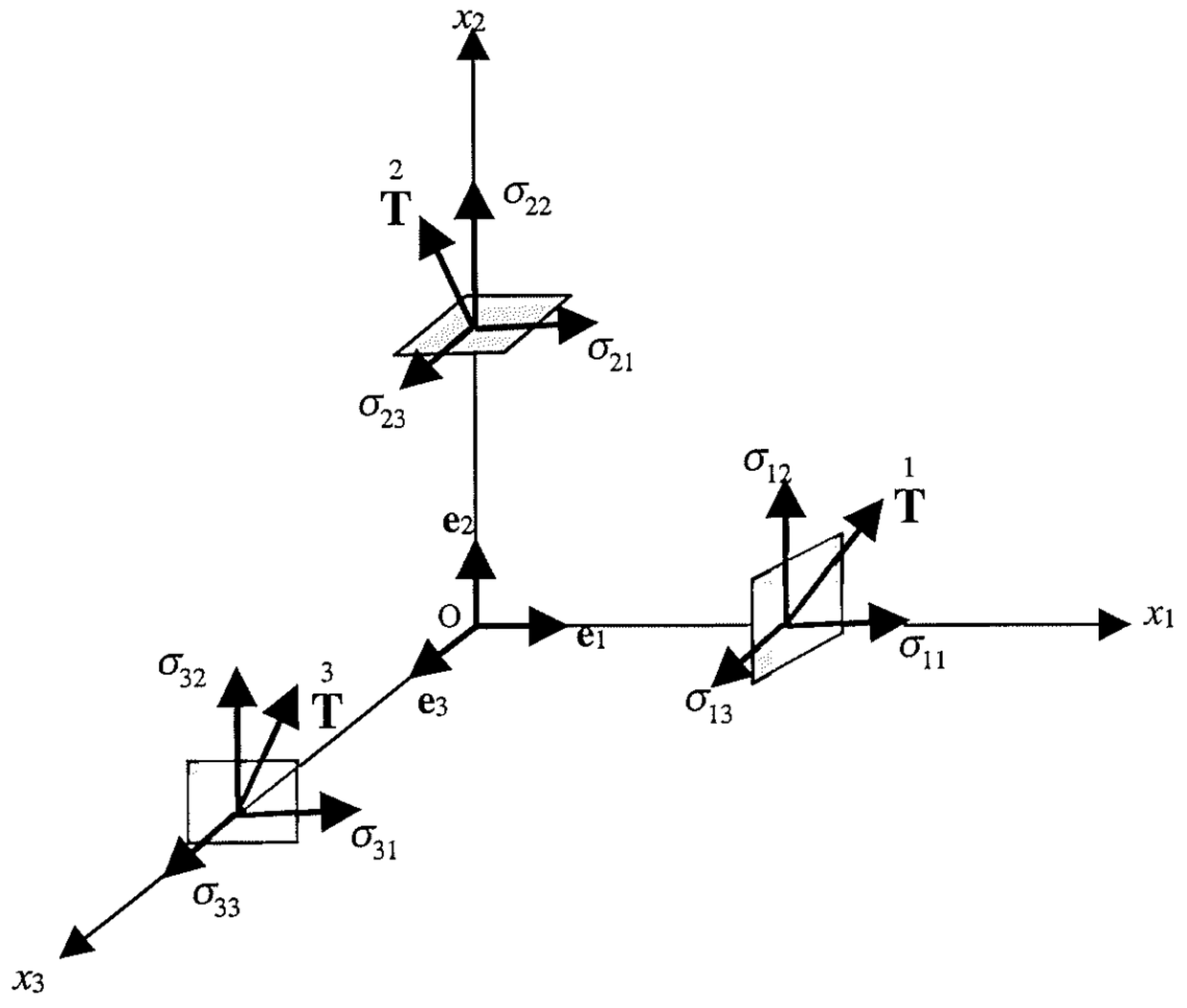

Fig. 2.2-3 Cartesian components of the stress vector $\overset{1}{\mathbf{T}}, \overset{2}{\mathbf{T}}, \overset{3}{\mathbf{T}}$ originating from point O in association with the Cartesian plane. Positions of these planes have been exaggerated from point O.

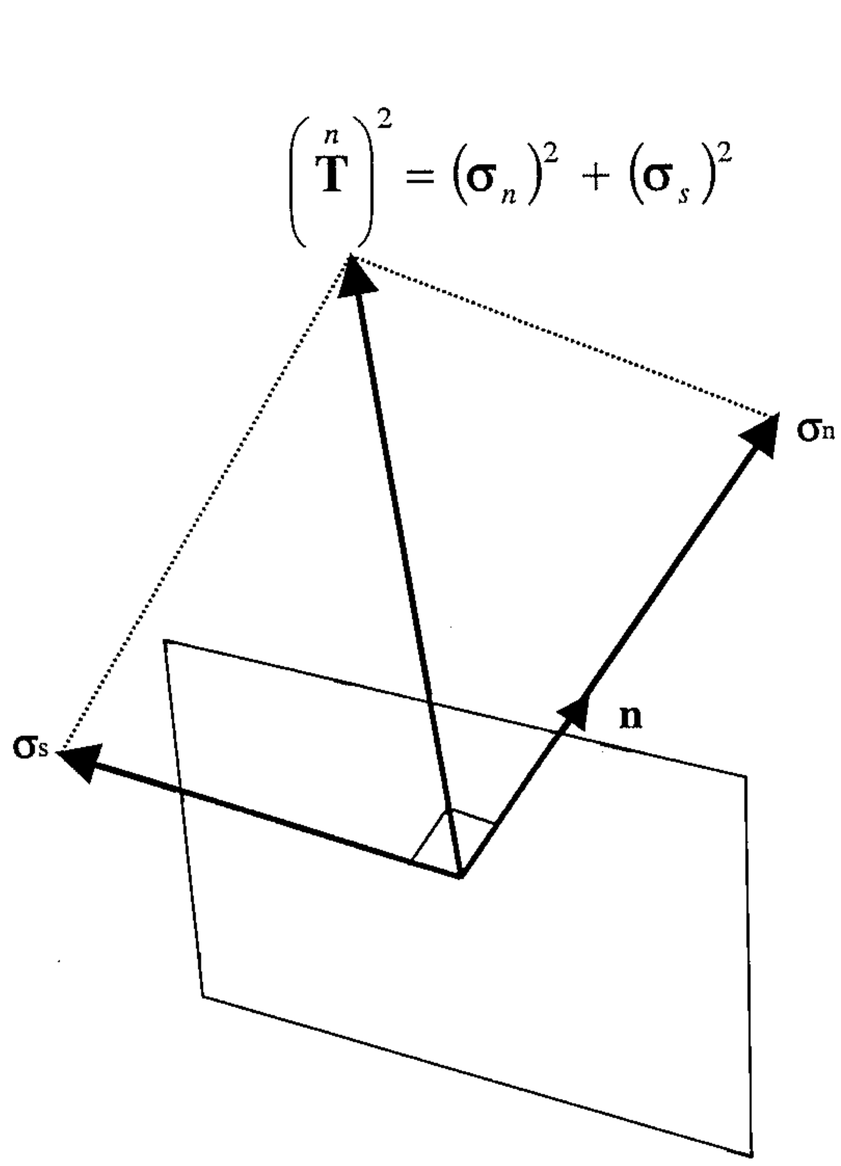

Fig. 2.2-4 The normal and shear components of the stress vector $\overset{n}{\mathbf{T}}$ acting on the arbitrary plane **n**.

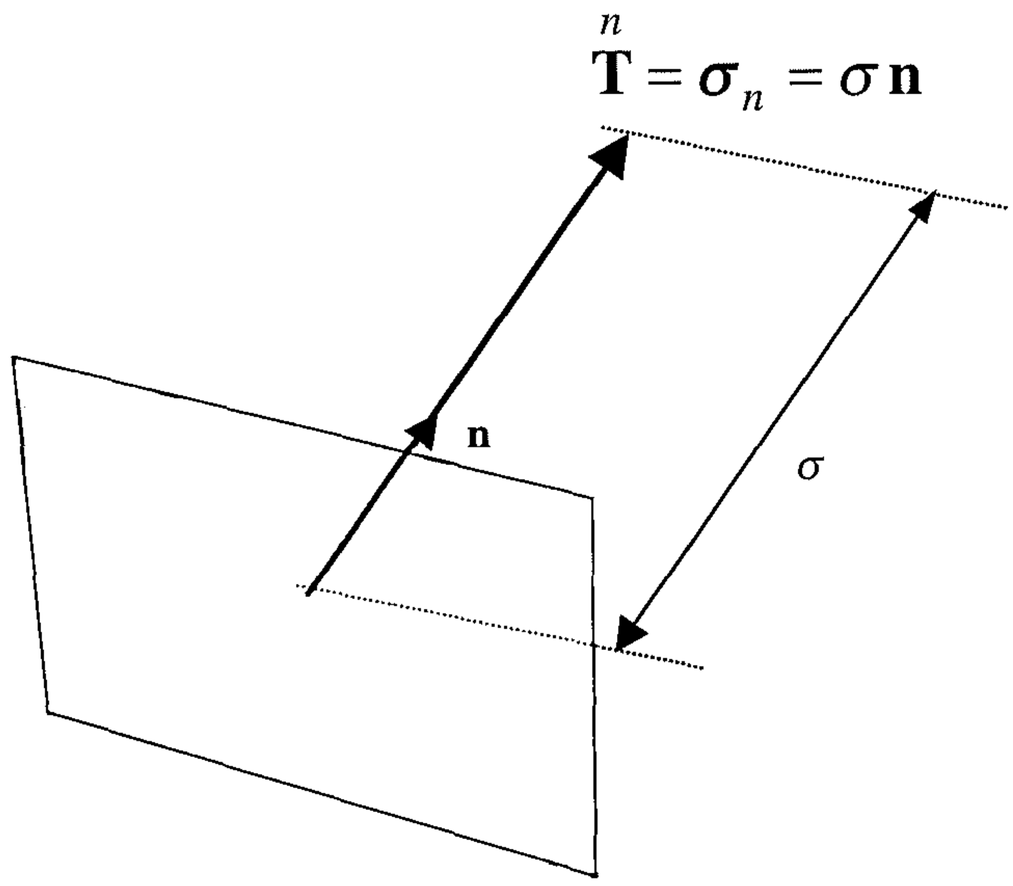

Fig. 2.2-5 Concept of Principal Stress axes.

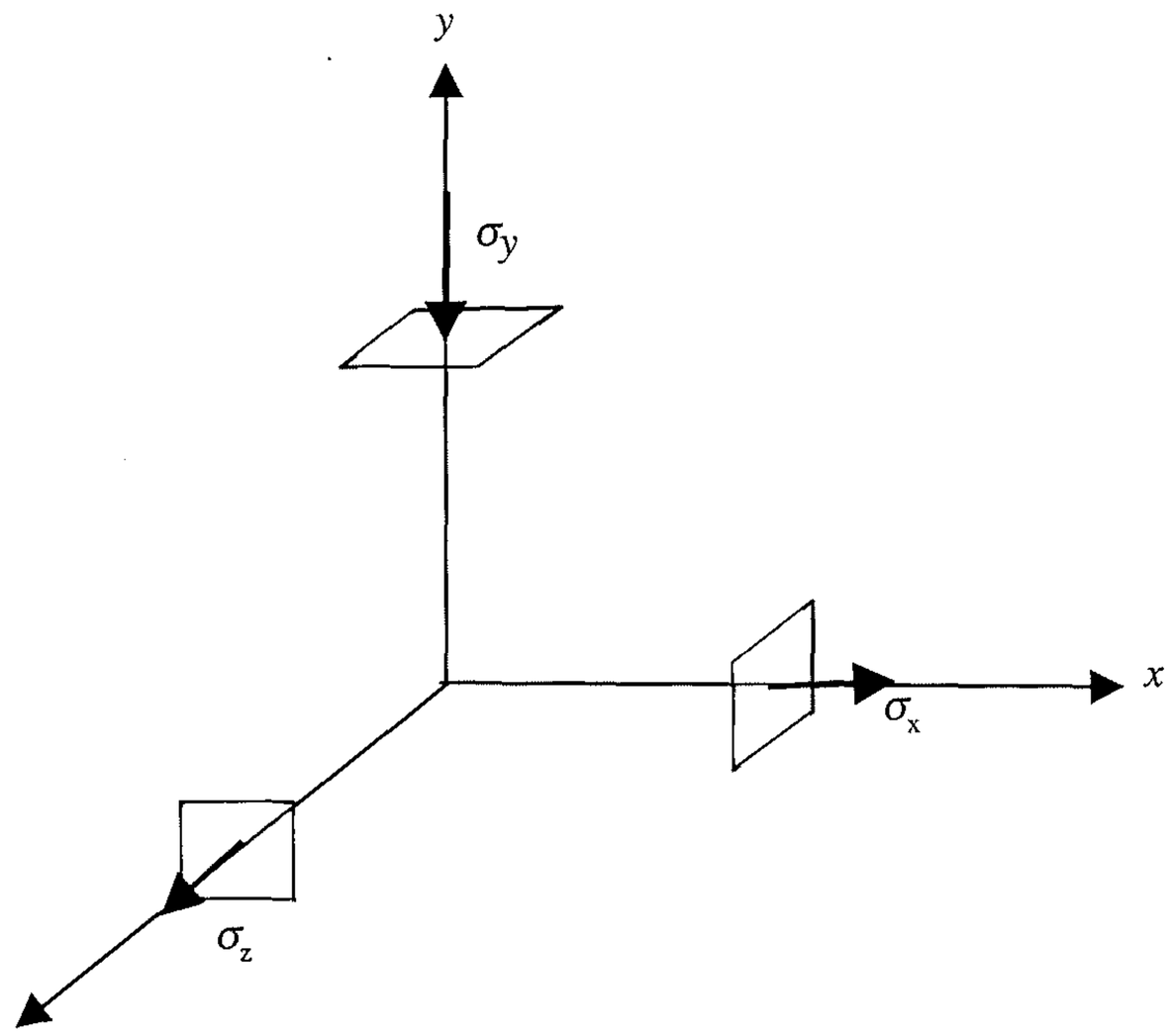

Fig. 2.2-6 A state of pure shear: $\sigma_x + \sigma_y + \sigma_z = 0$, where $\sigma_x > \sigma_y > 0$ and $\sigma_z < 0$.

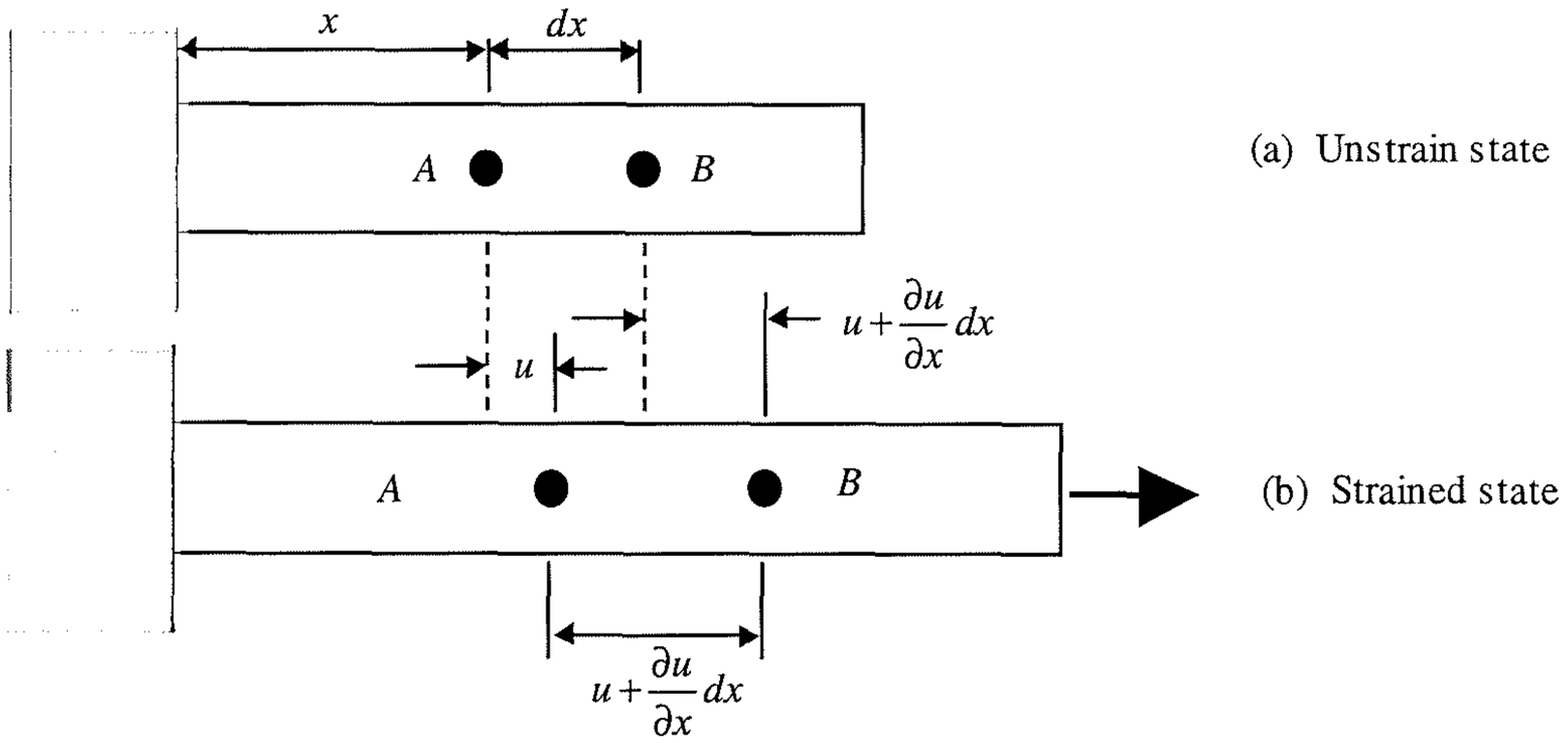

Fig. 2.3-1 Normal strain of a one-dimensional body.

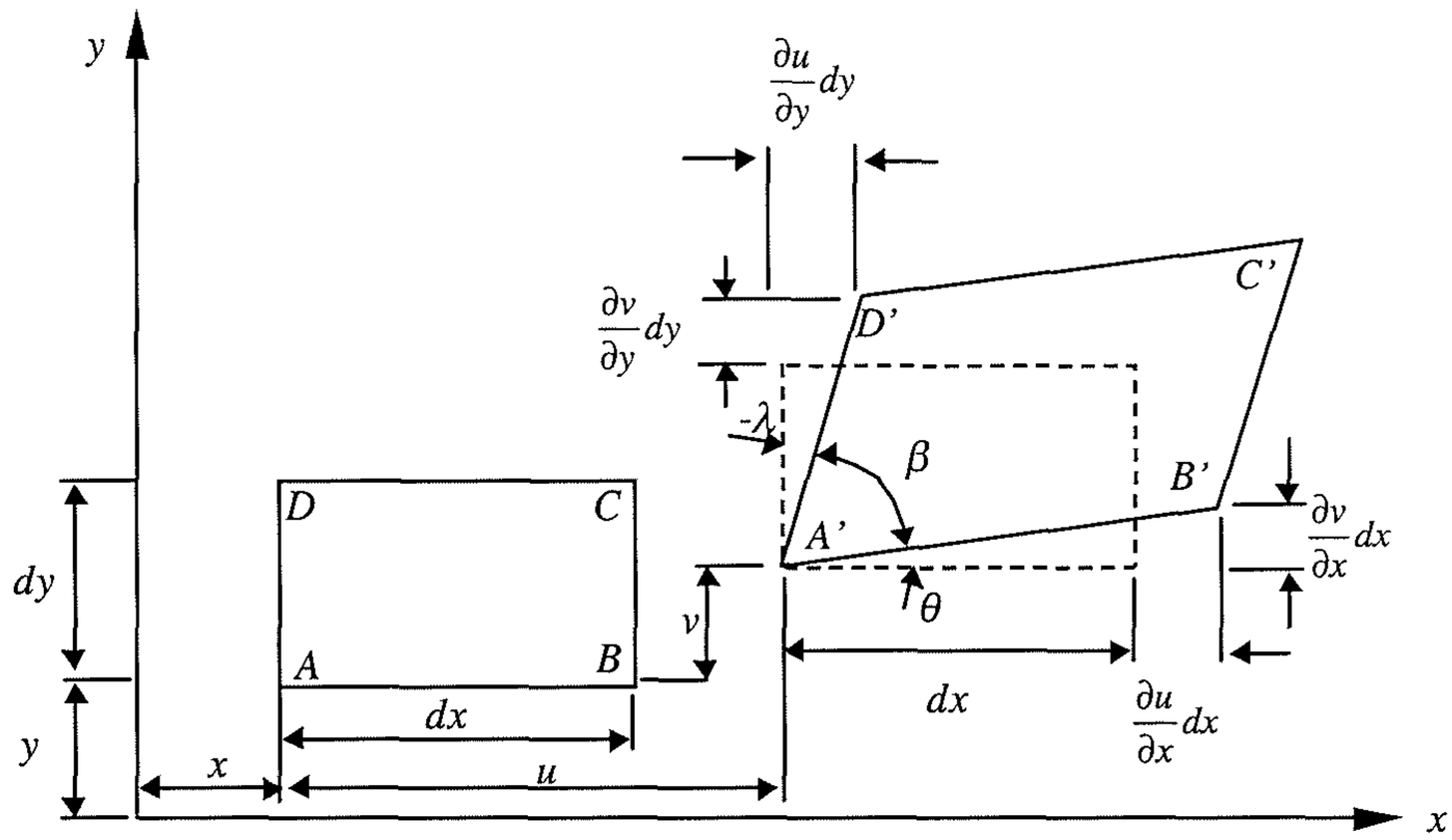

Fig. 2.3-2 Translation and normal and shear strains of a two-dimensional body

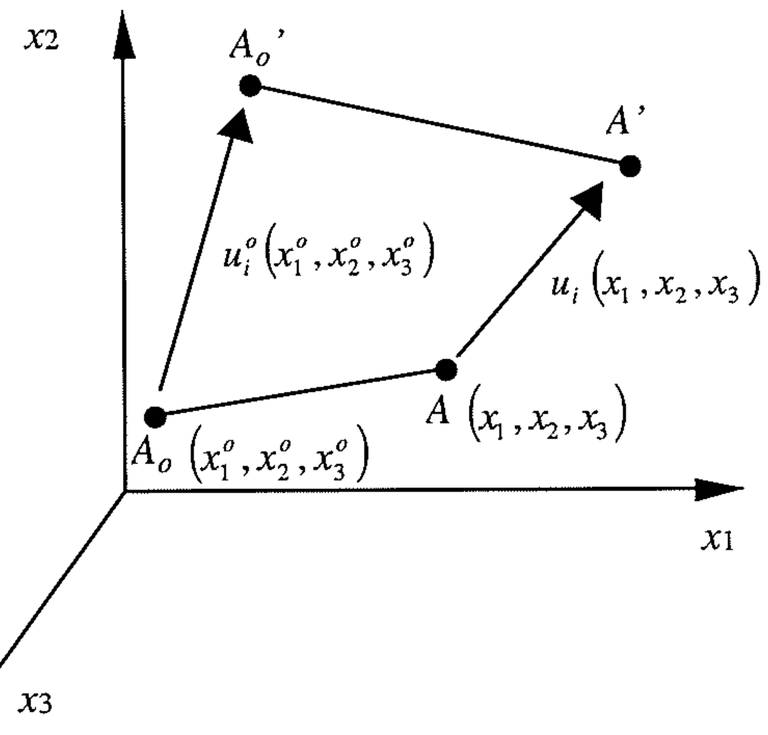

Fig. 2.3-3 Displacements of points based on Lagrangian co-ordinate system $x_i(x_1,x_2,x_3)$.

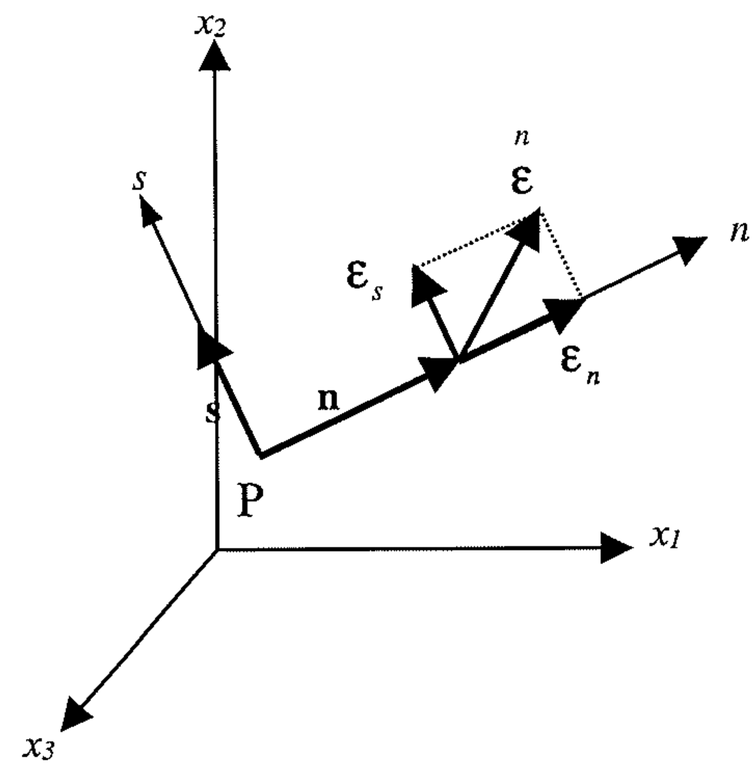

Fig. 2.3-4 Normal component ε_n and shear component ε_s and of the resultant strain vector at point P with unit normal **n**.

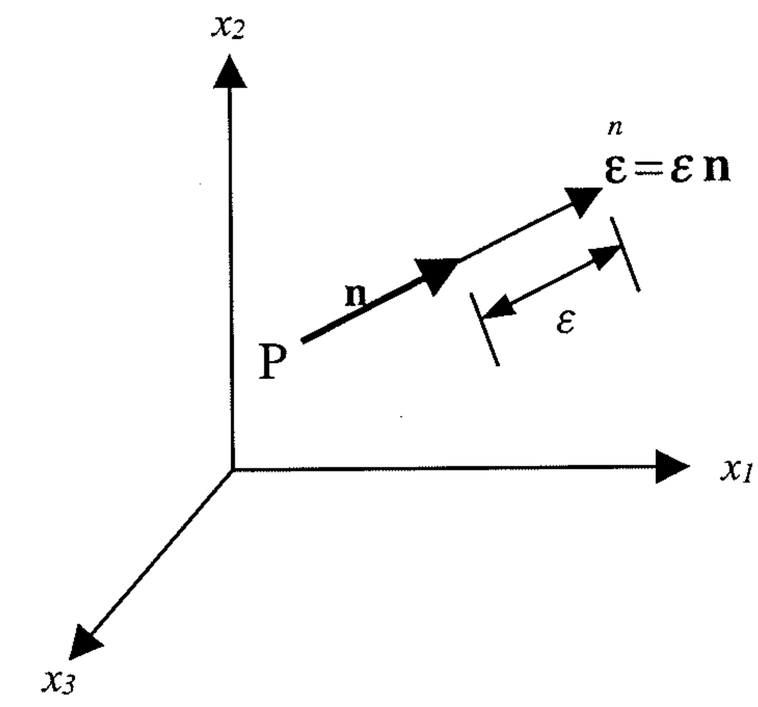

Fig. 2.3-5 The principal strain vector ε and the principal strain direction **n**.

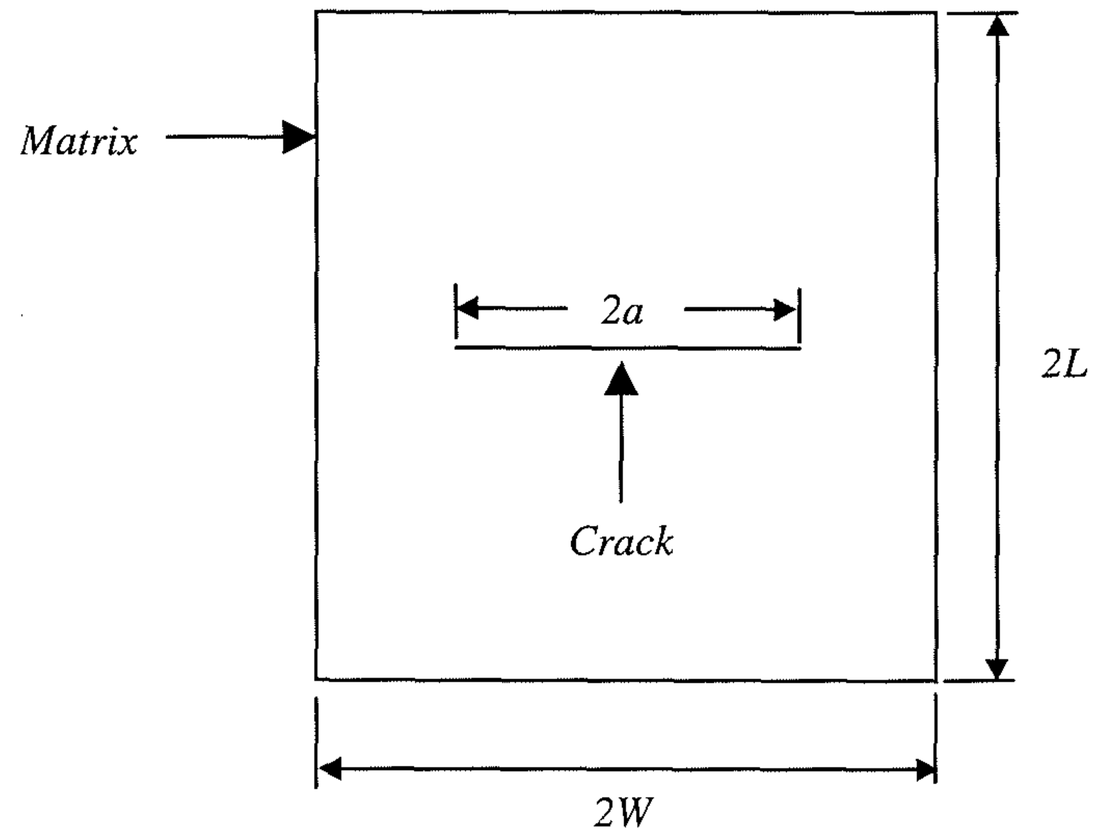

Fig 2.5.1-1 The elementary cell model of a cracked composite proposed by Burr *et al* (1997).

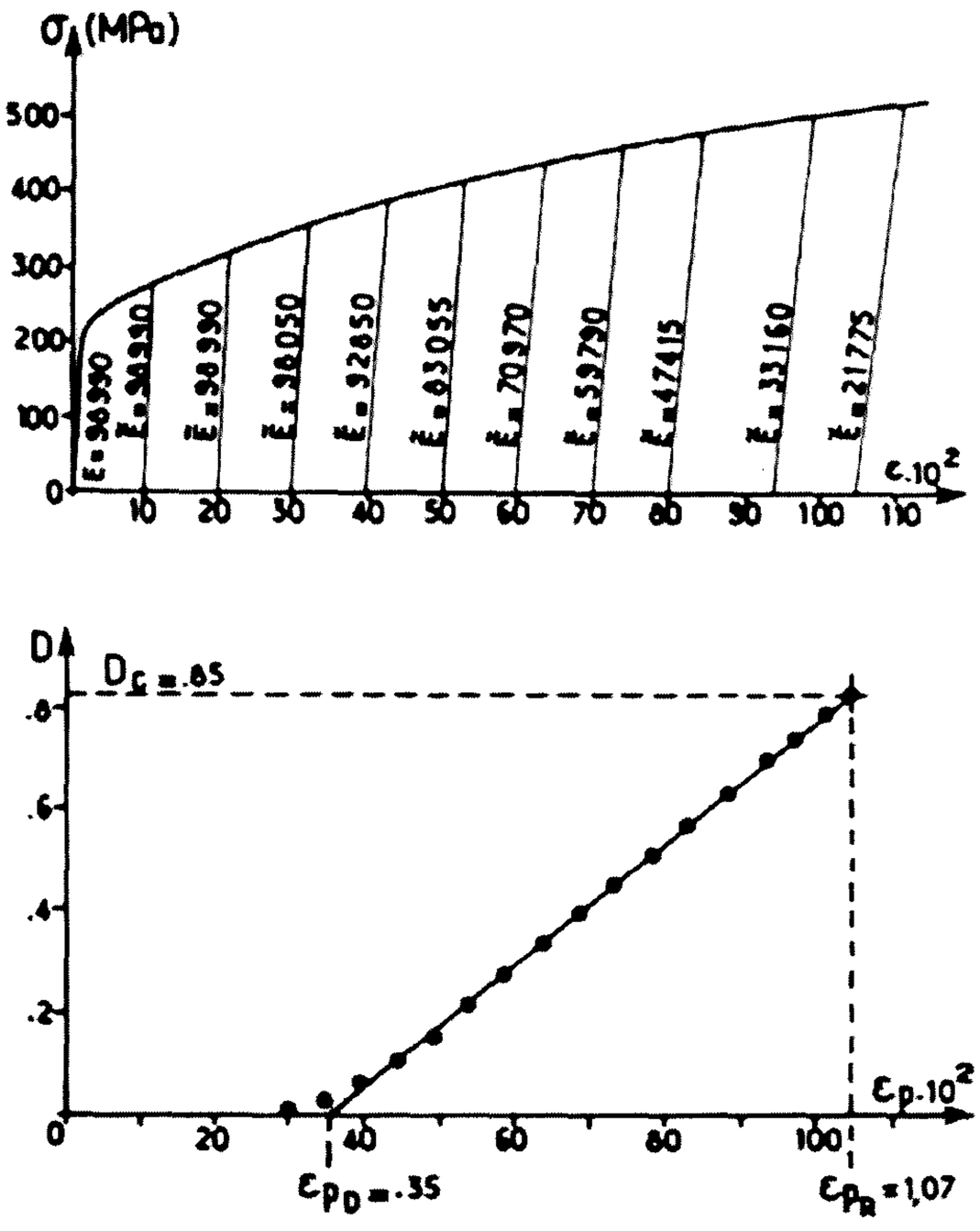

Fig. 2.5.3-1 Experimental derivation of the damage trend $D(\varepsilon)$ of copper 99.9% where damage $D = 1 - \overline{E}/E$ (adapted from Lemaitre 1984).

CHAPTER 3

Mechanical Properties of Brittle Matrix Composites

3.1 Introduction

The mechanical behaviour of unidirectional fibre-reinforced brittle matrix composites is highly non-linear and anisotropic. The ability to model composite behaviour and failure requires an understanding of composite's micromechanics, which depends on the matrix, fibre, fibre-matrix interface, damage, and fibre alignment. In this chapter, the mechanics of the elastic moduli, tensile stress-strain behaviour, matrix cracking initiation, and ultimate tensile strength are reviewed. This chapter concludes with a discussion of the effects of fibre misalignment on the composite strength.

3.2 Elastic Moduli

A central problem in predicting the elastic properties of composite materials arises from the complexity of the local stress and strain distributions when the constituents are elastically mismatched. Although exact solutions are difficult, bounds based on the theorems of minimum potential energy and minimum complementary energy can be used to make useful predictions.

When a shear strain γ is applied to a composite, the Voigt analysis (Hull & Clyne, 1997) assumes that the strain in the constituents is identical to that applied to the composite as a whole. As such, the shear stress in the composite is:

$$\tau = G_c \gamma = \left(V_m G_m + V_f G_f\right)\gamma \qquad (3.2.1)$$

where G_c, G_m, G_f are the shear modulus of the composite, matrix and fibres. The symbols V_m and V_f are the volume fractions of the matrix and fibres such that:

$$V_m + V_f = 1 \qquad (3.2.2)$$

The shear modulus of the composite from eqn (3.2.1) is then:

$$G_{Voigt} = V_m G_m + V_f G_f \qquad (3.2.3)$$

However, the assumption of homogeneous strain generally ($G_m \neq G_f$) violates the equilibrium equations because the stresses at the constituent boundaries are not in equilibrium. As such, Voigt's assumption is inadmissible. However, the theorem of

minimum potential energy indicates that, "The strain energy obtained from displacement compatible with any boundary conditions, integrated over the entire volume, is a minimum for the exact displacement distribution." (McClintock and Argon, 1966). Equivalently, the strain energy U^* of a body only satisfying compatibility conditions must be greater or equal to the strain energy U associated with actual strain distribution (when both equilibrium and compatibility are satisfied), i.e.

$$U \leq U^* \tag{3.2.4}$$

The strain energy is defined as:

$$U = \tfrac{1}{2}\int_V \sigma_{ij}\varepsilon_{ij}\ dV \tag{3.2.5}$$

and the stress-strain relations are (see eqn (2.4.48)):

$$\sigma_{ij} = \frac{E}{(1+\nu)}\varepsilon_{ij} + \frac{\nu E}{(1+\nu)(1-2\nu)}\varepsilon_{kk}\,\delta_{ij} \tag{3.2.6}$$

Given that the internal strain field, satisfying compatibility condition only, is such that:

$$\gamma^*_{12} = \gamma \qquad \text{and} \qquad \varepsilon^*_{11} = \varepsilon^*_{22} = \varepsilon^*_{33} = \gamma^*_{23} = \gamma^*_{31} = 0 \tag{3.2.7}$$

the inequality defined by eqn (3.2.4) becomes:

$$\tfrac{1}{2}\int_V G_c\gamma^2 dV \leq \tfrac{1}{2}\int_{V_m V} G_m\gamma^2 dV + \tfrac{1}{2}\int_{V_f V} G_f\gamma^2 dV \tag{3.2.8}$$

$$\frac{V}{2}G_c\gamma^2 \leq \frac{V}{2}\left(V_m G_m + V_f G_f\right)\gamma^2 \tag{3.2.9}$$

$$G_c \leq \left(G_{Voigt} = V_m G_m + V_f G_f\right) \tag{3.2.10}$$

Thus, Voigt's solution gives an upper bound to the shear modulus of the composite.

The lower bound estimate is associated with the name of Reuss (Hull & Clyne, 1997) and assumes that the stress in the constituents is identical to the stress in the composite. As such, the shear strain in the composite is:

$$\gamma = \frac{\tau}{G_c} = V_m\frac{\tau}{G_c} + V_f\frac{\tau}{G_f} \tag{3.2.11}$$

and the corresponding composite shear modulus is:

$$G_{Reuss} = \left(\frac{V_m}{G_c} + \frac{V_f}{G_f}\right)^{-1} \tag{3.2.12}$$

The Reuss stress assumption however generally ($G_m \neq G_f$) violates compatiblity at the constituents boundaries. As such, the assumption is inadmissible. However, the theorem of minimum complementary energy states that, "Among the stress distribution which satisfy equilibrium at every point and are in equilibrium with the external load, the

strain energy found for such distribution is a minimum for the exact distribution." (McClintock & Argon, 1966). This means that the strain energy U^o determined for equilibrium state is greater or equal to the strain energy U at which both equilibrium and compatibility is satisfied, i.e.

$$U \leq U^o \tag{3.2.13}$$

Given that the internal stress field, for satisfying equilibrium condition only, is such that:

$$\tau_{12}^o = \tau \qquad \text{and} \qquad \sigma_{11}^o = \sigma_{22}^o = \sigma_{33}^o = \tau_{23}^o = \tau_{31}^o = 0 \tag{3.2.14}$$

the inequality defined in eqn (3.2.13), after substituting for eqns (3.2.5 & 14), gives:

$$\tfrac{1}{2}\int_V \frac{\tau^2}{G_c} dV \leq \tfrac{1}{2}\int_{V_m V} \frac{\tau^2}{G_m} dV + \tfrac{1}{2}\int_{V_f V} \frac{\tau^2}{G_f} dV \tag{3.2.15}$$

$$\frac{\tau^2}{2G_c} V \leq \frac{\tau^2}{2}\left(\frac{V_m}{G_m} + \frac{V_f}{G_f}\right) V \tag{3.2.16}$$

The shear modulus of the composite is then defined as:

$$G_c \geq \left[G_{\mathrm{Re}uss} = \left(\frac{V_m}{G_m} + \frac{V_f}{G_f}\right)^{-1} \right] \tag{3.2.17}$$

where Reuss solution is a lower bound to the shear modulus of the composite. The composite shear modulus thus is bounded by:

$$G_{\mathrm{Re}uss} \leq G_c \leq G_{Voigt} \tag{3.2.18}$$

as shown in Fig 3.2.1.

Using the energy theorems, Young's modulus of a composite E_c can also be bounded in similar fashion. However, for Voigt's analysis, compatibility requires that Poisson's ratio of the composite constituents is identical. The Young's modulus of the composite is then bounded by:

$$E_{\mathrm{Re}uss} \leq E_c \leq E_{Voigt} \tag{3.2.19}$$

or

$$\left(\frac{V_m}{E_m} + \frac{V_f}{E_f}\right)^{-1} \leq E_c \leq V_m E_m + V_f E_f \tag{3.2.20}$$

A detailed derivation is given by Jones (1999). A particularly important case is that of a composite reinforced with continuous parallel fibres loaded in simple tension parallel to the fibre axis. In this case the Voigt analysis satisfies both equilibrium and compatibility

and as such is the exact solution, given that the Poisson's ratio of the matrix ν_m and fibres ν_f are identical, i.e.

$$E_c = V_m E_m + V_f E_f \qquad (\nu_f = \nu_m) \qquad (3.2.21)$$

3.3 Stress-Strain Behaviour

Aveston, Cooper & Kelly (1971) (henceforth ACK) first established the micromechanics for uni-directional fibre reinforced brittle matrix composites tensioned parallel to the fibre direction. These composites use fibres with strength σ_{fu} and an ultimate failure strain ε_{fu} that is greater than the matrix strength σ_{mu} and the ultimate strain of the matrix ε_{mu}. When the composite is subject to uniaxial tension parallel to the fibres, the Young's modulus of the composite E_c is initially:

$$E_c = V_m E_m + V_f E_f \qquad (3.3.1)$$

and the stress of the composite σ_c is:

$$\sigma_c = \sigma_f V_f + \sigma_m V_m \qquad (3.3.2)$$

where σ_f and σ_m are the stress in the fibres and matrix. When the applied strain ε exceeds the ultimate strain of the matrix ε_{mu}, the matrix will crack. At the crack plane, the load on the composite is entirely borne by the fibres. The fibre will fail at the crack plane if the fibres are unable to sustain the load:

$$\left(\sigma_c = \sigma_{mu} V_m + \sigma'_f V_f\right) \geq \sigma_{fu} V_f \qquad (3.3.3)$$

Here, σ'_f is the stress in the fibres when the matrix breaks. It includes the additional load transferred from the cracked matrix. However if fibres are able to bear the load transferred from the cracked matrix, i.e.

$$\left(\sigma_c = \sigma_{mu} V_m + \sigma'_f V_f\right) < \sigma_{fu} V_f \qquad (3.3.4)$$

the matrix will exhibit multiple matrix cracking and the composite will have a non-linear stress-strain response. The stress-strain responses for multiple matrix cracking and single crack failure are shown schematically in Fig 3.3-1. The inequality given by eqn (3.3.4) indicates that there is a critical fibre volume fraction V_f at which single fracture changes to multiple fracture:

$$V_{f\,\mathrm{crit}} > \frac{\sigma_{mu} + \sigma_{fu}}{\sigma_{fu} - \sigma_{mu} - \sigma'_f} \qquad (3.3.5)$$

which is schematically shown in Fig 3.3-2.

To describe the non-linear stress-strain response of the composite during multiple matrix cracking, ACK developed a shear-lag model, which is shown in Fig 3.3-3. The fibre-matrix interface is assumed to be unbonded and is frictionally constrained from slipping. At the crack plane ($x = 0$), the stress in the matrix is zero. This is because the stress borne in the matrix is totally transferred to the fibres. Following eqn (3.3.4), the total stress in the fibres at the crack plane is:

$$\sigma_f\Big|_{x=0} = \frac{\sigma_c}{V_f} = \sigma'_f + \sigma_{mu}\frac{V_m}{V_f} = \sigma'_f + \Delta\sigma \qquad (3.3.6)$$

where $\sigma_{mu}(V_m/V_f) = \Delta\sigma$ is the stress transferred onto the fibres. If the frictional shear stress τ at the fibre-matrix interface is constant, the transferred stress will be linearly transmitted back to the matrix by friction as $x \rightarrow x'$, such that at $x = x'$, the stress in the matrix and fibres is:

$$\sigma_m\Big|_{x=x'} = \sigma_{mu} \quad \text{and} \quad \sigma_f\Big|_{x=x'} = \sigma'_f \qquad (3.3.7)$$

Equilibrating the axial forces on the fibres over the region $0 \le x \le x'$, i.e.

$$F_{x=0} + dF = F_{x=x'} \qquad (3.3.8)$$

or
$$\pi r_o^2\left(\sigma'_f + \sigma_{mu}\frac{V_m}{V_f}\right) - 2\pi r_o x'\tau = \pi r_o^2\sigma'_f \qquad (3.3.9)$$

the critical distance x' to transfer load is defined as:

$$x' = \frac{\sigma_{mu}r_o}{2\tau}\left(\frac{V_m}{V_f}\right) \qquad (3.3.10)$$

ACK analysis shows that the minimum distance separating a new crack from the original crack cannot be less than x'. If another crack occurs at a distance less than $2x'$ from the original crack, the stress in the matrix would not reach the ultimate stress of the fibre and this prevents the creation of a new crack between the two existing cracks. As such, the minimum crack separation distance at saturation for multiple matrix cracking lies between x' and $2x'$. Kimber and Keer (1982) have used a statistical analysis to show that the matrix crack separation distance at saturation is $1.337x'$ or approximately $4/3x'$, i.e.

$$\overline{x'} \approx \frac{3\sigma_{mu}r_o}{2\tau}\left(\frac{V_m}{V_f}\right) \qquad (3.3.11)$$

Assuming that the matrix cracking strain is constant, matrix cracking will occur at a constant composite stress of $E_c\varepsilon_{mu}$ until the matrix is saturated with cracks with

separation distances between x' and $2x'$. At the matrix crack, the additional strain induced in the fibres $\Delta\varepsilon$ is:

$$\Delta\varepsilon = \frac{\Delta\sigma}{E_f} = \frac{\sigma_{mu}}{E_f}\left(\frac{V_m}{V_f}\right) = \varepsilon_{mu}\left(\frac{E_m V_m}{E_f V_f}\right) = \varepsilon_{mu}\alpha \qquad (3.3.12)$$

where $\Delta\sigma$ is defined in eqn (3.3.6) and

$$\alpha = \frac{V_m E_m}{V_f E_f} \qquad (3.3.13)$$

Over a crack separation distance of $2x'$, the average strain induced in the fibres is $\alpha\varepsilon_{mu}/2$. When the crack separation is x', the distance over which the fibre transmit stress back into the matrix is halved. As such, at a distance $x'/2$ from the crack plane, half of the transmitted matrix stress will remain within the fibres and the average stress transferred into the fibres is $\Delta\sigma = 3\sigma_{mu}(V_m/V_f)/4$. Substituting for eqn (3.3.12), the corresponding average strain induced in the fibre is $3\alpha\varepsilon_{mu}/4$. Consequently, the total strain of the composite at matrix cracking saturation $\varepsilon_{mc(sat)}$ is bounded by:

$$\varepsilon_{mu}\left(1+\frac{\alpha}{2}\right) < \varepsilon_{mc(sat)} < \varepsilon_{mu}\left(1+\frac{3\alpha}{4}\right) \qquad (3.3.14)$$

When further load is applied to the composite, the fibres will elongate resulting in sliding between the matrix and fibres so that the cracked matrix bears no additional load. Only the fibres are capable of sustaining additional load applied after matrix crack saturation. At this stage, the composite's Young's modulus becomes $E_f V_f$ and failure of the composite occurs when the fibres break, i.e. $\sigma_{cu} = V_f\sigma_{fu}$. Upper and lower bounds for the composite failure strain ε_{cu} are obtained using the crack separation distance at saturation of $2x'$ and x'. Solving for the composite modulus:

$$V_f E_f = \frac{\sigma_{fu}V_f - E_c\varepsilon_{mu}}{\left(\varepsilon_{cu} - \varepsilon_{mc(sat)}\right)} \qquad (3.3.15)$$

The bounds for the composite failure strain after substituting eqn (3.3.14) into eqn (3.3.15) are:

$$\left(\varepsilon_{fu} - \frac{\alpha\varepsilon_{mu}}{2}\right) < \varepsilon_{cu} < \left(\varepsilon_{fu} - \frac{\alpha\varepsilon_{mu}}{4}\right) \qquad (3.3.16)$$

The stress-strain curve resulting from the ACK analysis is shown in Fig 3.3-4.

Aveston and Kelly (1973) extended ACK analysis by considering fibre-matrix interfaces that remain bonded during matrix cracking. In this case, the interfacial shear stress τ is assumed a function of the distance x along the fibre. Consequently, the stress

transferred onto the fibres due to matrix cracking is also a function of the distance x. Following the shear-lag analysis, see Fig 3.3.5, the transferred matrix stress $\Delta\sigma$ and the shear stress τ as a function of x are:

$$\Delta\sigma = \Delta\sigma_o \exp\left(-\sqrt{\phi}x\right) \tag{3.3.17}$$

and

$$\tau = \frac{r_o}{2}\Delta\sigma_o \sqrt{\phi}\ \exp\left(-\sqrt{\phi}x\right) \tag{3.3.18}$$

where

$$\sqrt{\phi} = \left(\frac{2G_m E_c}{E_f E_m V_m}\right)^{1/2} \frac{1}{r_o\left[\ln\left(R/r_o\right)\right]^{1/2}} \tag{3.3.19}$$

Here, G_m denotes the shear modulus of the matrix and $2R$ is the centre-to-centre separation of the fibres. For a hexagonal array $R = r_o\left[\pi/2\sqrt{3}\,V_f\right]^{1/2}$. The symbol $\Delta\sigma_o$ denotes the stress transferred onto the fibres at the matrix crack plane which is given as:

$$\Delta\sigma_o = \sigma - E_f\varepsilon_{mu} \tag{3.3.20}$$

following eqn (3.3.6) in which σ denotes the applied stress. Importantly, the interfacial shear stress τ is independent of the fibre radius r_o due to the perfect bonding at the fibre-matrix interface. This differs significantly from the case where the fibre-matrix interface is not bonded. Further the maximum interfacial shear stress τ, i.e. τ_{max}, occurs at $x = 0$:

$$\tau\big|_{x=0} = \tau_{\max} = \frac{\Delta\sigma_o \sqrt{\phi}\, r_o}{2} \tag{3.3.21}$$

The fundamental equilibrium equation governing load transfer between the fibres and the matrix can be re-written generally as:

$$\frac{dF}{dx} = \frac{2V_f\tau}{r_o} \tag{3.3.22}$$

Substituting for eqn (3.3.18), the axial force F in the cracked matrix, as a function of distance l from the crack surface, is given as:

$$F = V_f\Delta\sigma_o\left[1 - \exp\left(-\sqrt{\phi}\,x\right)\right] \tag{3.3.23}$$

The relation shows that multiple matrix cracking can only occur if $\Delta\sigma_o$ increases. For small increments of $\Delta\sigma_o$, the crack spacing would be between the critical load transfer distance x' and $2x'$. The critical load transfer distance x' can be determined by letting $F = \sigma_{mu}V_m$, when:

$$x' = -\frac{1}{\sqrt{\phi}} \ln\left(1 - \frac{\sigma_{mu} V_m}{\Delta\sigma_o V_f}\right) \tag{3.3.24}$$

If $\Delta\sigma_o$ is greater than $\sigma_{mu} V_m / V_f$, the critical load transfer distance x' reduces to:

$$x' = \frac{1}{\sqrt{\phi}} \frac{\sigma_{mu} V_m}{\Delta\sigma_o V_f} \tag{3.3.25}$$

Essentially, the critical load transfer distance x' for the bonded case is the same as the critical load transfer distance x' for the unbonded case. The interfacial shear stress τ in eqn (3.3.10) is replaced by $\Delta\sigma_o \sqrt{\phi}\, r_o / 2$, which is the maximum shear stress τ_{max} at the fibre-matrix interface (see eqn (3.3.21)).

The critical load transfer distance x' given by eqn (3.3.24) allows the stress-strain response of the brittle matrix composite during multiple matrix cracking to be deduced. This can be achieved by determining the average additional strain increment in the fibres (or the composite) due to each matrix cracking event, i.e.:

$$\Delta\varepsilon = \frac{\Delta w}{x'} \tag{3.3.26}$$

Here, Δw denotes the total additional displacement of the fibres during a single matrix crack event which is defined as:

$$\Delta w = 2\int_0^{x'/2} \frac{\Delta\sigma}{E_f} dx = \frac{2\,\Delta\sigma_0}{E_f \sqrt{\phi}} \left\{1 - \left(1 - \frac{\sigma_{mu} V_m}{\Delta\sigma_0 V_f}\right)^{1/2}\right\} \tag{3.3.27}$$

Substituting eqn (3.3.24 & 27) into eqn (3.3.26) gives

$$\Delta\varepsilon = -\frac{2\,\Delta\sigma_0}{E_f} \left\{\frac{1 - \left(1 - \sigma_{mu} V_m / \Delta\sigma_0 V_f\right)^{1/2}}{\ln\left(1 - \sigma_{mu} V_m / \Delta\sigma_0 V_f\right)}\right\} \tag{3.3.28}$$

This expression shows that the additional strain increment in the composite is initially zero when a matrix crack forms. As $\Delta\sigma_o$ increases, the additional strain increment $\Delta\varepsilon$ increases to $\Delta\sigma_o / E_f$. The predicted stress-strain curves of steel reinforced Portland cement with perfectly bonded and unbonded fibre-matrix interface is shown in Fig 3.3.6 following Aveston & Kelly (1973). The predicted stress-strain curves show that the bonded interface analysis allows the stress in the matrix cracked region of the stress-strain curve to increase smoothly towards final failure of the composite. In the case of unbonded interfaces, a smooth increase in the matrix cracking region of the stress-strain curve is only possible if the matrix cracking strain is taken to be statistically distributed.

3.4 Matrix Crack Initiation

The initiation of matrix cracking is an important feature of fibre reinforced brittle matrix composites. It signifies the start of permanent damage to the matrix and results in the exposure of the fibres to environmental attack, e.g. corrosion and oxidation. In this section, the theoretical approaches used to predict matrix cracking initiation in unidirectional fibre reinforced brittle matrix composites are reviewed. These approaches can be divided into two categories: *energy balance approaches* and *fracture mechanics approaches*.

3.4.1 Energy Balance Approach

In the energy balance approach, the initiation of matrix cracking is predicted by an energy balance before and after a matrix crack is formed. The displacement at the crack surfaces is assumed to be uniform and the fibres bridging the crack remain intact, i.e. *steady-state matrix cracking*. The argument was originally introduced by ACK when analysing the tensile behaviour of unidirectional fibre reinforced brittle matrix composites loaded in the fibre direction (see Sect. 3.3). Steady-state matrix cracking is postulated to occur if the external work done ΔW equals or exceeds the energy consumed during the internal matrix cracking processes, i.e.

$$\left(U_c + \gamma_{db} + U_s + \Delta U_f - \Delta U_m\right) \leq \Delta W \tag{3.4.1.1}$$

Here, U_c is the matrix crack surface energy consumed and is given as:

$$U_c = 2\gamma_m V_m \tag{3.4.1.2}$$

in which γ_m is the fracture work required to form a crack surface in the matrix. The energy γ_{db} consumed to debond all fibres bridging a unit area of the matrix crack over the critical load transfer distance of $2x'$ is given as:

$$\gamma_{db} = \frac{2G_{II}\sigma_{mu}V_m}{\tau} \tag{3.4.1.3}$$

in which G_{II} is the critical energy required to debond a unit area of fibre-matrix interface. The increase in strain energy of the fibres ΔU_f after overcoming the constant frictional stress τ at the fibre-matrix interface is given as:

$$\Delta U_f = \frac{E_f E_m V_m}{2\tau}\varepsilon_{mu}^3 \alpha r_o \left(1+\frac{\alpha}{3}\right) \tag{3.4.1.4}$$

and the loss in matrix strain energy ΔU_m due to the strain relaxation in the fibre direction is:

$$\Delta U_m = \frac{E_f E_m V_m}{3\tau} \varepsilon_{mu}^3 \alpha r_o \qquad (3.4.1.5)$$

The energy dissipated due to frictional sliding U_s per unit area of the matrix crack is:

$$U_s = \frac{E_f E_m V_m}{6\tau} \varepsilon_{mu}^3 \alpha r_o (1+\alpha) \qquad (3.4.1.6)$$

The work done ΔW by the applied stress to create a steady-state matrix crack is given as:

$$\Delta W = \frac{E_f E_m V_m}{2\tau} \varepsilon_{mu}^3 \alpha r_o (1+\alpha) \qquad (3.4.1.7)$$

Substituting eqn (3.4.1.2 to 7) in eqn (3.4.1.1) gives:

$$2V_m \left(\gamma_m + G_{II} \frac{\sigma_{mu}}{\tau} \right) \leq \frac{E_c E_f \varepsilon_{mu}^3 \alpha^2 r_o}{6\tau} \qquad (3.4.1.8)$$

If the debond energy of the fibre-matrix interface G_{II} is assumed to equal the surface energy for a matrix crack γ_m, eqn (3.3.1.8) can be re-written as:

$$2V_m \gamma_m \left(1 + \frac{\sigma_{mu}}{\tau} \right) \leq \frac{E_c E_f \varepsilon_{mu}^3 \alpha^2 r_o}{6\tau} \qquad (3.4.1.9)$$

If the fibre-matrix interface is purely frictional, i.e. $G_{II} = 0$, the lower limit to eqn (3.4.1.8) is:

$$2V_m \gamma_m \leq \frac{E_c E_f \varepsilon_{mu}^3 \alpha^2 r_o}{6\tau} \qquad (3.4.1.10)$$

which gives the strain to initiate steady-state matrix cracking as:

$$\varepsilon_{mu} = \left(\frac{12 \tau \gamma_m E_f V_f^2}{E_c E_m^2 r_o V_m} \right)^{\frac{1}{3}} \qquad (3.4.1.11)$$

Eqn (3.4.1.11) indicates that the strain to initiate matrix cracking increases if the fibre radius r_o is decreased or if the frictional stress at the interface τ is increased. For sufficiently low r_o or high τ, matrix cracking can be suppressed and the composite would be brittle.

Aveston and Kelly (1973) extended the ACK analysis to predict the strain to initiate steady-state matrix cracking with perfectly bonded fibre-matrix interface. Since

no energy is consumed for debonding or frictional sliding, the energy criterion given in eqn (3.4.1.1) simplifies to:

$$U_c \leq \Delta W \tag{3.4.1.12}$$

The work done ΔW by the applied stress to create a steady-state matrix crack is given by the product of the stress in the composite $E_c\varepsilon_{mu}$ and increased fibre length Δw due to the transferred stress $\Delta\sigma_o = \sigma_{mu}V_m/V_f$, in which

$$\Delta w = 2\int_0^\infty \frac{\Delta\sigma}{E_f}dx = \frac{2}{E_f}\int_0^\infty \Delta\sigma_o \exp\left(-\sqrt{\phi}x\right)dx = \frac{2\Delta\sigma_o\phi^{-1/2}}{E_f} = 2\alpha\varepsilon_{mu}\phi^{-1/2} \tag{3.4.1.13}$$

using eqn (3.3.13 & 17). The work done by the applied stress is given as:

$$\Delta W = E_c\varepsilon_{mu}\Delta w = E_c\varepsilon_{mu}^2\alpha\phi^{-1/2} \tag{3.4.1.14}$$

and eqn (3.4.1.12) is re-written as:

$$2\gamma_m V_m \leq E_c\varepsilon_{mu}^2\alpha\phi^{-1/2} \tag{3.4.1.15}$$

The strain to initiate steady-state matrix cracking with perfectly bonded fibre-matrix interface is then given as:

$$\varepsilon_{mu} = \left[\frac{2\gamma_m V_m\phi^{1/2}}{\alpha E_c}\right]^{1/2} = \left[\frac{2\gamma_m V_m}{r_o\alpha E_c}\left(\frac{2G_m E_c}{\beta E_f E_m V_m}\right)^{1/2}\right]^{1/2} \tag{3.4.1.16}$$

where $\beta = \ln(R/r_o)$. The ratio of the strain initiating a matrix crack with perfectly bonded interface (eqn (3.4.1.16)) to the unbonded case (eqn (3.4.1.11)) is:

$$\frac{\varepsilon_{mu(AK)}}{\varepsilon_{mu(ACK)}} = \sqrt{\frac{\sigma_{mu}}{3\tau}} \tag{3.4.1.17}$$

If $\tau < \sigma_{mu}/3$, the strain to initiate a matrix crack with perfectly bonded fibre-matrix interface would be greater than the unbonded case.

Budiansky, Hutchinson and Evans (1986) have generalised the approaches developed by ACK and Aveston & Kelly (1973) using the principle of virtual work and the shear-lag model developed by Aveston & Kelly (1973). Partial debonding was allowed and the effects of thermal stresses were considered in the analysis. A schematic diagram of the virtual steady-state crack extension model used is shown in Fig 3.4-1. Initially, the composite contains a steady state matrix crack of length s in a wide specimen of width W and unit thickness and length $2L$. The matrix crack is then allowed to virtually advance a distance Δs from the initial crack front CC to the new crack front $C'C'$ in which that the average applied stress σ remains constant. This means the

stresses at the crack front, averaged through the thickness, remains unchanged during crack growth, and the stress states far ahead of and behind the crack front (hereafter, upstream and downstream stress-state) do not change. Assuming that the composite is elastic and solving the net upstream and downstream potential energy per unit cross-sectional area of the composite during steady-state matrix crack propagation, the steady-state matrix crack stress of a composite is generally given as:

$$\sigma_{mc} = \sigma_o - \frac{E_c}{E_m}{}^r\sigma_m \tag{3.4.1.18}$$

where ${}^r\sigma_m$ is the axial residual stress in the matrix.

For composites with unbonded fibre-matrix interfaces that are constrained with a constant interfacial frictional shear stress τ,

$$\sigma_o = \left(\frac{6\tau G_m V_f^2 E_f E_c^2}{V_m E_m^2 r_o} \right)^{1/3} \tag{3.4.1.19}$$

and for composites with bonded fibre-matrix interfaces,

$$\sigma_o = \left(\frac{V_f E_f E_c^2 G_{\mathrm{I}} \sqrt{\phi}}{E_m} \right)^{1/2} \tag{3.4.1.20}$$

where $\sqrt{\phi}$ is defined in eqn (3.3.19) and G_I denotes the critical mode I matrix fracture energy release rate. If initially no residual stresses exist in the matrix, i.e. ${}^r\sigma_m = 0$, the matrix cracking stresses predicted in eqn (3.4.1.19 and 20) are essentially the equivalent result of ACK for the unbonded case and Aveston & Kelly (1973) for the bonded case. For composites with initially bonded-debonding fibres,

$$\sigma_o = B\left[\frac{6V_f^2 G_I E_f E_c^3}{V_m^2 E_m (1+\nu_m) r_o} \right]^{1/4} \left[\frac{1 + \left(\frac{4V_f l_d G_{\mathrm{II}}}{V_m r_o G_{\mathrm{I}}} \right)}{1 + \frac{B^2}{V_m} \left[\frac{6E_c}{E_f (1+\nu_m)} \right]^{1/2} \left(\frac{l_d}{r_o} \right)} \right]^{1/2} \tag{3.4.1.20}$$

where
$$B = \left(\frac{V_m}{6 \log \overline{R}/r_o} \right)^{1/4} \tag{3.4.1.21}$$

and
$$\log \overline{R}/r = - \frac{2\log V_f + V_m (3 - V_f)}{4V_m^2} \tag{3.4.1.22}$$

According to Budiansky, Hutchinson and Evans (1986), the composite matrix cracking stress during debonding is expected to be less than the bonded case given in eqn (3.4.1.20).

In the limit, the matrix cracking strain ε_{mc} and stress σ_{mc} estimated using the energy balance approach apply only if the matrix cracking stress is single valued and independent of pre-existing crack size. In practice, however, the matrix is brittle which means that the matrix cracking stress σ_{mc} is both sensitive to the distribution of pre-existing flaws and flaw sizes. This implies that *non-steady state matrix cracking* can occur, however this possibility has not been considered by ACK, Aveston & Kelly (1973) or Budiansky, Hutchinson and Evans (1986). To overcome the limitation from the energy balance approaches, stress-intensity approaches have been developed and are reviewed next.

3.4.2 Stress Intensity Approach

Marshall, Cox & Evans (1985) first used a *stress-intensity approach* to analyse the stress required to initiate non-steady-state and steady-state matrix cracking. Essentially, a matrix crack bridged by the fibres in a uni-directional fibre reinforced composite can be represented as a semi-infinite crack centrally located in an infinite homogeneous elastic body which is subjected to a uniform far-field stress σ_∞ and an opposing closure pressure

$$p(X) = T(X)V_f \qquad (3.4.2.1)$$

at the crack surface, as shown in Fig 3.4.2-1. Here, *T(X)* denotes the closure traction applied by the bridging fibres along the normalised crack surface position *X*, which is the ratio of the distance *x* along the crack surface and the half-crack length *a*. The net pressure at the crack surface is the difference between the far-field stress σ_∞ and the fibre pressure *p(X)*.

Following Lawn & Wilshaw (1975) and Sih (1973), the effective stress intensity of the composite K^c can be approximated as:

$$K^c = 2\sqrt{\frac{a}{\pi}} \int_0^1 \frac{[\sigma_\infty - p(X)]}{\sqrt{1-X^2}} dX \qquad (3.4.2.2a)$$

if the matrix crack is straight or

$$K^c = 2\sqrt{\frac{a}{\pi}} \int_0^1 \frac{[\sigma_\infty - p(X)]X}{\sqrt{1-X^2}} dX \qquad (3.4.2.2b)$$

if the matrix crack is penny shaped and K^c is a function of the matrix stress intensity K^m. To determine the relationship between K^c and K^m, Marshall, Cox & Evans (1985) assumed that just ahead of the crack-tip the composite and matrix strain are equal and the composite and matrix stress intensities scale with the stresses. This implies that:

$$K^c = K^m \left(E_c / E_m\right) \qquad (3.4.2.3)$$

Crack propagation in the matrix occurs when the stress intensity factor of the matrix K^m reaches a critical value, i.e. K^m_{IC}. Similarly, matrix crack propagation in the composite occurs when:

$$K^c = K^c_{IC} = K^m_{IC}\left(E_c / E_m\right) \qquad (3.4.2.4)$$

By substituting eqn (3.4.2.4) in eqn (3.4.2.2), the far field stress required to initiate matrix cracking, i.e. $\sigma_\infty = \sigma_{mc}$, can be found.

However, before eqn (3.4.2.4) and eqn (3.4.2.2) is solved, the crack closure pressure *p(X)* given in eqn (3.4.2.1) must be defined. For a composite with unbonded frictionally constrained fibre-matrix interfaces, the fibre traction *T(X)* along the crack surface has been defined as:

$$T(X) = A\ \sqrt{u(X)} \qquad (3.4.2.5)$$

where
$$A = 2\left(E_f \tau \left(1+\alpha^{-1}\right)/r_o\right)^{1/2} \qquad (3.4.2.6)$$

Here, E_f is the elastic modulus of the fibres, τ is the constant frictional stress at the fibre-matrix interface, r_o is the fibre radius, α is the elastic constant given in eqn (3.3.13) and *u(X)* is the crack surface displacement as a function of the normalised distance *X*. For steady-state matrix cracking *u(X)* is constant. The fibre traction - crack opening displacement relation, given in eqn (3.4.2.5), was derived based on the ACK shear-lag analysis for steady-state matrix cracking (see eqn (3.3.6 to 13)). Along the crack surface, Sneddon & Lowengrub (1969) give the crack surface displacement as:

$$u(X) = \frac{4a\left(1-\nu^2\right)}{\pi E_c} \int_X^1 \frac{s}{\sqrt{s^2 - X^2}} \times \int_s^s \frac{\left[\sigma_\infty - p(t)\right]dt}{\sqrt{s^2 - t^2}}\, ds \qquad (3.4.2.7a)$$

if the matrix crack is straight or

$$u(X) = \frac{4a\left(1-\nu^2\right)}{\pi E_c} \int_X^1 \frac{1}{\sqrt{s^2 - X^2}} \times \int_s^s \frac{\left[\sigma_\infty - p(t)\right]t\, dt}{\sqrt{s^2 - t^2}}\, ds \qquad (3.4.2.7b)$$

if the matrix crack is penny shaped. Here, *s* and *t* denotes normalised position co-ordinates and ν denotes the Poisson's ratio of the composite.

Marshall, Cox & Evans (1985) have estimated that the stress to initiate steady-state matrix cracking is:

$$\sigma_{mc} = \delta' \left[\frac{\left(1-\nu^2\right) K_{IC}^{m\,2}\, \tau E_f V_f^2 V_m \left(1+\alpha^{-1}\right)^2}{E_m r_o} \right]^{1/3} \qquad (3.4.2.8)$$

where δ' is a dimensionless constant. Defining the transient crack length, i.e. the distance from the crack-tip before the crack surface displacement becomes uniform, as:

$$a_o = \left(\frac{\pi K_{IC}^{c}}{1.44 V_f^2 \omega} \right)^{2/3} \qquad (3.4.2.9)$$

in which

$$\omega = \frac{8\left(1-\nu^2\right)\tau V_f^2 E_f \left(1+\alpha^{-1}\right)}{\sqrt{\pi} E_c r_o} \qquad (3.4.2.10)$$

non-steady state matrix cracking was shown to occur if a pre-existing matrix crack length was less than $\sim a_o/3$. In that region, the stress inducing crack propagation was shown to increase as the pre-existing crack length decreases.

The stress intensity approach by Marshall, Cox & Evans (1985) is however questionable. The equal stress or strain condition assumed just ahead of the crack-tip to derive the stress intensity relations given in eqn (3.4.2.3 and 4) is arbitrary and possibly inappropriate. Stress concentration at the crack-tip can cause the stress and strain fields to be non-uniform. As such, the equal strain condition assumed for the composite and matrix may not be valid. McCartney (1987) has shown that the effective stress intensities of the composite given in eqn (3.4.2.3 and 4) are energetically inconsistent based on an energy balance framework. Instead, the effective critical stress intensity of the composite in eqn (3.4.2.4) should be:

$$K^c = K_{IC}^c = K_{IC}^m \left(V_m E_c / E_m\right)^{1/2} \qquad (3.4.2.11)$$

where

$$K_{IC}^m = \left(2\gamma_m E_m / 1-\nu^2\right)^{1/2} \qquad (3.4.2.12)$$

which is $\left(E_c / V_m E_m\right)^{1/2}$ times the estimate by Marshall, Cox & Evans (1985). When implemented into the stress intensity framework introduced by Marshall, Cox & Evans (1985), the McCartney (1987) analysis shows that the stress required to initiate steady-state matrix cracking is:

$$\sigma_{mc} = \left[\frac{3 V_m \gamma_m E_c \lambda^2}{2\pi\left(1-\nu^2\right)} \right]^{1/3} \qquad (3.4.2.13)$$

where $$\lambda = 2\frac{V_f}{V_m}\left(\frac{2\pi E_f E_c}{r_o E_m^2}\right)^{1/2} \qquad (3.4.2.14)$$

and the transition crack length is:

$$a_o = \left(\sqrt{\pi} K_{IC}^{c} / \lambda^2\right)^{2/3} \qquad (3.4.2.15)$$

The steady-state matrix cracking stress is identical to the estimate by ACK for plane strain condition. Non-steady state matrix cracking is shown to occur if the pre-existing crack lengths are less than ~$10a_o$.

Danchaivijit & Shetty (1993) have questioned the fibre traction - crack opening displacement relation given in eqn (3.4.2.5). They argued that the mechanics used to derive the traction-displacement relation is valid only during steady-state matrix cracking. However, near the crack-tip, a transient region exist in which non-steady state matrix cracking occurs. As such, eqn (3.4.2.5) is inappropriate. To improve the stress intensity approach, Danchaivijit & Shetty (1993) introduced a modified shear lag model to include the transient effects near the crack-tip. The new fibre traction - crack opening displacement relation is given as:

$$T = \frac{\sigma_\infty}{2\alpha V_f\left(1+\alpha^{-1}\right)}\left\{\left[1+\frac{16\left(1+\alpha^{-1}\right)^2\alpha^2 E_f V_f^2\,\tau u}{\sigma_\infty r_o}\right]^{1/2}+1\right\} \qquad (3.4.2.16)$$

In addition, by using the effective critical stress intensity relation developed by McCartney (1987), i.e. eqn (3.4.2.12), the steady-state matrix cracking stress was estimated to be:

$$\sigma_{mc} = \left[\frac{12\left(1-\nu^2\right)K_{IC}^{m\,2}\,\tau E_f V_f^2 V_m\left(1+\alpha^{-1}\right)^3}{E_m r_o\left(2+3\alpha^{-1}\right)}\right]^{1/3} \qquad (3.4.2.17)$$

and the transient crack length was defined as:

$$a_o = \pi\left(\frac{K_{IC}^{c}}{\zeta}\right)^{2/3} V_m^2\left(1+\alpha^{-1}\right)^2 \qquad (3.4.2.18)$$

in which $$\zeta = \frac{6\left(1-\nu^2\right)\tau V_m V_f^2 E_f\left(1+\alpha^{-1}\right)^2}{E_m r_o} \qquad (3.4.2.19)$$

Compared to the analysis of Marshall, Cox & Evans (1985) and McCartney (1987), an important result of Danchaivijit & Shetty (1993) is that the critical crack length for non-steady state matrix cracking is dependent on α, i.e. as α decreases the critical crack length for non-steady state matrix cracking increases.

Cao *et al* (1990) have shown that the theoretical steady-state matrix cracking stress correctly estimate the proportional limits for several uni-axially tensioned aligned SiC (Nicalon) fibre reinforced glass and glass-ceramic matrix composites. This was achieved using estimates of the interfacial friction stress independently assessed from the saturation crack spacing on tensile specimens and theoretical estimates of the composite residual stress. The result suggest that the pre-existing flaw length prior to the proportional limit is greater than the critical crack length required for non-steady state matrix cracking. The study by Kim & Pagano (1991) supports the finding of Cao *et al* (1990). However, their study also detected matrix micro-cracking at stresses 35% to 85% of the proportional limit based on acoustic emission and optical microscopy data. To reconcile the discrepancy between experiment and theory, Kim & Pagano (1991) reasoned that the micro-cracking at low stresses is sensitive to non-uniform fibre distribution. In regions where the fibre volume fraction is low or non-existent, the stress to propagate a matrix crack would be less than the matrix cracking stress calculated for the average fibre volume fraction. Numerical results on the matrix cracking stress as a function of crack size for different unbridged zone size in a penny shape crack of a SiC-LAS composite by Shetty (1995) have verified Kim & Pagano's argument. For increasing unbridged zone sizes, the stress required to extend the penny shaped matrix crack was shown to decrease. Hence, matrix microcracking can occur below the steady-state matrix cracking stress. The study by Baaklini & Batt (1991), Beyerle et al (1992), Wang & Parvizi-Maljidi (1992) and Karandikar & Chou (1993) on SiC fibre reinforced ceramic composites also detected the early initiation of micro-cracks which progressively accumulates before reaching the steady-state matrix cracking stress. Consequently, these studies illustrate the limitations of the current steady-state matrix cracking stress analysis.

3.5 Ultimate Tensile Strength

After matrix cracking has saturated, the ultimate failure of a fibre reinforced brittle matrix composite occurs when the fibres are unable to withstand the load on the composite. To predict the ultimate failure, deterministic or statistical approaches can be used.

For simplicity, the ultimate tensile strength of the composite can be estimated by assuming the fibre strength to be single-valued. Following ACK, the ultimate strength of the composite can be defined as:

$$\sigma_{cu} = V_f \sigma_{fu} \tag{3.5.1}$$

where σ_{fu} denotes the ultimate strength of the fibres. Prewo (1986) has compared the results from ACK model with experimental data of a unidirectional SiC-LAS composite. The ultimate strength of the fibres σ_{fu} was determined by individually testing fibres extracted from the composite in uniaxial tension. The strength of the extracted fibres was found to be 30% to 40% lower than the as received fibres. However, comparison with the ultimate tensile strength of the composite after multiplying the measured σ_{fu} with the fibre volume fraction V_f showed good agreement.

Alternatively, statistical approaches can be used. Weibull (1951) first considered the distributive strength characteristic of fibres. Conceptually, a fibre of length L can be likened to a chain with links of incremental lengths ΔL_1, ΔL_2, etc. When subjected to an applied stress σ, failure of the chain occurs when one of the links break, i.e. the fibre breaks when one of the incremental lengths contains n_σ critical number of cracks per unit length – *Weakest Link Theory*. In the first incremental length, the probability of failure can be defined as:

$$P_{F1} = n_\sigma \Delta L_1 \tag{3.5.2}$$

and the probability of survival is:

$$P_{S1} = 1 - P_{F1} \tag{3.5.3}$$

If so, the probability of survival of the entire fibre can be given as the product of the probabilities of survival of each of the N incremental lengths making up the fibre, i.e.

$$P_S = (1 - P_{F1})(1 - P_{F2})....(1 - P_{FN}) \tag{3.5.4}$$

For infinitesimal incremental length, eqn (3.5.4) can be approximated as:

$$P_S = \exp[-(P_{F1} + P_{F2} + ...P_{FN})] = \exp[-Ln_\sigma] \tag{3.5.5}$$

since $(1 - x) \approx \exp(-x)$ when $x << 1$ and substituting from eqn (3.5.2). In addition, for brittle materials, Weibull (1951) proposed that the critical number of crack per unit length sufficient to cause failure is of the form:

$$n_\sigma L_o = \left(\frac{\sigma}{\sigma_o}\right)^m \tag{3.5.6}$$

in which m is called the Weibull modulus and σ_o is a normalising strength expected from a fibre of length L_o. Substituting into eqn (3.5.5), the probability of failure of a fibre of length L for an applied stress σ is:

$$P_F = 1 - \exp\left[-\left(\frac{L}{L_o}\right)\left(\frac{\sigma}{\sigma_o}\right)^m\right] \tag{3.5.7}$$

The distribution of the fibre failure strengths, i.e. the probability density of failure, can be obtain by differentiating eqn (3.5.7) with respect to the stress (σ/σ_o), i.e.

$$p_F = m\frac{L}{L_o}\left(\frac{\sigma}{\sigma_o}\right)^{m-1}\exp\left[-\frac{L}{L_o}\left(\frac{\sigma}{\sigma_o}\right)^m\right] \tag{3.5.8}$$

The role of the Weibull modulus m can be seen from the results obtained from eqn (3.5.7 & 8). For high values of m, a low probability of failure is implied which mean that the fibre is very reliable. Conversely, low values of m would imply a high probability of failure and that the fibre is unreliable. The mean fibre failure stress can be obtained by differentiating the fibre failure probability density function p_F and equating it to zero, which gives

$$\overline{\sigma}_{fu} = \sigma_o\left[\left(1-\frac{1}{m}\right)\left(\frac{L_o}{L}\right)\right]^{1/m} \tag{3.5.9}$$

In the case of a loose bundle of fibres, the failure stress of the bundle is dependent on its fibres (Daniel (1945), Colemen (1958) & Rosen (1970)). When the bundle is stressed, the weaker fibres will break and the load previously borne is transferred to the stronger fibres. If the stronger fibres are able to withstand the load transferred by the broken fibres, the fibre bundle will not break. At a given stress (σ/σ_o), the stress in the bundle is:

$$\frac{\sigma_b}{\sigma_o} = \frac{\sigma}{\sigma_o}(1-P_F) = \frac{\sigma}{\sigma_o}\exp\left[-\frac{L}{L_o}\left(\frac{\sigma}{\sigma_o}\right)^m\right] \tag{3.5.10}$$

The ultimate strength of the bundle is obtained by differentiating eqn (3.5.10) and equating it to zero, i.e.

$$\sigma_{bu} = \sigma_o\left[\frac{1}{m}\left(\frac{L_o}{L}\right)\right]^{1/m} \tag{3.5.11}$$

The ratio of the ultimate bundle strength and the mean fibre strength is:

$$\frac{\sigma_{bu}}{\overline{\sigma}_{fu}} = \left(\frac{1}{m-1}\right)^{1/m} \tag{3.5.12}$$

The strength ratio shows that the ultimate bundle strength is less than the mean strength of a fibre and it decreases as the fibre becomes more unreliable (small values of m). The

reduction in the ultimate bundle strength can be overcome by increasing the number of fibres in the bundle. Daniel (1945) has showed that for a bundle with N number of fibres, the distribution of bundle strength is Gaussian and the standard deviation is proportional to $N^{-\frac{1}{2}}$. Therefore, as N increases to infinity, the deviation in strength reduces which ultimately produces a highly reliable bundle with a single-valued strength. Davidge & Briggs (1989) and Bhatt & Phililps (1990) have used the bundle-mean fibre strength ratio with eqn (3.5.1) to estimate the ultimate strength of SiC-RBSN and Nicalon-BSG composites. Reasonable agreement with experiment was obtained.

In applying the fibre bundle analysis to fibre composites, the load from the broken fibres is assumed to be homogeneously distributed to the unbroken fibres. However, in reality, the matrix does bear some load transferred from the broken fibres. Rosen (1970) has developed a cumulative weakening model to consider the matrix effect. To determine the composite strength, the composite is treated as a string of fibre bundles each with a unit length L_c. For each bundle, the probability of survival below a stress (σ/σ_o) is:

$$(1-P_F) = \exp\left[-\left(\frac{\sigma}{\sigma_o}\right)^m\right] \tag{3.5.13}$$

For a composite L times the unit bundle length L_c, the probability of survival is the product of the probabilities of survival of each of the unit bundle, i.e.

$$(1-P_f)^{\frac{L}{L_c}} = \exp\left[-\frac{L}{L_c}\left(\frac{\sigma}{\sigma_o}\right)^m\right] \tag{3.5.14}$$

By following the argument which leads to eqn (3.5.9), the bundle strength is given as:

$$\sigma_b = \sigma_o\left\{\left[\frac{1}{m}\left(\frac{L_o}{L}\right)\right]^{1/m}\exp\left(-\frac{1}{m}\right)\right\} \tag{3.5.11}$$

The stress in a composite, which allows multiple failure of the fibres, is given as:

$$\sigma_c = V_f\sigma_{fu} + V_m\sigma'_m \tag{3.5.12}$$

where σ'_m denote the stress in the matrix when the fibre breaks. Substituting eqn (3.5.11) into eqn (3.5.12) in place of the maximum fibre stress σ_{fu}, the stress of the composite is estimated to be:

$$\sigma_c = V_f\sigma_o\left\{\left[\frac{1}{m}\left(\frac{L_o}{L}\right)\right]^{1/m}\exp\left(-\frac{1}{m}\right)\right\} + V_m\sigma'_m \tag{3.5.13}$$

The statistical approaches presented so far are not designed specifically for ceramic matrix composites. In such composites, matrix cracking modifies the failure process. To include these effects, Cao & Thouless (1990) have used a statistical and micro-mechanical approach to estimate the composite strength. Assuming that the stress transferred at the fibre-matrix interface is controlled by a constant friction stress τ following ACK, the composite stress is approximated as:

$$\sigma_c = V_f \sum \left[\frac{\sum r_o}{m(m+1)\tau L} \right]^{1/m} \exp\left[-\frac{1}{m} \right] \tag{3.5.14}$$

where $$\sum = \left[\frac{A_o S_o \tau (m+1)}{2\pi r_o^2} \right]^{\frac{1}{m+1}} \quad \text{and} \quad S_o = \sigma_o \left[\frac{2\pi r_o L}{A_o} \right]^{\frac{1}{m}} \tag{3.5.15}$$

Here, L denote gauge length (i.e. the length of the specimen) and A_o is a normalising factor (= 1 m^2). For Nicalon-LAS composites, the agreement between theory and experiment was fairly good.

In the statistical and micro-mechanical approach by Curtin (1991), the ability to consider multiple fibre failure was included. The strength of the composite is given as:

1

$$\sigma_c = V_f S \left(\frac{2}{m+2} \right)^{\frac{1}{m+1}} \frac{m+1}{m+2} \tag{3.5.15}$$

where $$S = \left(\frac{\sigma_o^m \tau L_o}{r_o} \right)^{\frac{1}{m+1}} \tag{3.5.16}$$

The model has been shown to predict the ultimate tensile strength of the different Nicalon-LAS composites reported by Prewo (1986).

3.6 Failure Criteria

Three dominant failure processes may occur when a unidirectional composite is loaded in uniaxial tension at an arbitrary angle to the fibres. These are axial failure, tensile delamination and shear delamination. Schematic diagrams of these processes are shown in Fig 3.6-1. Following the maximum stress theory (Hull & Clyne, 1997), the criteria for these failure processes are:

$$\begin{aligned} \sigma_1 &\geq \sigma_{1u} \\ \sigma_2 &\geq \sigma_{2u} \\ \tau_{12} &\geq \tau_{12u} \end{aligned} \tag{3.6.1}$$

Here, σ_1, σ_2, τ_{12} are the axial, transverse and shear stress components on the composite with respect to the material-position-system 1 and 2 while σ_{1u}, σ_{2u}, τ_{12u} are the corresponding composite strengths. To relate the composite stresses in the material-position-system to the stress system (σ_x, σ_y, τ_{xy}) applied to the composite, the tensor transformation law described by eqn (2.4.12) may be used:

$$\begin{Bmatrix} \sigma_1 \\ \sigma_2 \\ \tau_{12} \end{Bmatrix} = [\boldsymbol{G}] \begin{Bmatrix} \sigma_x \\ \sigma_y \\ \tau_{xy} \end{Bmatrix} \tag{3.6.2}$$

The transformation matrix [$\boldsymbol{G}$] is given by:

$$[\boldsymbol{G}] = \begin{bmatrix} \cos^2\theta & \sin^2\theta & 2\cos\theta\sin\theta \\ \sin^2\theta & \cos^2\theta & -2\cos\theta\sin\theta \\ -\cos\theta\sin\theta & \cos\theta\sin\theta & \cos^2\theta - \sin^2\theta \end{bmatrix} \tag{3.6.3}$$

Here, θ is the angle between the loading axis and the fibre axis of the material-position-system. From these relations, it is possible to determine the stress to cause failure of a misaligned composite. The maximum stress criteria for axial failure, tensile delamination and shear delamination as a function of the loading angle θ is:

$$\begin{aligned} \sigma_x &\geq \frac{\sigma_{1u}}{\cos^2\theta} \\ \sigma_x &\geq \frac{\sigma_{2u}}{\sin^2\theta} \\ \sigma_x &\geq \frac{\tau_{12u}}{\sin\theta\cos\theta} \end{aligned} \tag{3.6.4}$$

The failure surface with respect to the loading angle θ is indicated by the solid line in Fig 3.6-2.

The predictions of anisotropic failure processes for unidirectionally reinforced composites can also be described by the Tsai-Hill criterion (Tsai, 1966). Hill (1950) first proposed this criterion as a modification of the von Mises yield criterion for metals with orthotropic symmetry. In plane stress, the criterion is:

$$\left(\frac{\sigma_1}{\sigma_{1Y}}\right)^2 + \left(\frac{\sigma_2}{\sigma_{2Y}}\right)^2 - \frac{\sigma_1\sigma_2}{\sigma_{1Y}^2} - \frac{\sigma_1\sigma_2}{\sigma_{2Y}^2} + \frac{\sigma_1\sigma_2}{\sigma_{3Y}^2} + \left(\frac{\tau_{12}}{\tau_{12Y}}\right)^2 = 1 \tag{3.6.5}$$

where σ_1, σ_2, τ_{12} are the stress components in the orthotropic material position system and σ_{1Y}, σ_{2Y}, σ_{3Y}, τ_{12Y} are the corresponding orthotropic yield strengths in tension and shear. The criterion was later modified by Tsai (1966) to model transverse-isotropic composites, i.e. $\sigma_{2Y} = \sigma_{3Y}$, where Hill's criterion becomes:

$$\left(\frac{\sigma_1}{\sigma_{1u}}\right)^2+\left(\frac{\sigma_2}{\sigma_{2u}}\right)^2-\frac{\sigma_1\sigma_2}{\sigma_{1u}^2}+\left(\frac{\tau_{12}}{\tau_{12u}}\right)^2=1 \qquad (3.6.6)$$

Here, σ_1, σ_2, τ_{12} are the composite stresses in the material-position system which can be related to an arbitrary applied stress system by the stress transformation given in eqn (3.6.2). In uniaxial tension, i.e. $\sigma_y = \tau_{xy} = 0$, the equation reduces to:

$$\begin{aligned}\sigma_1 &= \sigma_x \cos^2\theta\\ \sigma_2 &= \sigma_x \sin^2\theta\\ \tau_{12} &= -\sigma_x \cos\theta \sin\theta\end{aligned} \qquad (3.6.7)$$

Substituting into eqn (3.4.6), the Tsai-Hill criterion gives the applied stress to cause failure as a function of loading angle as:

$$\sigma_{x(\theta)} = \left[\frac{\cos^2\theta-\left(\cos^2\theta-\sin^2\theta\right)}{\sigma_{1u}^2}+\frac{\sin^4\theta}{\sigma_{2u}^2}+\frac{\cos^2\theta\sin^2\theta}{\tau_{12u}^2}\right]^{-\frac{1}{2}} \qquad (3.6.8)$$

The failure surface predicted by Tsai-Hill's criterion is compared with the maximum stress criterion in Fig 3.6.2.

The attractive feature of Tsai-Hill criterion is that the prediction of failure is compacted into a single expression which is simple to implement computationally. However, the criterion does not indicate a failure mode, in contrast to the maximum stress theory. This short-fall suppresses information necessary for improving the design of composites. Other failure criteria, similar in nature to the Tsai-Hill criterion, have also been proposed. These include the Hoffman failure criterion (Hoffman, 1967) and the Tsai-Wu failure criterion (Tsai & Wu, 1971), which also predicts the strength of a uni-directional composite in uniaxial tension to decrease smoothly as a function of loading angle. This is because the anisotropic strengths are assumed to be interactive, i.e the critical stress to trigger one failure process is affected by the stresses which trigger other failure processes. The interactive nature of the composite strengths has, however, recently been challenged. Hart-Smith (1993) has argued that the failure processes are unrelated (non-interactive) because composites are heterogeneous and the failure processes are different, unlike isotropic metals undergoing plastic deformation. Hence, the failure surface of composites arguably cannot be continuously smooth. Instead, it is more reasonable to expect the number of criterion for failure to correspond with the different failure processes, predicted by the maximum stress criterion.

To date, the issue of the interactive nature of failure criterion for composites is still contentious. A round-robin exercise to asses the merits of different failure criteria

has recently been undertaken by Hinton & Soden (1998). However, the results to compare the predictions of the failure criteria with experimental data are currently not available. The failure criteria considered includes McCartney (1998) fracture-energy-based approach, the mechanistic theory of Puck & Schurmann (1998), Rotem (1998) and Sun and Tao (1998), a strain-energy based-failure theory by Wolfe & Butalia (1998) and the Maximum-Strain and Truncated Maximum-Strain failure theories of Hart-Smith (1998), as well as a micromechanics model developed by NASA (Gotsis, Chamis & Minnetyan, 1998), British design codes for GFRP (Eckold, 1998), and the failure model of the aerospace company AEA (Edge, 1998).

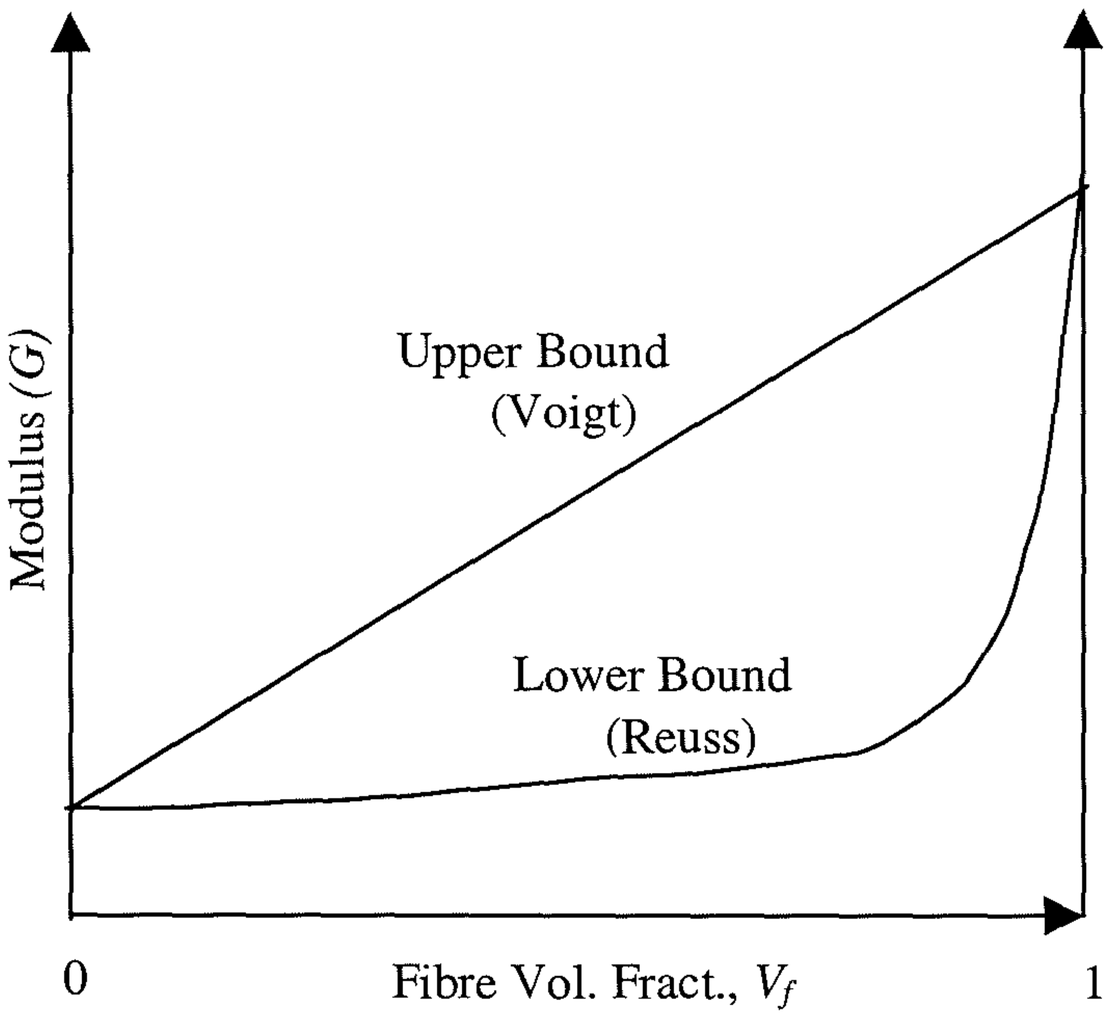

Fig. 3.2-1 Bounds for composite moduli.

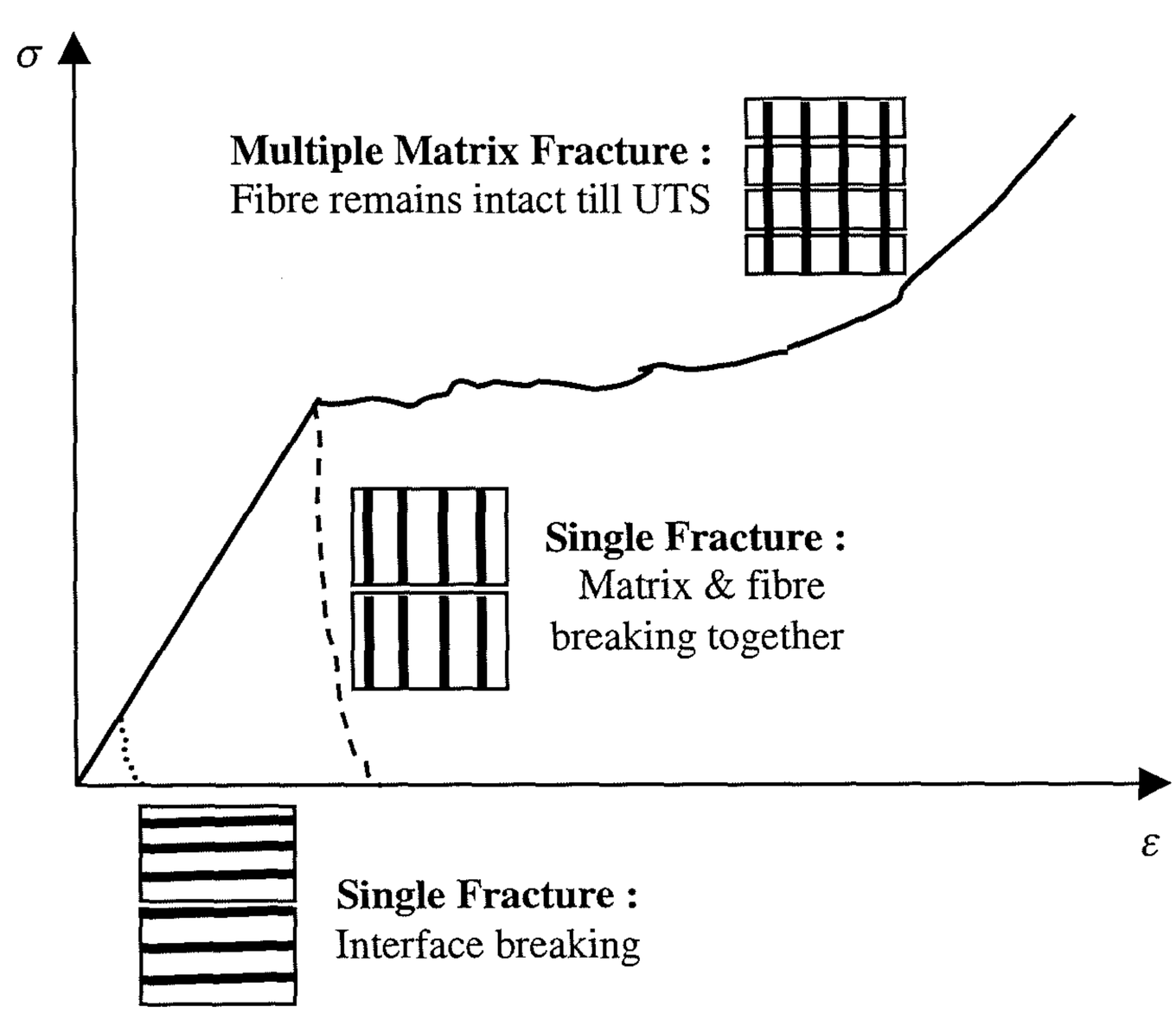

Fig. 3.3-1 Stress-strain behaviours of brittle matrix composite due to single fracture and multiple matrix fracture.

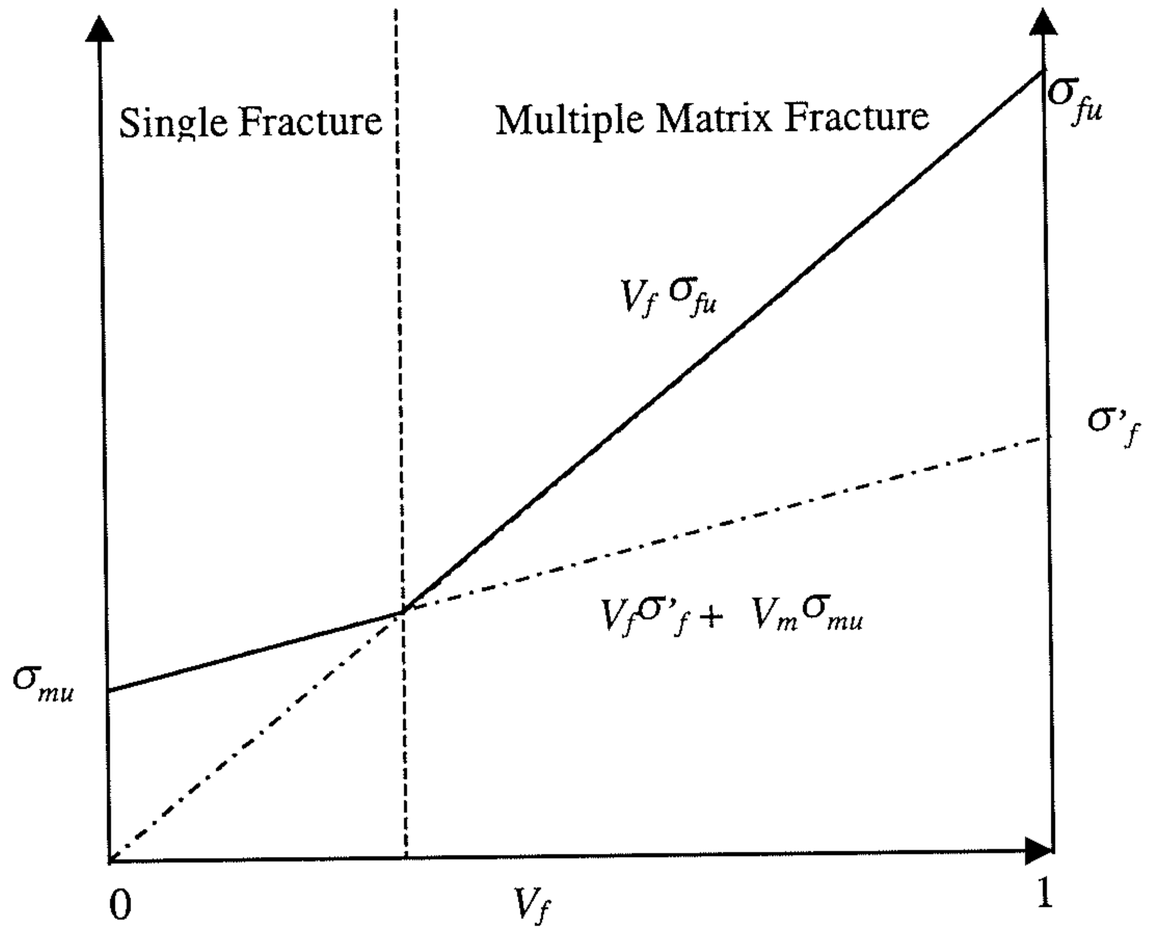

Fig. 3.3-2 Schematic diagram of the transition from single to multiple matrix fracture in ductile-fibre/brittle-matrix composites such that $\varepsilon_{fu} > \varepsilon_{mu}$ and $\sigma_{fu} > \sigma_{mu}$.

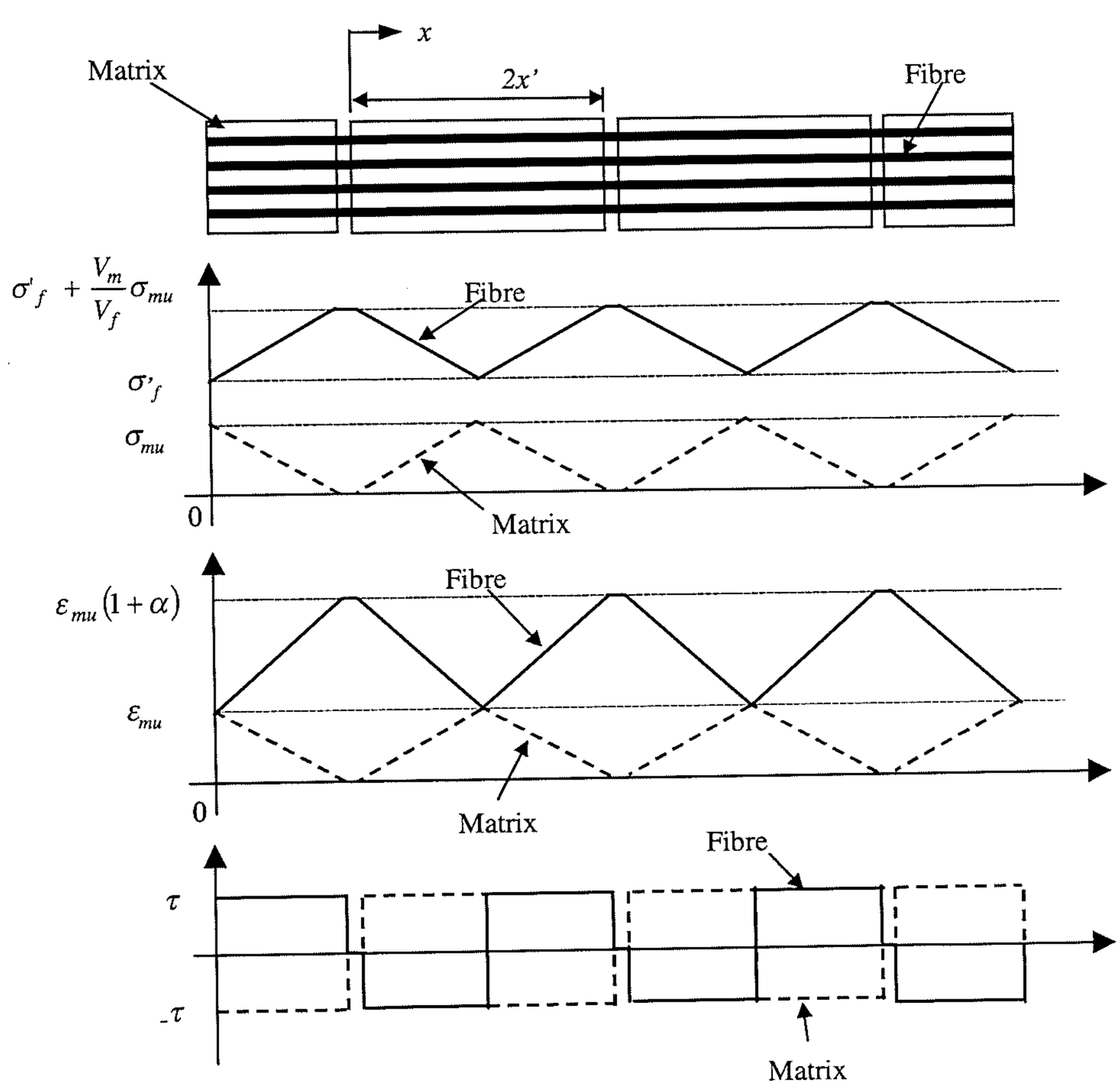

Fig. 3.3-3 Schematic diagram of the shear-lag model by ACK (1971).

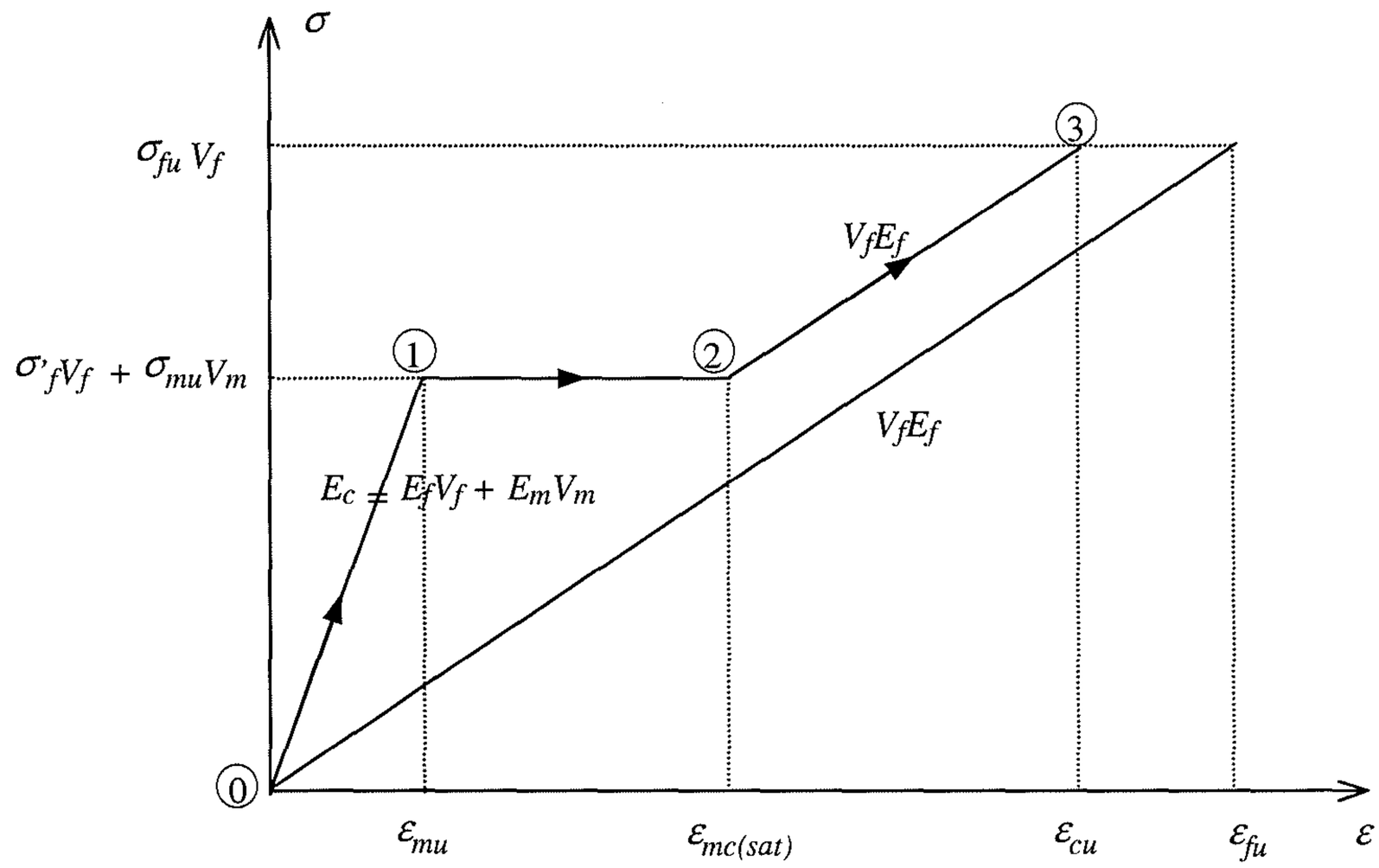

Legend :

σ_{fu} : fracture strength of the fibre.

σ_{mu} : fracture strength of the matrix.

ε_{fu} : fracture strain of the fibre.

ε_{mu} : fracture strain of the matrix.

ε_{cmf} : the composite strain at which multiple matrix cracking saturates .

ε_{cu} : fracture strain of the composite.

σ'_f : stress in fibre reinforcement when the strain of the composite reaches ε_{mu}.

V_f : volume fraction of fibre.

V_m : volume fraction of matrix.

(1) : Initiation of matrix cracking.

(2) : Saturation point of the multiple matrix cracking.

(3) : Final failure of composite due to fibre fracture.

Fig. 3.3-4 Tensile stress-strain curve of a brittle matrix composite during matrix cracking as proposed by ACK.

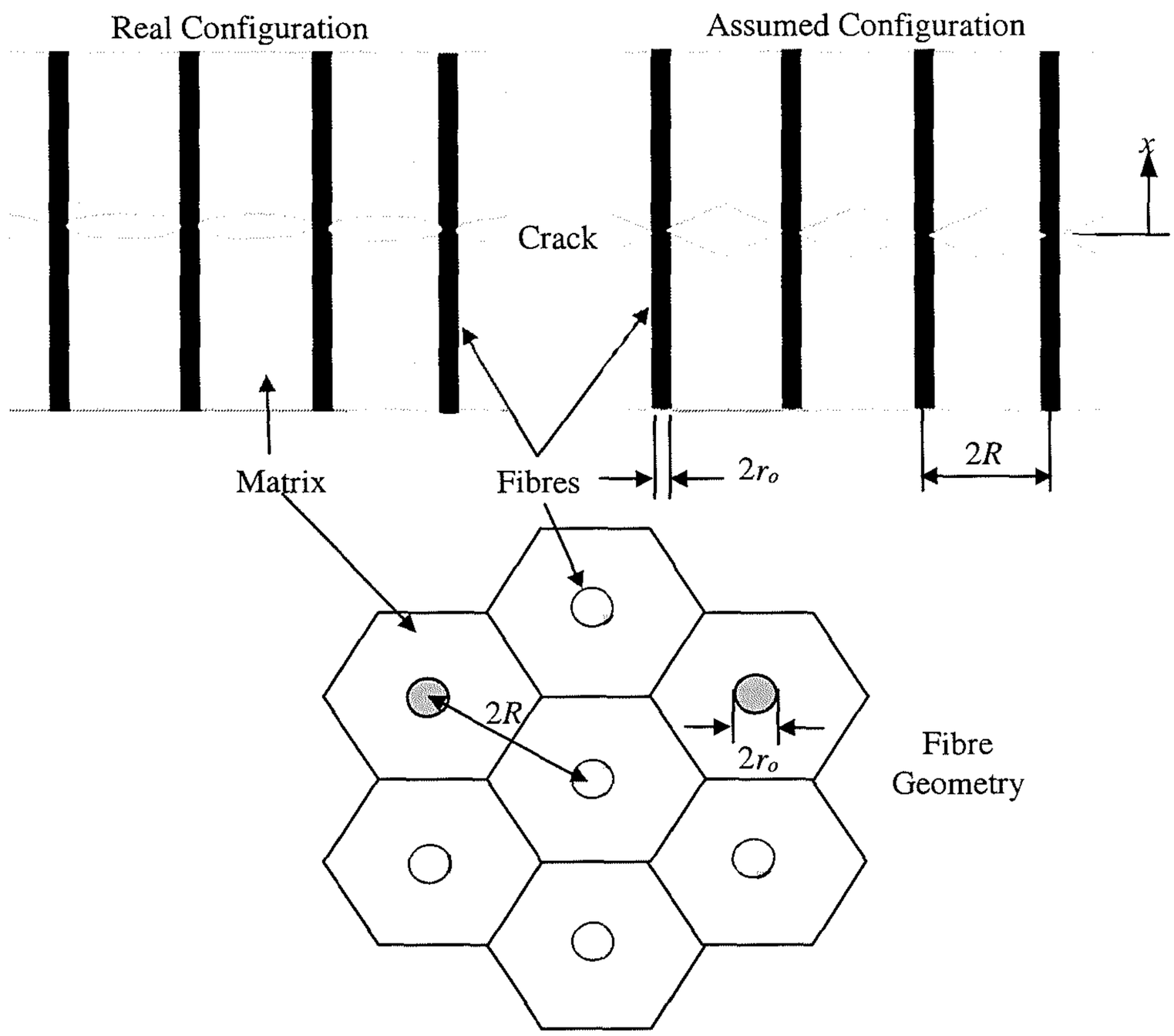

Fig. 3.3-5 Shear-lag model for matrix cracking with perfectly bonded elastic matrix and fibres following Aveston & Kelly (1973).

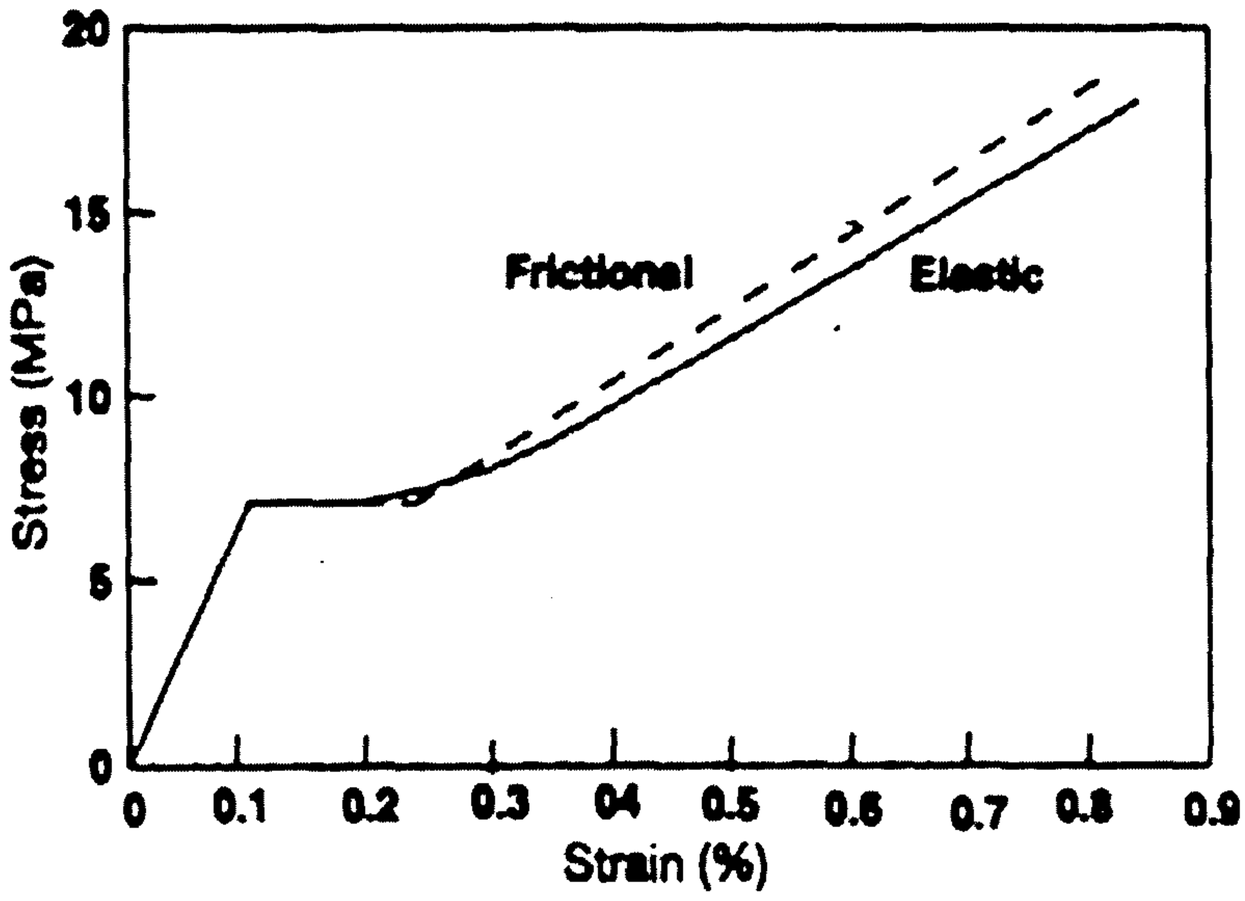

Fig. 3.3-6 Predicted stress-strain curve for Portland cement reinforced by long steel fibres with $V_f = 1\%$: Solid curve – perfectly bonded interface, broken curve – unbonded interface. Adapted from Aveston & Kelly (1973).

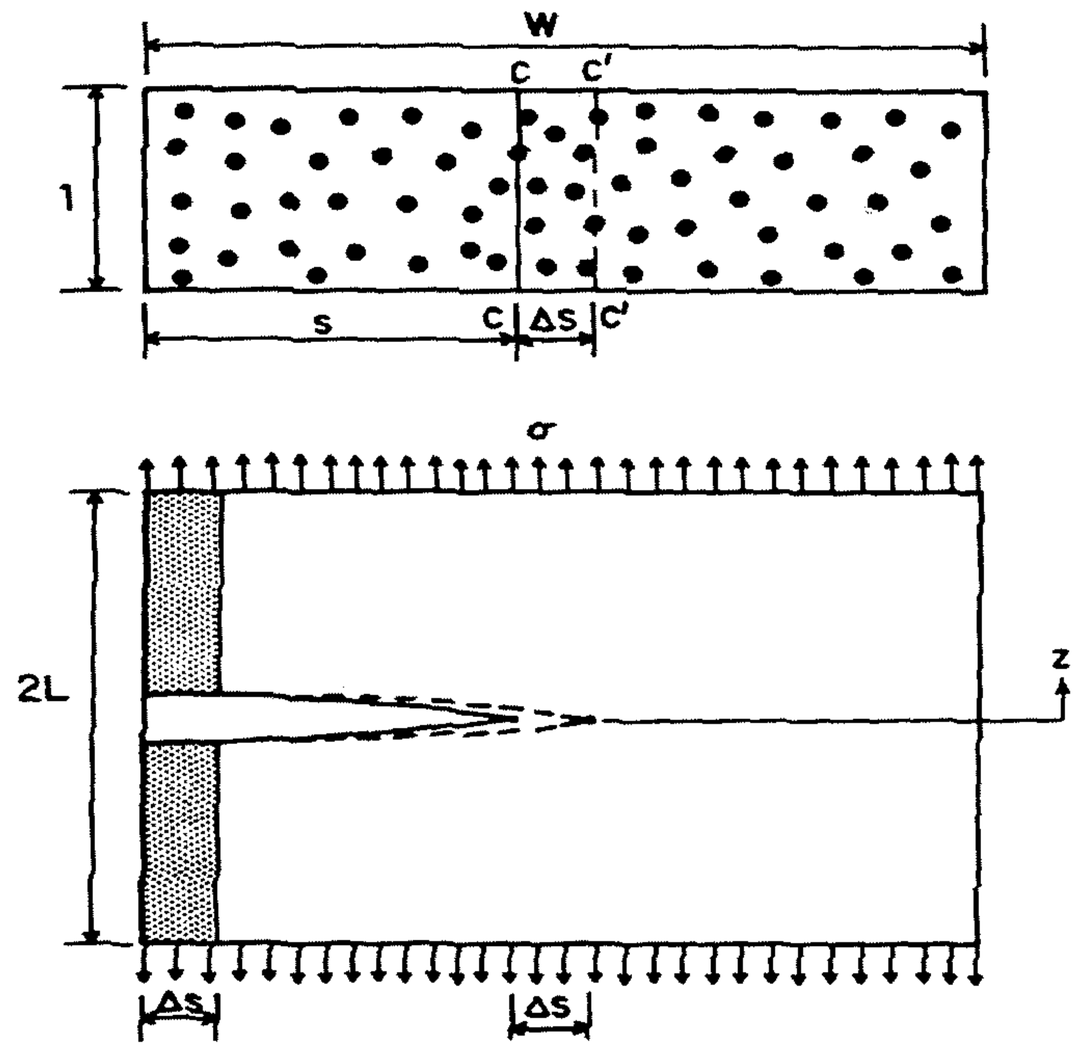

Fig. 3.4.1-1 The virtual crack extension model by Budiansky, Hutchinson and Evans (1986).

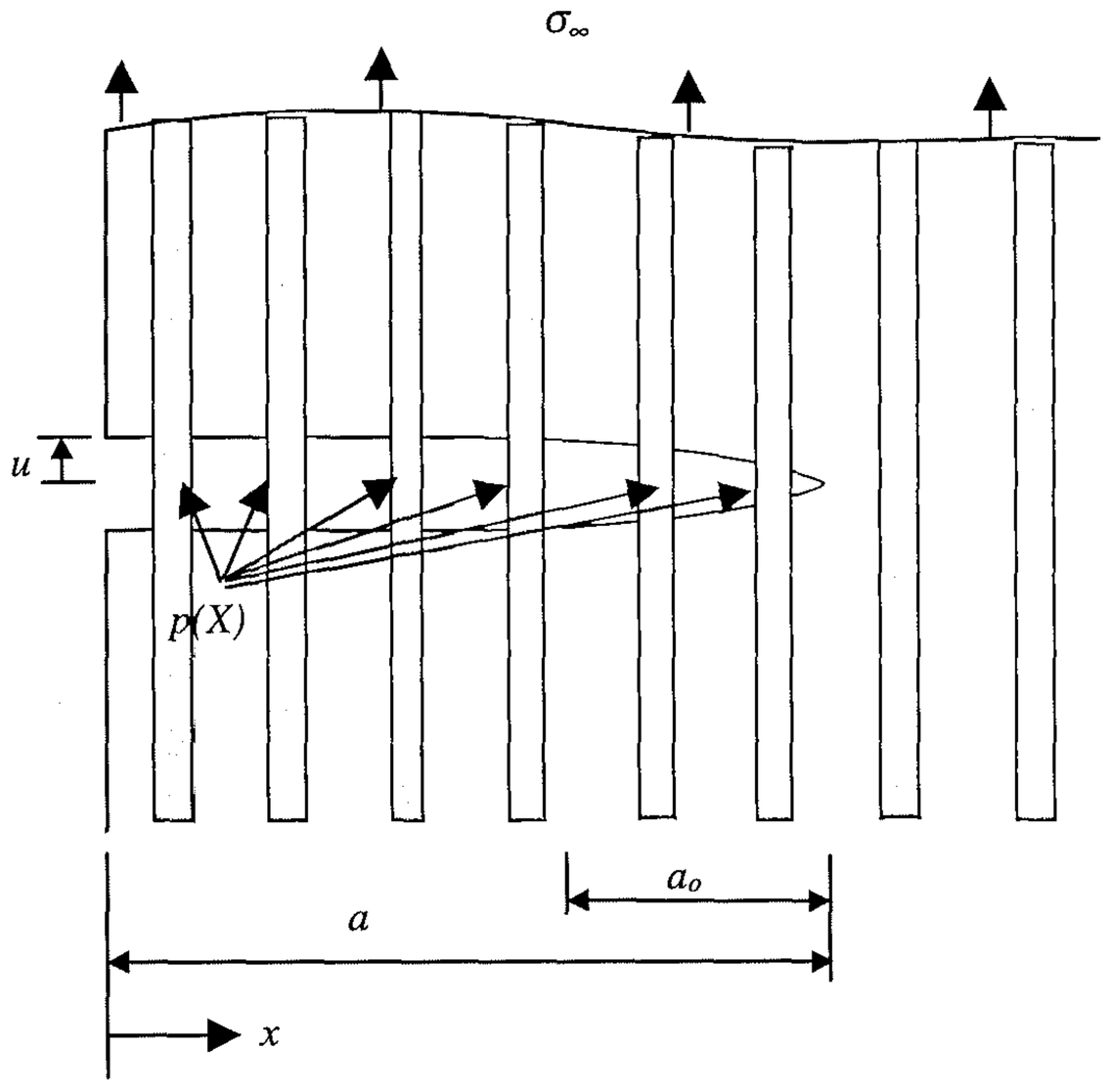

Fig. 3.4.2-1 Schematic representation of a steady-state matrix crack in a fibre composite following Marshall, Cox & Evans (1985).

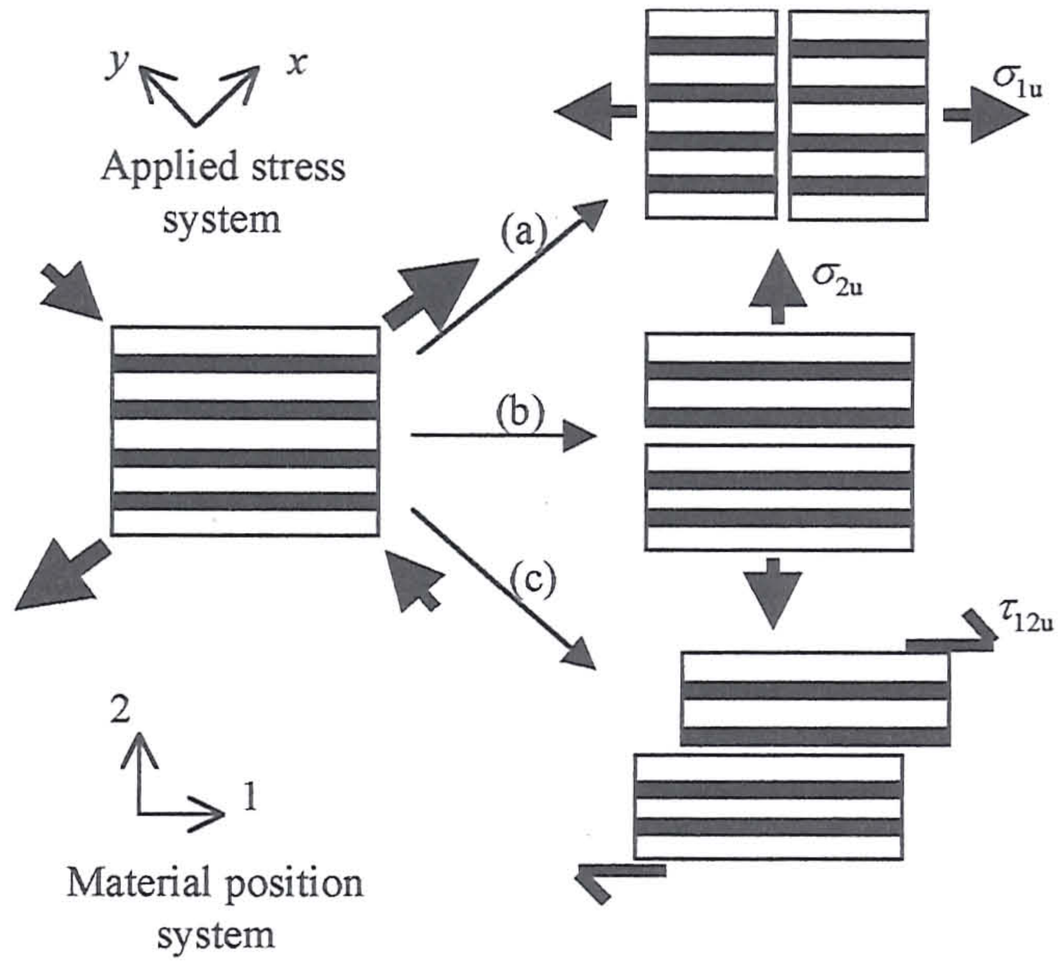

Fig. 3.6-1 Schematic illustration of the three dominant failure processes in a uni-directional composite in an arbitrary stress state (a) axial failure, (b) transverse failure and (c) shear failure.

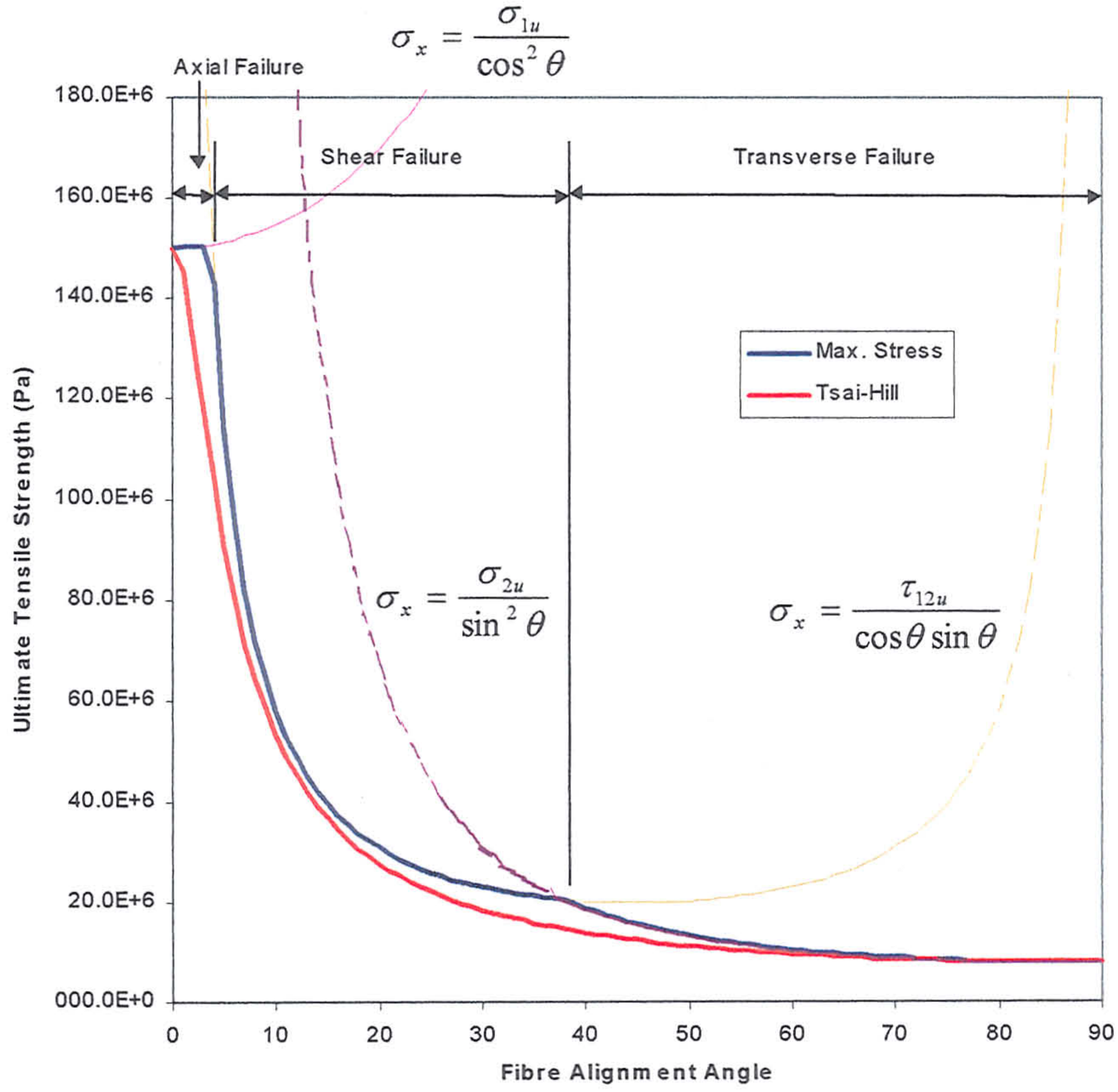

Fig. 3.6-2 Predicted failure surface for polyester/polyester composite with 18.5% fibres using Maximum Stress theory and Tsai-Hill criterion.

CHAPTER 4

The Experimental System

4.1 Introduction

Ceramic composites have the potential to revolutionise the design of high temperature engineering components and structures. In high temperature environments, their potential performance surpasses that of super-alloys. Rolls-Royce has considered replacing the super-alloy exhaust diffuser units of an EJ200 aero-engine with one made of ceramic composites (McCafferty, 1994). This non-critical component served as a test bed for subsequent introduction of other composite engine components. Of particular interest is the use of a SiC/SiC composite. This material has the ability to function at temperatures between 1200°C to 1500°C, which avoids the need for cooling systems in exhaust diffuser units. This results in weight saving and higher thrust-to-weight ratios. SiC/SiC composites exhibit low modulus and thermal expansion coefficient mismatch characteristics between fibres and matrix. This is a crucial factor for ceramic composites. In the manufacture of ceramic composites, two problems dominate – porosity and matrix microcracking. Porosity is a bi-product of the densification processes and kinetics of vapour deposition. Matrix microcracking results from residual stress fields arising from cooling from the manufacture temperature, and are caused by mismatches in elastic modulus and thermal expansion coefficient between fibres and matrix. By reducing the level of mismatch (i.e. using SiC/SiC composites), the extent of matrix microcracking can be minimised during fabrication.

To optimise the structural use of materials such as SiC/SiC composites, it is necessary to establish design and analysis guidelines. However, the material is relatively new and data is scarce. Typically, mechanical tests such as tensile and bend tests on plates and simple structures elements are done to determine constitutive relations and failure criteria. The mechanical data are then used for computational modelling, which is advantageous because it allows the analysis of full structures and complicated geometries that are not simple to manufacture or test. Computational modelling is also

cost effective because the manufacture of SiC/SiC composites by chemical vapour deposition is both expensive and slow.

In this chapter, the mechanical tests conducted to establish the constitutive relations and failure criteria of a SiC/SiC analogue in tension and shear are presented. Both uni-directional (one-dimensional) and balanced 0°-90° woven (two-dimensional) fibre architecture were considered. The objective was to establish a physical basis for computational modelling the mechanical behaviour of brittle matrix composites in general.

4.2 Materials

Characterisation of the mechanical behaviour of SiC/SiC composites involves mechanical tests, which are both expensive and time consuming to the manufacture process of the material. To overcome these constraints, Butler (1992) has proposed an analogue material system, which replicates the mechanical behaviour of SiC/SiC composites at ambient temperatures. The analogue material system exhibits low mismatch in elastic moduli and thermal expansion coefficient between the fibre and matrix. As a polymer system, it is cheap and easy to manufacture in the laboratory. McCafferty (1994) has compared the mechanical properties of the analogue system with a SiC/SiC composite with a balanced 0°-90° woven fibre architecture. The uniaxial tensile stress-strain response of both material systems parallel to the fibre direction is shown in Fig 4.2-1. The stress-strain response of the two materials are quite different. However, when normalised by the stress at which matrix cracking initiates and the corresponding matrix cracking strain, the normalised response of both material systems are similar. This is shown in Fig 4.2-2. The polymer system is used in the current thesis to establish the necessary basis and physics for computational modelling of SiC/SiC composites. The following sections contain descriptions of the analogue composite systems.

4.2.1 The Matrix

The matrix was a mixture of 85% polyester resin (471PALV) and 15% styrene monomer (Monomer C) by weight (Scott Bader, 1994). Preparation of the matrix first required the liquid polyester-styrene mixture to be degassed in an ultrasonic bath for 5-10 minutes. After eliminating entrapped gas bubbles, 2% weight of hardener (Catalyst

M) was introduced. At an ambient temperature of 20°C, the pot life of the liquid matrix was 12 minutes. To achieve the final solidified state, the polymer was cured at ambient temperature for 24 hours and post-cured in an oven for 16 hours at 40°C. To minimise the build up of residual stresses within the matrix, the solidified matrix was finally allowed to cool slowly in the oven to ambient temperature.

To determine the mechanical properties of the polyester matrix, the liquid matrix (prior to curing) was manually injected into a mould to form a square panel with dimensions of 240mm x 240mm x 4mm. Dog-bone shaped tensile specimens were CNC milled according to the dimensions illustrated in Fig 4.2.1-1. The tensile specimens were tested on a Lloyds 30R testing machine at a displacement rate of 2 mm/min with a strain gauge mounted directly on either side of the specimen to detect the normal and transverse strains. The stress-strain behaviour of the polyester matrix is shown in Fig 4.2.1-2. The polyester matrix was brittle linear elastic with a modulus E_m of 4.3GPa, a failure stress σ_{mu} of 32.4MPa, a failure strain ε_{mu} of 7.54E-3 and Poisson's ratio ν_m of 0.32.

4.2.2 The Fibres

The fibres were made of extruded polyester extracted from a woven polyester fabric. The average number of fibres in each tow was optically determined to be 210, with an average fibre diameter of 22.6μm ±0.2μm. The properties of the fibre were obtained from mechanical tests of the fibre tows. The tows were bonded at each end with thick industrial adhesive tapes, which served as tabs held in the grips of the test machine. General-purpose adhesive was also applied to improve load transfer and minimise stress concentrations at the grips. Fibre tows of length 180mm were loaded in tension at a displacement rate of 2 mm/min. The extensions were measured using a Lloyds laserscan 200 extensometer. The gauge length of each fibre tow, i.e. the separation between the leading edges of two reflective tapes adhered onto the fibre tow, was 125mm. The accuracy of the laser extensometer was ±0.5% of the working length.

The average stress-strain response of a typical polyester fibre tow compared with the matrix stress-strain relation is shown in Fig 4.2.2-1. The fibres are non-linear, having an initial average modulus of 4.3GPa at strains less than 0.005. At the failure strain of 0.014, the secant modulus of the fibre was ~7.15GPa, which is about 1.66

times the initial modulus. The average fibre failure stress σ_{fu} was 800MPa and the corresponding fibre failure strain ε_{fu} was 0.157.

4.2.3 The Composite

A description of the fabrication of one and two-dimensional polymer composites is now presented.

4.2.3.1 One-Dimensional Composite

One-dimensional polyester composite specimens were fabricated using 6 layers of lightly hand-tensioned continuous fibres, which were pre-aligned and secured in a custom-made mould. The fibres were obtained by discarding the transverse fibres from a balanced 0°-90° woven polyester fabric as described in Sect. 4.2.2. To impregnate the fibres, the polyester resin was initially poured onto the aligned fibres and distributed using paddle rollers. The roller facilitated the release of air bubbles trapped in the resin between fibre tows. This was performed in a ventilation chamber with an average air velocity of 0.47 m/sec to remove fumes. A cover was applied to seal the mould and the composite allowed to set (see Sect. 4.2.1). The thickness of the composite panel was controlled using height-adjustment attachments on the mould cover and an applied load of 100N. The quality of the composite panel is shown in Fig 4.2.3-1a. The composite panel exhibited highly aligned fibres with small levels of residual stress, as indicated by the slight curvature of the panel. However, a disadvantage of the fabrication technique was that the top surface of the panel was plagued with porosity. This was probably due to entrapment of air between the cover and the liquid resin during closure.

To overcome the porosity problem, a resin injection technique was developed. The contact between the cover and the mould was sealed to prevent leakage. The mould was then left standing on one edge with the aligned fibres in the horizontal direction. The polyester resin was slowly injected into the mould through an inlet located near the bottom edge. To allow the release of air from the mould, the top edge of the mould was opened. The quality of the composite panel is shown in Fig 4.2.3-1b. The porosity problem in the previous fabrication technique was eliminated, while retaining the good fibre alignment and low residual stress characteristics. This fabrication technique was used to fabricate one-dimensional polyester composite test specimens. A diagram of the mould with the encased impregnated fibres is shown in Fig 4.2.3-2.

4.2.3.2 Two-Dimensional Composites

Two-dimensional composites with a balanced 0°-90° array of fibres were fabricated using a hand-layup technique. The matrix was formed using a polyester gel-coat, Resin B, and 2% weight of hardener Catalyst M (Scott Bader, 1998). The mechanical properties were identical to the resin used for the one-dimensional composite. The work surface of the mould was coated with gel to provide an even surface finish for the composite. A woven fibre layer was then applied onto the gel. To ensure good impregnation, a subsequent layer of gel was applied to the woven layer and evenly distributed using a paddle roller. The process of fibre laying and gel application was repeated till the required amount of fibre layers was obtained. The mould cover, which was pre-coated with gel, was applied to finish the composite. A force of 100N was applied onto the cover during the curing process. Both the cure and post-cure duration were identical to the one-dimensional composite. The hand-layup technique was preferred over the liquid resin injection method because of better fibre impregnation, but this was achieved at the expense of fibre alignment.

4.3 Mechanical Tests

The mechanical test programme had two objectives. The first was to determine the anisotropic stress-strain relations and failure criteria for one-dimensional composites. The second objective was to compare the mechanical response of one and two-dimensional composites to determine the influence of transverse fibres. The mechanical test programme was intended to provide the data and physical basis for computational modelling.

4.3.1 Test Procedure

To measure the stress-strain relations and characterise the failure of one-dimensional composites, tensile tests were performed at fibre alignment angles, α, from 0° to 90° in ten degree intervals, plus 45°. Two test configurations were used: tabbed rectangular coupons and dog-bone specimens. The former follows the recommendations of national test standards such as BS EN ISO 527-5: 1997 for polymer matrix composites. The latter follows recommendations from an American national standard ASTM E8M-88 for tensile testing metals.

The rectangular coupons were bonded with square tabs. The square tabs were fabricated using a two-dimensional composite with reinforcement off-axis at ±45° to the loading direction. The dimensions of the rectangular coupon specimen and the square tabs are shown in Fig 4.3.1-1. The dimensions of the dog-bone shaped specimens are given in Fig 4.3.1-2. Specimens with fibre alignment of between 0° to 45° were considered. The average fibre volume fraction V_f the rectangular coupons and dogbone shaped specimens was 0.185 and 0.189. This was determined by calculating the average area of the fibres per unit area at the gauge section. The average fibre area was obtained by multiplying the area of the fibres per tow by the number of fibre tows in the section. Further details are given in sect. 4.2.2. For specimens with a fibre alignment of $\alpha = 0°$ to 45°, a displacement rate of 2 mm/min was used, while for fibre alignment of $\alpha = 60°$ to 90° a displacement rate of 0.2 mm/min was used. The Lloyds Laserscan 200 extensometer was used to measure the applied strains for specimens with fibre alignments between 0° to 60° while strain gauges of gauge length 6.5mm were used for the other tests. The temperature of the test environment was approximately 20°C. A Lloyds 30R test machine was used to load the specimens.

For specimens with a fibre alignment of $\alpha = 0°$, the evolution of matrix cracks as a function of strain was determined using both tabbed-coupon and dogbone shaped specimen by counting the number of cracks along the gauge length and recording the applied strain of the composite. Tabbed rectangular coupons were also used to investigate the debond characteristics of fibre tows caused by matrix cracking at applied strains of 0.02, 0.0.06, 0.10 and 0.12. The information was used to determine the interfacial shear strength of the fibre-matrix interface.

Rail shear tests (ASTM D4255/D4255M-83) were used to measure the shear strength and shear modulus of the one-dimensional composite. A schematic diagram of the rail shear specimen and its dimensions, following Method A, are shown in Fig 4.3.1-3. A photograph of the rail shear test configuration is shown in Fig 4.3.1-4. The strains were measured with strain rosettes of 0° and ±45° using an Orion 3531D data acquisition system (Schlumberger, 1987). The through thickness delamination stress of the one-dimensional composite was measured using the test configuration shown in Fig 4.3.1-5. The two-dimensional composite was also tested in tension and in shear. Tabbed-coupons with the dimensions are shown in Fig 4.3.1-6 and fibre alignment

angles between 0° to 45° were used for the tensile tests. The dimensions of the rail shear specimen are as shown in Fig 4.3.1-3. The shear was applied parallel to one of the reinforcement directions. The test parameters were identical to the one-dimensional composites. A Lloyds 10000 testing machine with an applied displacement rate of 0.2mm/min was used in these tests.

4.3.2 Results

Photographs of the broken one-dimensional tabbed rectangular coupons and the dogbone shaped specimens, for each fibre alignment angle tested in tension, are shown in Fig 4.3.2-1 and Fig 4.3.2-2. The corresponding stress-strain curves are shown in Fig 4.3.2-3. Material properties such as Young's modulus E_c, the ultimate tensile strength σ_{cu} and strain ε_{cu} are given in Table 4.3.2-1. The table also gives the failure mechanism as well as the matrix cracking stress σ_{mc} and strain ε_{mc}.

	Tabbed Coupons			**Dogbone**			**Damage Mechanism**
α (°)	σ_{cu} & σ_{mc} (MPa)	ε_{cu} & ε_{mc} $*10^{-3}$	E_c (GPa)	σ_{cu} & σ_{mc} (MPa)	ε_{cu} & ε_{mc} $*10^{-3}$	E_c (GPa)	
0	118 59.5	126 13.4	4.44	150 53.3	136 12.8	4.16	Matrix cracking
0	116 52.7	124 11.6	4.54	134 47.6	126 11.8	4.03	Matrix cracking
10	51.5	15.3	3.37	51.0	10.4	4.90	Matrix cracking & delamination
10	50.8	10.7	4.75	54.5	15.2	3.56	Matrix cracking & delamination
20	23.1	6.54	3.53	3.69	9.77	3.78	Matrix cracking & delamination
20	28.0	8.17	3.43	37.5	9.16	4.09	Matrix cracking & delamination
30	10.2	3.81	2.67	22.4	6.10	3.68	Delamination
30	20.4	4.76	4.28	18.3	5.93	3.09	Delamination
45	11.1	3.81	2.91	12.6	3.82	3.30	Delamination
45	10.5	3.81	2.75	-	-	-	Delamination
60	8.26	2.78	2.97	-	-	-	Delamination
60	5.99	1.61	3.72	-	-	-	Delamination
70	9.31	2.34	3.98	-	-	-	Delamination
70	9.76	2.98	3.28	-	-	-	Delamination
80	7.40	2.07	3.57	-	-	-	Delamination
80	8.83	1.85	4.77	-	-	-	Delamination
90	7.78	1.86	4.18	-	-	-	Delamination
90	7.73	2.34	3.30	-	-	-	Delamination

Table 4.3.2-1 Test data of the one-dimensional polyester/polyester composite.

Photographs illustrating the evolution of matrix cracks during tensile testing of the tabbed-coupon are presented in Fig 4.3.2-4. A plot of the matrix crack density as a function of applied strain for a one-dimensional tabbed-coupon and dogbone shaped specimen tension parallel to the reinforcement direction is shown in Fig 4.3.2-5. The crack density ρ is defined as the number of matrix cracks per unit length. This was normalised by the density at saturation ρ_{sat}, i.e. the maximum number of matrix cracks per unit length in the gauge length when the composite finally failed. The matrix crack density at saturation ρ_{sat} for the tabbed-coupon and the dog-bone shaped specimens were 6 cracks/cm and 7cracks/cm, respectively. The evolution of matrix cracks in the composite was initially a linear function of strain. However, prior to failure the damage density was constant as the matrix cracking had saturated.

A photograph of fibre debonding at a matrix crack is shown in Fig 4.3.2-6. From such micrographs, the average fibre debond lengths were determined for strains of 0.02, 0.06, 0.1 and 0.12. The results are presented in Table 4.3.2-2. A plot of the average fibre debond length (± 2 standard deviations) with respect to strain is shown in Fig 4.3.2-7. This shows that the debond length tends to increase with applied strain, although there is a great deal of scatter in the results.

Applied Strain	No. of data	Ave. debond length (mm)	1 Standard Deviation (mm)
0.02	72	0.508	0.146
0.06	152	0.569	0.155
0.1	287	0.744	0.213
0.12	54	1.005	0.155

Table 4.3.2-2 The measured debond length for one-dimensional composites.

A photograph of a broken one-dimensional Rail Shear specimen is shown in Fig 4.3.2-8. A distinct delamination plane parallel to the fibre reinforcement direction was observed near the rail-grips. The average shear modulus and the average shear strength obtained from the rail shear tests were 2.1GPa and 9.9MPa. Two specimens were examined. A plot of the typical shear stress-strain relations is shown in Fig 4.3.2-9.

A photograph of the one-dimensional composite delaminating in the thickness direction is shown in Fig 4.3.2-10. A plot of the stress-strain relation of the specimen is

shown in Fig 4.3.2-11. The average through-thickness delamination stress was 12.3MPa.

The uniaxial stress-strain relations of the two-dimensional tabbed-coupons for fibre alignments between 0° and 45° are shown in Fig 4.3.2-12. The stress-strain relations for all fibre alignment angles were similar in form to the aligned one-dimensional specimens. Failure occurred by matrix cracking and subsequent fibre failure. Photographs of the cracked specimens for the different fibre alignment angles are shown in Fig 4.3.2-13, indicating that matrix cracks were inclined to the principal reinforcement directions. Table 4.3.2-3 gives the stress σ_{mc} and strain ε_{mc} at which matrix cracking initiated, the final failure stress σ_{cu} and strain ε_{cu}, Young's modulus E_c and matrix crack orientations with respect to the loading direction.

α (°)	σ_{mc} (MPa)	ε_{mc} $*10^{-3}$	σ_{cu} (MPa)	ε_{cu}	E_c (GPa)	Crack plane angle w.r.t. loading
0°	20.0	5.58	132	0.155	4.01	90°
10°	15.0	4.40	118	0.165	3.55	65°
20°	14.6	4.48	918	0.199	3.71	70°
30°	10.0	2.84	852	0.237	2.87	80°
45°	17.0	10.4	937	0.306	2.07	90°

Table 4.3.2-3 Test data of the two-dimensional polyester/polyester composite.

A photograph of the broken two-dimensional composite from the rail shear test is shown in Fig 4.3.2-14. Matrix cracks orientated at 45° to the applied shear direction were observed. No in-plane delamination was visible.

4.4 Discussion

4.4.1 One-Dimensional Composites

Three types of damage were observed in the tensile tests. The first was matrix cracking followed by failure of the fibres, causing failure of the composite. This failure mechanism was observed in specimens loaded parallel to the reinforcement, i.e. at a fibre alignment angle of 0°. Matrix cracks give rise to a non-linearity in the composite stress-strain relations (Fig 4.3.2-3a). The second type of damage was delamination, in which the composite failed through the fibre-matrix interface, resulting in a catastrophic loss of strength. This failure mechanism was observed for specimens with fibre

alignment angles between 30° and 90°. The third type of damage involved a mixture of matrix cracking and delamination, and was observed in specimens with a fibre alignment angle between 10° and 20° (Fig 4.4.1-1). The damage consisted of a delamination plane along the fibre-matrix interface and matrix crack planes with normal *n* rotated 10°-20° from the loading axis, but in the opposite sense to the fibres. Fig 4.4.1-1 also shows that the damage zone becomes localised along the delamination plane as the fibre alignment angle approached 20°.

The ultimate tensile strength and the failure strain of the tabbed-coupons and dogbone shape specimens are shown in Fig 4.4.1-2 and Fig 4.4.1-3. The results show that one-dimensional composites exhibit the greatest strength and ductility parallel to the fibres. As the fibre axis rotates towards an orientation at right angles to the loading direction, the strength and ductility decrease due to delamination.

A comparison of the strengths predicted by the maximum stress and the Tsai-Hill (Tsai, 1966) failure criteria with the experimental data is shown in Fig 4.4.1-2. The shear strength obtained from the rail shear test and the tensile delamination stress for $\alpha = 90°$ and the ultimate tensile strength at $\alpha = 0°$ were used to establish the critical values in both criteria. Good agreement between both failure theories and experiments was obtained. In particular, the maximum stress criterion predicted multiple matrix cracking damage between 0° to 3°, shear delamination between 4° and 37° and tensile delamination between 38° and 90°. However, the maximum stress theory has limitations. Matrix cracking is assumed to occur normal to the direction of maximum stress of the composite, that is the matrix crack planes are implied to be normal to the fibre direction. Hence when the fibre orientation rotates, the orientation of the crack planes is expected to remain normal to the fibre direction. However, the off-axis tension test showed that the crack planes were inclined at an angle to the fibre axis. The results support the view that the matrix crack planes had initiated normal to the direction of the maximum principal stress in the matrix. This issue is further elaborated in Chapter 8.

Fig 4.4.1-4 shows a comparison of the ultimate tensile strength obtained from the dogbone shaped specimens and the tabbed-coupons. This is expressed as a ratio between the strength of the dogbone shaped specimen and the tabbed-coupons as a function of fibre alignment angle. The dogbone shaped specimens were generally stronger than the tabbed-coupons, except for $\alpha = 10°$. The superior strength of the

dogbone shaped specimens may be explained by comparing the failure location (Fig 4.3.2-1 and 2). For the tabbed-coupons, failure for $\alpha = 0°$, 20° and 30° occurred near the tabs indicating that the strengths measured were sensitive to the stress concentration at the tabs. For the dogbone shaped specimens, failure occurred within the gauge lengths. Based on the superior strengths measured from the dogbone shaped specimens, the dogbone configuration is recommended for tensile test of one-dimensional composites, for both aligned and off-axis conditions.

In Fig 4.4.1-5, the uniaxial tensile stress-strain behaviour of the one-dimensional composites parallel to the fibres is divided into three regions. The first region is linear elastic until the initiation of matrix cracking. Young's modulus of the composite E_c was well described by the rule of mixtures:

$$E_c = E_f V_f + E_m V_m \qquad (4.4.1\text{-}1)$$

In the second region multiple matrix cracking occurs. The tangent modulus reduced to approximately 6% of the initial modulus and the density of matrix cracks increased with strain (see. Fig 4.3.2-5). In the third region, matrix cracking saturated and the load in the composite was largely borne by the fibres. The average tangent modulus of the composite was close to $E_f V_f$.

Included in Fig 4.4.1-5 are the load bearing capacities of the fibres and matrix per unit area as a function of applied strain, i.e. $\sigma_f V_f$ and $\sigma_m V_m$. The load bearing capacity of the fibre weighted by it volume fraction was obtained by multiplying by the fibre stress σ_f determined from the experimental stress-strain of the fibre at the composite strain multiplied by V_f. The load bearing capacity of the matrix per unit area, $\sigma_m V_m$, was obtained by subtracting the stress of the volume fraction of fibres $\sigma_f V_f$ from the composite stress σ_c. Comparison of these stress-strain relations and the normalised matrix crack density plot in Fig 4.3.2-5 showed that the fibres become the dominant load bearing component when the level of matrix crack damage is approximately halved. The composite finally failed when the fibres failed, i.e. $\sigma_c = \sigma_{fu} V_f$.

The average stress-strain relation of the damage matrix shows four important regions. The first region is linear elastic with a Young's modulus of E_m until matrix cracking initiated. During matrix cracking, the matrix initially tension-hardened until the tangent modulus reduced to zero. Subsequently, as the applied strain increased the

matrix began to tension-soften at a constant tangent modulus of –0.277GPa. At a matrix crack damage level of 0.9, i.e. near saturation, the tangent modulus of the matrix becomes close to zero.

During matrix cracking, it is commonly assumed that the interfacial shear stress τ' of the debonded fibres near the matrix crack planes is constant. ACK (1971) give the interfacial shear stress τ' as (see eqn (3.3.10)):

$$\tau' = \frac{\sigma_{mu} r}{2x'}\left(\frac{V_m}{V_f}\right) \qquad (4.4.1\text{-}3)$$

Here, x' is the debond length in the fibres, r is the fibre radius and σ_{mu} is the matrix cracking stress of the composite. To determine if the interfacial shear stress is a function of applied strain is, two scenarios are considered. The first assumes the matrix cracking stress of the composite is constant at 56MPa, while the second uses the composite stress corresponding to the applied strain. In both scenarios, the fibre radius was 11.3μm and V_f was 0.185. The debond length as a function of applied strain is given in Fig 4.3.2-6. The interfacial shear stress ±2 standard deviations, are plotted in Fig 4.4.1-7. Using eqn. (4.4.1-3) to determine τ a decrease in interfacial shear stress with respect to strain is indicated. For a matrix cracking stress which is a function of strain, i.e.

$$\tau'(\varepsilon) = \frac{\sigma_{mu}(\varepsilon)\, r}{2\, x'(\varepsilon)}\left(\frac{V_m}{V_f}\right) \qquad (4.4.1\text{-}5)$$

the average values are more nearly constant despite the large standard deviations.

A photograph of the distribution of fibres in a fibre tow is shown in Fig 4.4.1-8. This shows the local volume fraction of fibres in fibre tows is significantly greater than in the composite. To determine the interfacial shear stress of the debonded fibres in a fibre tow, the same analysis was repeated by using a fibre volume fraction of 0.5. Results of the average interfacial shear stress for the fibres in fibre tows are plotted in Fig 4.4.1-9. The interfacial shear stress of the debonded fibres in the fibre tows was approximately one fifth of the average value calculated for the composite, which shows that shear failure could initiate at the interface of the fibres within the fibre tow.

4.4.2 Two-Dimensional Composites

The tensile stress-strain relation of all the balanced 0°-90° two-dimensional composites is broadly similar to the aligned one-dimensional composite. This is because

the two-dimensional composite fails by matrix cracking followed by fibre failure, irrespective of fibre alignment angle. The ultimate tensile strength and the failure strain of the two-dimensional composites as a function of fibre alignment angles are shown in Fig 4.4.2-1 and Fig 4.4.2-2. The results indicate that when the fibre alignment angle increased from 0° to 45°, the strength decreased by 30% but the ductility increased by a factor of 2.

To compare one- and two-dimensional composites, a plot of the uniaxial tensile stress-strain relations of the composites for a fibre alignment angle of 0° is shown in Fig 4.4.2-3 using tabbed-coupons specimens. The one-dimensional specimen shows a higher matrix micro-cracking stress. To investigate the reason for the lower matrix cracking stresses in the two-dimensional composites, the stress-strain relation of the matrix in the two-dimensional composite was derived following eqn. (4.4.1-2). This is given in Fig 4.4.2-4 with the stress-strain relations of the two-dimensional composite and fibre. The form of the matrix stress-strain relation is the same as the one-dimensional composite shown in Fig 4.4.1-6. Next, the stress-strain relation of the matrix in the two-dimensional composite and the stress-strain relation of the one-dimensional composite with a fibre alignment of $\alpha = 90°$ are compared in Fig 4.4.2-5. This shows the initiation stress (0.2% proof stress) for matrix cracking in two-dimensional composite was approximately 1.5 times the in-plane tensile delamination stress of the one-dimensional composite. The comparison suggests the low matrix cracking stress in the two-dimensional composite was influenced by the weak fibre-matrix interface of the fibres perpendicular to the applied stress. The crack initiation stress in the matrix was greater than the in-plane tensile delamination stress because of the strengthening effects of the woven fibre architecture.

4.5 Conclusions

The stress-strain relations and failure criteria of the one-dimensional composite are strongly anisotropic. Three modes of failure were observed: matrix cracking, delamination and a combination of the two. During matrix cracking, the orientation of the crack plane was not normal to the fibres or the tensile loading direction. The interfacial shear stress of the fibre-matrix interface was approximately constant. Because the tensile strengths measured using the dog-bone shaped specimens were greater than the tabbed-coupons, the dog-bone configuration is recommended for on-

and off-axis tensile testing of brittle matrix composites. The anisotropic stress-strain relations of two-dimensional composites were also determined. In comparison to the one-dimensional counterpart, the strength and ductility of the two-dimensional composites were significantly improved as a function of orientation. However, the stresses at which matrix cracking initiated were generally lower due to the weak fibre-matrix interfaces.

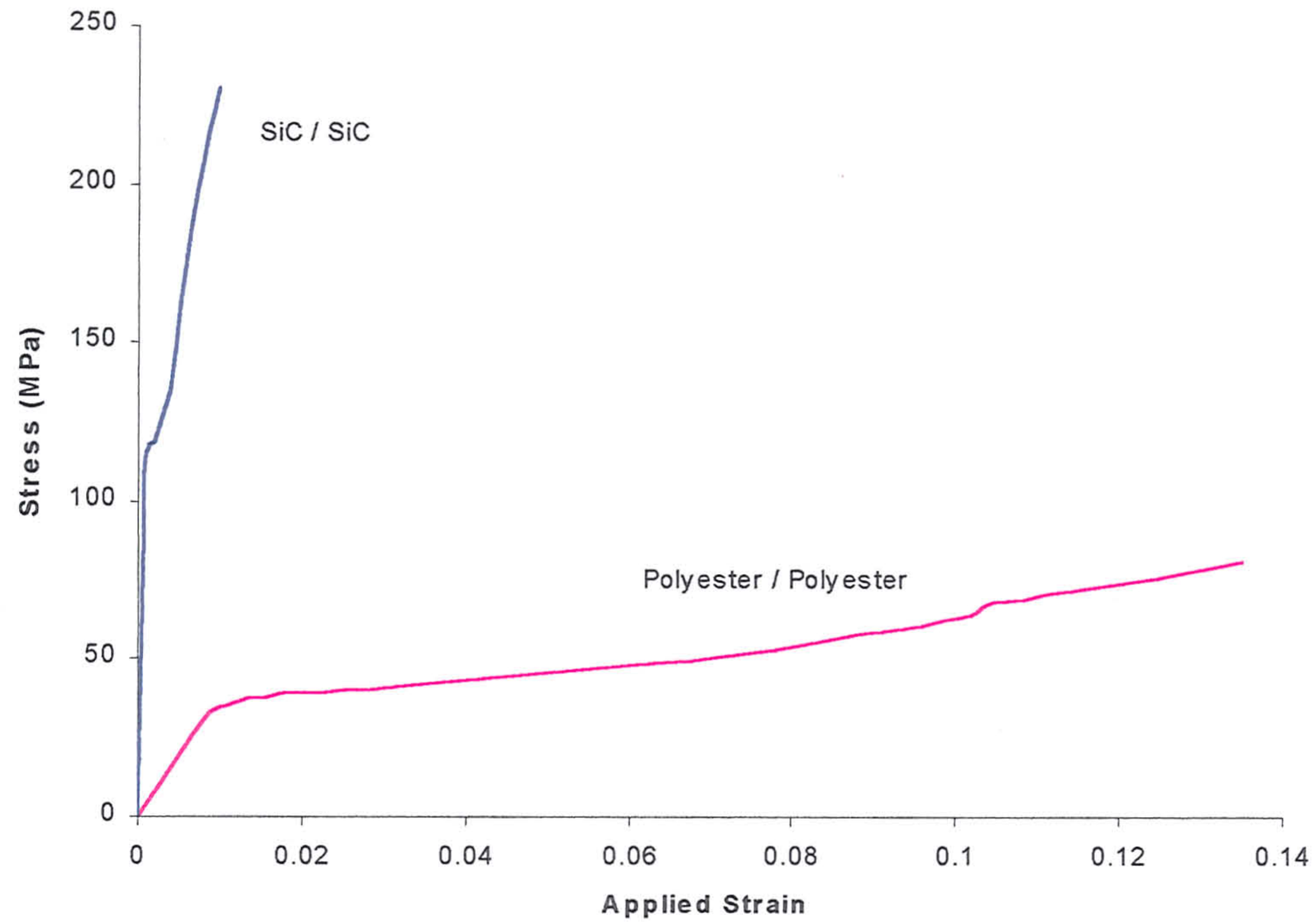

Fig 4.2-1 Absolute stress-strain response of balanced 0°-90° woven SiC/SiC and the SiC/SiC analogue system (Polyester/Polyester) in uniaxial tension parallel to the fibre direction (adapted from McCafferty, 1994).

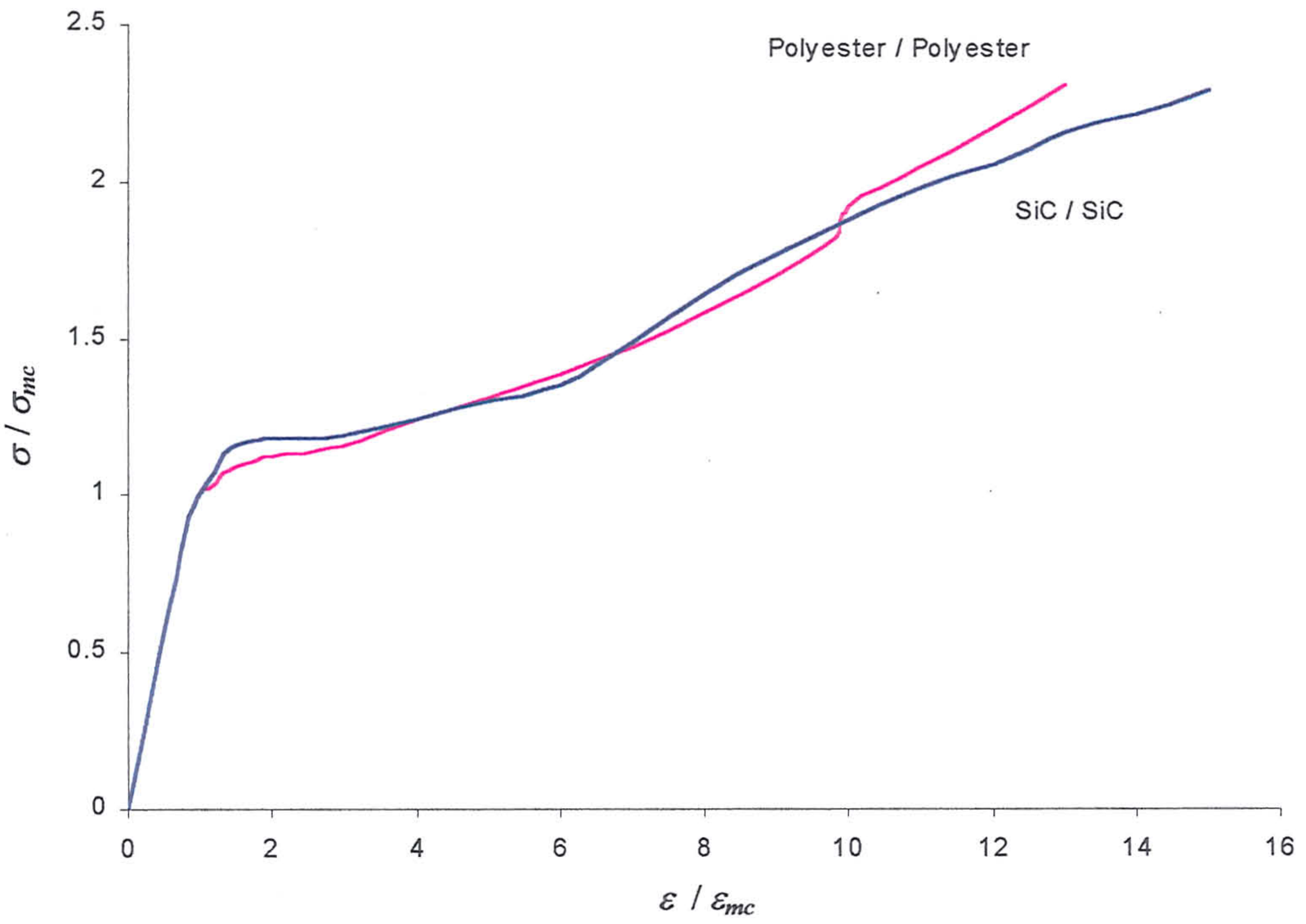

Fig 4.2-2 The normalised stress-strain response of balanced 0°-90° woven SiC/SiC and the SiC/SiC analogue system (Polyester/Polyester) in uniaxial tension parallel to the fibre direction (adapted from McCafferty, 1994).

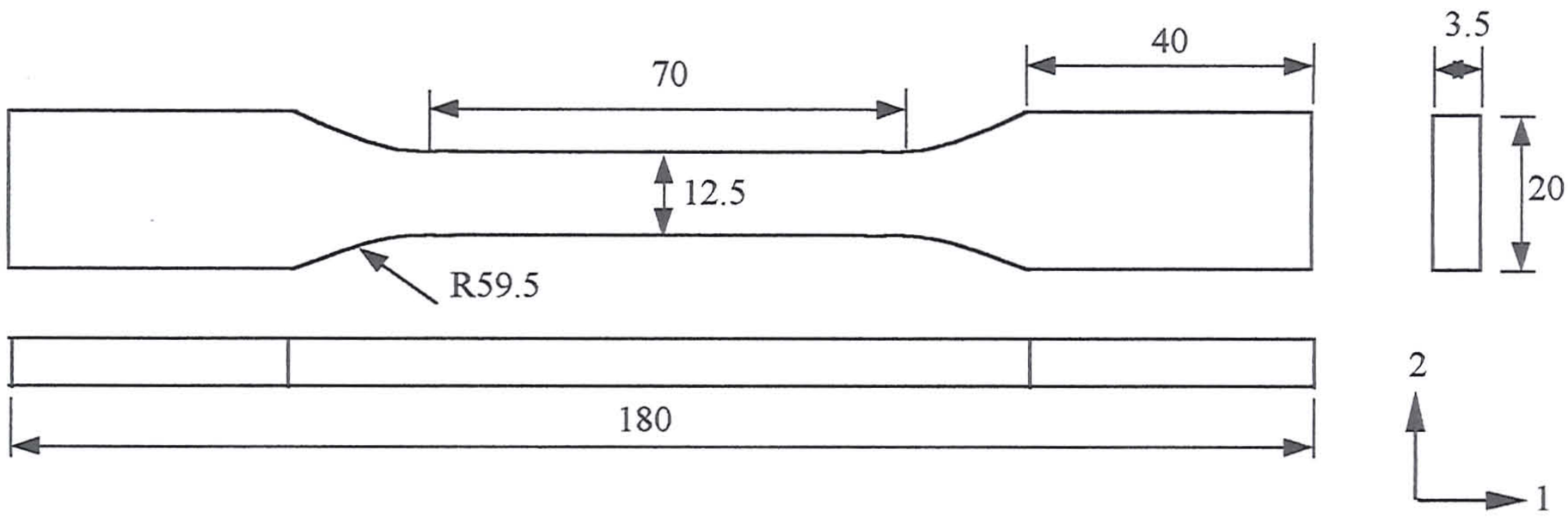

All dimensions are in mm.

Fig 4.2.1-1 Schematic diagram of tensile specimen for polyester resin.

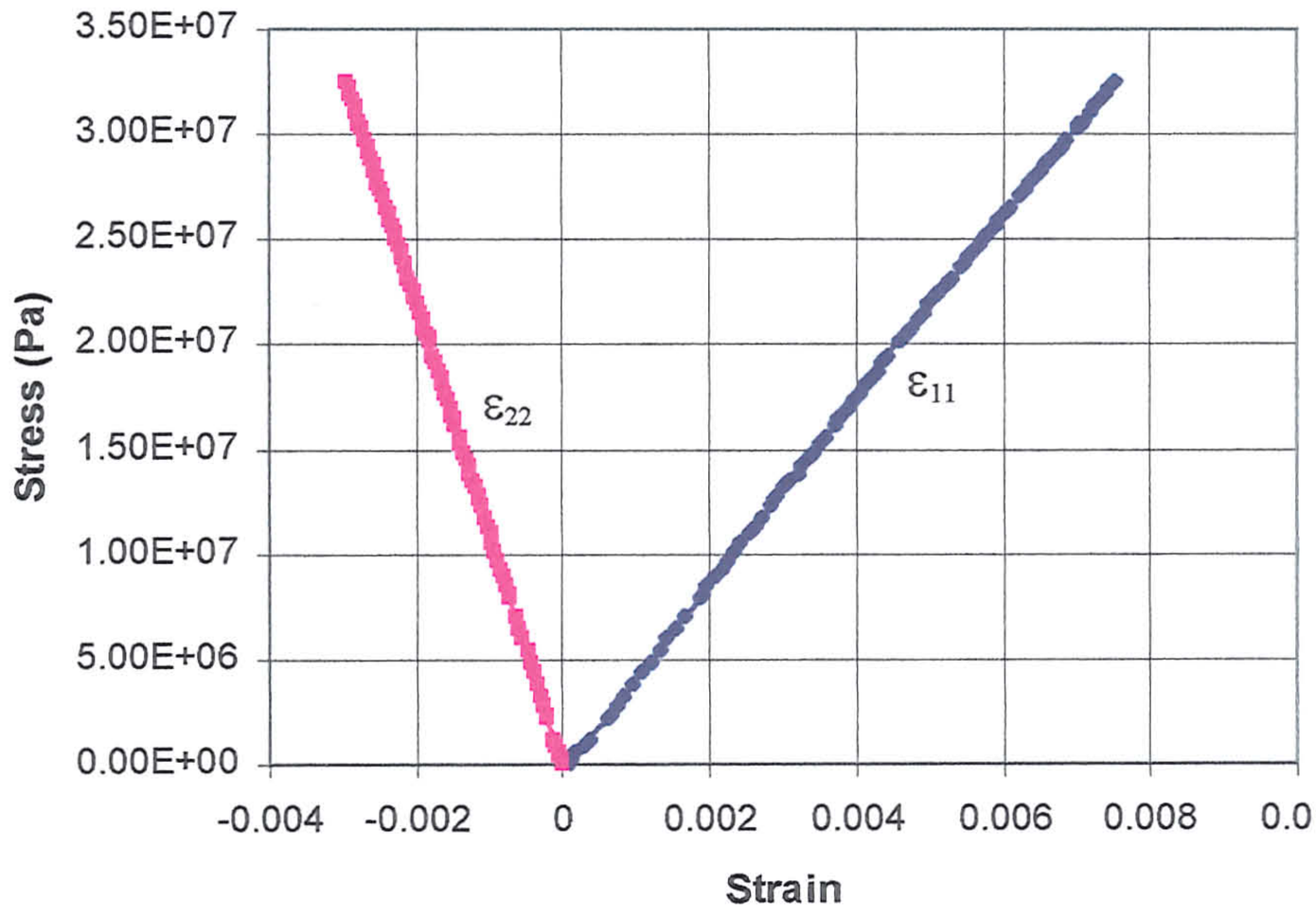

Fig 4.2.1-2 Uniaxial stress-strain relations of the polyester matrix.

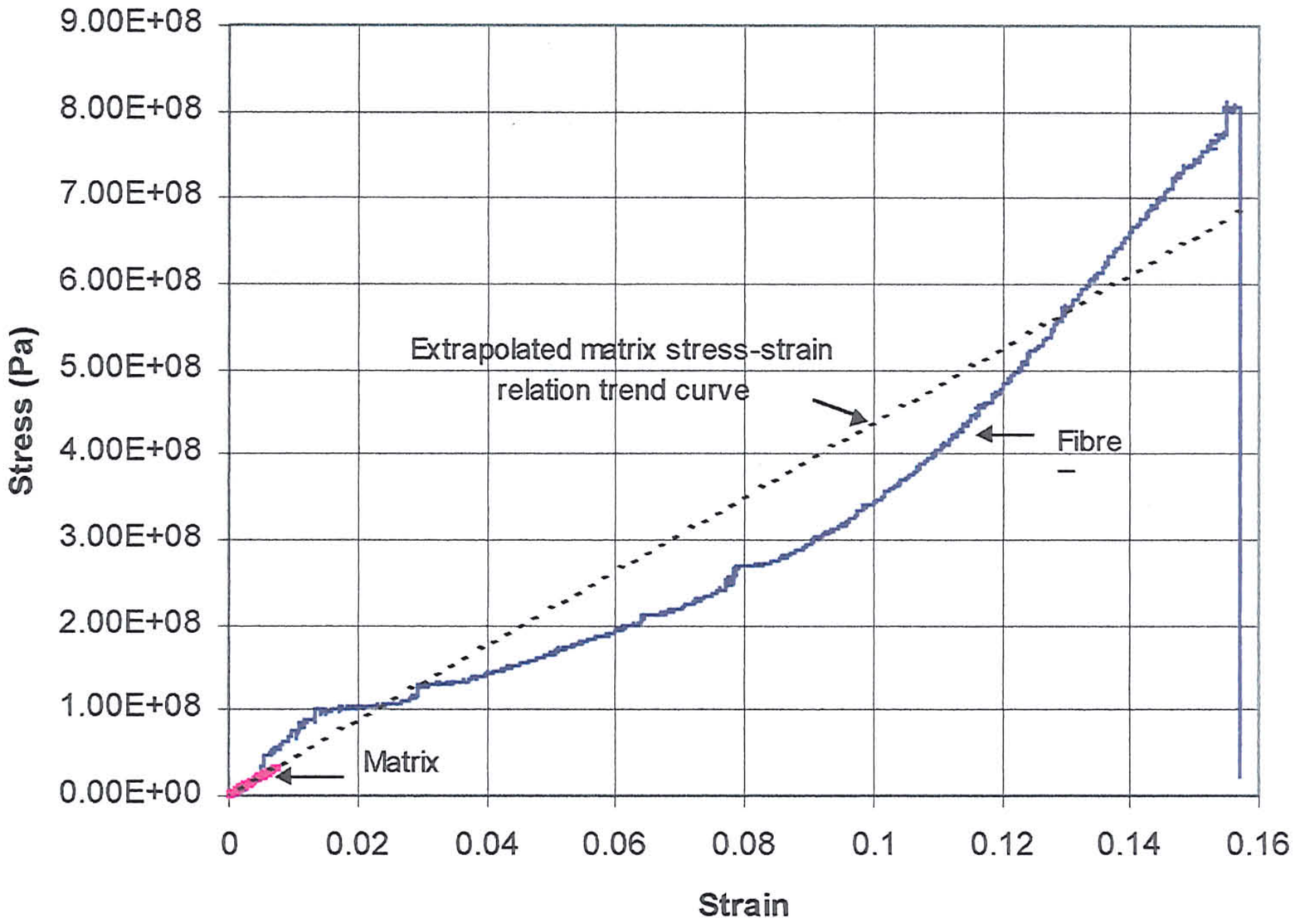

(a)

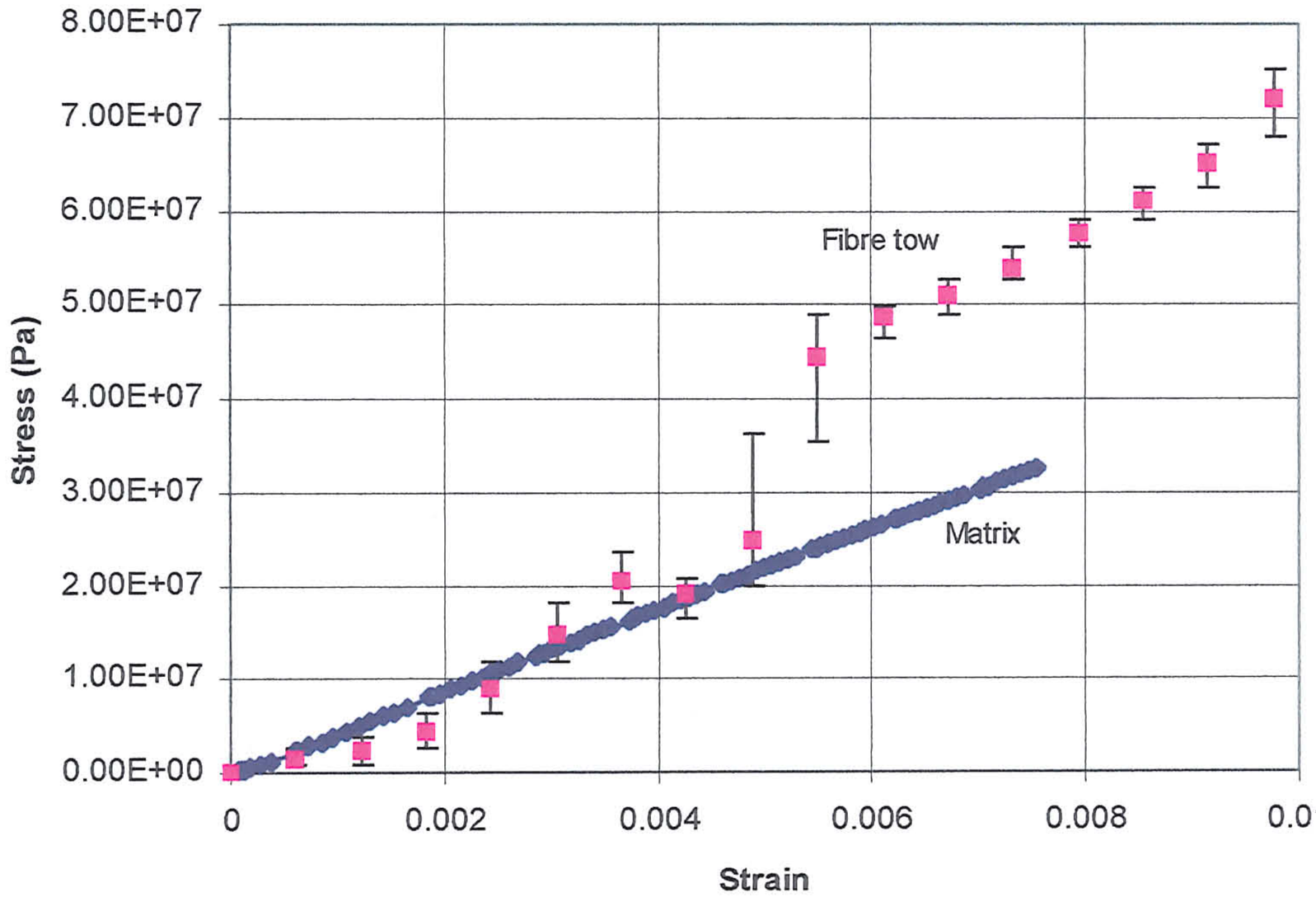

(b)

Fig 4.2.2-1 (a) Stress-strain relation for a polyester fibre tow (with 210 fibres) in uniaxial tension when compare with the polyester matrix; (b) Enlargement of the low strain region.

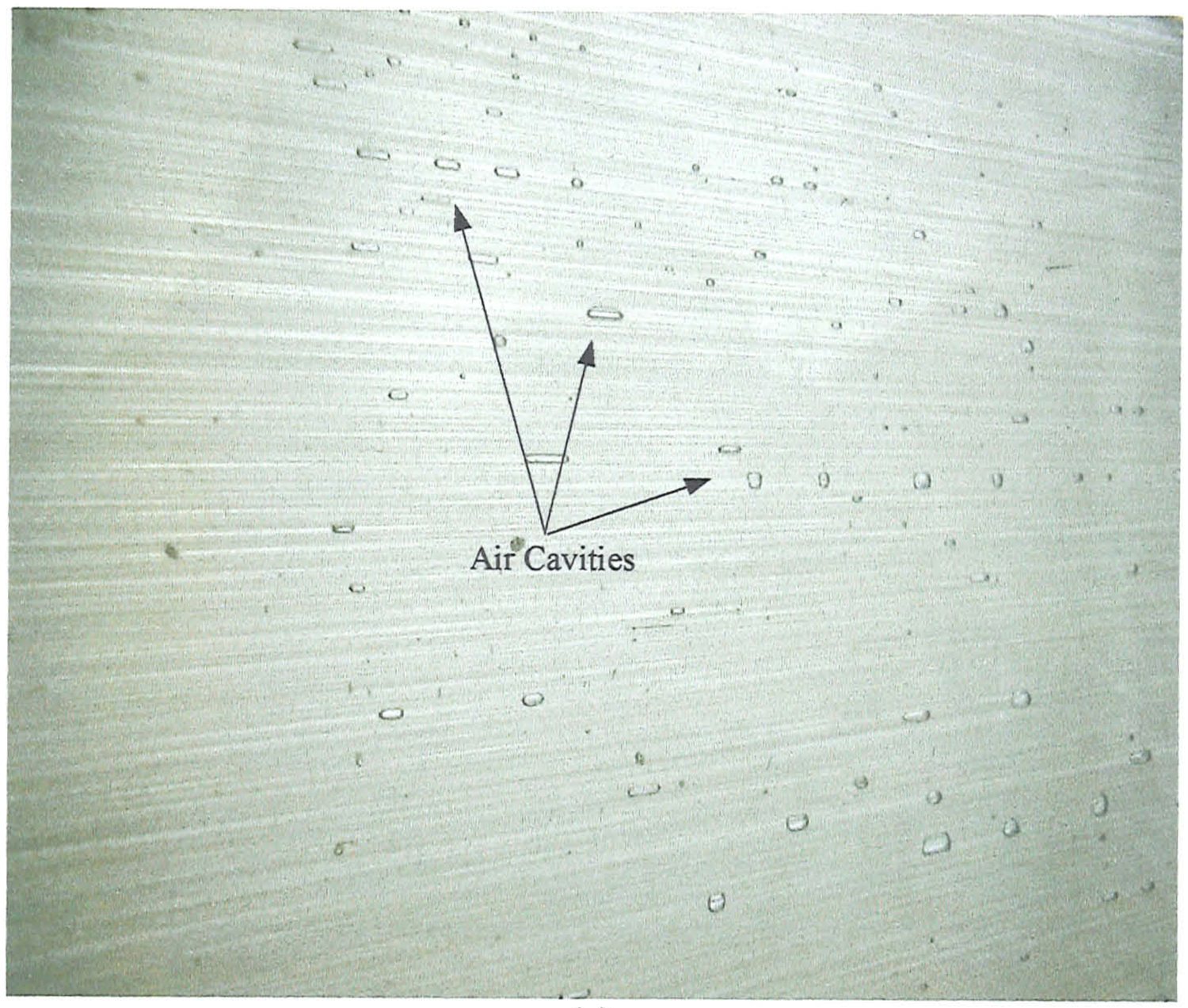

(a)

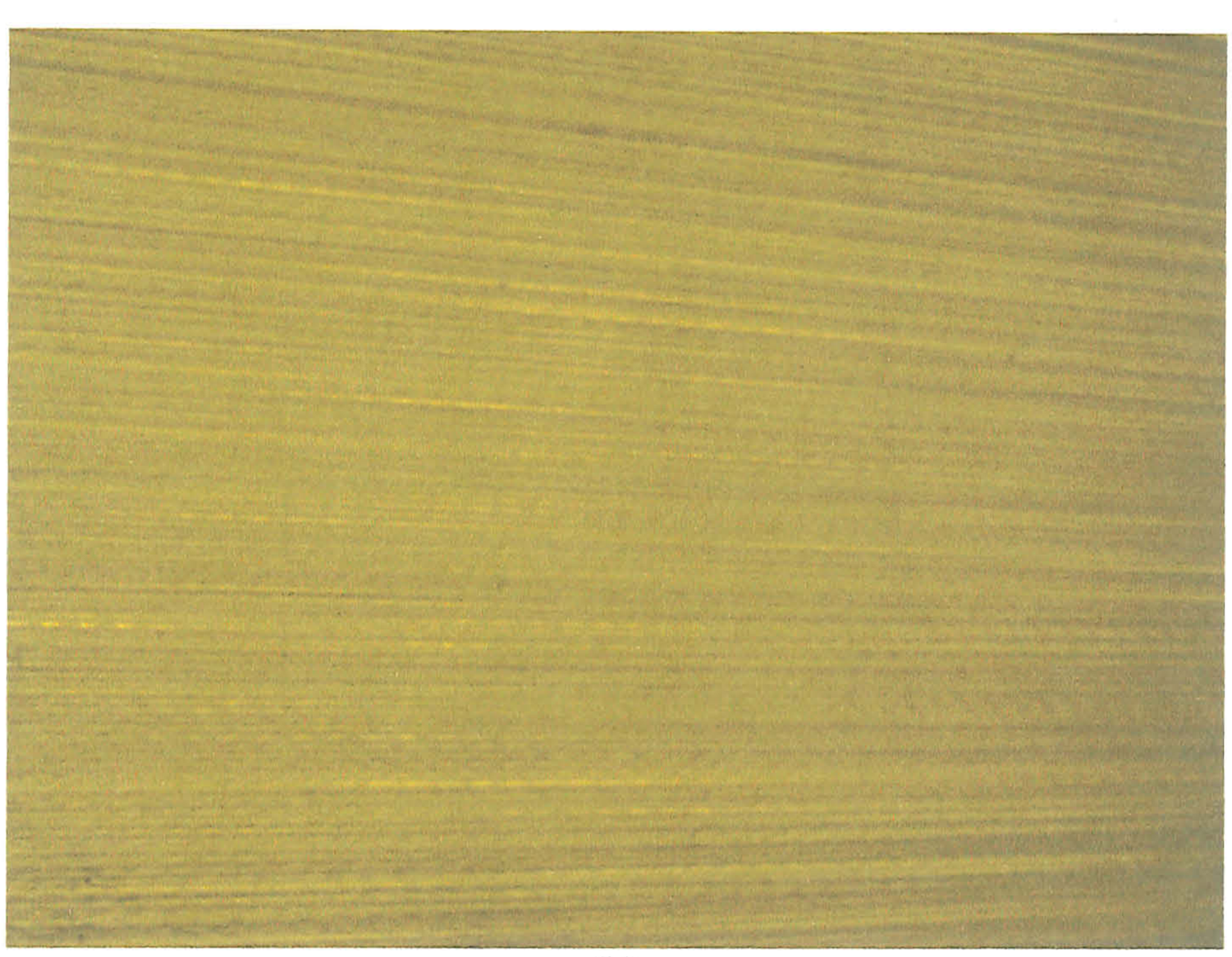

(b)

Fig 4.2.3-1 Quality of the one-dimensional polyester composite panel fabricated through (a) hand-laying technique and (b) resin injection technique.

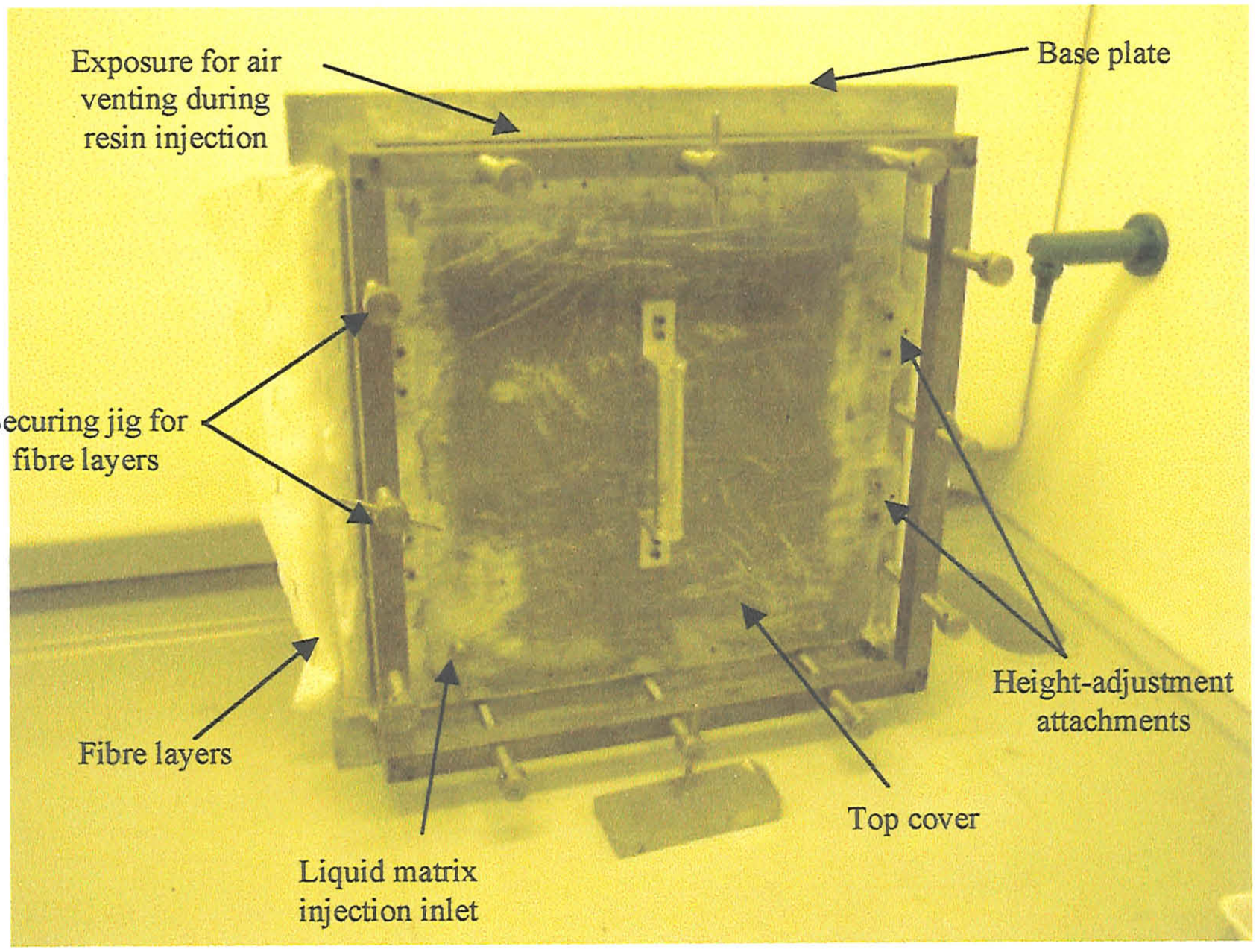

Note: The grips usually applied at the height–adjustment attachments have been removed to facilitate labelling purposes.

Fig 4.2.3-2 Custom-made mould for fabricating square polyester composite panels.

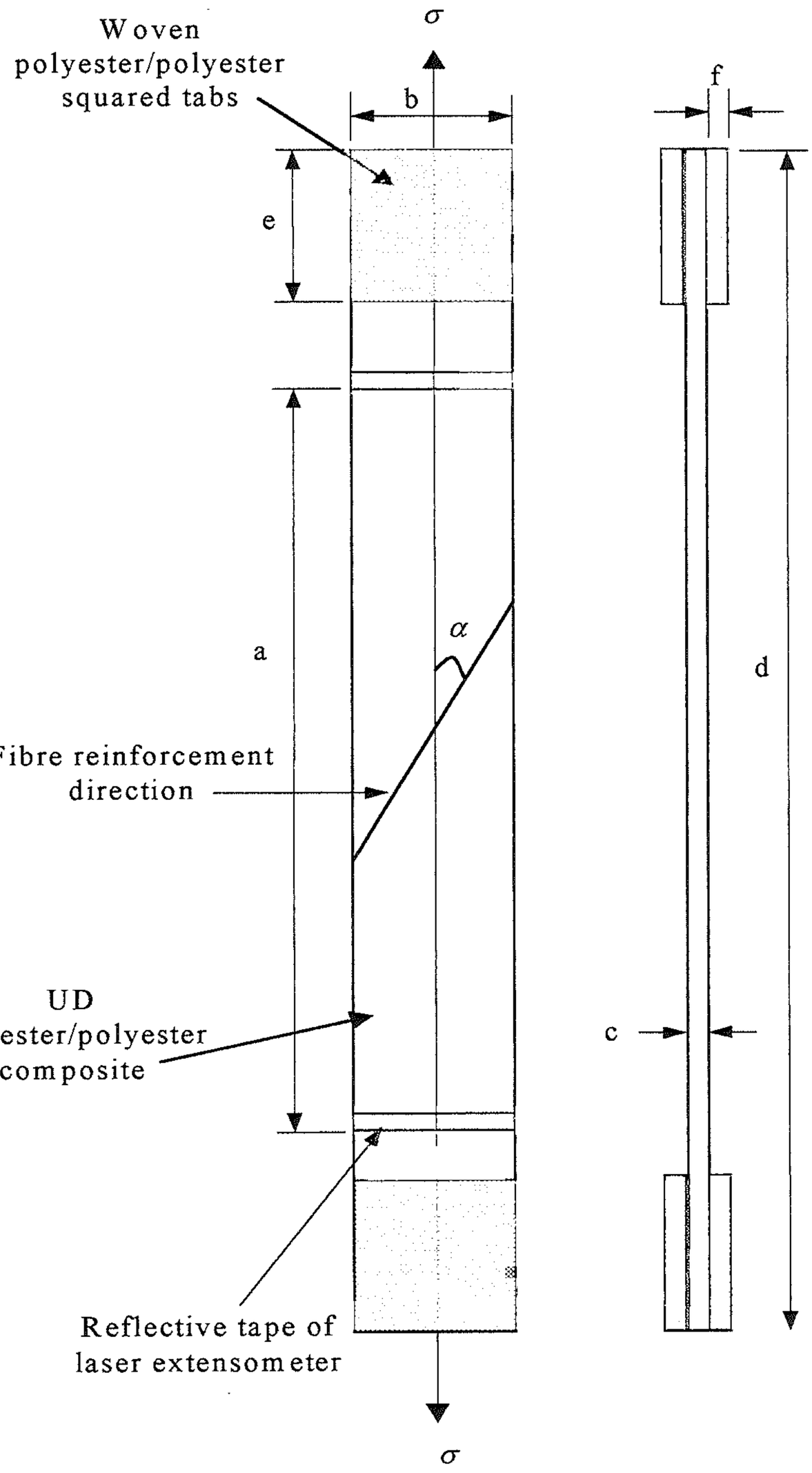

α	a (mm)	b (mm)	c (mm)	d (mm)	e (mm)	f (mm)
0°	125	15	2.1	210	38	1.2
10°	180	20	2.1	250	25	1.2
20°	140	20	2.1	200	25	1.2
30°	80	20	2.1	140	25	1.2
45° to 90°	40	20	2.1	100	25	1.2

Fig 4.3.1-1 Dimensions for the tabbed one-dimensional analogue rectangular coupons at fibre alignment angle $\alpha = 0°$, 10°, 20°, 30°, 45°, 60°, 70°, 80° and 90°.

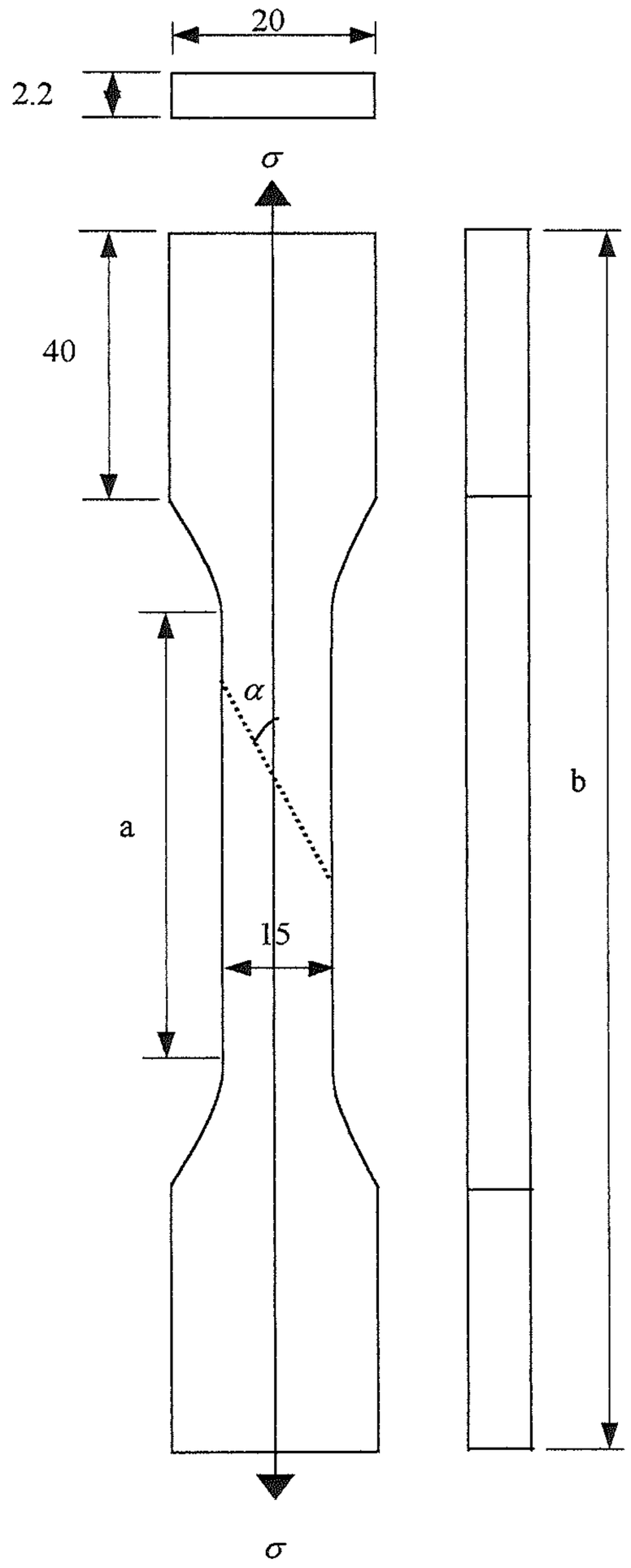

All dimensions are in mm.

α	a (mm)	b (mm)
0°	50	160
10°	110	225
20°	50	180
30°	50	180
45°	50	160

Fig 4.3.1-2 Dimensions for the one-dimensional analogue dog-bone specimens at fibre alignment angle $\alpha = 0°$, 10°, 20°, 30° and 45°.

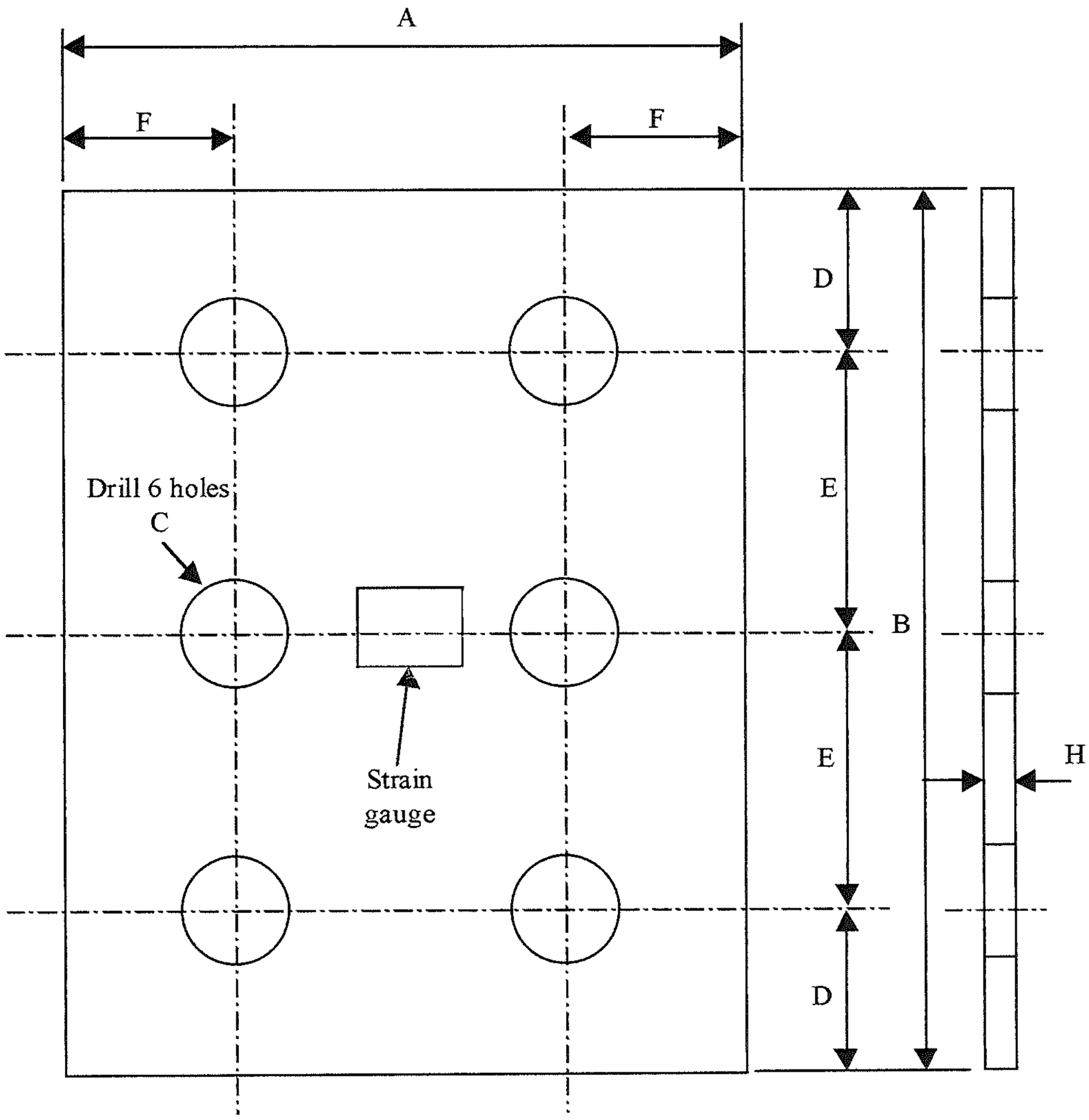

Dimension	mm
A	76
F	15.9
C	12.7
D	25.0
E	51.0
B	152.0
H	2.75

Fig 4.3.1-3 Method A Rail Shear Specimen (ASTM D4225/D4355M)

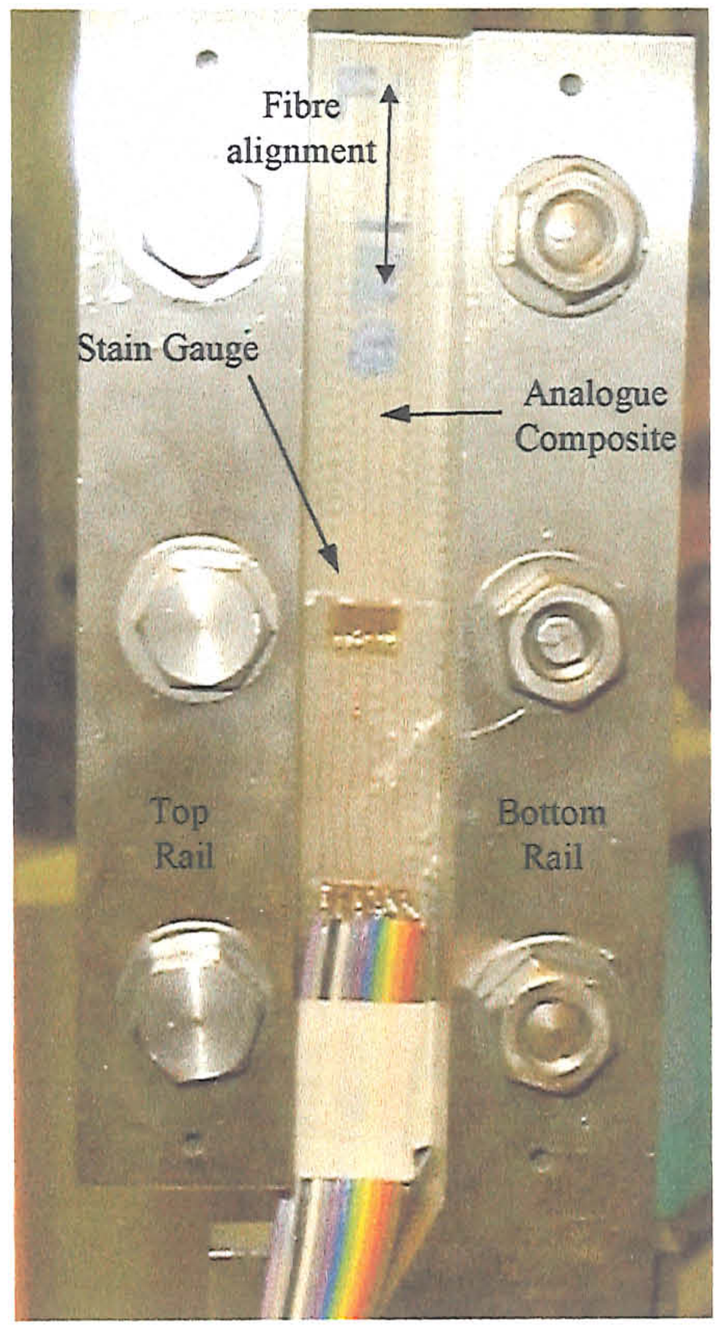

Fig 4.3.1-4 Photograph of the Rail Shear configuration.

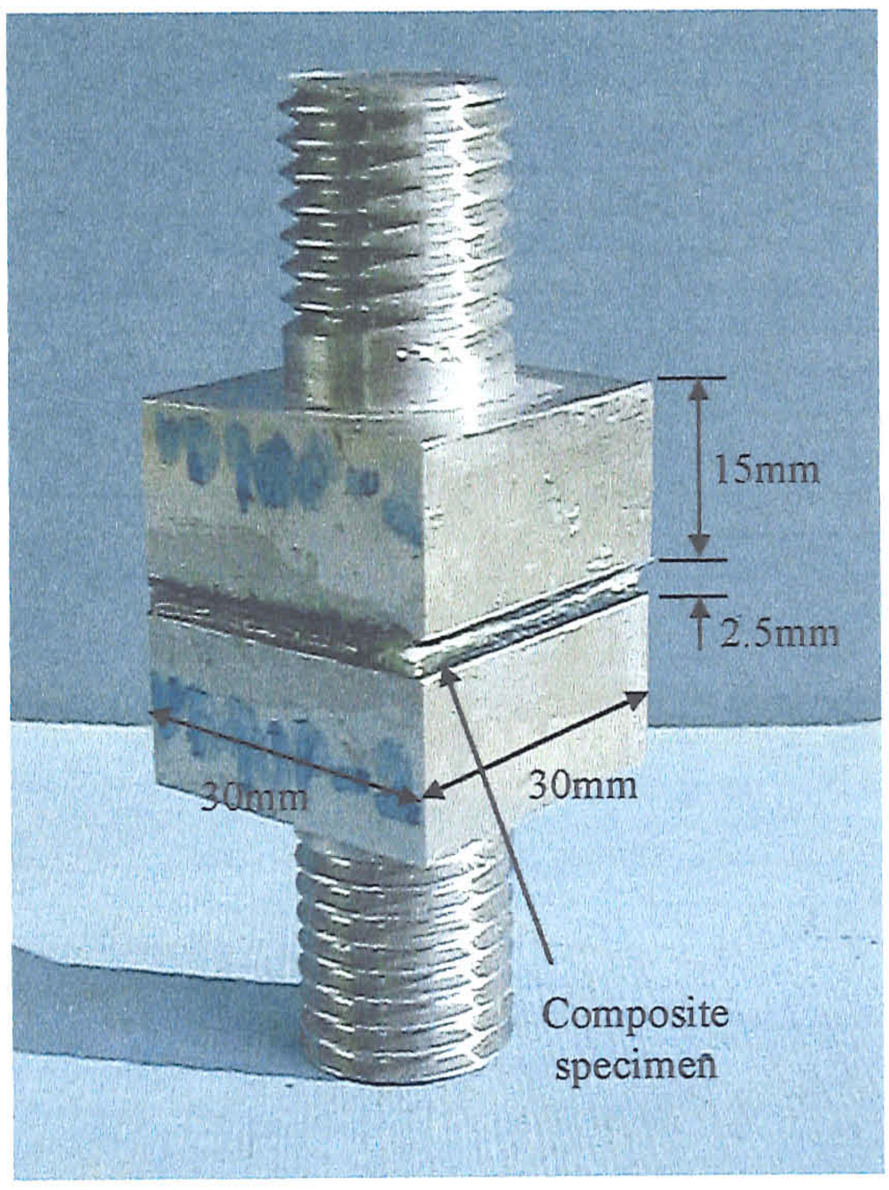

Fig 4.3.1-5 Photograph of the test configuration for determining the composite through thickness delamination strength.

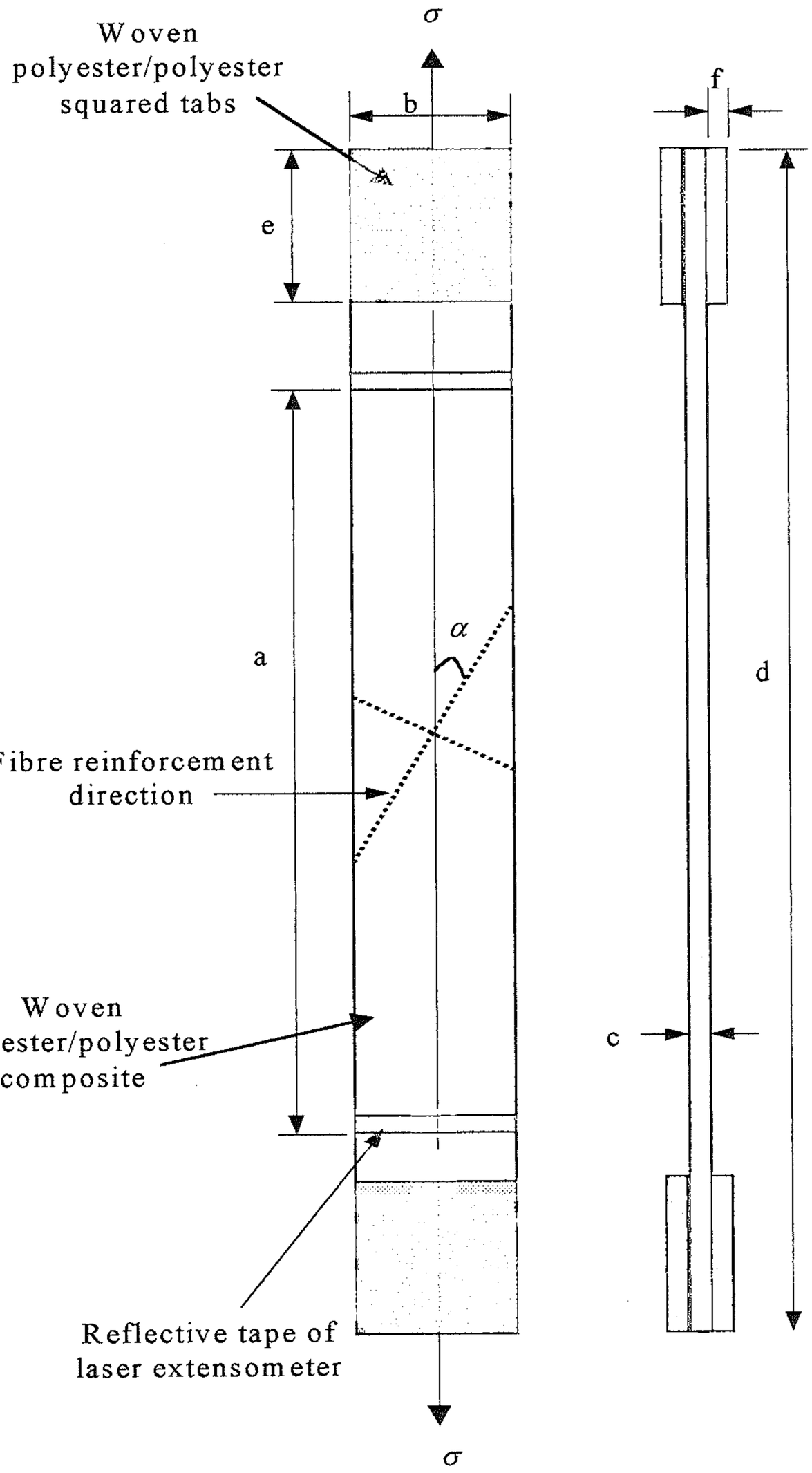

α	a (mm)	b (mm)	c (mm)	d (mm)	e (mm)	f (mm)
0°	115	15	2	200	38	1.2
10°	180	20	2	250	25	1.2
20°	125	20	2	185	25	1.2
30°	70	20	2	130	25	1.2
45°	35	20	2	95	25	1.2

Fig 4.3.1-6 Dimensions for the tabbed two-dimensional analogue rectangular coupon at fibre alignment angle of $\alpha = 0°$, 10°, 20°, 30° and 45°.

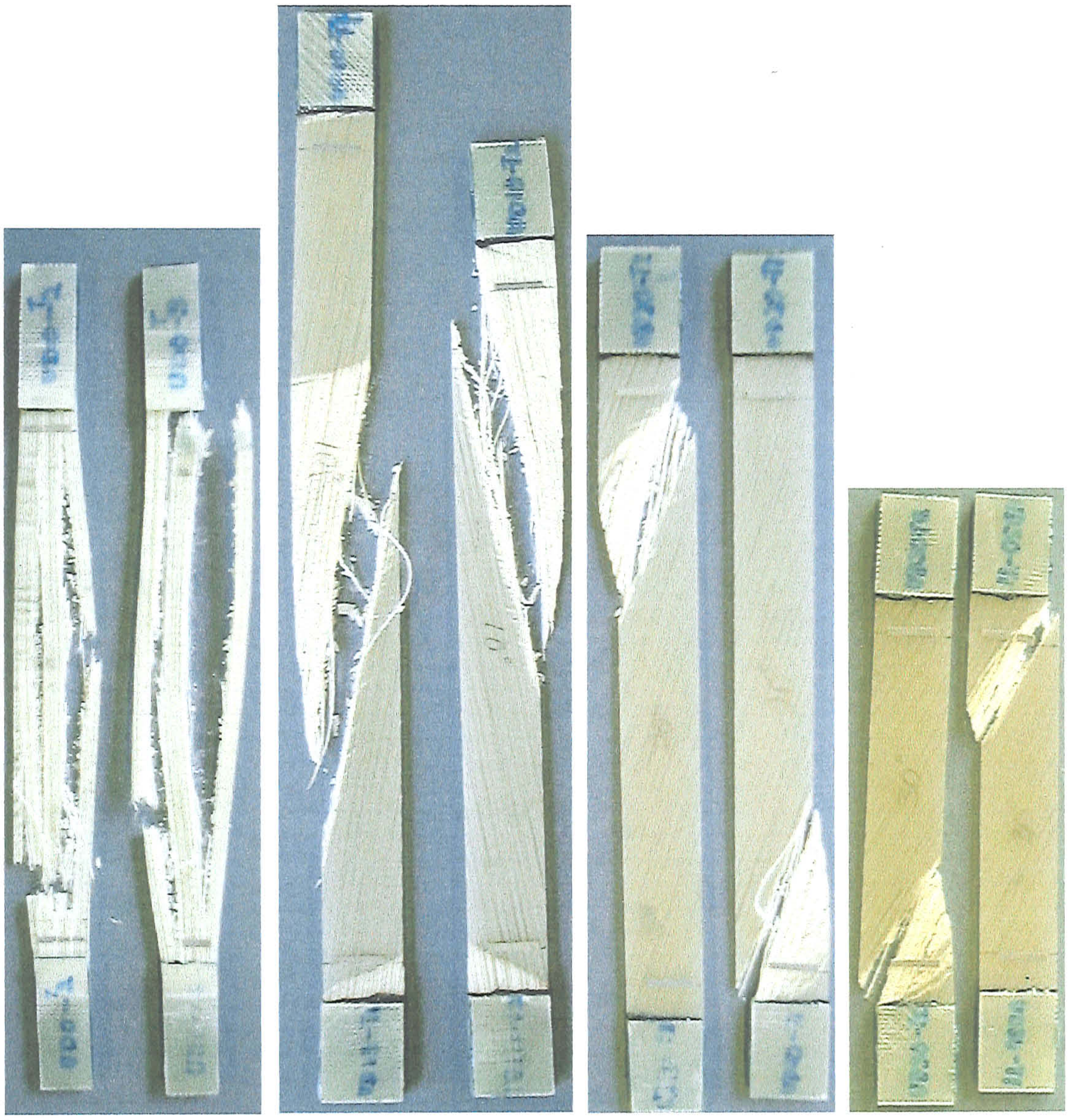

(a) **(b)** **(c)** **(d)**

Fig 4.3.2-1. Photographs of the fractured one-dimensional analogue tabbed-coupons in uniaxial tension at various fibre alignment angle: (a) $\alpha = 0°$, (b) $\alpha = 10°$, (c) $\alpha = 20°$, (d) $\alpha = 30°$, (e) $\alpha = 45°$, (f) $\alpha = 60°$, (g) $\alpha = 70°$, (h) $\alpha = 80°$ and (i) $\alpha = 90°$.

(e)

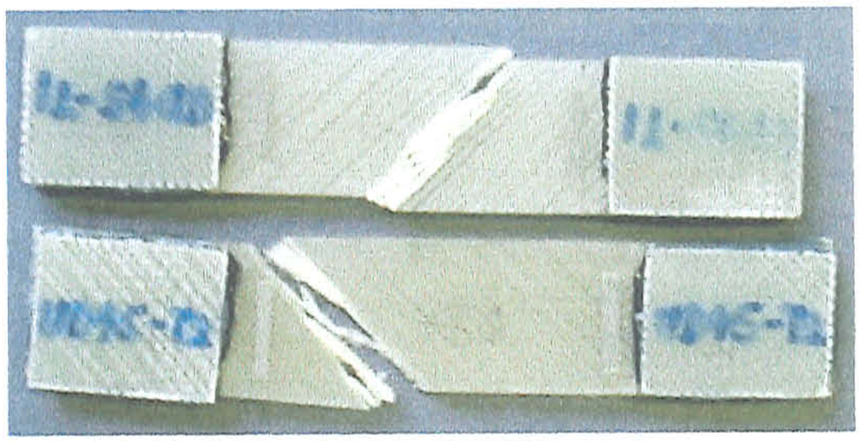

(f)

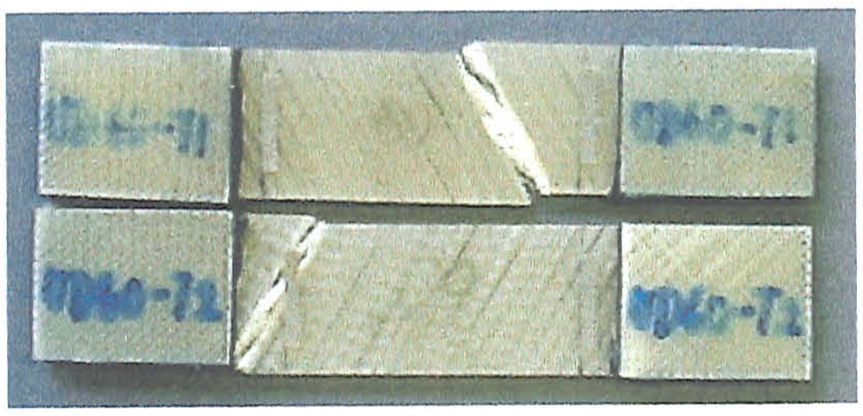

(g)

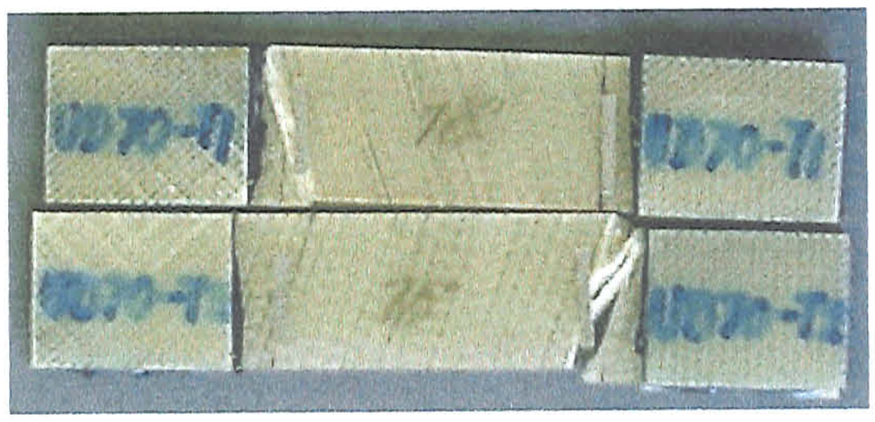

(h)

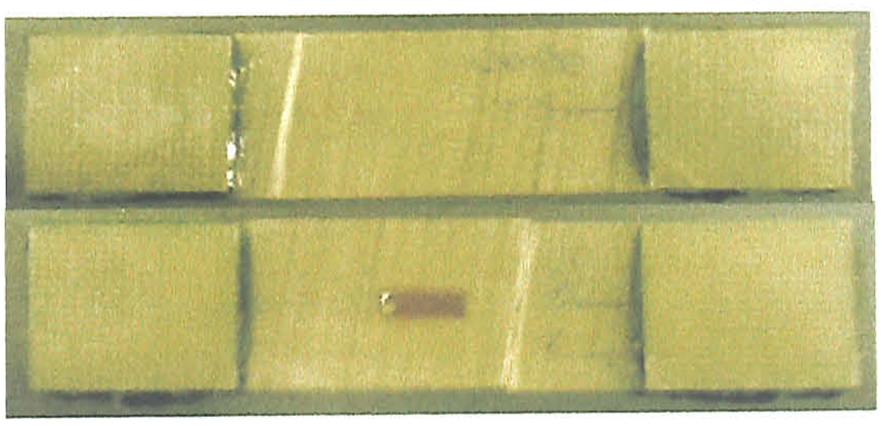

(i)

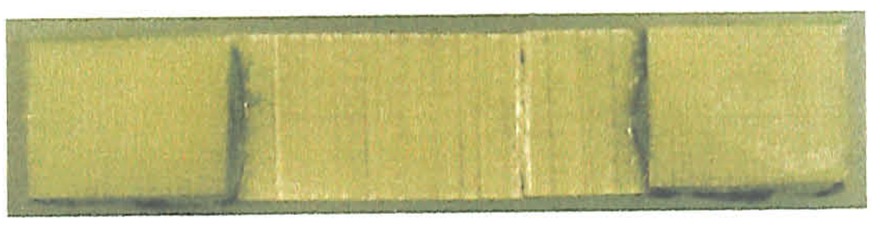

Fig 4.3.2-1 *cont.*

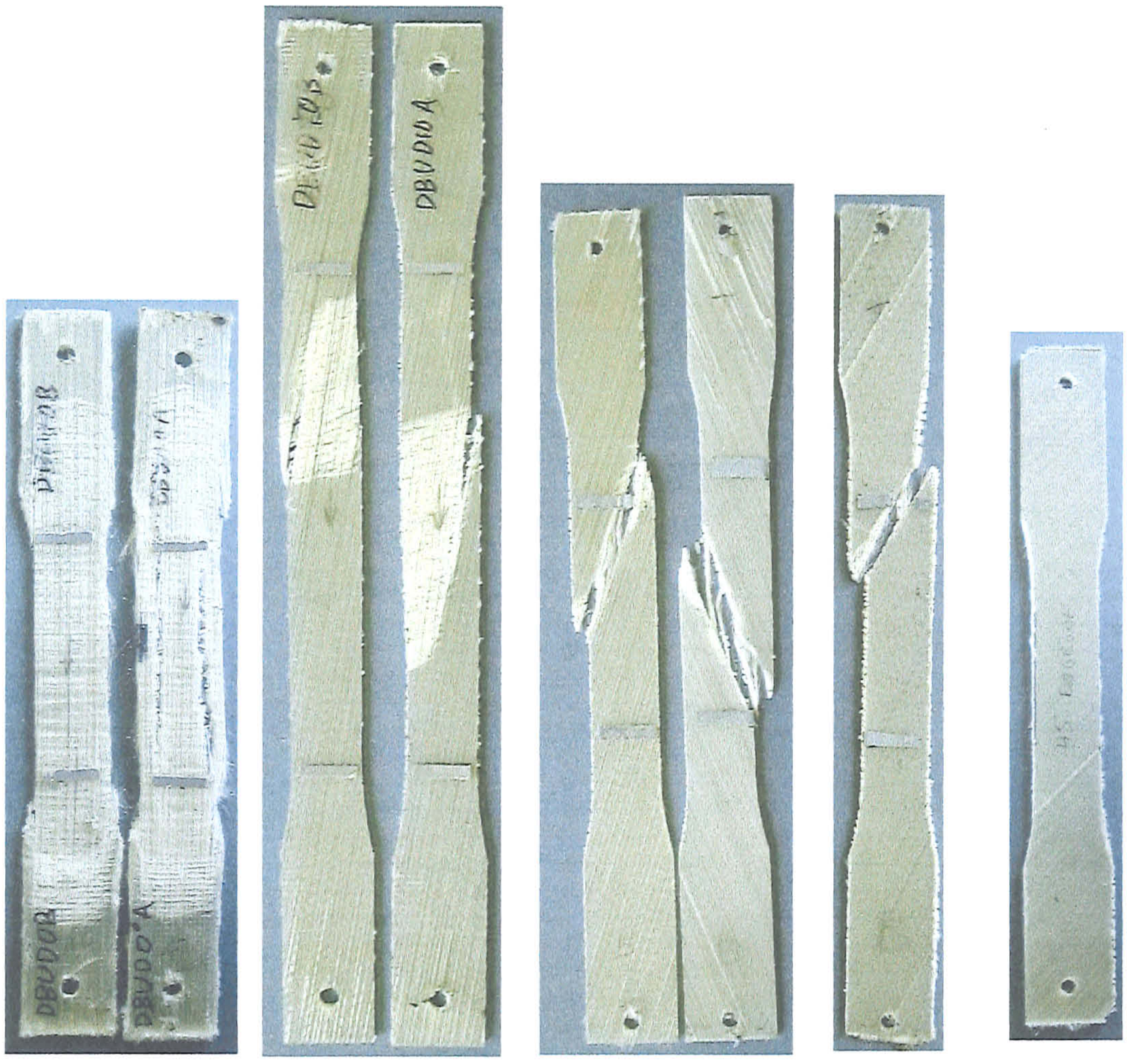

(a) **(b)** **(c)** **(d)** **(f)**

Fig 4.3.2-2. Photographs of the fractured one-dimensional analogue dogbone shaped specimens in uniaxial tension at various fibre alignment angle: (a) $\alpha = 0°$, (b) $\alpha = 10°$, (c) $\alpha = 20°$, (d) $\alpha = 30°$ and (e) $\alpha = 45°$.

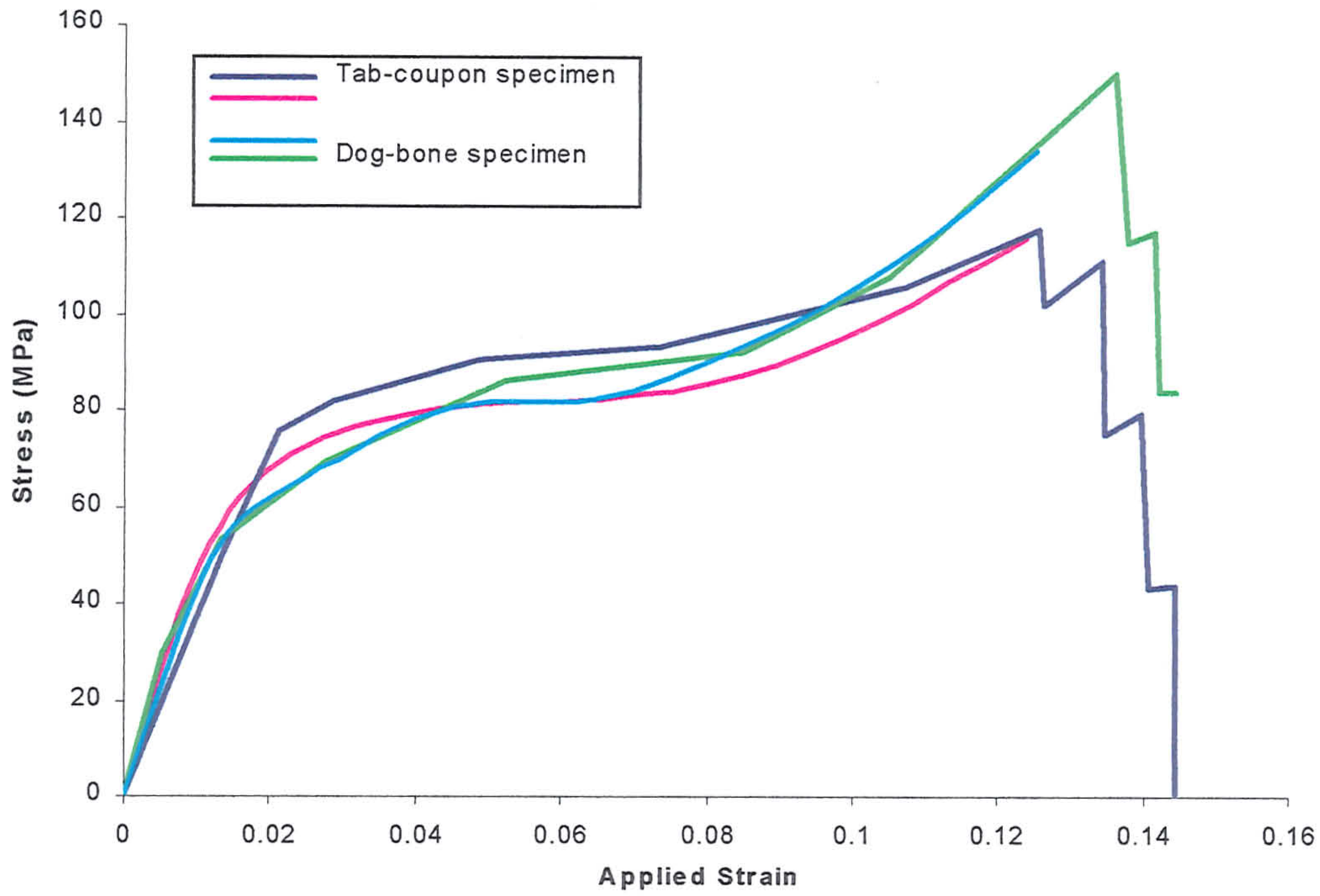

(a) $\alpha = 0°$

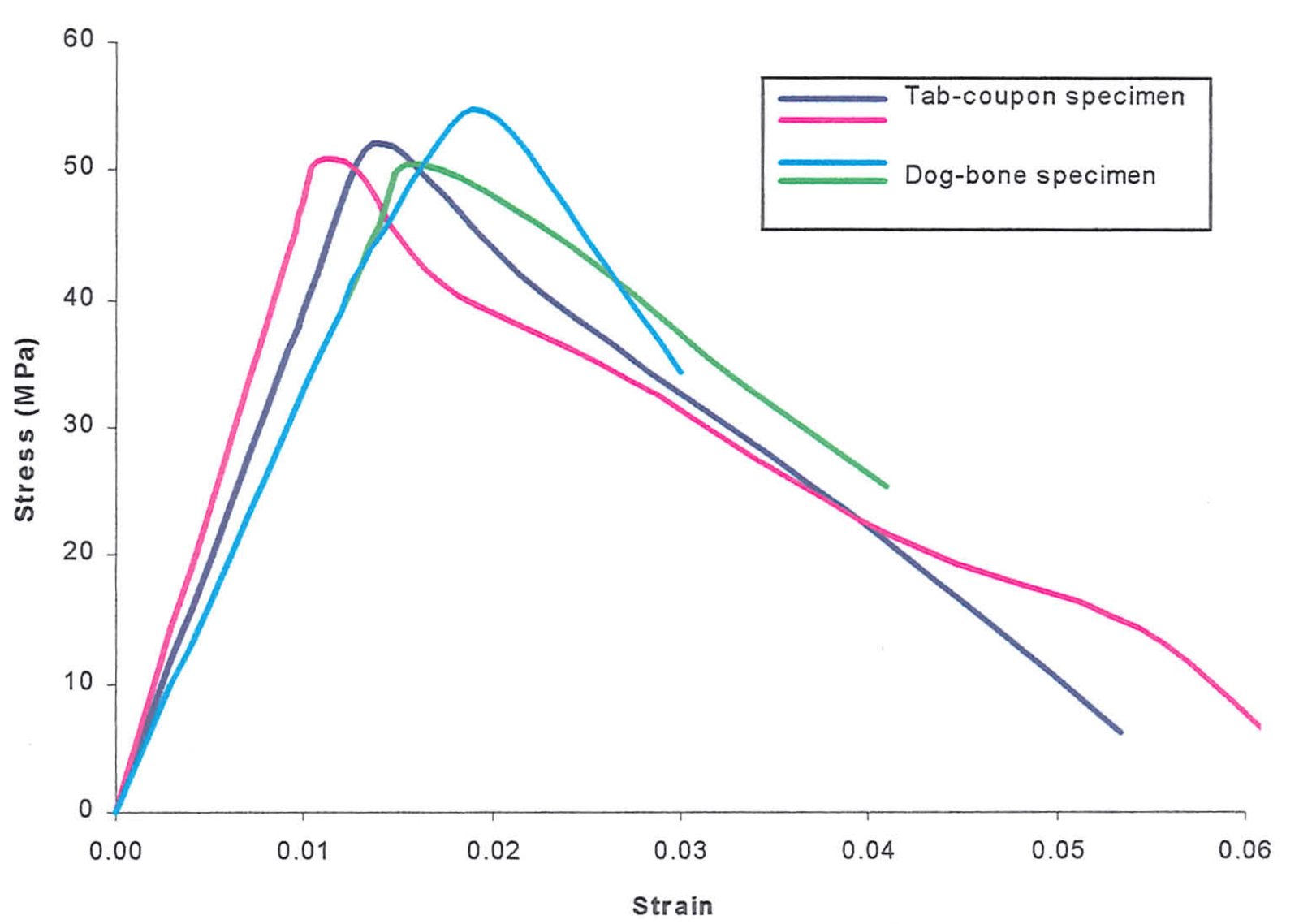

(b) $\alpha = 10°$

Fig 4.3.2-3 Stress-strain relations of one-dimensional analogue composite in uniaxial tension for fibre angle: (a) $\alpha = 0°$, (b) $\alpha = 10°$, (c) $\alpha = 20°$, (d) $\alpha = 30°$, (e) $\alpha = 45°$, (f) $\alpha = 60°$, (g) $\alpha = 70°$, (h) $\alpha = 80°$ and (i) $\alpha = 90°$.

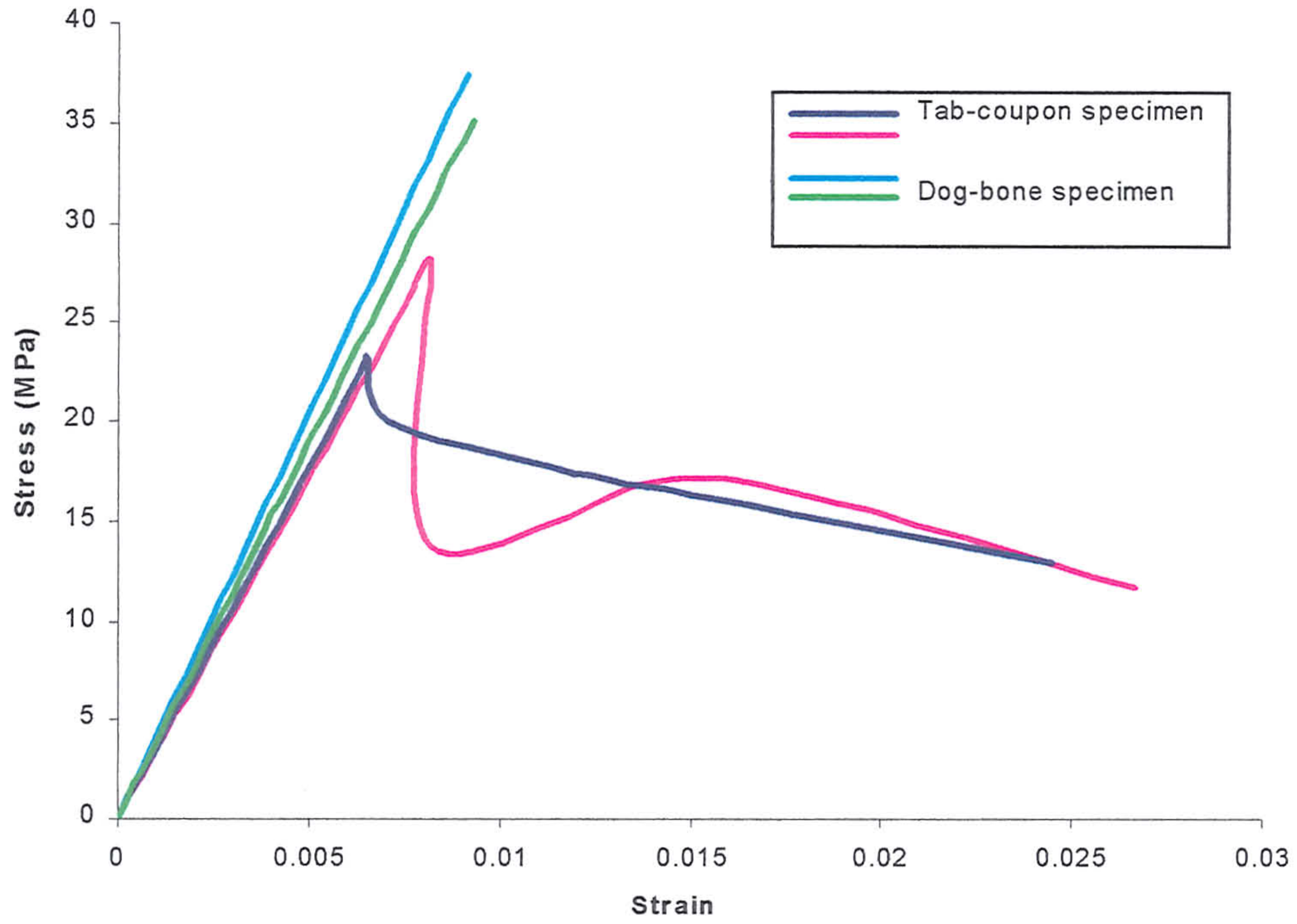

(c) $\alpha = 20°$

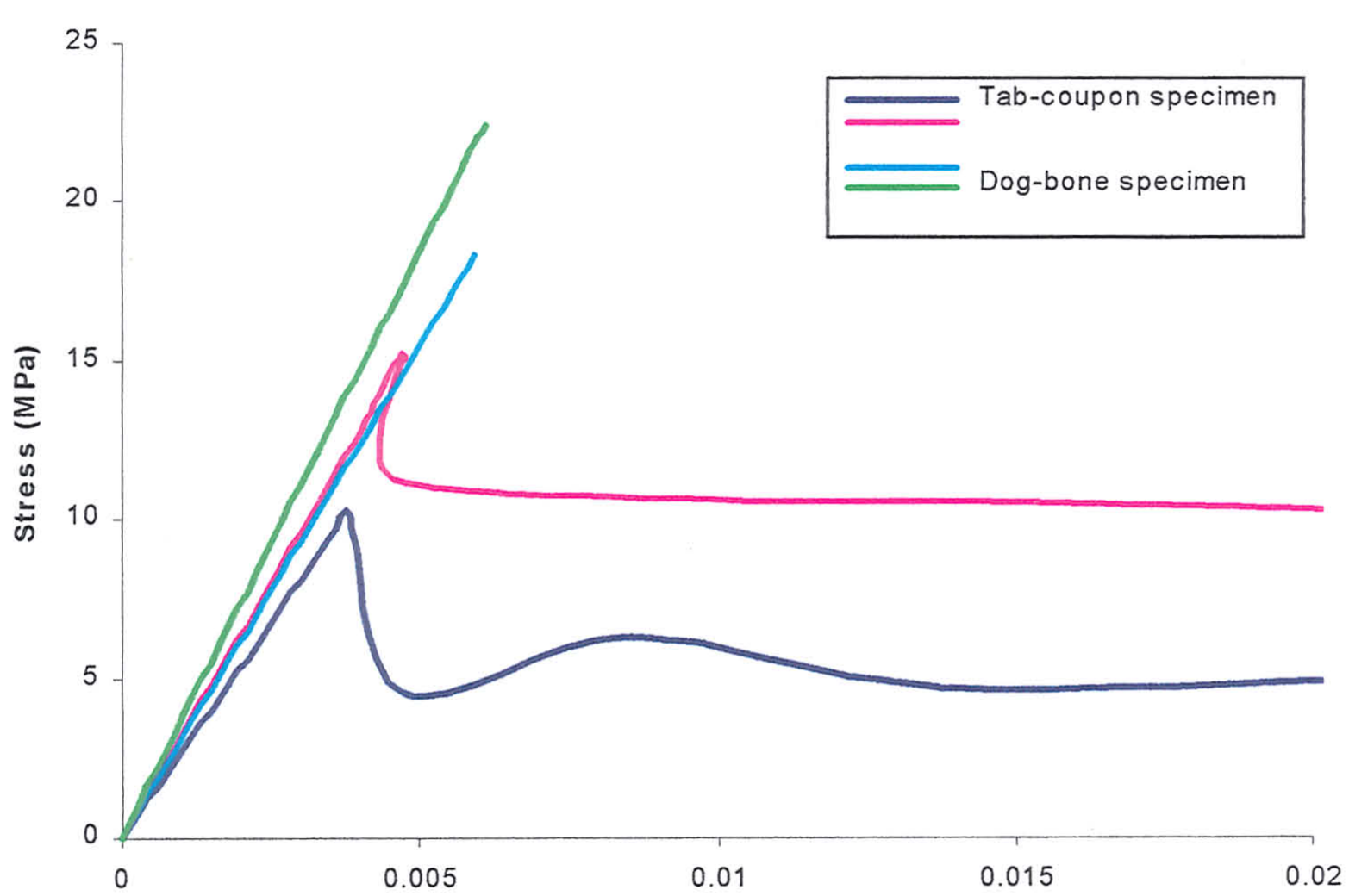

(d) $\alpha = 30°$

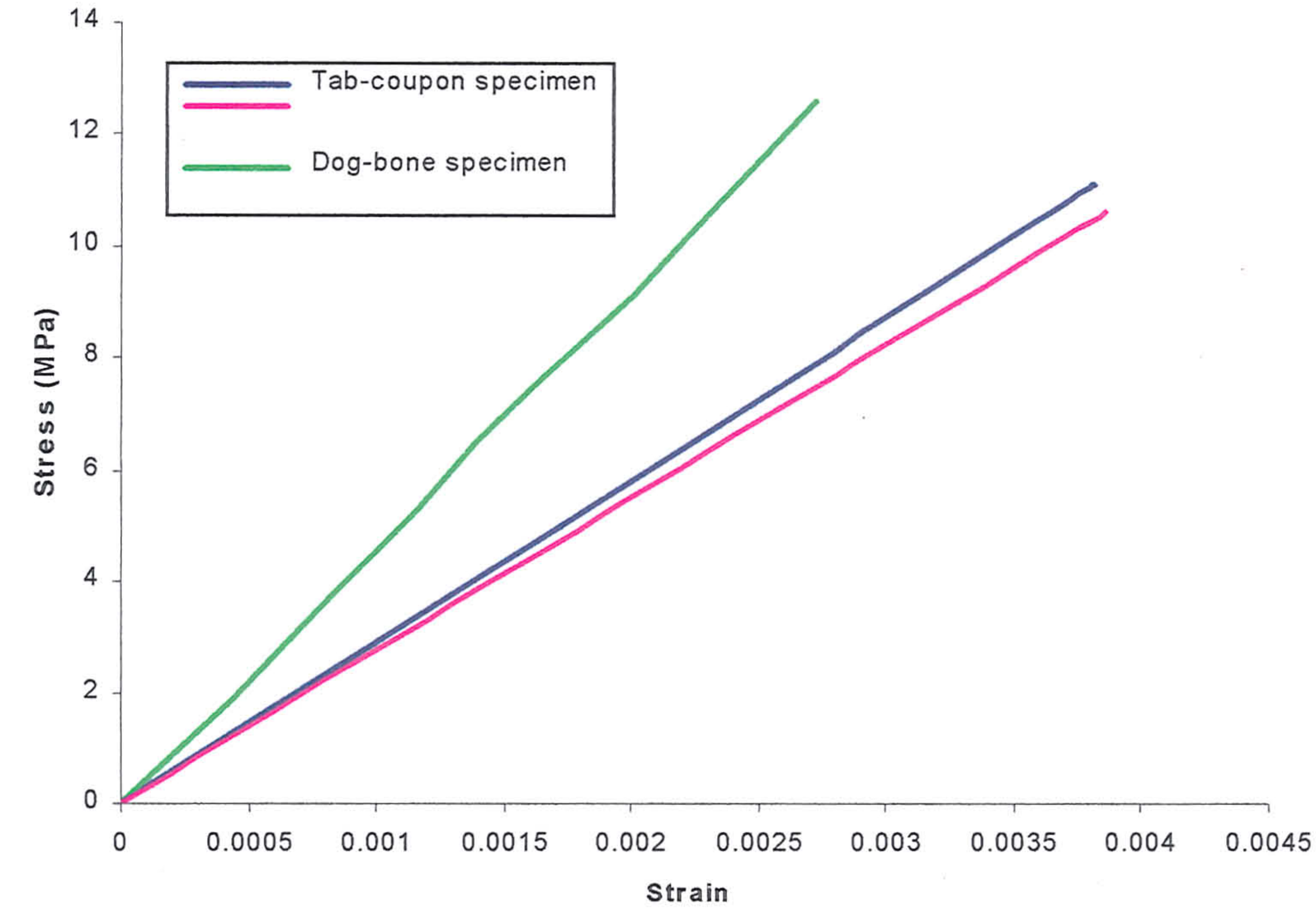

(e) $\alpha = 45°$

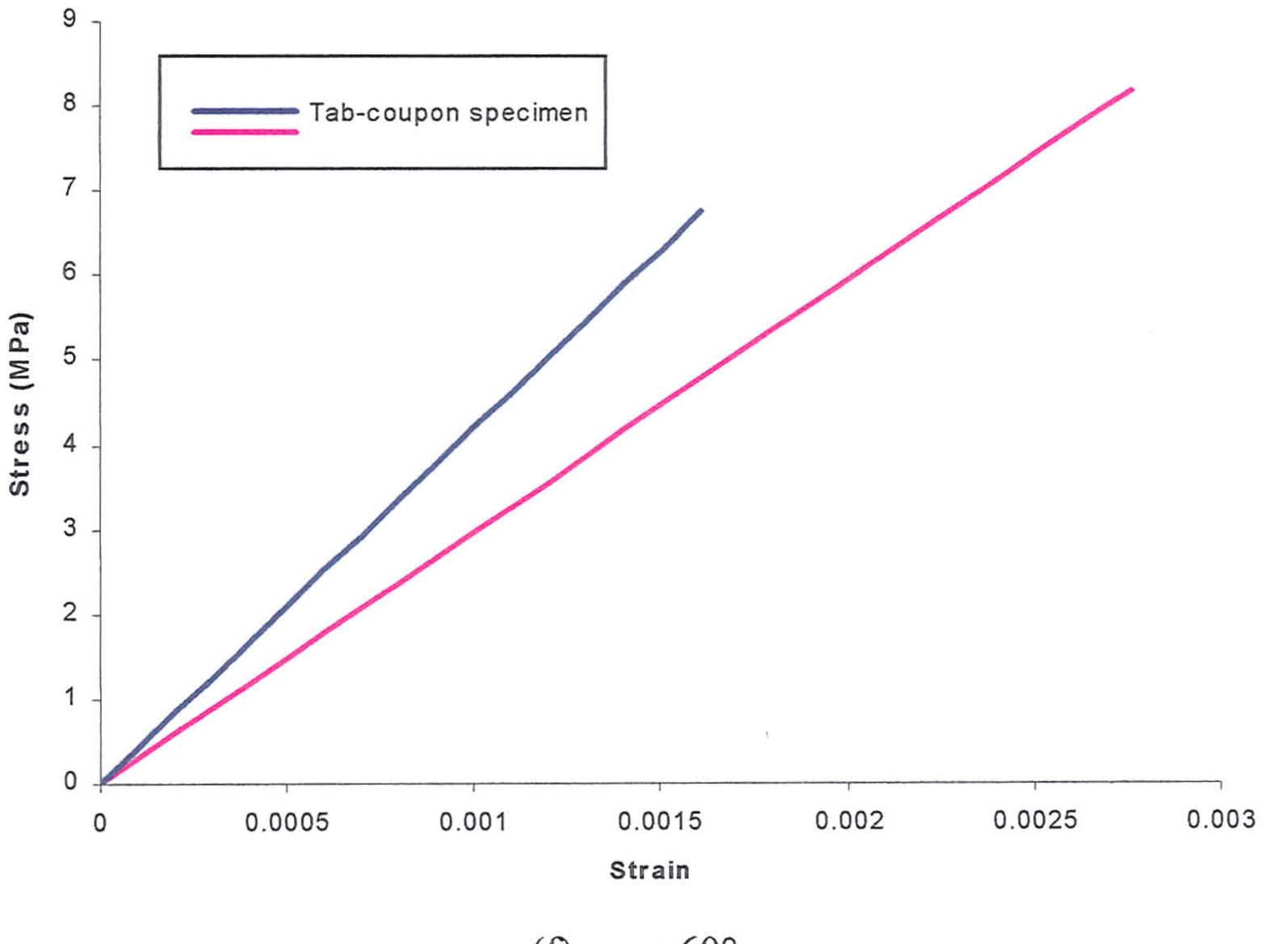

(f) $\alpha = 60°$

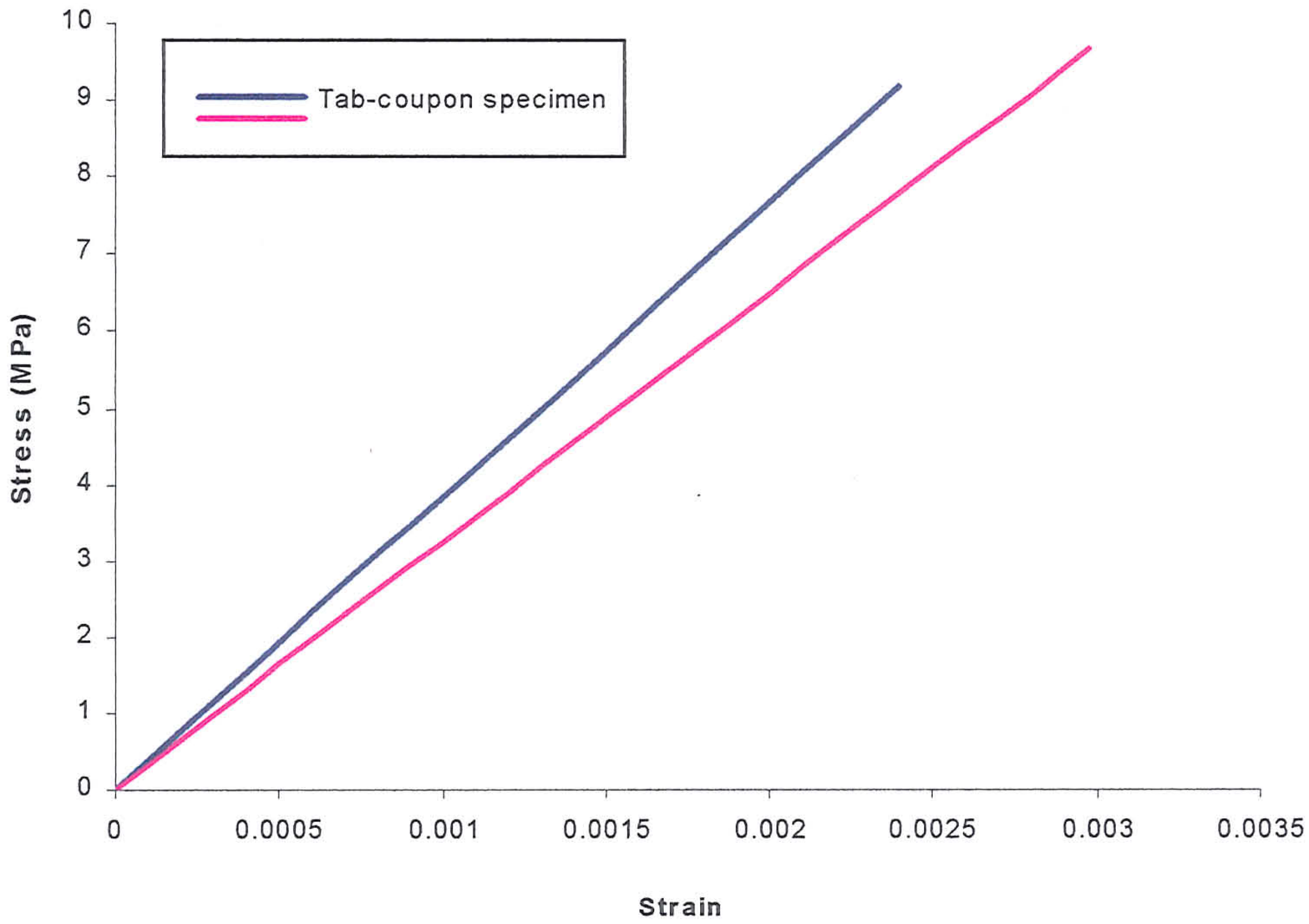

(g) $\alpha = 70°$

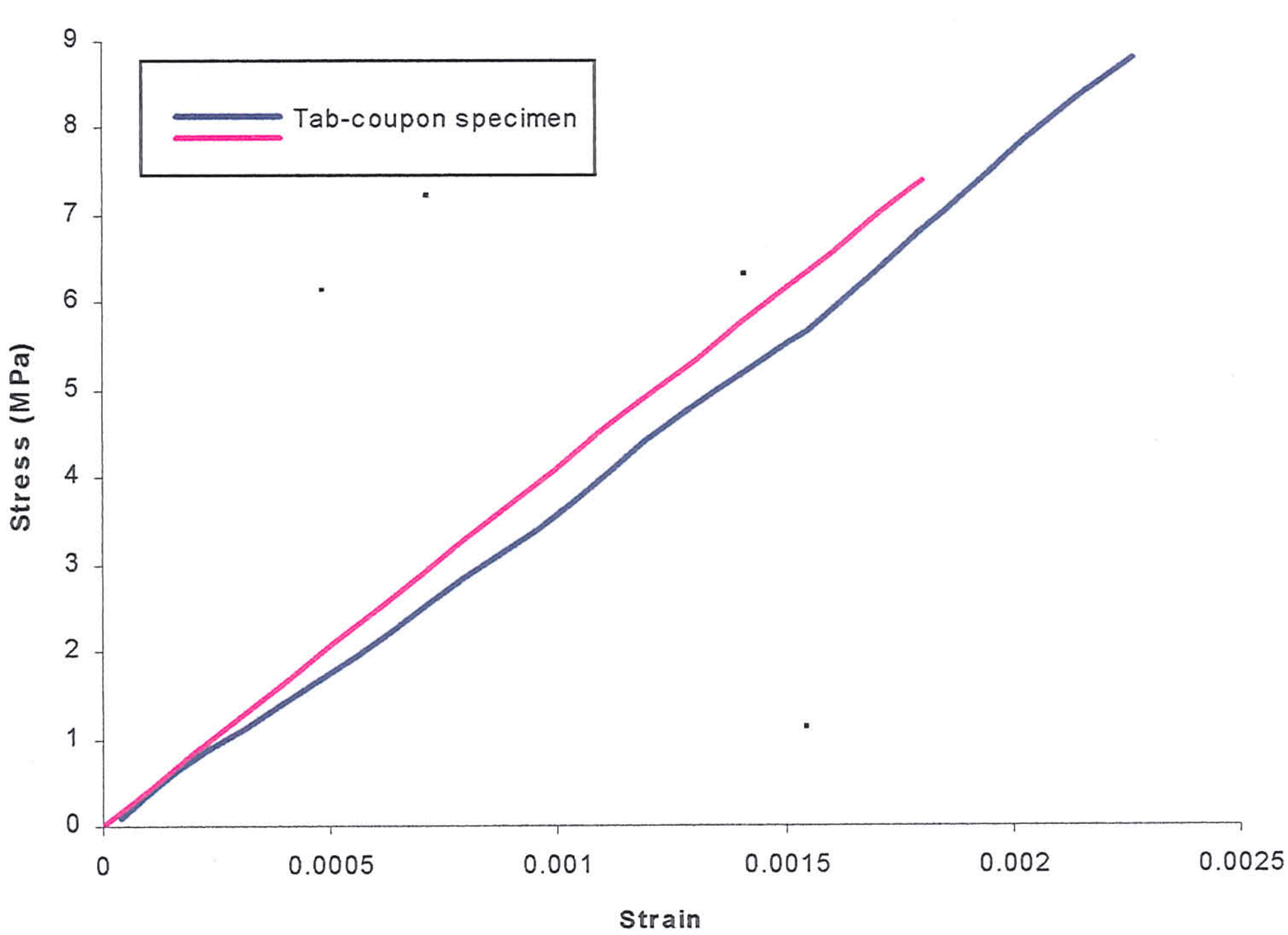

(h) $\alpha = 80°$

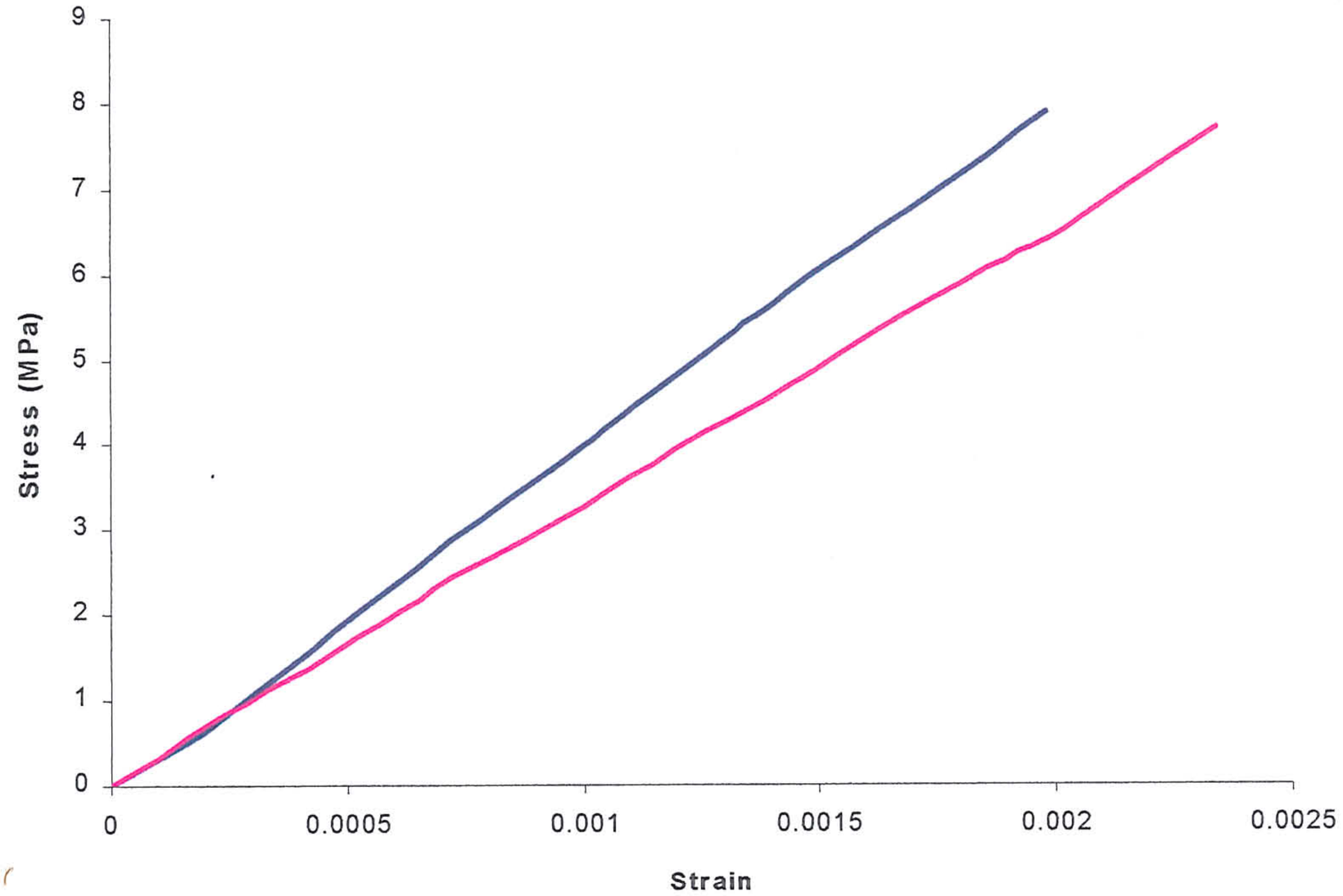

(i) $\alpha = 90°$

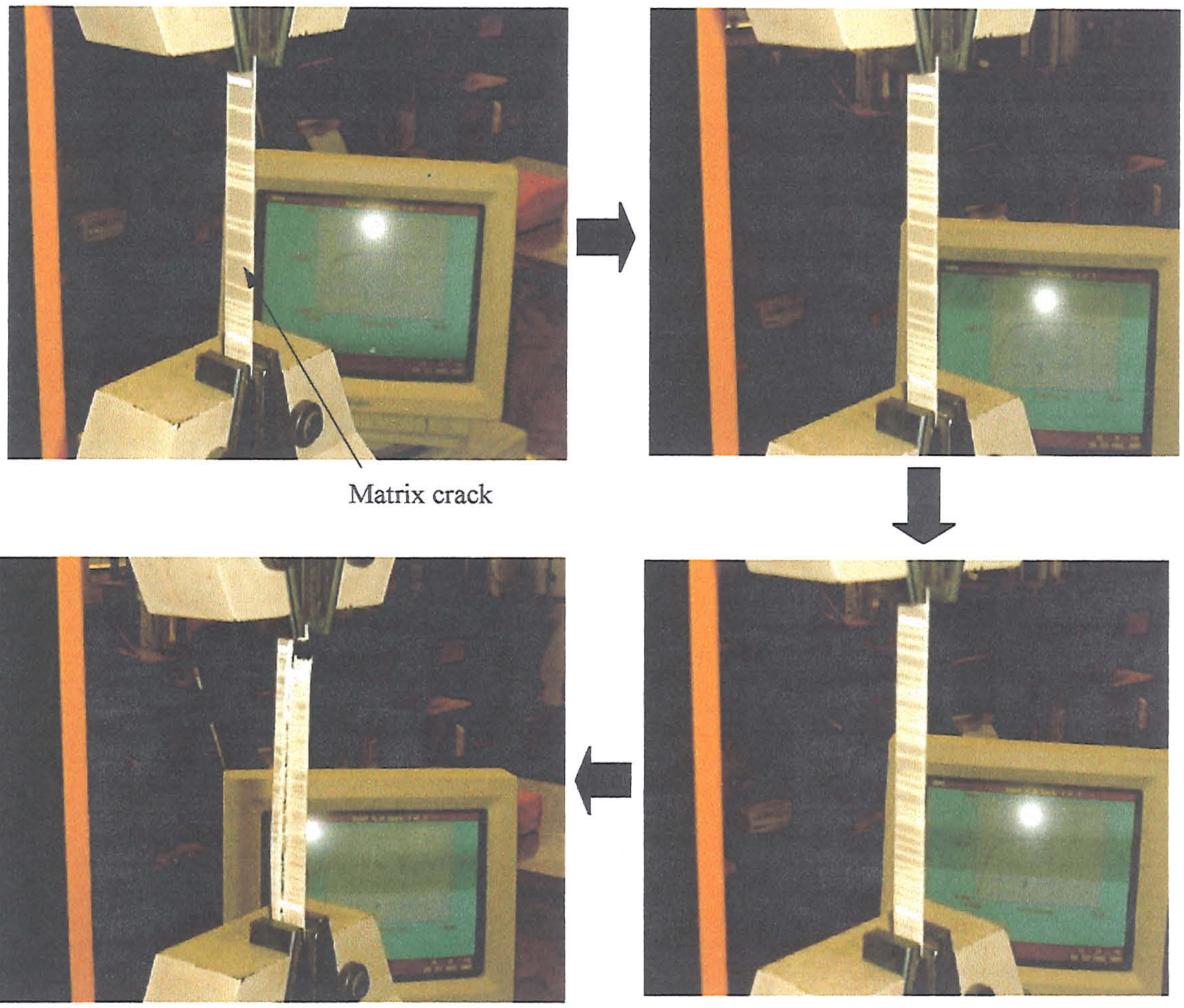

Fig 4.3.2-4 Photographs of matrix cracks distribution in the one-dimensional analogue composite during uniaxial tension.

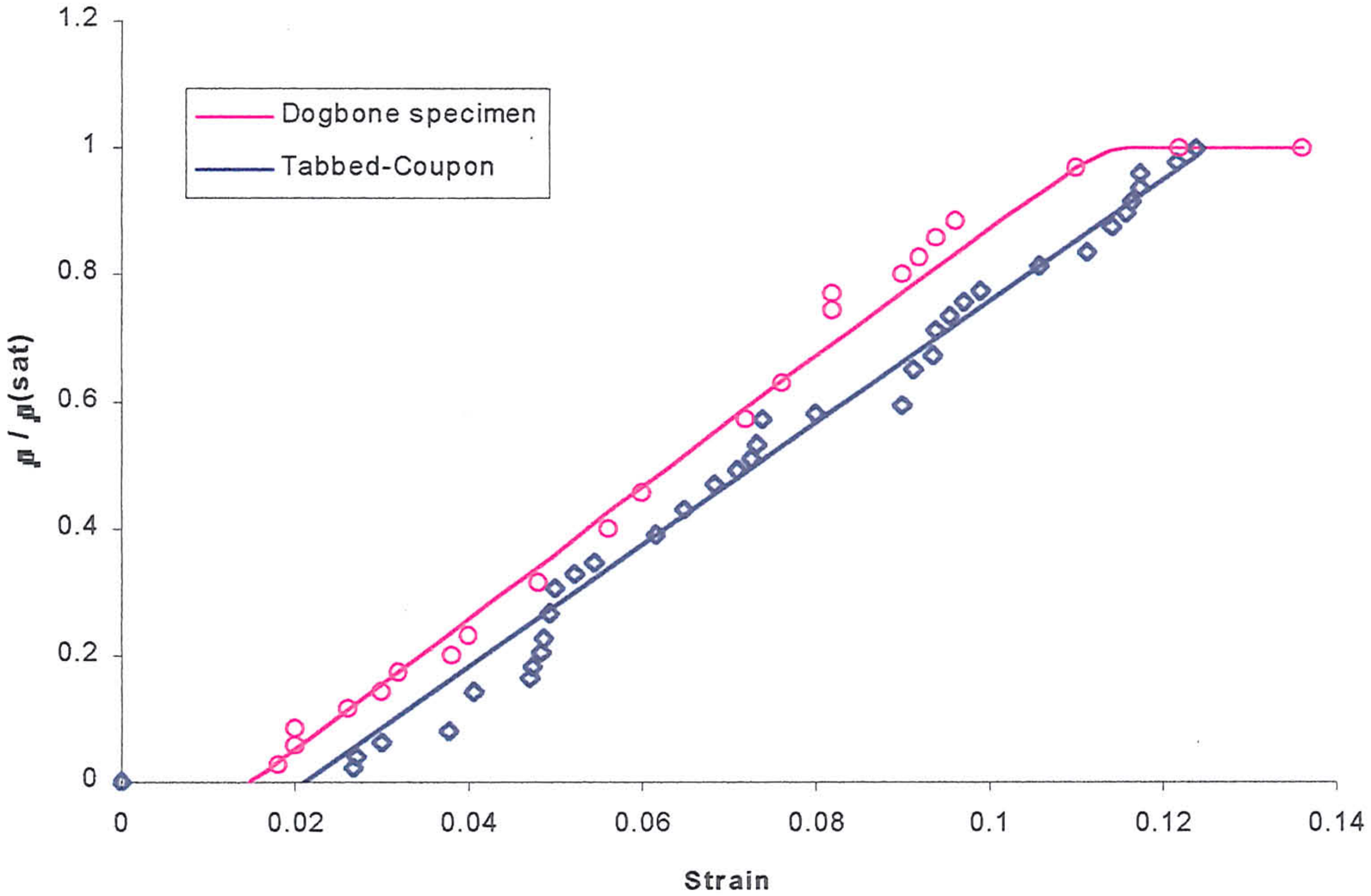

Fig 4.3.2-5 The normalised damage density plot for the one-dimensional analogue composite tensioned in the reinforcement direction. The damage density at saturation for the tabbed-coupon and dogbone specimen were $\rho_{sat} = 6$ cracks/cm and 7cracks/cm, respectively.)

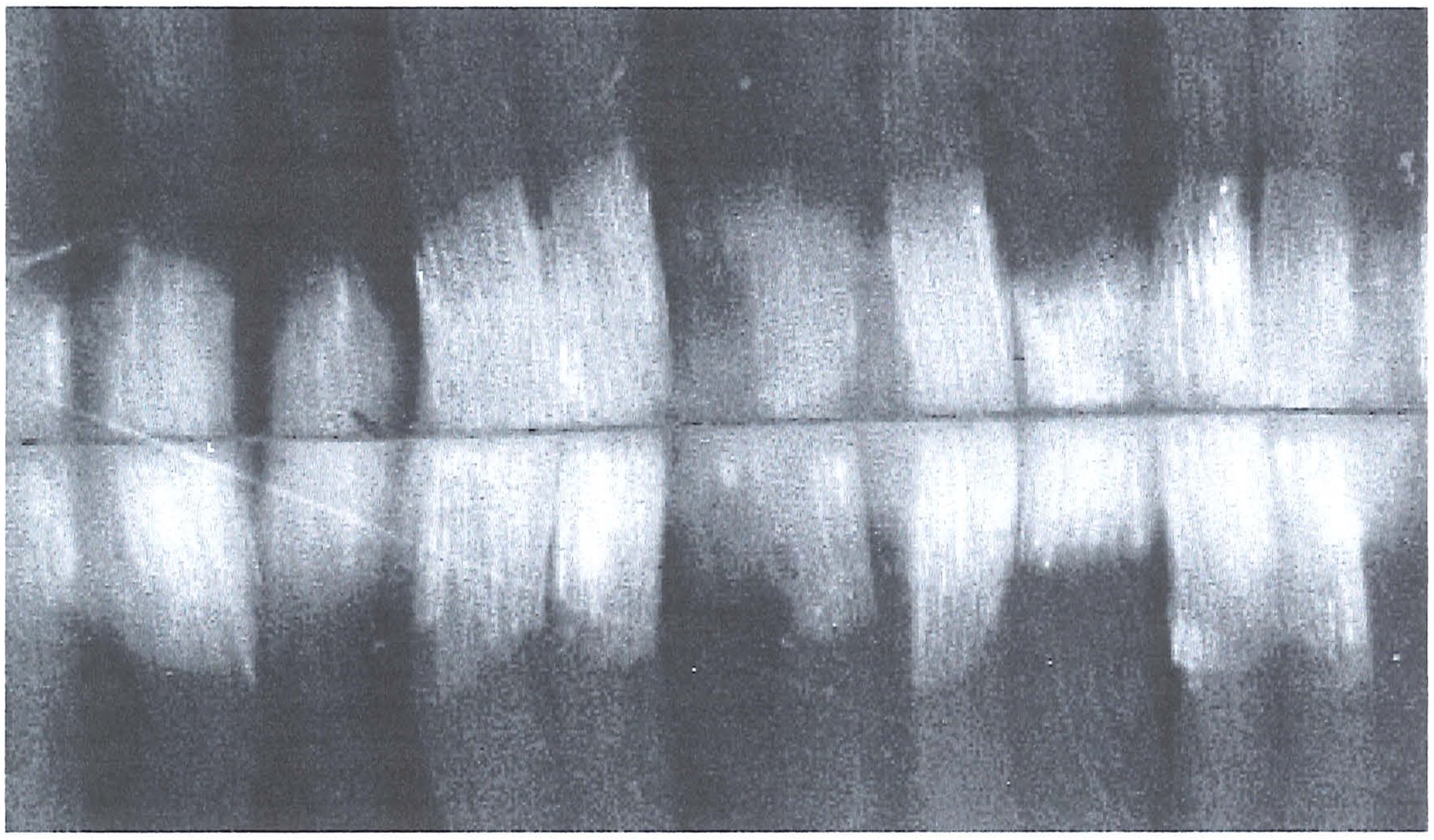

Fig 4.3.2-6 Photograph of typical debond lengths of fibre tows during multiple matrix cracking.

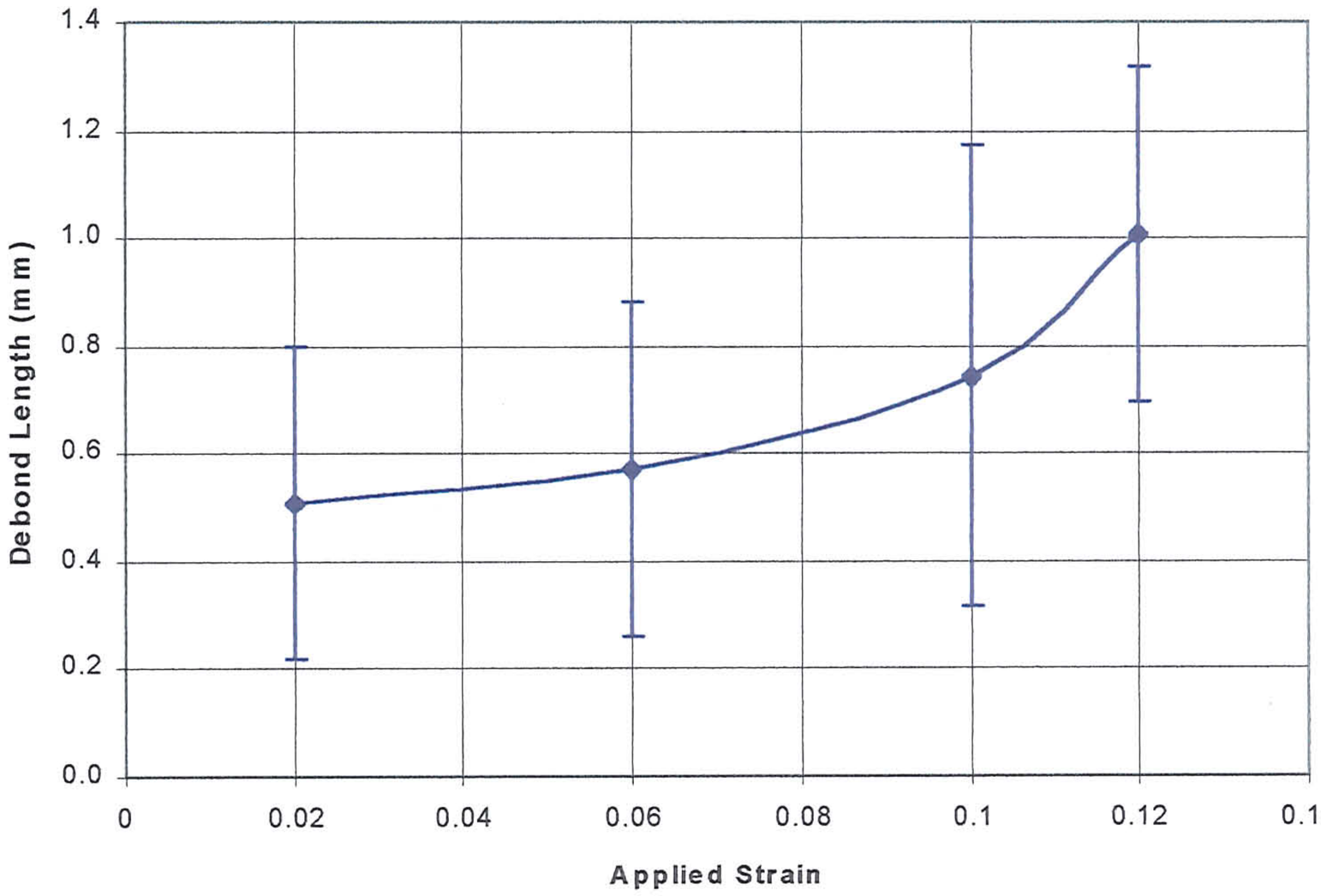

Fig 4.3.2-7 The average fibre tow debond lengths during matrix cracking as a function of applied strain.

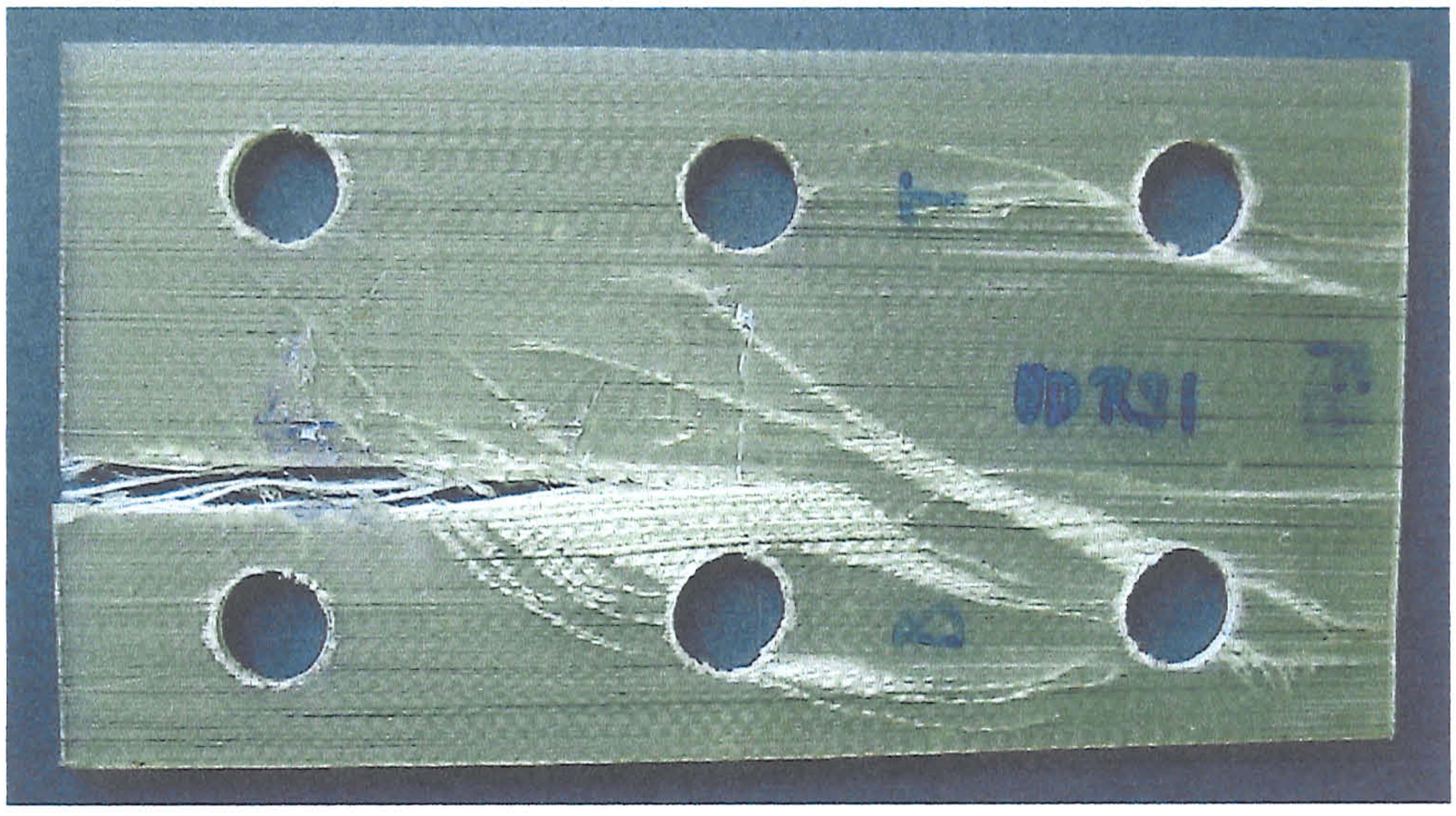

Fig 4.3.2-8 Photograph of the rail sheared one-dimensional polymer composite.

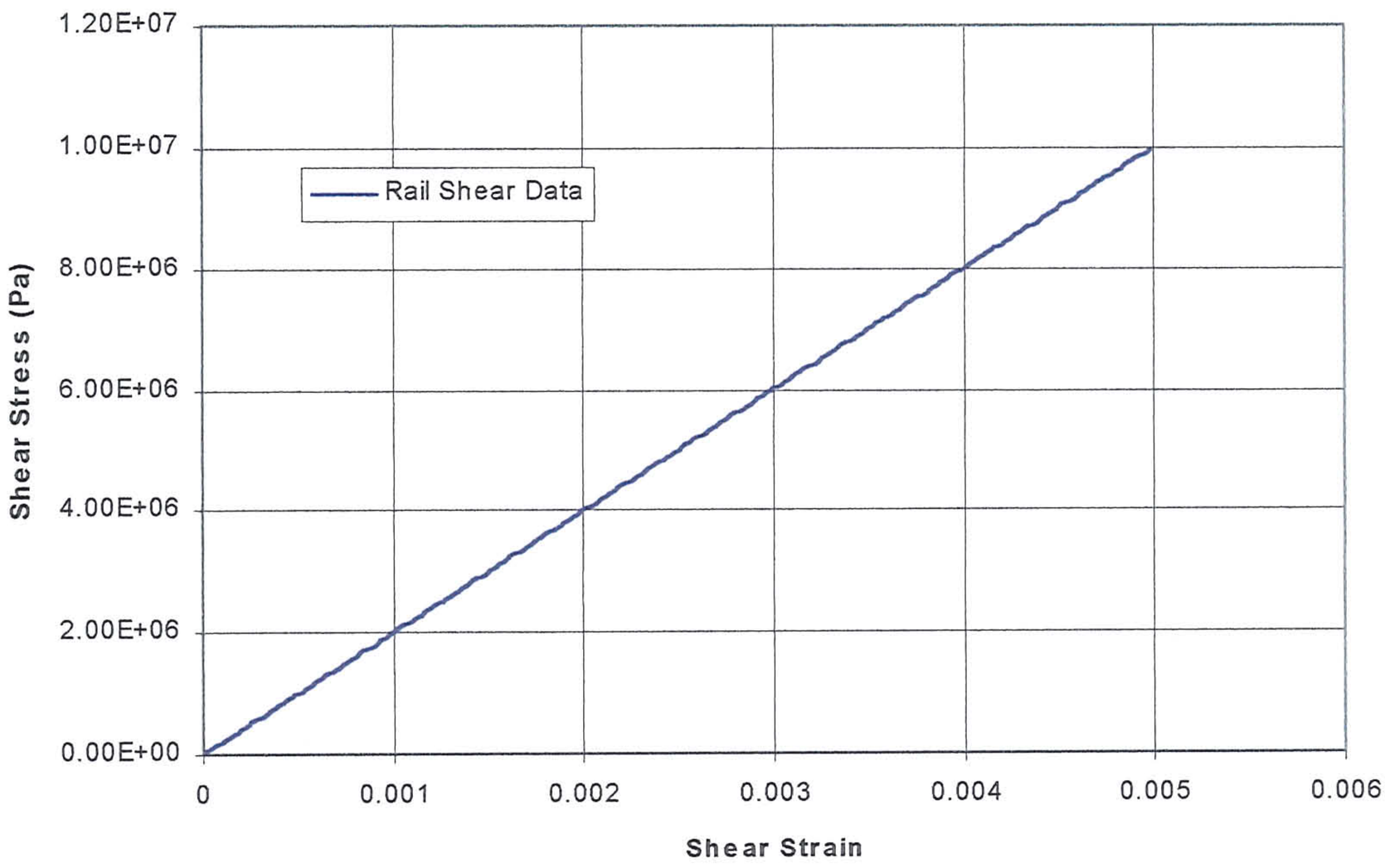

Fig 4.3.2-9 Shear stress – shear strain relations of the one-dimensional polymer composite rail shear tested parallel to the fibre alignment direction.

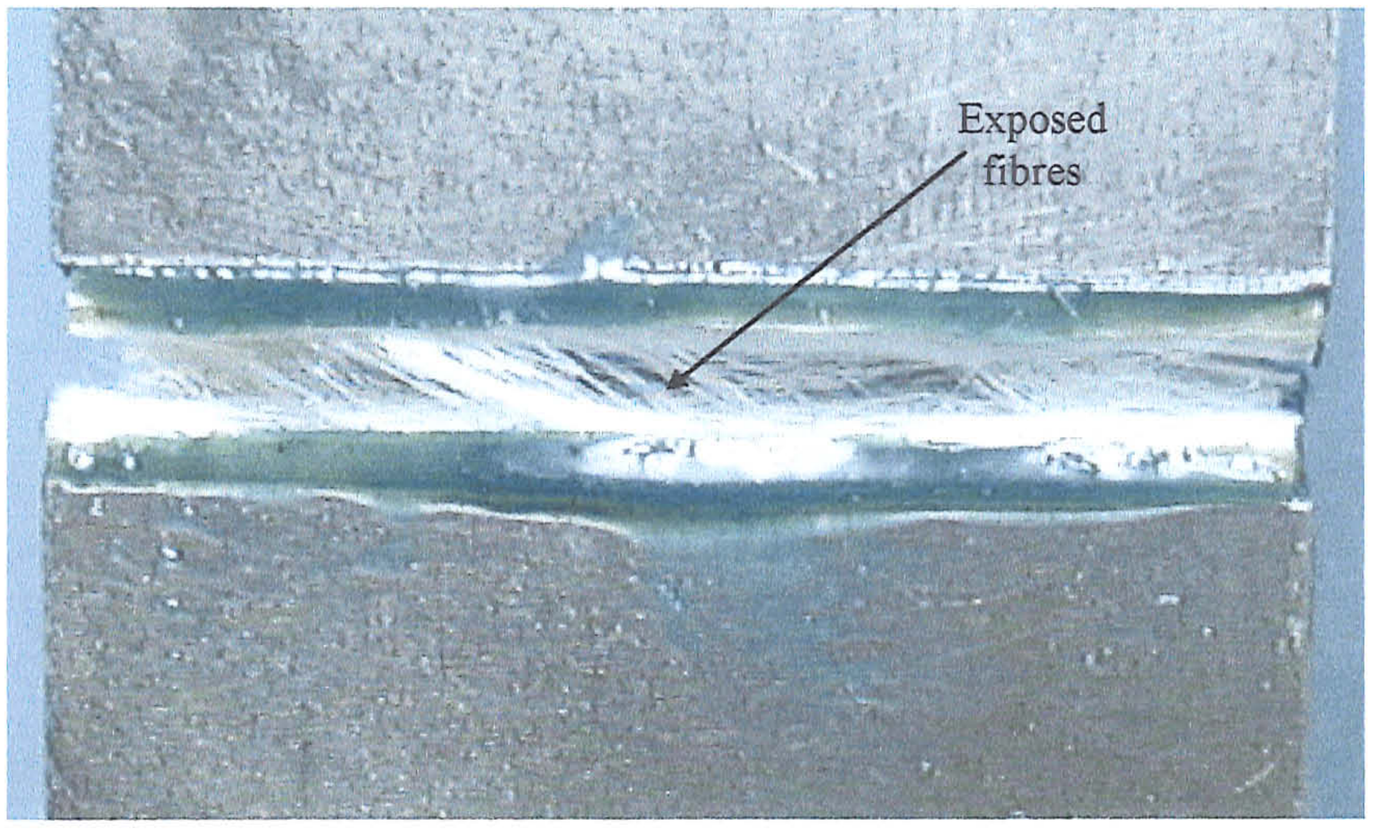

Fig 4.3.2-10 Photograph of the delamination in the through thickness direction.

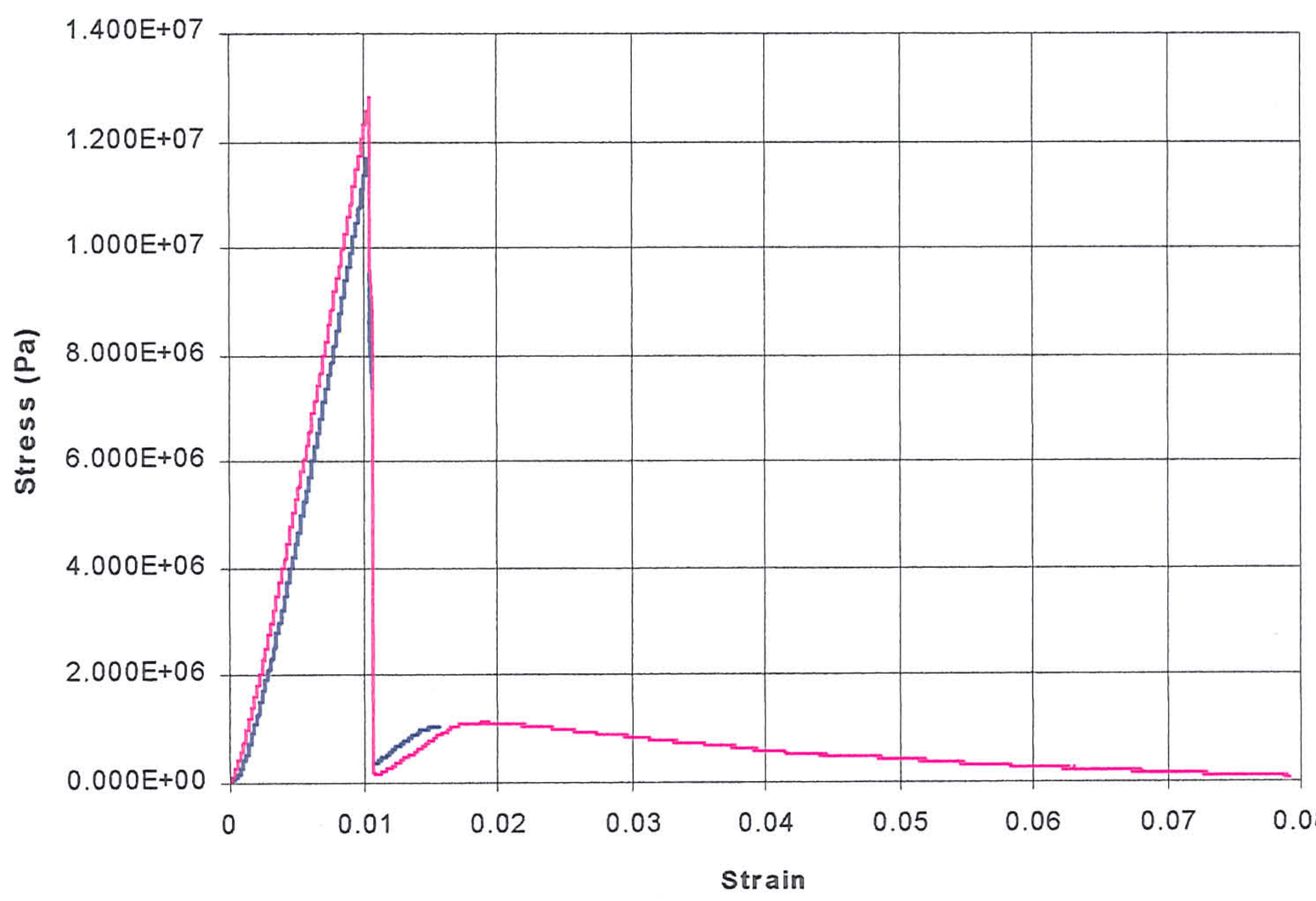

Fig 4.3.2-11 Stress-strain relations of the one-dimensional composite tensioned in the thickness direction.

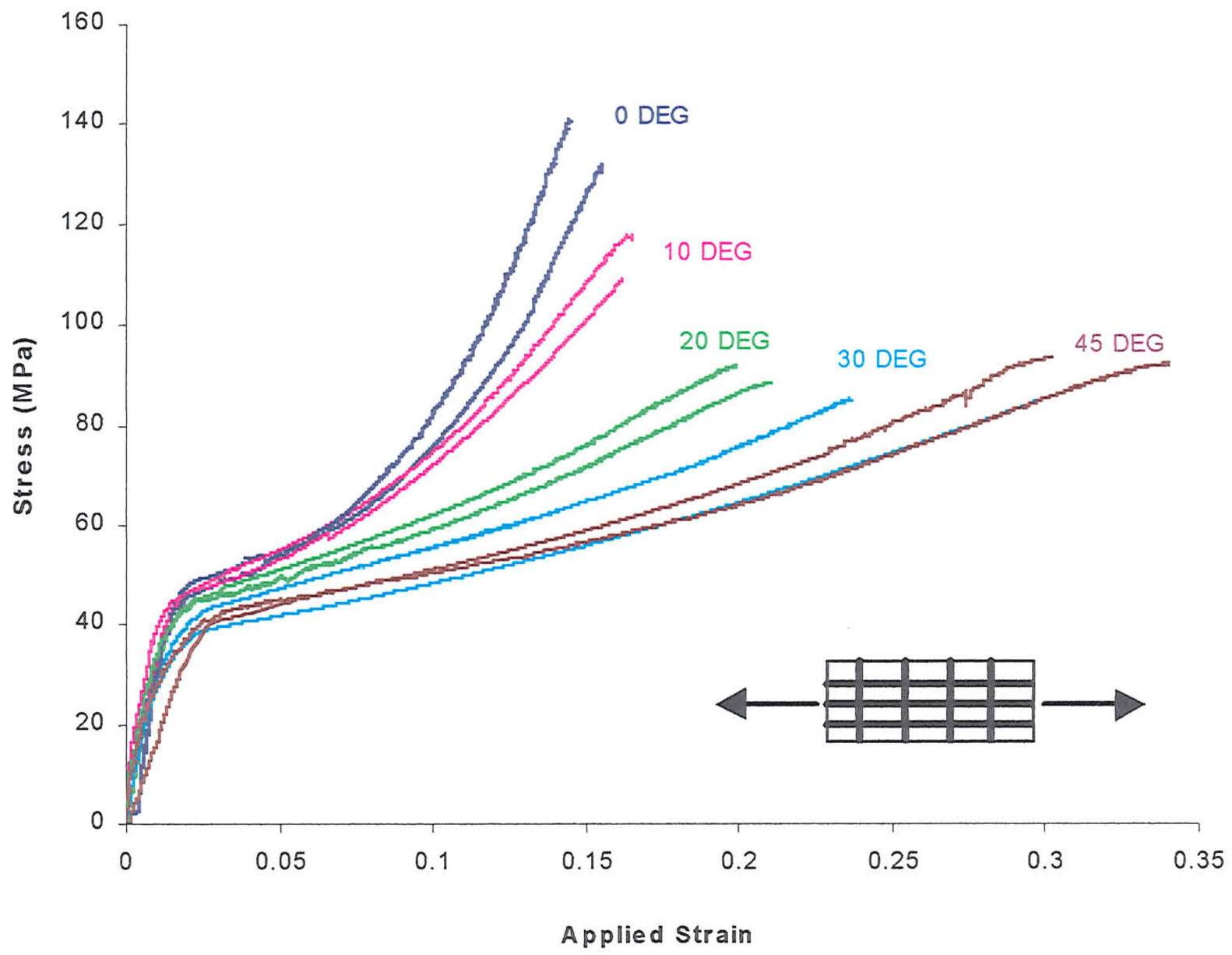

Fig 4.3.2-12 Uniaxial stress-strain relations of the two-dimensional composite at fibre alignment angle $\alpha = 0°$, 10°, 20°, 30° and 45°.

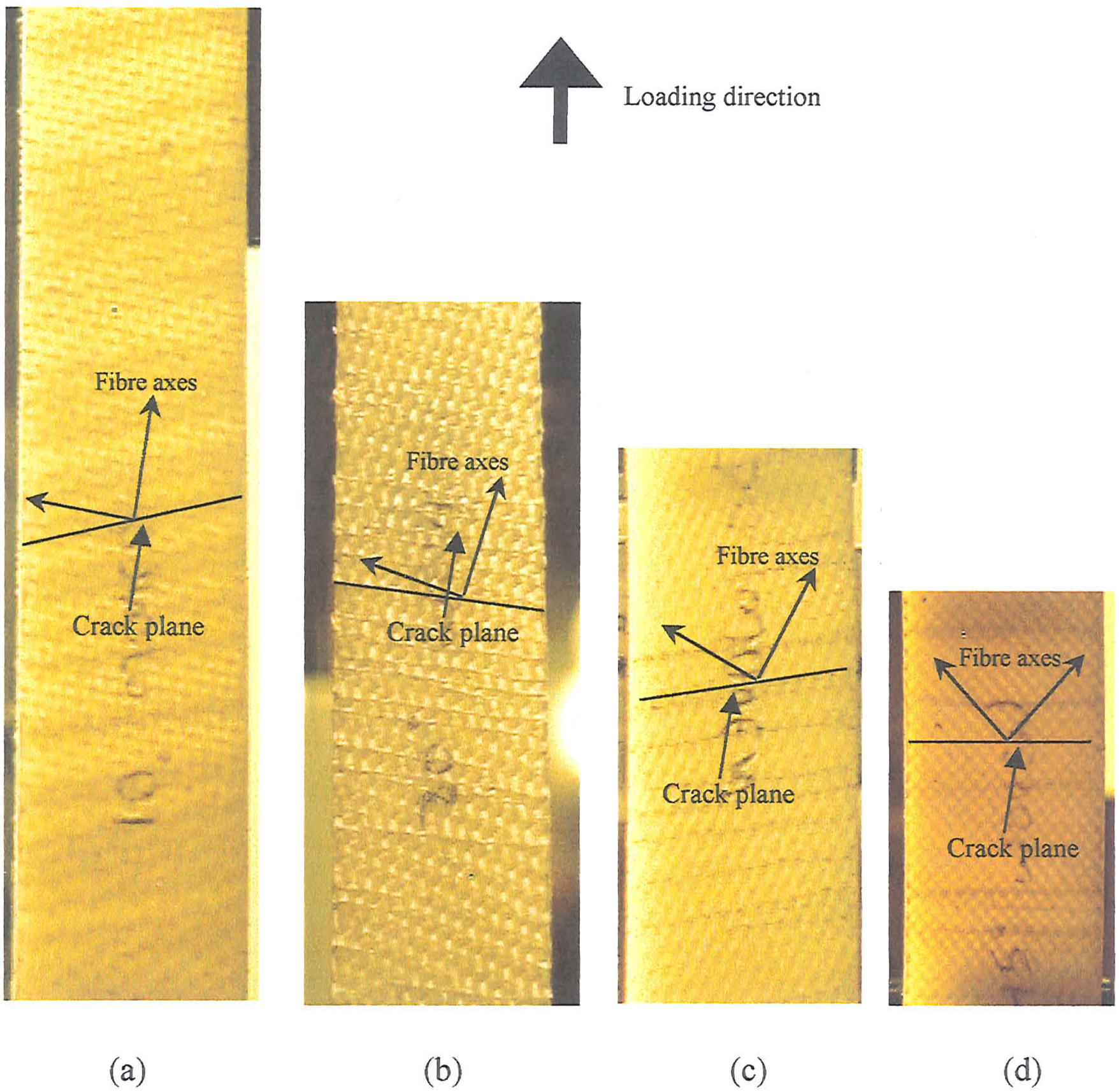

Fig 4.3.2-13 Photographs of the crack orientation in the two-dimensional tabbed coupons for $\alpha = 10°$, 20°, 30° and 45°

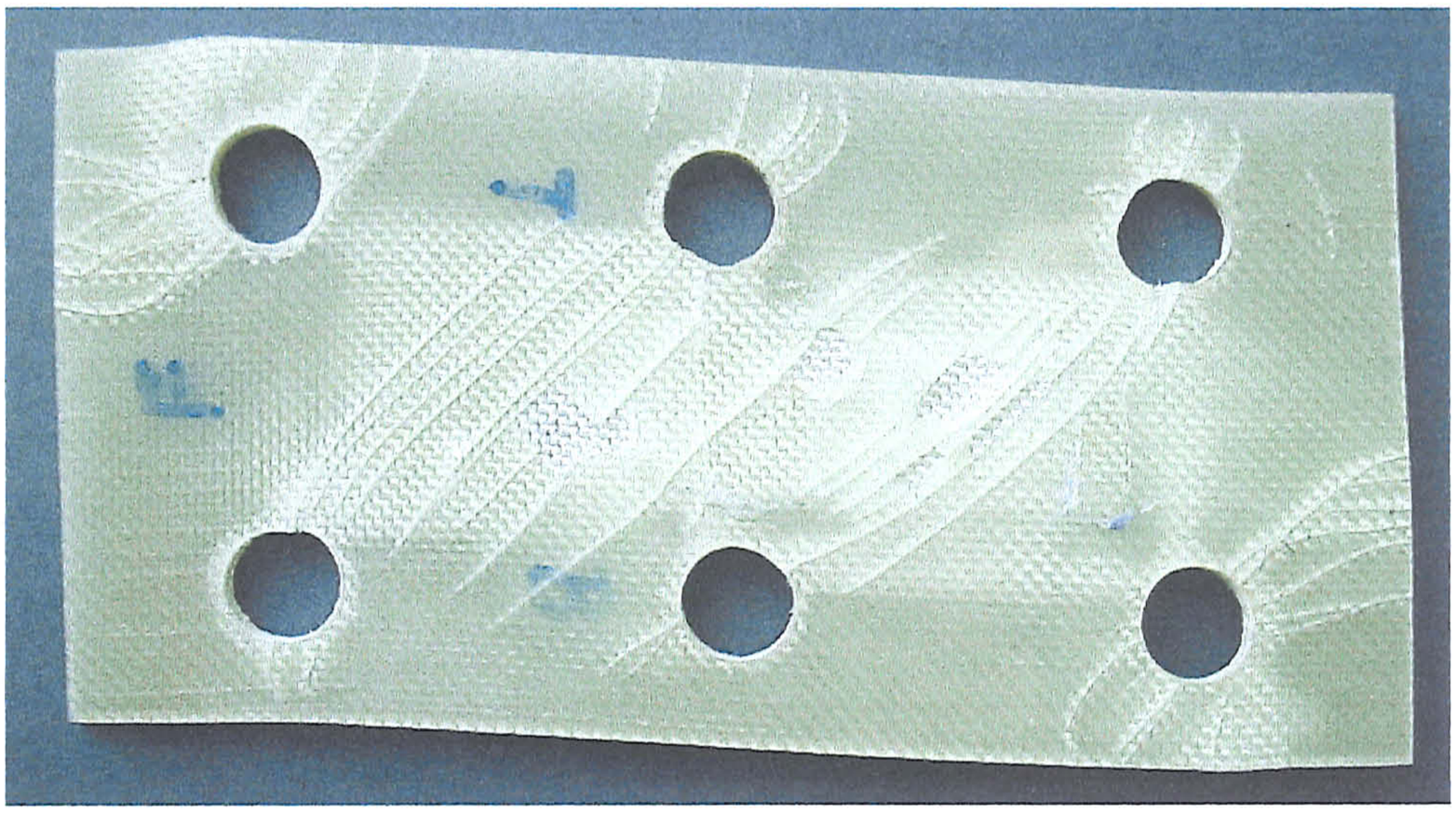

Fig 4.3.2-14 Photograph of the two-dimensional composite tested using the Rail Shear method.

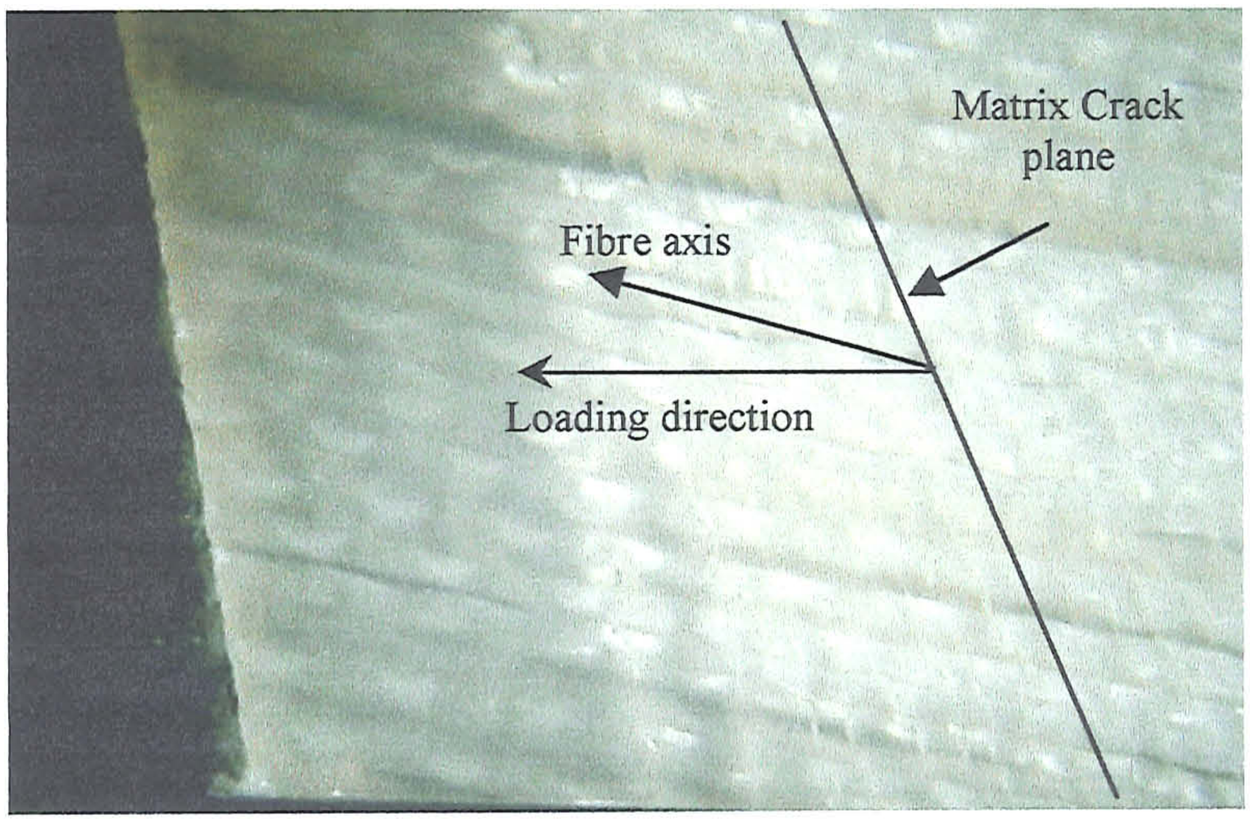

Fig 4.4.1-1 Photographs of the damages in the one-dimensional composite with $\alpha =$ 10°.

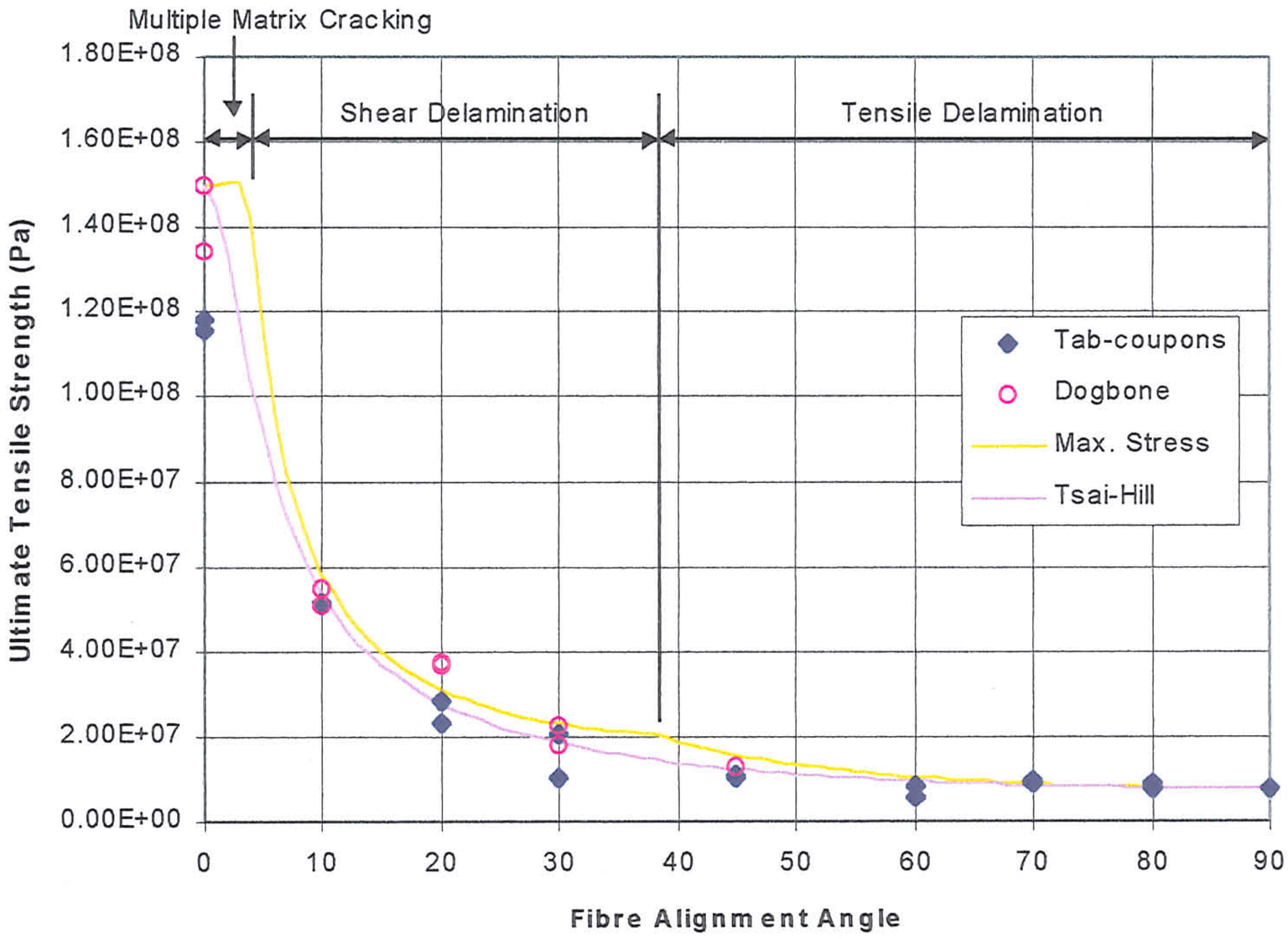

Fig 4.4.1-2 A plot of the ultimate tensile strength (UTS) of the one-dimensional composite with respect to fibre alignment angles α.

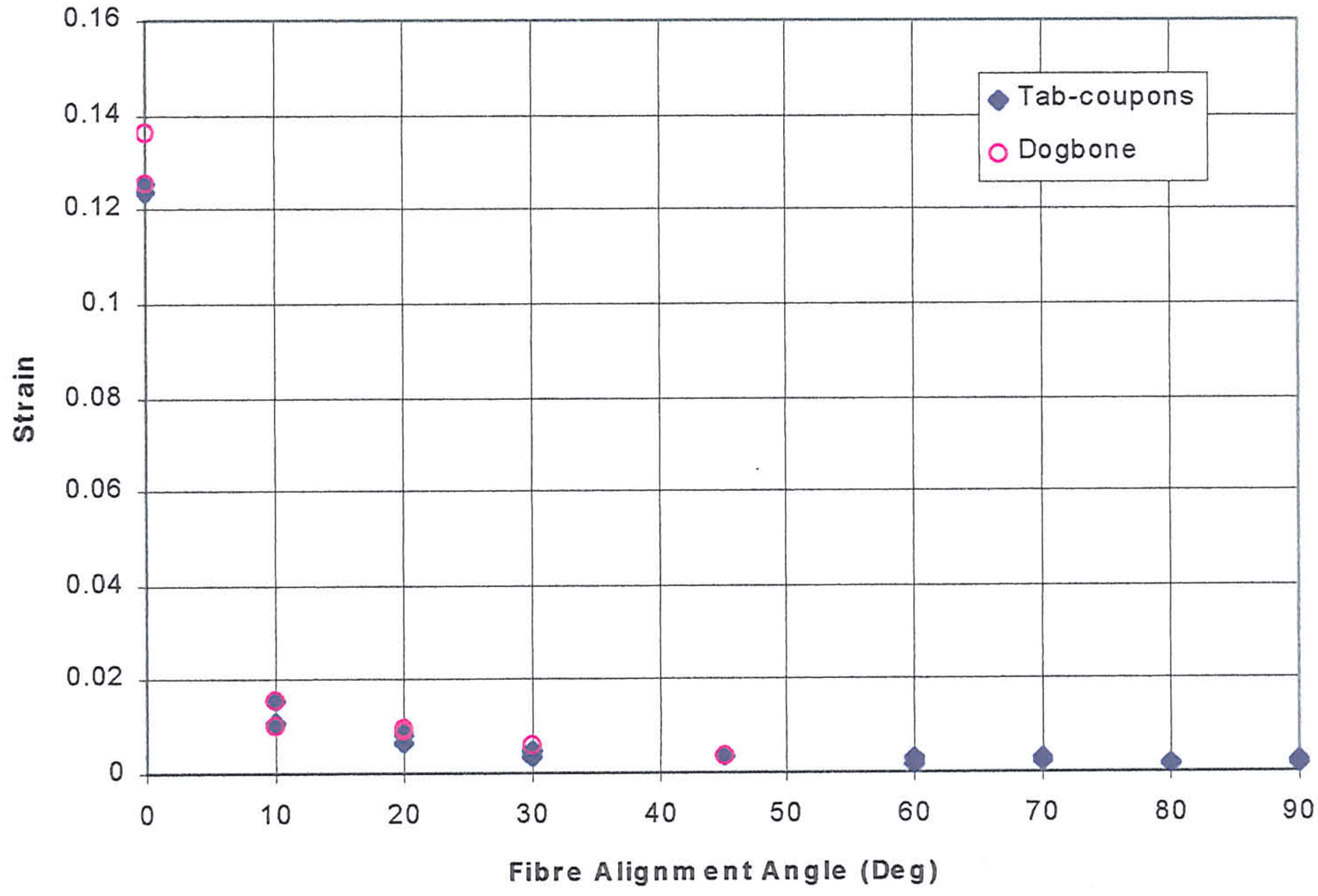

Fig 4.4.1-3 A plot of the ultimate tensile strength (UTS) of the one-dimensional composite with respect to fibre alignment angles α.

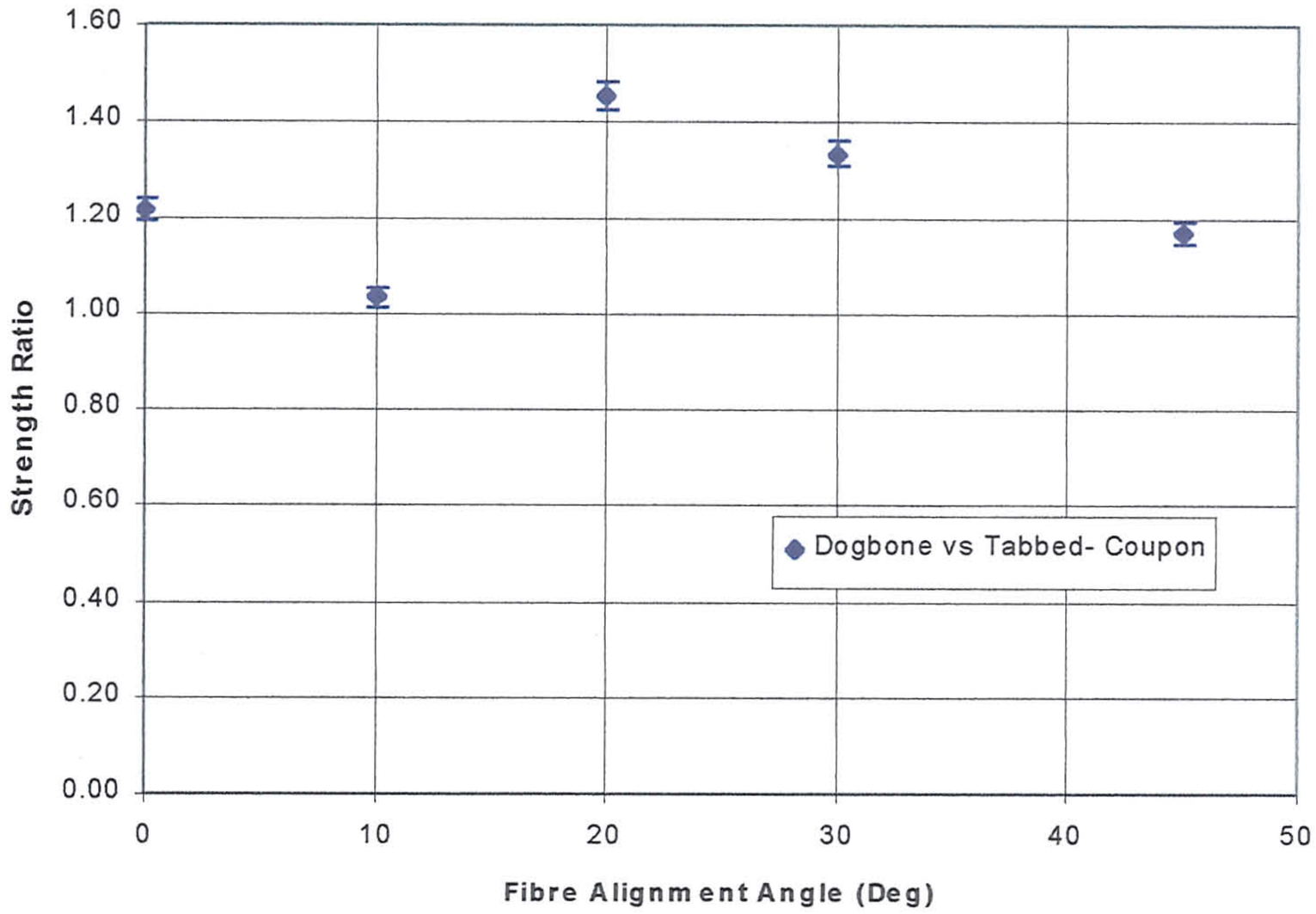

Fig 4.4.1-4 A ratio of the average tensile strengths between the dogbone shaped specimen and tabbed-coupon specimens with respect to fibre alignment angle.

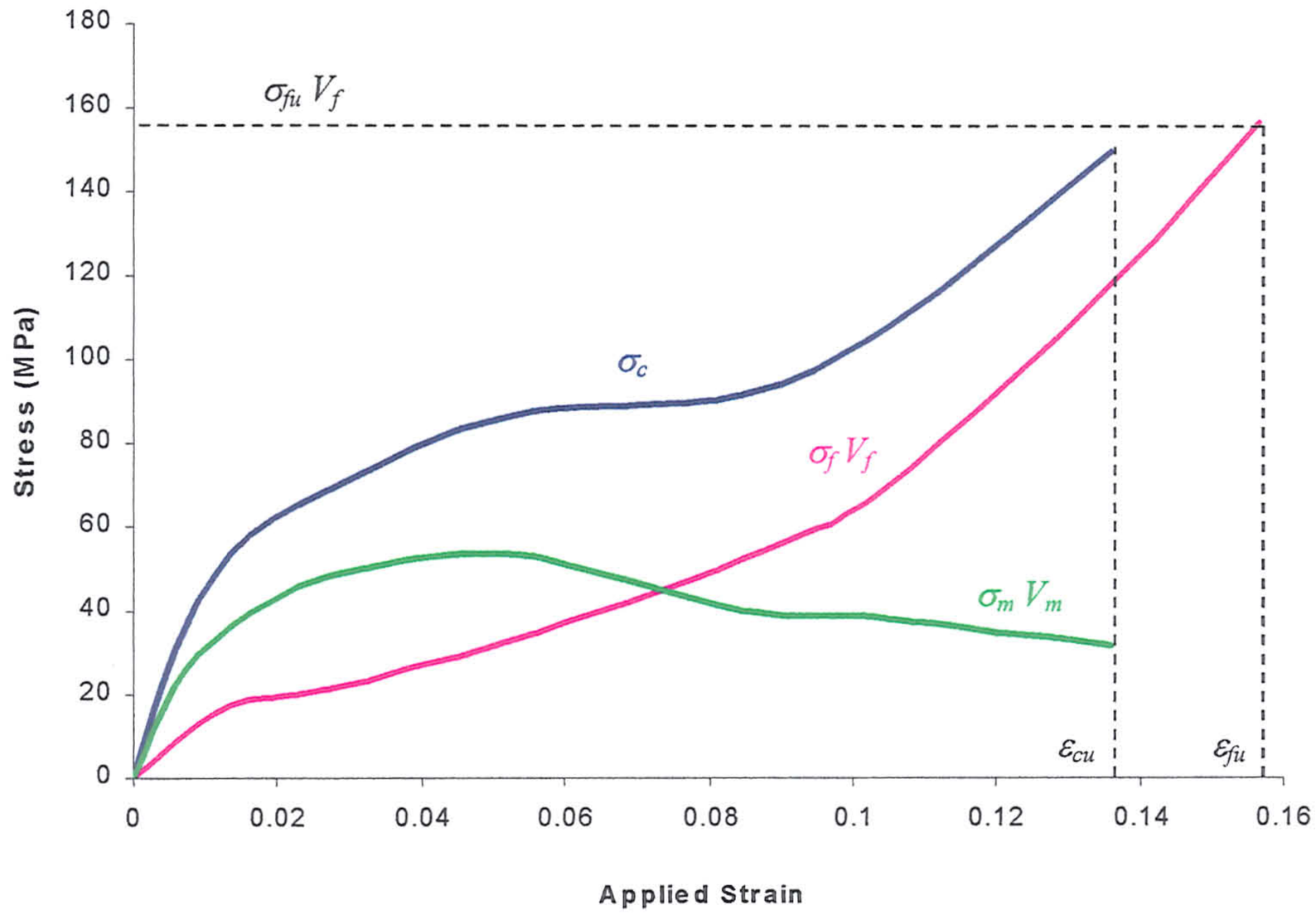

Fig 4.4.1-5 Stress-strain relations of the one-dimensional composite, the volume fraction of fibres and the volume fraction of matrix.

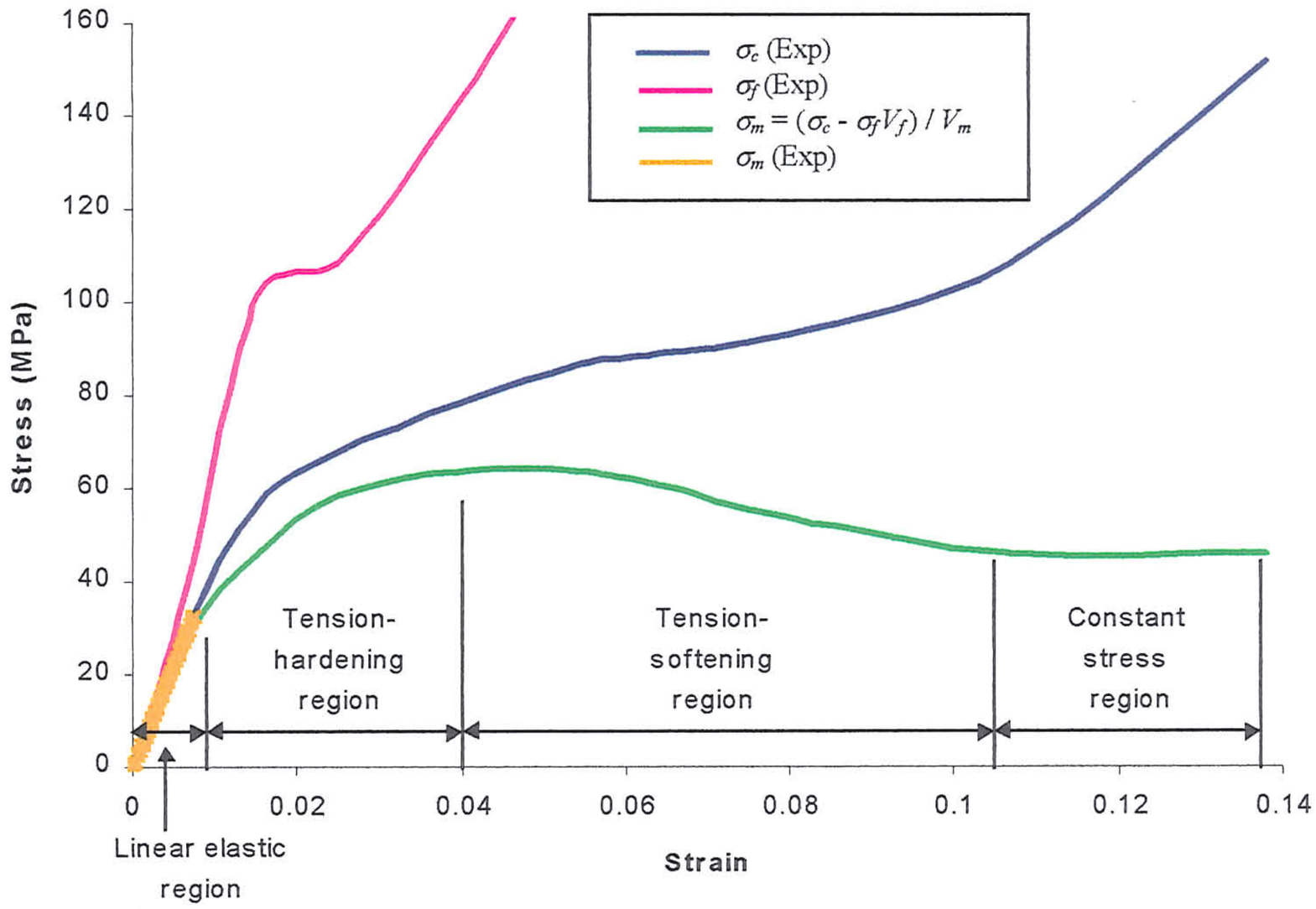

Fig 4.4.1-6 Stress-strain relations of the one-dimensional composite, fibres, matrix and monolithic matrix. Note, the fibre response is truncated.

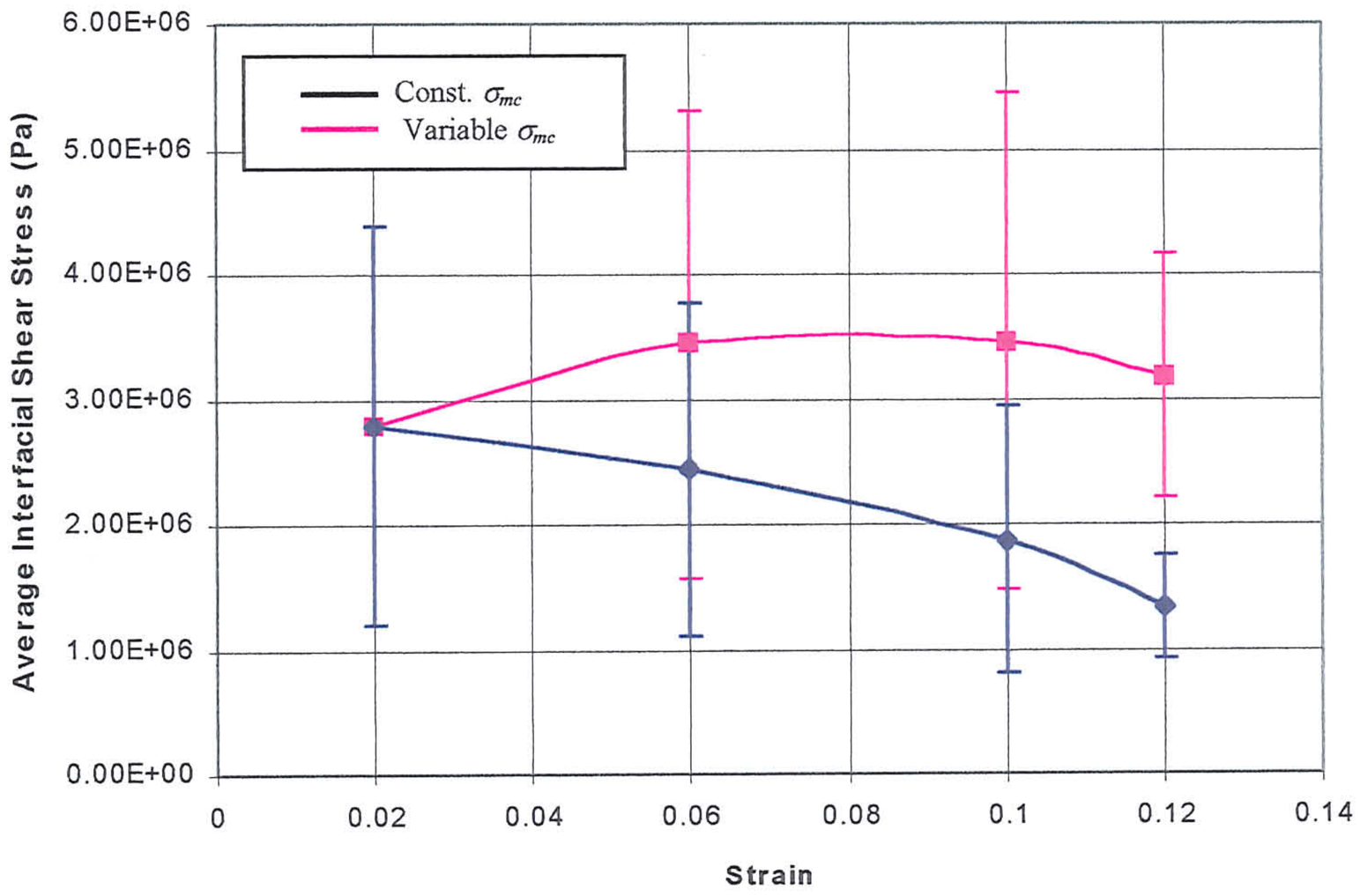

Fig 4.4.1-7 The average interfacial shear stress of debonded fibre tows in the analogue composite with respect to applied strain.

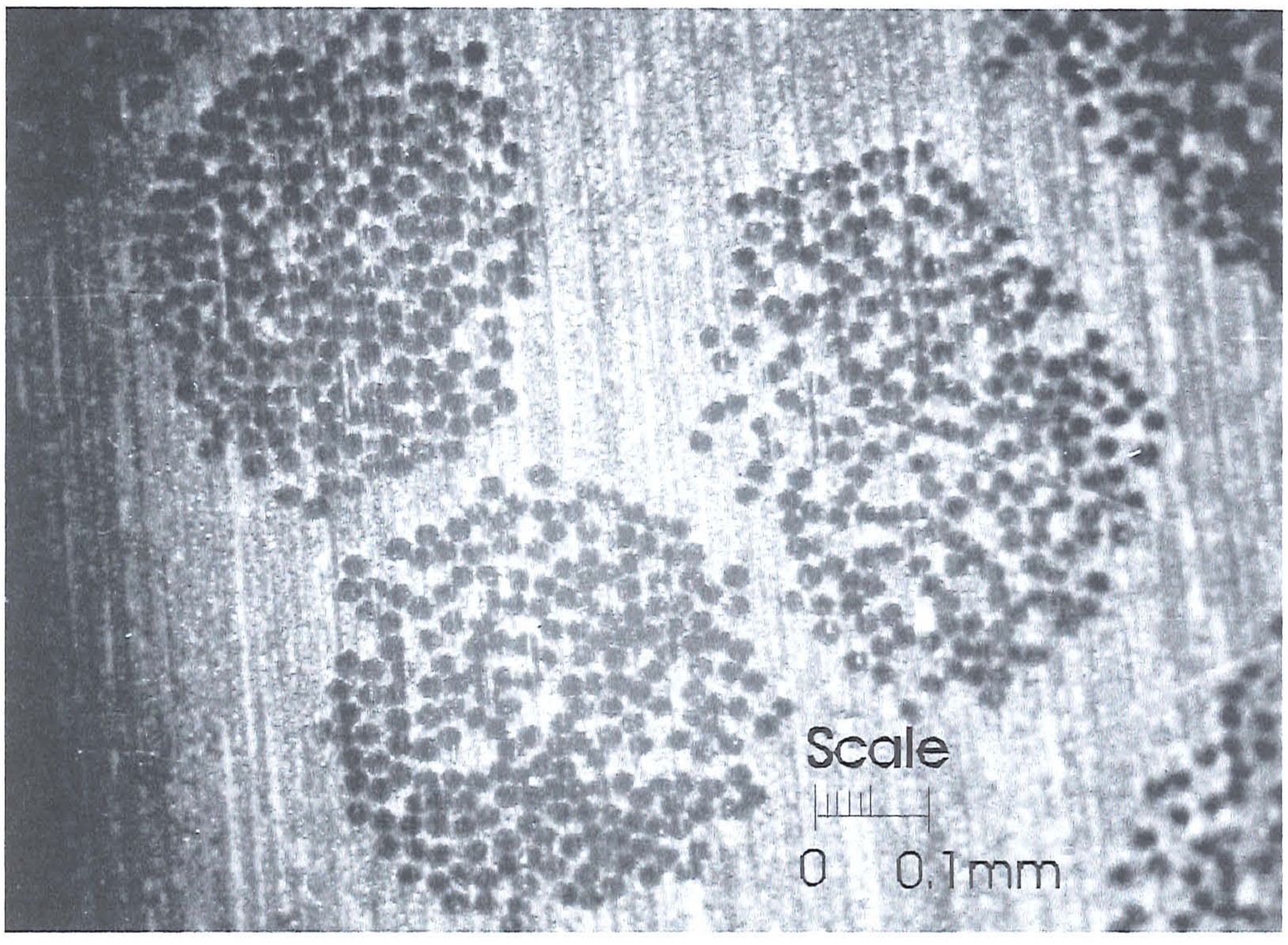

Fig 4.4.1-8 Photograph of the number of fibres in fibre tows.

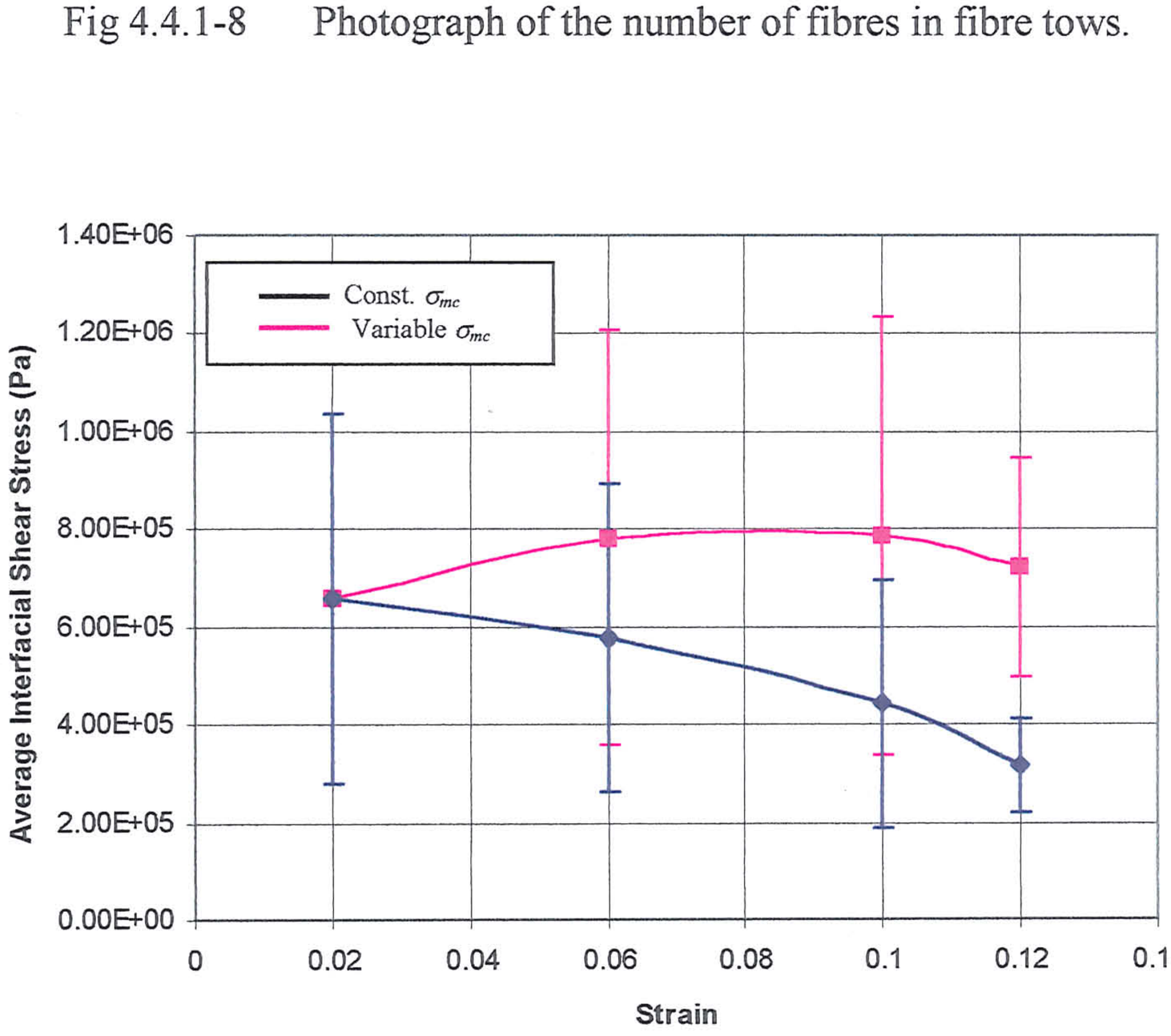

Fig 4.4.1-9 The average interfacial shear stresses of debonded fibres in a fibre tow with respect to applied strain.

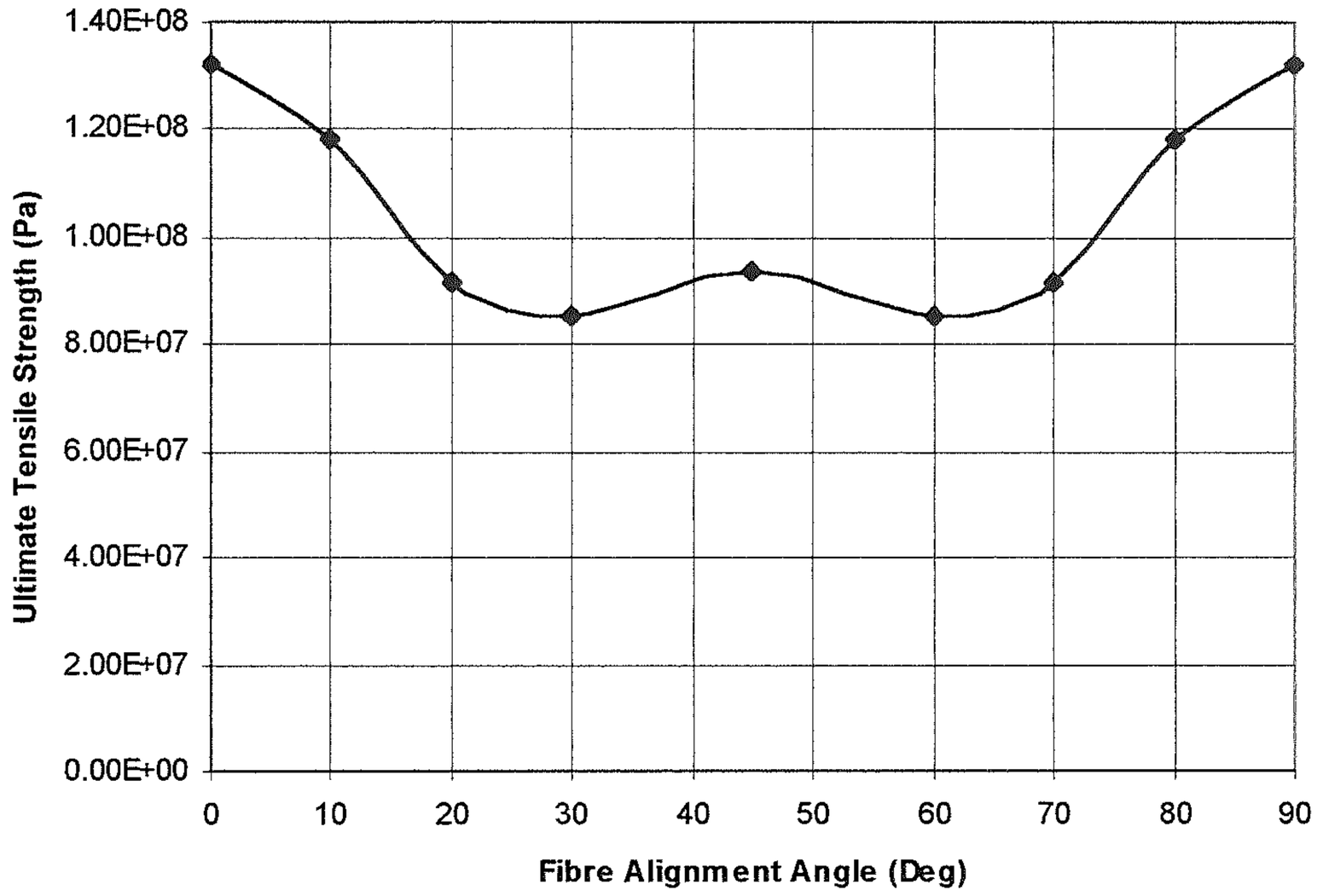

Fig 4.4.2-1 The ultimate tensile strength plotted with respect to fibre alignment angle for the two-dimensional analogue composite.

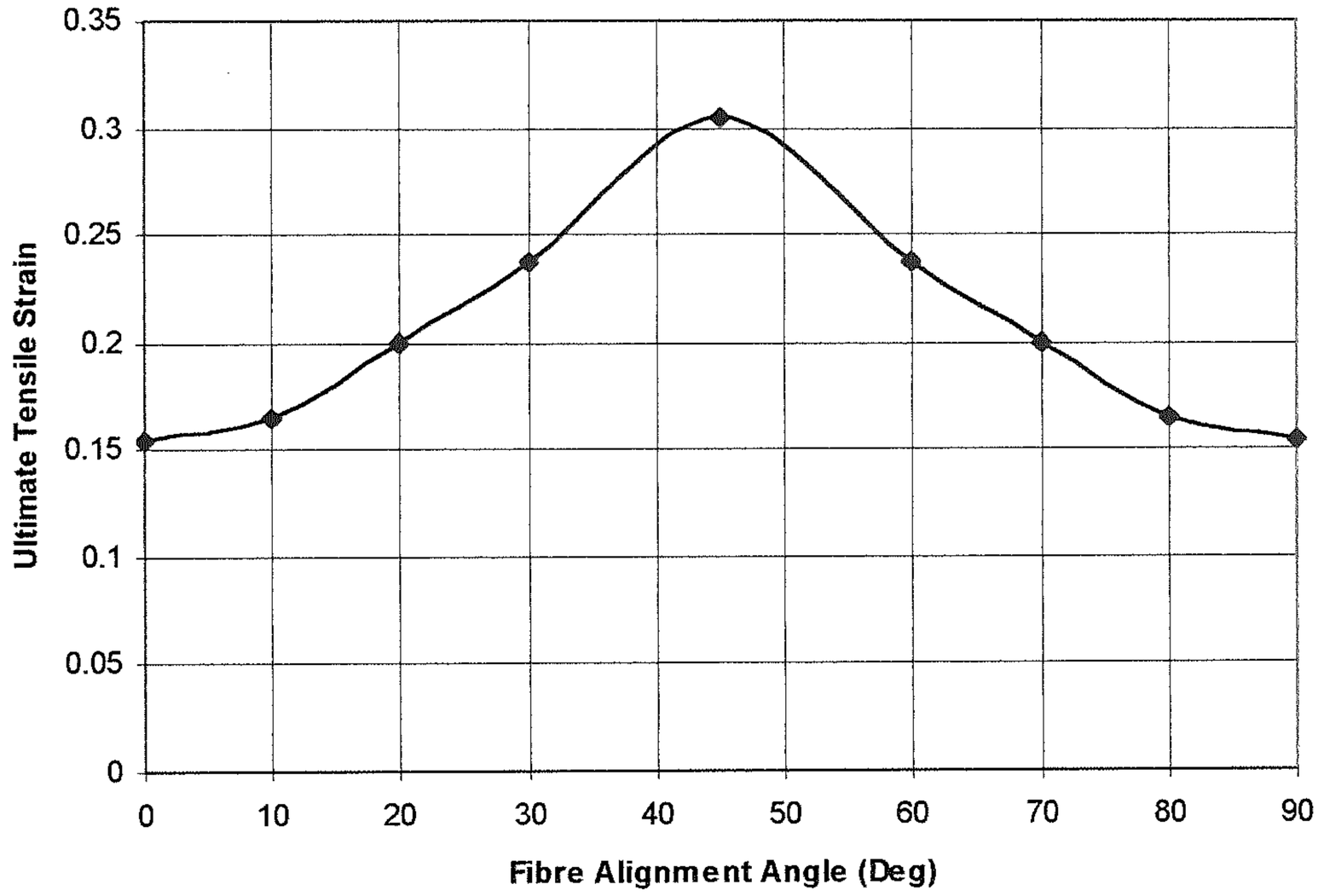

Fig 4.4.2-2 The ultimate tensile strain plotted with respect to fibre alignment angle for the two-dimensional analogue composite.

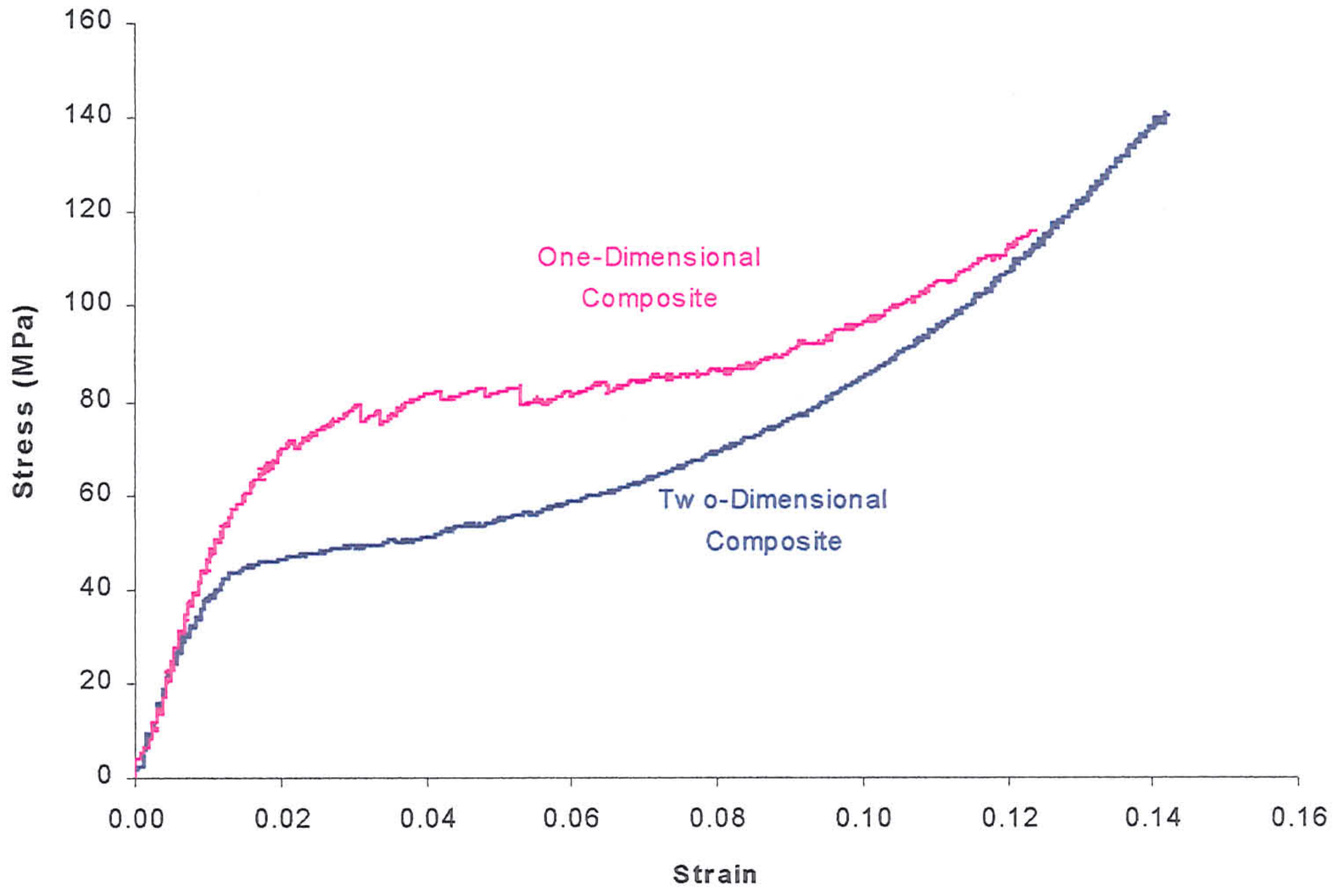

Fig 4.4.2-3 Comparison of the stress-strain relations of the one- and two-dimensional tabbed-coupons.

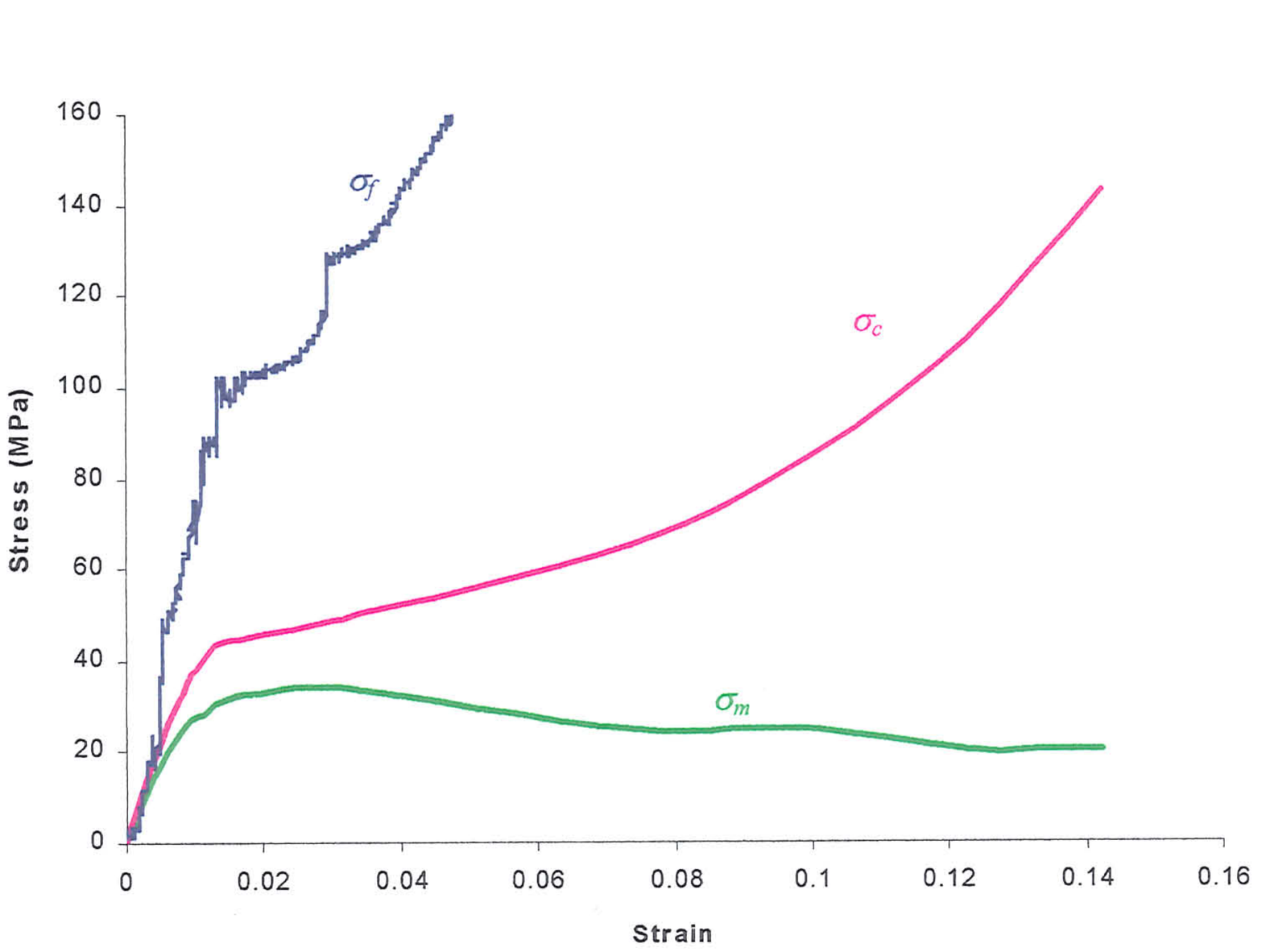

Fig 4.4.2-4 Stress-strain relations of the two-dimensional composite, fibres and damaged matrix. The fibre response is truncated.

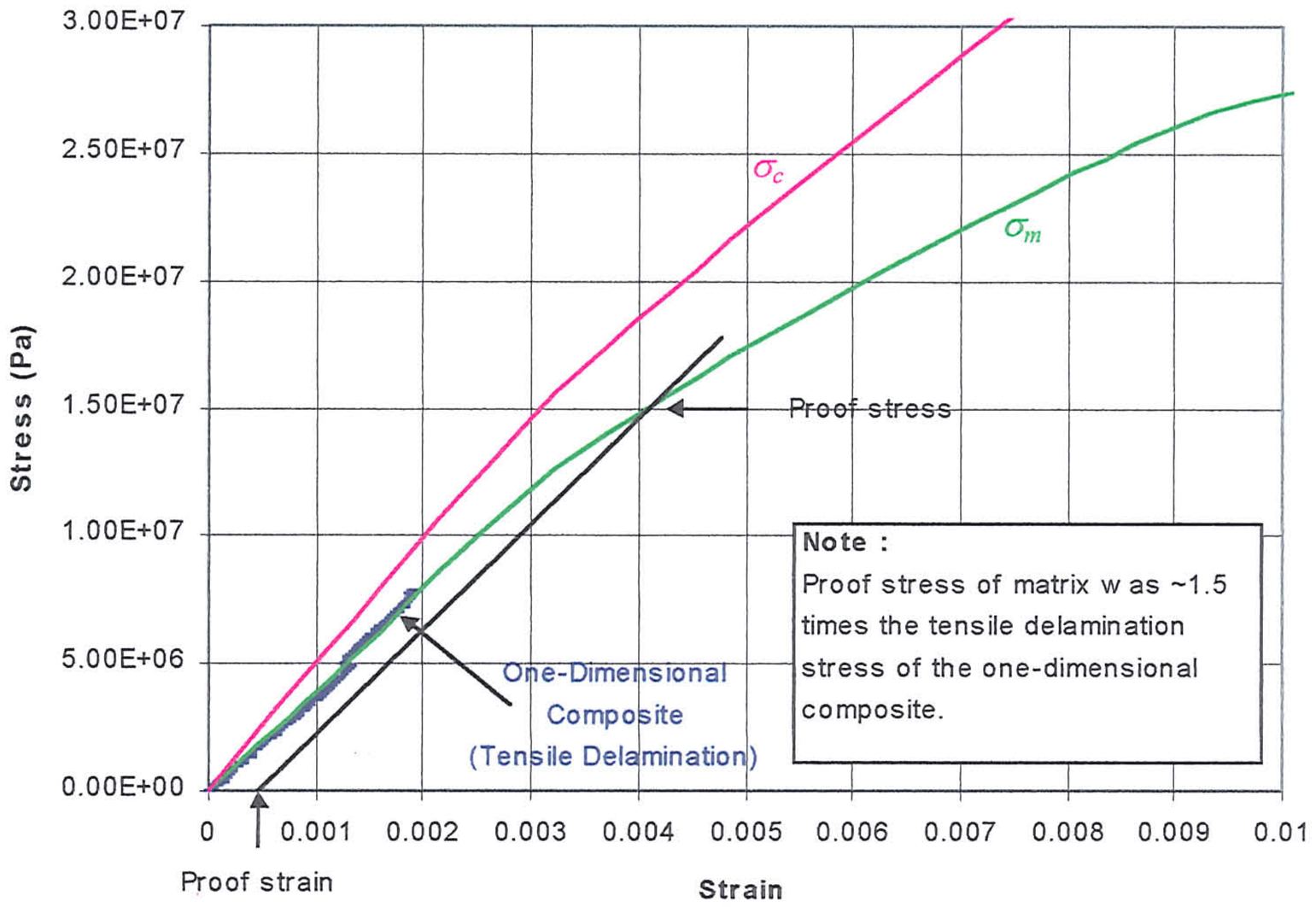

Fig 4.4.2-5 Stress-strain relations of the two-dimensional composite, damaged matrix and one-dimensional composite with $\alpha = 90°$.

CHAPTER 5

Sub-Structures

5.1 Introduction

In Chapter 4, the mechanical properties and damage mechanisms of one- and two-dimensional composites were measured in uni-axial tension. The purpose of the tests was to provide data to establish the physical basis for computational modelling brittle matrix composites. From this base, an ability to consider more complex geometries and loadings is a step towards full structural analysis. Following McCafferty (1994), three different geometries known as sub-structures are considered. These were suggested by Rolls-Royce as features which were representative of a structures found in the exhaust diffuser unit of the EJ200 aero-engine. Fig 5.1-1 to 3 show the sub-structures. These include a rectangular bar, a T-shaped bar and a wedged bar. These sub-structures were fabricated using the material system discussed in Chapter 4, using both one- and two-dimensional reinforcements. The work described in this chapter has two objectives. The first is to describe the role of one- and two-dimensional reinforcements for different sub-structures. The second is to derive experimental data to check the numerical model developed for brittle matrix composites

5.2 Fabrication Techniques

Two techniques were used to fabricate the sub-structures. In the first, liquid polyester resin was injected into a mould with pre-aligned fibres as described in Chapter 4. This technique was used to make rectangular bars with one-dimensional reinforcements. To make the 'T' and wedged shaped sub-structures, a hand lay-up technique was adopted. This allowed better control of the fibre orientation. The moulds for fabricating the 'T' and wedge shaped sub-structural elements are shown in Fig 5.2-1 and Fig 5.2-2. The mould surfaces were coated with a PTFE release agent. A polyester gel-coat (Resin B) with 2% weight of hardener (Catalyst M) from Scott Bader (1994) was then applied to the mould surfaces and the corresponding fibre layer applied. The lamina was allowed to harden to a tacky state before repeating the procedure for the

required number of fibre layers. The curing procedure is described in Sect. 4.2.3. To make the sub-structures with two-dimensional reinforcements, hand-laying technique was used as this allowed better wetting and control of the reinforcements.

5.3 Experiments

The sub-structures were all loaded in three-point bending using a Lloyd 10000 testing machine at a displacement rate of 1mm/min. The test configurations and the dimensions are given in Fig 5.1-1 to 3. The sub-structures were tested to complete failure or until the displacement limit of the test configuration. The sub-structures test were also tested until the initiation of damage was detected visually or audibly. After testing, optical microscopy was used to determine the damage mechanisms and the extent of damage.

5.4 Results and Analysis

5.4.1 Bend Bars

Typical load-displacement response of the rectangular bend bars with one- and two-dimensional fibre reinforcements are shown in Fig 5.4.1-1. The initial elastic stiffness were 292KN/m and 235KN/m, respectively.

For the sub-structures with one-dimensional reinforcements, matrix cracking started at an applied displacement of 0.618mm and load of 202N. The formation of a matrix crack was audible and was reflected distinctly in the force-displacement curve as a sudden loss in load. As the applied load increased, subsequent matrix cracking was heard and load drops occurred in the force-displacement curve. The test was stopped at an applied displacement of ~3mm and a load of 578N. The damage zone is shown in Fig 5.4.1-2. Matrix cracks and debonding of the fibre-matrix interfaces adjacent to the crack planes were observed. The length of the damage zone along the reinforcement direction was 8mm and contained approximately 5 matrix cracks. A photograph of the corresponding crack depths is given in Fig 5.4.1-3. The average crack depth was 1.71mm and the average crack separation distance was 1.37mm.

For sub-structures with two-dimensional reinforcements, matrix cracking started at an applied displacement of 1.36mm and load of 309N. The event was audible but was not clearly reflected in the force-displacement curve. As the applied load increased, further cracking sounds were heard. The test was stopped at an applied displacement of

3.8mm and a corresponding load of 556N. A photograph of the damaged zone is shown in Fig 5.4.1-4. Approximately 7 evenly distributed matrix cracks were seen along the length of the damage zone. The average crack separation distance was 1.1mm in a damage zone of 8.6mm in length. A photograph of a section of the specimen side profile is shown in Fig 5.4.1-5. The average crack depth was 0.87mm.

The sub-structure with two-dimensional reinforcement was observed to be less stiff than the one-dimensionally reinforced sub-structure after matrix cracking had initiated. An explanation of this phenomenon can be derived by considering the findings given in Sect. 4.4.2, in which the matrix cracking stresses of two-dimensional composites were shown to be significantly lower due to the low interfacial strength of the orthogonal reinforcements. As such, the early development of matrix cracks in the two-dimensionally reinforced sub-structure gives rise to a lower stiffness. This agrees with the optical observations of matrix cracking. However, the acoustic data suggests that matrix cracking in the two-dimensionally reinforced sub-structure occurred at a higher applied load than in the one-dimensionally reinforced sub-structures. An explanation may be obtained by comparing the matrix cracks of the sub-structures (see Fig 5.4.1-2 to 5). The matrix cracks in the two-dimensionally reinforced sub-structures are smaller, suggesting that matrix cracks in the two-dimensionally reinforced sub-structure may have developed from the accumulations of microcracks, which might not have been sufficient to be detected acoustically.

5.4.2 T-Shaped Sub-Structures

The load-displacement curves of T-shaped sub-structures with one- and two-dimensional reinforcements are shown in Fig 5.4.2-1. The initial elastic stiffness of the sub-structures were 418KN/m and 343KN/m, respectively.

In the sub-structure with one-dimensional reinforcements, damage initiated by matrix cracking at the fillet was reflected as a load drop in the force-displacement curve. The matrix crack occurred at an applied displacement of 0.677mm and a load of 271N. The maximum load borne by the sub-structure was 299N with a corresponding displacement of 1.5mm. The test was finally stopped at an applied displacement of 2.23mm and a load of 224N because the sub-structure had slipped from the outer load points.

The damaged T-shaped sub-structure with one-dimensional fibres are shown in Fig 5.4.2-2. Three types of damage were observed: matrix cracking at the fillet,

delamination along the fillet and cracks in the matrix core. The delamination plane in the fillet was not initially obvious. This was verified after sectioning the specimen and optically inspecting the fillet, when a distinct delamination plane became visible. The delamination plane was formed by the linkage of debonded fibre-matrix interfaces in fibre tows and cracks in the matrix separating the fibre tows. A photograph of the delamination plane is shown in Fig 5.4.2-3.

Optical microscopy and the force-displacement curve allow the sequence of damage events to be reconstructed. In bending, the tensile stress is highest at the outer surface of the fillet. When the stress in the matrix reaches a critical value the matrix cracked. The cracks propagated across the layers of reinforcement but stopped at the matrix core. Across the matrix crack plane, some debonding of the fibre-matrix interfaces also occurred. Due to these weakened interfaces and the shear stresses introduced by the applied load, the formation of a delamination plane developed, as observed in Fig 5.4.2-3. The initial load loss in the force-displacement curve shown in Fig 5.4.2-1 is believed to encompass all these damage mechanisms. When further load was applied, the extent of delamination in the fillet increased until the maximum load was reached. Finally, when the stress was sufficiently high, cracks initiated in the matrix core. The load drop near the end of the force-displacement curve reflects this. The location of cracking in the matrix core is shown in Fig 5.4.2-2c.

For the T-shaped sub-structures with two-dimensional reinforcements, cracking was audible at an applied displacement of 0.58mm and a load of 169N. This correspond to the first departure from linearity in the force-displacement curve. As the applied displacement increased, a maximum load of ~236N was obtained at a displacement of ~1.08mm. With further displacement applied, the load bearing capacity gradually reduced to approximately 200N. This was followed by a catastrophic load drop near the end of the force-deflection curve when the sub-structure delaminated. A micrograph of the T-shaped sub-structure fillet surface, loaded to the first departure from linearity in the force-displacement curve, is shown in Fig 5.4.2-4a. Some microcracks were observed in the matrix. In addition, the colour of the matrix at the fillet turned white, indicating delamination. In Fig 5.4.2-4b, a photograph of the delamination plane at the end of the test is shown.

McCafferty (1994) has described the damage mechanisms and failure of T-shaped sub-structures with two-dimensional reinforcements. The author has attributed the failure mechanism to be caused by tensile delamination, as the tensile delamination

stress obtained from experiment was ~0.6MPa and is significantly lower than the matrix cracking stress of the composite.

5.4.3 Wedged-Shaped Sub-Structure

The load-displacement curves of a wedged-shaped sub-structure with one- and two-dimensional reinforcements are shown in Fig 5.4.3-1. The initial elastic stiffness of the sub-structures was 318KN/m and 185KN/m, respectively. This is because the thickness of the sub-structure with one-dimensional reinforcements was thicker. The total thickness for the wedged-shaped sub-structure with one- and two-dimensional reinforcements was ~9.4mm and ~7mm.

For the wedged-shaped sub-structure with one-dimensional reinforcements, matrix cracks were observed and heard at an applied load of 554N and a displacement of 1.82mm. The matrix cracks occurred at the wedge, and resulted in load drops in the force-displacement curve. When further bending was applied, the load on the sub-structure continued to increase until a maximum load of 1.01KN and a deflection of 3.78mm. This was followed by matrix cracking in the undamaged wedge of the sub-structure, which resulted in the final load drop in the force-displacement curve. A micrograph of the damage in the sub-structure is shown in Fig 5.4.3-2.

For the wedged-shaped sub-structure with two-dimensional reinforcements, cracking was audible at an applied load of 280N and a deflection of 1.9mm. Subsequent cracking was heard at an applied load of 415N and a deflection of 3.4mm and finally at a maximum load of 500N and a deflection of 5.2mm. The initial cracking events were not distinctly reflected in the force-displacement curve. Only the final cracking event was seen in the force-displacement curve by catastrophic load loss. As in the one-dimensionally reinforced sub-structure, matrix cracks were observed in the wedge. This is shown in Fig 5.4.3-3.

5.5 Conclusions

Experimental analyses of composite sub-structures with one- and two-dimensional reinforcements were conducted in three-point bending. It was found that the type of reinforcement influenced the force-deflection response of the sub-structures. Generally, the damage force-deflection response of sub-structures with two-dimensional reinforcements was less stiff than sub-structures with one-dimensional reinforcements.

In the rectangular bend bar, the difference in force-deflection response during damage was due to the different matrix cracking stresses induced by the reinforcements. The two-dimensional reinforcement exhibited in a lower matrix cracking stress due to the weak interfacial strength of the orthogonal reinforcements. In the T-shaped sub-structure, the orthogonal fibres in the two-dimensional reinforcement architecture significantly reduced the tensile delamination stress. In the case of the wedge-shaped sub-structures, results were not conclusive because the geometries of the sub-structure were differently. Finally, the experimental data collected from the tests on the substructures formed a basis for numerical modelling.

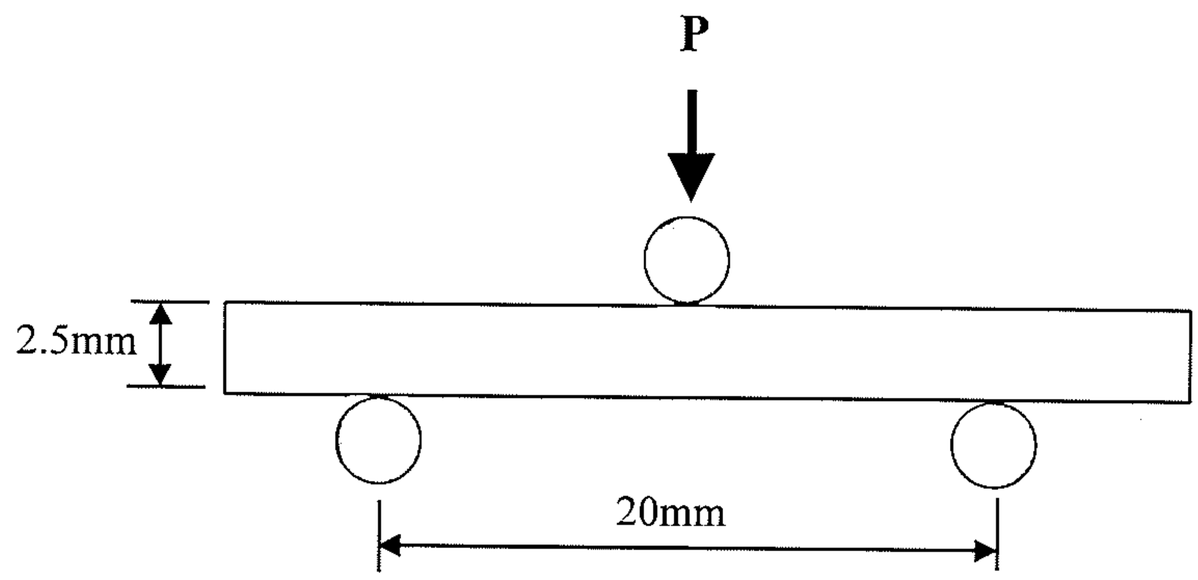

Fig. 5.1-1 Three point bend test configuration for rectangular polyester composite 10mm wide.

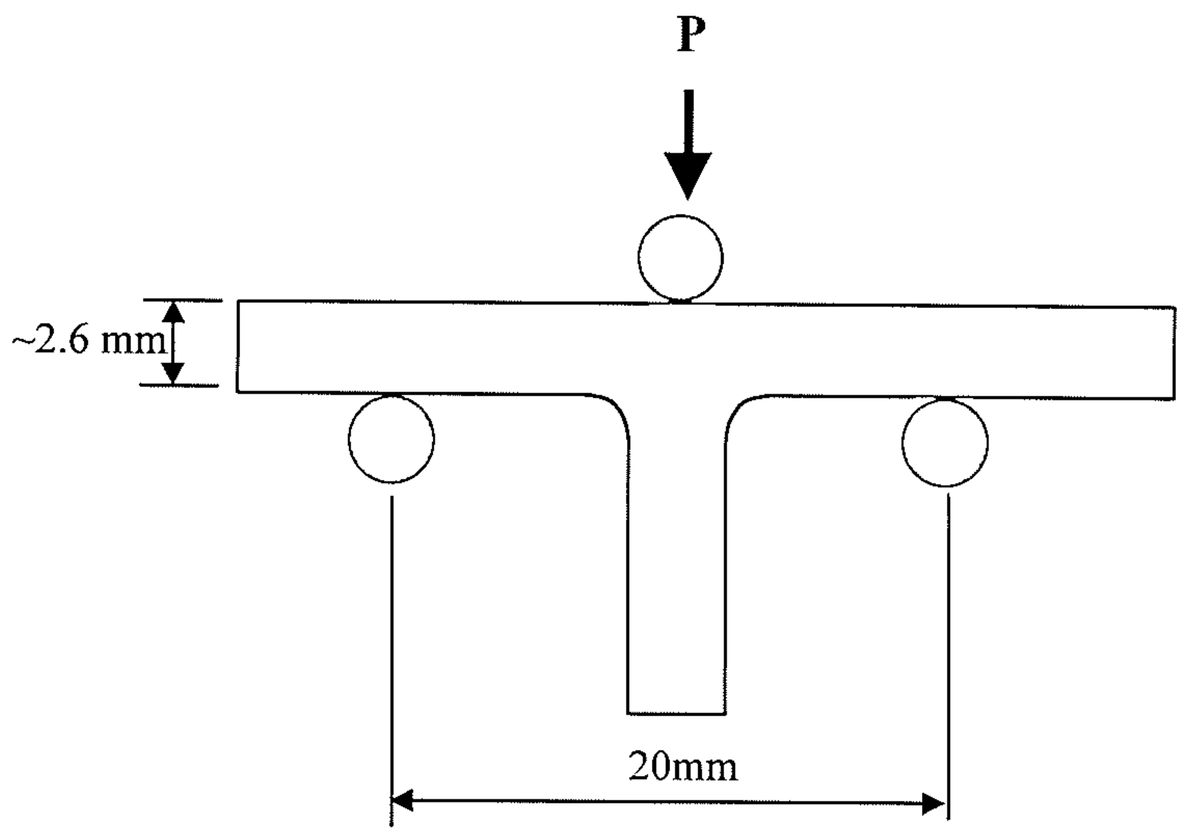

Fig. 5.1-2 Three point bend test configuration for 'T' shaped polyester composite bar 10mm wide.

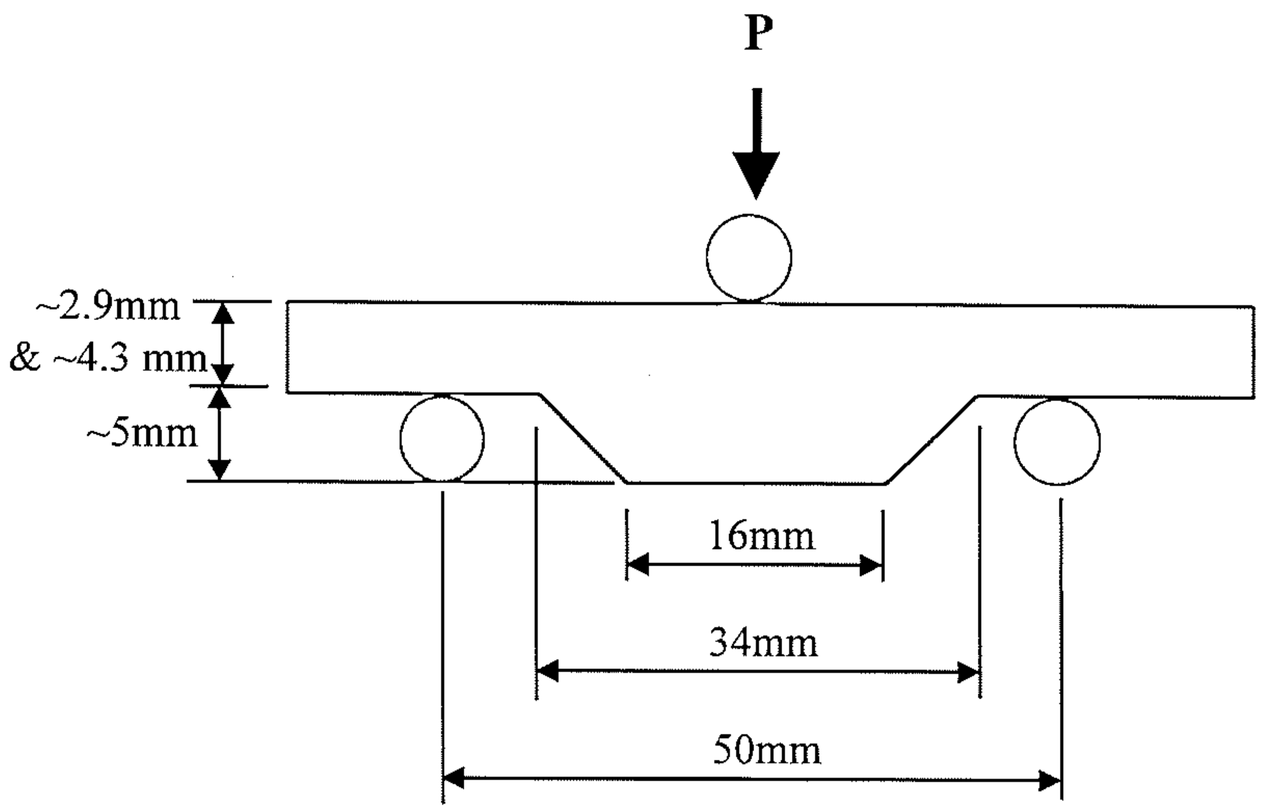

Fig. 5.1-3 Three point bend test configuration for thicken polyester composite bar 10mm wide.

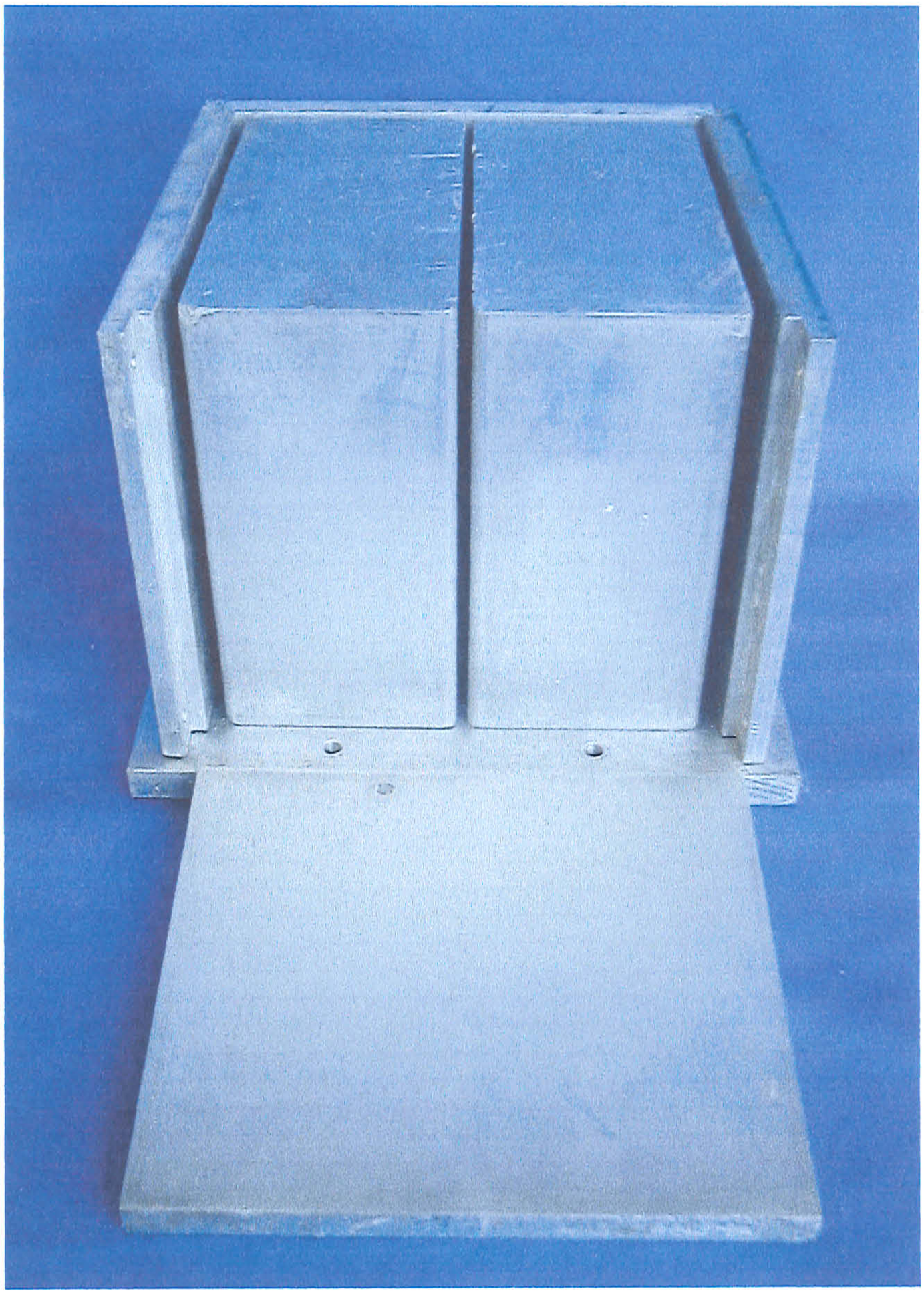

Fig. 5.2-1 Mould for fabrication of T-shaped composite specimens

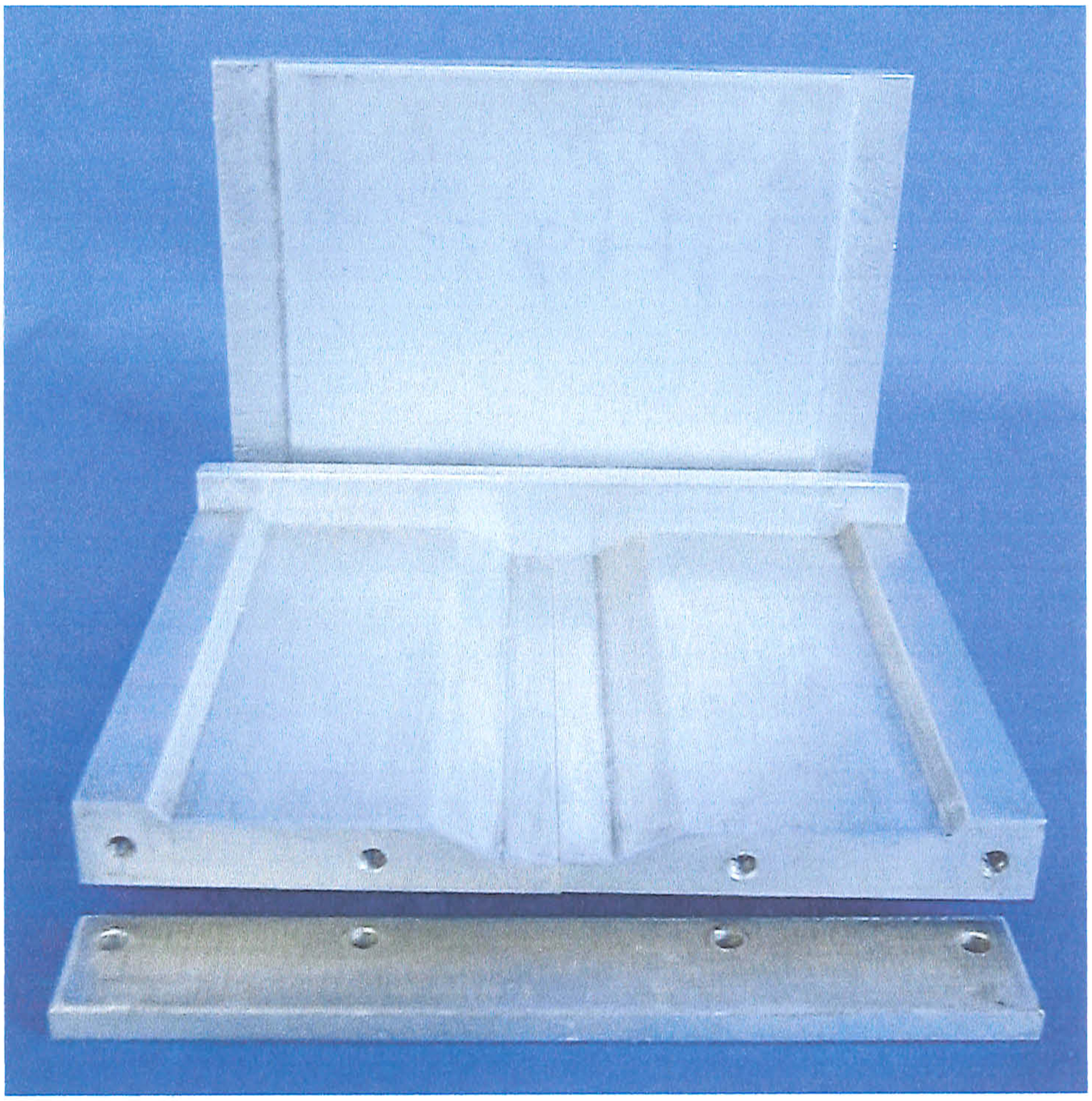

(a)

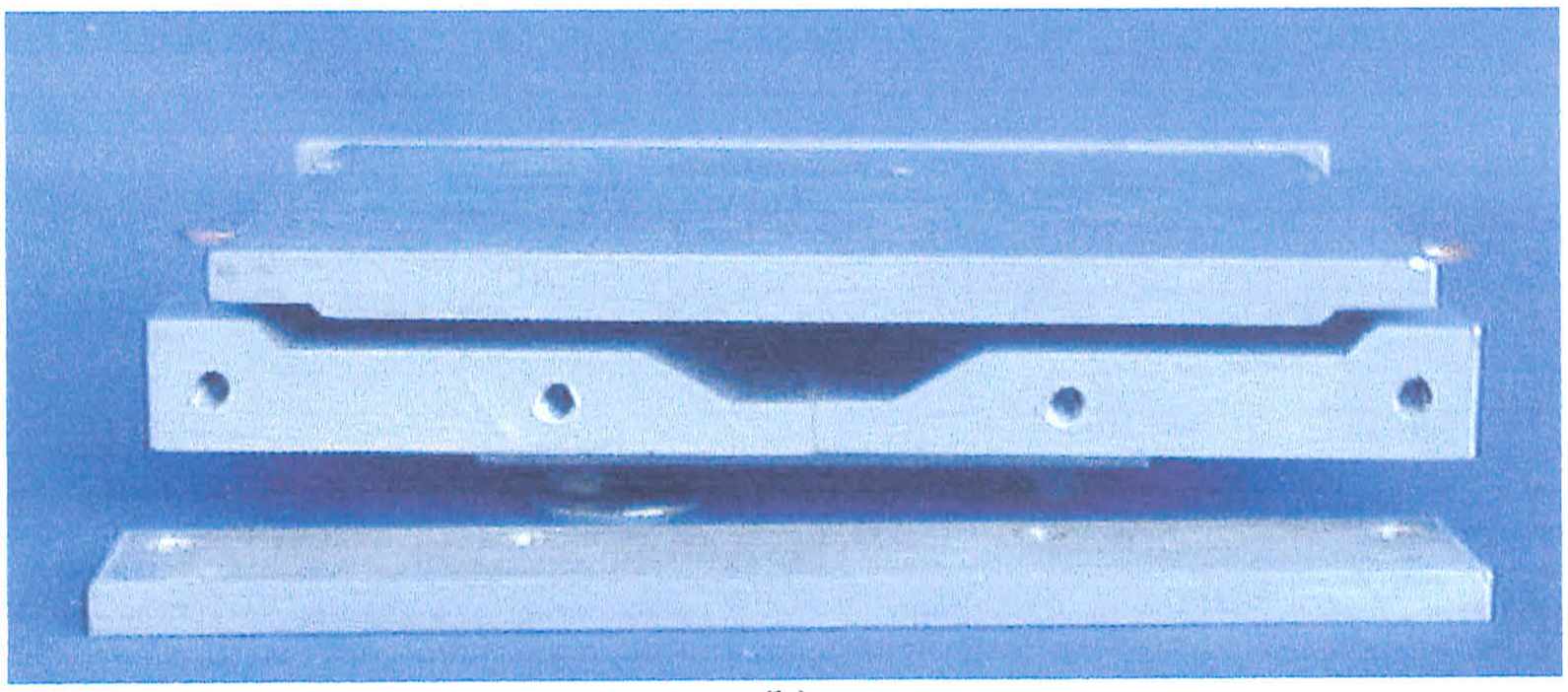

(b)

Fig. 5.2-2 Mould for fabrication of Wedge-shaped composite specimens

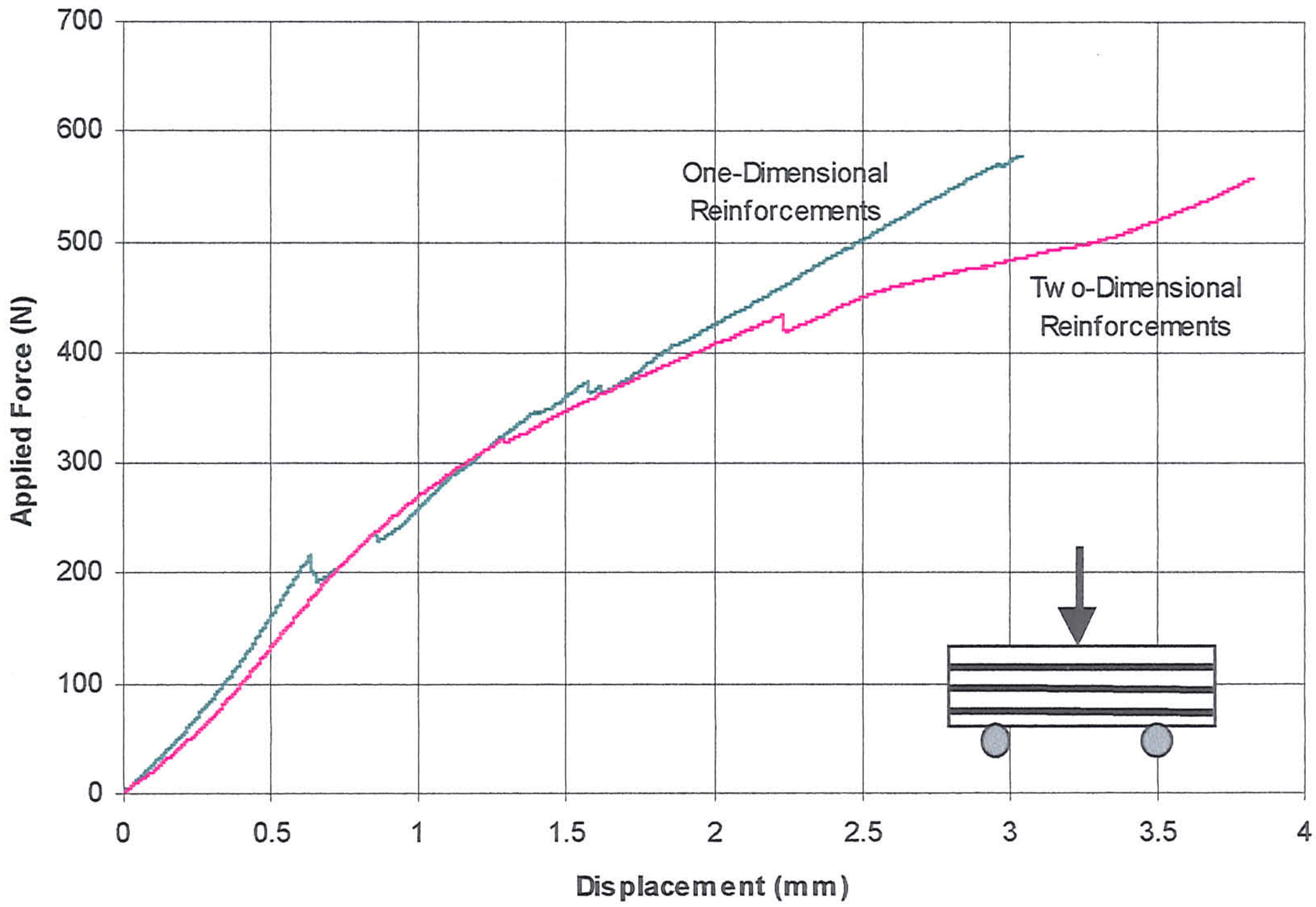

Fig. 5.4.1-1 Experimental force-displacement curves of the rectangular sub-structures with one- and two-dimensional reinforcements.

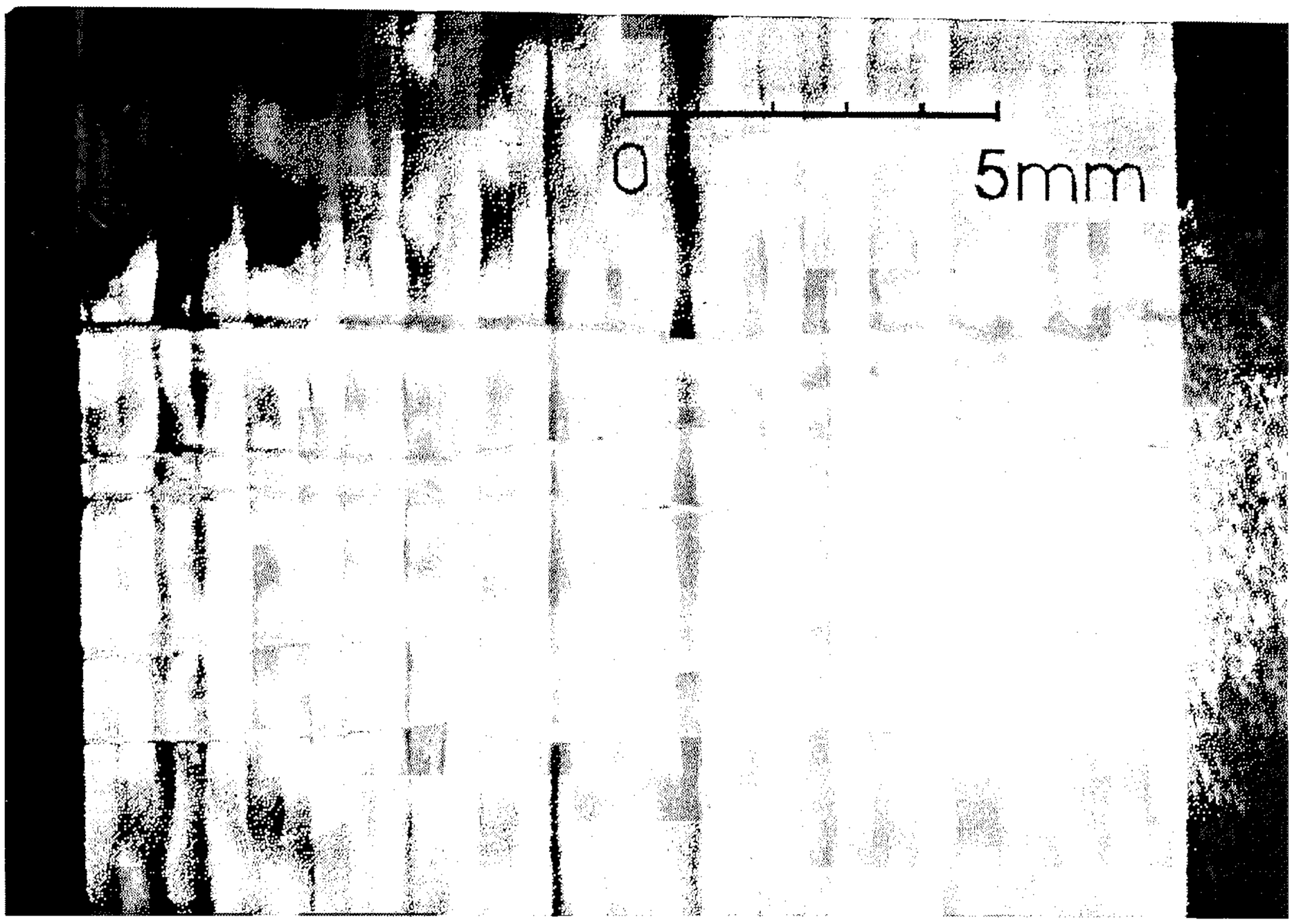

Fig. 5.4.1-2 Damage in one-dimensionally reinforced rectangular sub-structure after three-point bending at an applied displacement of 3mm.

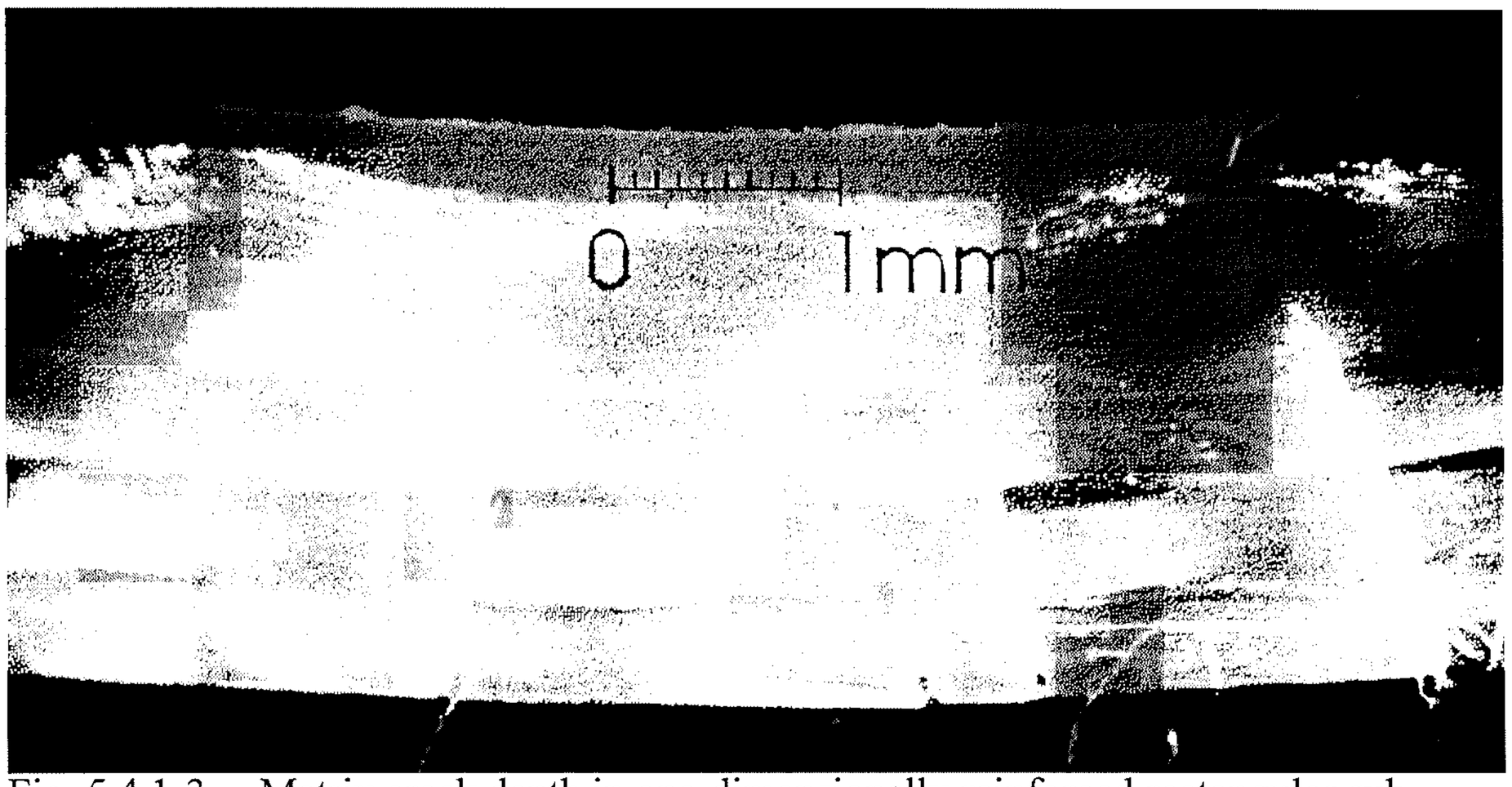

Fig. 5.4.1-3 Matrix crack depth in one-dimensionally reinforced rectangular sub-structure after three-point bending at an applied displacement of 3mm.

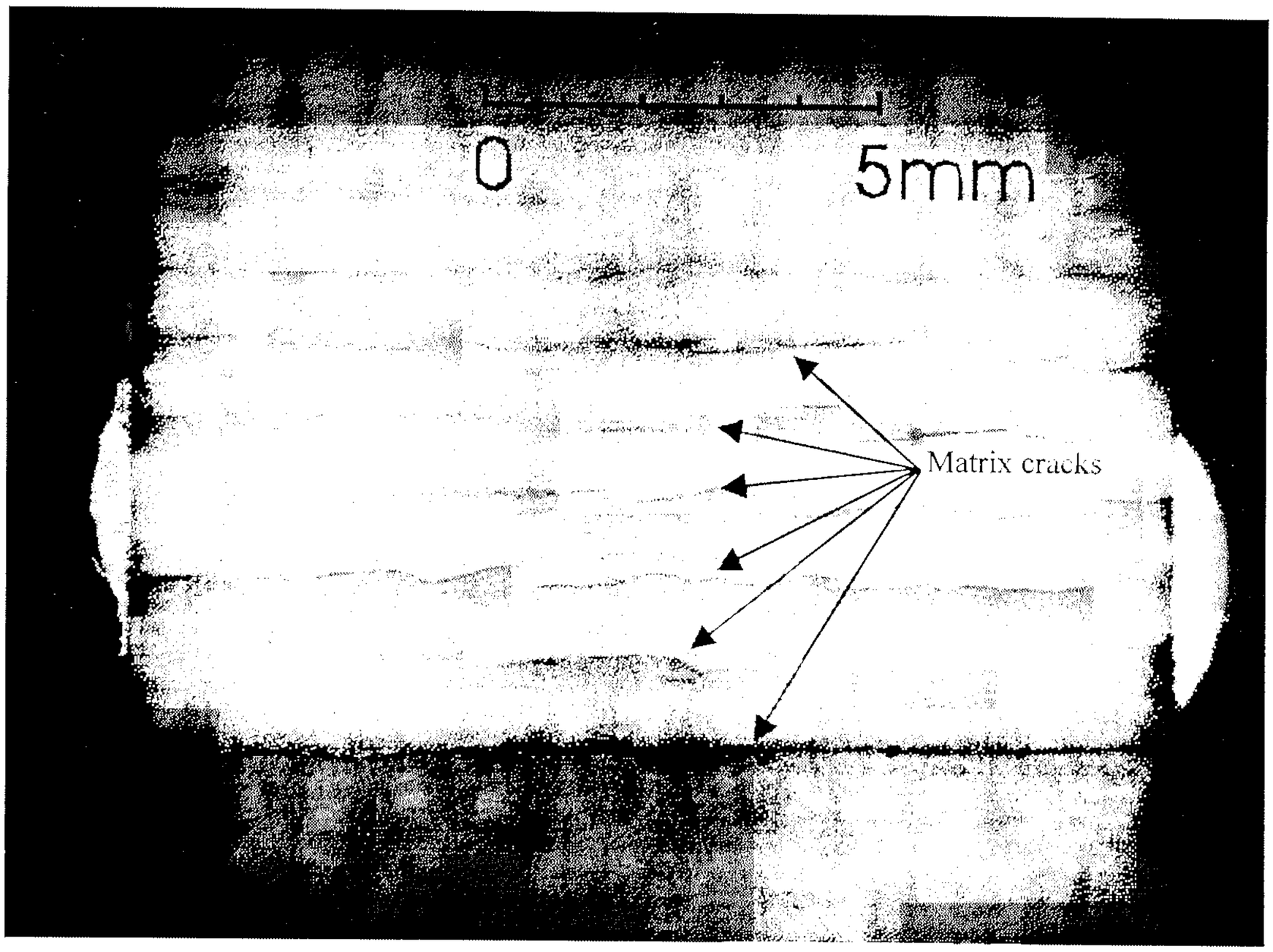

Fig. 5.4.1-4 Damage in two-dimensionally reinforced rectangular sub-structure after three-point bending with an applied displacement of 3.8mm.

Fig. 5.4.1-5 Side profile of two-dimensionally reinforced rectangular sub-structure after three-point bending with an applied displacement of 3.8mm.

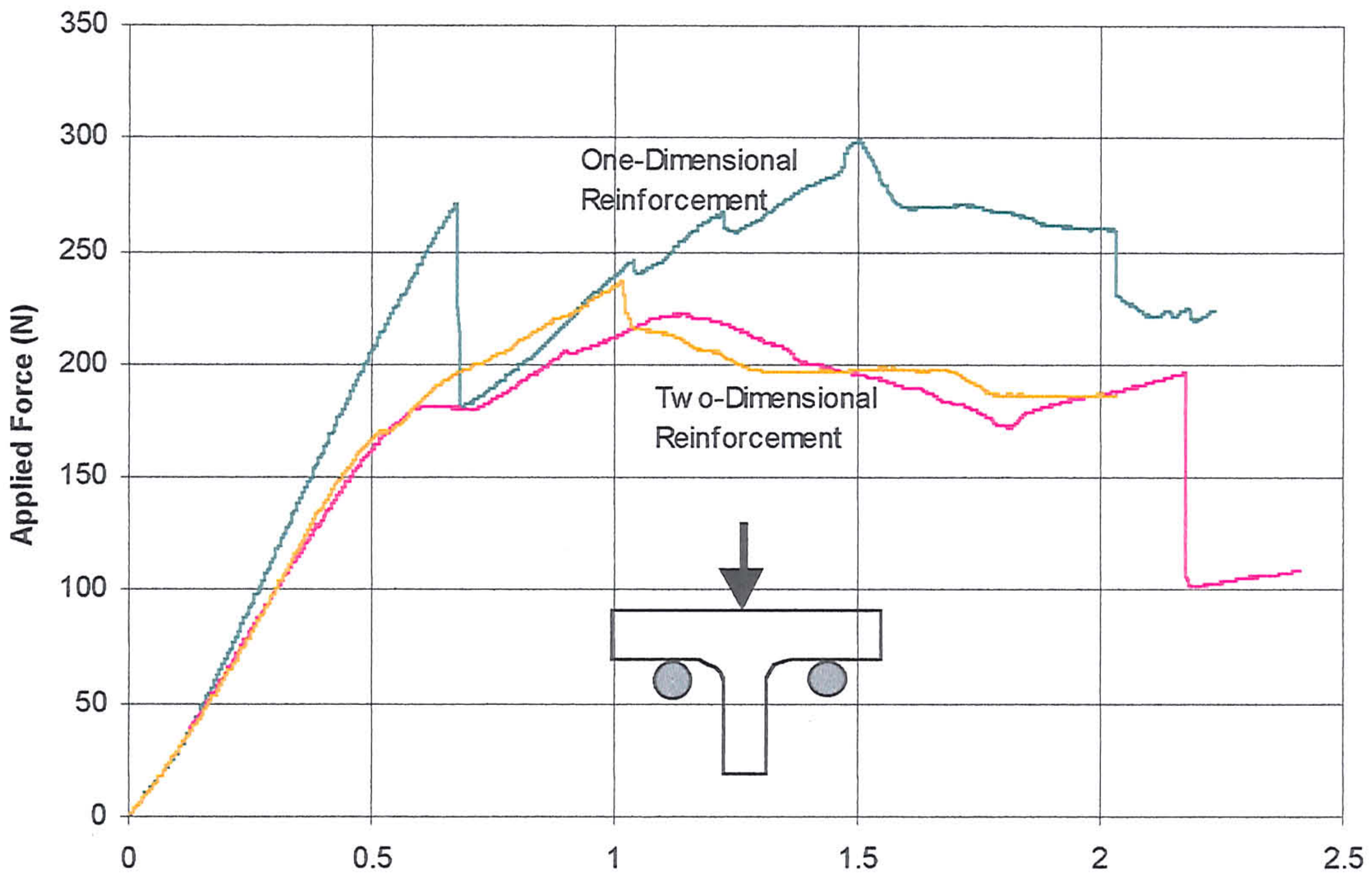

Fig. 5.4.2-1 Experimental force-displacement curves of the T-shaped sub-structures with one- and two-dimensional reinforcements.

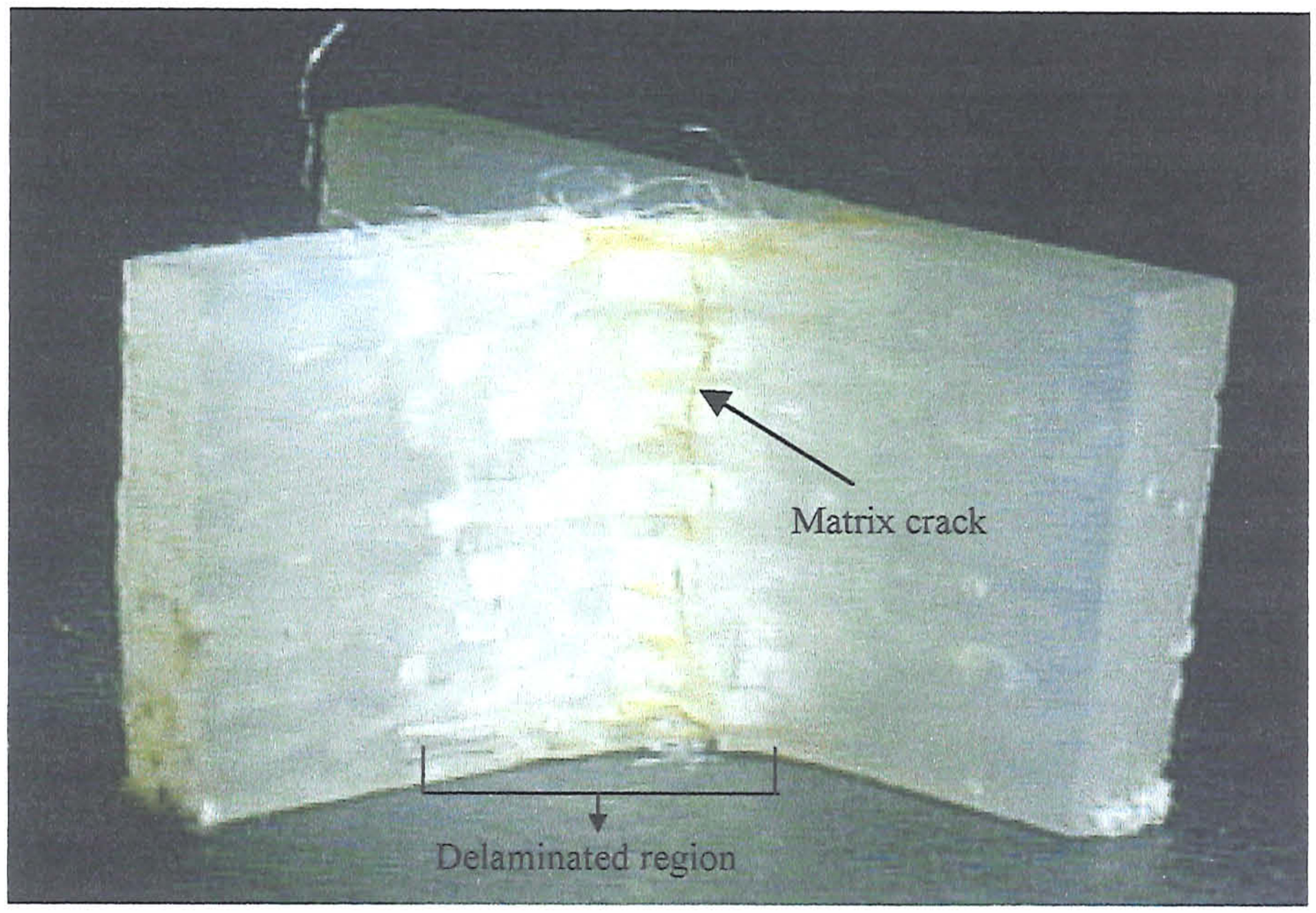
Matrix crack
Delaminated region

(a)

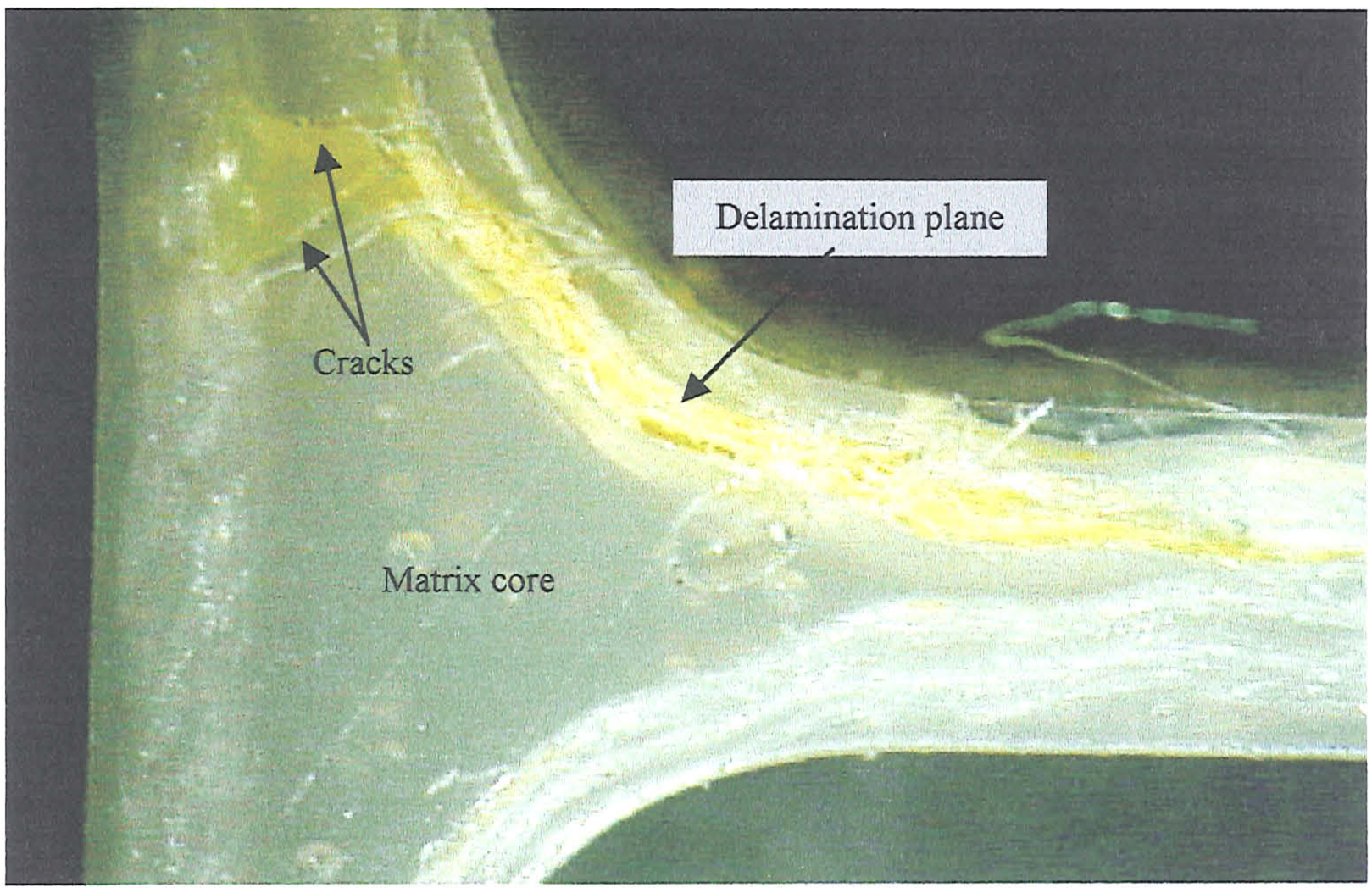
Delamination plane
Cracks
Matrix core

(b)

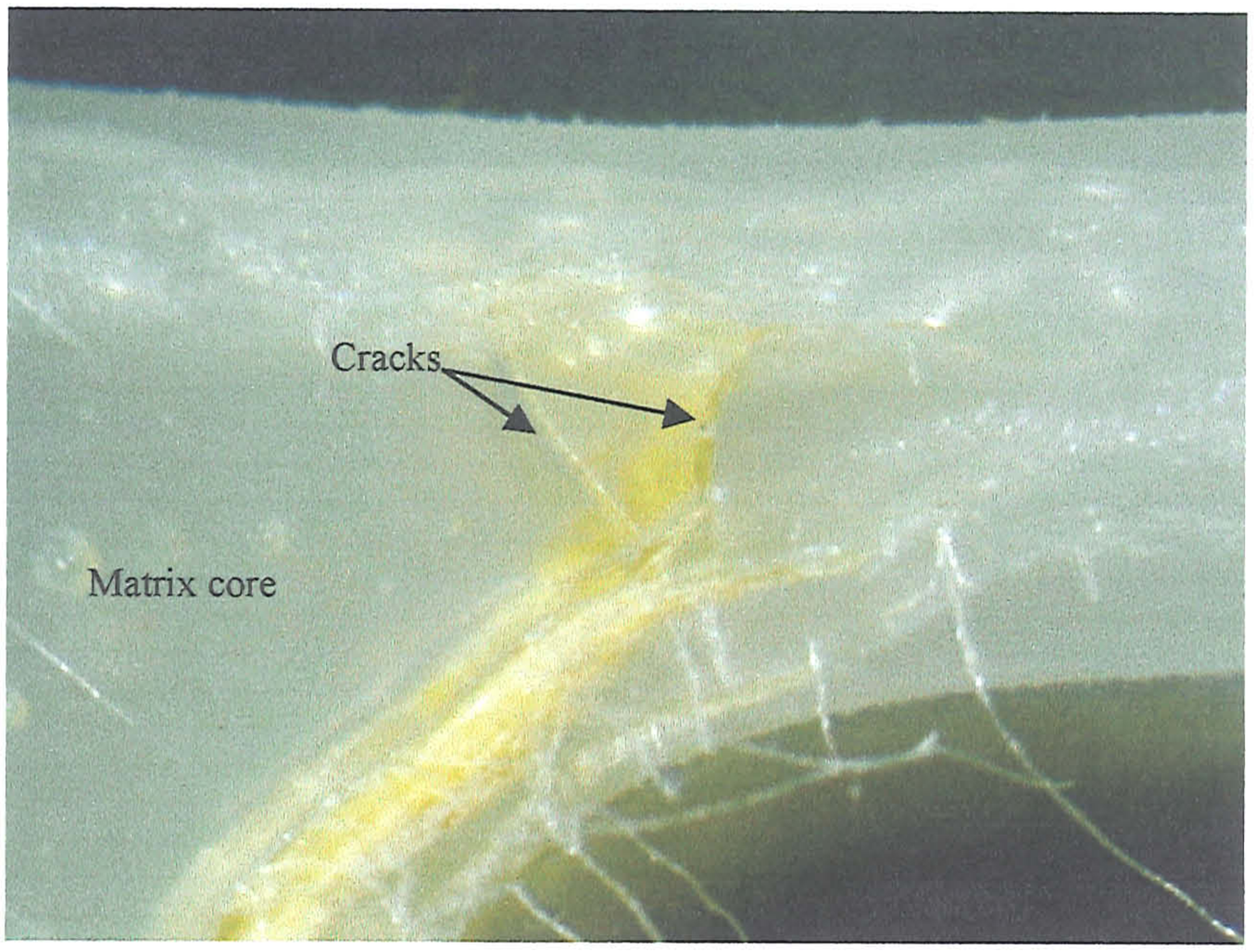

(c)

Fig. 5.4.2-2 Photographs of damaged T-shaped sub-structure with one-dimensional reinforcements after three-point bending:
(a) profile showing matrix crack and delamination region.
(b) profile showing delamination plane and cracks in matrix core.
(c) close-up of cracks in the ligament of the matrix core.

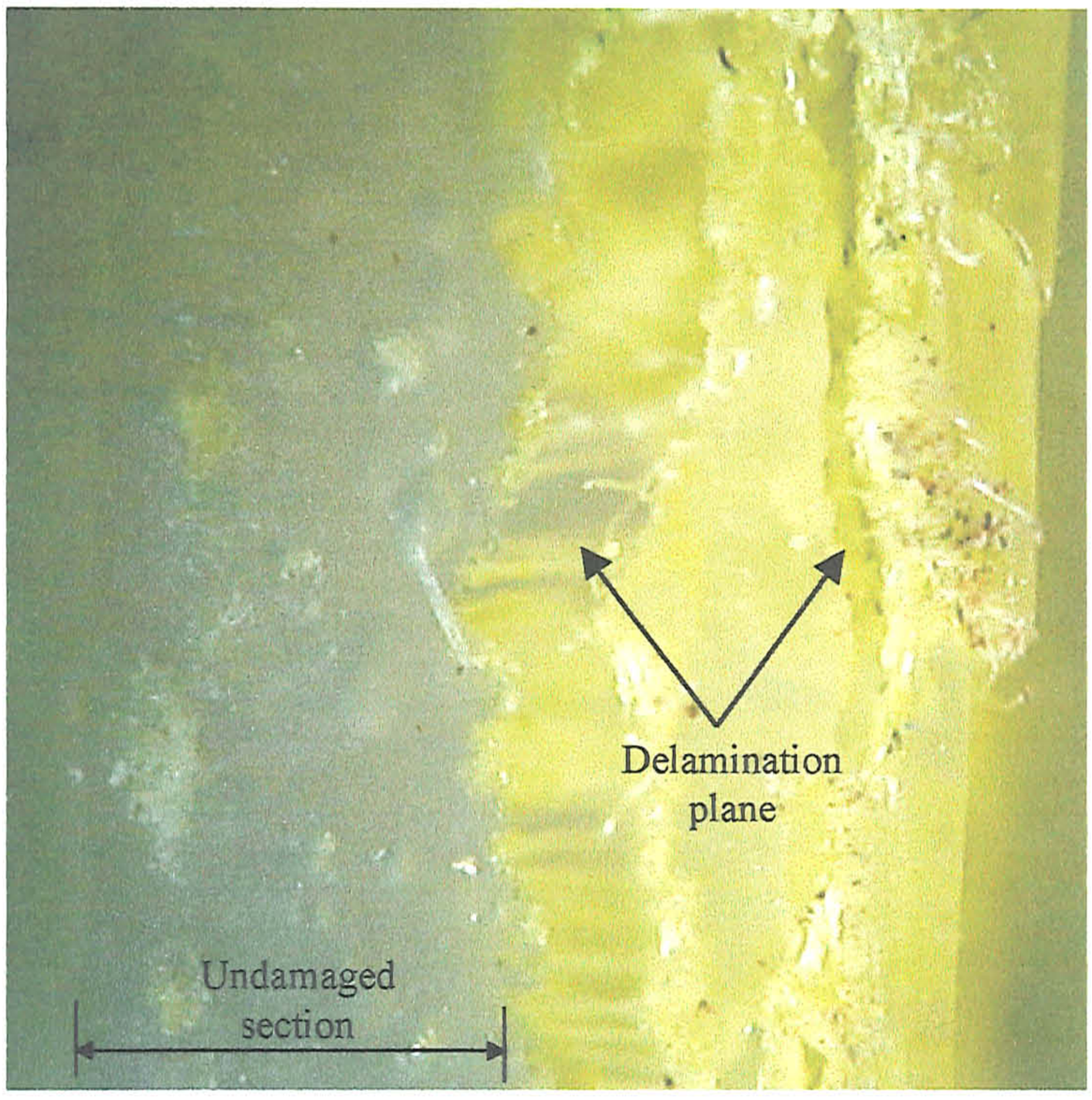

Fig. 5.4.2-3 The delamination plane in the fillet of the T-shaped sub-structure with one-dimensional reinforcement.

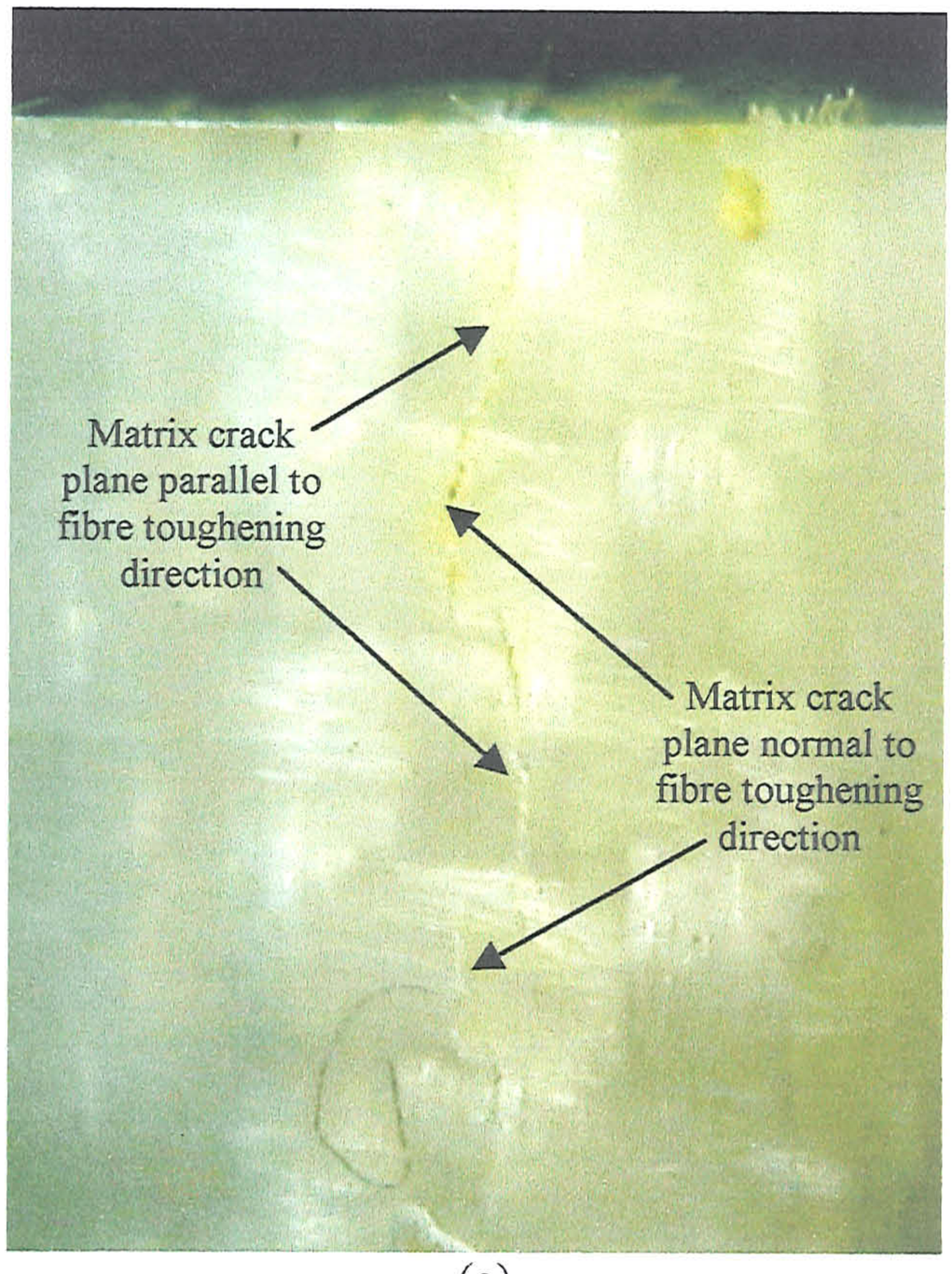

(a)

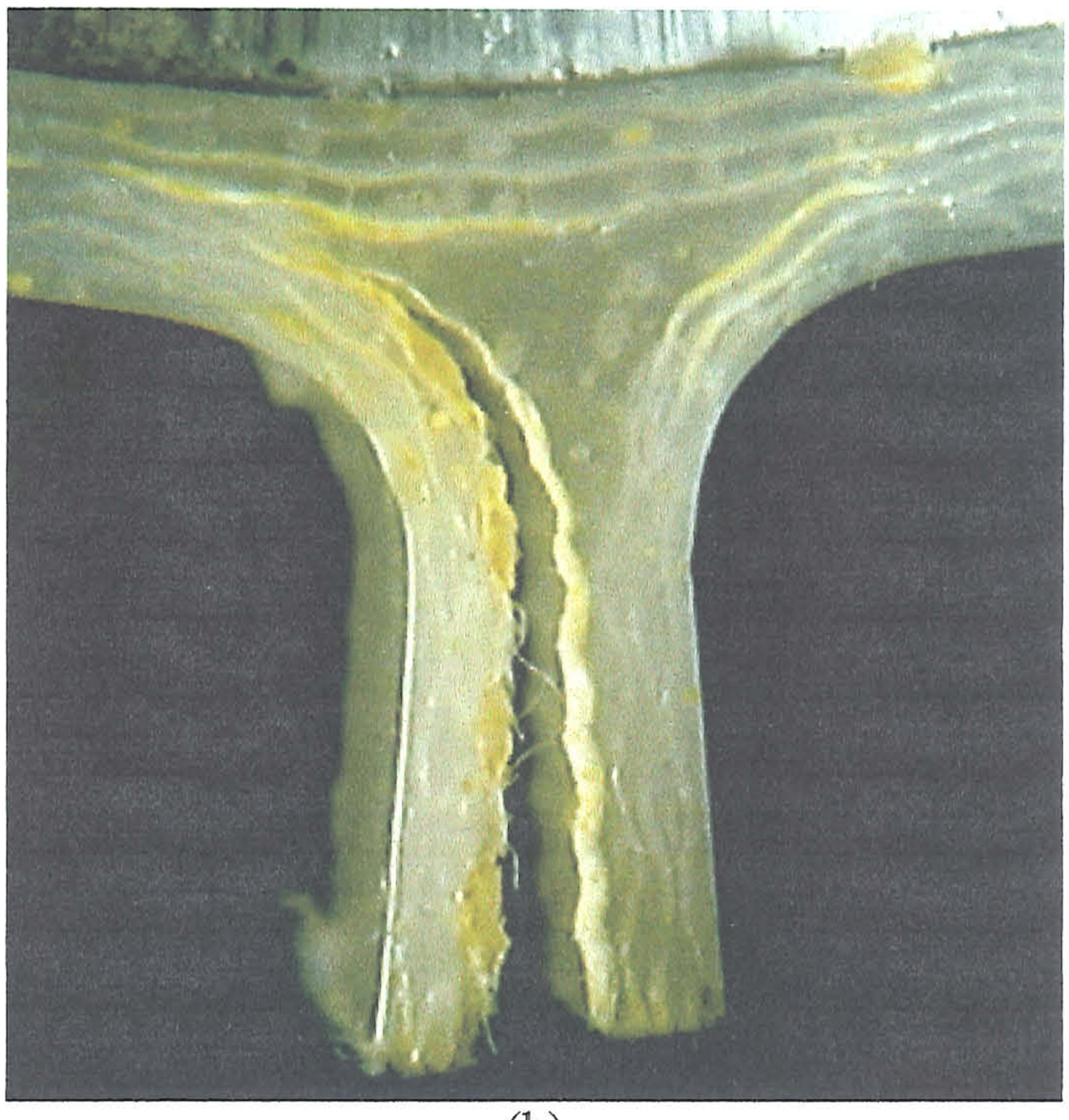

(b)

Fig. 5.4.2-4 Photographs of the fractured two-dimensionally toughened T-shaped sub-structure (a) Matrix crack plane at fillet, and (b) Delamination plane along fillet.

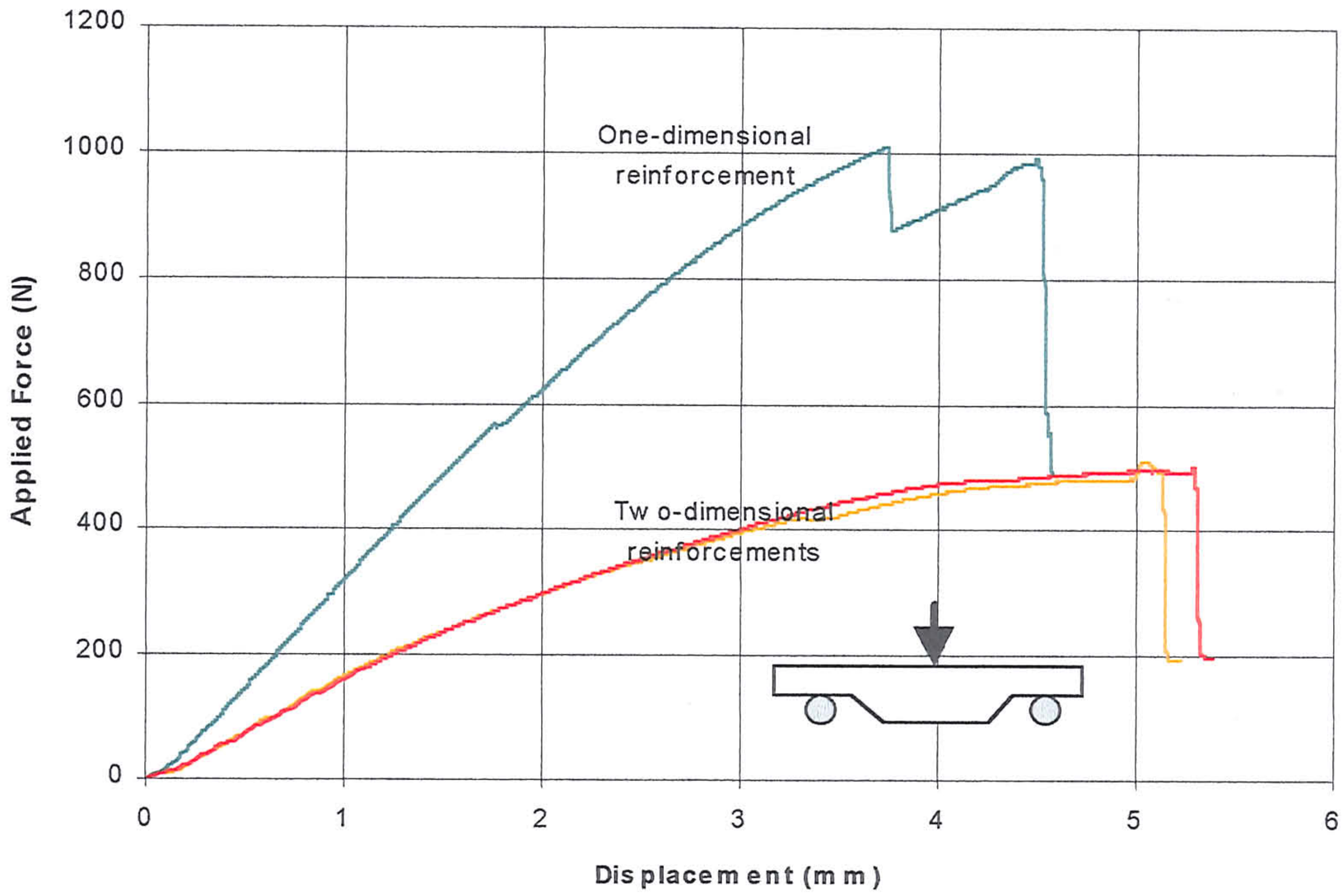

Fig. 5.4.3-1 Experimental force-displacement curves of the wedged-shaped sub-structures with one- and two-dimensional reinforcements.

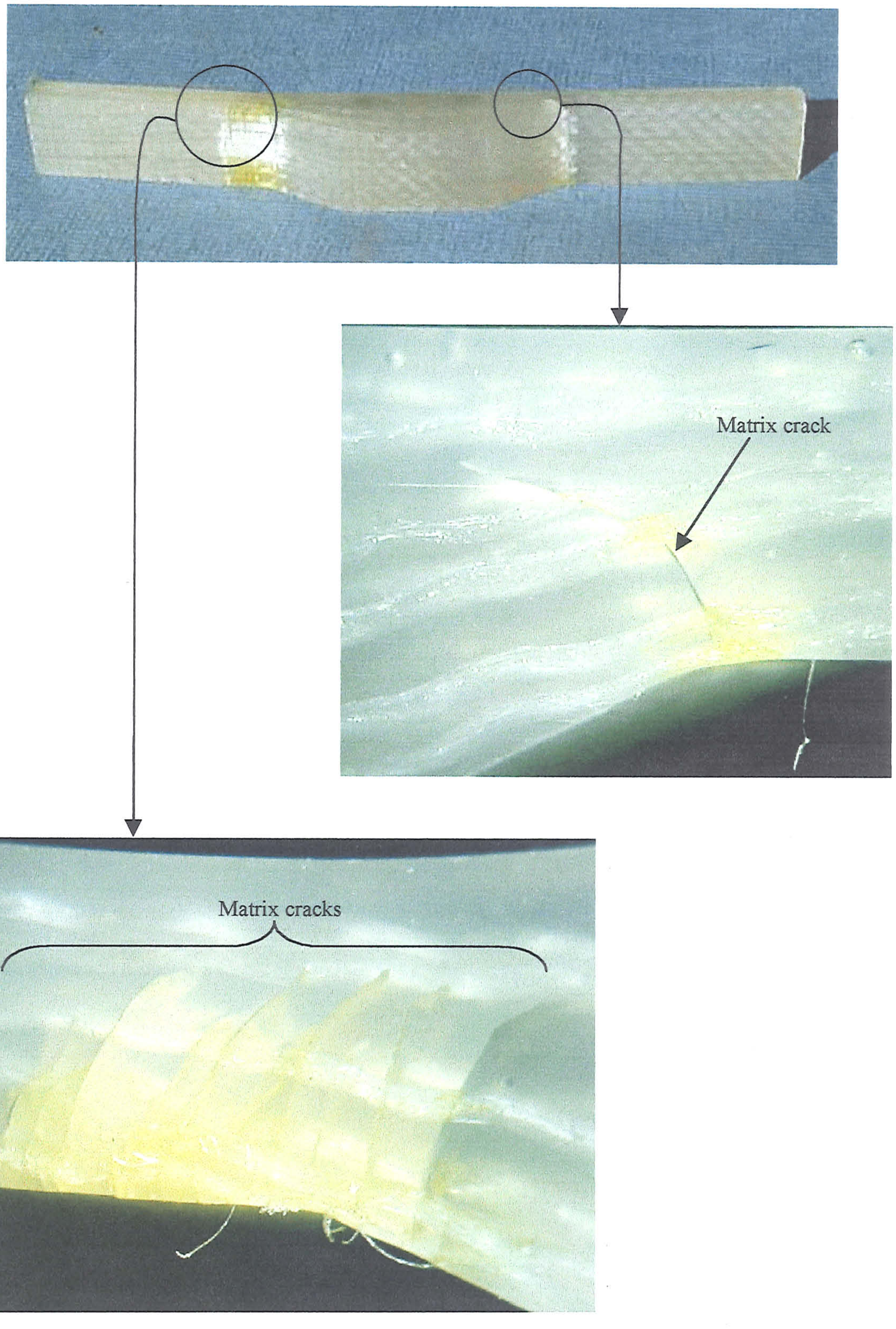

Fig 5.4.3-2 Photographs of the fractured one-dimensionally toughened wedged shape specimen.

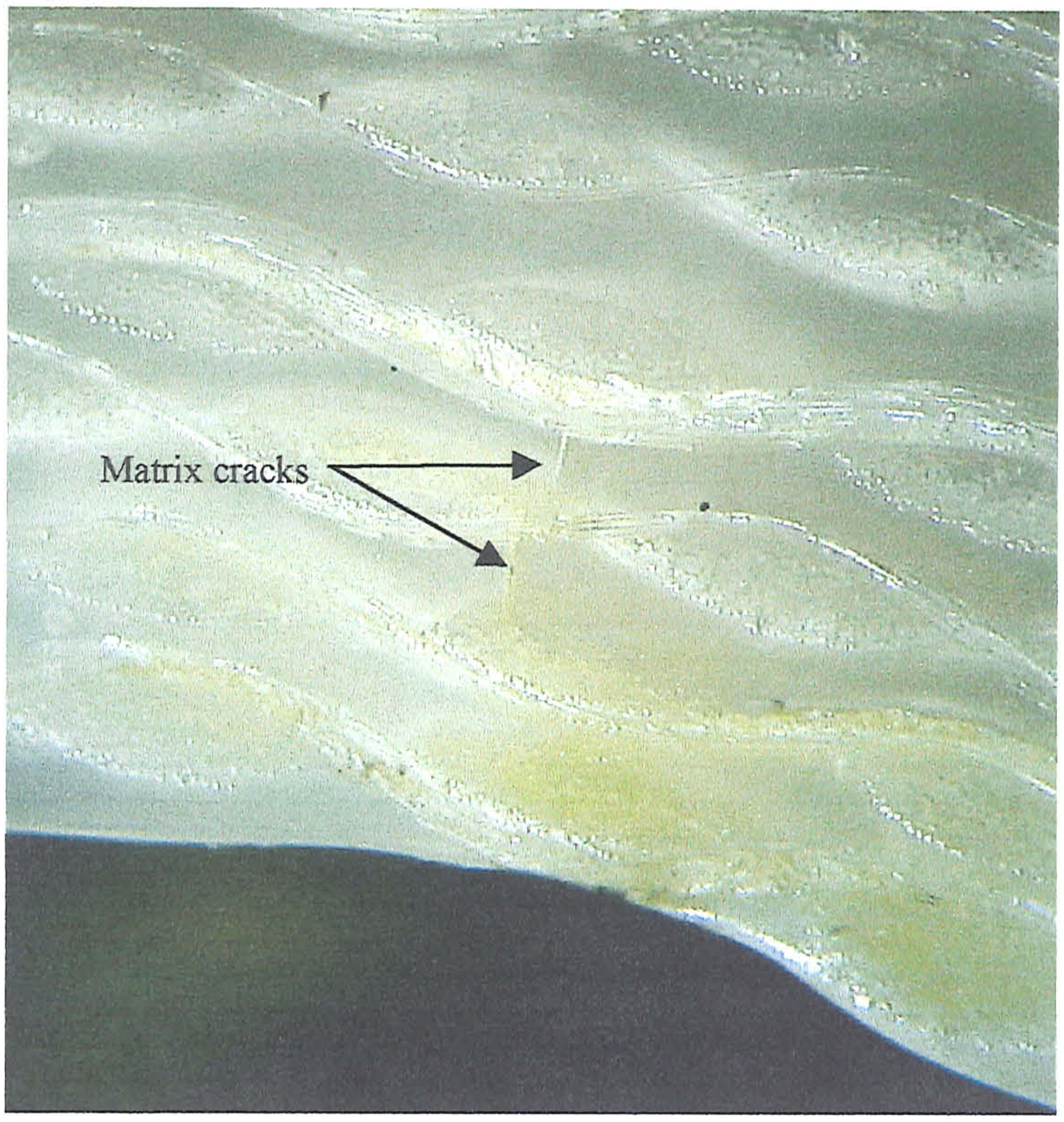

(a)

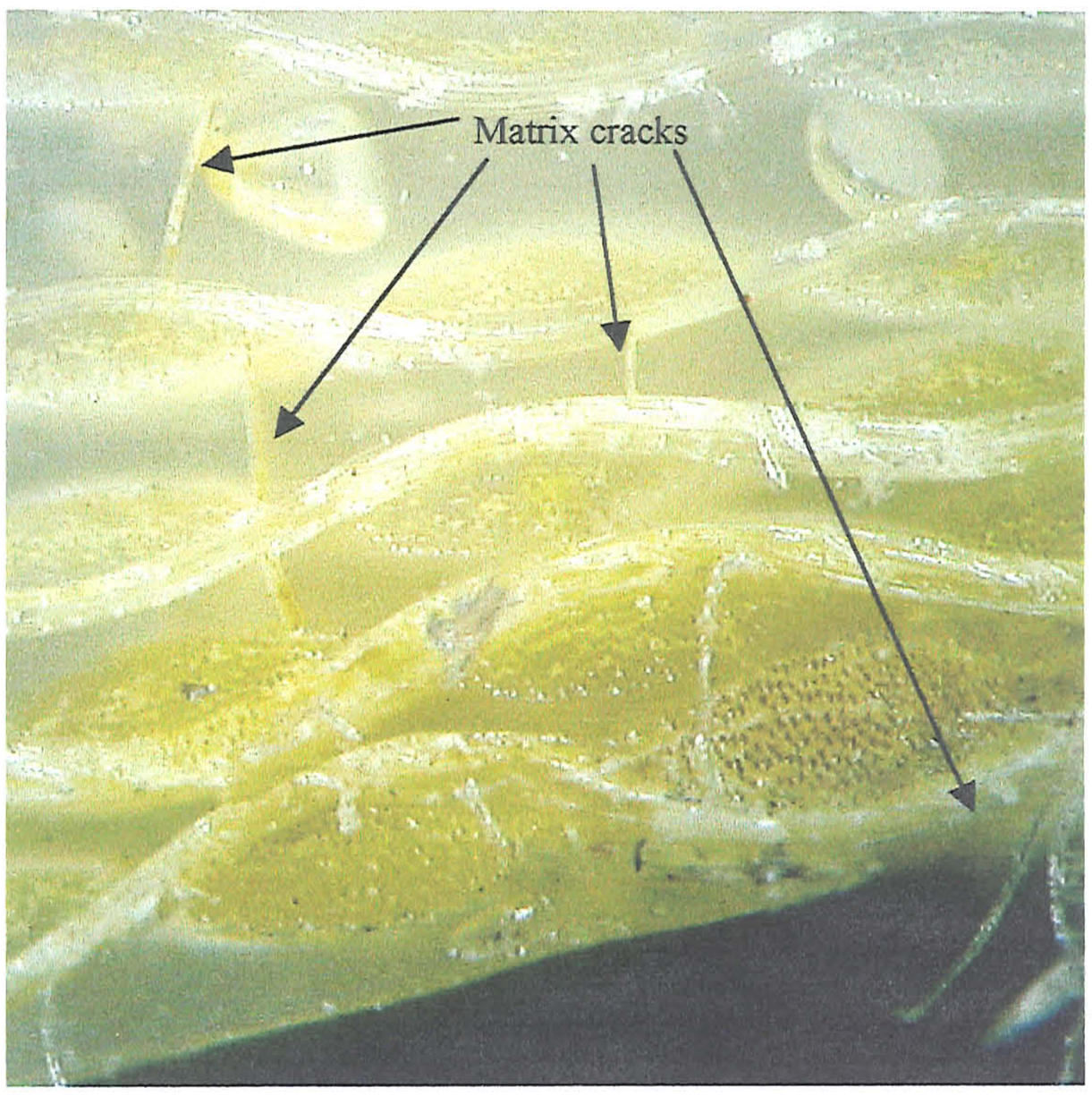

(b)

Fig. 5.4.3-3 Photographs of fractured surfaces of the two-dimensionally toughened wedged-shaped sub-structure: (a) left wedge and (b) right wedge.

CHAPTER 6

Finite Element Modelling Techniques for Composites

6.1 Introduction

Finite element methods are extensively employed in the analysis of solids and structures (Bathe 1996). In essence, the method involves solving engineering problems by solving a set of governing algebraic equations using fast digital computers. In the finite element analysis of composites, the central issue is how to reinforcement is represented. Three main modelling techniques are used: *embedded*, *discrete* and *distributed* representation.

The embedded reinforcement representation was developed in the early 1970s to analyse civil engineering composite materials such as steel-reinforced concrete. The technique models the concrete using two- or three dimensional isoparametric elements, while the steel reinforcements are represented by line elements embedded into the isoparametric elements. Significant contributors to the development and application of this technique include Zienkiewicz et al (1972), Phillips & Zienkiewicz (1976) and Hibbitt, Karlsson & Sorensen (1998a). The line elements are only capable of a one-dimensional response and their shape functions are similar to isoparametric elements. As such, compatibility between the line elements and the isoparametric element is satisfied, since the displacement fields of the line elements and the isoparametric elements are identical. However, line elements do not contribute to the mass or volume of the model. This is not a problem when modelling reinforced concrete as the volume fraction of reinforcement is very low, typically of the order of 1% to 2%. Hence when developing a mesh to model reinforced concrete, the overall geometrical properties of the isoparametric elements represents the reinforced concrete. Because the technique allows strategic placement of the line elements within isoparametric elements, the ability to analyse composites with complex reinforcement architectures is advantageous.

In the discrete reinforcement representation, the individual constituents of a composite are also modelled using separate element types. However, the underlying difference to the embedded reinforcement technique stems from the elements used to

model the reinforcement. Typically, one-dimensional (truss/bar) elements or two/three-dimensional (beam/solid/shell) elements are used. These are connected to the elements representing the matrix, typically two/three-dimensional elements, by node sharing or node tying techniques. In one-dimensional reinforcements, only the axial force of the reinforcements is taken into account. In two/three dimensional reinforcements, the axial force, shear and bending effects are taken into account. The response of the reinforcement and matrix is coupled such that the integrated response of the assembly of elements is modelled. This implies that both equilibrium and compatibility between the constituents is satisfied. This has advantage over the embedded reinforcement representation, which satisfies only compatibility. Another advantage of the technique is the ability to model interfacial effects, such as friction and damage, of the constituents. This is significant because the mechanical properties of composites, such as strength and stiffness, are dependent on interfacial behaviour. Connector elements such as line-springs elements have also been used to model the interface.

Examples of the discrete reinforcement representation include Grande et al (1988), Needleman (1990), Mukherjee & Rao (1995), Goda (1999) and Cox *et al* (1994). To predict the interfacial shear and tensile strength when debonding occurred, Grande et al (1988) used two-dimensional elements to model both the fibre and matrix. The plane of nodes at which the constituent elements met, defined the interface. To model the decohesion process, Needleman (1990) modelled the imperfect interfaces using spring elements whose traction-displacement relations was the differential of a potential function. The use of one-dimensional elements to model the interface however does have the major limitation that the compatibility condition along the interface is not perfectly satisfied. The shape function of the one-dimensional element is not necessarily compatible with higher order elements modelling the matrix as the reinforcement response is limited to discrete nodal points and not the entire length of the element. Under a compressive normal force, overlapping of nodal points commonly occurs, which violates the interface compatibility conditions. As a solution, Mukherjee & Rao (1995) utilised six noded isoparametric-interface elements, which allowed improved modelling of interfaces in whisker reinforced ceramic matrix composites. Recently, Goda (1999) utilised the discrete reinforcement representation to establish a macro model for unidirectional fibrous composites tensioned parallel to the fibres. The matrix was modelled using 4-noded isoparametric elements, the fibres were represented by 2-

noded truss elements and the interface using 2-noded spring elements. Using a Monte-Carlo simulation technique, the effects of interfacial debonding on strength and reliability were analysed. The approach is similar to the Binary Model of Cox *et al* (1994). However in the case of Cox *et al* (1994), the Monte-Carlo technique was used to model random fibre strength resulting from irregular fibre positioning.

In the distributed reinforcement technique, the composite is modelled as a continuum. The reinforcements are assumed to be homogeneously smeared-out within the matrix. The composite is represented using second or third order continuum (solid/shell) elements, in which lamina theory or anisotropic elasticity theory is used to model the average mechanical response of the composite (Hibbitt, Karlsson & Sorensen (1998b)). Advances to the distributed technique have been introduced by the development of damage mechanics (Sect. 2.5), that is the smearing out of damage such as inter-lamina and intra-lamina cracks. To model the resulting response, damage variables and damage evolutionary laws are introduced into the constitutive relations of the composite. Chen & Saleb (1994) have used the technique to analyse steel reinforced concrete structures. Voyiadjis and Kattan (1999) have studied the effects of damage in metal matrix composites. To alow the analysis to include damage in laminated composites, (Hibbitt, Karlsson & Sorensen (1998b) have also introduced layered continua that allow the damaged mechanical behaviour of individual layers of a laminate to be modelled using a single element.

In this chapter, the suitability of the embedded, discrete and distributed reinforcement techniques for modelling brittle matrix composites with high fibre volume fraction in structural analysis is considered. Specifically, the technique should:

- satisfy both equilibrium and compatibility and the appropriate boundary conditions
- allow efficient representation of the composite constituents architecture, and
- have a physical based interpretation of damage

To compare existing modelling techniques, simple benchmark studies are initially considered. These are described in detail in the following section. The finite element analysis was conducted using the ABAQUS/Standard solver, developed by Hibbitt, Karlsson & Sorensen (1998a).

6.2 The Benchmark Studies & Model

Four simple benchmark studies were considered to assess the suitability of each modelling technique for uni-directional composites:

Case (1): Tension parallel to the reinforcement direction with no modulus mismatch ($V_f = V_m = 0.5$ and $E_f = E_m = 4.732$GPa),

Case (2): Tension parallel to the reinforcement direction with a higher fibre volume fraction but no modulus mismatch ($V_f = 3V_m = 0.75$ and $E_f = E_m = 4.732$GPa),

Case (3): Tension parallel to the reinforcement direction with modulus mismatch ($V_f = V_m = 0.5$ and $E_f = 10E_m = 47.32$GPa), and,

Case (4): Tension normal to the reinforcement direction with no modulus mismatch ($V_f = V_m = 0.5$ and $E_f = E_m = 4.732$GPa).

Here, V_m and V_f are the volume fraction of the matrix and fibres; E_m and E_f is the Young's modulus of the matrix and fibres. The Poisson's ratio of the composite and its constituents were taken to be identical, i.e. $\nu_c = \nu_f = \nu_m = 0.3$. The dimensions of the composite were 0.015m x 0.015m x 0.002m and magnitude of the applied displacement in the global 1-direction was 0.001m. The composite constituents were assumed to be isotropic linear elastic and perfectly bonded. Diagrams of the benchmark studies are shown in Fig. 6.2-1. The figure also defines the Cartesian co-ordinate and node numbering systems

In the embedded reinforcement model, the matrix was represented using a 4-noded plane stress solid element with in plane dimensions of 0.015m x 0.015m. The thickness of the elements were 0.002m and 0.001m; the first thickness follows current modelling practice and represents the thickness of the composite while the latter models the area of the matrix only. The fibres were modelled using an embedded line element positioned central to the element. For cases 1 to 3, the line element was aligned in the global 1-direction, while in case 4 the line element was aligned in the global 2-direction. The cross-sectional area of fibres was represented by specifying in the finite element code. In cases 1, 3 & 4, a fibre cross-sectional area of 1.5E-5m^2 was used while a fibre cross-sectional area of 2.25E-5m^2 was used in case 2.

In the discrete reinforcement model, the matrix was represented by a 4-noded plane stress solid element. In all cases, the in-plane cross section dimensions were 0.015m x 0.015m. In cases 1, 3 & 4, the thickness of the matrix was 0.001m while a thickness of 0.0005m was used in case 2. The reinforcement was modelled using two truss elements. In cases 1 to 3, the truss elements were connected between nodes 1 & 2 and nodes 4 & 3. In case 4, the truss elements were connected between nodes 1 & 4 and nodes 2 & 3. In cases 1, 3 & 4, the area of each truss element was 0.75E-5m^2 while the area of each truss element in case 2 was 1.125E-5m^2.

In the distributed reinforcement model, a 4-noded plane stress solid element with dimensions 0.015m x 0.015m x 0.002m was used to represent the composite, which consisted the properties of the matrix and reinforcements. In case 3, where modulus mismatch was present, the composite was modelled as transversely-isotropic linear elastic.

In the models, the applied boundary conditions were identical. Node 1 was pinned in the global 1 & 2 direction while a displacement u_1 in the global 1-direction of 0.001m was applied onto node 2 and 3. Node 4 was constrained from moving in the global 1-direction to prevent rigid body motion.

6.3 The Benchmark Results

To compare solutions from the modelling techniques, exact solutions were determined where possible. For cases 1, 2, 3 & 4, the composite reduces to a simple isotropic homogeneous elastic solid. The relevant numerical results are presented in Table 6.3-1 to 6.3-4. Incorporated into the tables are the finite element results for the embedded, discrete and distributed reinforcement models. The results are defined in terms of the global co-ordinate system as shown in Fig. 6.2-1. The symbols F_c, F_m and F_f denote the applied force on the composite, matrix and fibres. The symbols σ_c, σ_m and σ_f denote the stress in the composite, matrix and fibres and ε_c is the strain in the composite. The suffices 1 and 2 denote components with respect to the global co-ordinate system. To emphasise discrepancies in the finite element results, italic values are used.

	Exact Solution	**Embedded Model**			**Discrete Model**	**Distributed Model**
		Matrix thickness 0.002m with fibres	Matrix thickness 0.002m w/o fibres	Matrix thickness 0.001m with fibres		
F_{m1} *(KN)*	4.72	*9.46*	*9.46*	4.72	4.72	-
F_{f1} *(KN)*	4.72	4.72	-	4.72	4.72	-
F_{c1} *(KN)*	9.45	*14.2*	9.46	9.46	9.45	9.45
σ_{m1} *(MPa)*	315	315	315	315	315	-
σ_{f1} *(MPa)*	315	315	-	315	315	-
σ_{c1} *(MPa)*	315	*473*	315	315	315	315
ε_{c1}	0.0666	0.0666	0.0666	0.0666	0.0666	0.0666
ε_{c2}	-0.020	-0.020	-0.020	-0.020	-0.020	-0.020

Table 6.3-1: Case 1 Tension parallel to reinforcement where $V_f = V_m = 0.5$ and $E_f = E_m = 4.732$GPa.

	Exact Solution	**Embedded Model**		**Discrete Model**	**Distributed Model**
		Matrix thickness 0.002m with fibres	Matrix thickness 0.0005m with fibres		
F_{m1} *(KN)*	2.37	*9.46*	2.37	2.36	-
F_{f1}*(KN)*	7.08	7.08	7.08	7.08	-
F_{c1} *(KN)*	9.45	*16.54*	9.45	9.45	9.45
σ_{m1} *(MPa)*	315	315	315	315	-
σ_{f1} *(MPa)*	315	315	315	315	-
σ_{c1} *(MPa)*	315	*551*	315	315	315
ε_{c1}	0.0666	0.0666	0.0666	0.0666	0.0666
ε_{c2}	-0.020	-0.020	-0.020	-0.020	-0.020

Table 6.3-2: Case 2 Tension parallel to reinforcement with $V_f = 3V_m = 0.75$ and $E_f = E_m = 4.732$GPa.

	Exact Solution	**Embedded Model**		**Discrete Model**	**Distributed Model**
		Matrix thickness 0.002m with fibres	Matrix thickness 0.001m with fibres		
F_{m1} *(KN)*	4.72	*9.54*	4.77	4.72	-
F_{f1} *(KN)*	47.23	47.23	47.23	47.23	-
F_{c1} *(KN)*	52.00	*56.77*	52.00	52.00	52.05
σ_{m1} *(MPa)*	315	315	318	315	-
σ_{f1} *(MPa)*	3149	3149	3149	3149	-
σ_{c1} *(MPa)*	1735	*1892*	1733	1732	1735
ε_{c1}	0.0666	0.0666	0.0666	0.0666	0.0666
ε_{c2}	-0.020	-0.020	-0.020	-0.020	-0.020

Table 6.3-3: Case 3 Tension parallel to reinforcement with $V_f = V_m = 0.5$ and $E_f = 10E_m = 47.32$GPa.

	Exact Solution	Embedded Model Matrix thickness 0.002m with fibres	Discrete Model	Distributed Model
F_{m1} *(KN)*	4.72	*9.45*	4.95	-
F_{m2} *(KN*	0	0	*0.74*	-
F_{f1} *(KN)*	4.72	-	-	-
F_{f2} *(KN)*	0	*-1.42*	*-0.74*	-
F_{c1} *(KN)*	9.45	9.45	*4.95*	9.45
F_{c2} *(KN)*	0	*-1.42*	0	0
σ_{m1} *(MPa)*	315	315	*330*	-
σ_{m2} *(MPa)*	0	0	*4.95*	-
σ_{f1} *(MPa)*	315	-	-	-
σ_{f2} *(MPa)*	0	*-94.4*	*-4.95*	-
σ_{c1} *(MPa)*	315	315	*330*	315
σ_{c2} *(MPa)*	0	*-94.4*	0	0
ε_{c1}	0.0666	0.0666	0.0666	0.0666
ε_{c2}	-0.020	-0.020	*-0.0105*	-0.020

Table 6.3-4: Case 4 Tension transverse to reinforcement with $V_f = V_m = 0.5$ and $E_f = 10E_m = 47.32$GPa.

6.4 Discussion

6.4.1 The Embedded Reinforcement Model

In general, the forces in the embedded reinforcement model were not correctly equilibrated when the matrix element was modelled using the overall geometry of the complete composite. In case 1, the composite force is overestimated by 50% compared with the exact solution. The overestimate can be understood by comparing with the results for a matrix element without the embedded line element (see Table 6.3-1). The total force of the matrix element without the line element was identical to the total force of the matrix in the embedded model. This showed that the stiffness of the line element was not included into the analysis and that equilibrium was only satisfied in the matrix element, giving an erroneous estimate of the composite force. This may be acceptable for composites with low volume fractions of reinforcement such as reinforced concrete, but presents significant difficulties for composites with a high volume fraction of reinforcement. The forces obtained in case 4 also support this finding. Though the transverse line element developed a compressive force, no counteracting force occurred in the matrix. The composite thus has a compressive force component, which is not equilibrated with the externally applied loads.

To satisfy equilibrium using the embedded reinforcement technique, the geometry should represent the matrix and not the composite. This is shown in cases 1 & 3 where a

matrix thickness of 0.001m was used and in case 2 where a matrix thickness of 0.0005m was used. In all these cases, the total force applied onto the composite was reported to be correct. The correct force is however obtained at the expanse of geometrical accuracy of the model. For three-dimensional modelling, this approach maybe undesirable, though application can be justified for two-dimensional applications.

Alternatively, the applied force on the composite can be correctly obtained by substituting the matrix stress and the stress from the line element into the rule of mixture and multiplying the composite stress by the composite area. This results in correct composite force and stress. In three-dimensional models and models involving many elements, this approach is cumbersome, but has the advantage that no alteration to the mesh is involved.

6.4.2 The Discrete Reinforcement Model

An advantage of the discrete reinforcement technique is that the forces in the matrix and the reinforcement are in equilibrium. Compatibility between the different elements is also satisfied. This allows the response of the composite to be correctly modelled for loading parallel to the reinforcement. A problem arises when the reinforcement is transversely aligned to the loading direction. This occurs because the truss elements are incapable of representing transverse loading effects.

The meshing procedure is cumbersome. The dimensions of the mesh have to represent the volume of the matrix instead of the composite. In two-dimensional modelling, this was controlled by the varying the thickness of the matrix element. In three-dimensional modelling, the predicted response is questionable since the dimensions of the mesh are not representative of the composite dimensions. Also, the implementation of the reinforcement is node dependent. For off-axis reinforcement problems, the diagonal implementation of the reinforcement would require the matrix mesh dimensions to correspond to the required alignment angle. In complicated geometries, the implementation of the reinforcement would be extremely difficult and cost-ineffective.

6.4.3 The Distributed Reinforcement Model

The distributed reinforcement technique correctly models the composite response regardless of the reinforcement orientation, in that both equilibrium and compatibility

are satisfied. The technique is simple and efficient to implement. The mesh represents the geometry of the composite, unlike the embedded and discrete reinforcement techniques. Changes in material properties such as volume fraction of the constituents do not require any changes to the mesh geometry. However, a setback in the model was that the forces and stresses of the composite constituents were not reported directly in ABAQUS.

6.4.4 Summary

The objective of the chapter is to assess the suitability of current finite element techniques for modelling high fibre volume fraction composites, subjected to the criteria listed in Sect. 6.1.

The embedded model has the advantage that it allows arbitrary positioning of reinforcements within each matrix element. In the discrete model, implementation of the reinforcement is node dependent. In off-axis problems, the dimensions of the matrix element have to be fixed to implement the reinforcement orientation. This is highly cost ineffective and computationally inefficient. In the distributed model, implementation of the reinforcement was achieved by defining appropriate stiffnesses in the finite element code. This did not affect the meshing process, which is advantageous. However, the technique assumes the reinforcements within composite to be homogeneously distributed over an element.

If complicated reinforcement architectures are to be implemented, both the embedded and discrete technique require more elements or special elements to sustain the simulation. Both methods result in an increase in computation cost. In the case of the distributed technique, the complicated reinforcement geometry only requires appropriate material constants or components of the stiffness matrix of the elements modelling the composite. This is easy to implement and cost effective.

Finally, the embedded and discrete models do not satisfy equilibrium condition for the entire composite. In the embedded technique, equilibrium of the matrix element is satisfied only. To obtain the correct applied force in the composite, post-processing of the constituent stress using the rule of mixtures or by changing the mesh geometry to represent the volume of matrix has to be adopted. In the discrete technique, equilibrium is not satisfied when the one-dimensional reinforcements are transverse to the loading direction. To obtain the stress of the composite post-processing is involved. In the

distributed model, the geometry of the mesh represents the whole composite and equilibrium is satisfied for all reinforcement orientations. However, a problem with the model is that the forces and stresses of the composite constituents had to be obtained by post-processing with a specially written procedure.

6.5 Conclusion

A comparative study of three finite element modelling techniques was conducted to assess their suitability for modelling high fibre volume fraction composites. In meeting the criteria listed in Sect. 6.1, the distributed reinforcement technique was preferred over the embedded and discrete reinforcement technique. The technique satisfies both the equilibrium and compatibility conditions of the composite, and, allows an efficient representation of composite constituents architecture, orientation and damage. The distributed reinforcement technique is therefore selected as the basis for development of a micromechanics-based continuum damage mechanics model for numerical modelling brittle matrix composites.

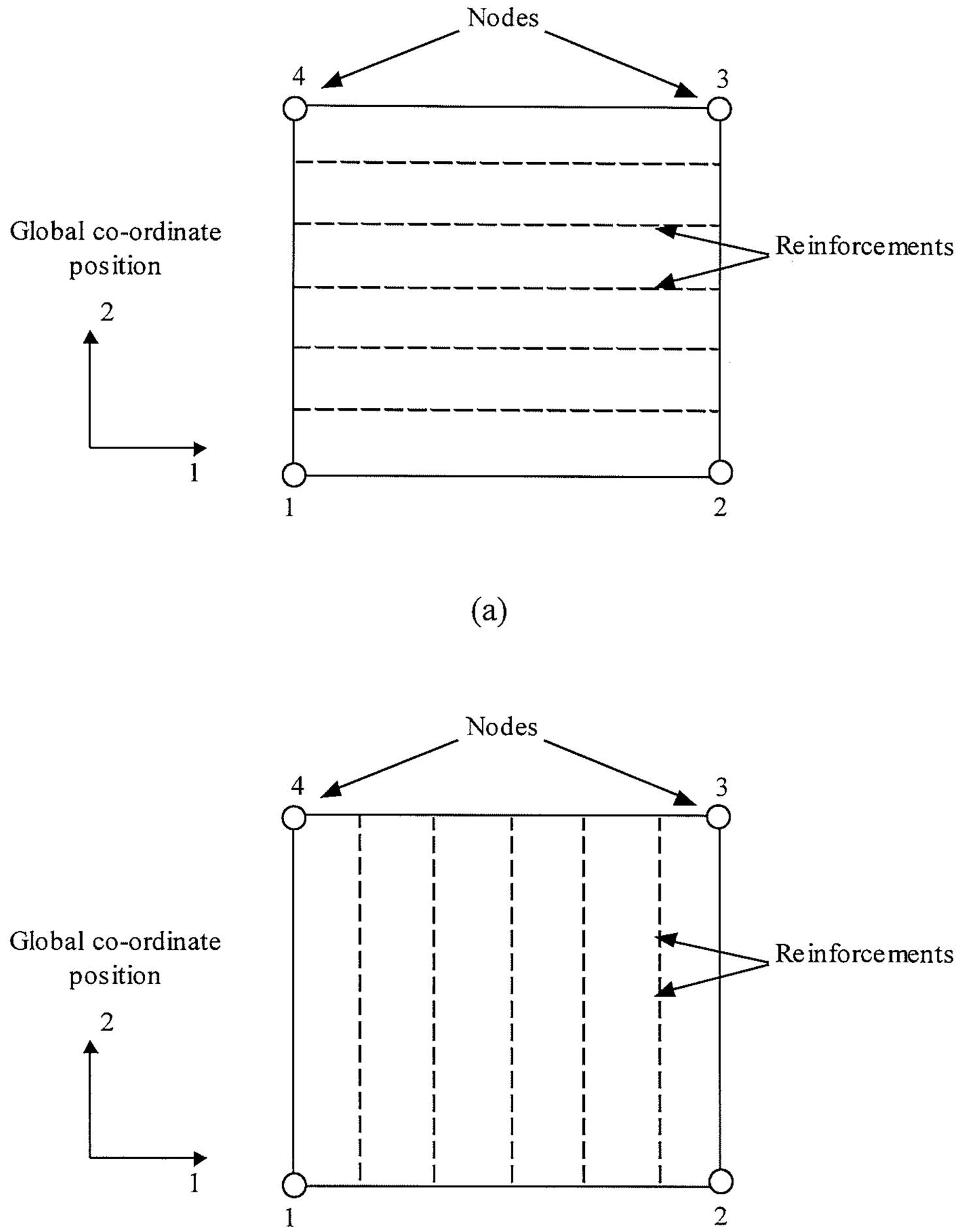

(a)

(b)

Fig. 6.2-1 Schematic diagrams of the benchmark studies for (a) cases 1, 2 & 3, and (b) case 4.

CHAPTER 7

A Damage Mechanics Approach to Model Deformation and Failure of Brittle Matrix Composites

7.1 Introduction

Computational models of the deformation of brittle matrix composite materials require the ability to deal with general stress states and anisotropy. The anisotropy is primarily caused by fibre architecture, modulus mismatch between the fibres and matrix, and damage. McCafferty (1994) developed a computational model that allowed the mechanical behaviour of the fibre and matrix to be modelled explicitly. This is an attractive approach since it allows a comprehensive description of factors such as fibre architecture and damage. The undamaged matrix was modelled using isotropic two-dimensional continuum elements, while the fibres were modelled separately using embedded one-dimensional line elements. However, this approach has limitations. First, damage was limited to matrix cracking and delamination could not be considered. Second, the full equilibrium conditions of the composite were not properly accounted for, as discussed in Chapter 6. The force in the embedded line element was a function of the displacements in the matrix element, as such the force in the line element was not equilibrated with adjacent elements.

In this chapter, a computational damage model, which overcomes the limitations faced by McCafferty (1994) is presented. The computational model is developed using a micromechanics-based continuum damage mechanics approach to model deformation and failure. It is under-pinned by the micromechanics theory of Aveston, Copper and Kelly (1971), which allows mechanical behaviour of a composite to be modelled through the tangent-stiffness of its constituents obtained from monotonic experiments. The advantages are that the approach is able to model damages such as matrix cracking, delamination and fibre failure as well as fibre architecture, and satisfies equilibrium. The approach is unlike classical continuum damage mechanics theory reviewed in Sect 2.5, which requires a formal thermo-mechanical analysis of a state potential with associated state variables. However, both approaches are similar in that the tensor nature

of damage in a composite is recognised and the evolution of damage is modelled. Despite the differences, the need to segregate the current proposed micromechanics-based continuum damage mechanics approach from classical continuum damage mechanics approach is considered to be philosophical. Hence, attempts to discriminate in the current thesis are considered unnecessary and are avoided.

The computational damage model was implemented through FORTRAN algorithms in the *user-defined material* (UMAT) subroutine of the finite element solver ABAQUS/STANDARD (Hibbitt, Karlsson & Sorenson, 1998a), hereafter ABAQUS. The following sections briefly describe the subroutine UMAT and the constitutive and strength theories for modelling the deformation of composites with one- and two-dimensional reinforcements. To limit the scope, only plane stress conditions are considered. For two-dimensional reinforcements the fibre directions are orthogonal, although it would not be difficult to include non-orthogonal fibre architectures.

7.2 Nomenclature and Position Systems

A nomenclature table is given at the start of the thesis, but is usefully summarised here:

Symbols

σ	- stress
ε	- strain
S	- compliance
C	- stiffness
E	- Young's modulus
G	- shear modulus
ν	- Poisson's ratio
T	- transformation
D	- an increment of
V	- volume fraction
A	- area fraction
$\{\ \}$	- 3 x 1 vector
$[\ ]$	- 3 x 3 matrix
$\|\ \|$	- magnitude of

Subscripts

c	- composite
f	- fibre
m	- matrix
mc	- matrix cracking
mc(sat)	- matrix crack saturation
ms	- matrix softening
td	- tensile delamination
sd	- shear delamination
u	- ultimate failure

Superscripts

n	- current increment
n-1	- previous increment
c	- composite position system
f	- fibre position system
m	- matrix principal stress position system

A contracted tensor notation described in Chapter 2 is used with a labelling system, which is shown below:

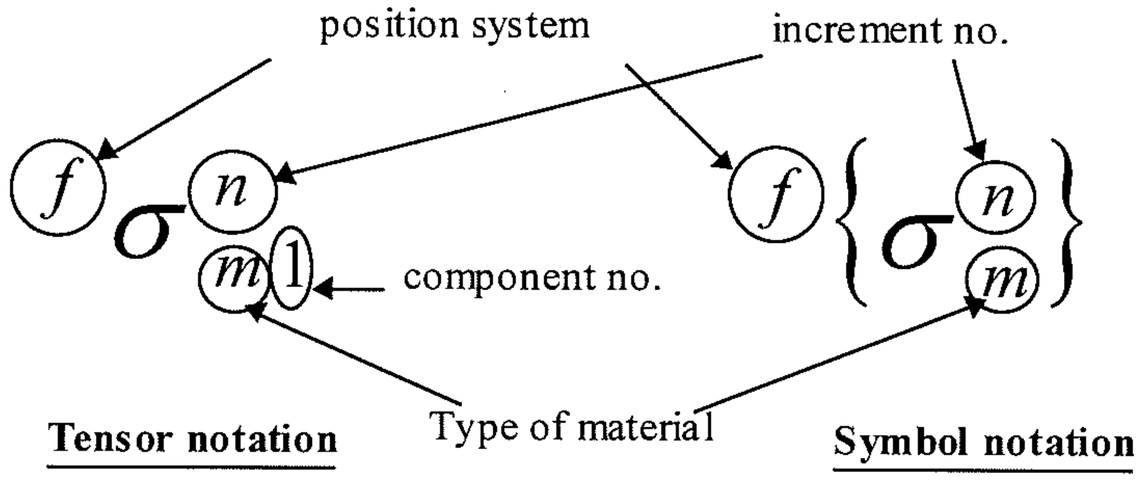

Three Cartesian position systems were used: the composite system is denoted with the superscript, *c*, the fibre system is denoted with the superscript, *f,* and the matrix-principal-stress system is denoted with the superscript, *m*. A schematic diagram of the position systems is shown in Fig 7.2-1. The composite position system defines the axes in which the UMAT subroutine interacts with ABAQUS and is identical to the global co-ordinate system of the finite element analysis. The interaction between the UMAT subroutine and ABAQUS is explained in sect. 7.3. The fibre position system implements the constitutive relations of the fibres and the constitutive relations of the matrix after delamination has initiated. For one-dimensional reinforcements, the 1-direction defined the fibre reinforcement direction (fibre axis) while the 2-direction is normal to the fibre axis. For composites with two-dimensional reinforcements, the 1- and 2-directions define the fibre axes of the first and second set of fibres. The matrix-principal-stress position system was used to define the mechanical properties of the matrix during matrix cracking.

7.3 The User-Defined Material Subroutine (UMAT)

The UMAT subroutine is a computational interface to ABAQUS, which allows mechanical constitutive models to be implemented. Its primary functions are to update the stress and solution-dependent state variables to their values at the end of each increment, and, to define the incremental stiffness matrix in the composite position system. To compute the stress and solution-dependent state variables, the incremental strain in the composite position system in each new increment *n* is provided by ABAQUS. Symbolically, the composite stress at the end of each increment is:

$$ {}^{c}\{\sigma_c^n\} = {}^{c}\{\sigma_c^{n-1}\} + {}^{c}\{d\sigma_c^n\} \qquad (7.3.1) $$

where

$$ {}^{c}\{d\sigma_c^n\} = {}^{c}[dC_c^n]\,{}^{c}\{d\varepsilon_c^n\} \qquad (7.3.2) $$

Here ${}^{c}\{\sigma_c^n\}$ and ${}^{c}\{\sigma_c^{n-1}\}$ denote the composite stress defined in the composite position system for the current increment *n* and in the previous increment *n-1*. The terms ${}^{c}\{d\sigma_c^n\}$ and ${}^{c}\{d\varepsilon_c^n\}$ denote the incremental stress and incremental strain of the composite in the composite position system for the current increment *n*. The incremental stiffness of the composite ${}^{c}[dC_c^n]$ can also be expressed in terms of an incremental compliance:

$$ {}^{c}[dC_c^n] = {}^{c}[dS_c^n]^{-1} \tag{7.3.3} $$

Substituting into eqn (7.3.2), the stress at the end of each increment becomes:

$$ {}^{c}\{\sigma_c^n\} = {}^{c}\{\sigma_c^{n-1}\} + {}^{c}[dS_c^n]^{-1}\ {}^{c}\{d\varepsilon_c^n\} \tag{7.3.4} $$

7.4 The Damage Model

7.4.1 General

The model is based on a micro-mechanics damage approach, which allows a mechanistic description of the composite behaviour through the undamaged and damaged properties of its constituents. The following simplifying assumptions are used to develop the model:

1. Firstly, the fibres and micro-cracked or delaminated matrix are regarded as a continua, so that discrete cracks and fibres are not represented. Their contribution to the behaviour of the composite is modelled in a way which can be sensibly interpreted over size scales large compared to the fibre or micro-crack spacing. Over such distances the average strain in the fibres, matrix and composite are identical.
2. The fibres are assumed to be weakly bonded to the matrix. This is a good assumption for ceramic composites, which are deliberately designed to have weak fibre-matrix interfaces. As a result fibres do not contribute significantly to the stiffness normal to the fibre axis, and their main role is to transmit axial loads.
3. Before damage, the matrix is assumed to be isotropic linear elastic while the fibres are one-dimensionally elastic along the fibre axis and the Poisson's ratio of the matrix, fibre and composite are identical.

4. Micro-cracking of the matrix is assumed to occur normal to the maximum principal stress direction in the matrix. The orientation of the crack planes is fixed in subsequent deformation, so that the model essentially considers proportional loading.
5. Tensile or shear delamination in the composite is assumed to occur parallel to the fibre axis, at a critical direct or shear stress.

To develop the damage model, elasticity theory is used at an incremental level. The stress-state of the composite before and during damage is defined by eqn (7.3.4) in which the incremental compliance of the composite $\left[dS_c^n\right]$ consists of matrix and fibre terms. In the following sections, the structure and components of the incremental compliance of the matrix and fibres used to model the undamaged and damaged mechanical behaviour is described for plane stress conditions.

7.4.2 Pre-Damage Constitutive Relations

Before damage, the matrix is treated as isotropic elastic while the fibre is one-dimensionally elastic. The incremental stiffness of the composite in the composite position system is given as:

$$^{c}\left[dS_c^n\right]^{-1} = \left[S_m\right]^{-1} + \left[T_\sigma\right]^{-1}\ {}^{f}\left[dS_f^n\right]^{-1}\left[T_\varepsilon\right] \qquad (7.4.2.1)$$

Here, $\left[S_m\right]$ is the isotropic elastic compliance of the volume fraction of matrix:

$$\left[S_m\right] = \begin{bmatrix} \frac{1}{E_m V_m} & \frac{-\nu}{E_m V_m} & 0 \\ \frac{-\nu}{E_m V_m} & \frac{1}{E_m V_m} & 0 \\ 0 & 0 & \frac{1}{G_m V_m} \end{bmatrix} \qquad (7.4.2.2)$$

in which the shear modulus of the matrix G_m is defined as:

$$G_m = \frac{E_m}{2(1+\nu)} \qquad (7.4.2.3)$$

The symbols E_m and V_m denote the Young's modulus and volume fraction of the matrix, and the symbol ν denotes Poisson ratio of the matrix.

The symbol ${}^{f}\left[dS_f^n\right]$ denotes the incremental compliance of the fibres in the fibre position system. For one-dimensional fibre reinforcement,

$$ {}^{f}\left[dS_f^n\right] = \begin{bmatrix} \frac{1}{E_f V_f} & 0 & 0 \\ 0 & 0 & 0 \\ 0 & 0 & 0 \end{bmatrix} \qquad (7.4.2.4) $$

for two-dimensional fibre reinforcements,

$$ {}^{f}\left[dS_f^n\right] = \begin{bmatrix} \frac{1}{E_{f1} A_{f1}} & 0 & 0 \\ 0 & \frac{1}{E_{f2} A_{f2}} & 0 \\ 0 & 0 & 0 \end{bmatrix} \qquad (7.4.2.5) $$

and

$$ A_{f1} + A_{f2} = V_f \qquad (7.4.2.6) $$

in which E_{f1} & E_{f2} are the tangent modulii and A_{f1} & A_{f2} are the area fractions of the fibres in the 1- and 2-directions of the fibre position system. Eqns (7.3.2.4 & 5) indicate that the fibres are assumed to make negligible contributions to the shear and transverse deformation of the composite in the fibre position system. This simplification can be relaxed if transverse stiffness terms are available.

The terms $\left[T_\sigma\right]$ and $\left[T_\varepsilon\right]$ denote the transformation matrix for stresses and engineering strains in fibre position system with respect to the composite position system. For plane stress condition,

$$ \left[T_\sigma\right] = \begin{bmatrix} l_{11}^2 & l_{12}^2 & 2\,l_{11}l_{21} \\ l_{21}^2 & l_{22}^2 & 2\,l_{22}l_{12} \\ l_{11}l_{12} & l_{21}l_{22} & l_{11}l_{22} + l_{21}l_{12} \end{bmatrix} \qquad (7.4.2.7) $$

following eqn (2.4.15), and

$$ \left[T_\varepsilon\right] = \begin{bmatrix} l_{11}^2 & l_{12}^2 & l_{11}l_{12} \\ l_{21}^2 & l_{22}^2 & l_{22}l_{21} \\ 2l_{11}l_{21} & 2l_{12}l_{22} & l_{11}l_{22} + l_{12}l_{21} \end{bmatrix} \qquad (7.4.2.8) $$

following eqn (2.4.16), while l_{ij} is the direction cosine of the fibre position system with respect to the composite position system which is defined as:

$$l_{ij} = \begin{pmatrix} l_{11} & l_{12} & l_{13} \\ l_{21} & l_{22} & l_{23} \\ l_{31} & l_{32} & l_{33} \end{pmatrix} = \begin{pmatrix} \cos\alpha & \sin\alpha & 0 \\ -\sin\alpha & \cos\alpha & 0 \\ 0 & 0 & 1 \end{pmatrix} \qquad (7.4.2.9)$$

Here, α denotes the fibre alignment angle.

7.4.3 Damage Criteria

Maximum stress theory is used to model the initiation of matrix cracking and delamination. The damage criteria are defined with respect to the current increment *n*.

Matrix cracking is assumed to initiate when

$$\frac{{}^{m}\sigma_{m(\max)}}{\sigma_{mc}} \geq 1 \qquad (7.4.3.1)$$

Here, σ_{mc} denotes the critical matrix cracking stress while ${}^{m}\sigma_{m(\max)}$ denotes the maximum principal stress in the matrix. The principal stress position system at which matrix cracking first initiated is fixed to model the subsequent constitutive response of the cracked matrix. Matrix cracking thus is allowed to occur on two orthogonal planes, which are not permitted to rotate after matrix cracking has initiated. In addition, the ultimate failure of the composite is modelled when the fibres failed, i.e.

$$\frac{{}^{f}\sigma_{f1}}{\sigma_{f}(\varepsilon_{cu})} \geq 1 \qquad \text{or} \qquad \frac{{}^{f}\sigma_{f2}}{\sigma_{f}(\varepsilon_{cu})} \geq 1 \qquad (7.4.3.2)$$

Here, ${}^{f}\sigma_{f1}$ and ${}^{f}\sigma_{f2}$ are the direct stress component of the fibres in the fibre position system while $\sigma_{f}(\varepsilon_{cu})$ denotes the average stress in the fibres at the failure strain of the composite when tensioned parallel to the fibre axis.

Maximum stress theory (Hull & Clyne, 1996) incorporates two delamination modes: tensile and shear delamination. The normal to the failure plane in both modes is normal to the fibre axis. The theory agrees well with the delamination experiments reported in Sect. 4.4. However, the correlation for shear delamination is not simple. The experiments showed that shear delamination occurred concurrently with matrix cracking, so that a range of potential failure planes form at the same time. Because the mechanics of damage interaction are not fully understood, the criteria for modelling cannot be implemented at this time. Although maximum stress theory for shear delamination may be a simplification of the experimental observations, the need to

develop a tractable computational procedure advocates its use. As such, maximum stress theory is used to model both tensile and shear delamination. Because the fibres do not contribute to the shear and transverse deformation of the elements, tensile delamination is modelled when

$$\frac{{}^{f}\sigma_{m2}}{\sigma_{td}} \geq 1 \qquad (7.4.3.3)$$

and shear delamination occurs when

$$\frac{{}^{f}\left|\tau_{m12}\right|}{\left|\tau_{sd}\right|} \geq 1 \qquad (7.4.3.4)$$

Here, the symbols σ_{td} and ${}^{f}\sigma_{m2}$ denote the tensile delamination strength of the composite and the transverse stress component of matrix in the fibre position system. The symbols $|\tau_{sd}|$ and ${}^{f}|\tau_{m12}|$ denote the magnitude of the shear strength of the composite and the magnitude of the matrix shear stress in the fibre position system. When delamination initiates, constitutive modelling of the matrix was implemented using the fibre position system.

To simplify the computational procedures, each integration point in the composite elements can exhibit either matrix cracking or tensile or shear delamination. Thus, simultaneous occurrences of different damages at the same integration point are not permitted. However, since each composite element comprises several integration points, it implies that the modelling procedure allows different damages to be modelled in a single composite element.

7.4.4 Constitutive Relations Incorporating Damage

7.4.4.1 Matrix cracking and Fibre failure

During matrix cracking, the incremental stiffness of the composite in the composite position system is given as:

$${}^{c}\left[dS_{c}^{n}\right]^{-1} = \left[P_{\sigma}\right]^{-1}\,{}^{m}\left[dS_{m}^{n}\right]^{-1}\left[P_{\varepsilon}\right] + \left[T_{\sigma}\right]^{-1}\,{}^{f}\left[dS_{f}^{n}\right]^{-1}\left[T_{\varepsilon}\right] \qquad (7.4.4.1.1)$$

Here, $[P_{\sigma}]$ and $[P_{\varepsilon}]$ denotes the transformation matrix of the matrix stresses and strains in the matrix position system with respect to the composite position system. Explicitly,

$$[P_\sigma] = \begin{bmatrix} b_{11}^2 & b_{12}^2 & 2\,b_{11}b_{21} \\ b_{21}^2 & b_{22}^2 & 2\,b_{22}b_{12} \\ b_{11}b_{12} & b_{21}b_{22} & b_{11}b_{22}+b_{21}b_{12} \end{bmatrix} \qquad (7.4.4.1.2)$$

following eqn (2.4.15), and

$$[P_\varepsilon] = \begin{bmatrix} b_{11}^2 & b_{12}^2 & b_{11}b_{12} \\ b_{21}^2 & b_{22}^2 & b_{22}b_{21} \\ 2b_{11}b_{21} & 2b_{12}b_{22} & b_{11}b_{22}+b_{12}b_{21} \end{bmatrix} \qquad (7.4.4.1.3)$$

following eqn (2.4.14). The symbol b_{ij} denotes the direction cosine of the matrix stress in the matrix position system with respect to the composite position system and is defined as:

$$b_{ij} = \begin{pmatrix} b_{11} & b_{12} & b_{13} \\ b_{21} & b_{22} & b_{23} \\ b_{31} & b_{32} & b_{33} \end{pmatrix} = \begin{pmatrix} \cos\theta & \sin\theta & 0 \\ -\sin\theta & \cos\theta & 0 \\ 0 & 0 & 1 \end{pmatrix} \qquad (7.4.4.1.4)$$

where θ denotes the maximum principal stress direction in the matrix before cracking initiated.

The symbol ${}^{m}\left[dS_{m}^{n}\right]$ denotes the incremental compliance of the cracked matrix defined in the matrix position system and its components are dependent on the effective stress-strain response of the cracked matrix. For brittle matrix composites in tension parallel to the fibres, the effective response of the cracked matrix can be derived from ACK theory. At any applied strain state, the effective stress in the cracked matrix can be obtained by subtracting the stress of the volume fraction of fibres from the composite stress, and dividing the resultant stress with the matrix volume fraction, i.e.

$$\sigma_m = \frac{\sigma_c - \sigma_f V_f}{V_m} \quad \text{if} \quad \left(\varepsilon_c = \varepsilon_m = \varepsilon_f = \varepsilon\right) \qquad (7.4.4.1.5)$$

Here, ε_c, ε_m and ε_f denote the strain components in the composite, matrix and fibres parallel to the loading direction and ε is the applied strain. Eqn (7.4.4.1.5) allows the effective tangent modulii of the cracked matrix which is a function of the applied strain to be obtained from experimental data.

The effective stress-strain response of the cracked matrix is shown schematically in Fig 7.4.4.1-1 to consist of hardening and softening regions. The hardening region describes the effective behaviour of the matrix from the onset of matrix microcracks to the initiation of steady-state matrix cracking, which is the maximum effective stress in

the matrix. The softening region models steady-state matrix cracking through cracking saturation and fibre failure. After which, the matrix response is unloaded exponentially.

During matrix cracking, ACK, Prewo (1986) and McCafferty (1994) have shown the tensile response of brittle matrix composites is inelastic when cyclically loaded in the fibre direction. This is due to frictional sliding at the fibre-matrix interface during matrix crack opening, crack closure and crack re-opening (Evans & Marshall, 1989). In the current damage model, the frictional effects during crack-opening (I), crack-closure (II) and crack-reopening (III) modes of deformation are modelled in both the hardening and softening regions of the damage matrix response by treating the matrix as an elastic-damaged material. The incremental compliance of the cracked matrix is assumed transversely-isotropic in the matrix position system and modifications to the effective engineering constants allow the components of the incremental compliance in the different deformation modes to be represented. The case where the matrix crack plane is normal to the 1-direction of the matrix position system is now described. During crack opening (mode I), the incremental compliance of the cracked matrix is given as:

$$ {}^{m}\left[dS_{m}\right] = \begin{bmatrix} \frac{1}{E_{mc}} & \frac{\nu_{mc}}{E_{mc}} & 0 \\ \frac{\nu_{mc}}{E_{mc}} & \frac{1}{V_{m}E_{m}} & 0 \\ 0 & 0 & \frac{1}{\beta V_{m}G_{m}} \end{bmatrix} \qquad (7.4.4.1.6) $$

Here, E_{mc} denotes the effective tangent modulii of the volume fraction of matrix derived from experiments (see eqn (7.4.4.1.5)). Experiments on one- and two-dimensional polyester composites conducted in Chapter 4 observed that the matrix strain parallel to the crack plane is relaxed during matrix cracking. To model this relaxation, a damaged Poisson's ratio term ν_{mc} was introduced which smoothly decays the isotropic undamaged Poisson ratio value ν of the matrix to zero:

$$ \nu_{mc} = \nu - \left[(0.37\nu - 0.001)\exp\left(1 - \frac{a}{\left({}^{m}\varepsilon_{m1}\right)^{2}}\right)\right] \qquad (7.4.4.1.7) $$

Here, ${}^{m}\varepsilon_{m1}$ denotes the matrix strain component normal to the crack plane and a is a constant. Poisson's ratio for the cracked matrix ν_{mc} is given as a function of different initial Poisson's ratios ν as a function of the matrix strain component ${}^{m}\varepsilon_{m1}$ in Fig

7.4.4.1-2. To improve numerical stability, a constant β of a magnitude of 1.0E-6 is introduced to eliminate the matrix shear modulus G_m. This circumvents 'shear locking' of the composite element during plane stress in-plane bending.

To model crack opening (mode I) and reopening (mode III) the incremental matrix strain normal to the crack plane must be positive while for crack closure (mode II) the incremental strain normal to the crack plane must be negative. The incremental compliance of the matrix during crack closure and crack reopening (modes II & III) is defined as:

$$ {}^{m}\left[dS_m\right] = \begin{bmatrix} \frac{1}{E_{\sec}} & \frac{\nu_{mc}}{E_{\sec}} & 0 \\ \frac{\nu_{mc}}{E_{\sec}} & \frac{1}{V_m E_m} & 0 \\ 0 & 0 & \frac{1}{\beta V_m G_m} \end{bmatrix} \qquad (7.4.4.1.8) $$

where E_{sec} is the secant modulus of the matrix with respect to the origin.

During matrix cracking, it is assumed that the fibres remain elastic and the incremental compliance of the fibres is defined either by eqn (7.4.2.4 or 5). However when the fibres start to break, the fibres unload and eqn (7.4.2.4 & 5) are invalid. For one-dimensional fibre reinforcement, the incremental compliance of the fibres in the fibre position system during unloading is:

$$ {}^{f}\left[dS''_f\right] = \begin{bmatrix} \frac{1}{E_{fu}} & 0 & 0 \\ 0 & 0 & 0 \\ 0 & 0 & 0 \end{bmatrix} \qquad (7.4.4.1.9) $$

and for two-dimensional fibre reinforcements,

$$ {}^{f}\left[dS''_f\right] = \begin{bmatrix} \frac{1}{E_{fu}} & 0 & 0 \\ 0 & \frac{1}{E_{f2}A_{f2}} & 0 \\ 0 & 0 & 0 \end{bmatrix} \qquad (7.4.4.1.10) $$

when fibre failure occurred in the fibre 1-direction. The symbol E_{fu} denotes the effective modulus of the failed fibres which decays to zero by an expression of the form:

$$E_{fu} = -a^{f}\left|\sigma_{f1}^{n-1}\right| \exp\left(-b^{f}\left|\varepsilon_{f1}^{n-1}\right|^{-c}\right) \qquad (7.4.4.1.11)$$

Here, a, b and c are curve fitting constants while ${}^{f}\left|\sigma_{f1}^{n-1}\right|$ and ${}^{f}\left|\varepsilon_{f1}^{n-1}\right|$ are the stress and strain magnitudes of the volume fraction of fibres in the 1-direction of the fibre position system from the previous increment n-1. Concurrently, the modulus of the cracked matrix E_{mc} in eqn (7.4.4.1.6) during fibre unloading is modelled as:

$$E_{mc} = -a^{m}\left|\sigma_{m1}^{n-1}\right| \exp\left(-b^{m}\left|\varepsilon_{m1}^{n-1}\right|^{-c}\right) \qquad (7.4.4.1.12)$$

in which ${}^{m}\left|\sigma_{m1}^{n-1}\right|$ and ${}^{m}\left|\varepsilon_{m1}^{n-1}\right|$ denotes the matrix stress and strain magnitudes in the 1-direction of the matrix position system from the previous increment n-1.

7.4.4.2 Tensile delamination

During tensile delamination, the damage response of the composite is modelled through the effective properties of the matrix as the fibres are assumed to be one-dimensional. The matrix is transversely-isotropic in the fibre position system while the fibres remain one-dimensionally non-linear elastic. The corresponding effective stress-strain response of the matrix in the 2-direction of the fibre position system during tensile delamination is shown in Fig 7.4.4.2-1. As with matrix cracking, three modes of tensile delamination are allowed: crack-opening (I), crack-closure (II) and crack-reopening (III).

Crack-opening (I) is modelled using the incremental matrix compliance:

$${}^{f}\left[dS_{m}^{n}\right] = \begin{bmatrix} \frac{1}{E_m V_m} & \frac{\nu_{td}}{E_m V_m} & 0 \\ \frac{\nu_{td}}{E_m V_m} & \frac{1}{E_{td}} & 0 \\ 0 & 0 & \frac{1}{G_{td} V_m} \end{bmatrix} \qquad (7.4.4.2.1)$$

where E_{td} denotes the effective incremental modulus of the volume fraction of the matrix during tensile delamination. The transition from an undamaged composite to full delamination is modelled by an exponential decay curve such that:

$$E_{td} = -a^{f}\left|\sigma_{m2}^{n-1}\right| \exp\left(-b^{f}\left|\varepsilon_{m2}^{n-1}\right|^{-c}\right) \qquad (7.4.4.2.2)$$

in which ${}^{f}\left|\sigma_{m2}^{n-1}\right|$ and ${}^{f}\left|\varepsilon_{m2}^{n-1}\right|$ are the matrix stress and strain magnitudes in the 2-direction of the fibre position system from the previous increment n-1, and a, b, c are constants. Poisson's ratio during tensile delamination ν_{td} is modelled as:

$$\nu_{td} = -\nu \left|\frac{E_{td}}{E_m}\right| \qquad (7.4.4.2.3)$$

while the matrix shear modulus is modelled as:

$$G_{td} = \frac{E_m}{2\left(1+\nu_{td}\right)} \qquad (7.4.4.2.4)$$

Modelling crack opening (mode I) requires that the matrix incremental strain normal to the delamination plane is positive.

During crack closure and crack reopening (modes II & III), the incremental compliance of the matrix is defined as:

$${}^{f}\left[dS_m^n\right] = \begin{bmatrix} \frac{1}{E_m V_m} & \frac{-\nu_{td}^{n-1}}{E_m V_m} & 0 \\ \frac{-\nu_{td}^{n-1}}{E_m V_m} & \frac{1}{E_{\text{sec}}} & 0 \\ 0 & 0 & \frac{1}{G_{td} V_m} \end{bmatrix} \qquad (7.4.4.2.5)$$

Here, ν_{td}^{n-1} denotes the matrix Poisson's ratio during tensile delamination in the previous increment. Crack closure (II) is modelled when matrix strain increment normal to the delamination plane is negative while a positive incremental strain models crack reopening (III). During crack reopening (III), deformation of the matrix is modelled by eqn. (7.4.4.2.1) when the matrix stress exceeds the stress at which crack closure initiates.

The incremental stiffness of the composite in the composite position system is given as:

$${}^{c}\left[dS_c^n\right]^{-1} = \left[T_\sigma\right]^{-1} {}^{f}\left[dS_m^n\right]^{-1} \left[T_\varepsilon\right] + \left[T_\sigma\right]^{-1} {}^{f}\left[dS_f^n\right]^{-1} \left[T_\varepsilon\right] \qquad (7.4.4.2.6)$$

7.4.4.3 Shear delamination

During shear delamination, the damage response of the composite is also modelled by the effective properties of the matrix and the incremental stiffness of the composite in the composite position system is given by eqn (7.4.4.2.6). The effective

shear stress-strain response during shear delamination in the fibre position system is shown in Fig 7.4.4.3-1. Shear delamination can occur in both positive and negative shear stress-strain spaces. In each of these regions, the shear delamination plane can exhibit open (I), closed (II) and re-opening (III) modes of deformation.

In either polarity, mode I in the matrix was modelled when the magnitude of the incremental shear strain was greater than zero. The incremental compliance of the volume fraction of matrix was modelled as:

$$ {}^{f}\left[dS_m\right] = \begin{bmatrix} \frac{1}{E_{sd}} & \frac{-\nu}{E_{sd}} & 0 \\ \frac{-\nu}{E_{sd}} & \frac{1}{E_m V_m} & 0 \\ 0 & 0 & \frac{1}{G_{sd} V_m} \end{bmatrix} \qquad (7.4.4.3.1) $$

in which G_{sd}, the effective incremental shear modulus of the delaminated matrix, was allowed to decay from the undamaged to the fully delaminated state by a relation of the form:

$$ G_{sd} = -a \; {}^{f}\left|\tau_{m12}^{n-1}\right| \exp\left(-b \; {}^{f}\left|\gamma_{m12}^{n-1}\right|^{-c}\right) \qquad (7.4.4.3.2) $$

Here, ${}^{f}\left|\tau_{m12}^{n-1}\right|$ and ${}^{f}\left|\gamma_{m12}^{n-1}\right|$ are the shear stress and shear strain magnitudes of the matrix in the fibre 12-plane in the previous increment, and, a, b, c are constants. The tangent modulus of the matrix in the fibre axis E_{sd} was modelled by:

$$ E_{sd} = E_m V_m \left[2(1+\nu)^2\right] \qquad (7.4.4.3.3) $$

This procedure ensured numerical convergence.

To model both mode II and mode III, the matrix incremental compliance was defined by:

$$ {}^{f}\left[dS_m\right] = \begin{bmatrix} \frac{1}{E_{sd}} & \frac{-\nu}{E_{sd}} & 0 \\ \frac{-\nu}{E_{sd}} & \frac{1}{E_m V_m} & 0 \\ 0 & 0 & \frac{1}{G_{\text{sec}}} \end{bmatrix} \qquad (7.4.4.3.4) $$

where G_{sec} denotes the matrix secant shear modulus. The criteria for modelling mode II in the positive stress & positive strain space were:

$$\left({}^{f}\gamma_{m12} > 0\right) \text{ and } \left(d^{f}\gamma_{m12} < 0\right) \qquad (7.4.4.3.5)$$

while the criteria for modelling in the negative stress & negative strain space were:

$$\left({}^{f}\gamma_{m12} < 0\right) \text{ and } \left(d^{f}\gamma_{m12} > 0\right) \qquad (7.4.4.3.6)$$

The criteria for modelling mode III in the positive stress & positive strain space were:

$$\left({}^{f}\gamma_{m12} > 0\right), \ \left(\left|{}^{f}\gamma_{m12}\right| > \left|\gamma_{m(\mathrm{II})}\right|\right) \text{ and } \left(d^{f}\gamma_{m12} > 0\right) \qquad (7.4.4.3.7)$$

while the criteria for modelling in the negative stress & negative strain space were:

$$\left({}^{f}\gamma_{m12} < 0\right), \ \left(\left|{}^{f}\gamma_{m12}\right| > \left|\gamma_{m(\mathrm{II})}\right|\right) \text{ and } \left(d^{f}\gamma_{m12} < 0\right) \qquad (7.4.4.3.8)$$

Here, $\left|{}^{f}\gamma_{m(\mathrm{II})}\right|$ is the magnitude of the shear strain at which closure initiated.

7.5 The Computation Algorithm

7.5.1 Overview

The computation algorithms of the damage model implemented in the subroutine UMAT were developed using FORTRAN77 (Ellis, 1993). A generalised flow chart of the damage model is shown schematically in Fig 7.5.1-1. Essentially, it consists of the subroutine UMAT, which initialises the local material variables and the state-dependent variables, and checks the damage analysis required. If a matrix cracking analysis is required only the subroutine KDMC is activate, otherwise the subroutine KDMCDEL is activated to allow matrix cracking or delamination analyses. The options are introduced to allow a comparison of results from different subroutines. In either case, before damage the subroutine KELAS is inherently active by default. During damage, the subroutines KMC or KDEL are made active to perform matrix cracking or delamination analysis through the subroutine KDMCDEL while the subroutine KDMC activates the subroutine KMC to perform only matrix cracking analysis.

The algorithm of the subroutine UMAT is presented schematically in Fig 7.5.1-2. Initially, a logical variable *TEST* with a default value of *FALSE*, and the global common block ABA_INPUT.INC and local common blocks INPUTA.INC, INPUTB.INC, …etc, are defined. The function of the local common blocks is to store the material properties of individual element sets listed in the '*.inp*' file. Through a logic loop of the variable *TEST*, the material data are read by subroutines KPROP3A, KPROP3B, …etc, during

the first incremental analysis and stored into the respective local common blocks INPUTA.INC, INPUTB.INC, …etc. Unlike the local common blocks, the function of the global common block ABA_INPUT.INC is to provide the material data required during the current analysis. To update the global common block ABA_INPUT.INC, the variable CMNAME which contains the material names of the element sets listed in the '*.inp*' file is used in an 'if-loop'. Corresponding to the material names, i.e. *MAT0, MAT1, ...etc*, the respective subroutines KCBA, KCBB, …etc, are activate to perform the corresponding updates. A list of the variables in the local and global common blocks is shown Table 7.5.1-1. After preliminary initialisations, the subroutines KDMCDEL or KDMC are activate depending on the value of the variable *PTYPE*. If *PTYPE* is zero, the subroutine KDMCDEL is activate while a value of one activates the subroutine KDMC. If any other values occur, an error message is written to the ABAQUS *.dat* file and the analysis terminates using the subroutine XIT provided by ABAQUS.

The algorithm of the subroutine KPROP3A, which reads in material data from the element set with a material name *MAT0*, is shown schematically in Fig 7.5.1-3. First, material data are read from two locations: the '*.inp*' file and data files located in a remote directory. The '*.inp*' file passes material data into the subroutine UMAT through the variable *PROPS(NPROPS)*. The material data are listed in Table 7.5.1-2. To simplify presentation, only two element sets are considered. Separately, the effective stress-strain data of the matrix and fibres are stored in remote data files. After reading in the effective stress-strain data, the tangent modulii of the volume fraction of matrix and fibres are evaluated. The effective stress at which matrix tension-softening initiates is determined through the subroutine KMAX and the subroutine KCONVER converts the fibre orientations from degrees to radians. The algorithms of the subroutines KMAX and KCONVER are shown in Fig 7.5.1-4 and 5.

For element sets with the material names *MAT1, MAT2, ...etc*, the subroutines KPROP3B, KPROP3C, …etc, are used to update the local common blocks INPUTB.INC, INPUTC.INC, …etc. In general, the structure of the subroutines KPROP3B, KPROP3C, …etc, are similar to KPROP3A. However, instead of using the local common block INPUTA.INC and having the letter '*A*' precede every local variable, the local common blocks INPUTB.INC, INPUTC.INC, …etc. are use and the local variables that are preceded with letters *B, C, ...etc*. An example is shown in Table 7.5.1-1 & 2.

The algorithm of the subroutine KCBA, which updates the global common block, is shown schematically in Fig 7.5.1-6. In general, the structure of the subroutine KCBA is similar with the subroutines KCBB, KCBC, …etc. The exceptions are that the local common block and local variable must be replaced with the one in use. Finally, the algorithm of the subroutines KDMCDEL and KDMC, which permits matrix cracking or delamination analysis and only matrix cracking analysis are shown schematically in Fig 7.5.1-7 & 8.

Before presenting the algorithm of the subroutine KELAS, KMC and KDEL, it is appropriate here to introduce the state dependent variables *STATEV(NSTATV)* which must be updated at every analysis. In Table 7.5.1-3, a list of the state-dependent variables are presented and briefly described.

CMNAME	NPROPS	Variables	CMNAME	NPROPS	Variables
MAT0	1	APOIS	MAT1	25	BPOIS
	2	ASSD		26	BSSD
	3	ASTD2		27	BSTD2
	4	ANDATAM		29	BNDATAM
	5	AGCONST		30	BGCONST
	6	ANOF		31	BNOF
	7	AANG1		32	BANG1
	8	AVF1		33	BVF1
	9	AAF1		34	BAF1
	10	ANDATAF1		35	BNDATAF1
	11	AANG2		36	BANG2
	12	AVF2		37	BVF2
	13	AAF2		38	BAF2
	14	ANDATAF2		39	BNDATAF2
	15	APTYPE		40	BPTYPE
	16	AFIB		41	BFIB
	17	ASMC1		42	BSMC1
	18-24	*Unused*		43-48	*Unused*

Table 7.5.1-2 The data PROPS(NPROPS) supplied from the *.inp* file into the subroutine UMAT.

Global Common Block	Local Common Block		Description
ABA_INPUT.INC	**INPUTA.INC**	**INPUTB.INC**	
ANG1	AANG1	BANG1	Angle (Deg. units) between the composite 1-dir and the fibre 1-dir.
ANG2	AANG2	BANG2	Angle (Deg. units) between the composite 2 dir and the fibre 2 dir.
POIS	APOIS	BPOIS	Poisson's ratio ν
SMC1	ASMC1	BSMC1	Matrix cracking initiation stress.
SMC2	ASMC2	BSMC2	Effect stress in vol. fraction of matrix when softening initiates.
SMC3	ASMC3	BSMC3	Effective stress in vol. fraction of matrix when fibres fails.
SSD	ASSD	BSSD	Shear delamination stress σ_{sd}
STD2	ASTD2	BSTD2	Tensile delamination stress σ_{td}
VF1	AVF1	BVF1	Vol. fraction of fibres in fibre 1-dir.
VF2	AVF2	BVF2	Vol. fraction of fibres in fibre 2-dir.
VM1	AVM1	BVM1	Vol. fraction of matrix in fibre 1-dir.
VM2	AVM2	BVM2	Vol. fraction of matrix in fibre 2-dir.
NDATAM	ANDATAM	BNDATAM	Number of rows of data in remote file *datam.exp*
NDATAF1	ANDATAF1	BNDATAF1	Number of rows of data in remote file *dataf.exp*
NDATAF2	ANDATAF2	BNDATAF2	Number of rows of data in remote file *dataf.exp*
NMAX	ANMAX	BNMAX	Date row number of remote file *datam.exp* when softening initiates
GCONST	AGCONST	BGCONST	Constant β
PCONST	APCONST	BPCONST	Constant P
AF1	AAF1	BAF1	Area of fibres in the fibre 1 dir.
AF2	AAF2	BAF2	Area of fibres in the fibre 2 dir.
NOF	ANOF	BNOF	Number of fibre reinforcement directions : (1 or 2)
STRESM(34)	ASTRESM(34)	BSTRESM(34)	Effective stress data of matrix.
STRANM(34)	ASTRANM(34)	BSTRANM(34)	Effective strain data of matrix.
EMODM(34)	AEMODM(34)	BEMODM(34)	Effective tangent modulii of matrix.
STRESF1(34)	ASTRESF1(34)	BSTRESF1(34)	Experimental stress data of fibres in fibre 1-dir.
STRESF2(34)	ASTRESF2(34)	BSTRESF2(34)	Experimental stress data of fibres in fibre 2-dir.
STRANF1(34)	ASTRANF1(34)	BSTRANF1(34)	Experimental strain data of fibres in fibre 1-dir.
STRANF2(34)	ASTRANF2(34)	BSTRANF2(34)	Experimental strain data of fibres in fibre 2-dir.
EMODF1(34)	AEMODF1(34)	BEMODF1(34)	Experimental tangent modulii of fibres in fibre 1-dir.
EMODF2(34)	AEMODF2(34)	BEMODF2(34)	Experimental tangent modulii of fibres in fibre 2-dir.
FIB	AFIB	BFIB	Compressive modulus of fibres: 0 => zero modulus 1 => modulus same as in tension
TEST	-	-	Logical variable (default FALSE)
PTYPE	APTYPE	BPTYPE	Compressive modulus of fibres: 0 => zero modulus 1 => modulus same as in tension

Table 7.5.1-1 The variables listed in the global and local common blocks of the subroutine UMAT.

STATEV	Descriptions
1-3	${}^{c}\sigma_{m1}$, ${}^{c}\sigma_{m2}$, ${}^{c}\tau_{m12}$
4-6	${}^{m}\sigma_{m1}$, ${}^{m}\sigma_{m2}$, ${}^{m}\tau_{m12}$
7-9	${}^{f}\sigma_{m1}$, ${}^{f}\sigma_{m2}$, ${}^{f}\tau_{m12}$
10-12	${}^{m}\varepsilon_{1}$, ${}^{m}\varepsilon_{2}$, ${}^{m}\gamma_{12}$
13-15	${}^{f}\varepsilon_{1}$, ${}^{f}\varepsilon_{2}$, ${}^{f}\gamma_{12}$
16-24	The direction cosine when matrix cracking initiated: 16-18 → component (11, 12, 13), 19-21 → component (21, 22, 23), 22-24 → component (31, 32, 33)
25	ε_{mc} - strain at which matrix cracking initiated in the matrix 1-direction.
26	ε_{mc} - strain at which matrix cracking initiated in the matrix 2-direction.
27	ε_{fd} - strain at which tensile delamination initiated in the fibre 2-direction .
28	γ_{sd} - shear strain at which shear delamination initiated in the fibre 12-plane.
29	State of matrix cracking in the matrix 1-direction 0 = no damage, 1=tension stiffening, 2=tension softening, 3=final failure
30	State of matrix cracking in the matrix 2-direction 0 = no damage, 1=tension stiffening, 2=tension softening, 3=final failure
31	*POISM* – matrix Poisson's ratio as a function of strain
32	Material state: 0=Pre-damage, 1=Matrix cracking, 2=Shear Delamination, 3=Tensile Delamination
33	${}^{m}\sigma_{m1}/\sigma_{mc1}$
34	${}^{m}\sigma_{m2}/\sigma_{mc1}$
35	${}^{f}\sigma_{m2}/\sigma_{fd}$
36	$\left\lvert {}^{f}\tau_{m12}/\tau_{sd}\right\rvert$
37	${}^{m}\sigma_{m1}$ at which mode II initiates during matrix cracking in matrix 1-direction
38	${}^{m}\sigma_{m2}$ at which mode II initiates during matrix cracking in matrix 2-direction
39	dC_{33}
40-42	${}^{f}\sigma_{f1}$, ${}^{f}\sigma_{f2}$, ${}^{f}\tau_{f12}$
43-45	${}^{c}\sigma_{f1}$, ${}^{c}\sigma_{f2}$, ${}^{c}\tau_{f12}$
46	Subroutines used to implement the incremental stiffness of the matrix
47	${}^{m}d\varepsilon_{1}$
48	E_{mc1}
49	E_{mc2}
50	State of tensile delamination in the fibre 2-direction 0 = no damage, 1 = mode I, 2 = mode II, 3 = mode III, 4 = compressive state
51	State of shear delamination in the fibre 2-direction 0 = no damage, 1 = mode I, 2 = mode II and III
52	${}^{f}\sigma_{m2}$ at which mode II initiates after tensile delamination
53	${}^{f}\varepsilon_{2}$ at which mode II initiates after tensile delamination
54	${}^{f}\tau_{m12}$ at which mode II initiates after tensile delamination

55	${}^{f}\gamma_{12}$ at which mode II initiates after tensile delamination
56	${}^{m}\varepsilon_{1}$ at which mode II initiates during matrix cracking in matrix 1-direction
57	${}^{m}\varepsilon_{2}$ at which mode II initiates during matrix cracking in matrix 2-direction
58	State of fibre deformation in fibre 1 –direction: 0 = linear elastic, 1 = non-linear elastic, 2 = broken fibres with +'ve ${}^{f}d\varepsilon_{1}$, 3 = broken fibres with -'ve ${}^{f}d\varepsilon_{1}$, 4 = compressive state
59	State of fibre deformation in fibre 2 –direction: 0 = linear elastic, 1 = non-linear elastic, 2 = broken fibres with +'ve ${}^{f}d\varepsilon_{2}$, 3 = broken fibres with -'ve ${}^{f}d\varepsilon_{2}$, 4 = compressive state
60	Broken fibre strain when +'ve ${}^{f}d\varepsilon_{1}$ initiates.
61	Broken fibre strain when +'ve ${}^{f}d\varepsilon_{2}$ initiates.
62	Broken fibre strain when -'ve ${}^{f}d\varepsilon_{1}$ initiates.
63	Broken fibre strain when -'ve ${}^{f}d\varepsilon_{2}$ initiates.

Table 7.5.1-3 Definition of the solution-dependent state variables (STATEV) at the end of each increment

7.5.2 The Elastic Subroutine KELAS

The function of the subroutine KELAS is to model the undamaged elastic stress-strain behaviour of the composite according to the micro-mechanical theory described in Sect. 7.4.2, and introduce the damage criteria described in Sect. 7.4.3. The structure of the algorithm is presented in Table 7.5.2-1.

Subroutine **KELAS**	
1. Initialisation of internal variables.	
2. Matrix Analyses in the Composite Position System	
2.1 Calculation of strain.	${}^{c}\{\varepsilon^{n}\} = {}^{c}\{\varepsilon^{n-1}\} + {}^{c}\{d\varepsilon^{n}\}$
2.2 Definition of stiffness for the vol. fraction of matrix	$[S_{m}^{n}]_{elas}^{-1} = [dS_{m}^{n}]_{elas}^{-1}$
2.3 Calculation of stress in vol. fraction of matrix.	${}^{c}\{\sigma_{m}^{n}\} = {}^{c}[S_{m}^{n}]_{elas}^{-1}\ {}^{c}\{\varepsilon^{n}\}$
3. Matrix Analyses in the Matrix Position System	
3.1 Calculation of principal stresses and principal strain and principal direction cosines.	${}^{m}\{\sigma_{m}^{n}\},\ {}^{m}\{\varepsilon^{n}\}\&[b]$
4. Matrix Analyses in the Fibre Position System	
4.1 Definition of stress transformation matrix.	$[T_{\sigma}]$
4.2 Definition of strain transformation matrix.	$[T_{\varepsilon}]$
4.3 Calculation of stress in volume fraction of matrix.	${}^{f}\{\sigma_{m}^{n}\} = [T_{\sigma}]\ {}^{c}\{\sigma_{m}^{n}\}$
4.4 Calculation of strain.	${}^{f}\{\varepsilon^{n}\} = [T_{\varepsilon}]\ {}^{c}\{\varepsilon^{n}\}$

5. Fibre Analyses in the Fibre Position System	
5.1 Calculation of strain increment	${}^{f}\{d\varepsilon^{n}\} = [T_{\varepsilon}]\ {}^{c}\{d\varepsilon^{n}\}$
5.2 Definition of the incremental stiffness of vol. fraction of fibres	${}^{f}[dS_{f}^{n}]^{-1}$
5.3 Calculation of stress increment in vol. fraction of fibres	${}^{f}\{d\sigma_{f}^{n}\} = {}^{f}[dS_{f}^{n}]^{-1}\ {}^{f}\{d\varepsilon^{n}\}$
5.4 Calculation of stress in vol. fraction of fibres	${}^{f}\{\sigma_{f}^{n}\} = {}^{f}\{\sigma_{f}^{n-1}\} + {}^{f}\{d\sigma_{f}^{n}\}$
6. Fibre Analyses in the Composite Position System	
6.1 Definition of transformation matrix	$[T_{\sigma}]^{-1}$
6.2 Definition of the fibre incremental stiffness	${}^{c}[dS_{f}^{n}]^{-1} = [T_{\sigma}]^{-1}\ {}^{f}[dS_{f}^{n}]^{-1}\ [T_{\varepsilon}]$
6.3 Calculation of stress increment of vol. fraction of fibres	${}^{c}\{d\sigma_{f}^{n}\} = {}^{c}[dS_{f}^{n}]^{-1}\ {}^{c}\{d\varepsilon^{n}\}$
6.4 Calculation of stress in vol. fraction of fibres	${}^{c}\{\sigma_{f}^{n}\} = {}^{c}\{\sigma_{f}^{n-1}\} + {}^{c}\{d\sigma_{f}^{n}\}$
7. Composite Analyses in the Composite Position System	
7.1 Definition of composite incremental stiffness	${}^{c}[dS_{c}^{n}]^{-1} = {}^{c}[dS_{m}^{n}]^{-1} + {}^{c}[dS_{f}^{n}]^{-1}$
7.2 Calculation of stress increment	${}^{c}\{d\sigma_{c}^{n}\} = {}^{c}[dS_{c}^{n}]^{-1}\ {}^{c}\{d\varepsilon^{n}\}$
7.3 Calculation of stress	${}^{c}\{\sigma_{f}^{n}\} = {}^{c}\{\sigma_{f}^{n-1}\} + {}^{c}\{d\sigma_{f}^{n}\}$
8. Updating of solution-dependent state variables.	

Table 7.5.2-1 Computation algorithm of KELAS

The flow diagram of KELAS is shown schematically in Fig 7.5.2-1. The subroutine KELAS begins with several initialising procedures. First, *STATEV(32)* is given the value 0 while the subroutine KZEROVEC and KZEROMAT, shown schematically in Fig 7.5.2-2 & 3, initialises the internal variables of the subroutine KELAS with zero values. KZEROVEC is designed for 3x1 vectors while KZEROMAT is designed for 3x3 matrices. Next, the subroutine KINI (Fig 7.5.2-4) updates the variables *SFF3* and *SF3* with the fibre stresses ${}^{f}\{\sigma_{f}^{n-1}\}$ and ${}^{c}\{\sigma_{f}^{n-1}\}$ stored in *STATEV* (40-42 and 43-45).

After initialisation, analyses of the stresses and strains in the volume fraction of matrix (hereafter, matrix) in the composite, matrix and fibre position systems are performed. In the composite position system, the matrix strain *STRAN* is determined using the incremental strain *DSTRAN* provided by ABAQUS and the subroutine KVECTPLUS3 (Fig 7.5.2-5), which performs vector addition of two 3x1 vectors. After

defining the stiffness of the matrix *CM* through the subroutine KCPM1 (Fig 7.5.2-6), the matrix stress *STRESM3* is determined through the subroutine KFILLVECT3 (Fig 7.5.2-7), which calculates the product of a 3x3 matrix with a 3x1 vector. In the matrix position system, the principal stresses of the matrix *SPM*, its direction cosines *PTRANS*, and the principal strains *EP*, are analysed by implementing the matrix stress *STRESM3* and strain *STRAN* in the ABAQUS subroutines SPRIND and SPRINC. In the fibre position system, the matrix stress and strain are obtained by first defining the stress transformation matrix *TFT3* and the engineering-strain transformation matrix *TFTTI3*, using the subroutines KT3 (Fig 7.5.2-8) and KTTI3 (Fig 7.5.2-9). After implementing the transformation matrices *TFT3* and *TFTTI3* with the stress *STRESM3* and strain *STRAN* in the subroutine KFILLVECT3, respectively, the matrix stress *STRESMF3* and strain *STRANF3* in the fibre position system are obtained.

After analysing the stresses and strains in the matrix, analyses for the stresses in the volume fraction of fibres (hereafter fibres) in the fibre and composite position systems are performed. In the fibre position system, the incremental strain of the fibres *DEF3* is first calculated using the subroutine KFILLVECT3. Next, the direct strain components of the fibres in the previous increment are rename as *X1* and *X2* by the subroutine KX (Fig 7.5.2-10). This is followed by a procedure which renames *STATEV(58,59,40,41,13,14,60 to 63)* and *DEF3* to *B1, B2, C1, C2, D1, D2, E1, E2, G1, G2, F1* and *F2*. Essentially, the variables with digits 1 or 2 denote the fibres in the 1 or 2 axes of the fibre position system. To determine the tangent modulus of the fibres corresponding to the level of applied strain in the fibre position system, the renamed variables and experimental stress-strain data of the fibres are submitted to the subroutine KEMF (Fig 7.5.2-11). After which, the embedded subroutine KEMOD (Fig 7.5.2-12) acquires the fibres tangent modulus in a piece-wise linear fashion. In addition, the subroutine KEMF also implements the failure criterion for the fibres and defines the tangent modulus to unload the fibres. After the tangent modulus is determine, the subroutine KCPSFF2 (Fig 7.5.2-13) then defines the incremental stiffness *CFF* of the fibres. To determine the incremental stress *DSFF3* and the total stress *SFF3* of the fibres, the subroutines KFILLVECT3 and KVECTPLUS3 are used. To determine the fibre stresses in the composite position system, a stress transformation matrix *TFTI3* is initially defined by the subroutine KTI3 (Fig 7.5.2-14). After which, the incremental stiffness of the fibres *CFF* in the fibre position system is transformed to the composite

position system through the 3x3 matrix multiplication subroutine KMATPRODUCT (Fig 7.5.2-15). By substituting the new incremental fibre stiffness *CF* and the incremental strain *DSTRAN* into the subroutine KFILLVECT3, the fibre stress increments *DSF3* are solved. By further substituting *DSF3* into KVECTPLUS3, the total stress *SF3* in the fibres in the composite position system is obtained.

To determine the composite incremental stiffness in the composite position system *DDSDDE*, the incremental stiffnesses *CF* and *CM* are submitted to the subroutine KMATPLUS3 (Fig 7.5.2-16); essentially the subroutine performs addition of two 3x3 matrices. The corresponding incremental stress of the composite *DSTRESS* is calculated using the subroutine KFILLVECT3 and the variables *DSTRAN* and *DDSDDE*. After which, the composite stress *STRESS* in the composite position system is determine by substituting the variable *DSTRESS* into the subroutine KVECTPLUS3.

To update the solution-dependent state variables *STATEV*, five subroutines are used. The subroutine KSDVA (Fig 7.5.2-17) updates *STATEV (1-3)* while the subroutine KSDVB (Fig 7.5.2-18) updates *STATEV (4,5,10,11,25,26,29,30,32-34,37,38,56,57)* and checks for matrix cracking. Both the subroutines KSDVC (Fig 7.5.2-19) and KSDVCELAS (Fig 7.5.2-20) updates *STATEV (7-9,13-15,27,28,32,35,36,50-55)*. However, the former is active when the variable *PTYPE=0* and checks for tensile and shear delamination while latter is active when the variable *PTYPE=1*. The subroutine KSDVPORIEN (Fig 7.5.2-21) updates *STATEV(16-24)* and finally the subroutine SDVFIB (Fig 7.5.2-22) updates *STATEV(40-45)*.

7.5.3 The Matrix Cracking Subroutine KMC

The function of the subroutine KMC is to model the damage stress-strain behaviour of the composite during matrix cracking according to the micro-mechanical theory described in Sect. 7.4.4. The structure of the computation algorithm is presented in Table 7.5.3-1.

Subroutine **KMC**	
1. Initialisation of internal variables.	
1.1 Internal variable with zero value	
1.2 Definition of the matrix stresses and strains in the matrix position system and the fibres stresses in the fibre and composite position system, from the previous increment.	${}^{m}\left\{\sigma_{m}^{n-1}\right\}, {}^{m}\left\{\varepsilon^{n-1}\right\}, {}^{f}\left\{\sigma_{f}^{n-1}\right\}, {}^{c}\left\{\sigma_{f}^{n-1}\right\}$

1.3 Definition of the stress transformation matrix.	$[P_\sigma]$
1.4 Definition of the inverted stress transformation matrix	$[P_\sigma]^{-1}$
1.5 Definition of the strain transformation matrix	$[P_\varepsilon]$
2. Matrix Analyses in the Matrix Position System	
2.1 Calculation of the incremental strain	${}^{m}\{d\varepsilon^n\} = [P_\varepsilon]\,{}^{c}\{d\varepsilon^n\}$
2.2 Definition of the incremental stiffness of the volume fraction of matrix	${}^{m}[dS_m^n]^{-1}$
2.3 Calculation of stress increment in matrix	${}^{m}\{d\sigma_m^n\} = {}^{m}[dS_m^n]^{-1}\,{}^{m}\{d\varepsilon^n\}$
2.4 Calculation of stress in matrix	${}^{m}\{\sigma_m^n\} = {}^{m}\{\sigma_m^{n-1}\} + {}^{m}\{d\sigma_m^n\}$
3. Matrix Analyses in the Composite Position System	
3.1 Calculation of stress in matrix	${}^{c}\{\sigma_m^n\} = [P_\sigma]^{-1}\,{}^{m}\{\sigma_m^n\}$
3.2 Calculation of strain	${}^{c}\{\varepsilon^n\} = {}^{c}\{\varepsilon^{n-1}\} + {}^{c}\{d\varepsilon^n\}$
3.3 Calculation of incremental stiffness of the volume fraction of matrix in the composite position system	${}^{c}[dS_m^n]^{-1} = [P_\sigma]^{-1}\,{}^{m}[dS_m^n]^{-1}\,[P_\varepsilon]$
4. Matrix Analyses in the Matrix Position System	
4.1 Calculation of strain	${}^{m}\{\varepsilon^n\} = [P_\varepsilon]\,{}^{c}\{\varepsilon^n\}$
5. Matrix Analyses in the Fibre Position System	
5.1 Definition of stress transformation matrix.	$[T_\sigma]$
5.2 Definition of strain transformation matrix.	$[T_\varepsilon]$
5.3 Calculation of stress in matrix.	${}^{f}\{\sigma_m^n\} = [T_\sigma]\,{}^{c}\{\sigma_m^n\}$
5.4 Calculation of strain.	${}^{f}\{\varepsilon^n\} = [T_\varepsilon]\,{}^{c}\{\varepsilon^n\}$
6. Fibre Analyses in the Fibre Position System	
6.1 Calculation of strain increment	${}^{f}\{d\varepsilon^n\} = [T_\varepsilon]\,{}^{c}\{d\varepsilon^n\}$
6.2 Definition of the fibre incremental stiffness	${}^{f}[dS_f^n]^{-1}$
6.3 Calculation of stress increment in fibres	${}^{f}\{d\sigma_f^n\} = {}^{f}[dS_f^n]^{-1}\,{}^{f}\{d\varepsilon^n\}$
6.4 Calculation of stress in fibres	${}^{f}\{\sigma_f^n\} = {}^{f}\{\sigma_f^{n-1}\} + {}^{f}\{d\sigma_f^n\}$
7. Fibre Analyses in the Composite Position System	
7.1 Definition of transformation matrix	$[T_\sigma]^{-1}$
7.2 Definition of the fibre incremental stiffness of vol. fraction of fibres	${}^{c}[dS_f^n]^{-1} = [T_\sigma]^{-1}\,{}^{f}[dS_f^n]^{-1}\,[T_\varepsilon]$
7.3 Calculation of stress increment in fibres	${}^{c}\{d\sigma_f^n\} = {}^{c}[dS_f^n]^{-1}\,{}^{c}\{d\varepsilon^n\}$
7.4 Calculation of stress in fibres	${}^{c}\{\sigma_f^n\} = {}^{c}\{\sigma_f^{n-1}\} + {}^{c}\{d\sigma_f^n\}$
8. Composite Analyses in the Composite Position System	
8.1 Definition of composite incremental stiffness	${}^{c}[dS_c^n]^{-1} = {}^{c}[dS_m^n]^{-1} + {}^{c}[dS_f^n]^{-1}$

8.2 Calculation of stress increment in composite	${}^{c}\{d\sigma_c^n\} = {}^{c}[dS_c^n]^{-1}\ {}^{c}\{d\varepsilon^n\}$
8.3 Calculation of stress in composite	${}^{c}\{\sigma_f^n\} = {}^{c}\{\sigma_f^{n-1}\} + {}^{c}\{d\sigma_f^n\}$
9. Updating of solution-dependent state variable.	

Table 7.5.3-1 Computation algorithm of KMC

The flow diagram of the subroutine KMC is shown schematically in Fig 7.5.3-1. The subroutine begins with several initialisation procedures. First, *STATEV(32)* is given a value of 1 and the internal variables are initialised with zero values using the subroutines KZEROVEC and KZEROMAT. After which, the subroutine KINIMC (Fig 7.5.3-2) updates the variables *SFF3* & *SF3* with the fibre stresses ${}^{f}\{\sigma_f^{n-1}\}$ and ${}^{c}\{\sigma_f^{n-1}\}$ that are stored in *STATEV* (40-42 and 43-45), and updates the variables *SPM* and *EP* with the matrix stress ${}^{m}\{\sigma_m^{n-1}\}$ and strain ${}^{m}\{\varepsilon^{n-1}\}$ stored in *STATEV* (4-6 and 10-12). In addition, the stress and engineering-strain transformation matrices *PTRANS3*, *PTRANSI3* and *PTRANE3* are defined by the subroutines KPTRANS3, KPTRANSI3 and KPTRANE3 (Fig 7.5.3-3 to 5). Here, *PTRANS3* and *PTRANE3* describe the transformation to the fibre position system with respect to the composite position system, while *PTRANSI3* is the inverse of *PTRANS3*.

After initialisation, the stresses and strains of the matrix are analysed in the matrix, composite and fibre position systems. First in the matrix position system, the local strain increment *DEP* is determined by transforming the strain increment *DSTRAN* in the composite position system using the subroutine KFILLVECT3 (Fig 7.5.2-7) and the transformation matrix *PTRANE3*. The local incremental stiffness of the matrix *C3* is defined by the subroutine KSTRIFFCRIT3MC (Fig 7.5.3-6). After which, the incremental stress of the matrix *DSPM* is determined as a product of the incremental stiffness *C3* and incremental strain *DEP* through the subroutine KFILLVECT3. To determine the matrix stress *SPM*, the subroutine KVECTPLUS3 (Fig 7.5.2-5) adds the incremental stress *DSPM* to the stress *SPM* from the previous increment. In the composite position system, the local stress in the matrix *STRESM3* is determined by transforming of the matrix stress *SPM* with the transformation matrix *PTRANSI3* in the subroutine KFILLVECT3. The local incremental stiffness of the matrix is determined by transforming the incremental stiffness *C3* using the subroutine KMATPRODUCT

(Fig 7.5.2-7) and the transformation matrices *PTRANSI3* and *PTRANE3*. The matrix strain *STRAN* is determined by adding the strain increment *DSTRAN* and the strain *STRAN* from the previous increment. In the matrix position system, the matrix strain *EP* is determined by transforming the matrix strain *STRAN* using the transformation matrix *PTRANE3* in the subroutine KFILLVECT3.

The subroutine KSTIFFCRIT3MC shown in Fig 7.5.3-6 models matrix cracking when the normal of the matrix crack plane is in the 1 or 2 direction of the matrix position system; this is dependent on the values of *STATEV(29)* and *STATEV(30)*, respectively. If either state variable is 1 or greater, matrix cracking is indicated in the respective matrix direction and the subroutine KSTIFFCRIT3MC1 (Fig 7.5.3-7) or KSTIFFCRIT3MC2 (Fig 7.5.3-8) is correspondingly active. Locally, the values of *STATEV(29)* or *STATEV(30)* are check to establish the matrix cracking mode in the previous increment. The meanings of the different values of the state variables *STATEV(29)* and *STATEV(30)* are shown in Table 7.5.1-3. Base to these reference states, the polarity of the current strain increment in the 1 or 2 direction of the matrix position system, i.e. *DSTRAN3M(1)* or *DSTRAN3M(2)*, indicates the matrix cracking mode in the current increment and activates the subroutine KSTIFF3 to define the local incremental stiffness of the matrix. The convention use to name the subroutines which implements the incremental stiffness of the matrix is as follows:

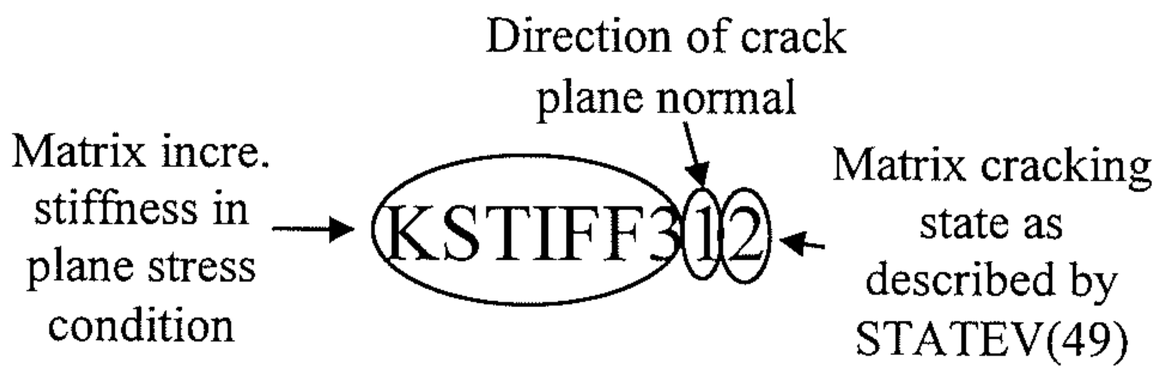

In the hardening region, subroutine KSTIFF311 or KSTIFF321 is active (see Fig 7.5.3-9 & 15) while in the softening region subroutine KSTIFF314 or KSTIFF324 (see Fig 7.5.3-12 & 18) is active. The effects of crack closure (mode II) and crack re-opening (model III) are modelled by subroutines KSTIFF312 and KSTIFF313 (see Fig 7.5.3-10 & 11) or KSTIFF322 and KSTIFF322 (see Fig 7.5.3-16 & 17). During fibre failure, the subroutine KSTIFF3111 and KSTIFF3112 (see Fig 7.5.3-13 & 14) or KSTIFF3211 and KSTIFF3212 (see Fig 7.5.3-19 & 20) are active to model the corresponding matrix behaviour.

The algorithms to analyse the matrix stress and strain in the fibre position system are identical to the subroutine KELAS. Similarly, the algorithm to analyse the stress, strain and incremental stiffness of the fibres and the composites are identical to the subroutine KELAS.

Finally to update the state variable STATEV, subroutines KSDV3A (Fig 7.5.2-17), KSDV3BMC (Fig 7.5.3-21), KSDV3CELAS (Fig 7.5.2-23), KSDVPORIENMC (Fig 7.5.3-24) and KSDVFIB (Fig 7.5.2-25) are active. In subroutine KSDV3BMC, the subroutines KSDV3BMC1 (Fig 7.5.3-22) and KSDV3BMC2 (Fig 7.5.3-23) update the relevant STATEV when the normal of the crack planes is in the 1 or 2 direction of the matrix position system.

7.5.4 The Delamination Subroutine KDEL

The subroutine KDEL models the mechanical behaviour of the composite during tensile or shear delamination. The structure of the computation algorithm is presented in Table 7.5.4-1.

Subroutine **KDEL**	
1. Initialisation of internal variables.	
1.1. Internal variable with zero value	
1.2. Definition of the matrix stresses and strains in the fibre position system and the fibres stresses in the fibre and composite position system, from the previous increment.	${}^{f}\{\sigma_m^{n-1}\}, {}^{f}\{\varepsilon^{n-1}\}, {}^{f}\{\sigma_f^{n-1}\}, {}^{c}\{\sigma_f^{n-1}\}$
2. Analyses in the Composite Position System	
2.1. Calculation of strain	${}^{c}\{\varepsilon^{n}\} = {}^{c}\{\varepsilon^{n-1}\} + {}^{c}\{d\varepsilon^{n}\}$
3. Matrix Analyses in the Fibre Position System	
3.1. Definition of strain transformation matrix.	$[T_\varepsilon]$
3.2. Calculation of incremental strain.	${}^{f}\{d\varepsilon^{n}\} = [T_\varepsilon]\ {}^{c}\{d\varepsilon^{n}\}$
3.3. Definition of the incremental stiffness of the volume fraction of matrix	${}^{f}[dS_m^{n}]^{-1}$
3.4. Calculation of stress increment in matrix	${}^{f}\{d\sigma_m^{n}\} = {}^{f}[dS_m^{n}]^{-1}\ {}^{f}\{d\varepsilon^{n}\}$
3.5. Calculation of stress in matrix	${}^{f}\{\sigma_m^{n}\} = {}^{f}\{\sigma_m^{n-1}\} + {}^{f}\{d\sigma_m^{n}\}$
3.6. Calculation of strain	${}^{f}\{\varepsilon^{n}\} = [T_\varepsilon]^{-1}\ {}^{c}\{\varepsilon^{n}\}$
4. Matrix Analyses in the Composite Position System	

4.2. Calculation of stress in matrix.	${}^{c}\{\sigma_m^n\} = [T_\sigma]^{-1}\ {}^{f}\{\sigma_m^n\}$
4.3. Definition of the incremental stiffness of the volume fraction of matrix	${}^{c}[dS_m^n]^{-1} = [T_\sigma]^{-1}\ {}^{f}[dS_m^n]^{-1}[T_\varepsilon]$
5. Matrix Analyses in the Matrix Position System	
5.1. Calculation of principal stresses and principal strain and principal direction cosines.	${}^{m}\{\sigma_m^n\},\ {}^{m}\{\varepsilon^n\}\ \&\ [P]$
6. Fibre Analyses in the Fibre Position System	
6.1. Definition of the fibre incremental stiffness for the vol. fraction of fibres	${}^{f}[dS_f^n]^{-1}$
6.2. Calculation of stress increment in fibres	${}^{f}\{d\sigma_f^n\} = {}^{f}[dS_f^n]^{-1}\ {}^{f}\{d\varepsilon^n\}$
6.3. Calculation of stress in fibres	${}^{f}\{\sigma_f^n\} = {}^{f}\{\sigma_f^{n-1}\} + {}^{f}\{d\sigma_f^n\}$
7. Fibre Analyses in the Composite Position System	
7.1. Definition of the fibre incremental stiffness	${}^{c}[dS_f^n]^{-1} = [T_\sigma]^{-1}\ {}^{f}[dS_f^n]^{-1}[T_\varepsilon]$
7.2. Calculation of stress increment of fibres	${}^{c}\{d\sigma_f^n\} = {}^{c}[dS_f^n]^{-1}\ {}^{c}\{d\varepsilon^n\}$
7.3. Calculation of stress in fibres	${}^{c}\{\sigma_f^n\} = {}^{c}\{\sigma_f^{n-1}\} + {}^{c}\{d\sigma_f^n\}$
8. Composite Analyses in the Composite Position System	
8.1. Definition of composite incremental stiffness	${}^{c}[dS_c^n]^{-1} = {}^{c}[dS_m^n]^{-1} + {}^{c}[dS_f^n]^{-1}$
8.2. Calculation of stress increment in composite	${}^{c}\{d\sigma_c^n\} = {}^{c}[dS_c^n]^{-1}\ {}^{c}\{d\varepsilon^n\}$
8.3. Calculation of stress in composite	${}^{c}\{\sigma_f^n\} = {}^{c}\{\sigma_f^{n-1}\} + {}^{c}\{d\sigma_f^n\}$
9. Updating of solution-dependent state variable.	

Table 7.5.4-1 Computation algorithm of KDEL

A flow diagram of KDEL is shown in Fig 7.5.4-1. The subroutine begins with several initialisation procedures. The subroutines KZEROVEC and KZEROMAT are initially active to initialise the internal variables with zero values and the subroutine KINIDEL (Fig 7.5.4-2) initialises the variables *SFF3*, *SF3*, *STRESMF3* and *STRANF3* with the fibre stresses in the fibre and composite position system and the matrix stress and strain in the fibre position system.

After initialisation, the stresses and strains of the matrix are analysed in the fibre, composite and matrix position system. Before the analyses in the fibre position system, the matrix strains in the composite position system *STRAN* is first determined through the subroutine KVECTPLUS3 (Fig 7.5.2-5). In addition, the subroutine KTTI3 is active to define the engineering strain transformation matrix *TFTTI3* for the fibre position

incremental strain of the matrix *DEF3* is determined as the product of the engineering strain transformation matrix *TFFTI3* and the incremental strain of the matrix in the composite position system *DSTRAN* through the subroutine KFILLVECT3 (Fig 7.5.2-7). The subroutine KSTIFFCRIT3DEL (Fig 7.5.4-3) defines the incremental stiffness of the matrix *C3*. After which, the incremental stress of the matrix *DSTRESMF3* is determined as the product of *C3* and *DEF3* while the stress in the matrix *STRESMF3* is the sum of *DSTRESMF3* and *STRESMF3,* which is the matrix stress in the previous increment. The subroutine KFILLVECT3 defines the local strain in the matrix *STRANF3* by transforming the matrix strain *STRAN* with the transformation matrix *TFFTI3*.

To initiate the analyses of the matrix properties in the composite position system, the subroutine KTI3 (Fig 7.5.2-14) first defined the inverse stress transformation matrix *TFTI3*. After which, the product of *TFTI3* and *STRESMF3*, which is the matrix stress in the fibre position system, determines the local matrix stress *STRESM3*. The local incremental stiffness of the matrix *CM* is determined as the product of *TFTI3*, *C3* and *TFTTI3*, which is calculated using the subroutine KMATPRODUCT (Fig 7.5.2-15).

A description of the subroutine KSTIFFCRIT3DEL (Fig 7.5.4-3) is given next. During delamination, identification of tensile or shear delamination is through the state variables *STATEV(50)* and *STATEV(51)*. For tensile delamination, the value of *STATEV(50)* must be one or greater. For shear delamination, the same criterion applies for *STATEV(51)*. During tensile delamination, the subroutine KSTIFFCRIT3TD (Fig 7.5.4-4) is active to determine the tensile delamination mode of the composite and define the incremental stiffness of the matrix. The subroutines KSTIFFTD31 (Fig 7.5.4-5), KSTIFFTD32 (Fig 7.5.4-6), KSTIFFTD33 (Fig 7.5.4-7) and KSTIFFTD34 (Fig 7.5.4-8) are active to model the deformation modes (I, II & III) of the composite during tensile delamination and during compression. In the case of shear delamination, the subroutine KSTIFFCRIT3SD (Fig 7.5.4-9) is active to determine the shear delamination mode of the composite and define the incremental stiffness of the matrix.
During mode I deformation, the subroutines KSTIFFSD31 (Fig 7.5.4-10) is active while the subroutine KSTIFFSD32 (Fig 7.5.4-11) is active for modes II and III deformation.

The subsequent sequences of the algorithm in the subroutine KDEL are identical

KSDV3BDEL (Fig 7.5.4-12) and KSDV3CDEL (Fig 7.5.4-13) to update the state variables. In the subroutine KSDV3CDEL, the subroutine KSDV3CTD (Fig 7.5.4-14) is active during tensile delamination while the subroutine KSDV3CSD (Fig 7.5.4-15) is active during shear delamination.

7.6 Benchmarking

Benchmarking is necessary to verify the damage model. In this section, benchmark procedures were developed for the UMAT subroutine. Initially, a single first-order quadrilateral plane stress solid element with dimensions 0.015m x 0.015m x 0.002m to represent a composite material was tested in simple stress states where exact solutions or bounds exist. After which, the composite was tested for matrix cracking, tensile delamination and shear delamination, and benchmarked using the experimental data of the one-dimensional polyester composite described in Chapter 4.

7.6.1 Pre-Damage State

7.6.1.1 Problem description

The benchmark studies are summarised in Table 7.6.1.1-1. For load cases 1, 2, 5 & 6, the composite was uniaxially tensioned parallel to the fibre axis, while in load cases 3 & 4, uniaxial tension was applied transverse to the fibre axis. In all load cases, Poisson's ratio of both the fibre and matrix was 0.3 and Young's modulus of the matrix was 4.732GPa. The volume fractions of the fibre and matrix were 0.5. The boundary conditions and position system of the composite and the fibres are shown in Fig 7.6.1.1-1. A displacement of 0.001m was applied in the composite 1 direction.

Load Cases	Description
1	One-dimensional composite tension parallel to fibre $E_f = E_m$
2	One-dimensional composite tension parallel to fibre $E_f = 10E_m$
3	One-dimensional composite tension transverse to fibre $E_f = E_m$
4	One-dimensional composite tension transverse to fibre $E_f = 10E_m$
5	Two-dimensional composite tension parallel to fibre $E_f = E_m$
6	Two-dimensional composite tension parallel to fibre $E_f = 10E_m$

Table 7.6.1.1-1 Load cases for benchmarking the pre-damage state

7.6.1.2 Reference Solutions & Bounds

To benchmark the solutions from the damage model, exact solutions or bounds were determined. For load cases 1, 3 & 5, the composite reduces to an isotropic homogeneous elastic solid. A bound for load case 2 was calculated using Voigt's analysis (see Sect. 3.2). No exact solution exists for load case 4. Instead, bounds were established using the Voigt and Reuss analyses. To verify the computational algorithm for load case 4, Voigt's analysis for a matrix containing voids was used as the fibre-matrix interface is taken to be very weakly bonded or unbonded so that the fibres make no contribution perpendicular to their length. The use of the Reuss analysis is not helpful in this case because the transverse modulus of the composite is only established to be greater than zero. No exact solution is available for load case 6. As such, Voigt's analysis was used to provide an upper bound to benchmark the numerical solution of the damage model. The exact solutions and bounds for the load cases are shaded in Table 7.6.1.3-1 and Table 7.6.1.3-2.

7.6.1.3 Results & Analyses

The numerical solutions for the load cases of the one- and two-dimensional composites in the composite position system are presented in Table 7.6.1.3-1 and Table 7.6.1.3-2. For load cases 3 to 6, a compressive strain was generated in the fibres and the analyses have been performed with both zero and a finite fibre moduli in compression. The label (a) indicates that the compressive modulus of the fibres was zero while the label (b) indicates that the same modulus was used in tension and compression. The stress-strain relations of the one- and two-dimensional composites, the fibres and matrix are shown in Fig 7.6.1.3-1 to 4 and Fig 7.6.1.3-5 to 6.

For load cases 1 and 2, where loading is applied parallel to the fibres, the numerical and exact solutions agree. For loading transverse to the fibres with no modulus mismatch (load case 3), the numerical solutions were underestimated by 50% if the fibres are taken to be fully bonded to the matrix. However treating the fibres as unbonded inherently gives agreement. In the case of modulus mismatch (load case 4), the numerical solution was less than Reuss's estimate by a factor of ~3. However, the numerical solution was identical to the upper bound for a matrix containing voids when

	Tension parallel to fibre axis				Tension transverse to fibre axis					
Load Case	**1**	**1**	**2**	**2**	**3**	**3a**	**3b**	**4**	**4a**	**4b**
ε_1	0.0666	0.0666	0.0666	0.0666	0.0666	0.0666	0.0666	0.0666	0.0666	0.0666
ε_2	-0.02	-0.02	-0.02	-0.02	-0.02	-0.02	*-0.0105*	-0.02	-0.02	-0.002
σ_1 (MPa)	315	315	1736	1740	315	*158*	*165*	$573 < \sigma_1 < 1733$ 158	158	172
E_1 (GPa)	4.74	4.74	26.0	26.0	4.74	*2.37*	*2.48*	$8.60 < E_1 < 26.0$ 2.37	2.37	2.58
F_1 (KN)	9.46	9.46	52.1	52.1	9.46	*4.73*	*4.96*	$17.19 < F_1 < 52.1$ 4.73	4.73	5.15
F_2 (KN)	0	0	0	0	0	0	0	0	0	0

Note : Exact solution or bounds (shaded); numerical solution (unshaded)

ble 7.6.1.3-1 Results of the UMAT subroutine and the exact solutions (or bounds) for one-dimensional composites before damage.

Load Case	**5**	**5a**	**5b**	**6**	**6a**	**6b**
ε_1	0.0666	0.0666	0.0666	0.0666	0.0666	0.0666
ε_2	-0.02	-0.02	*-0.0153*	<-0.02	-0.02	-4.96e-3
σ_1 (MPa)	315	315	*321*	<1735	1025	1043
E_1 (GPa)	4.74	4.74	*4.81*	<26.0	15.4	15.6
F_1 (KN)	9.46	9.46	*9.63*	<52.05	30.8	31.3
F_2 (KN)	0	0	0	0	0	0

Note : Exact solution or bounds (shaded); numerical solution (unshaded)

Table 7.6.1.3-2 Results of the UMAT subroutine and exact solutions (or bound) for two-dimensional composites.

to the upper bound. For two-dimensional composites, the numerical solution for load case 5 agreed with the exact solution when the fibre modulus in compression was zero. By introducing a finite compressive fibre modulus, the numerical solutions were greater than the exact solution by 2%. In the case of modulus mismatch (load case 6), the numerical solution was lower than the upper bound.

From these results, the simplification of the fibres as a one-dimensional load bearing member may underestimate the transverse modulus and stress of a fully bonded one-dimensional composite. However, the assumption that the fibre-matrix is weak or unbonded is well represented by the simplification that the fibres only transmit axial loads. The results also showed that the damage model usefully represents the elastic response of two-dimensional composites.

7.6.2 Matrix Cracking

7.6.2.1 Problem description

A one-dimensional composite was stretched parallel to the fibres until matrix cracking initiated. After cracking, the composite was cyclically unloaded and reloaded until the composite finally failed by fibre failure. A schematic diagram of the composite and the boundary conditions is shown in Fig 7.6.1.1-1a. The mechanical properties of the one-dimensional polyester composite presented in Chapter 4 were used to model the composite. The volume fraction of the fibres was 0.185 and simulations of the composite with and without a compressive fibre modulus were considered.

7.6.2.2 Results & Analyses

The numerical stress-strain relations for the composite and the volume fraction of fibre and matrix are shown in Figs 7.6.2.2-1 to 3. Superimposed on the data are the experimental stress-strain data for the one-dimensional dogbone specimen, the fibre and the average response of the damaged matrix. The results show that the UMAT algorithm is able to model the non-linear elastic response of the fibres, and the non-linear elastic-damaged response of the composite and the matrix response. Further, after fibre failure, the damage model is able to unload the composite in an elastic-damage manner.

In Fig 7.6.2.2-4, the deformed meshes before matrix cracking and at final failure are shown. The deformed meshes show the transverse strain of the composite is relaxed

that the crack plane normal was parallel to the composite 1 direction, i.e. the direction of the applied displacement. This however is not shown in the deformed mesh.

7.6.3 Tensile Delamination

7.6.3.1 Problem description

A schematic diagram of the composite and the applied boundary conditions is shown in Fig 7.6.1.1-1b. The composite was initially stretched transverse to the fibre axis to induce tensile delamination. Subsequently, the composite was cyclically compressed and reloaded. The mechanical properties of the composite are as described in Sect. 7.6.2.1. The tensile delamination stress of the composite was 7.79MPa while the transverse modulus of the composite was 3.74GPa (see Sect. 4.3.2). The analysis was performed for fibres with zero and a finite compressive modulus.

7.6.3.2 Results & Analyses

The numerical stress-strain response of the composite, matrix and fibres are shown Fig 7.6.3.2-1. The result shows that the composite was successfully modelled as non-linear damaged elastic. The composite delaminated at approximately 8MPa, which is close to the experimental value. This indicates that the damage criterion modelling tensile delamination was correctly implemented. The modulus of the composite normal to the fibre axis, when the fibres compressive modulus was zero and finite, was predicted as 3.50GPa and 3.67GPa, respectively. In comparison to the experimental data, the predicted modulus was underestimated by between 2% and 7%, which suggest that the transverse modulus of the polyester fibres have little contribution to transverse modulus of the composite. As such, the fibres may be treated as one-dimensional and the modulus of the volume fraction of matrix may be used to model the transverse modulus of the composite. The deformed mesh after tensile delamination is shown in Fig 7.6.3.2-2. The deformed mesh demonstrates that the composite strain parallel to the tensile delamination plane was relaxed.

7.6.4 Shear Delamination

7.6.4.1 Problem description

are shown in Fig 7.6.4.1-1. First, the composite was subjected to a positive shear parallel to the fibre 12-plane. After shear delamination, the composite was cyclically unloaded and reloaded. Next, the test was repeated with a negative shear. Finally, the composite was cyclically sheared in the positive and negative direction sequentially. Mechanical properties of the polyester composite mentioned in Chapter 4 were used. The fibre volume fraction was 0.185, the composite shear modulus was 2.10GPa and the shear delamination stress was 9.96MPa.

7.6.4.2 Results & Analyses

The numerical shear stress-strain response of the composite, matrix and fibre tested in the positive and negative shear directions are shown in Fig 7.6.4.2-1. The shear stress and shear strain response of the composite changing from the positive to the negative shear direction is shown in Fig 7.6.4.2-2. These results demonstrate that the composite was successfully modelled after shear delamination and that the damage criterion for shear delamination was not dependent on the polarity of the shear stress. The predicted shear delamination stress of the composite was 10.2MPa. This slightly overestimated the shear stress of the composite by about 2%. The agreement demonstrates that the shear delamination criterion was correctly implemented. The shear modulus of the composite was predicted to be 1.34GPa, which is 19% less than the upper bound estimate of the composite shear modulus of 1.65GPa. In Fig 7.6.4.2-3, the deformed mesh in the positive shear direction is shown. The deformation modelled after shear delamination is shown to be correct.

7.6.5 The Damage Criterion

7.6.5.1 Problem description

During uni-axial tension, the experiments described in Chapter 4 have shown that damage modes in one-dimensional composites change with fibre alignment. To benchmark the damage model ability to model the damage mechanisms with respect to fibre alignment, a series of fibre alignment angles ranging from $\alpha = 0°$ to $90°$ was considered. A schematic diagram of the mesh and the boundary conditions and position system of the composite and fibre is as shown in Fig 7.6.5.1-1. To compare the

stress of the composite was taken as 55.3MPa and the critical shear and tensile delamination stresses of the composite were 9.94MPa and 7.79MPa.

7.6.5.2 Results & Analyses

The predicted ultimate tensile strengths of the one-dimensional composite as a function of the fibre alignment angles are plotted in Fig 7.6.5.2-1. The damage model predicted matrix cracking for fibre alignment angles of $\alpha = 0°$ to 9°, shear delamination for $\alpha = 10°$ to 38°, and tensile delamination for $\alpha = 39°$ to 90°. The figure also show the experimental data points and estimates using the maximum stress and Tsai-Hill criteria.

The predicted strengths are shown to be in close agreement with the experimental data. In addition, the predicted strengths agree well with the estimates from the maximum stress criterion, which implies that the subroutine UMAT correctly implemented the delamination criterion in the subroutine KSDVC. During matrix cracking, the predicted strength of the composite decreased as the fibre alignment angle increased. This is because the composite was allowed to fail when the fibres failed. The decrease in UTS predicted is different to the estimates of the maximum stress theory, which suggest that the composite strength increase initially with fibre misalignment. However, it supports the Tsai-Hill criterion, which predicts a decrease in UTS with respect to fibre misalignment. Though no experimental data are available to validate the controversy surrounding the UTS trend at small fibre misalignments, mechanistically the current damage mechanics approach shows that the strength of the composite does decrease with fibre misalignment, but at a lower rate than expected from the Tsai-Hill criterion.

7.7 Discussion

The analysis of composites tensioned parallel to the fibre axis established the abilities of the model to represent the axial properties of the composite. Before damage (see load cases 1 & 2), the numerical solutions agreed with the exact solutions. During matrix cracking, the numerically determined stress-strain curve of the composite modelled the experiment as required. Crack-closure and crack-reopening were demonstrated through the unloading and reloading paths of the damage-elastic matrix and the elastic fibres. The crack orientation was predicted on the plane of maximum

cracks showed no influence on the axial properties of the composite after crack closure; the modulus of the matrix in compression was described by the Young's modulus of the volume fraction of matrix.

Experiments by ACK and McCafferty (1994) have shown that when brittle matrix composites are cyclically tensioned parallel to the fibre axis, a permanent strain results in the composite. ACK (1971) has attributed this phenomenon to slippage at the debonded fibre-matrix interfaces near the matrix cracks. As such, the composite modulus during unloading and reloading will initially be E_c, but decrease to the limiting value of $E_f V_f$. Though the damage model did not attempt to model the permanent strain, the approach adopted to model the unloading and re-loading path of the composite was simple and appropriate for handling stress-redistribution during largely proportional loading. It is observed that by treating the matrix as elastic-damage and the fibres as non-linear elastic, the unloading and reloading response of the composite is non-linear due to the non-linear fibre responses.

When transversely loaded, load cases 3 & 4 show that the damage model underestimates the elastic response of the composite if the matrix and fibres are isotropic and perfectly bonded. This is because in the model the fibres do not contribute any stiffness normal to the fibre axis. To overcome this problem, the fibres can be modelled as transversely-isotropic. In load case 5a, the numerical results satisfied the exact solutions after the transverse modulus of the fibres were introduced. The added flexibility of representing the fibre with two-dimensional stiffness however requires the transverse modulus of the composite to be known. In the case of the one-dimensional polyester composite, the effective transverse modulus of the fibres was obtained as a difference between the transverse modulus of the composite and the modulus of the volume fraction of matrix, divided by the volume fraction of fibres, which was deduced to be 1.27GPa. In comparison with the fibre axial modulus of 4.3GPa, the transverse modulus of the fibres is shown to be lower, which indicates the polyester fibres may be transversely-isotropic. This is possible since the fibres were fabricated by extrusion. An alternative may be due to an imperfect fibre-matrix interface, which would reduce the transverse stiffness of the composite. This has been studied in Chapter 9.

During tensile delamination, the unloading-reloading stress-strain curve of the composite was treated by damaged elasticity. The benchmark results verified the

compression normal to the delamination plane, delamination was shown to have no influence on the response of the composite after crack closure since the modulus of the composite in compression was allowed to be the same as in tension. Similarly, the damage model is able to account for both positive and negative shears. After shear delamination in either direction, the composite was able to unload by softening in the direction of the shear damage. When the direction of the shear strain was reversed, i.e. 'closed', the unloading response was modelled using the secant modulus with respect to the origin.

The analysis of the two-dimensional composites indicated that the modulus did not exceed the established upper bound. For composites without modulus mismatch, the transverse strain of the composite was best modelled by eliminating the fibre modulus when the fibres are in compression. This recommendation may apply for modelling two-dimensional composites with modulus mismatch. However, this recommendation could not be verified, as a lower bound was not established.

7.8 Conclusion

A damage mechanics approach for modelling the deformation and failure of brittle matrix composites with one- and two-dimensional reinforcements was developed. This was achieved first at a micro-level in which the effective incremental compliance of the matrix and fibres were modelled separately for matrix cracking, fibre failure, and shear or tensile delamination. During damage the matrix was assumed to be transversely-isotropic, capable of crack opening, crack closure and crack re-opening. Before damage the matrix was treated as isotropic linear elastic. The fibres were assumed to transmit only axial loads and follow a non-linear elastic response until failure. The composite compliance was modelled as the sum of the matrix and fibres compliances within the context of ACK (1971) theory. The damage mechanics approach was developed into a computation algorithm using FORTRAN and implemented into the finite element solver ABAQUS through the interface subroutine UMAT. The code was successfully benchmarked for a first order plane stress quadrilateral solid element in the pre-damage regime and during matrix cracking, shear delamination and tensile delamination.

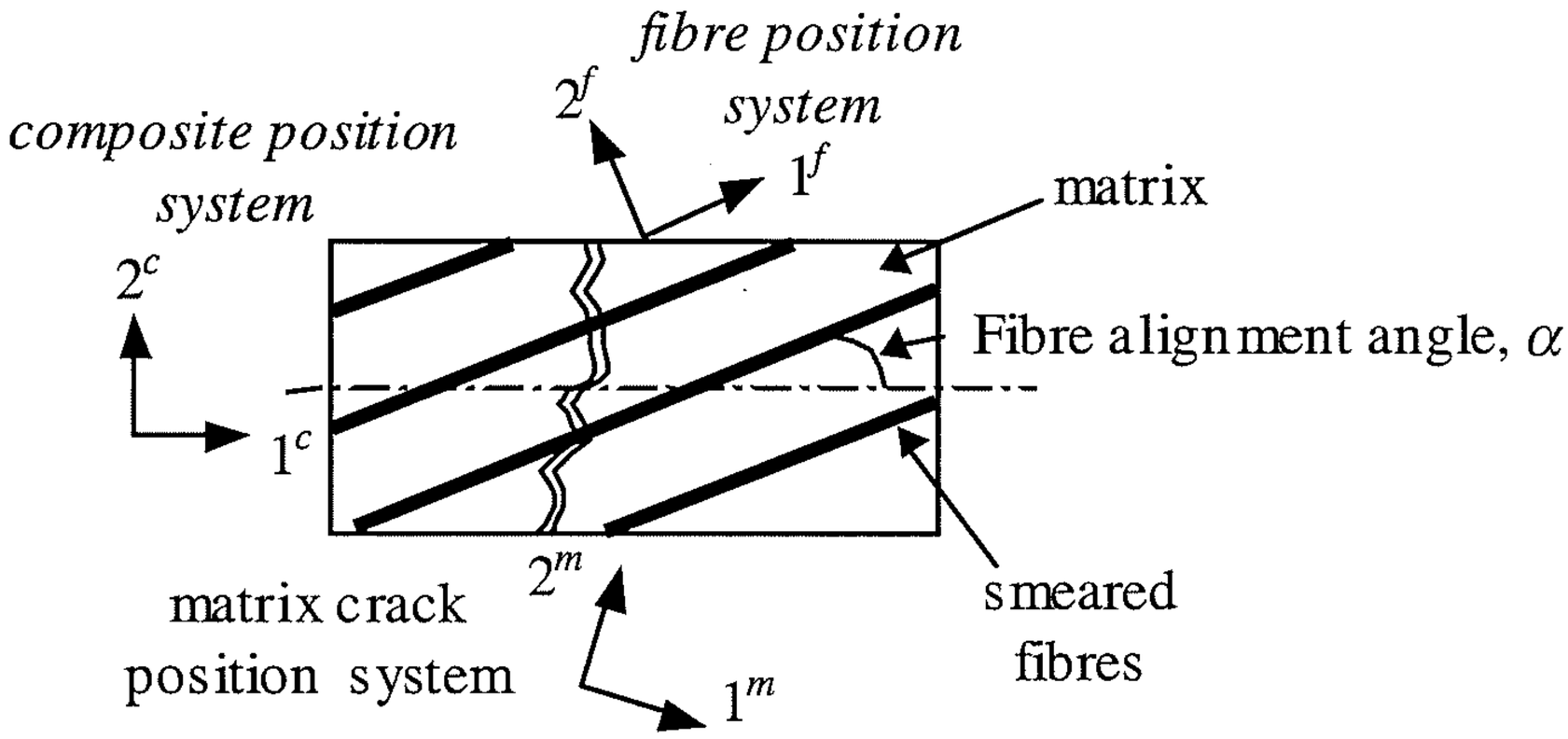

Fig 7.2-1 The position systems of the damage model.

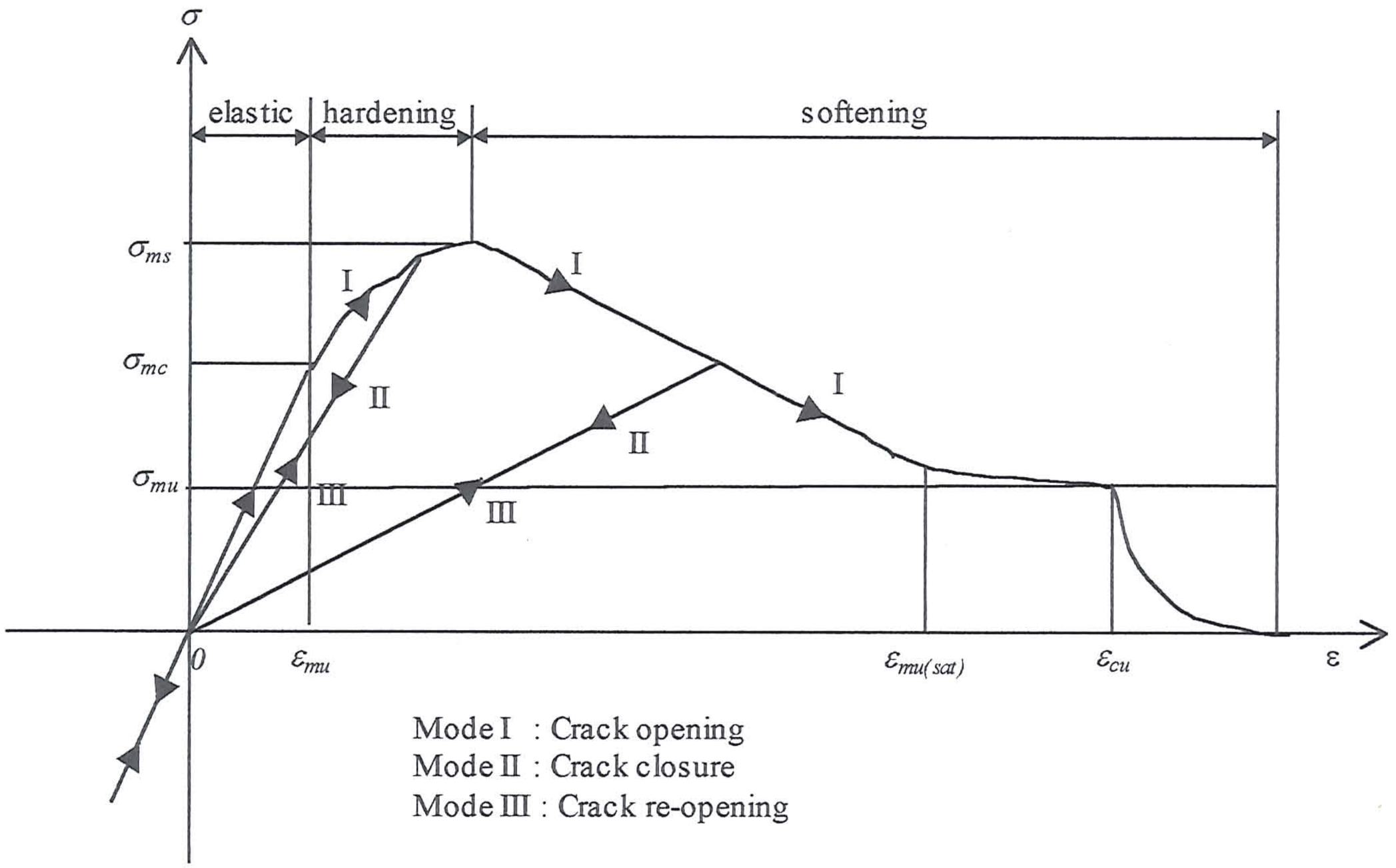

Fig 7.4.4.1-1 The effective stress-strain behaviour and deformation modes of the matrix during matrix cracking.

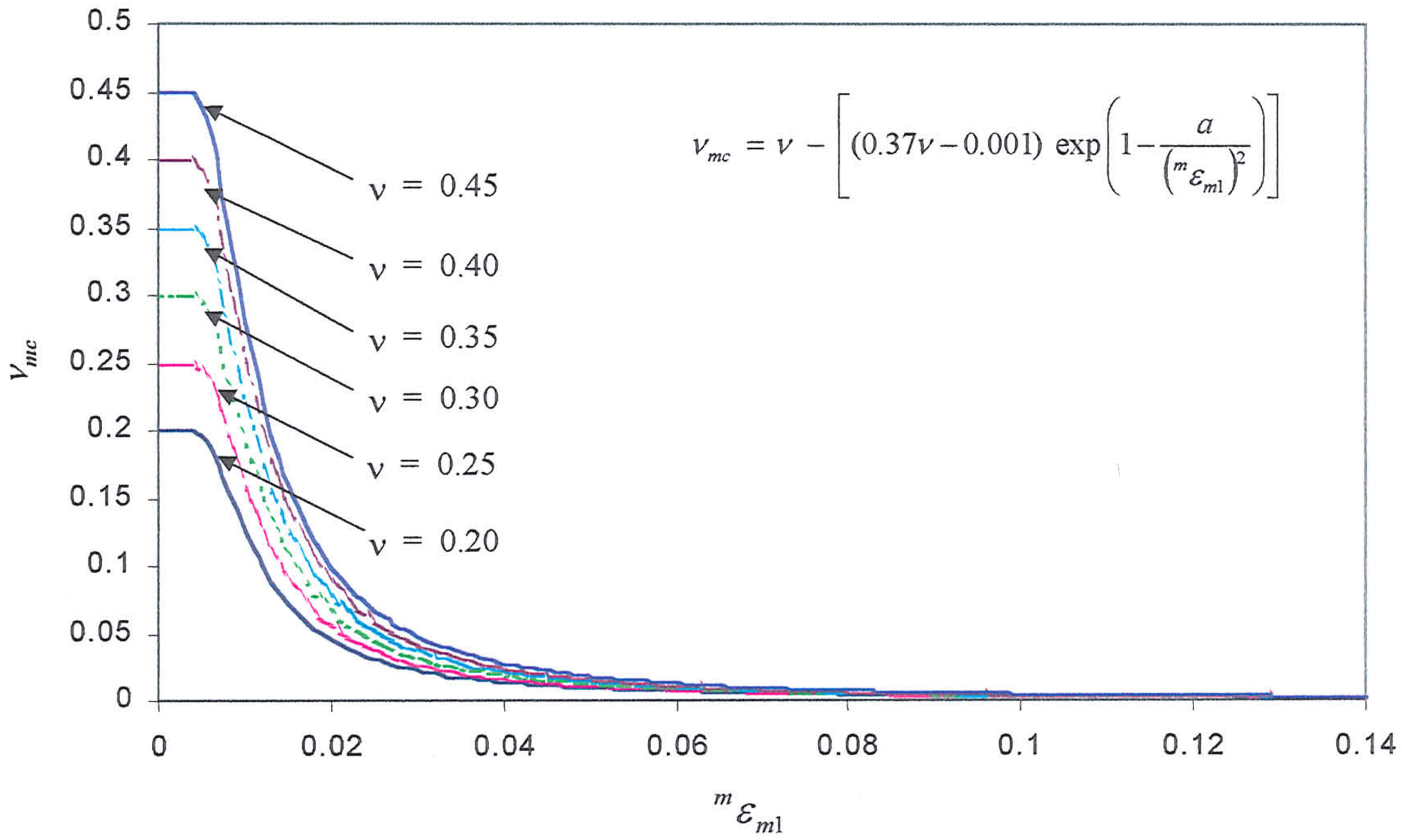

Fig 7.4.4.1-2 Plots of the Poisson's ratio ν_{mc} during matrix cracking as a function of

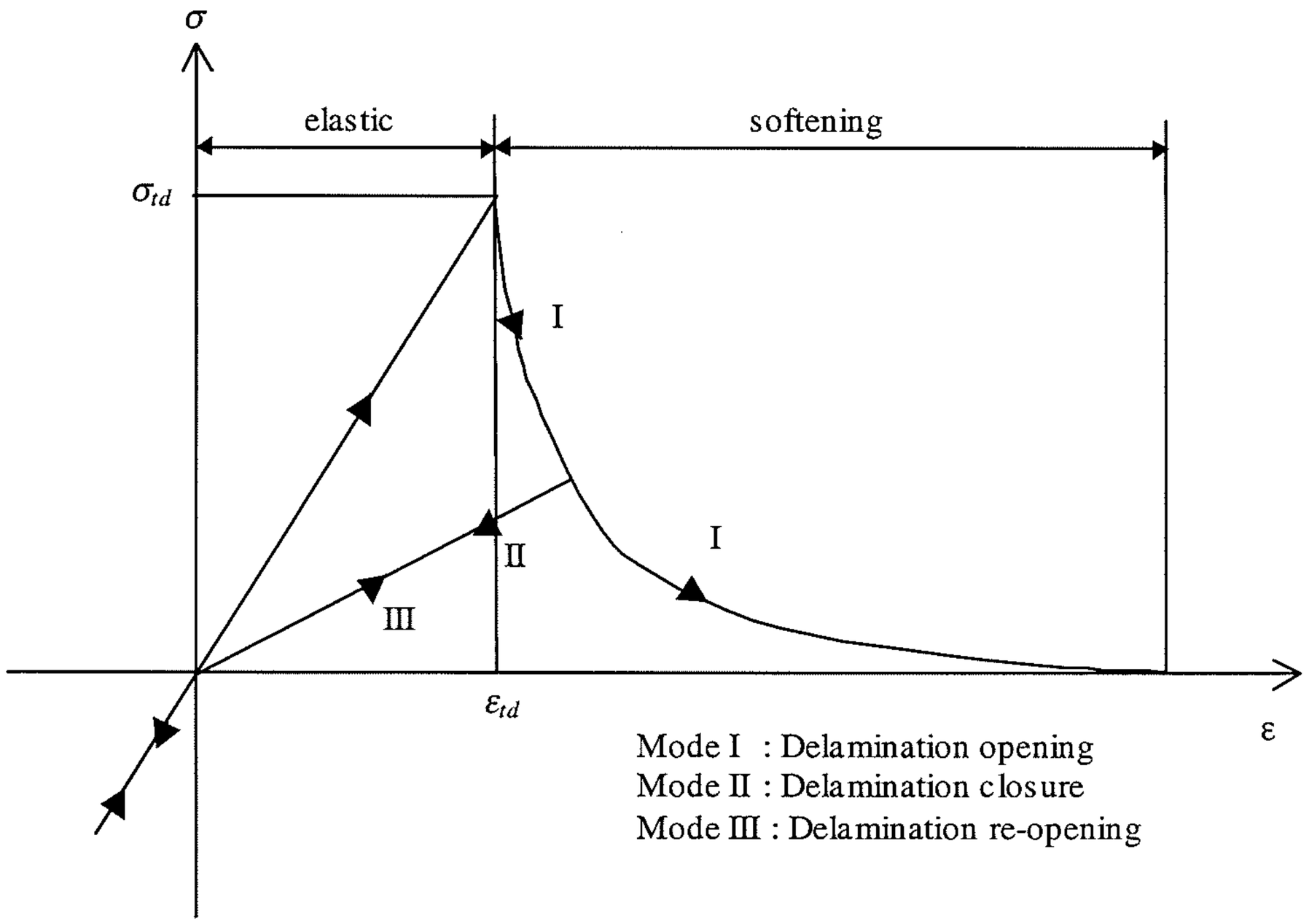

Fig 7.4.4.2-1 The effective stress-strain behaviour and deformation modes of the matrix during tensile delamination.

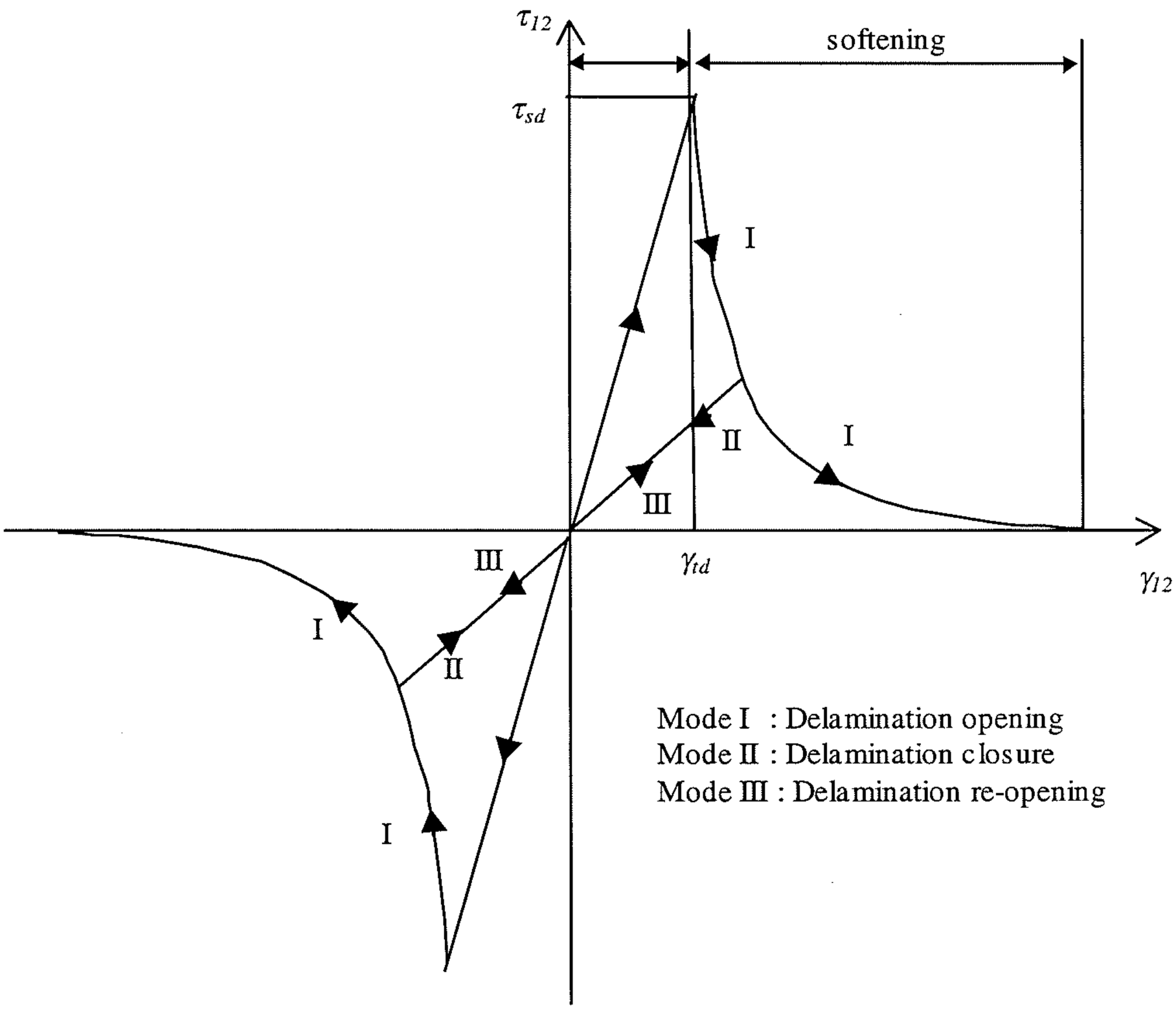

Fig 7.4.4.3-1 The effective shear stress-strain behaviour and deformation modes of the

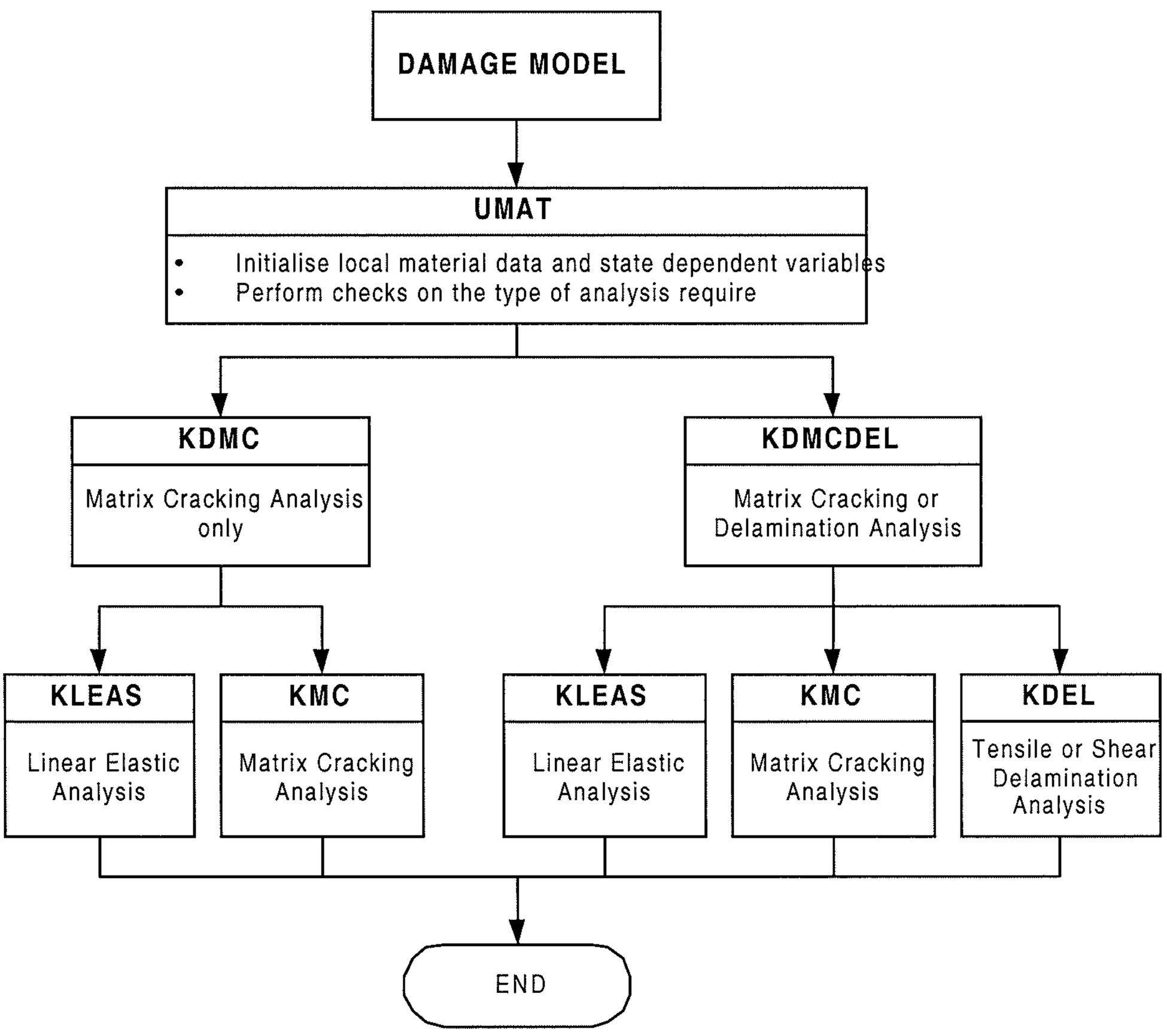

Fig 7.5.1-1

Flow diagram of the general computation algorithm of the Damage Model.

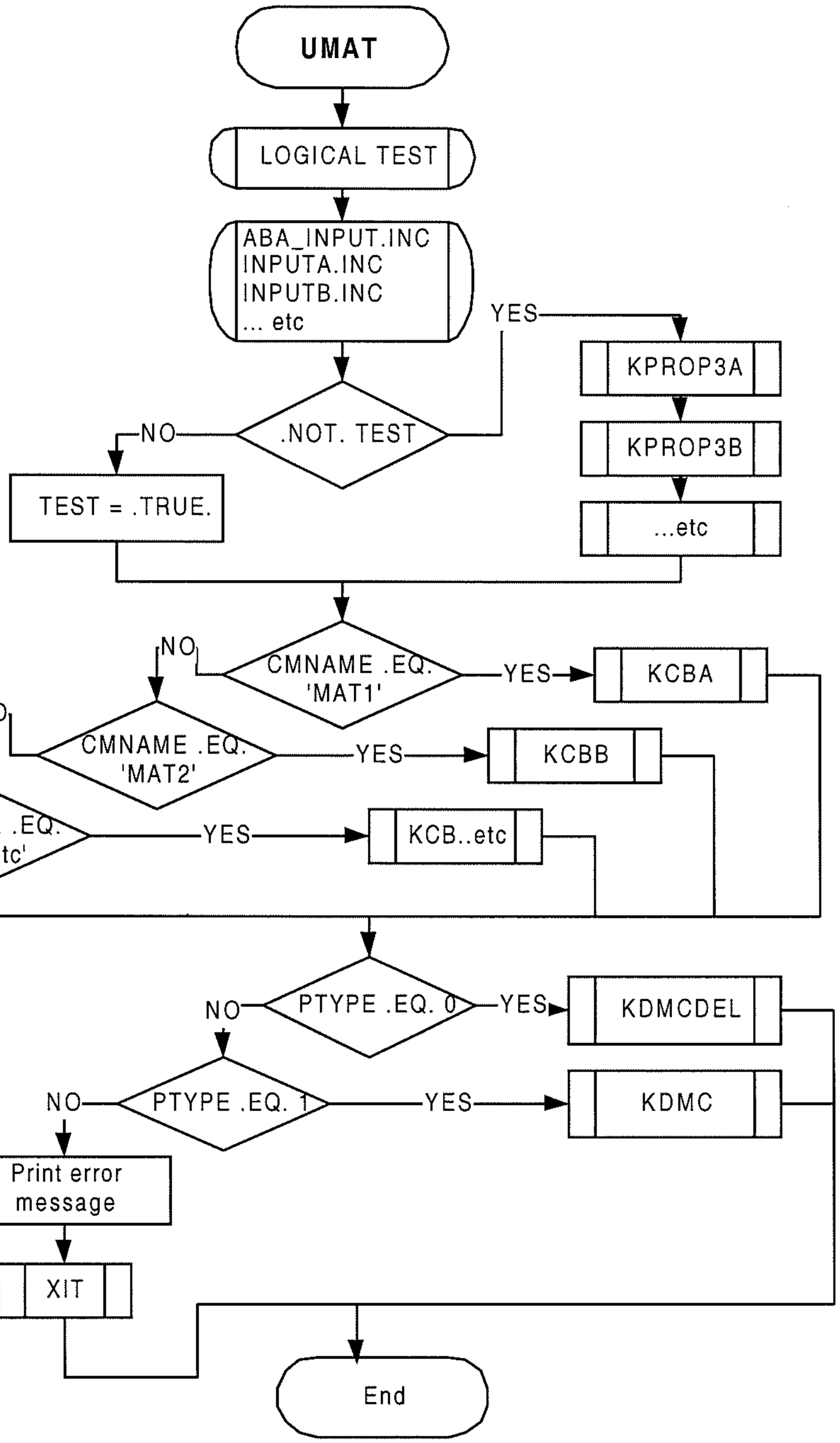

Fig, 7.5.1-2 Flow diagram of the subroutine UMAT.

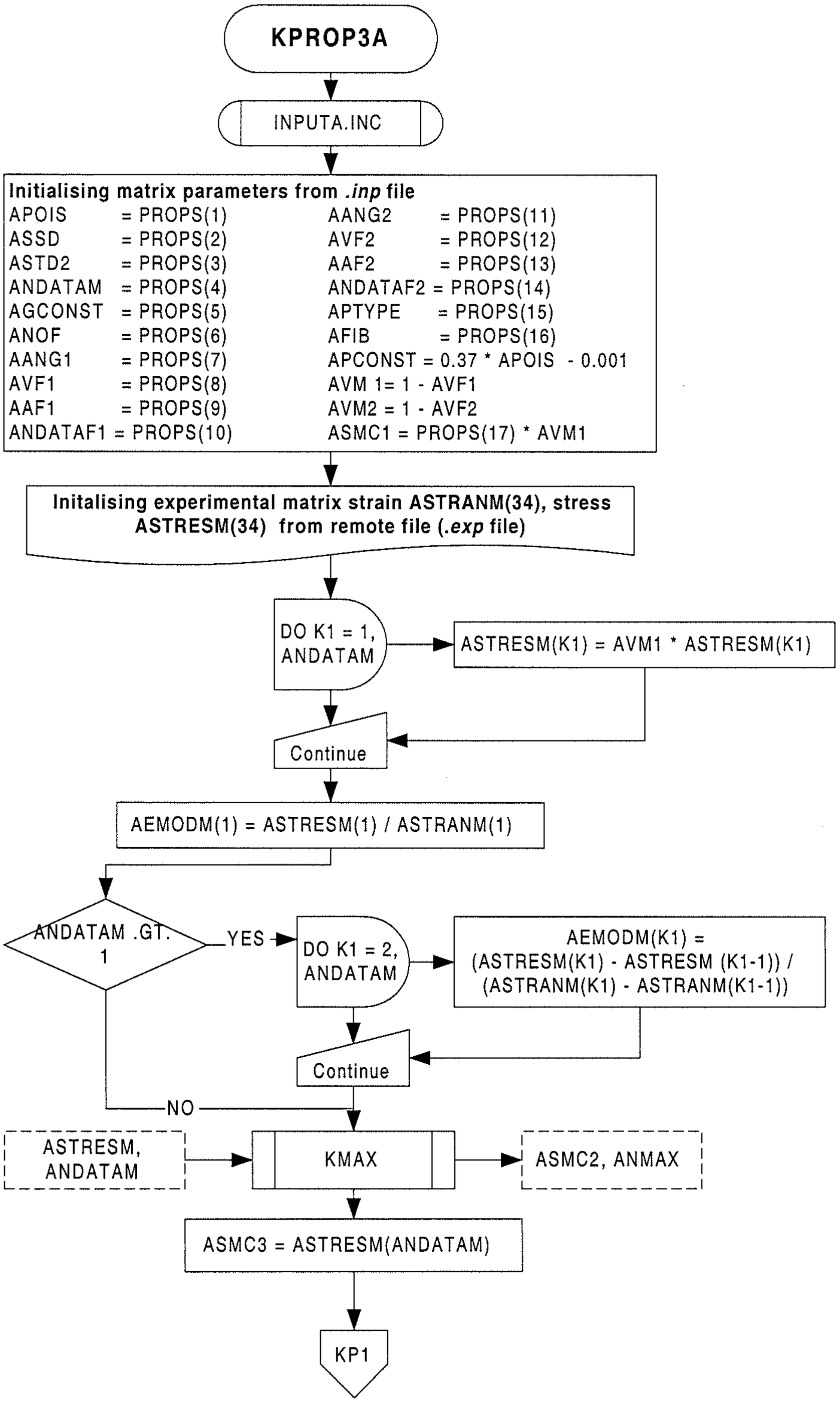

Fig, 7.5.1-3a Flow diagram of the subroutine KPROP3A (part1/2)

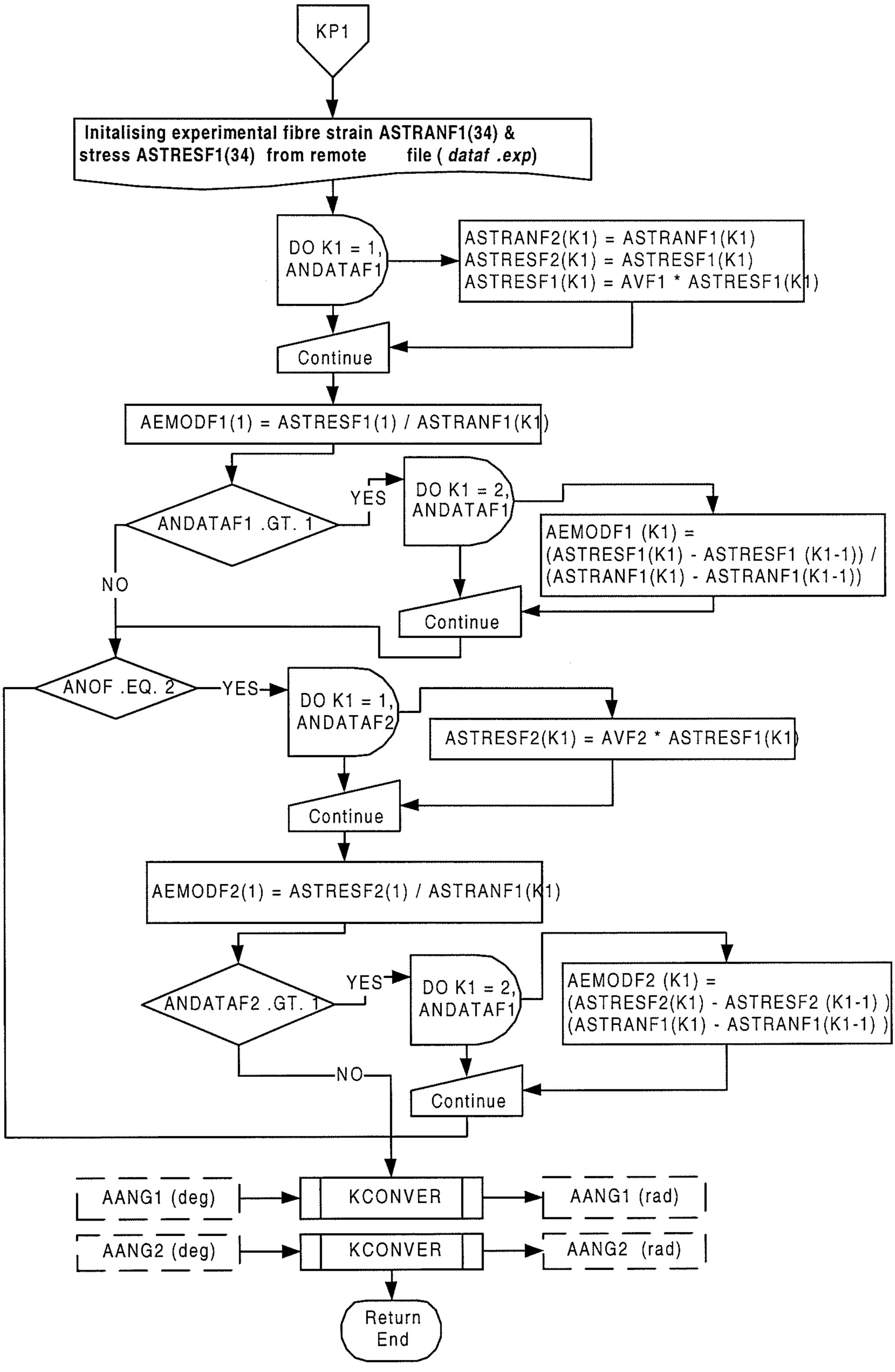
KP1
Initalising experimental fibre strain ASTRANF1(34) & stress ASTRESF1(34) from remote file (dataf .exp)
DO K1 = 1, ANDATAF1
ASTRANF2(K1) = ASTRANF1(K1)
ASTRESF2(K1) = ASTRESF1(K1)
ASTRESF1(K1) = AVF1 * ASTRESF1(K1)
Continue
AEMODF1(1) = ASTRESF1(1) / ASTRANF1(K1)
ANDATAF1 .GT. 1
YES
DO K1 = 2, ANDATAF1
AEMODF1 (K1) = (ASTRESF1(K1) - ASTRESF1 (K1-1)) / (ASTRANF1(K1) - ASTRANF1(K1-1))
Continue
NO
ANOF .EQ. 2
YES
DO K1 = 1, ANDATAF2
ASTRESF2(K1) = AVF2 * ASTRESF1(K1)
Continue
AEMODF2(1) = ASTRESF2(1) / ASTRANF1(K1)
ANDATAF2 .GT. 1
YES
DO K1 = 2, ANDATAF1
AEMODF2 (K1) = (ASTRESF2(K1) - ASTRESF2 (K1-1)) / (ASTRANF1(K1) - ASTRANF1(K1-1))
Continue
NO
AANG1 (deg)
KCONVER
AANG1 (rad)
AANG2 (deg)
KCONVER
AANG2 (rad)
Return End

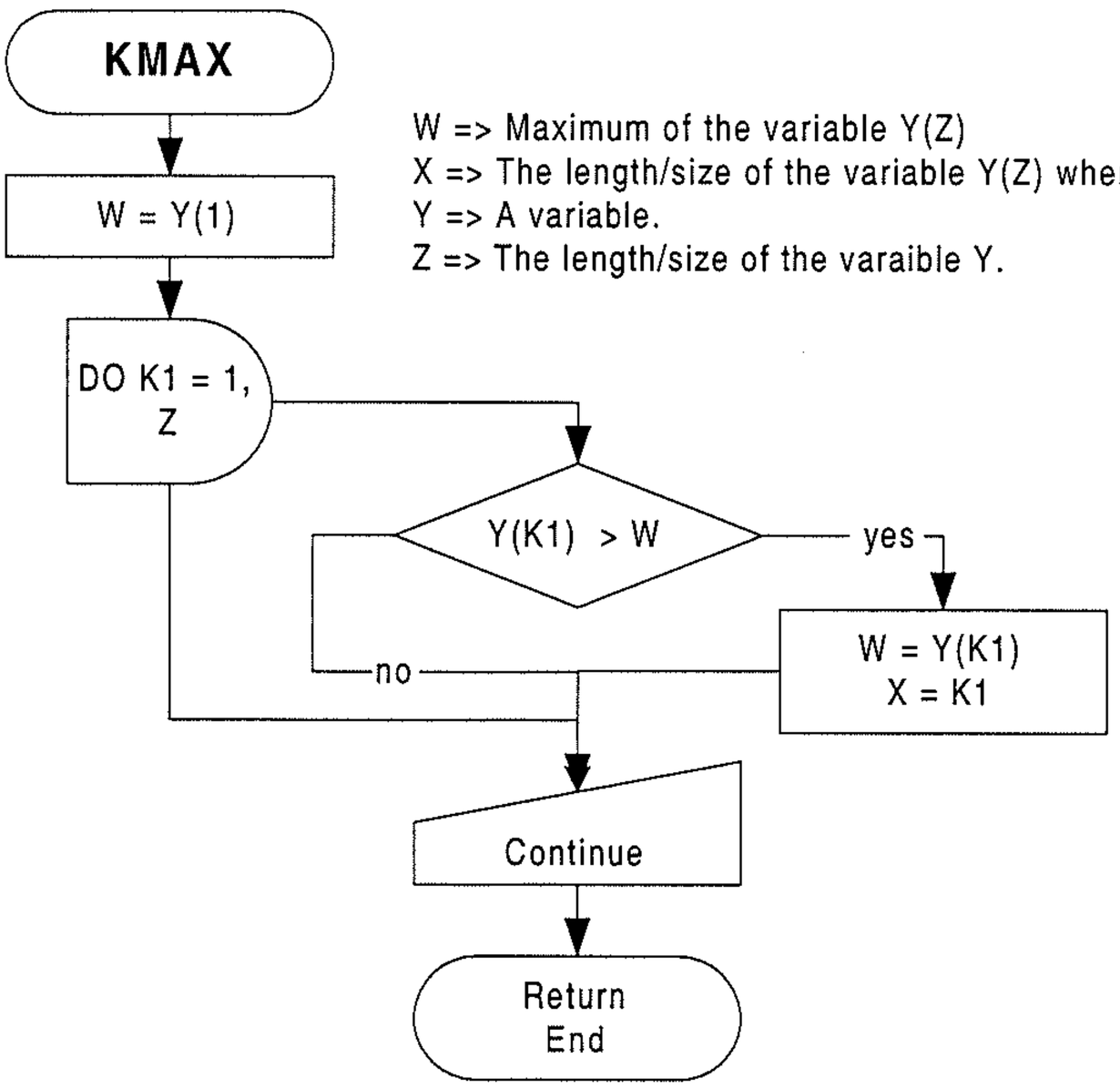

Fig 7.5.1-4 Flow diagram of subroutine KMAX

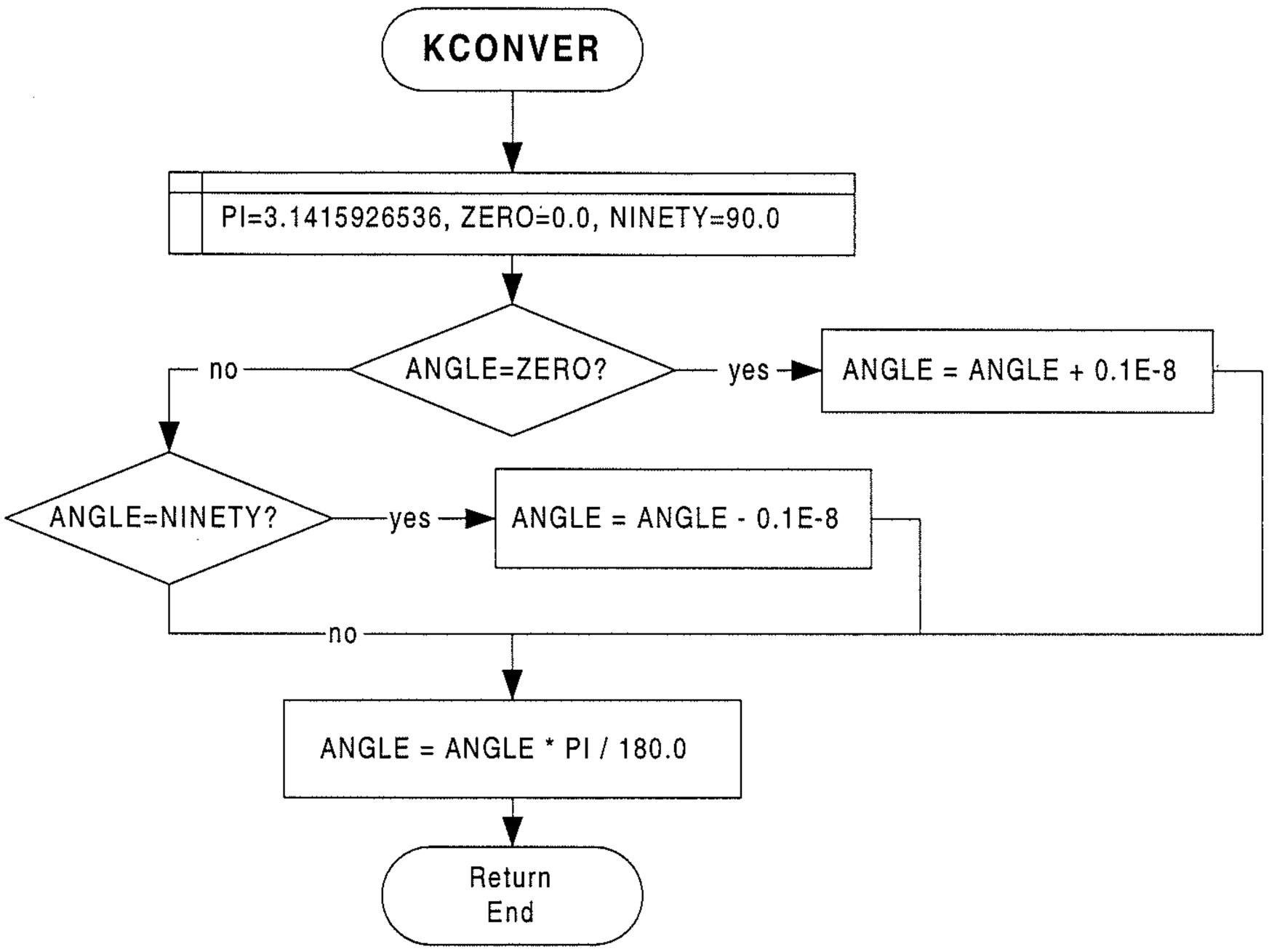

Fig 7.5.1-5 Flow diagram of subroutine KCONVER

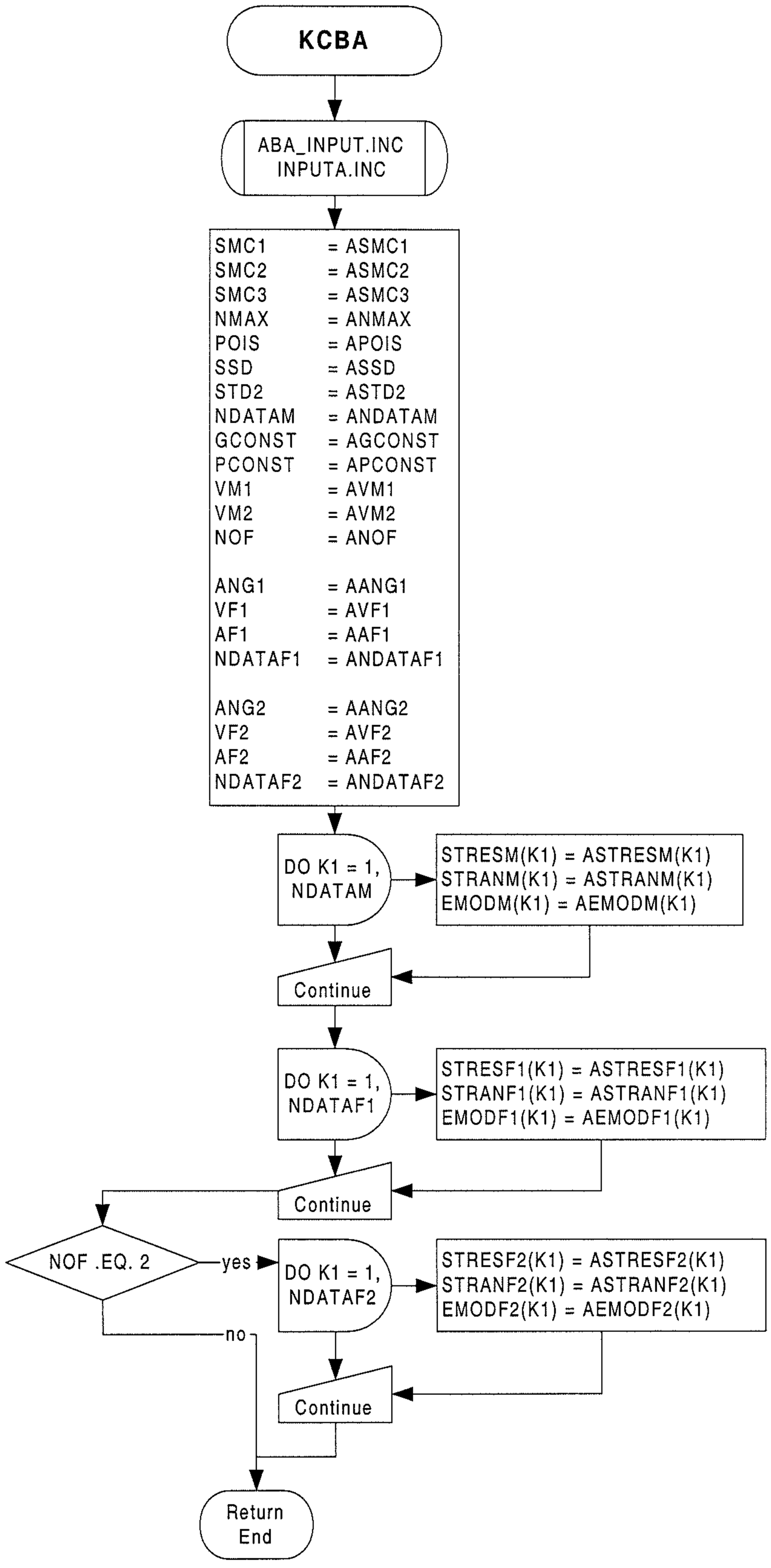
KCBA
ABA_INPUT.INC
INPUTA.INC
SMC1 = ASMC1
SMC2 = ASMC2
SMC3 = ASMC3
NMAX = ANMAX
POIS = APOIS
SSD = ASSD
STD2 = ASTD2
NDATAM = ANDATAM
GCONST = AGCONST
PCONST = APCONST
VM1 = AVM1
VM2 = AVM2
NOF = ANOF
ANG1 = AANG1
VF1 = AVF1
AF1 = AAF1
NDATAF1 = ANDATAF1
ANG2 = AANG2
VF2 = AVF2
AF2 = AAF2
NDATAF2 = ANDATAF2
DO K1 = 1, NDATAM
STRESM(K1) = ASTRESM(K1)
STRANM(K1) = ASTRANM(K1)
EMODM(K1) = AEMODM(K1)
Continue
DO K1 = 1, NDATAF1
STRESF1(K1) = ASTRESF1(K1)
STRANF1(K1) = ASTRANF1(K1)
EMODF1(K1) = AEMODF1(K1)
Continue
NOF .EQ. 2
yes
DO K1 = 1, NDATAF2
STRESF2(K1) = ASTRESF2(K1)
STRANF2(K1) = ASTRANF2(K1)
EMODF2(K1) = AEMODF2(K1)
no
Continue
Return
End

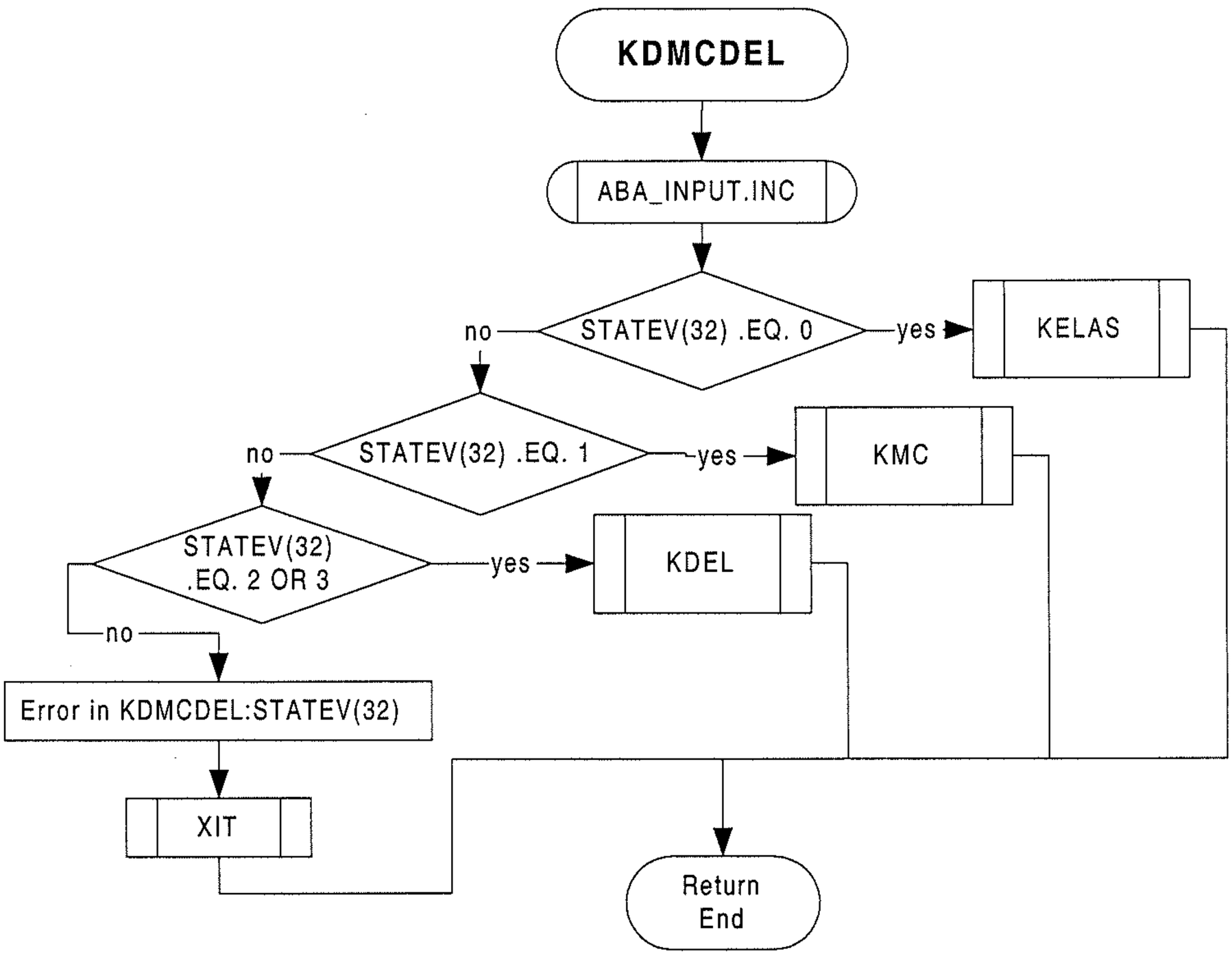

Fig 7.5.1-7 Flow diagram of subroutine KDMCDEL

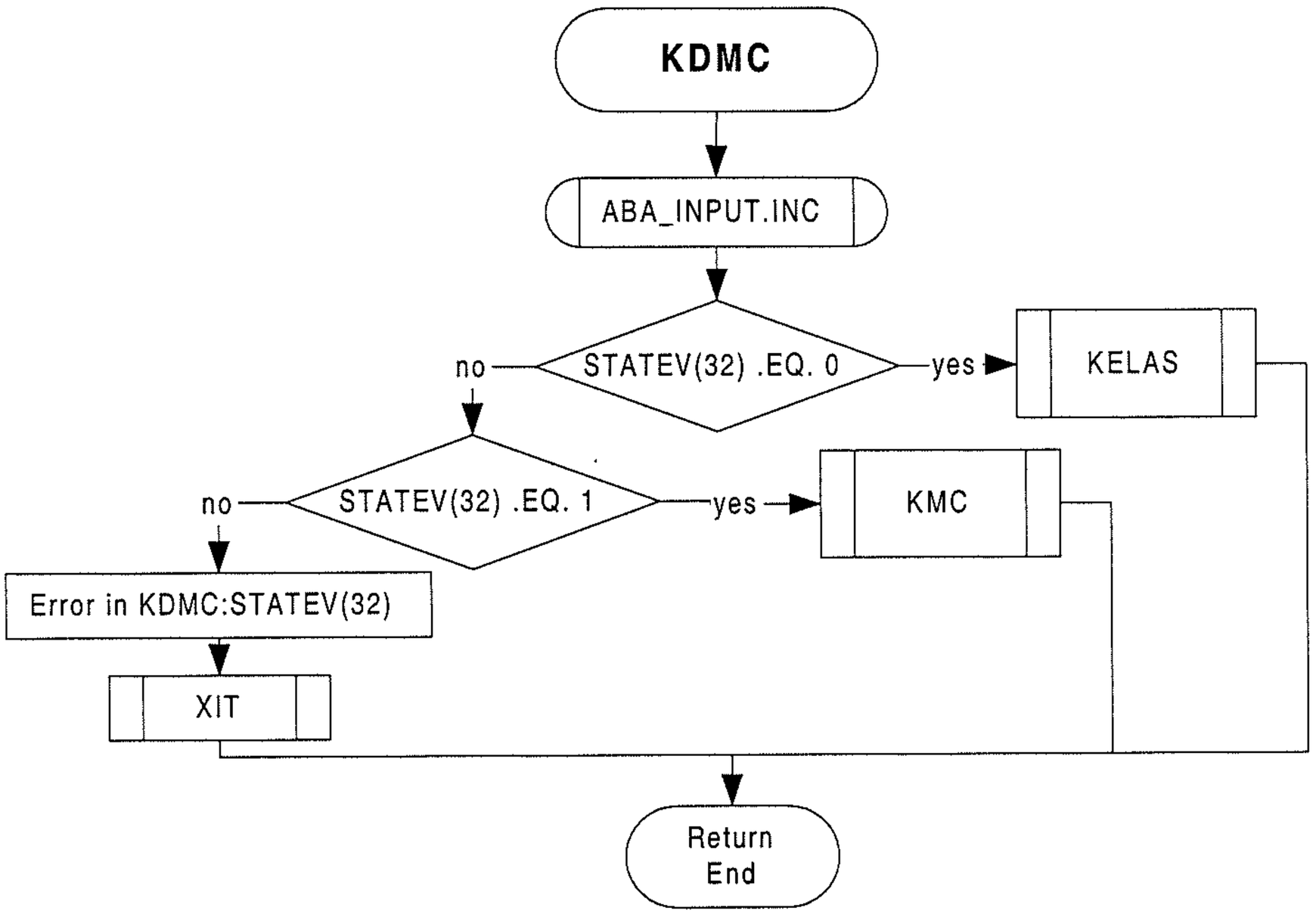

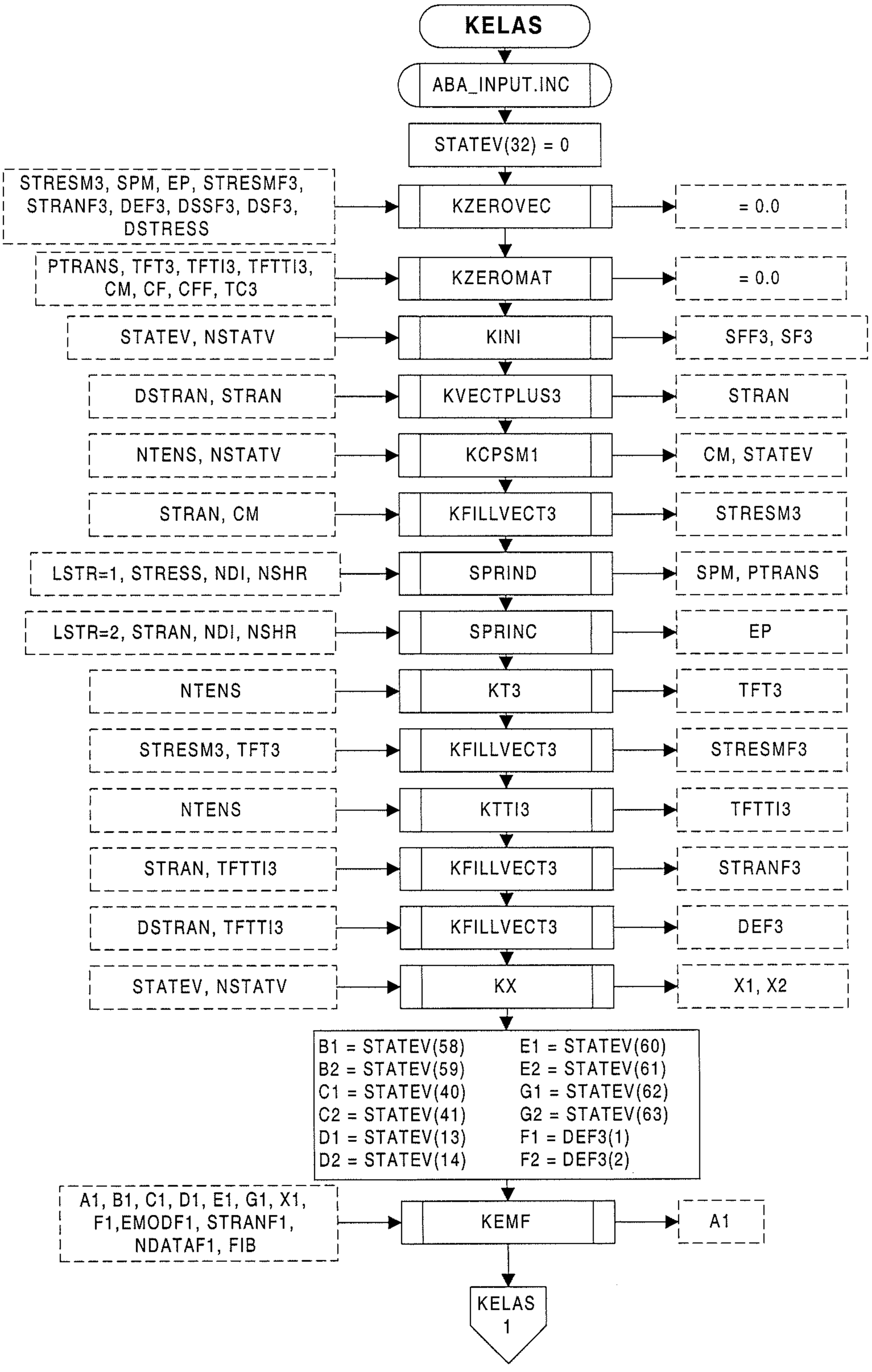

Fig 7.5.2-1a Flow diagram of the subroutine KELAS (Part 1/2)

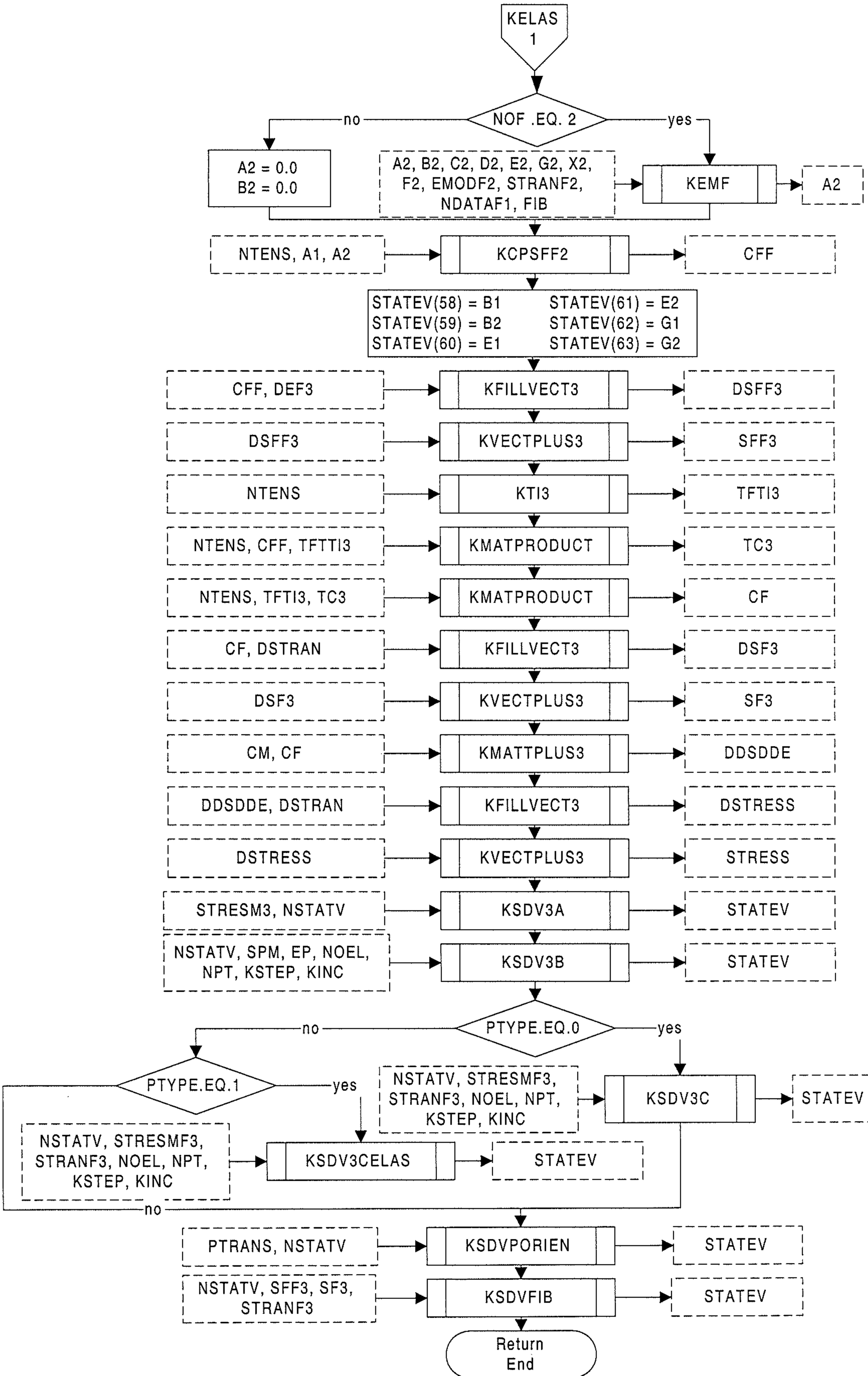
KELAS
1
NOF .EQ. 2
no
yes
A2 = 0.0
B2 = 0.0
A2, B2, C2, D2, E2, G2, X2,
F2, EMODF2, STRANF2,
NDATAF1, FIB
KEMF
A2
NTENS, A1, A2
KCPSFF2
CFF
STATEV(58) = B1
STATEV(59) = B2
STATEV(60) = E1
STATEV(61) = E2
STATEV(62) = G1
STATEV(63) = G2
CFF, DEF3
KFILLVECT3
DSFF3
DSFF3
KVECTPLUS3
SFF3
NTENS
KTI3
TFTI3
NTENS, CFF, TFTTI3
KMATPRODUCT
TC3
NTENS, TFTI3, TC3
KMATPRODUCT
CF
CF, DSTRAN
KFILLVECT3
DSF3
DSF3
KVECTPLUS3
SF3
CM, CF
KMATTPLUS3
DDSDDE
DDSDDE, DSTRAN
KFILLVECT3
DSTRESS
DSTRESS
KVECTPLUS3
STRESS
STRESM3, NSTATV
KSDV3A
STATEV
NSTATV, SPM, EP, NOEL,
NPT, KSTEP, KINC
KSDV3B
STATEV
PTYPE.EQ.0
no
yes
PTYPE.EQ.1
yes
NSTATV, STRESMF3,
STRANF3, NOEL, NPT,
KSTEP, KINC
KSDV3C
STATEV
NSTATV, STRESMF3,
STRANF3, NOEL, NPT,
KSTEP, KINC
KSDV3CELAS
STATEV
no
PTRANS, NSTATV
KSDVPORIEN
STATEV
NSTATV, SFF3, SF3,
STRANF3
KSDVFIB
STATEV
Return
End

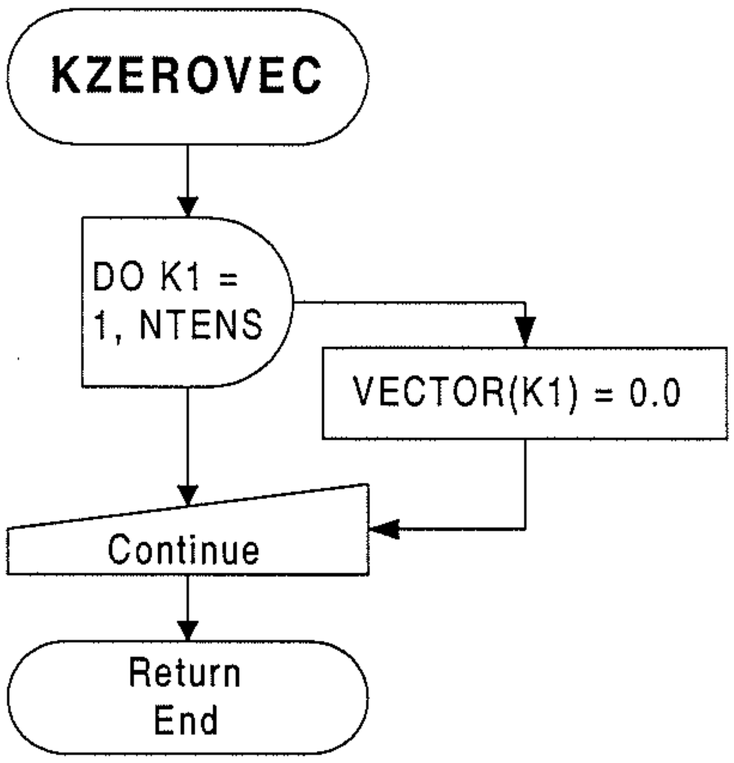

Fig 7.5.2-2
Flow diagram of subroutine KZEROVEC

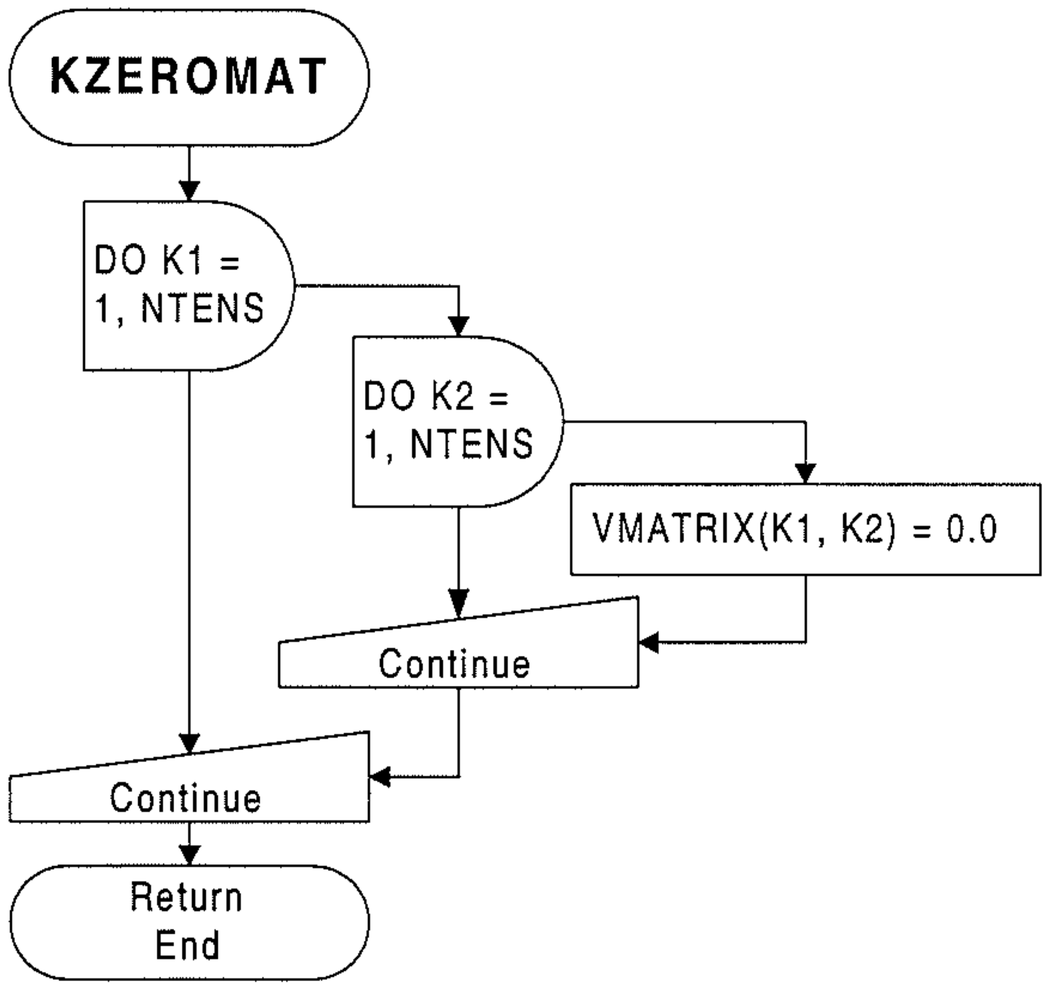

Fig 7.5.2-3
Flow diagram of subroutine KZEROMAT

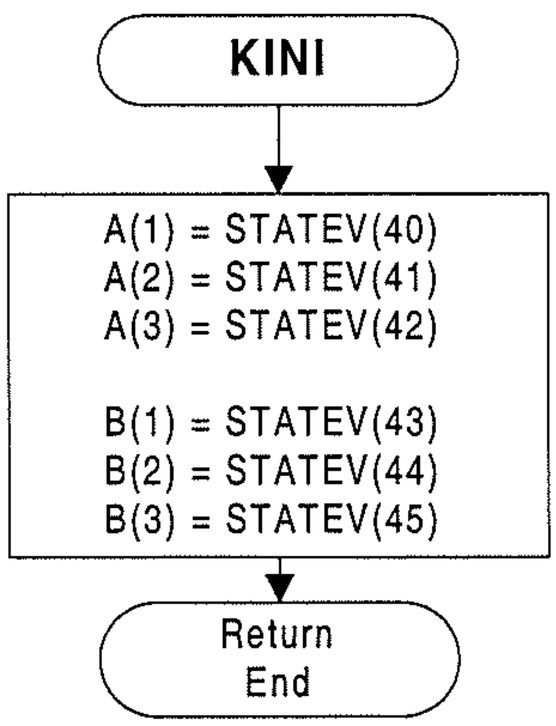

Fig 7.5.2-5
Flow diagram of subroutine KINI

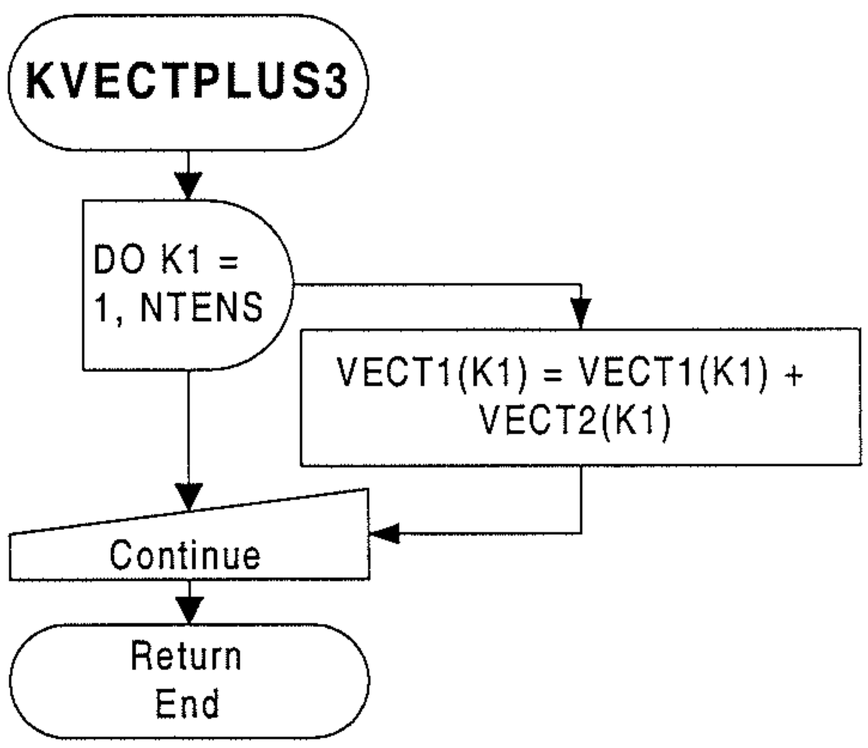

Fig 7.5.2-5
Flow diagram of subroutine KVECTPLUS3

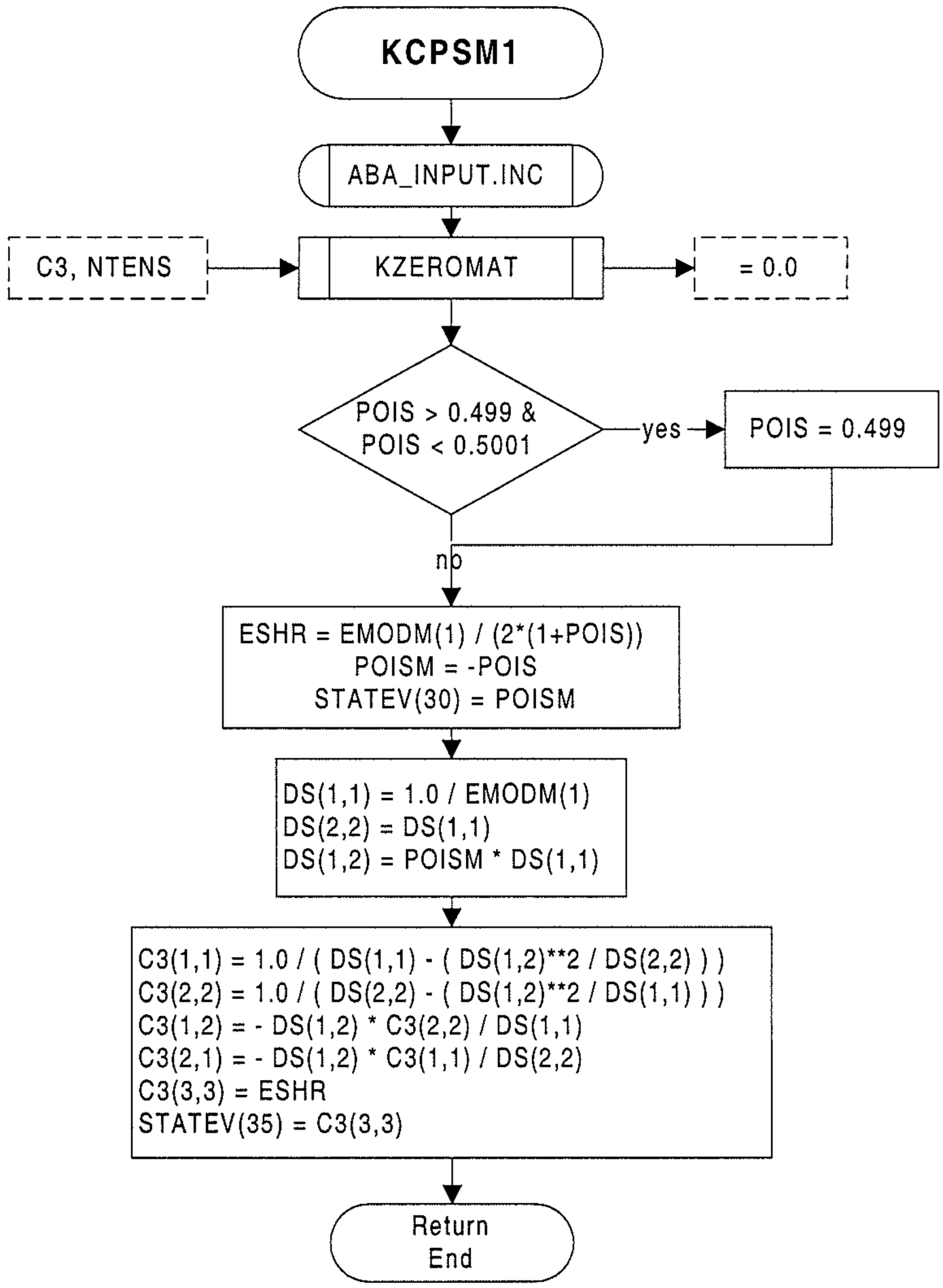

Fig 7.5.2-6 Flow diagram of subroutine KCPSM1

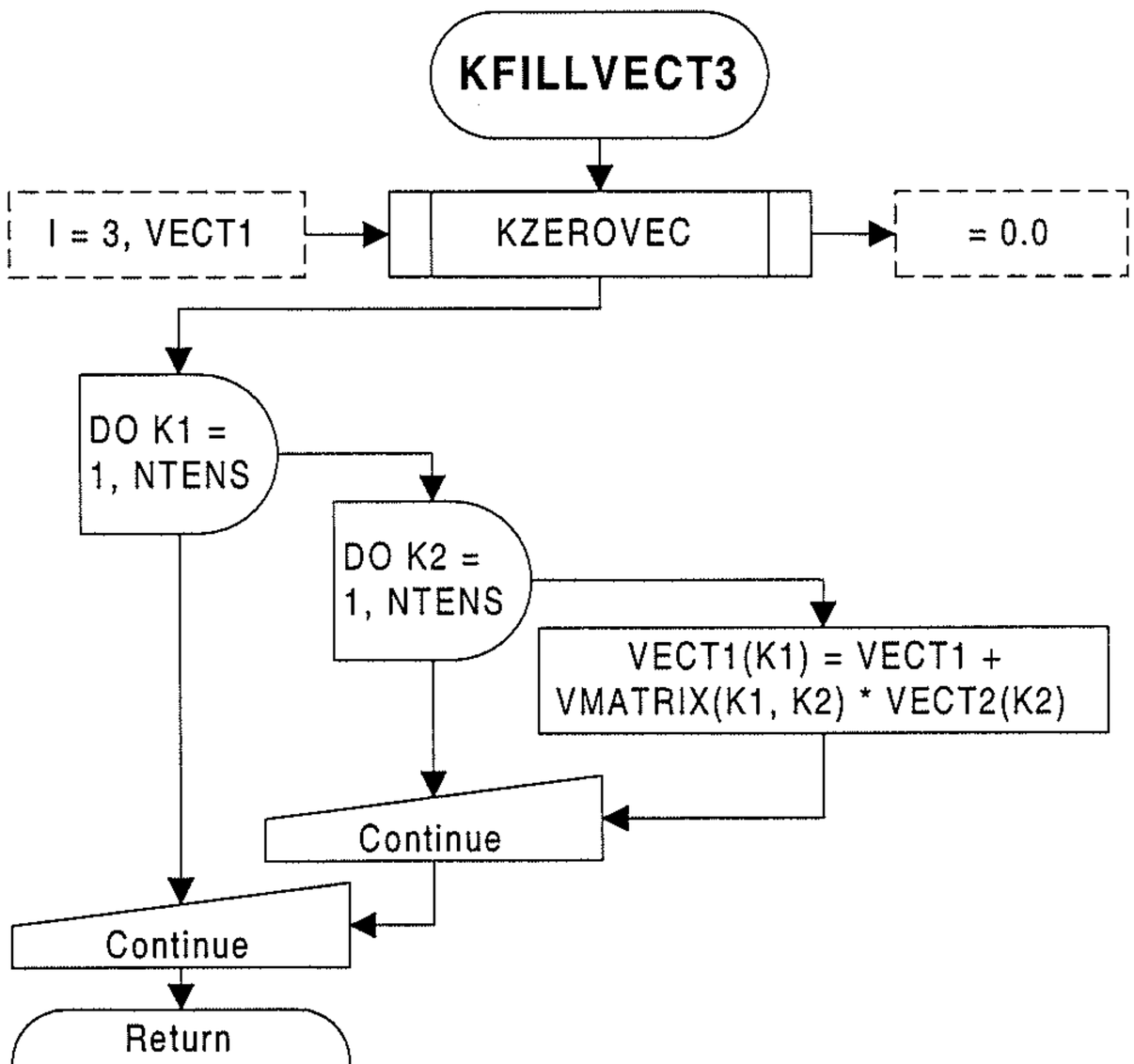

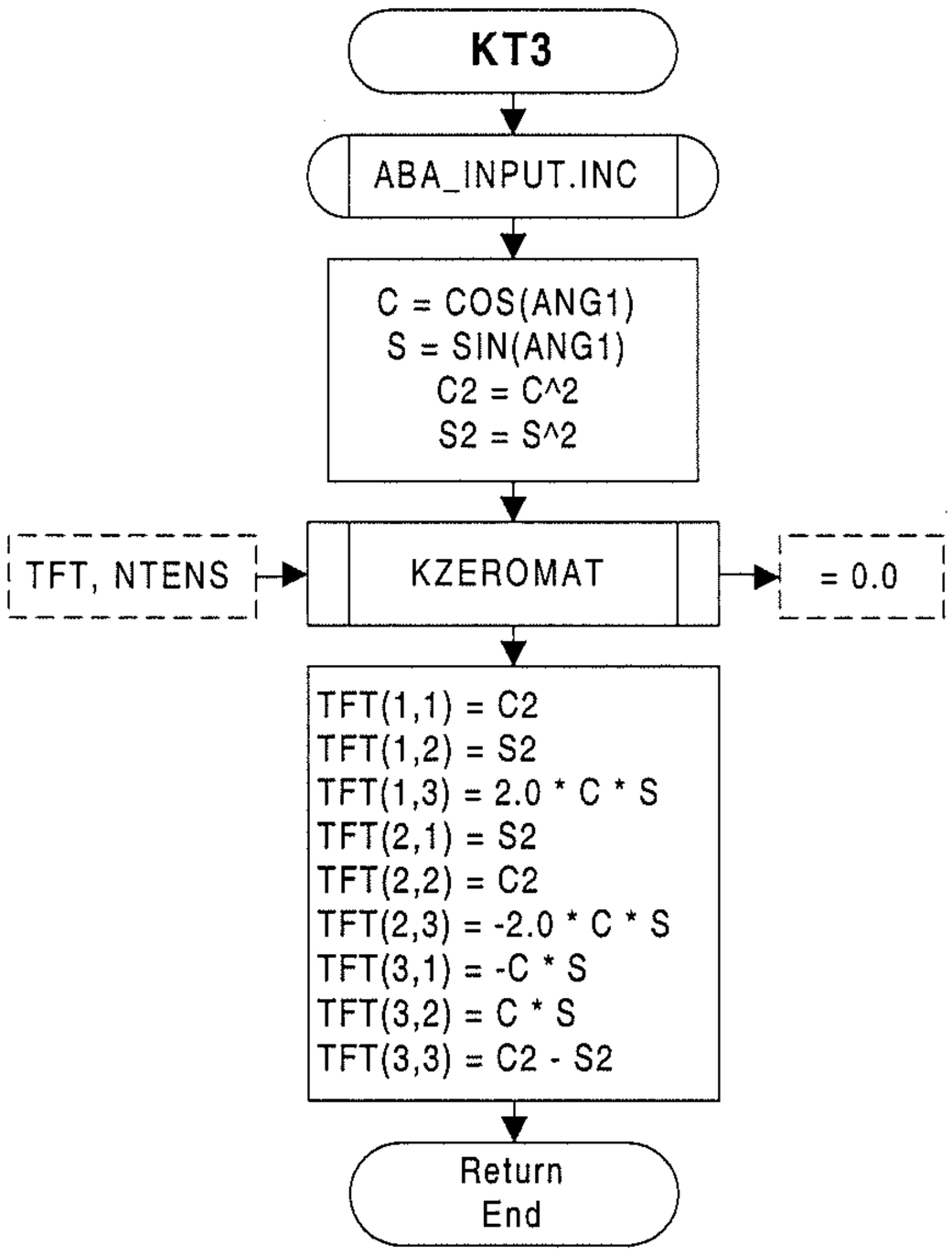

Fig 7.5.2-8
Flow diagram of subroutine KT3

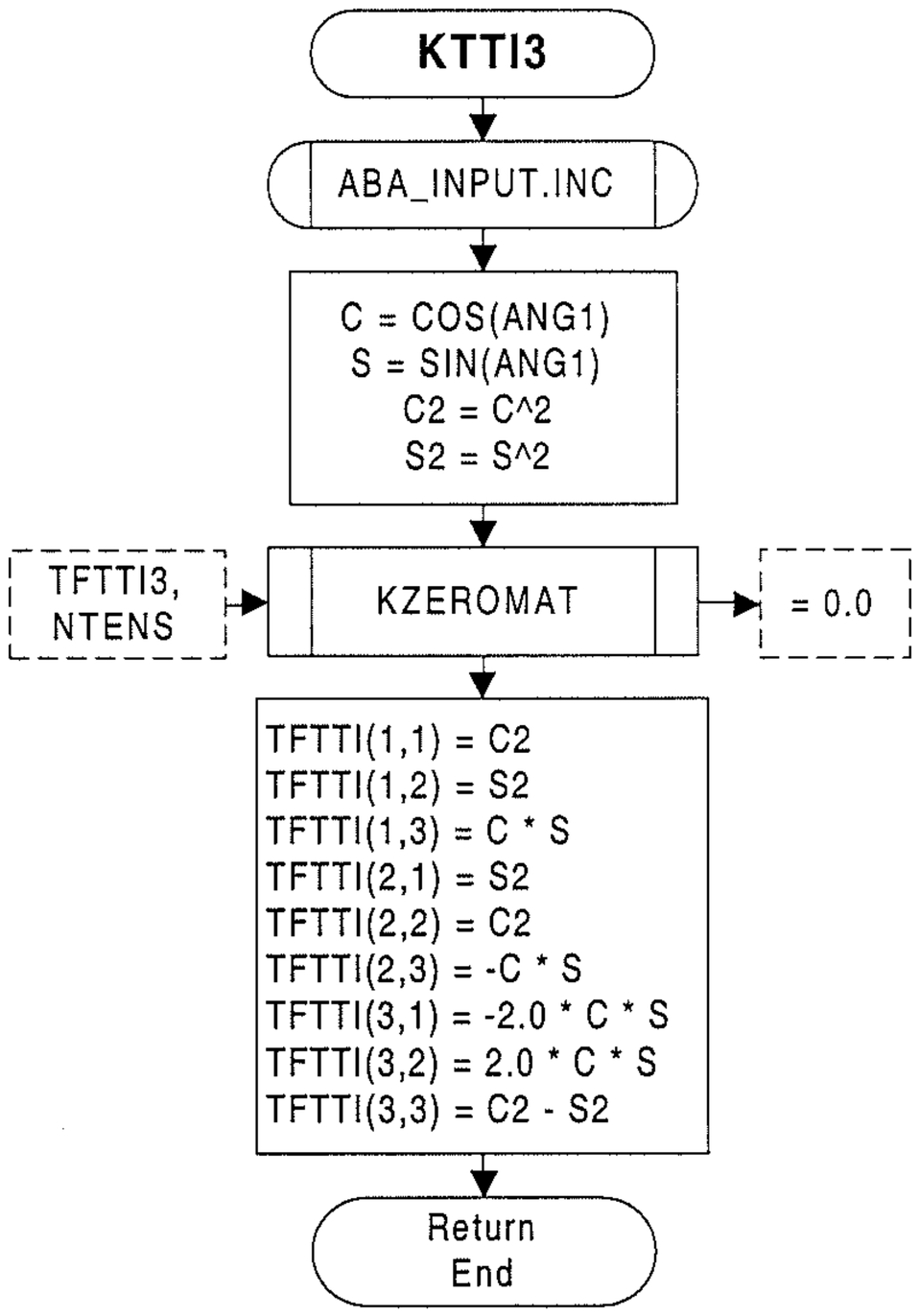

Fig 7.5.2-9
Flow diagram of subroutine KTTI3

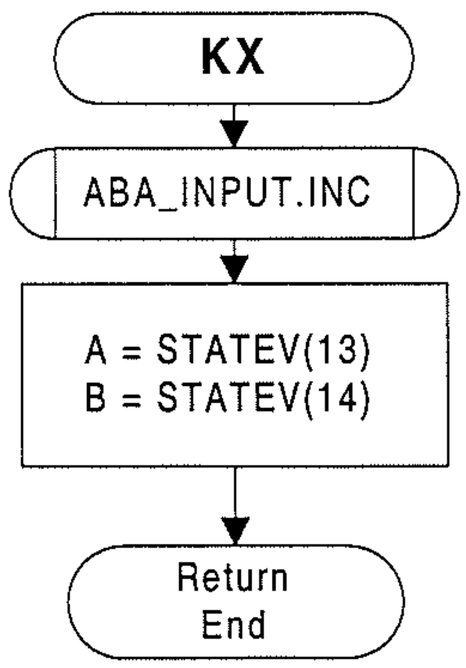

Fig 7.5.2-10 Flow diagram of subroutine KX

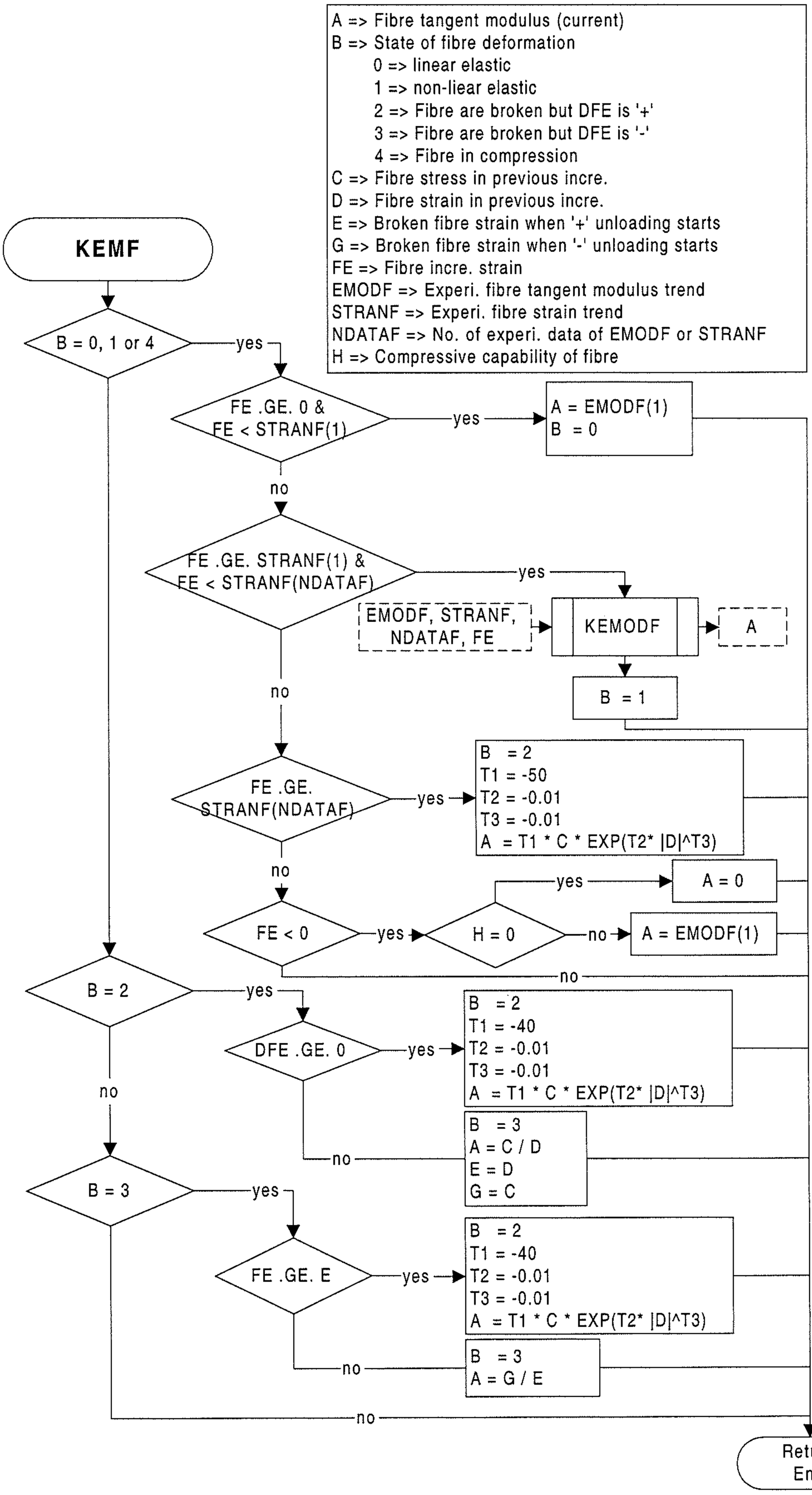
A => Fibre tangent modulus (current)
B => State of fibre deformation
0 => linear elastic
1 => non-liear elastic
2 => Fibre are broken but DFE is '+'
3 => Fibre are broken but DFE is '-'
4 => Fibre in compression
C => Fibre stress in previous incre.
D => Fibre strain in previous incre.
E => Broken fibre strain when '+' unloading starts
G => Broken fibre strain when '-' unloading starts
FE => Fibre incre. strain
EMODF => Experi. fibre tangent modulus trend
STRANF => Experi. fibre strain trend
NDATAF => No. of experi. data of EMODF or STRANF
H => Compressive capability of fibre
KEMF
B = 0, 1 or 4
yes
FE .GE. 0 & FE < STRANF(1)
yes
A = EMODF(1)
B = 0
no
FE .GE. STRANF(1) & FE < STRANF(NDATAF)
yes
EMODF, STRANF, NDATAF, FE
KEMODF
A
B = 1
no
FE .GE. STRANF(NDATAF)
yes
B = 2
T1 = -50
T2 = -0.01
T3 = -0.01
A = T1 * C * EXP(T2* |D|^T3)
no
FE < 0
yes
H = 0
yes
A = 0
no
A = EMODF(1)
no
B = 2
yes
DFE .GE. 0
yes
B = 2
T1 = -40
T2 = -0.01
T3 = -0.01
A = T1 * C * EXP(T2* |D|^T3)
no
B = 3
A = C / D
E = D
G = C
no
B = 3
yes
FE .GE. E
yes
B = 2
T1 = -40
T2 = -0.01
T3 = -0.01
A = T1 * C * EXP(T2* |D|^T3)
no
B = 3
A = G / E
no
Return
End

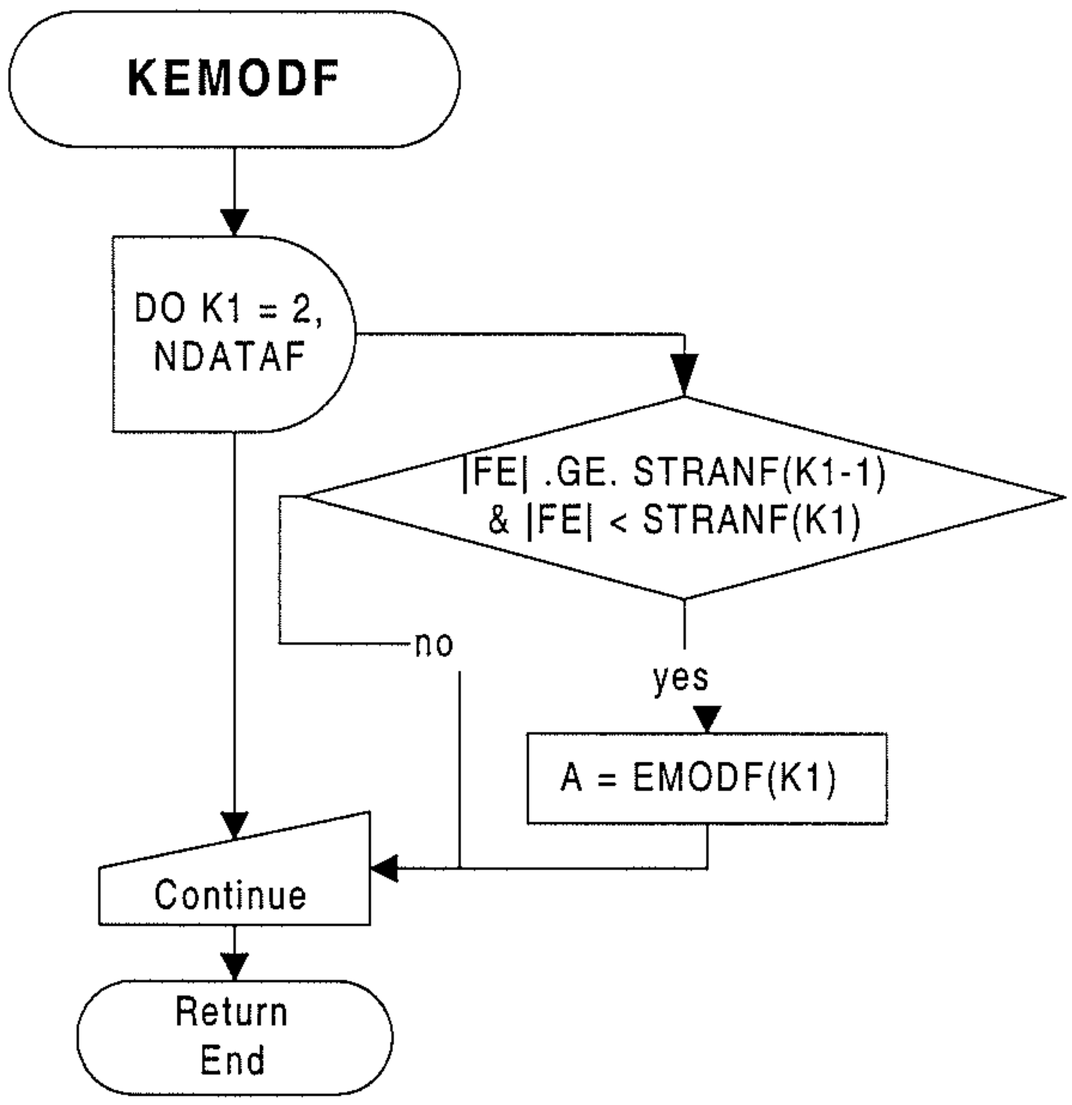

Fig 7.5.2-12
Flow diagram of subroutine KEMODF

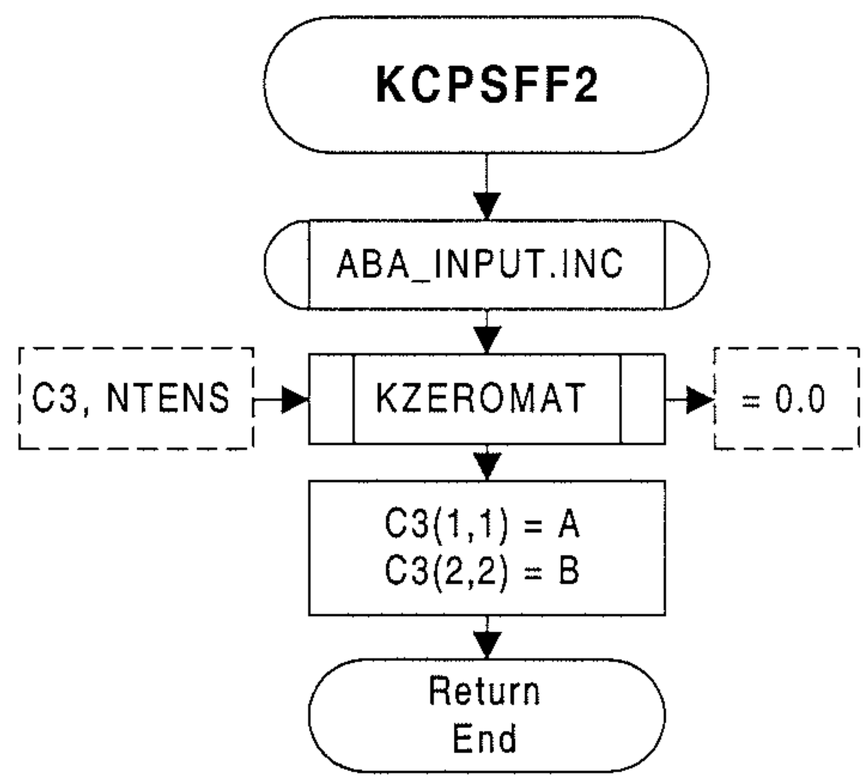

Fig 7.5.2-13
Flow diagram of subroutine KCPSFF2

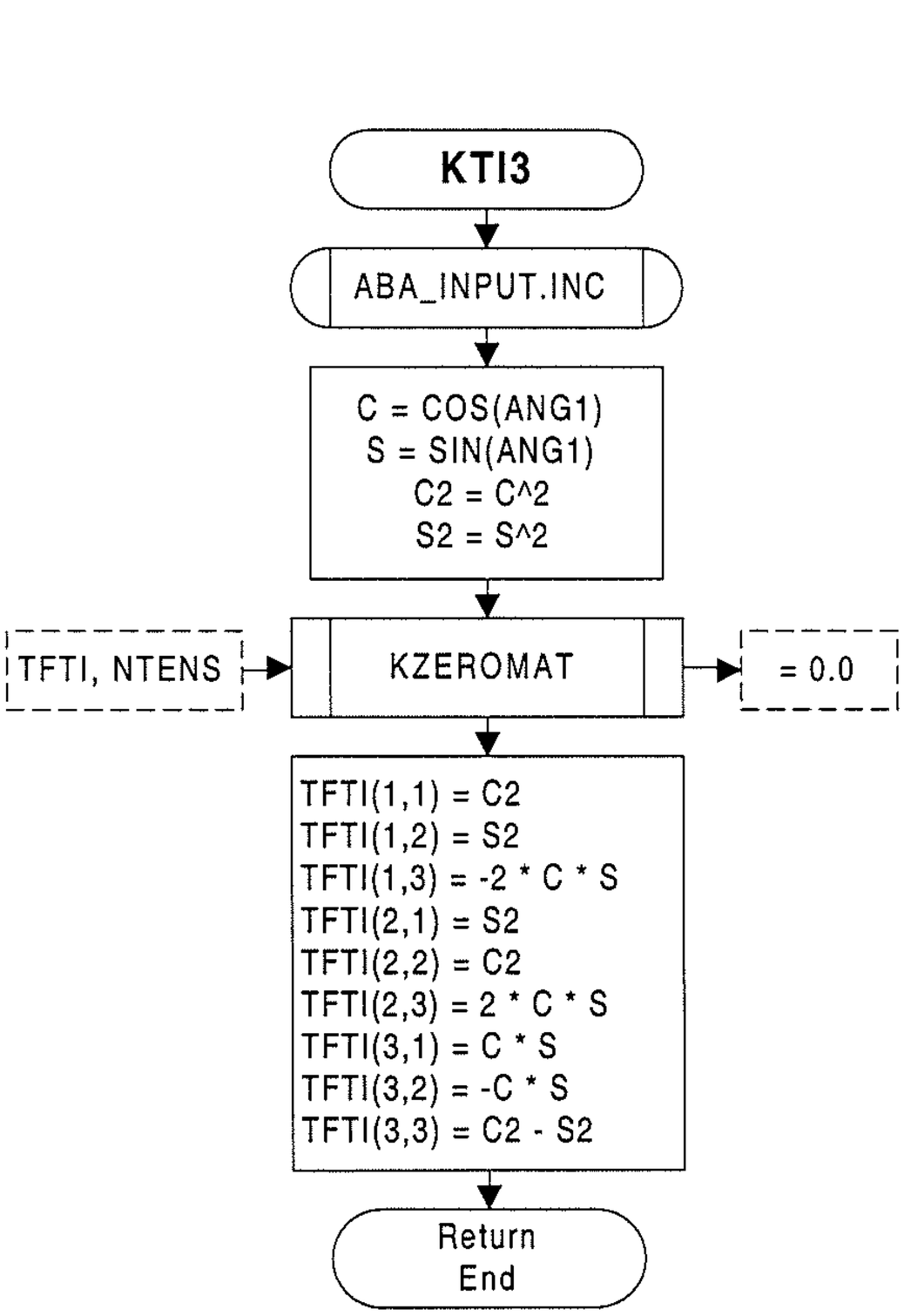

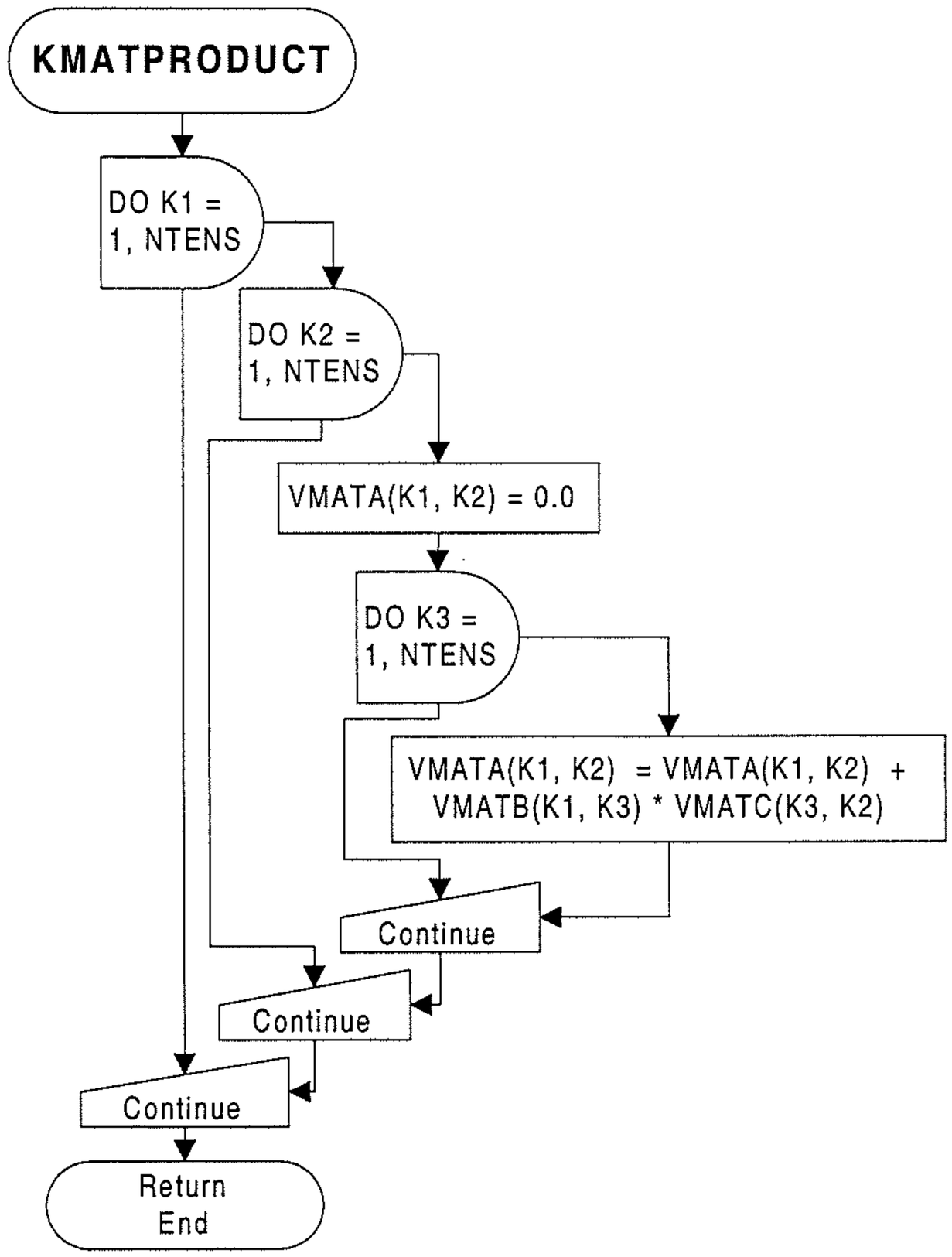

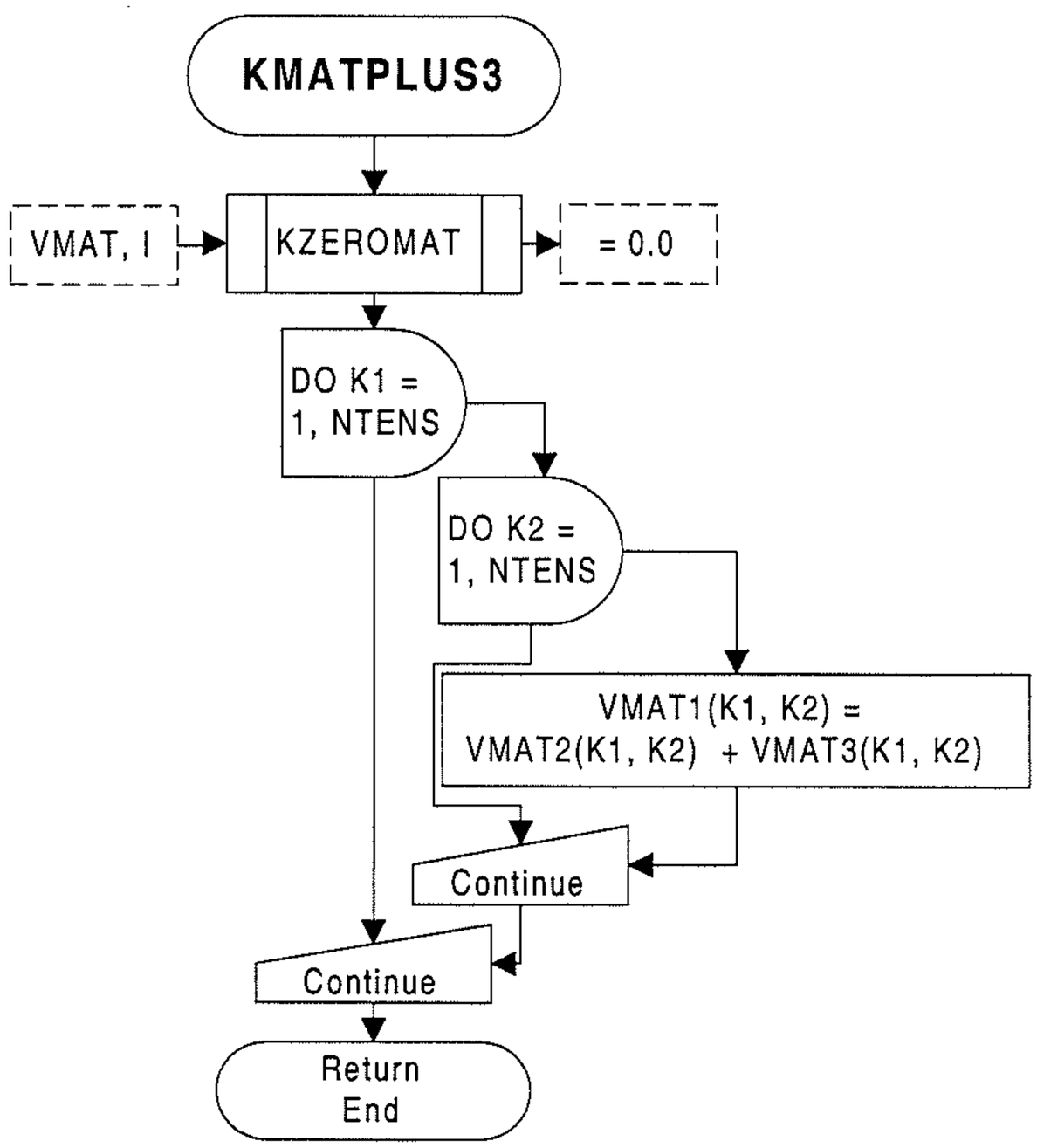

Fig 7.5.2-16
Flow diagram of subroutine KMATPLUS3

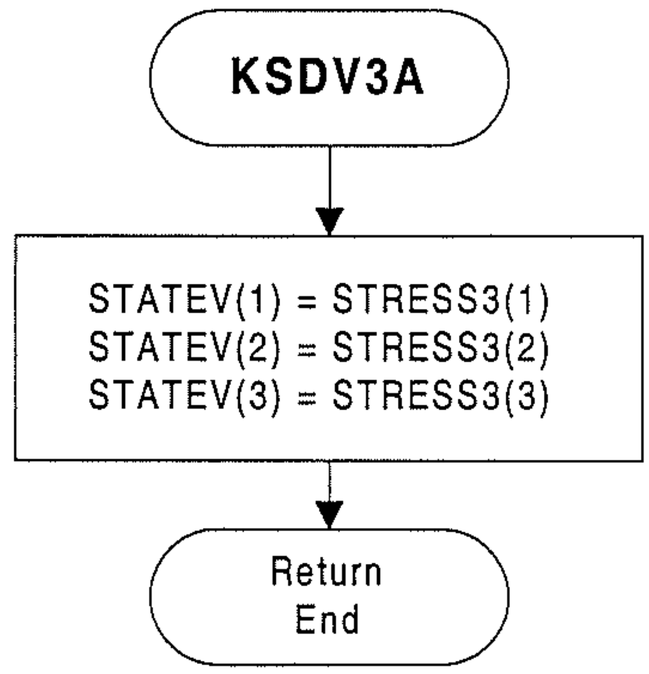

Fig 7.5.2-17
Flow diagram of subroutine KSDVA

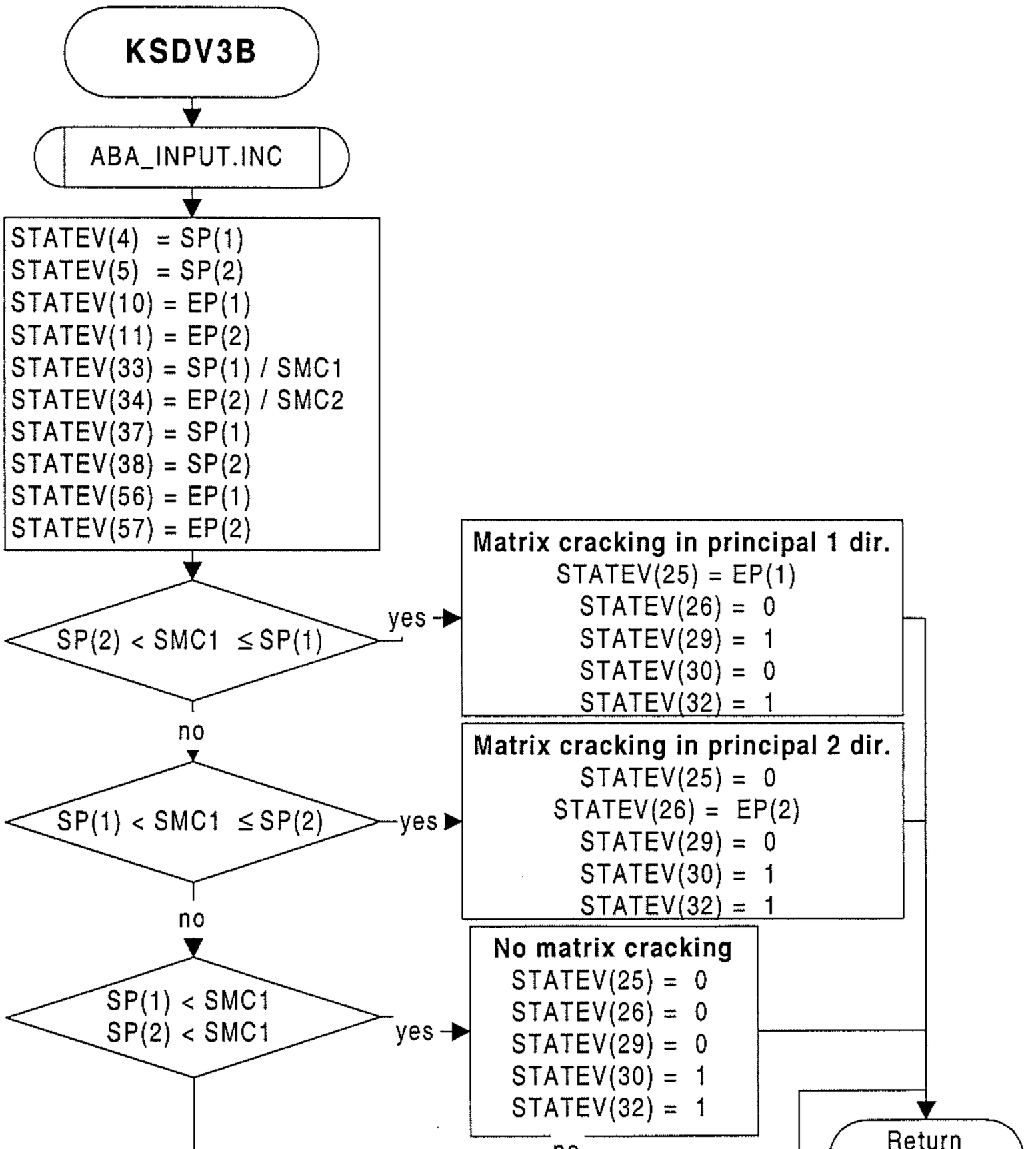

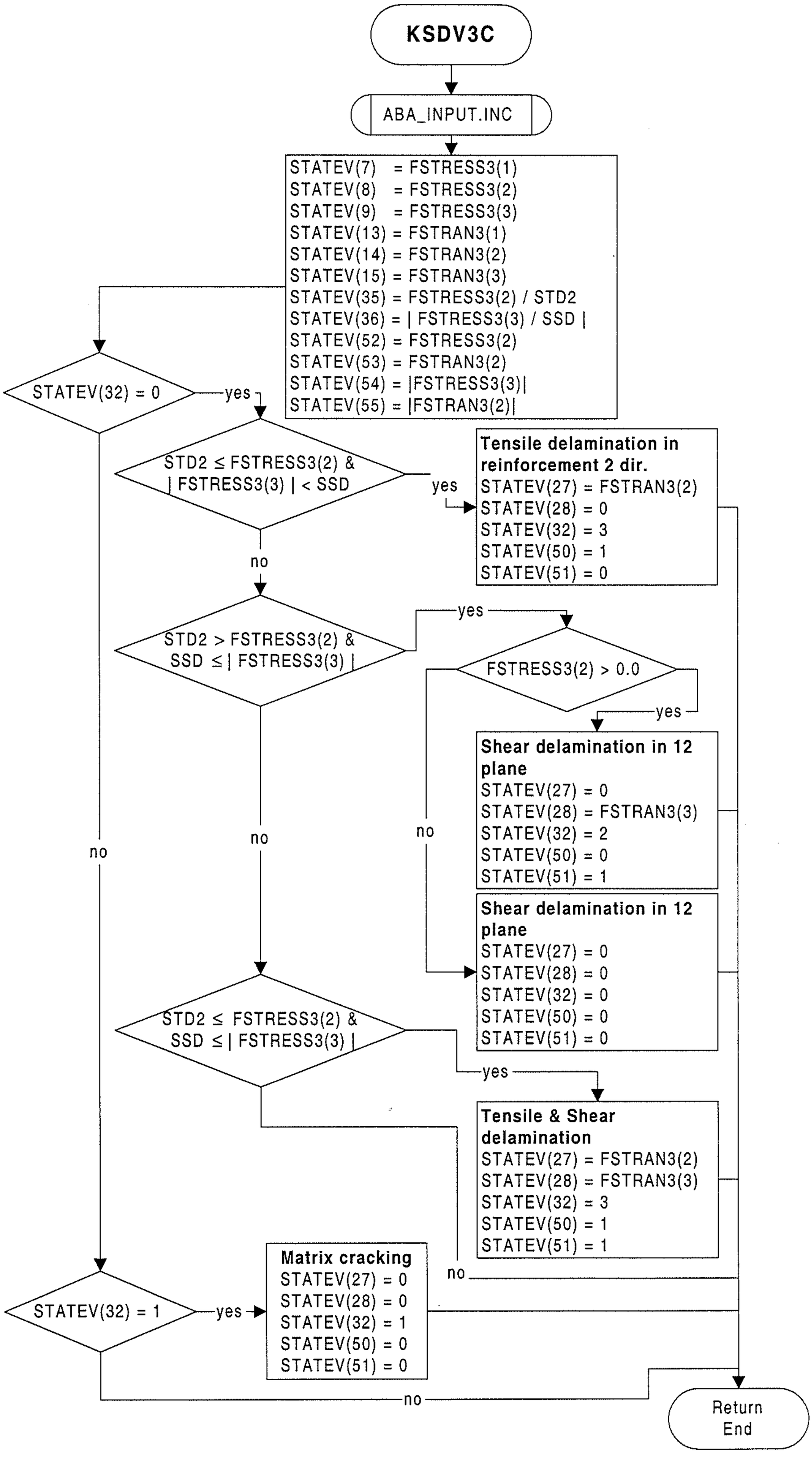
KSDV3C
ABA_INPUT.INC
STATEV(7) = FSTRESS3(1)
STATEV(8) = FSTRESS3(2)
STATEV(9) = FSTRESS3(3)
STATEV(13) = FSTRAN3(1)
STATEV(14) = FSTRAN3(2)
STATEV(15) = FSTRAN3(3)
STATEV(35) = FSTRESS3(2) / STD2
STATEV(36) = | FSTRESS3(3) / SSD |
STATEV(52) = FSTRESS3(2)
STATEV(53) = FSTRAN3(2)
STATEV(54) = |FSTRESS3(3)|
STATEV(55) = |FSTRAN3(2)|
STATEV(32) = 0
yes
STD2 ≤ FSTRESS3(2) & | FSTRESS3(3) | < SSD
yes
Tensile delamination in reinforcement 2 dir.
STATEV(27) = FSTRAN3(2)
STATEV(28) = 0
STATEV(32) = 3
STATEV(50) = 1
STATEV(51) = 0
no
STD2 > FSTRESS3(2) & SSD ≤ | FSTRESS3(3) |
yes
FSTRESS3(2) > 0.0
yes
Shear delamination in 12 plane
STATEV(27) = 0
STATEV(28) = FSTRAN3(3)
STATEV(32) = 2
STATEV(50) = 0
STATEV(51) = 1
no
Shear delamination in 12 plane
STATEV(27) = 0
STATEV(28) = 0
STATEV(32) = 0
STATEV(50) = 0
STATEV(51) = 0
no
no
STD2 ≤ FSTRESS3(2) & SSD ≤ | FSTRESS3(3) |
yes
Tensile & Shear delamination
STATEV(27) = FSTRAN3(2)
STATEV(28) = FSTRAN3(3)
STATEV(32) = 3
STATEV(50) = 1
STATEV(51) = 1
no
STATEV(32) = 1
yes
Matrix cracking
STATEV(27) = 0
STATEV(28) = 0
STATEV(32) = 1
STATEV(50) = 0
STATEV(51) = 0
no
Return
End

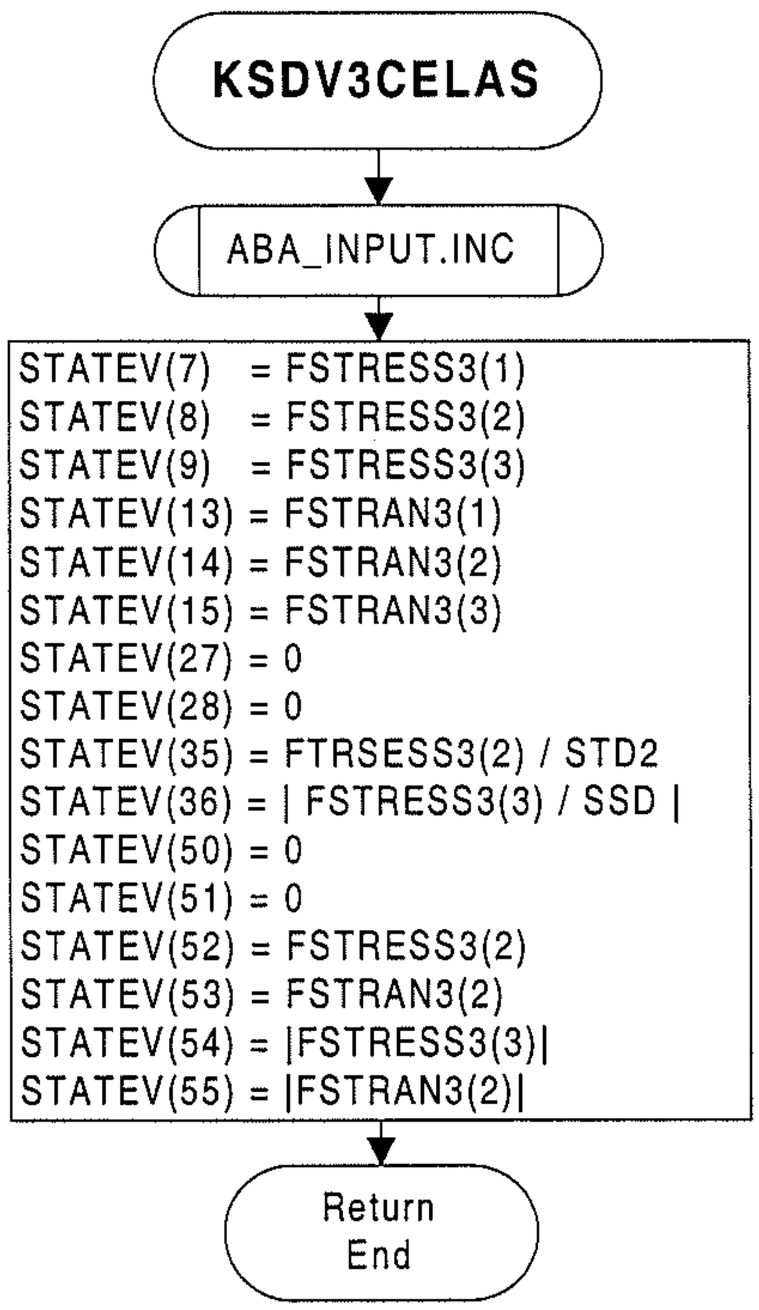

Fig 7.5.2-20 Flow diagram of subroutine KSDVCELAS

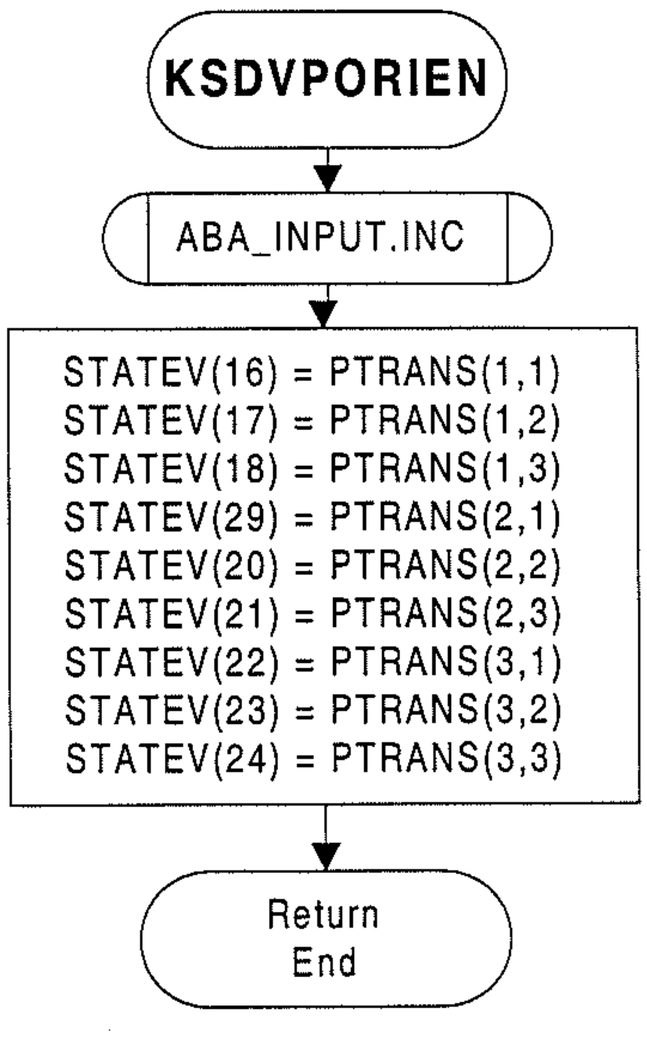

Fig 7.5.2-21
Flow diagram of subroutine KSDVPORIEN

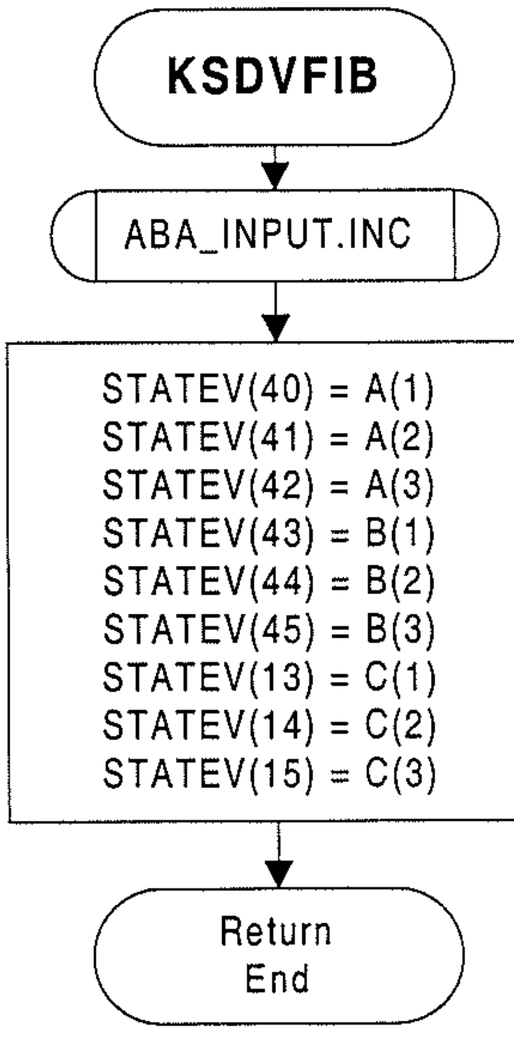

Fig 7.5.2-22
Flow diagram of subroutine KSDVFIB

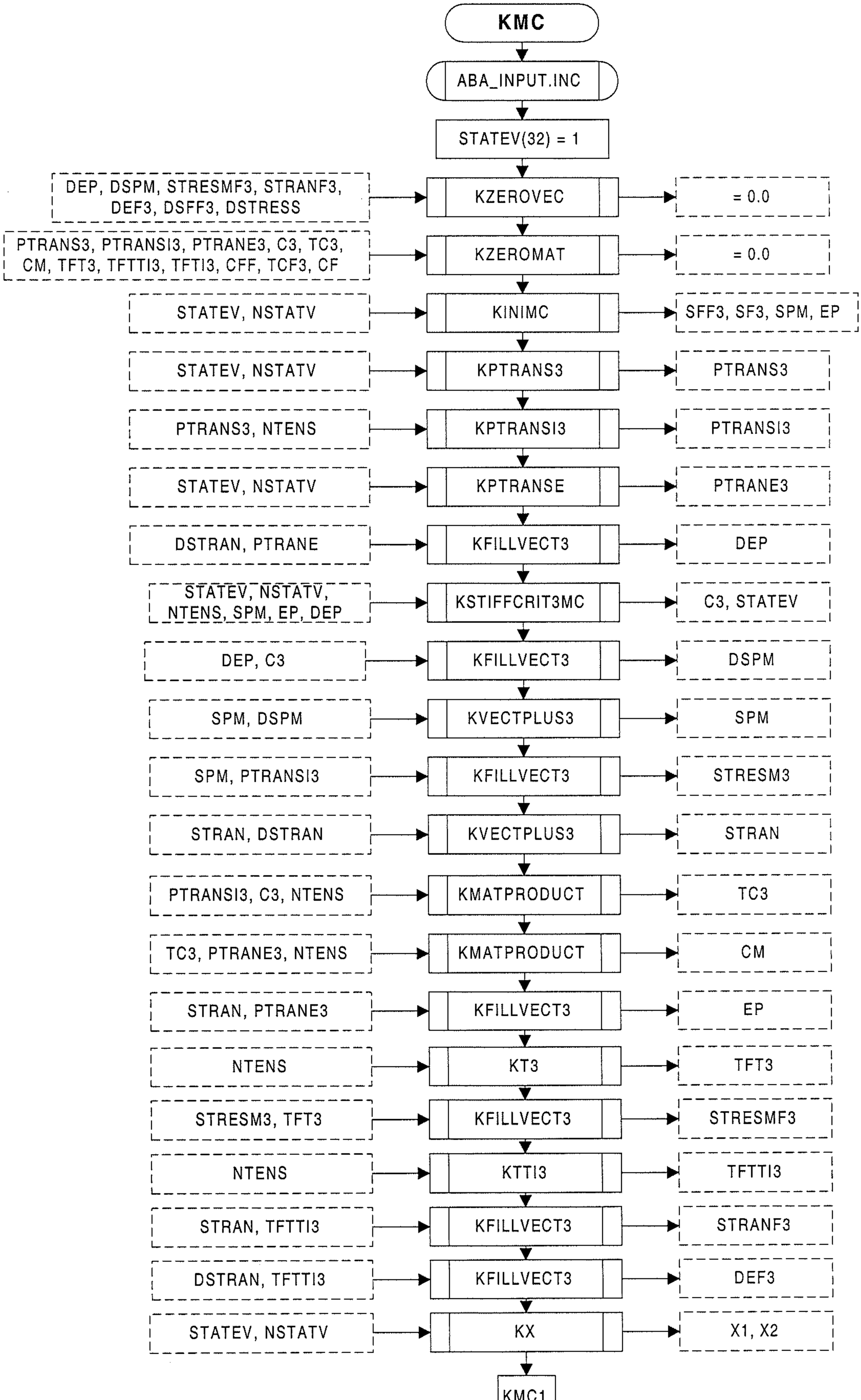
KMC
ABA_INPUT.INC
STATEV(32) = 1
DEP, DSPM, STRESMF3, STRANF3, DEF3, DSFF3, DSTRESS
KZEROVEC
= 0.0
PTRANS3, PTRANSI3, PTRANE3, C3, TC3, CM, TFT3, TFTTI3, TFTI3, CFF, TCF3, CF
KZEROMAT
= 0.0
STATEV, NSTATV
KINIMC
SFF3, SF3, SPM, EP
STATEV, NSTATV
KPTRANS3
PTRANS3
PTRANS3, NTENS
KPTRANSI3
PTRANSI3
STATEV, NSTATV
KPTRANSE
PTRANE3
DSTRAN, PTRANE
KFILLVECT3
DEP
STATEV, NSTATV, NTENS, SPM, EP, DEP
KSTIFFCRIT3MC
C3, STATEV
DEP, C3
KFILLVECT3
DSPM
SPM, DSPM
KVECTPLUS3
SPM
SPM, PTRANSI3
KFILLVECT3
STRESM3
STRAN, DSTRAN
KVECTPLUS3
STRAN
PTRANSI3, C3, NTENS
KMATPRODUCT
TC3
TC3, PTRANE3, NTENS
KMATPRODUCT
CM
STRAN, PTRANE3
KFILLVECT3
EP
NTENS
KT3
TFT3
STRESM3, TFT3
KFILLVECT3
STRESMF3
NTENS
KTTI3
TFTTI3
STRAN, TFTTI3
KFILLVECT3
STRANF3
DSTRAN, TFTTI3
KFILLVECT3
DEF3
STATEV, NSTATV
KX
X1, X2
KMC1

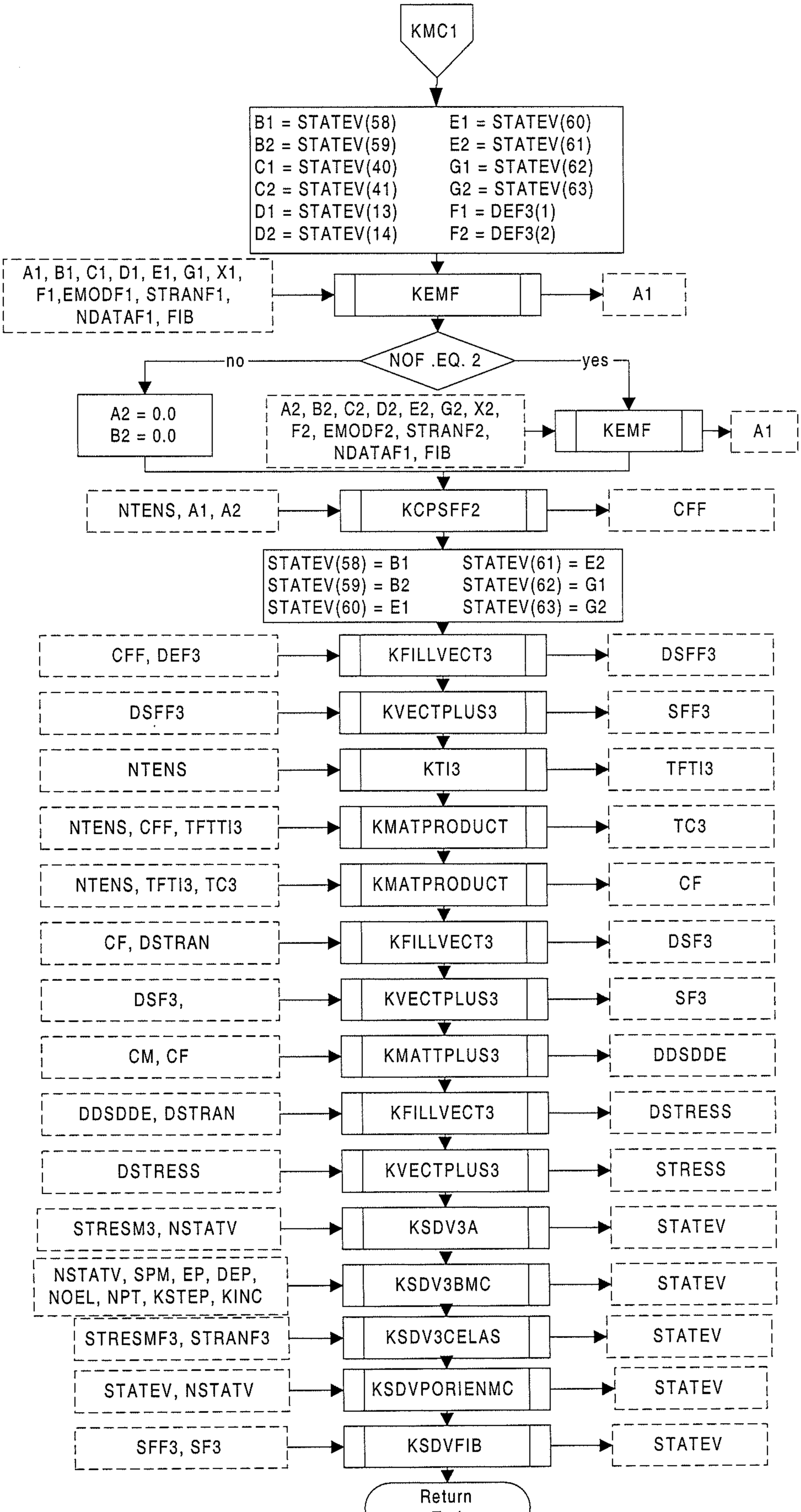
KMC1
B1 = STATEV(58)
B2 = STATEV(59)
C1 = STATEV(40)
C2 = STATEV(41)
D1 = STATEV(13)
D2 = STATEV(14)
E1 = STATEV(60)
E2 = STATEV(61)
G1 = STATEV(62)
G2 = STATEV(63)
F1 = DEF3(1)
F2 = DEF3(2)
A1, B1, C1, D1, E1, G1, X1, F1,EMODF1, STRANF1, NDATAF1, FIB
KEMF
A1
NOF .EQ. 2
no
yes
A2 = 0.0
B2 = 0.0
A2, B2, C2, D2, E2, G2, X2, F2, EMODF2, STRANF2, NDATAF1, FIB
KEMF
A1
NTENS, A1, A2
KCPSFF2
CFF
STATEV(58) = B1
STATEV(59) = B2
STATEV(60) = E1
STATEV(61) = E2
STATEV(62) = G1
STATEV(63) = G2
CFF, DEF3
KFILLVECT3
DSFF3
DSFF3
KVECTPLUS3
SFF3
NTENS
KTI3
TFTI3
NTENS, CFF, TFTTI3
KMATPRODUCT
TC3
NTENS, TFTI3, TC3
KMATPRODUCT
CF
CF, DSTRAN
KFILLVECT3
DSF3
DSF3,
KVECTPLUS3
SF3
CM, CF
KMATTPLUS3
DDSDDE
DDSDDE, DSTRAN
KFILLVECT3
DSTRESS
DSTRESS
KVECTPLUS3
STRESS
STRESM3, NSTATV
KSDV3A
STATEV
NSTATV, SPM, EP, DEP, NOEL, NPT, KSTEP, KINC
KSDV3BMC
STATEV
STRESMF3, STRANF3
KSDV3CELAS
STATEV
STATEV, NSTATV
KSDVPORIENMC
STATEV
SFF3, SF3
KSDVFIB
STATEV
Return

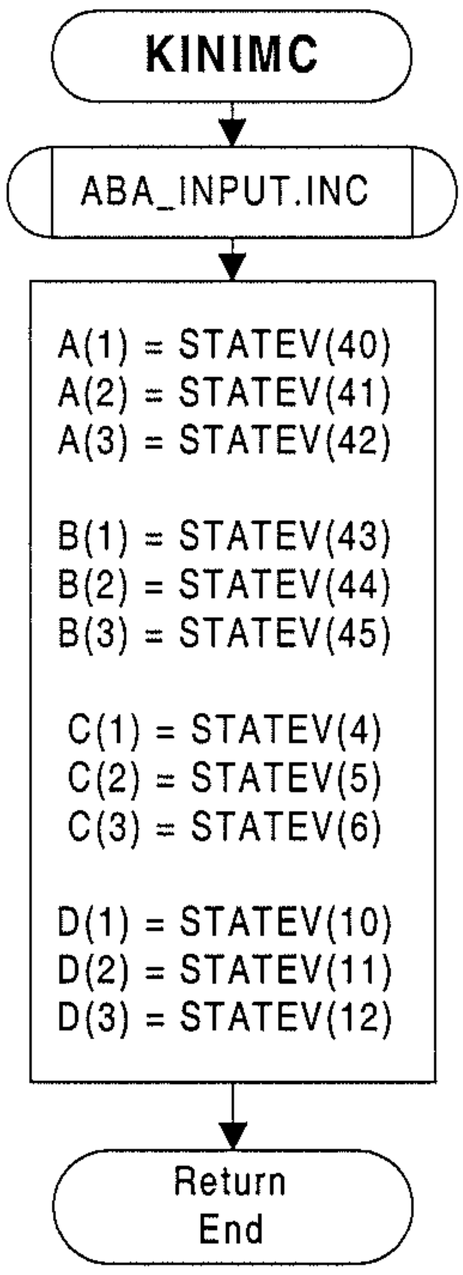

Fig 7.5.3-2
Flow diagram of the subroutine KINIMC

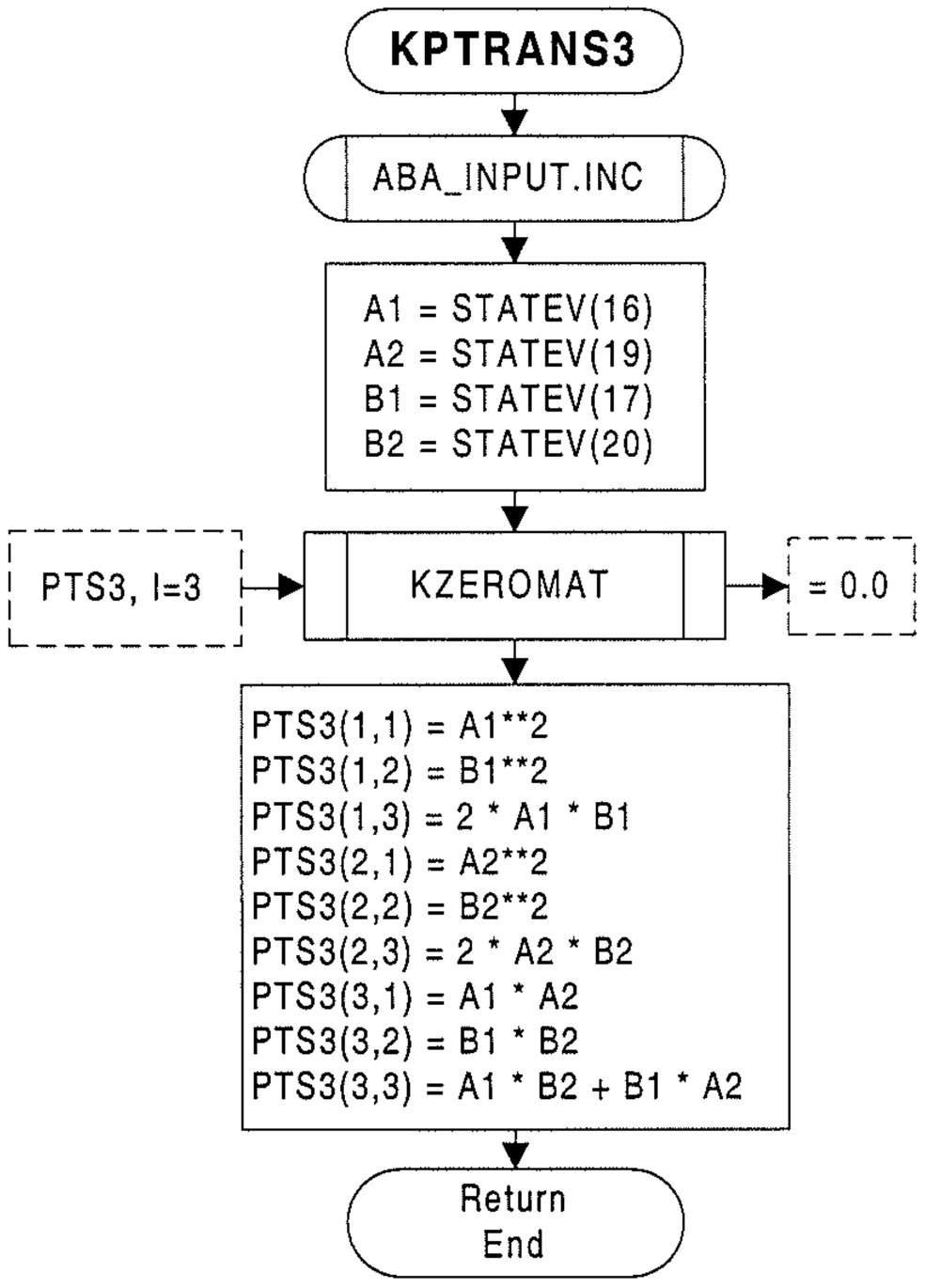

Fig 7.5.3-3
Flow diagram of the subroutine KPTRANS3

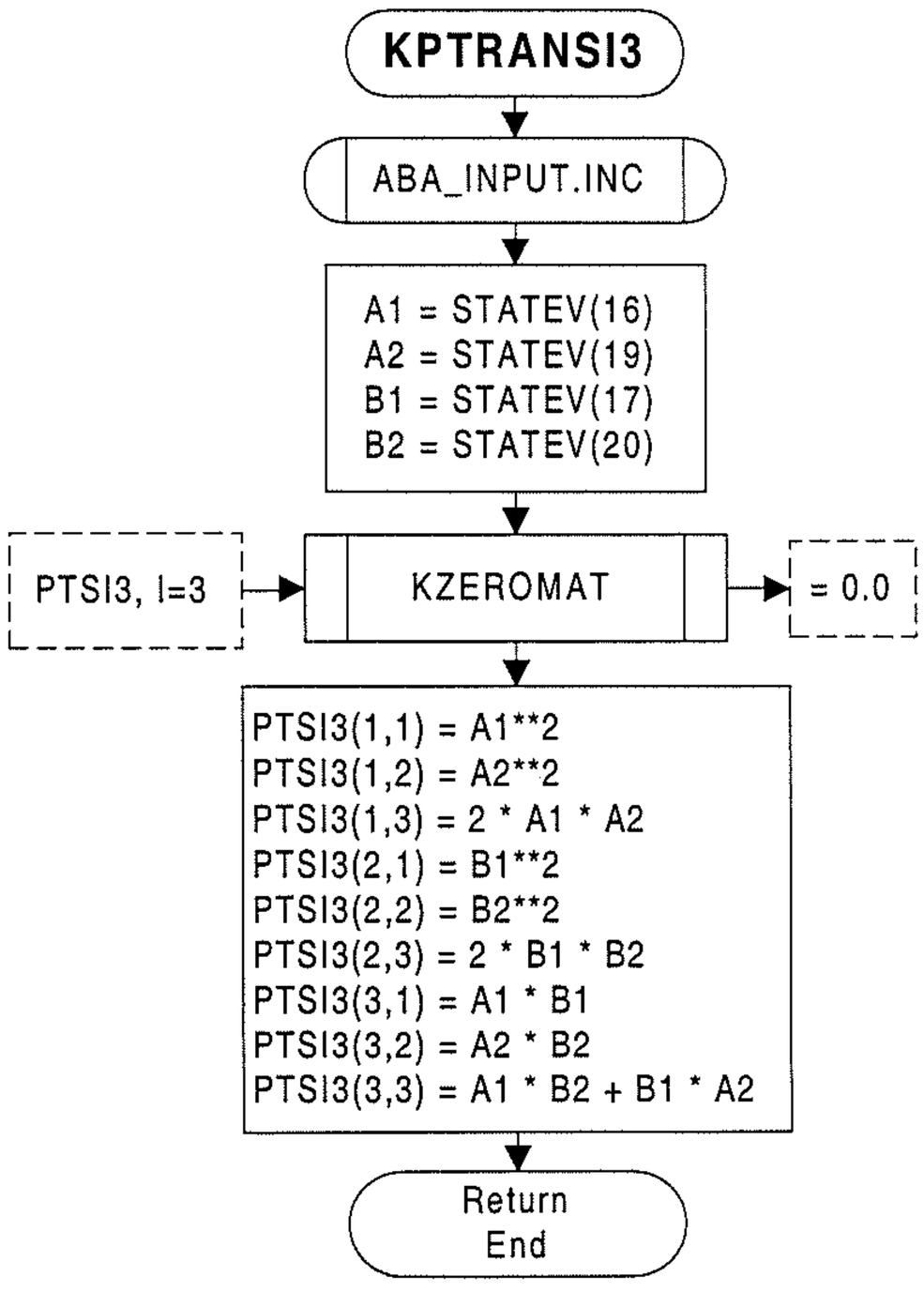

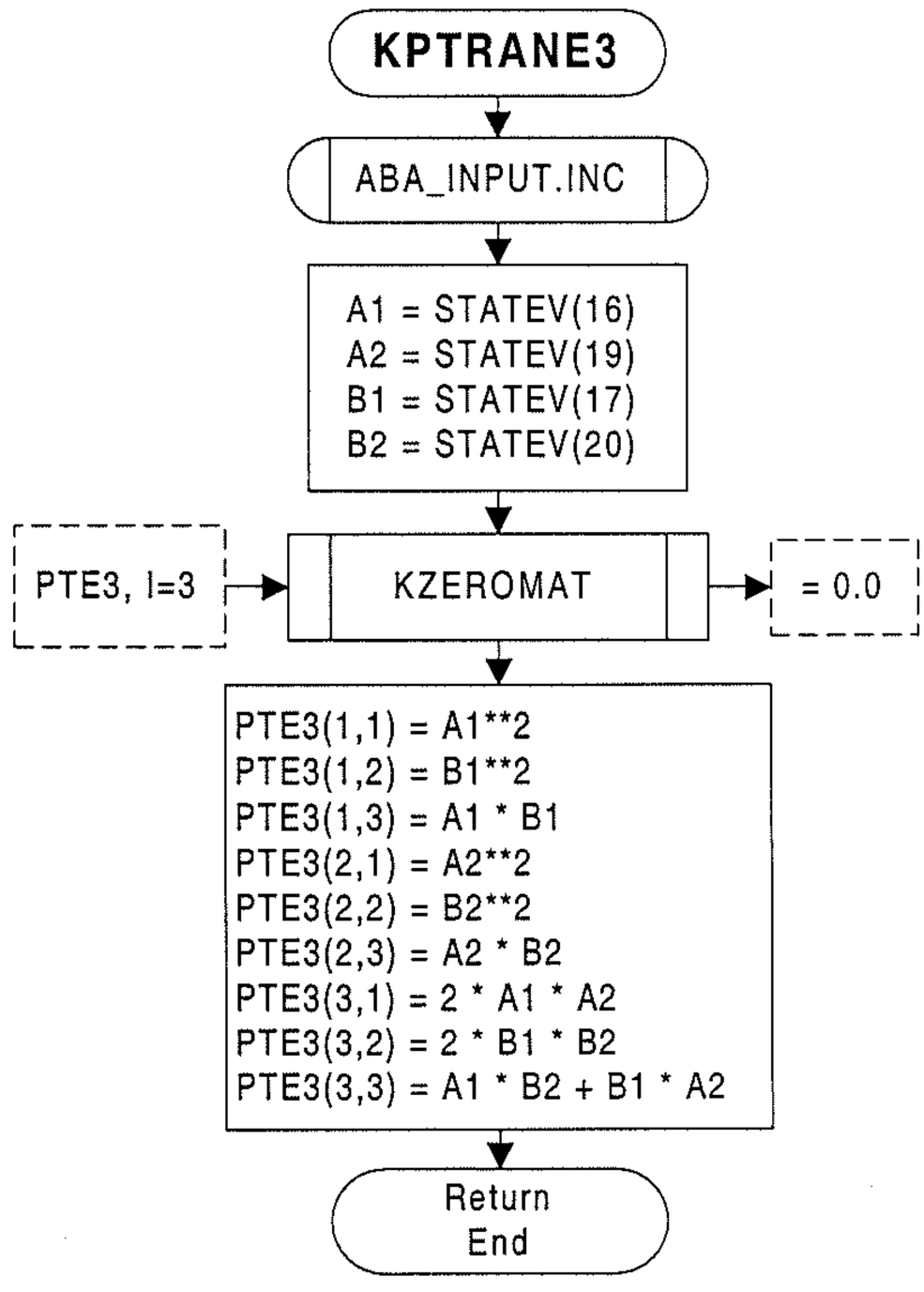

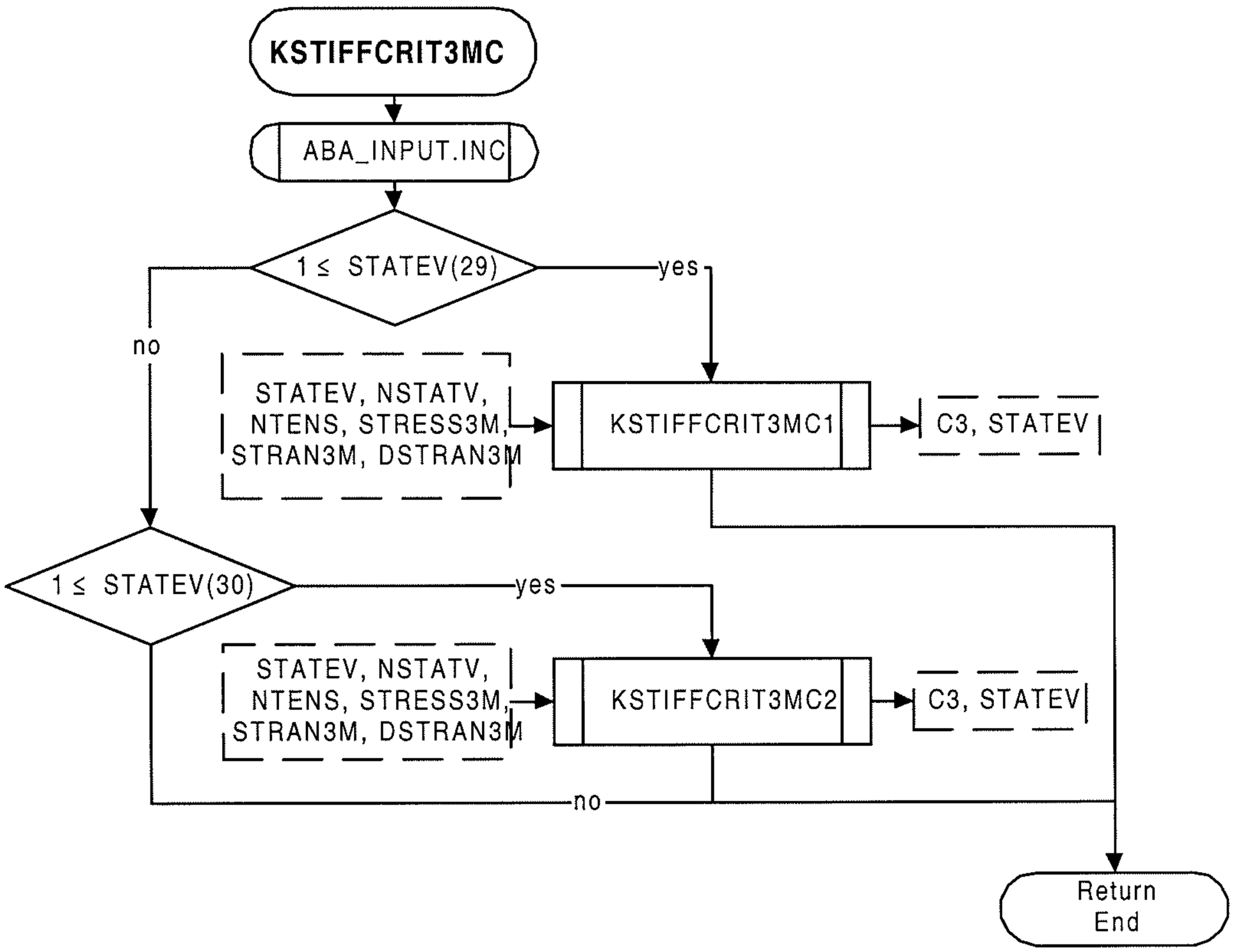

Fig 7.5.3-6 Flow diagram of the subroutine KSTIFFCRIT3MC

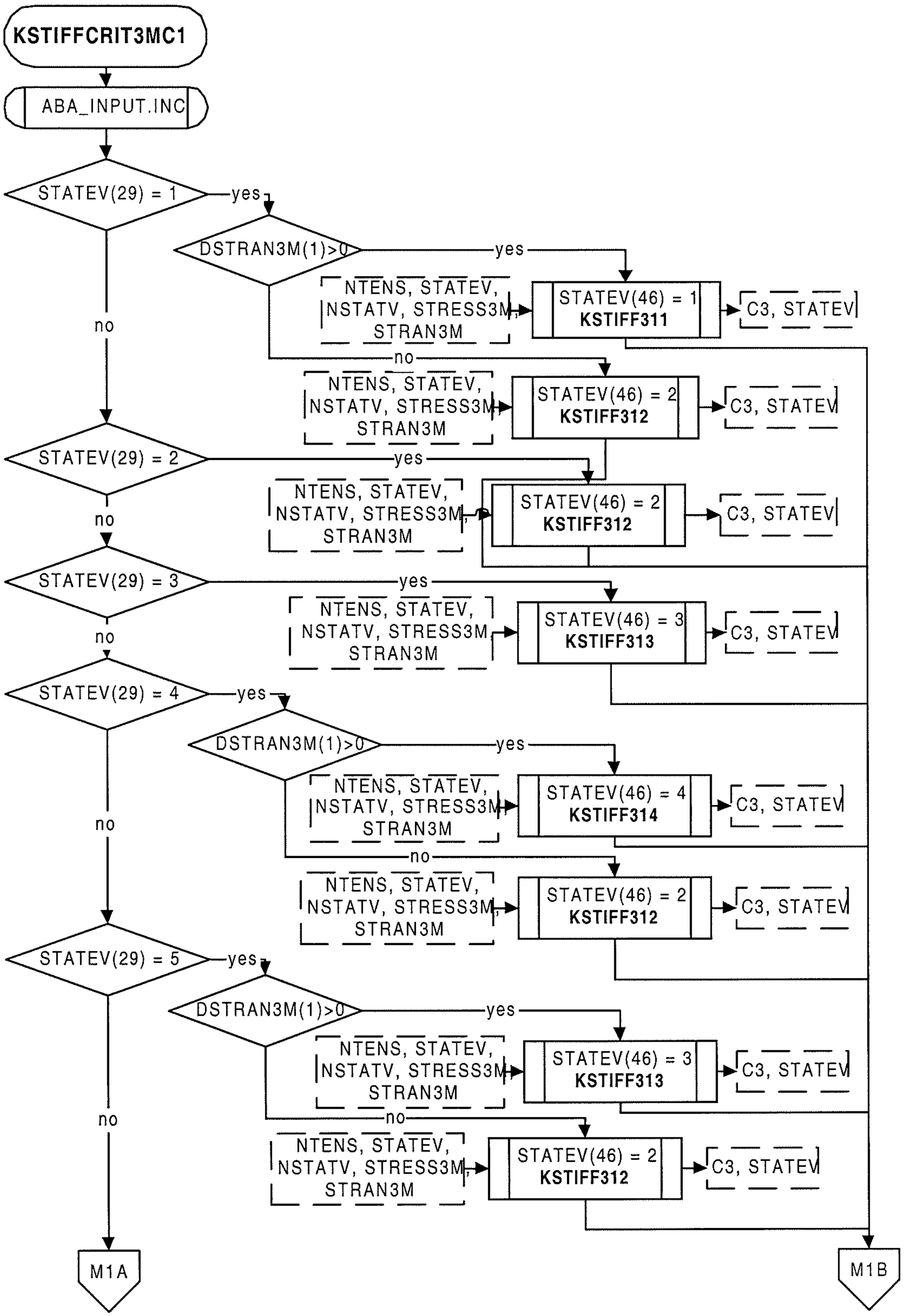
KSTIFFCRIT3MC1
ABA_INPUT.INC
STATEV(29) = 1
yes
DSTRAN3M(1)>0
yes
NTENS, STATEV, NSTATV, STRESS3M, STRAN3M
STATEV(46) = 1
KSTIFF311
C3, STATEV
no
no
NTENS, STATEV, NSTATV, STRESS3M, STRAN3M
STATEV(46) = 2
KSTIFF312
C3, STATEV
STATEV(29) = 2
yes
no
NTENS, STATEV, NSTATV, STRESS3M, STRAN3M
STATEV(46) = 2
KSTIFF312
C3, STATEV
STATEV(29) = 3
yes
no
NTENS, STATEV, NSTATV, STRESS3M, STRAN3M
STATEV(46) = 3
KSTIFF313
C3, STATEV
STATEV(29) = 4
yes
DSTRAN3M(1)>0
yes
NTENS, STATEV, NSTATV, STRESS3M, STRAN3M
STATEV(46) = 4
KSTIFF314
C3, STATEV
no
NTENS, STATEV, NSTATV, STRESS3M, STRAN3M
STATEV(46) = 2
KSTIFF312
C3, STATEV
STATEV(29) = 5
yes
DSTRAN3M(1)>0
yes
NTENS, STATEV, NSTATV, STRESS3M, STRAN3M
STATEV(46) = 3
KSTIFF313
C3, STATEV
no
NTENS, STATEV, NSTATV, STRESS3M, STRAN3M
STATEV(46) = 2
KSTIFF312
C3, STATEV
no
M1A
M1B

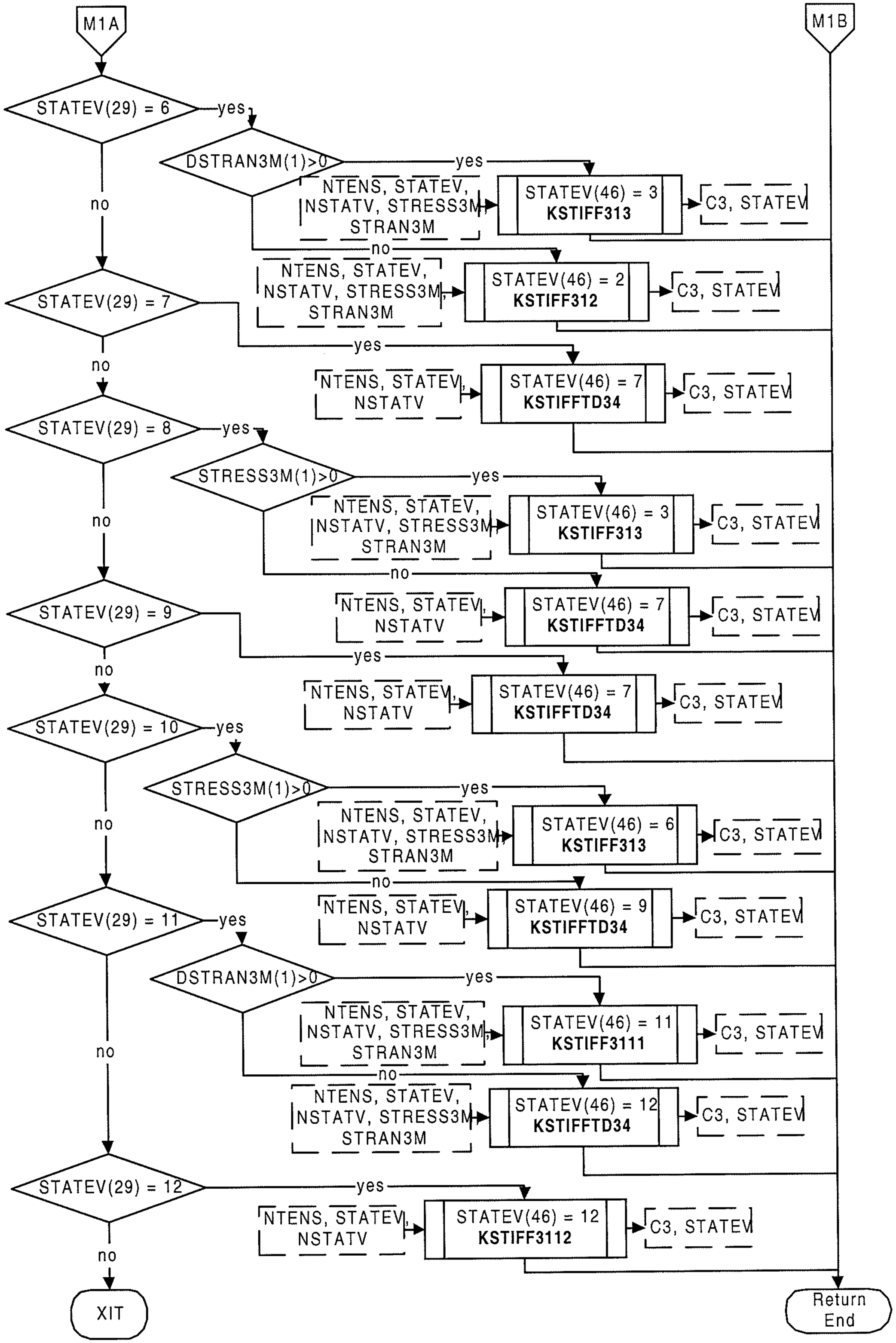
M1A
STATEV(29) = 6
yes
DSTRAN3M(1)>0
yes
NTENS, STATEV, NSTATV, STRESS3M, STRAN3M
STATEV(46) = 3 KSTIFF313
C3, STATEV
no
NTENS, STATEV, NSTATV, STRESS3M, STRAN3M
STATEV(46) = 2 KSTIFF312
C3, STATEV
no
STATEV(29) = 7
yes
NTENS, STATEV, NSTATV
STATEV(46) = 7 KSTIFFTD34
C3, STATEV
no
STATEV(29) = 8
yes
STRESS3M(1)>0
yes
NTENS, STATEV, NSTATV, STRESS3M, STRAN3M
STATEV(46) = 3 KSTIFF313
C3, STATEV
no
NTENS, STATEV, NSTATV
STATEV(46) = 7 KSTIFFTD34
C3, STATEV
no
STATEV(29) = 9
yes
NTENS, STATEV, NSTATV
STATEV(46) = 7 KSTIFFTD34
C3, STATEV
no
STATEV(29) = 10
yes
STRESS3M(1)>0
yes
NTENS, STATEV, NSTATV, STRESS3M, STRAN3M
STATEV(46) = 6 KSTIFF313
C3, STATEV
no
NTENS, STATEV, NSTATV
STATEV(46) = 9 KSTIFFTD34
C3, STATEV
no
STATEV(29) = 11
yes
DSTRAN3M(1)>0
yes
NTENS, STATEV, NSTATV, STRESS3M, STRAN3M
STATEV(46) = 11 KSTIFF3111
C3, STATEV
no
NTENS, STATEV, NSTATV, STRESS3M, STRAN3M
STATEV(46) = 12 KSTIFFTD34
C3, STATEV
no
STATEV(29) = 12
yes
NTENS, STATEV, NSTATV
STATEV(46) = 12 KSTIFF3112
C3, STATEV
no
XIT
M1B
Return End

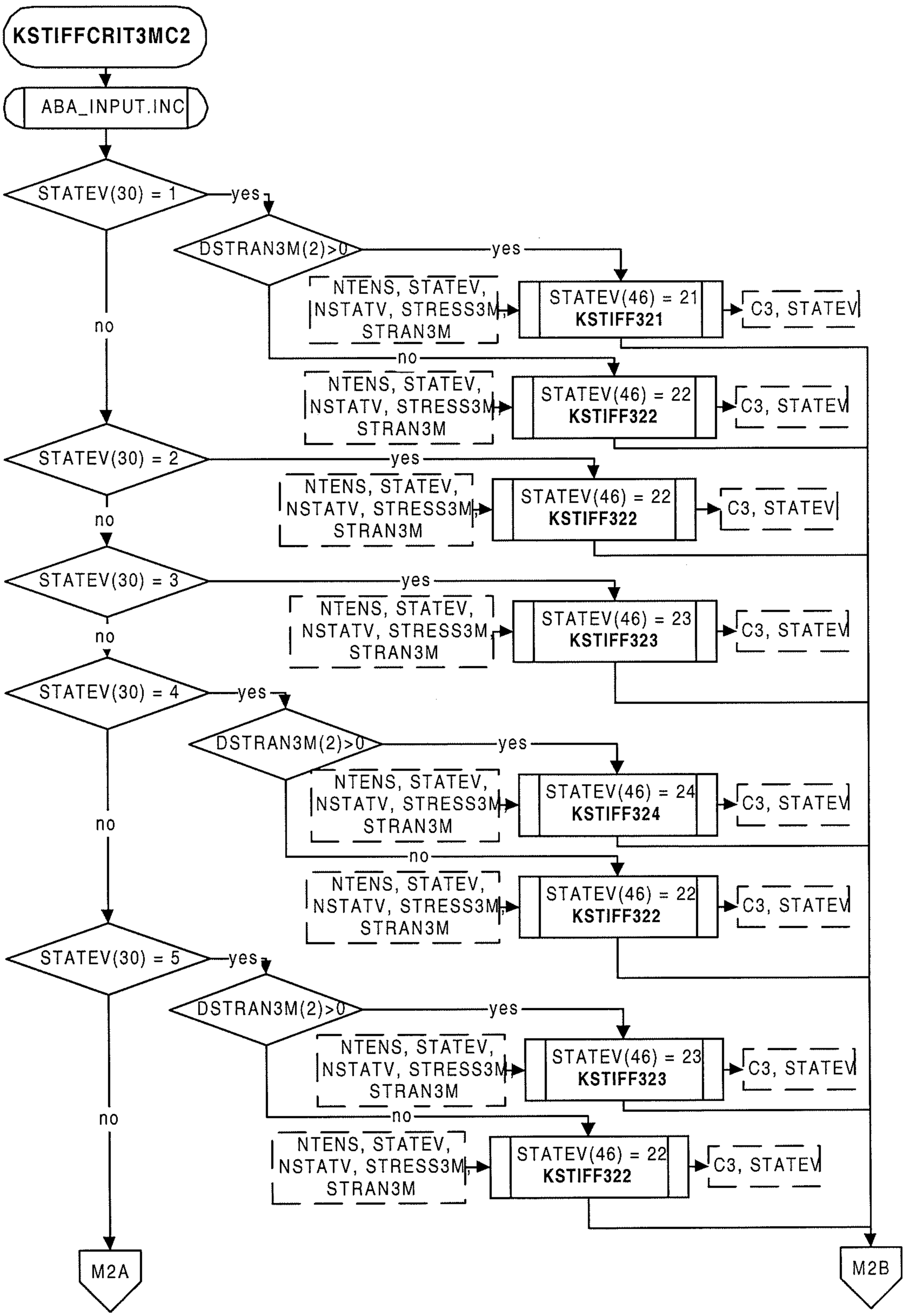

Fig 7.5.3-8a Flow diagram of the subroutine KSTIFFCRIT3MC2 (Part 1/2)

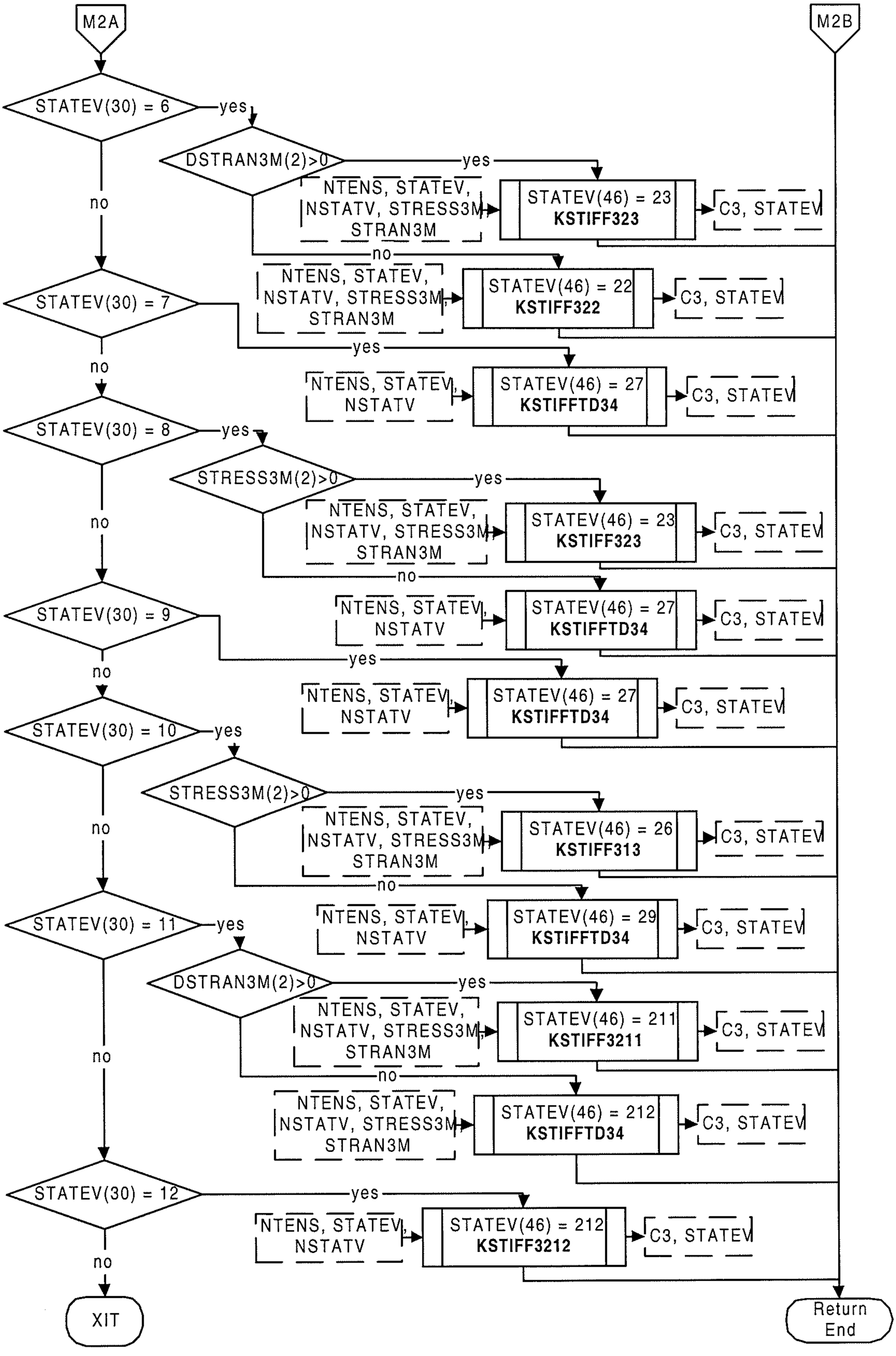
M2A
M2B
STATEV(30) = 6
yes
no
DSTRAN3M(2)>0
yes
no
NTENS, STATEV, NSTATV, STRESS3M, STRAN3M
STATEV(46) = 23 KSTIFF323
C3, STATEV
STATEV(30) = 7
NTENS, STATEV, NSTATV, STRESS3M, STRAN3M
STATEV(46) = 22 KSTIFF322
C3, STATEV
yes
no
NTENS, STATEV, NSTATV
STATEV(46) = 27 KSTIFFTD34
C3, STATEV
STATEV(30) = 8
yes
no
STRESS3M(2)>0
yes
no
NTENS, STATEV, NSTATV, STRESS3M, STRAN3M
STATEV(46) = 23 KSTIFF323
C3, STATEV
STATEV(30) = 9
NTENS, STATEV, NSTATV
STATEV(46) = 27 KSTIFFTD34
C3, STATEV
yes
no
NTENS, STATEV, NSTATV
STATEV(46) = 27 KSTIFFTD34
C3, STATEV
STATEV(30) = 10
yes
no
STRESS3M(2)>0
yes
no
NTENS, STATEV, NSTATV, STRESS3M, STRAN3M
STATEV(46) = 26 KSTIFF313
C3, STATEV
STATEV(30) = 11
yes
no
NTENS, STATEV, NSTATV
STATEV(46) = 29 KSTIFFTD34
C3, STATEV
DSTRAN3M(2)>0
yes
no
NTENS, STATEV, NSTATV, STRESS3M, STRAN3M
STATEV(46) = 211 KSTIFF3211
C3, STATEV
NTENS, STATEV, NSTATV, STRESS3M, STRAN3M
STATEV(46) = 212 KSTIFFTD34
C3, STATEV
STATEV(30) = 12
yes
no
NTENS, STATEV, NSTATV
STATEV(46) = 212 KSTIFF3212
C3, STATEV
XIT
Return End

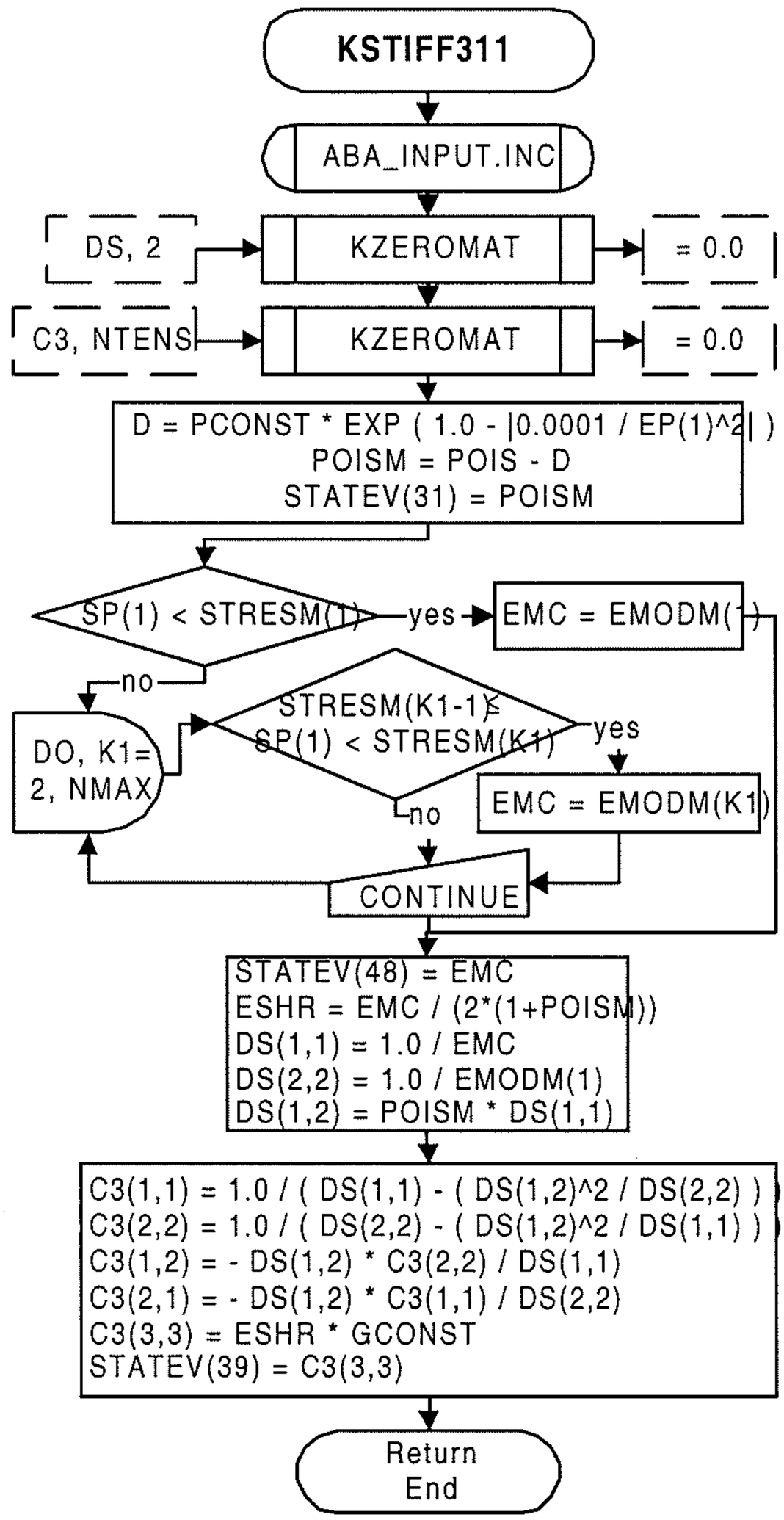

Fig 7.5.3-9
Flow diagram of the subroutine KSTIFF311

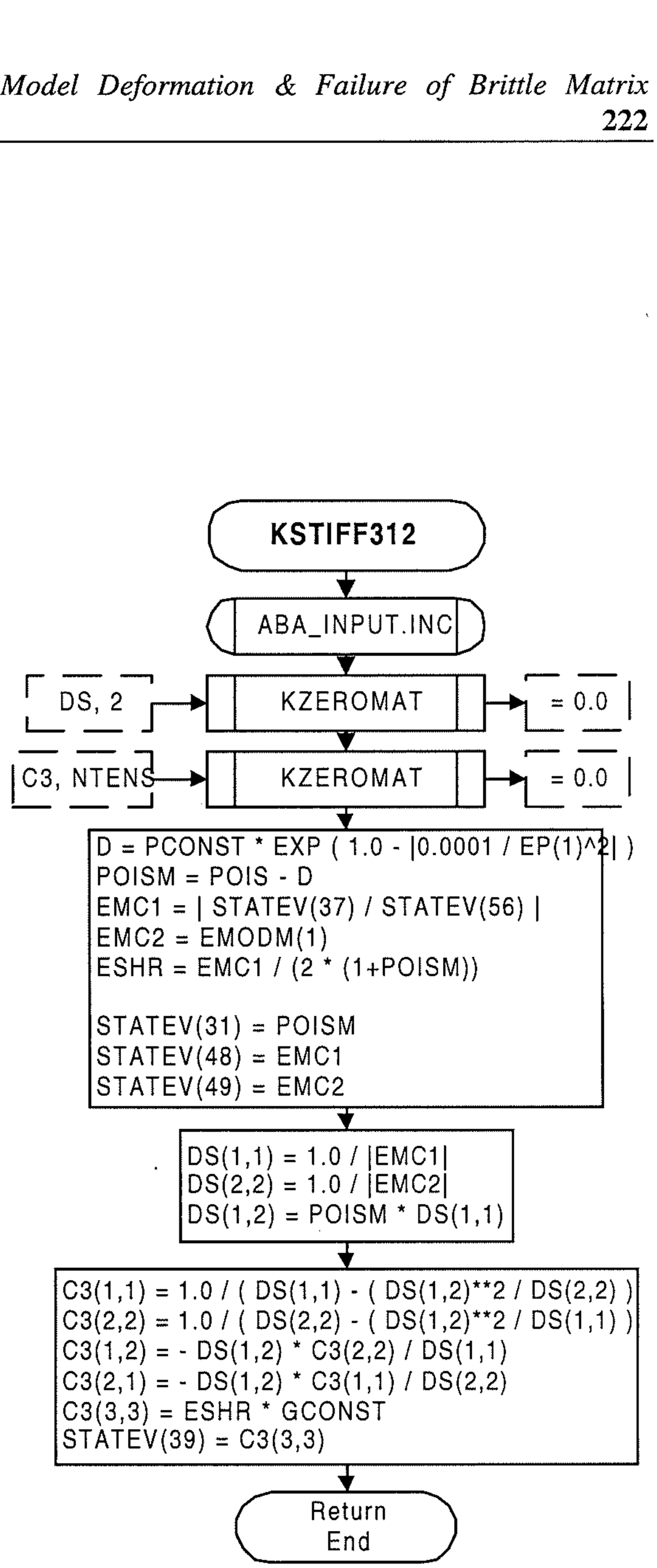

Fig 7.5.3-10
Flow diagram of the subroutine KSTIFF312

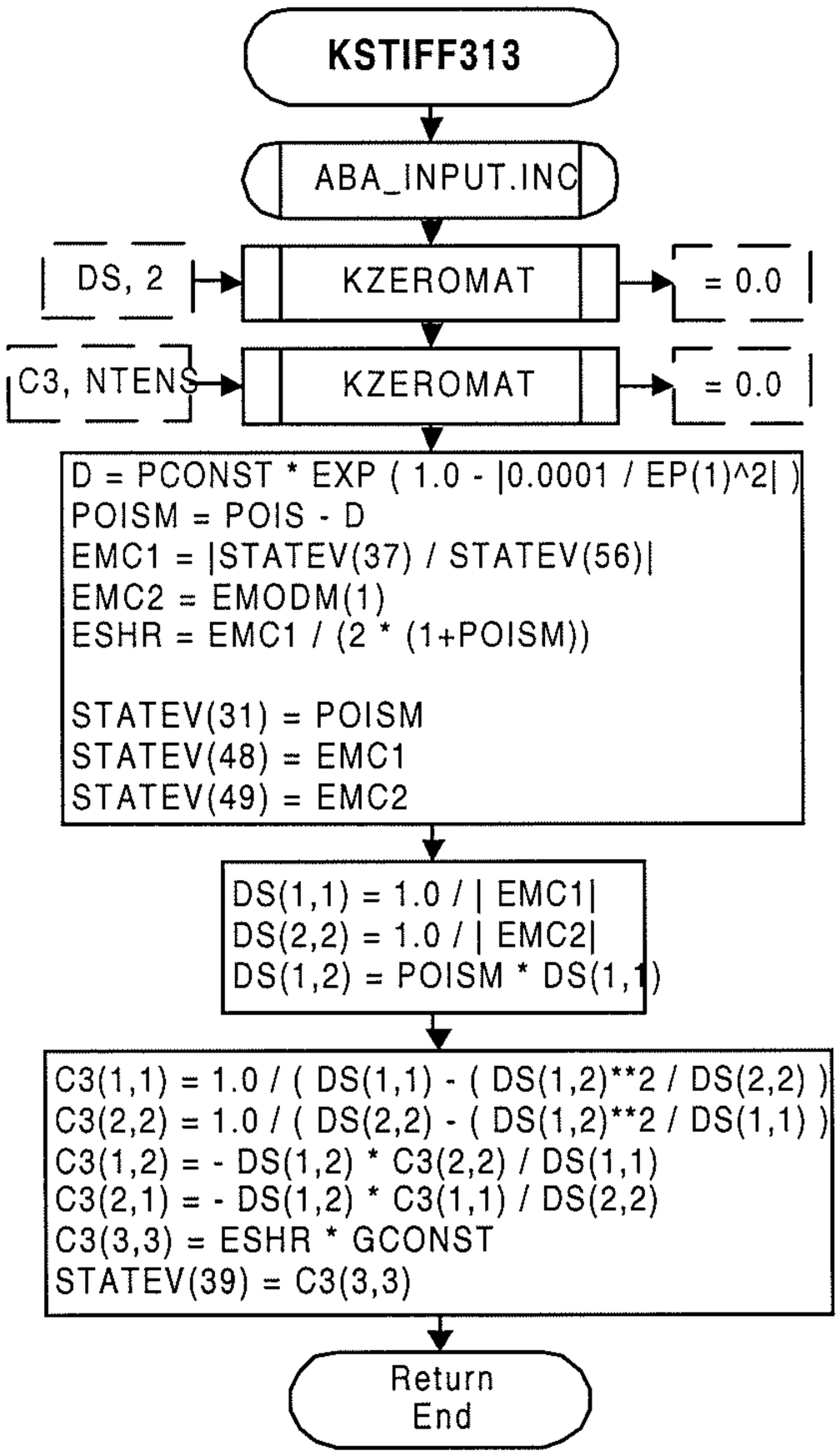

Fig 7.5.3-11
Flow diagram of the subroutine KSTIFF313

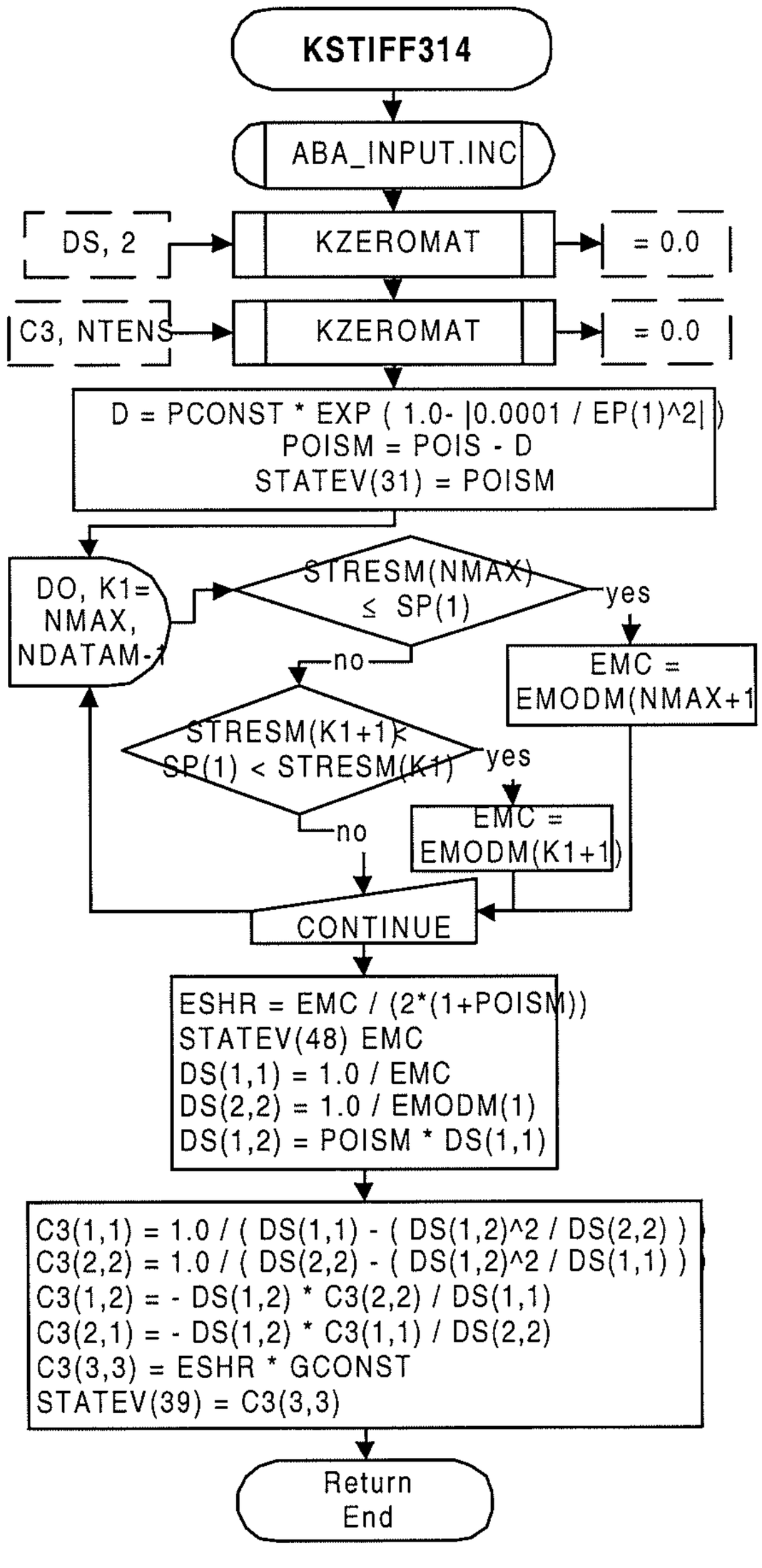

Fig 7.5.3-12
Flow diagram of the subroutine KSTIFF314

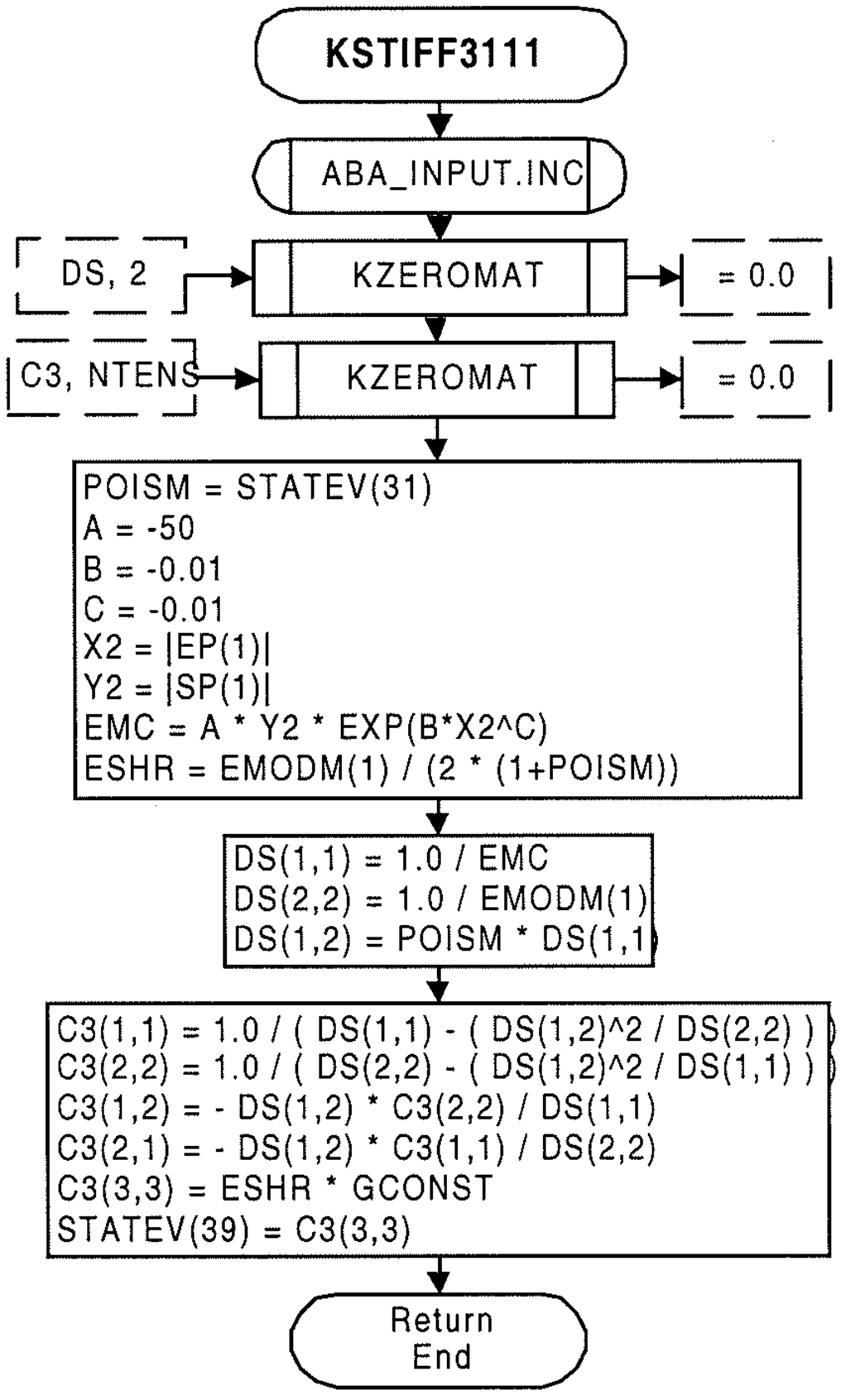

Fig 7.5.3-13
Flow diagram of the subroutine KSTIFF3111

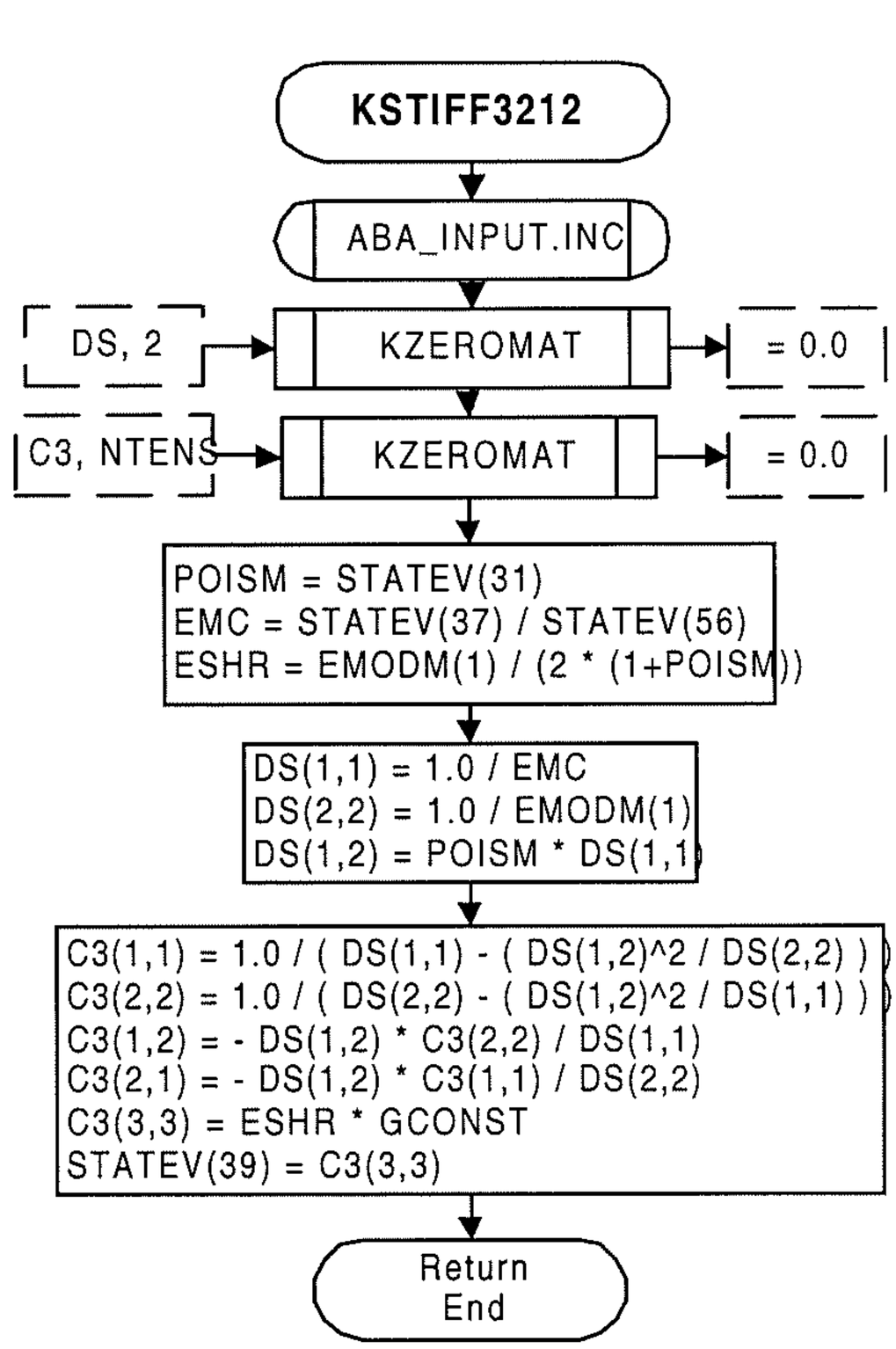

Fig 7.5.3-14
Flow diagram of the subroutine KSTIFF3112

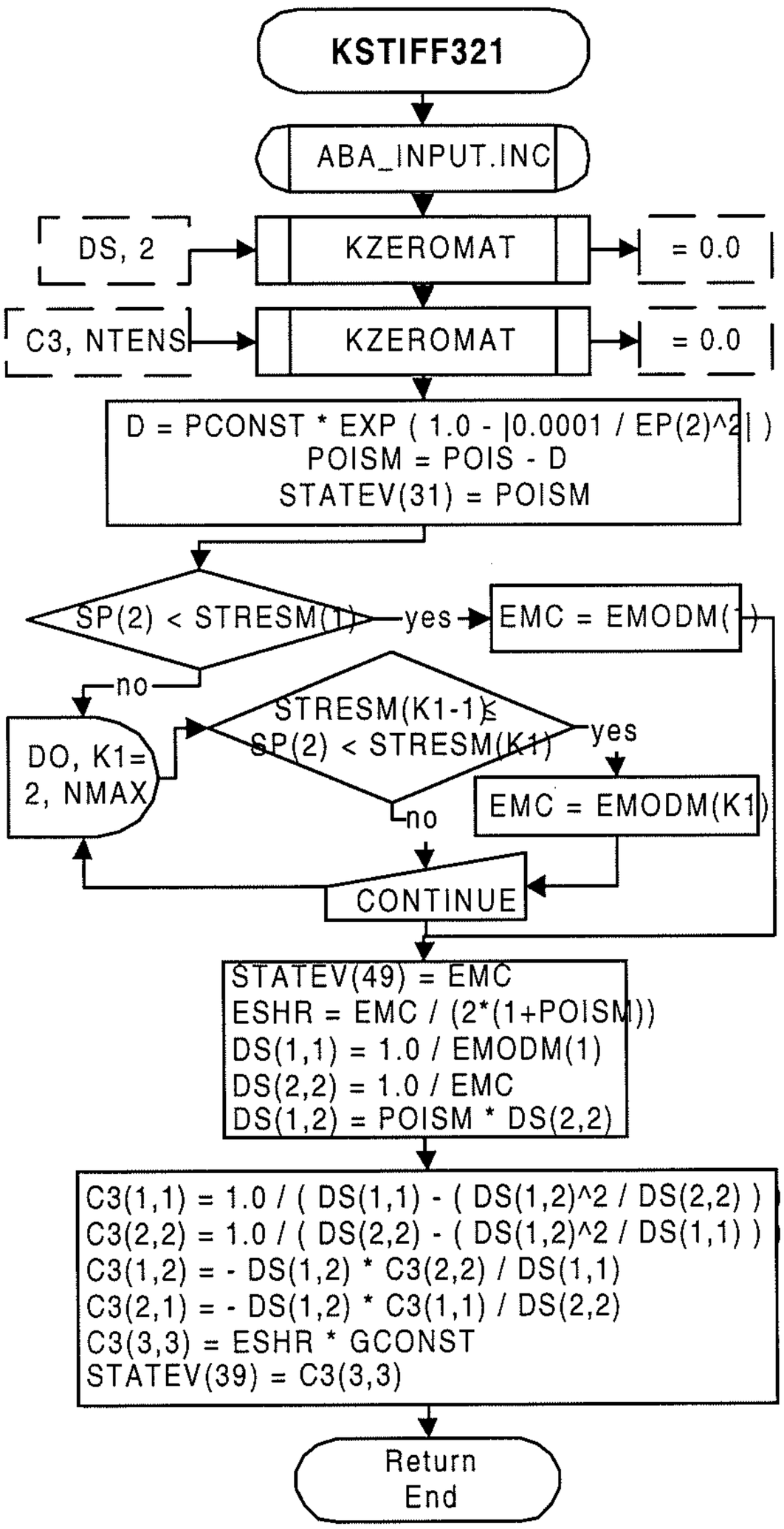

Fig 7.5.3-15
Flow diagram of the subroutine KSTIFF321

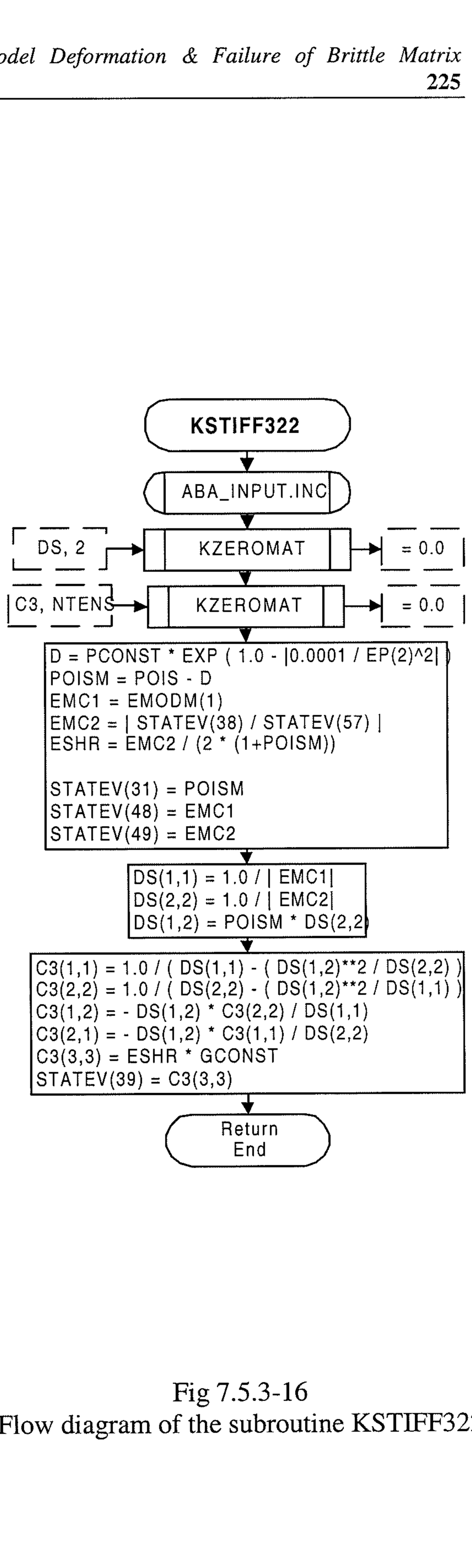

Fig 7.5.3-16
Flow diagram of the subroutine KSTIFF322

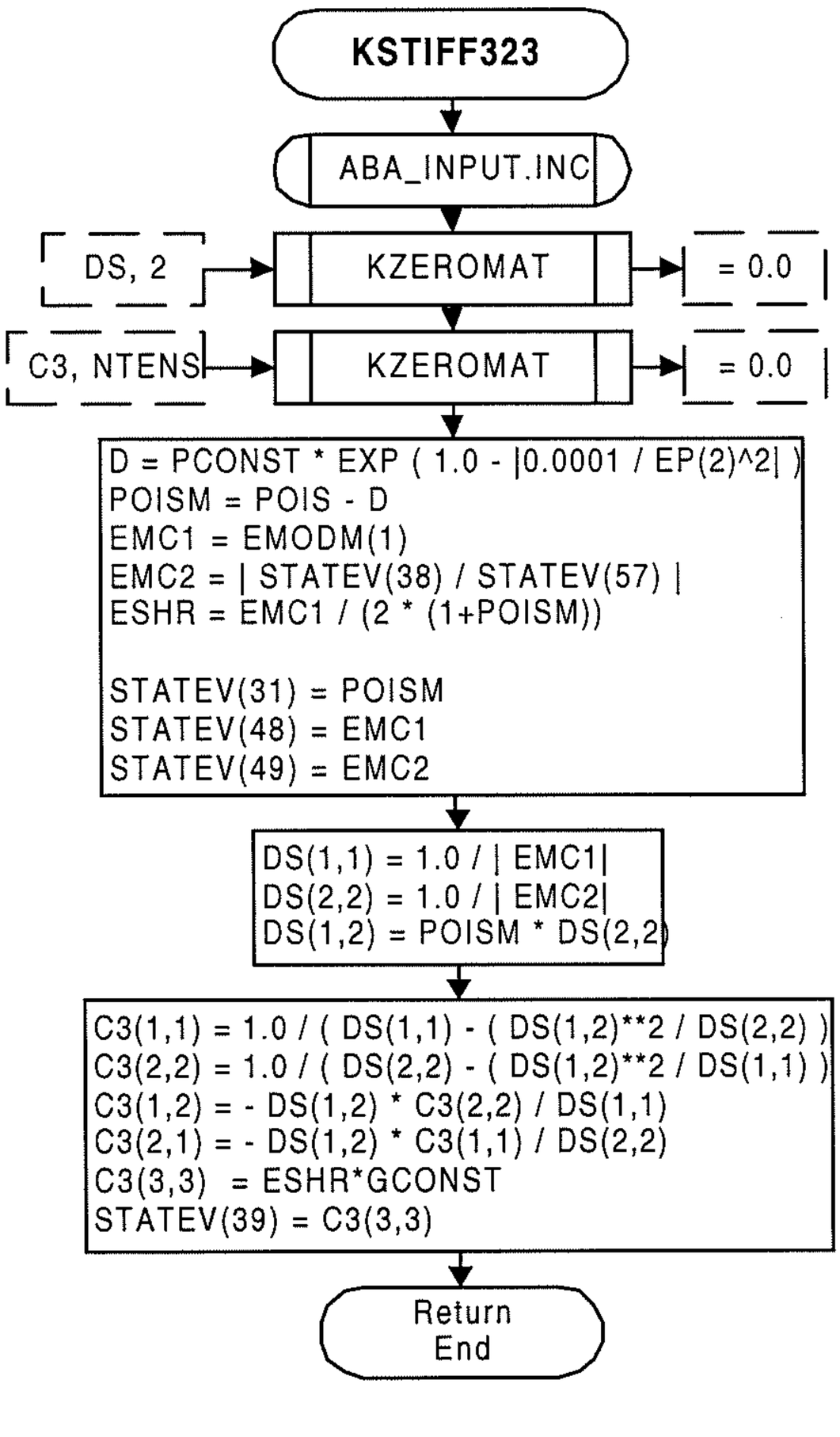

Fig 7.5.3-17
Flow diagram of the subroutine KSTIFF323

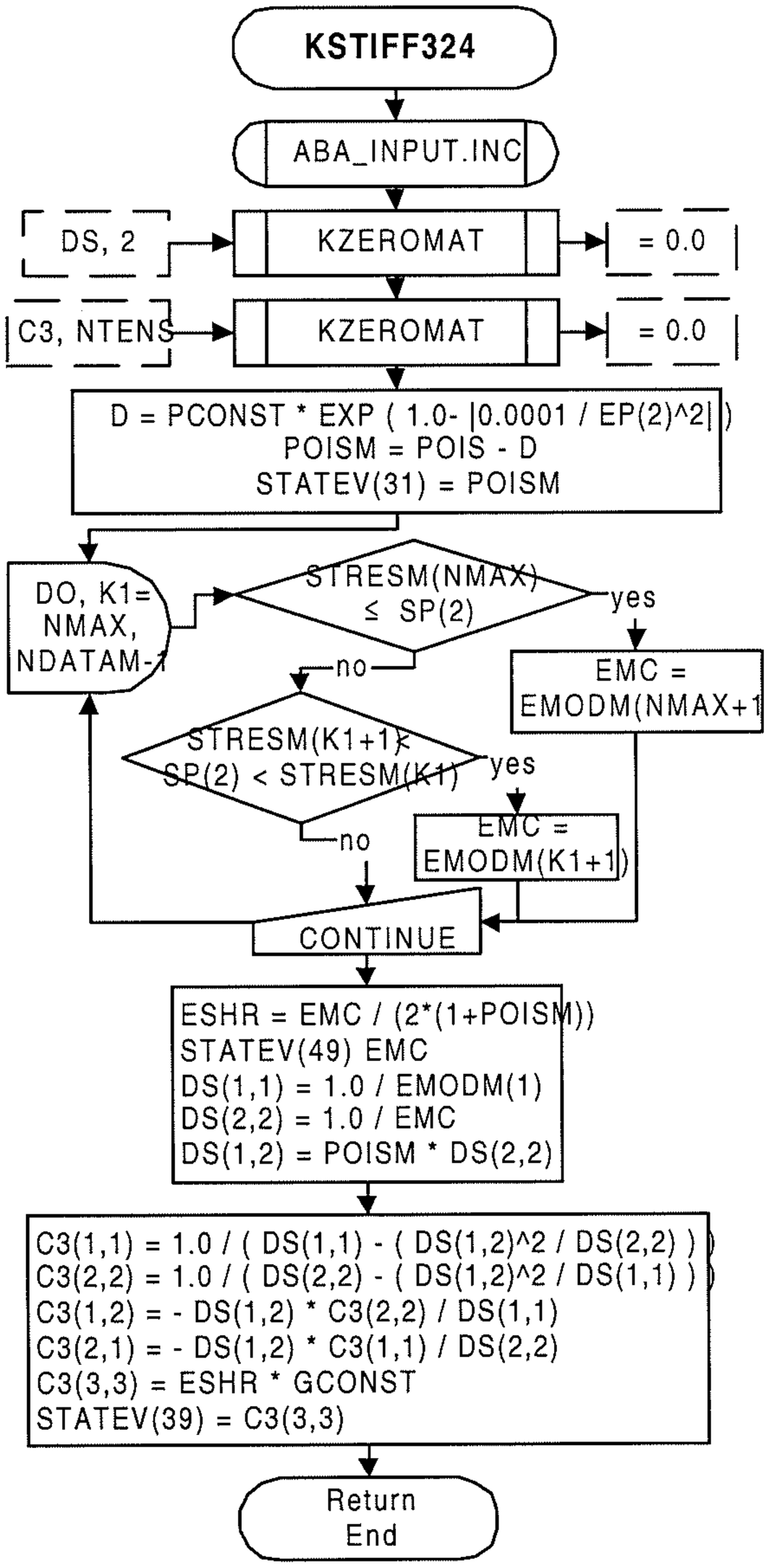

Fig 7.5.3-18
Flow diagram of the subroutine KSTIFF324

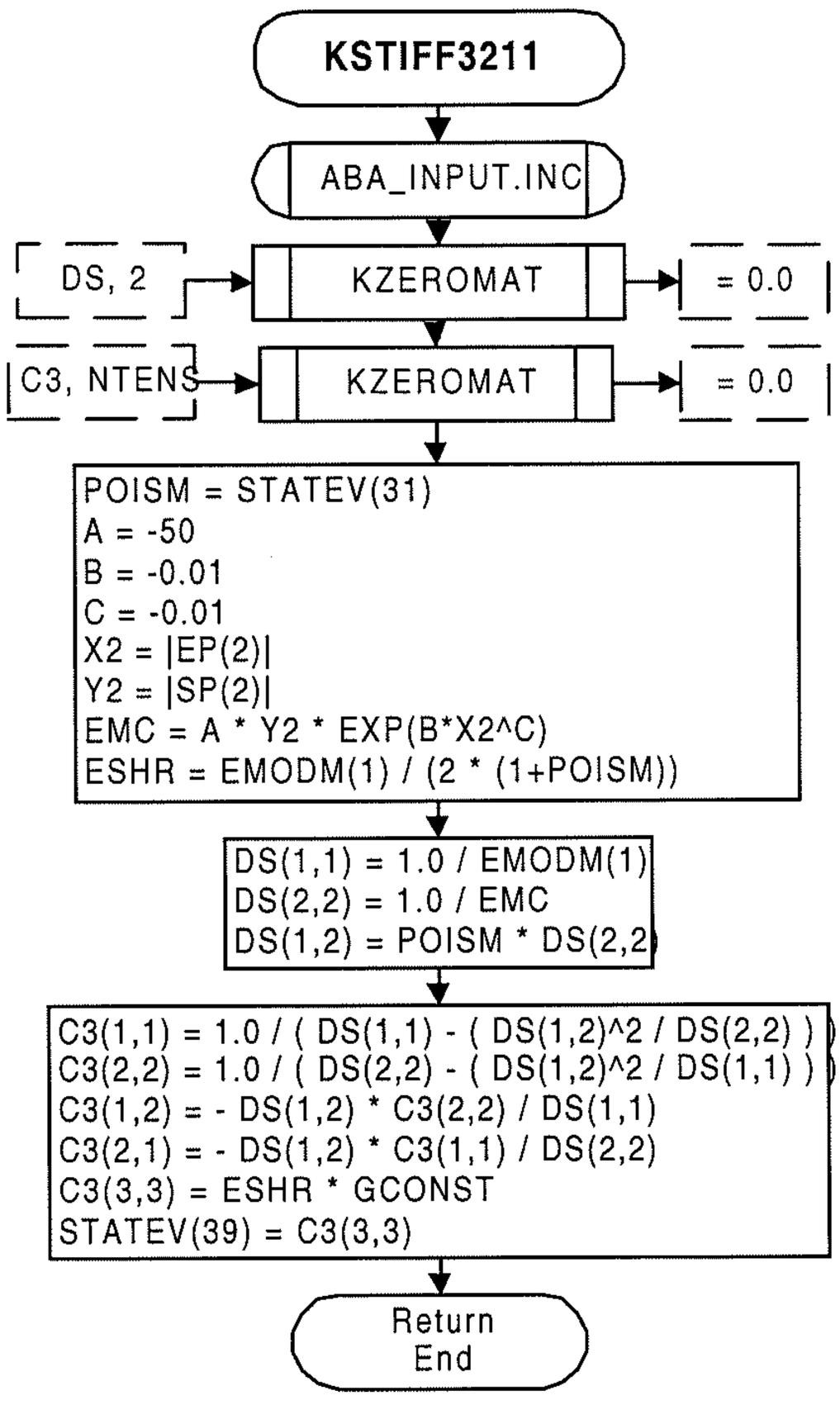

Fig 7.5.3-19
Flow diagram of the subroutine KSTIFF3211

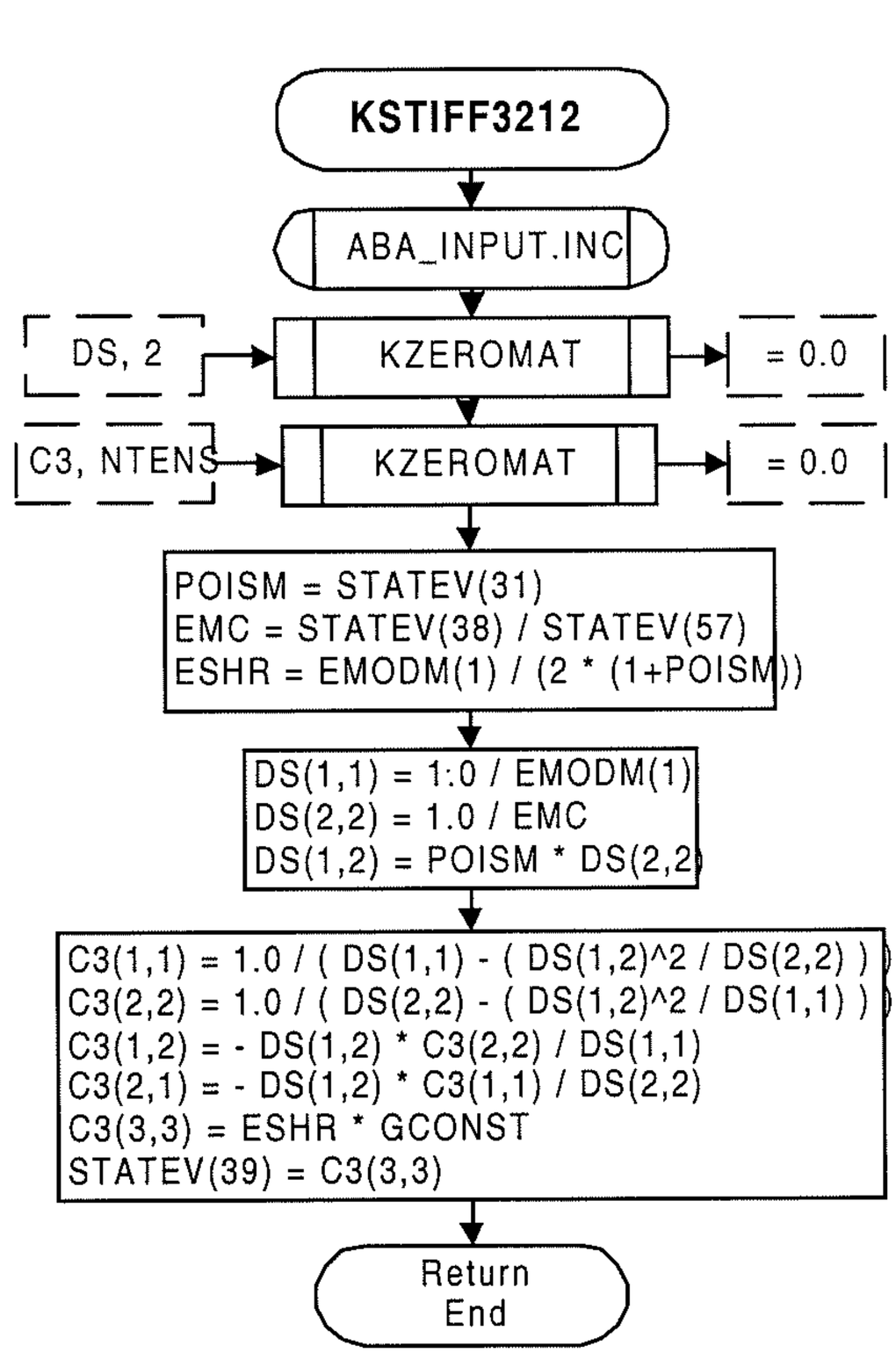

Fig 7.5.3-20
Flow diagram of the subroutine KSTIFF3212

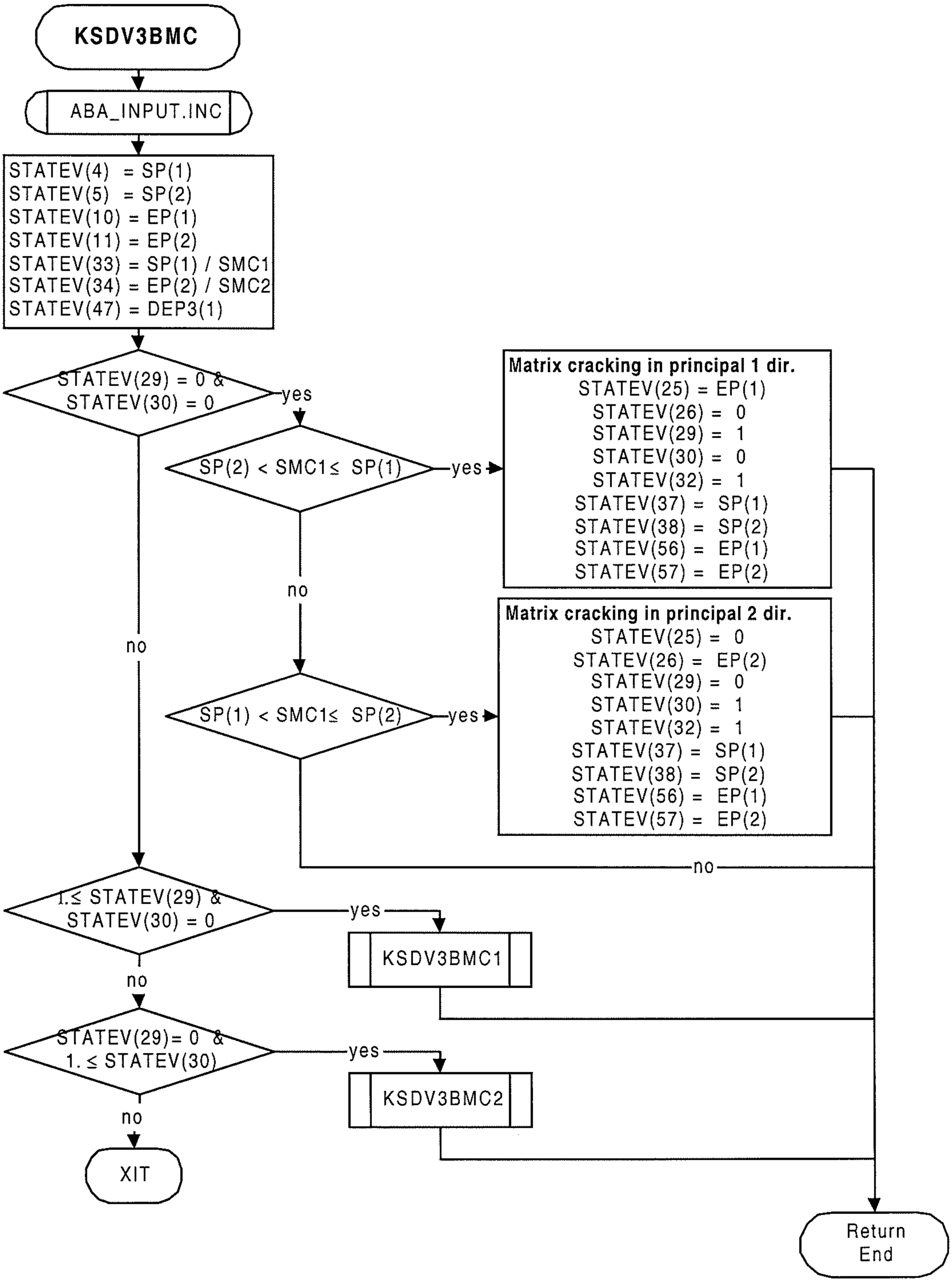

Fig 7.5.3-21 Flow diagram of the subroutine KSDVBMC

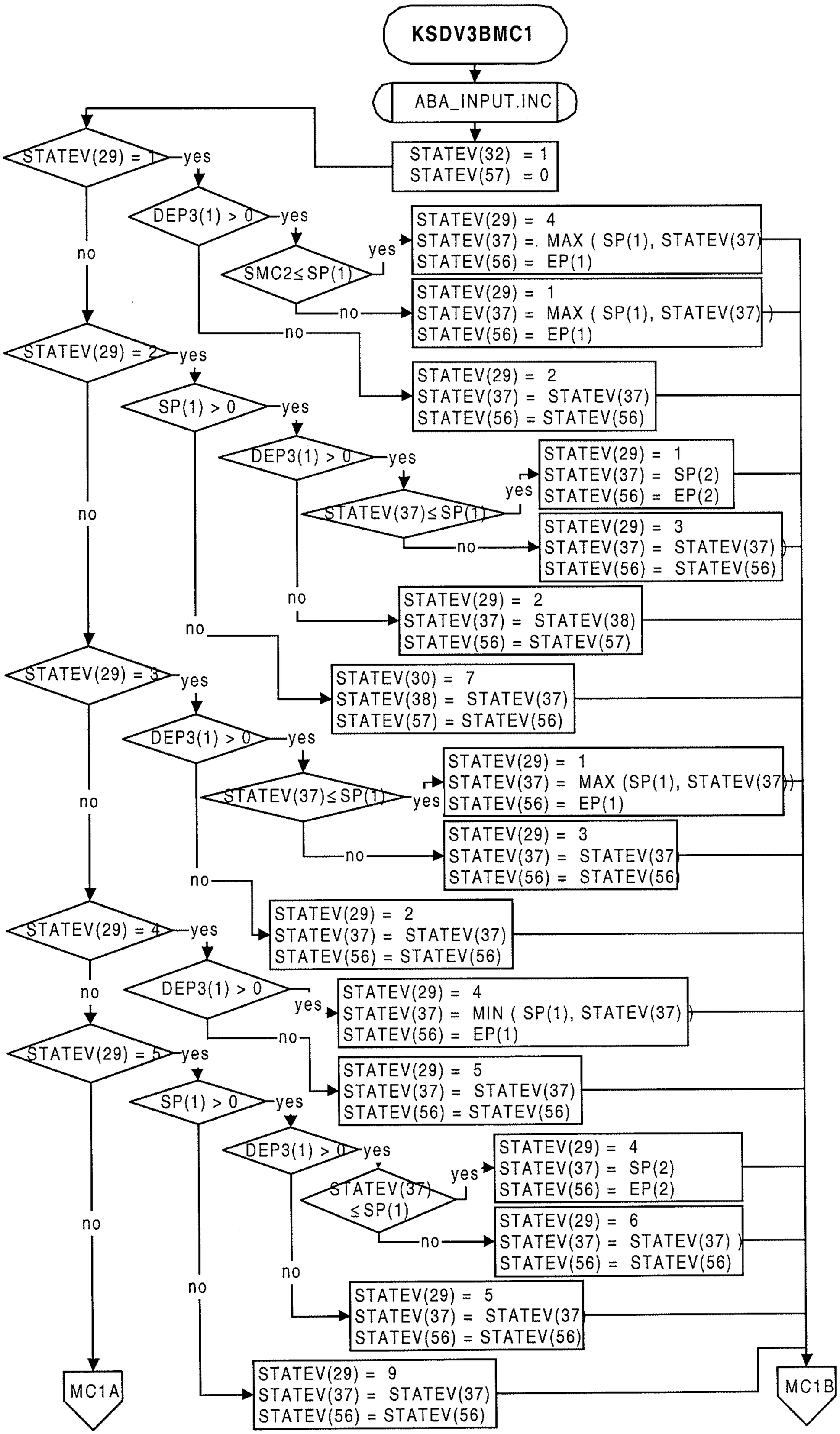
KSDV3BMC1
ABA_INPUT.INC
STATEV(32) = 1
STATEV(57) = 0
STATEV(29) = 1
yes
DEP3(1) > 0
yes
SMC2≤ SP(1)
yes
STATEV(29) = 4
STATEV(37) = MAX (SP(1), STATEV(37))
STATEV(56) = EP(1)
no
STATEV(29) = 1
STATEV(37) = MAX (SP(1), STATEV(37))
STATEV(56) = EP(1)
no
STATEV(29) = 2
STATEV(37) = STATEV(37)
STATEV(56) = STATEV(56)
no
STATEV(29) = 2
yes
SP(1) > 0
yes
DEP3(1) > 0
yes
STATEV(37)≤ SP(1)
yes
STATEV(29) = 1
STATEV(37) = SP(2)
STATEV(56) = EP(2)
no
STATEV(29) = 3
STATEV(37) = STATEV(37)
STATEV(56) = STATEV(56)
no
STATEV(29) = 2
STATEV(37) = STATEV(38)
STATEV(56) = STATEV(57)
no
STATEV(29) = 3
yes
DEP3(1) > 0
yes
STATEV(37)≤ SP(1)
yes
STATEV(29) = 1
STATEV(37) = MAX (SP(1), STATEV(37))
STATEV(56) = EP(1)
no
STATEV(29) = 3
STATEV(37) = STATEV(37
STATEV(56) = STATEV(56)
no
STATEV(30) = 7
STATEV(38) = STATEV(37)
STATEV(57) = STATEV(56)
no
STATEV(29) = 2
STATEV(37) = STATEV(37)
STATEV(56) = STATEV(56)
no
STATEV(29) = 4
yes
DEP3(1) > 0
yes
STATEV(29) = 4
STATEV(37) = MIN (SP(1), STATEV(37))
STATEV(56) = EP(1)
no
STATEV(29) = 5
STATEV(37) = STATEV(37)
STATEV(56) = STATEV(56)
no
STATEV(29) = 5
yes
SP(1) > 0
yes
DEP3(1) > 0
yes
STATEV(37) ≤SP(1)
yes
STATEV(29) = 4
STATEV(37) = SP(2)
STATEV(56) = EP(2)
no
STATEV(29) = 6
STATEV(37) = STATEV(37)
STATEV(56) = STATEV(56)
no
STATEV(29) = 5
STATEV(37) = STATEV(37
STATEV(56) = STATEV(56)
no
STATEV(29) = 9
STATEV(37) = STATEV(37)
STATEV(56) = STATEV(56)
MC1A
MC1B

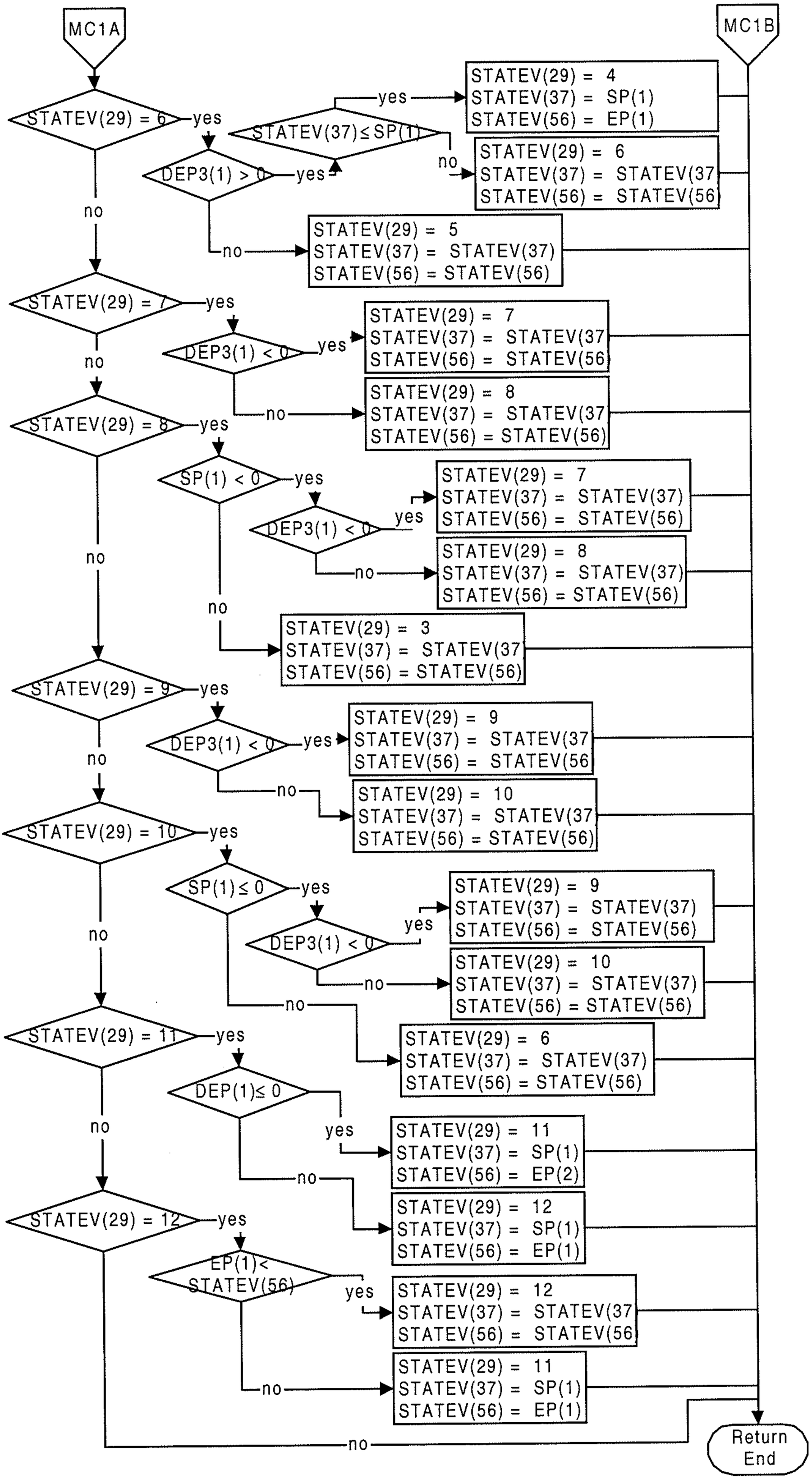
MC1A
STATEV(29) = 6
yes
DEP3(1) > 0
yes
STATEV(37)≤ SP(1)
yes
STATEV(29) = 4
STATEV(37) = SP(1)
STATEV(56) = EP(1)
no
STATEV(29) = 6
STATEV(37) = STATEV(37
STATEV(56) = STATEV(56)
no
STATEV(29) = 5
STATEV(37) = STATEV(37)
STATEV(56) = STATEV(56)
no
STATEV(29) = 7
yes
DEP3(1) < 0
yes
STATEV(29) = 7
STATEV(37) = STATEV(37
STATEV(56) = STATEV(56)
no
STATEV(29) = 8
STATEV(37) = STATEV(37
STATEV(56) = STATEV(56)
no
STATEV(29) = 8
yes
SP(1) < 0
yes
DEP3(1) < 0
yes
STATEV(29) = 7
STATEV(37) = STATEV(37)
STATEV(56) = STATEV(56)
no
STATEV(29) = 8
STATEV(37) = STATEV(37)
STATEV(56) = STATEV(56)
no
STATEV(29) = 3
STATEV(37) = STATEV(37
STATEV(56) = STATEV(56)
no
STATEV(29) = 9
yes
DEP3(1) < 0
yes
STATEV(29) = 9
STATEV(37) = STATEV(37
STATEV(56) = STATEV(56)
no
STATEV(29) = 10
STATEV(37) = STATEV(37
STATEV(56) = STATEV(56)
no
STATEV(29) = 10
yes
SP(1)≤ 0
yes
DEP3(1) < 0
yes
STATEV(29) = 9
STATEV(37) = STATEV(37)
STATEV(56) = STATEV(56)
no
STATEV(29) = 10
STATEV(37) = STATEV(37)
STATEV(56) = STATEV(56)
no
STATEV(29) = 6
STATEV(37) = STATEV(37)
STATEV(56) = STATEV(56)
no
STATEV(29) = 11
yes
DEP(1)≤ 0
yes
STATEV(29) = 11
STATEV(37) = SP(1)
STATEV(56) = EP(2)
no
STATEV(29) = 12
STATEV(37) = SP(1)
STATEV(56) = EP(1)
no
STATEV(29) = 12
yes
EP(1)< STATEV(56)
yes
STATEV(29) = 12
STATEV(37) = STATEV(37
STATEV(56) = STATEV(56)
no
STATEV(29) = 11
STATEV(37) = SP(1)
STATEV(56) = EP(1)
no
Return
End
MC1B

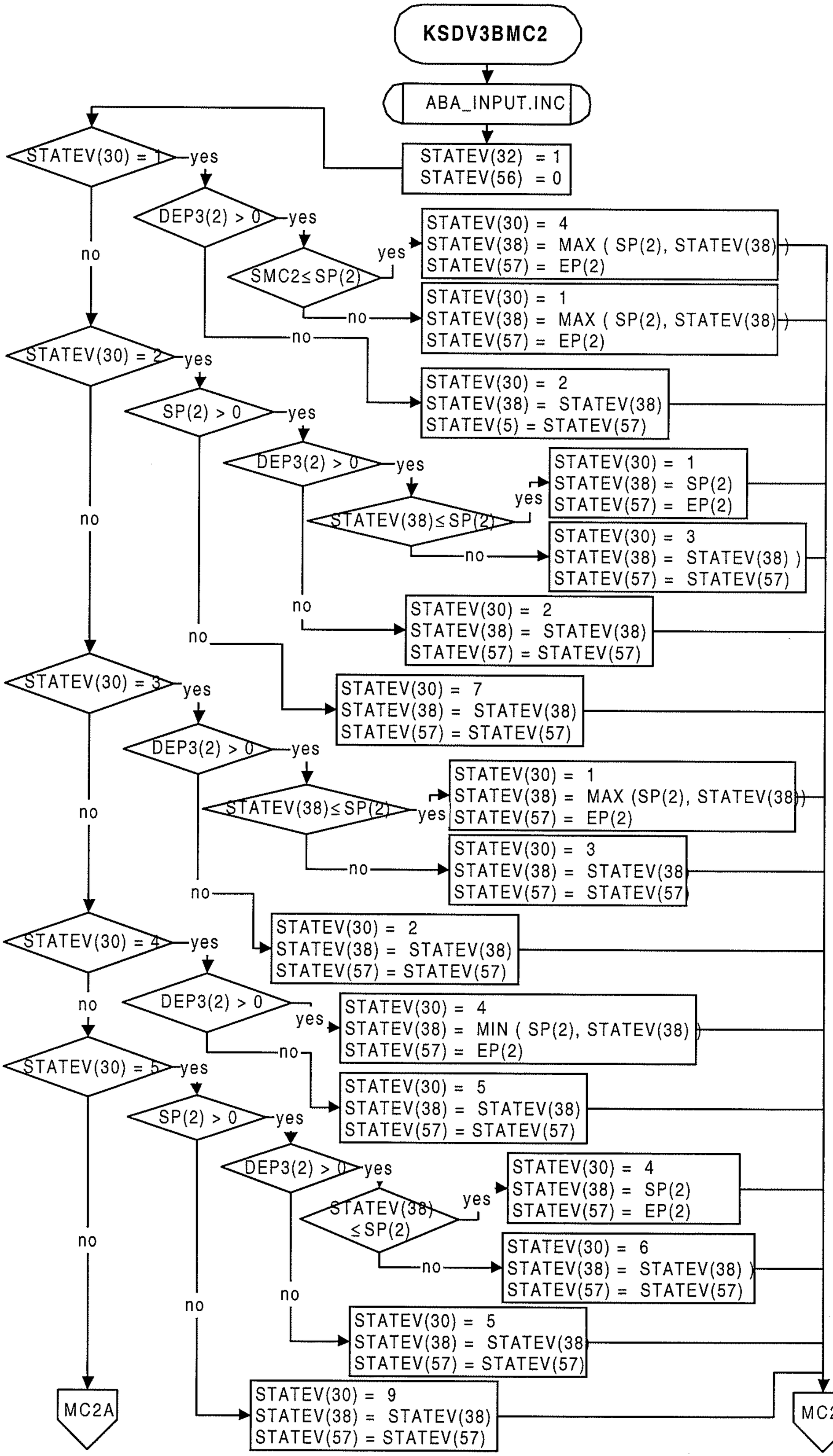
KSDV3BMC2
ABA_INPUT.INC
STATEV(30) = 1
yes
STATEV(32) = 1
STATEV(56) = 0
DEP3(2) > 0
yes
no
SMC2≤ SP(2)
yes
STATEV(30) = 4
STATEV(38) = MAX (SP(2), STATEV(38))
STATEV(57) = EP(2)
no
STATEV(30) = 1
STATEV(38) = MAX (SP(2), STATEV(38))
STATEV(57) = EP(2)
no
STATEV(30) = 2
yes
STATEV(30) = 2
STATEV(38) = STATEV(38)
STATEV(5) = STATEV(57)
SP(2) > 0
yes
DEP3(2) > 0
yes
STATEV(38)≤ SP(2)
yes
STATEV(30) = 1
STATEV(38) = SP(2)
STATEV(57) = EP(2)
no
STATEV(30) = 3
STATEV(38) = STATEV(38))
STATEV(57) = STATEV(57)
no
STATEV(30) = 2
STATEV(38) = STATEV(38)
STATEV(57) = STATEV(57)
no
STATEV(30) = 2
STATEV(38) = STATEV(38)
STATEV(57) = STATEV(57)
no
STATEV(30) = 3
yes
STATEV(30) = 7
STATEV(38) = STATEV(38)
STATEV(57) = STATEV(57)
DEP3(2) > 0
yes
STATEV(38)≤ SP(2)
yes
STATEV(30) = 1
STATEV(38) = MAX (SP(2), STATEV(38))
STATEV(57) = EP(2)
no
STATEV(30) = 3
STATEV(38) = STATEV(38
STATEV(57) = STATEV(57
no
STATEV(30) = 4
yes
STATEV(30) = 2
STATEV(38) = STATEV(38)
STATEV(57) = STATEV(57)
DEP3(2) > 0
yes
STATEV(30) = 4
STATEV(38) = MIN (SP(2), STATEV(38))
STATEV(57) = EP(2)
no
STATEV(30) = 5
yes
STATEV(30) = 5
STATEV(38) = STATEV(38)
STATEV(57) = STATEV(57)
SP(2) > 0
yes
DEP3(2) > 0
yes
STATEV(38) ≤SP(2)
yes
STATEV(30) = 4
STATEV(38) = SP(2)
STATEV(57) = EP(2)
no
STATEV(30) = 6
STATEV(38) = STATEV(38))
STATEV(57) = STATEV(57)
no
STATEV(30) = 5
STATEV(38) = STATEV(38
STATEV(57) = STATEV(57)
no
STATEV(30) = 9
STATEV(38) = STATEV(38)
STATEV(57) = STATEV(57)
MC2A
MC2B

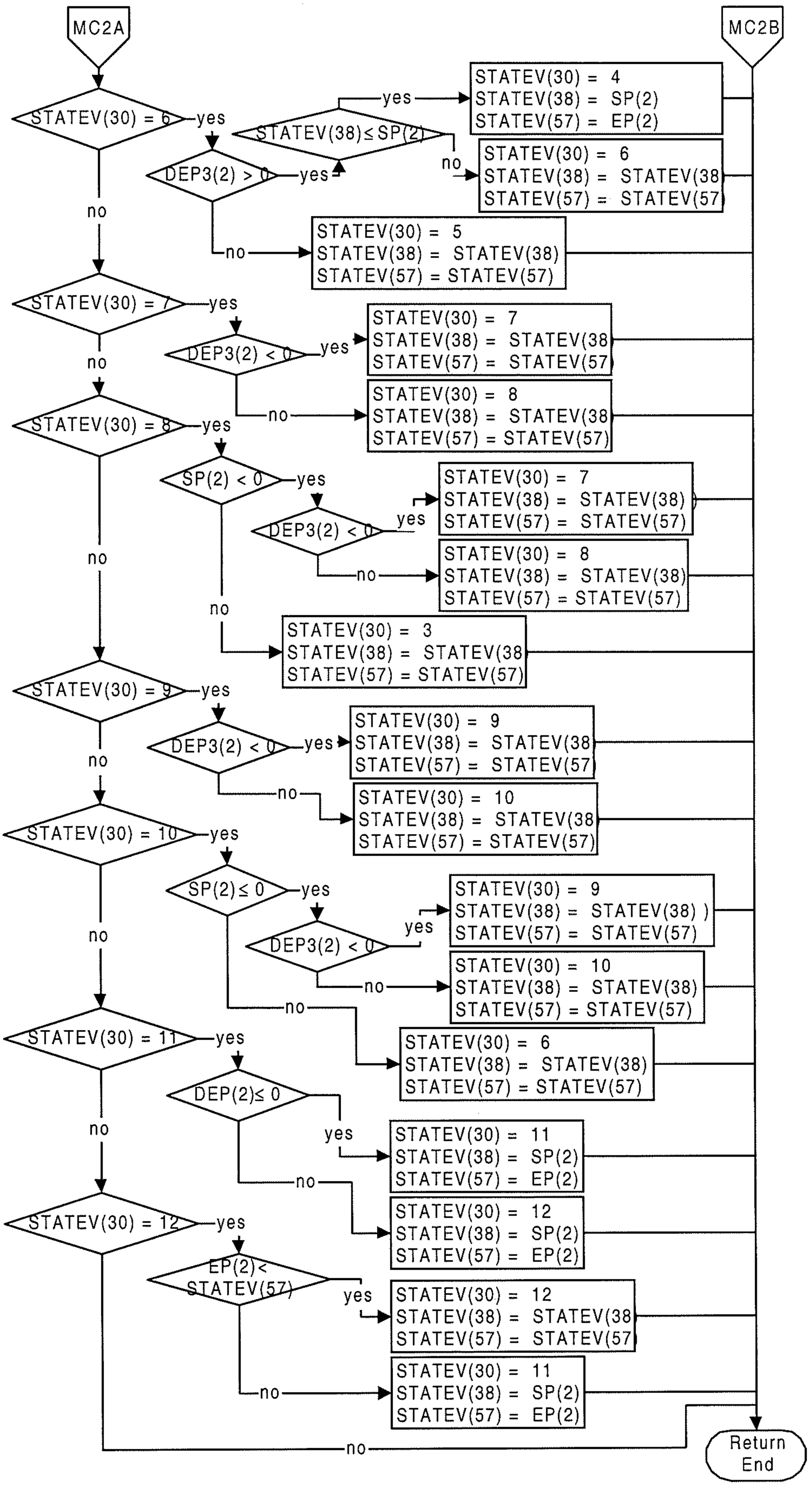
MC2A
STATEV(30) = 6
yes
STATEV(38)≤ SP(2)
yes
STATEV(30) = 4
STATEV(38) = SP(2)
STATEV(57) = EP(2)
no
DEP3(2) > 0
yes
STATEV(30) = 6
STATEV(38) = STATEV(38
STATEV(57) = STATEV(57
no
STATEV(30) = 5
STATEV(38) = STATEV(38)
STATEV(57) = STATEV(57)
STATEV(30) = 7
yes
DEP3(2) < 0
yes
STATEV(30) = 7
STATEV(38) = STATEV(38
STATEV(57) = STATEV(57
no
STATEV(30) = 8
STATEV(38) = STATEV(38
STATEV(57) = STATEV(57)
STATEV(30) = 8
yes
SP(2) < 0
yes
DEP3(2) < 0
yes
STATEV(30) = 7
STATEV(38) = STATEV(38)
STATEV(57) = STATEV(57)
no
STATEV(30) = 8
STATEV(38) = STATEV(38)
STATEV(57) = STATEV(57)
no
STATEV(30) = 3
STATEV(38) = STATEV(38
STATEV(57) = STATEV(57)
STATEV(30) = 9
yes
DEP3(2) < 0
yes
STATEV(30) = 9
STATEV(38) = STATEV(38
STATEV(57) = STATEV(57
no
STATEV(30) = 10
STATEV(38) = STATEV(38
STATEV(57) = STATEV(57)
STATEV(30) = 10
yes
SP(2)≤ 0
yes
DEP3(2) < 0
yes
STATEV(30) = 9
STATEV(38) = STATEV(38))
STATEV(57) = STATEV(57)
no
STATEV(30) = 10
STATEV(38) = STATEV(38)
STATEV(57) = STATEV(57)
no
STATEV(30) = 6
STATEV(38) = STATEV(38)
STATEV(57) = STATEV(57)
STATEV(30) = 11
yes
DEP(2)≤ 0
yes
STATEV(30) = 11
STATEV(38) = SP(2)
STATEV(57) = EP(2)
no
STATEV(30) = 12
STATEV(38) = SP(2)
STATEV(57) = EP(2)
STATEV(30) = 12
yes
EP(2)< STATEV(57)
yes
STATEV(30) = 12
STATEV(38) = STATEV(38
STATEV(57) = STATEV(57
no
STATEV(30) = 11
STATEV(38) = SP(2)
STATEV(57) = EP(2)
no
MC2B
Return
End

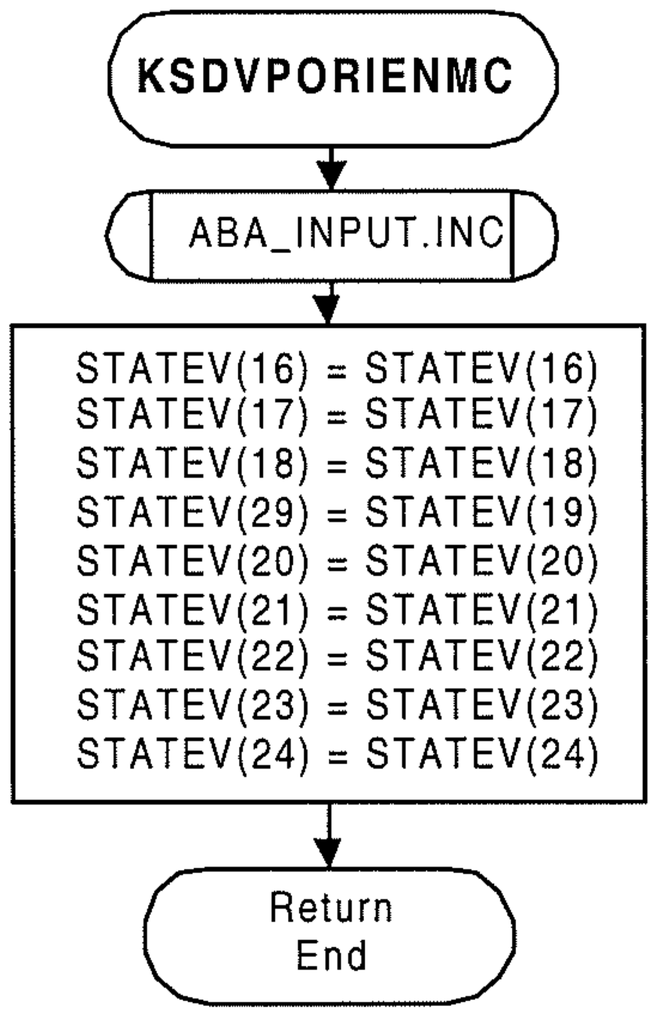

Fig 7.5.3-24 Flow diagram of the subroutine KSDVPORIENMC

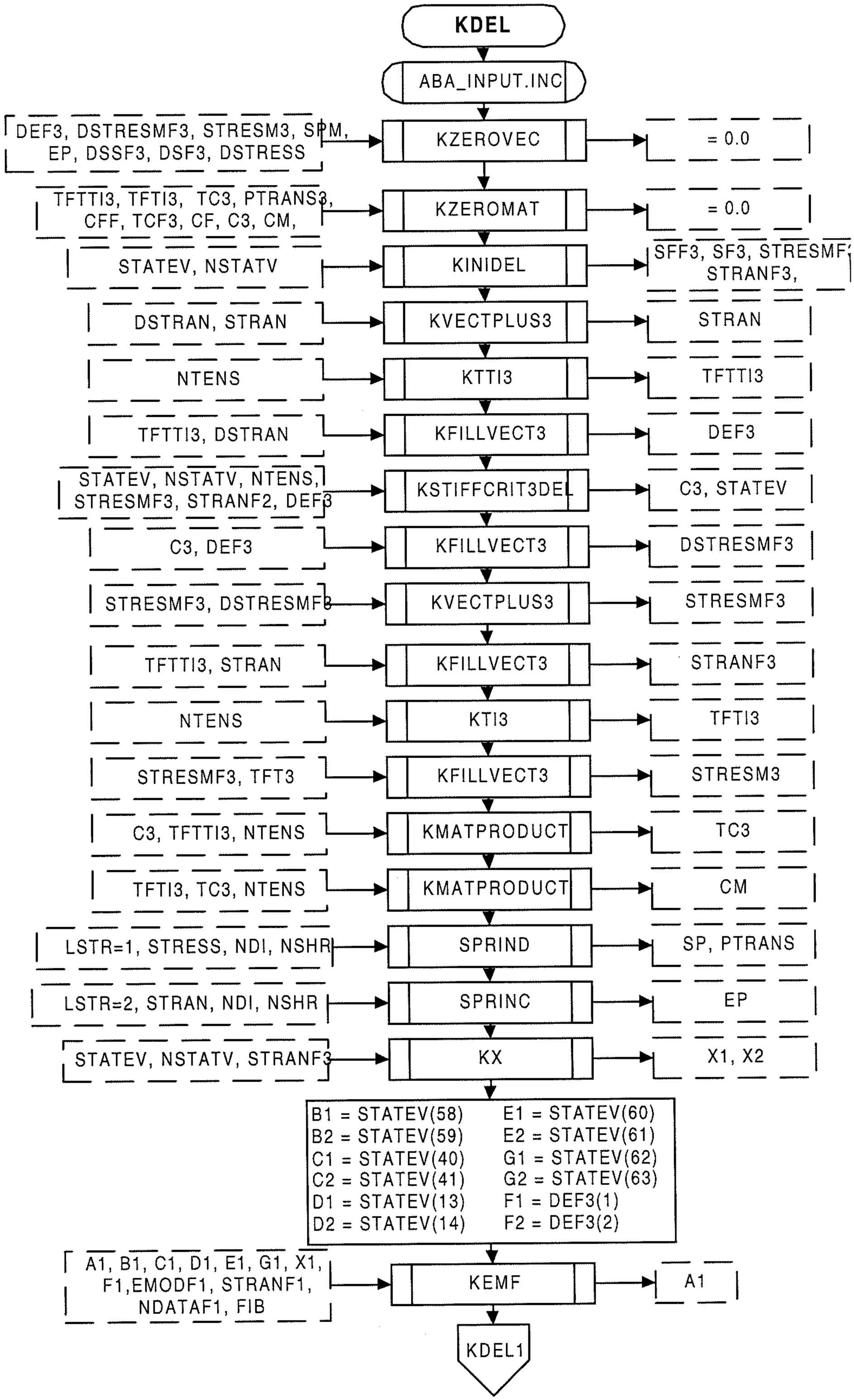
KDEL
ABA_INPUT.INC
DEF3, DSTRESMF3, STRESM3, SPM, EP, DSSF3, DSF3, DSTRESS
KZEROVEC
= 0.0
TFTTI3, TFTI3, TC3, PTRANS3, CFF, TCF3, CF, C3, CM,
KZEROMAT
= 0.0
STATEV, NSTATV
KINIDEL
SFF3, SF3, STRESMF3, STRANF3,
DSTRAN, STRAN
KVECTPLUS3
STRAN
NTENS
KTTI3
TFTTI3
TFTTI3, DSTRAN
KFILLVECT3
DEF3
STATEV, NSTATV, NTENS, STRESMF3, STRANF2, DEF3
KSTIFFCRIT3DEL
C3, STATEV
C3, DEF3
KFILLVECT3
DSTRESMF3
STRESMF3, DSTRESMF3
KVECTPLUS3
STRESMF3
TFTTI3, STRAN
KFILLVECT3
STRANF3
NTENS
KTI3
TFTI3
STRESMF3, TFT3
KFILLVECT3
STRESM3
C3, TFTTI3, NTENS
KMATPRODUCT
TC3
TFTI3, TC3, NTENS
KMATPRODUCT
CM
LSTR=1, STRESS, NDI, NSHR
SPRIND
SP, PTRANS
LSTR=2, STRAN, NDI, NSHR
SPRINC
EP
STATEV, NSTATV, STRANF3
KX
X1, X2
B1 = STATEV(58)
B2 = STATEV(59)
C1 = STATEV(40)
C2 = STATEV(41)
D1 = STATEV(13)
D2 = STATEV(14)
E1 = STATEV(60)
E2 = STATEV(61)
G1 = STATEV(62)
G2 = STATEV(63)
F1 = DEF3(1)
F2 = DEF3(2)
A1, B1, C1, D1, E1, G1, X1, F1,EMODF1, STRANF1, NDATAF1, FIB
KEMF
A1
KDEL1

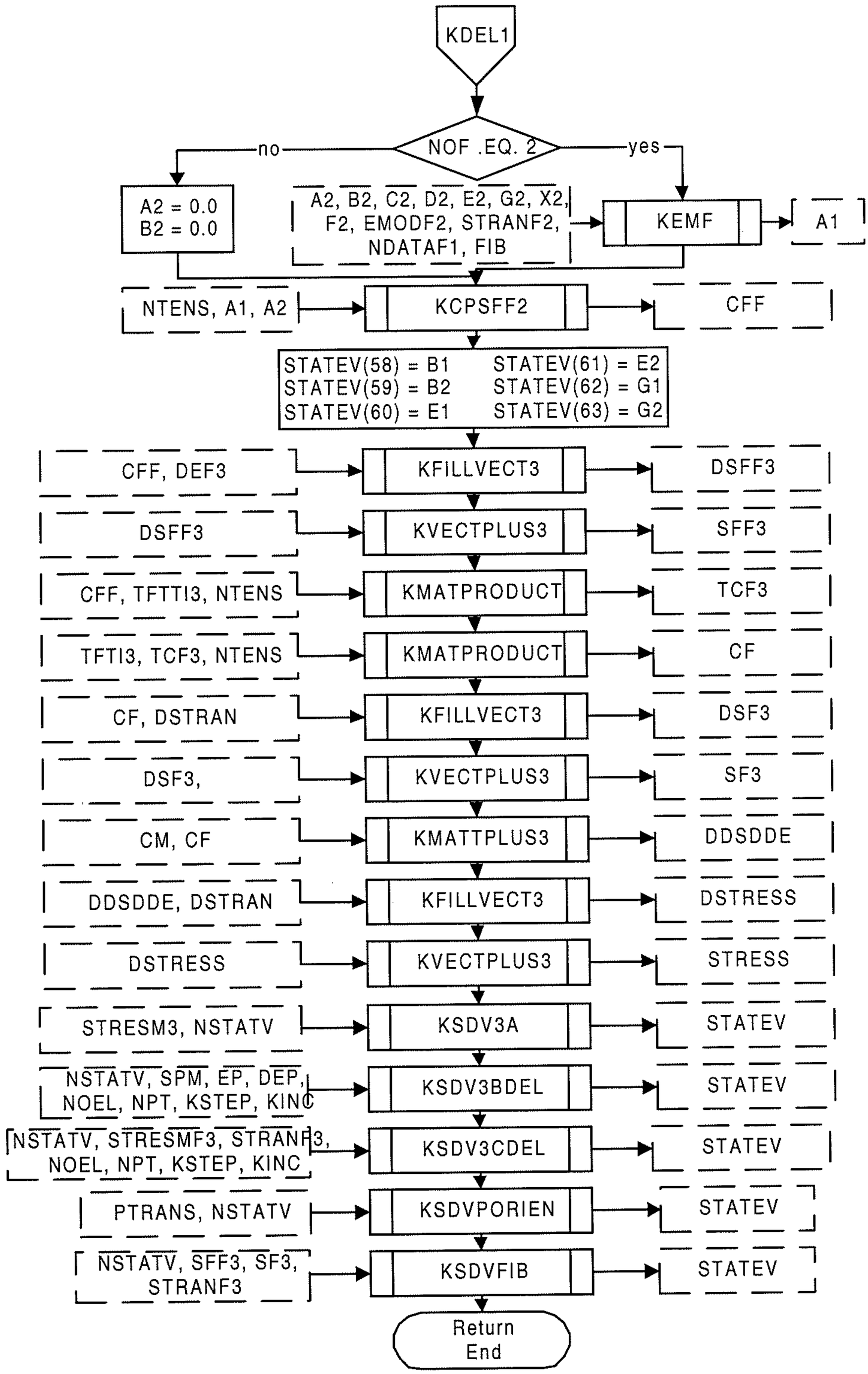

Fig 7.5.4-1b Flow diagram of the subroutine KDEL (Part 2/2)

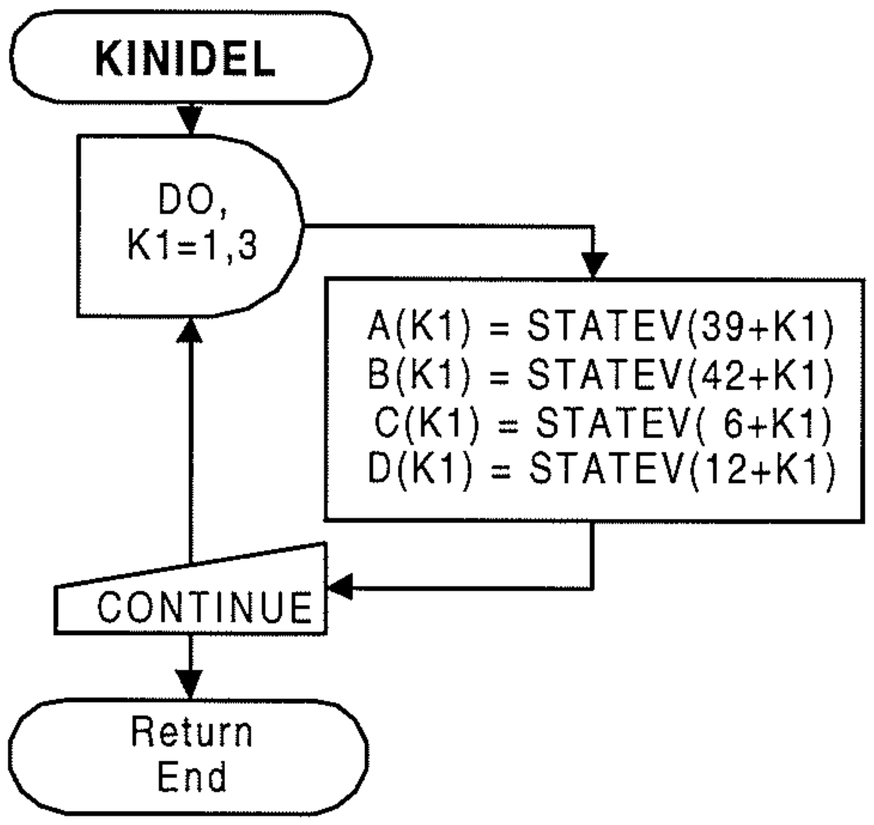

Fig 7.5.4-2 Flow diagram of the subroutine KINIDEL

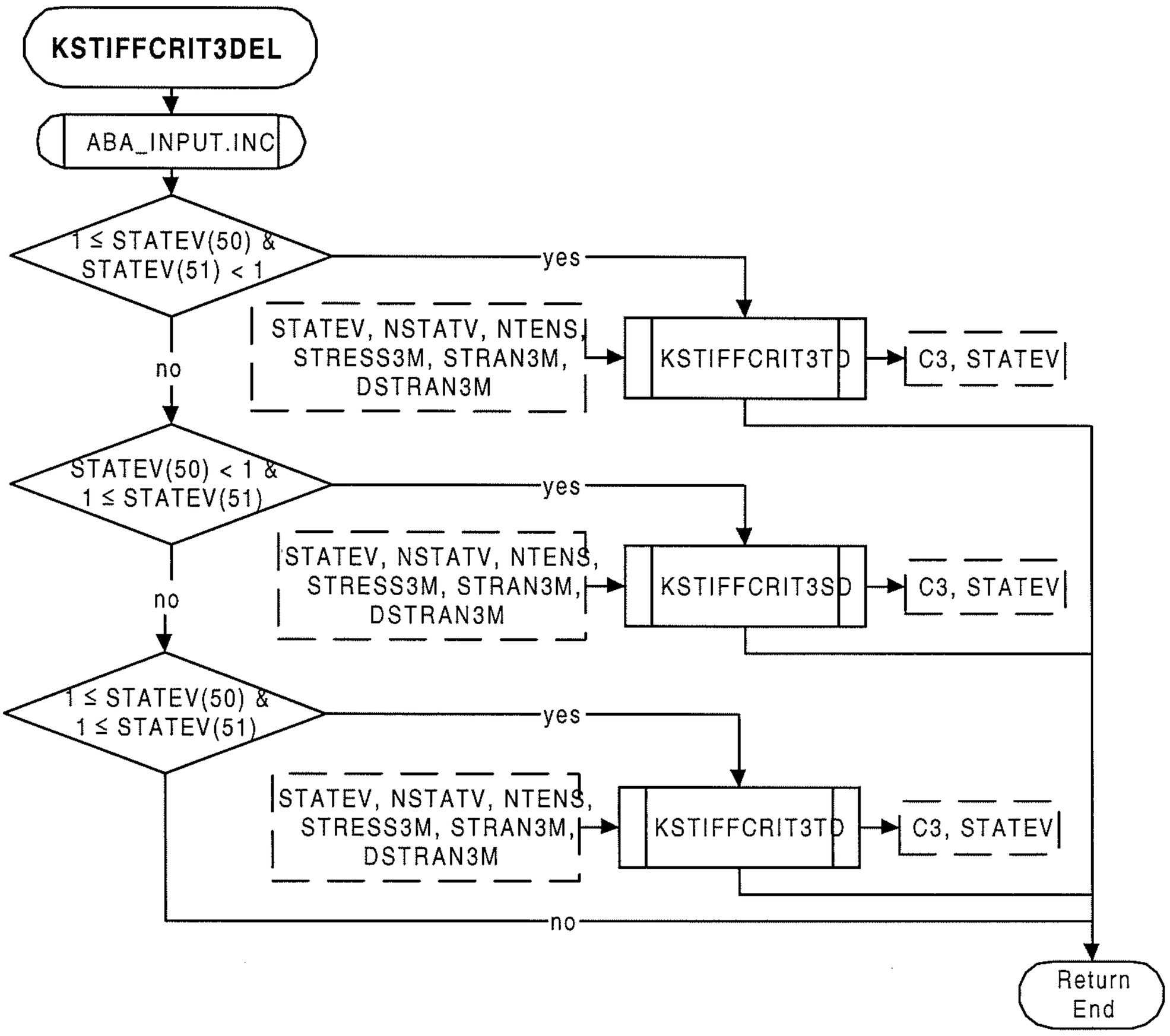

Fig 7.5.4-3 Flow diagram of the subroutine KSTIFFCRIT3DEL

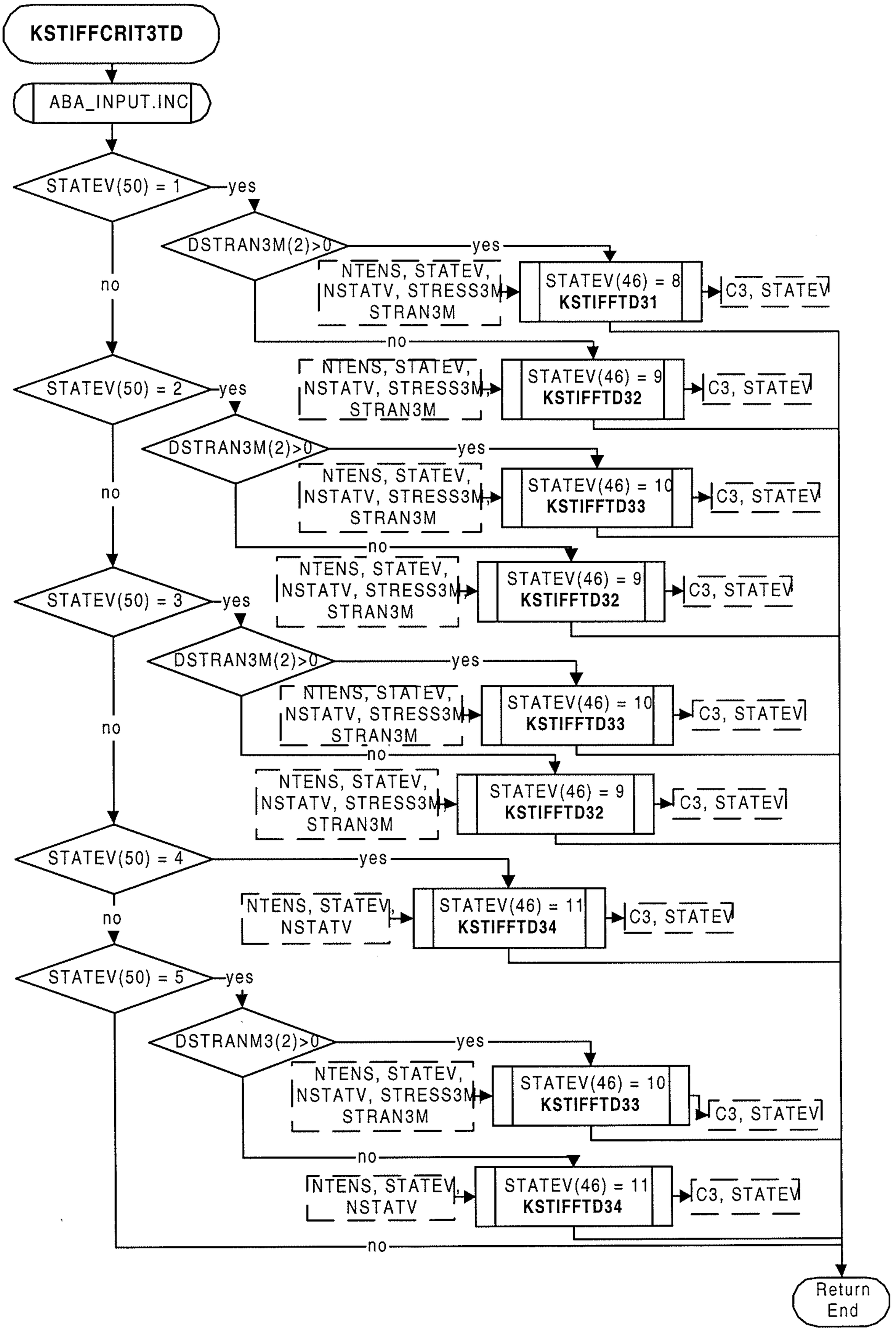

Fig 7.5.4-4 Flow diagram of the subroutine KSTIFFCRIT3TD

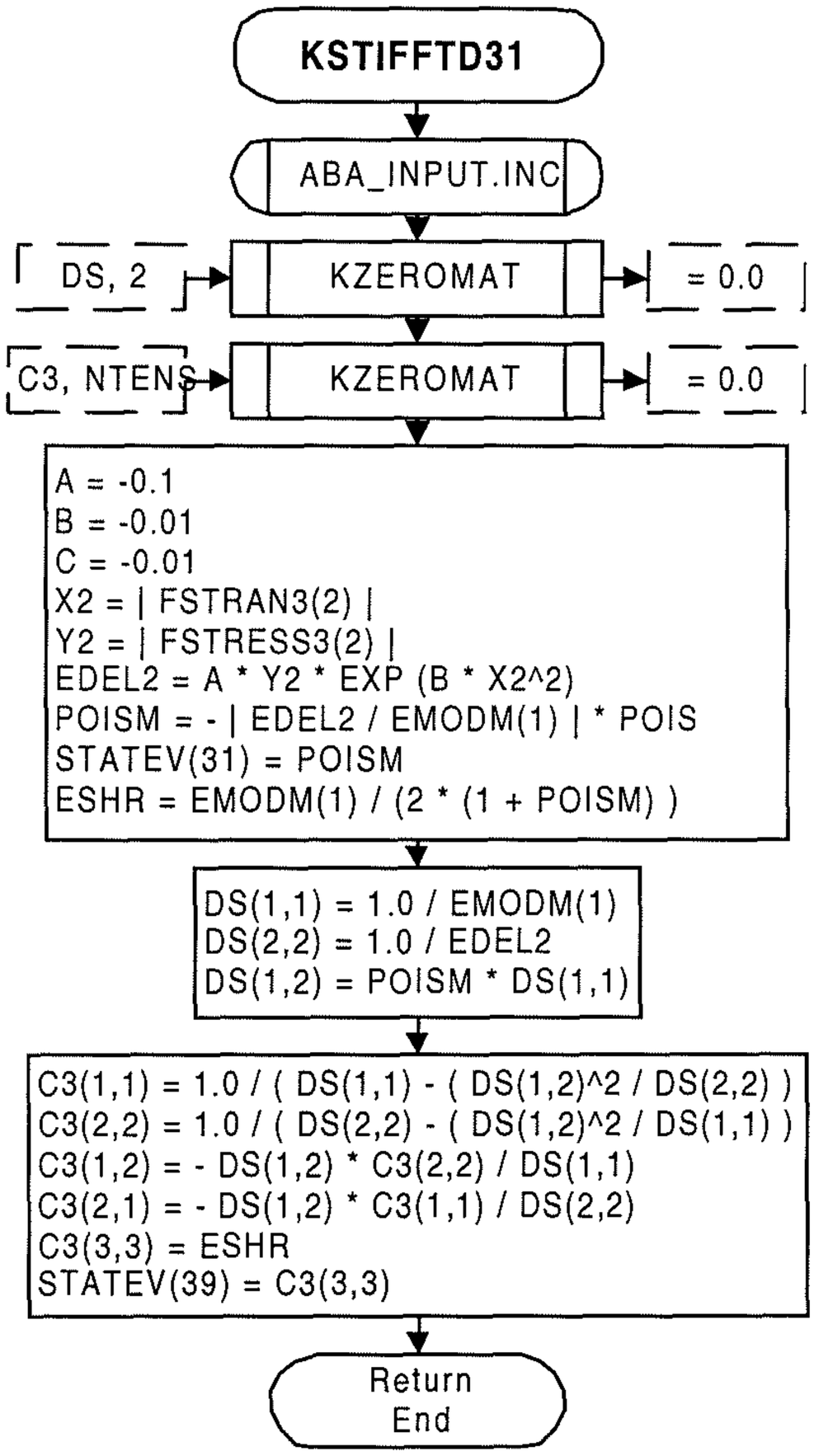

Fig 7.5.4-5
Flow diagram of the subroutine KSTIFFTD31

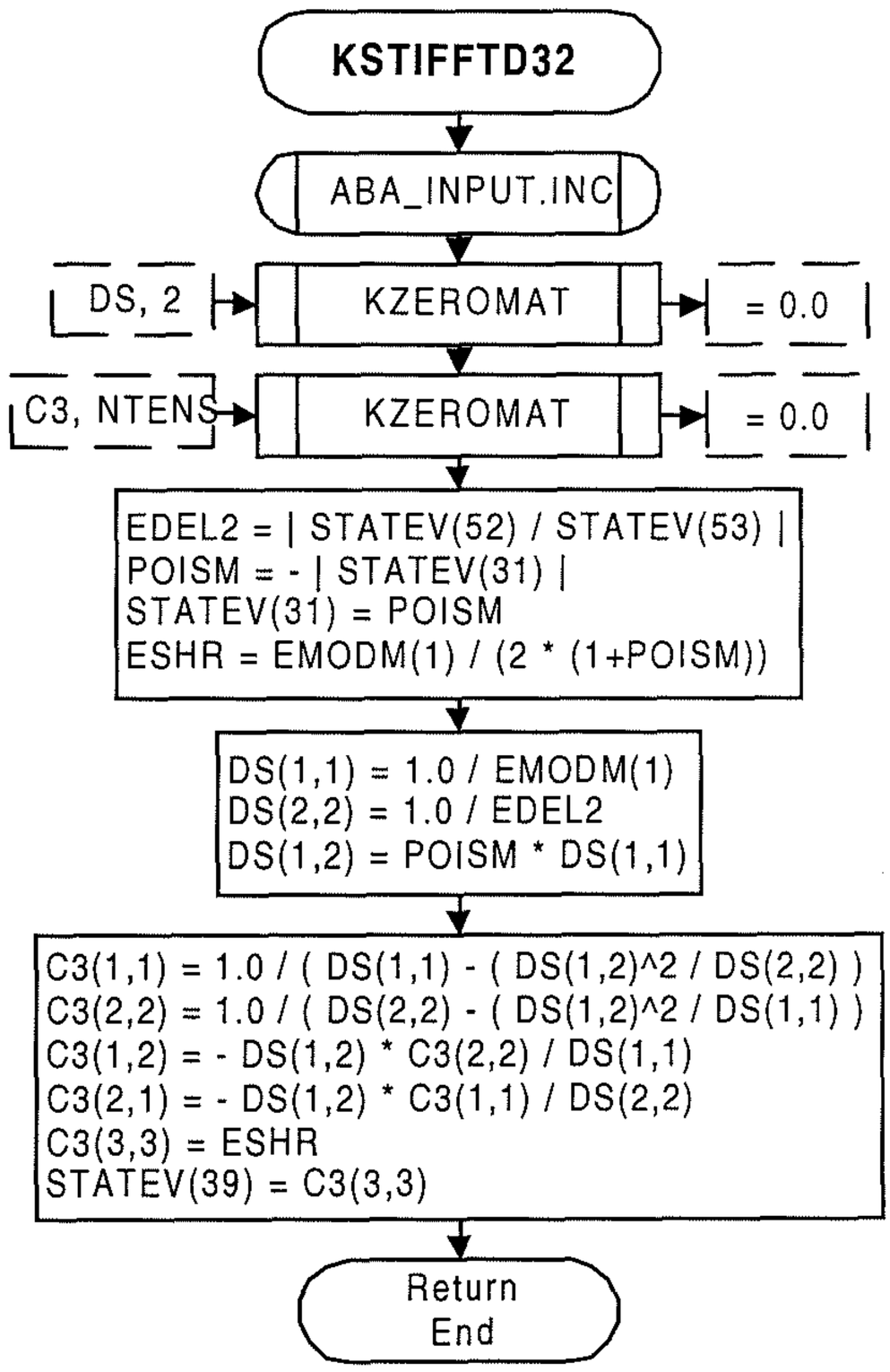

Fig 7.5.4-6
Flow diagram of the subroutine KSTIFFTD32

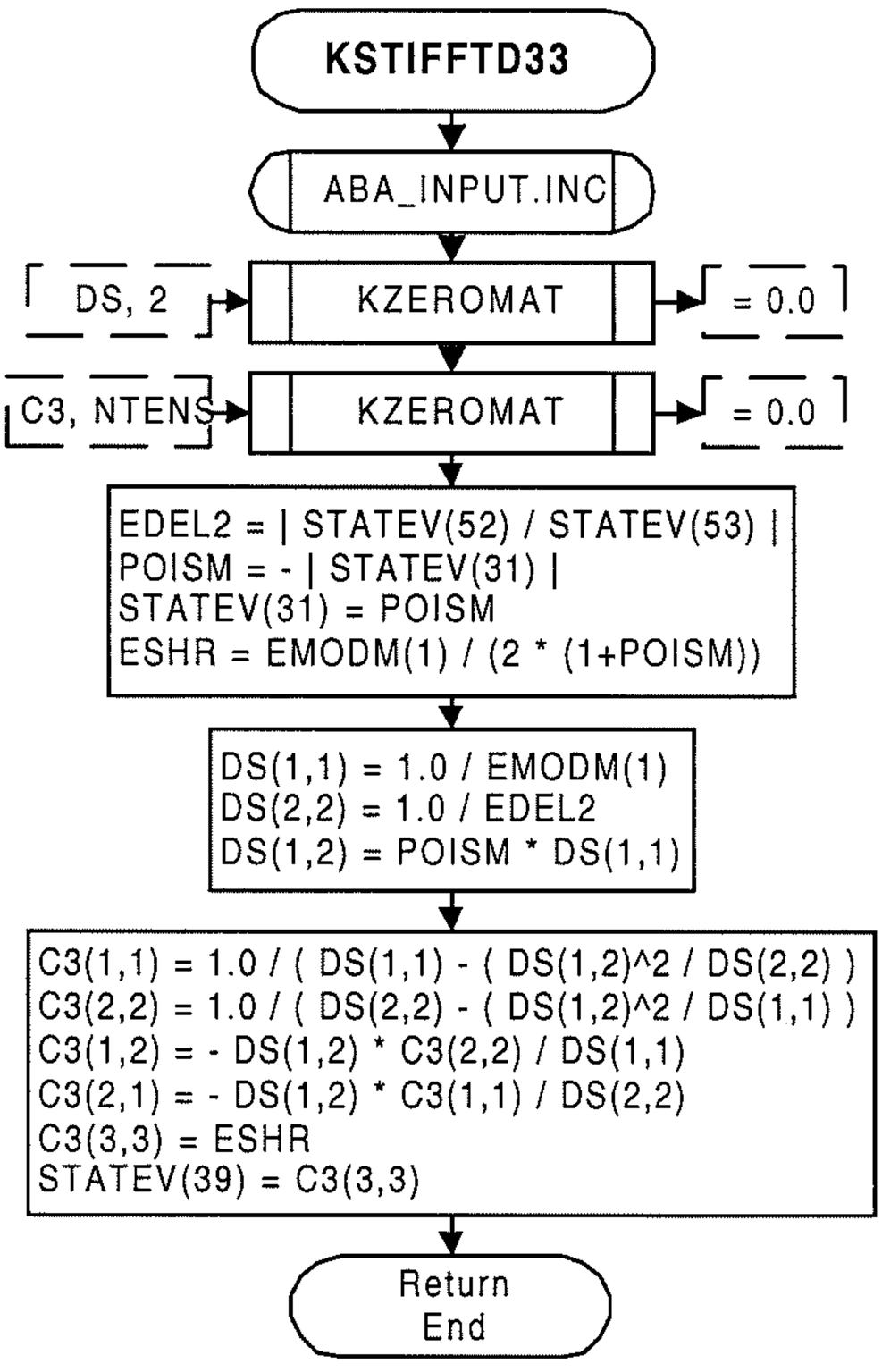

Fig 7.5.4-7
Flow diagram of the subroutine KSTIFFTD33

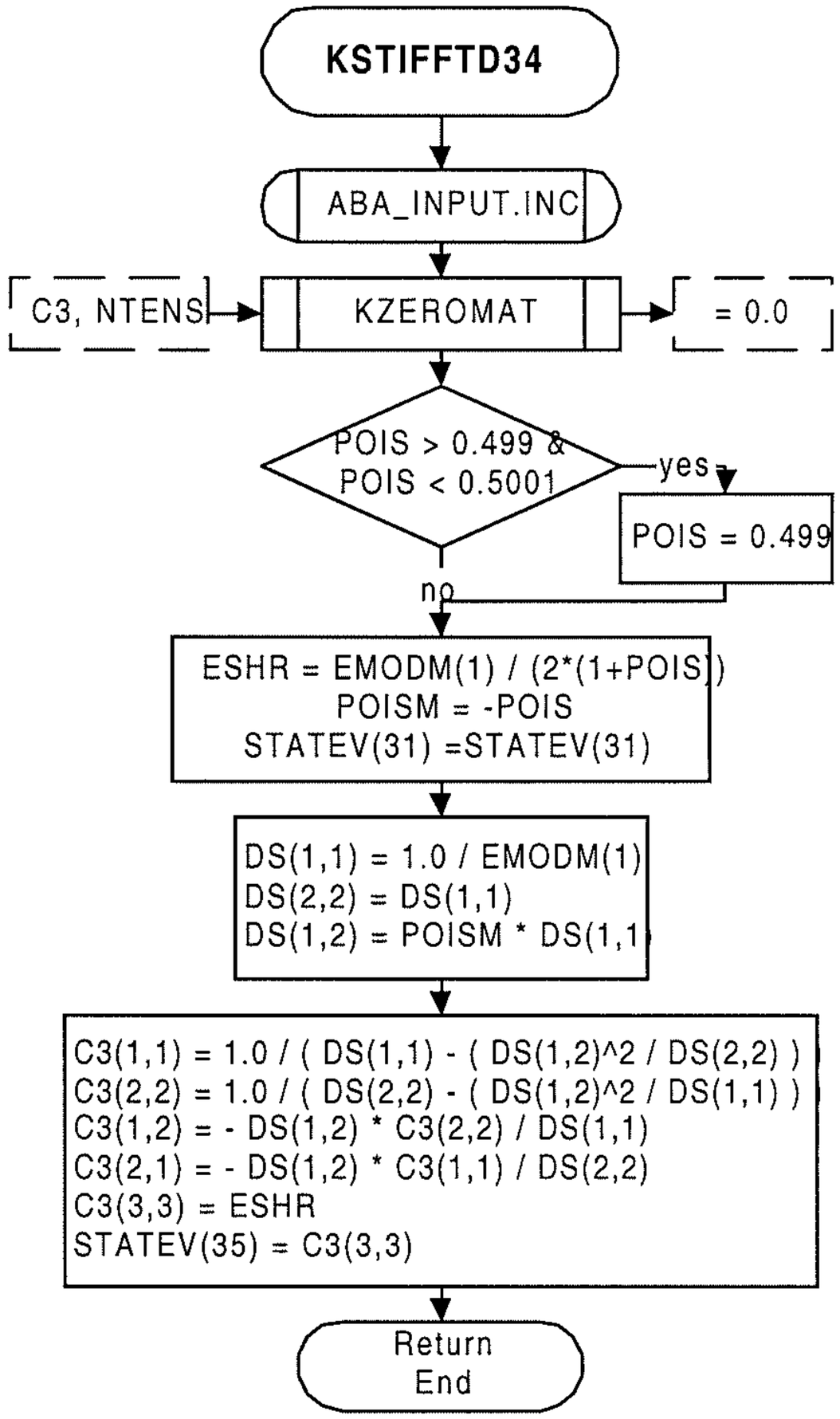

Fig 7.5.4-8
Flow diagram of the subroutine KSTIFFTD34

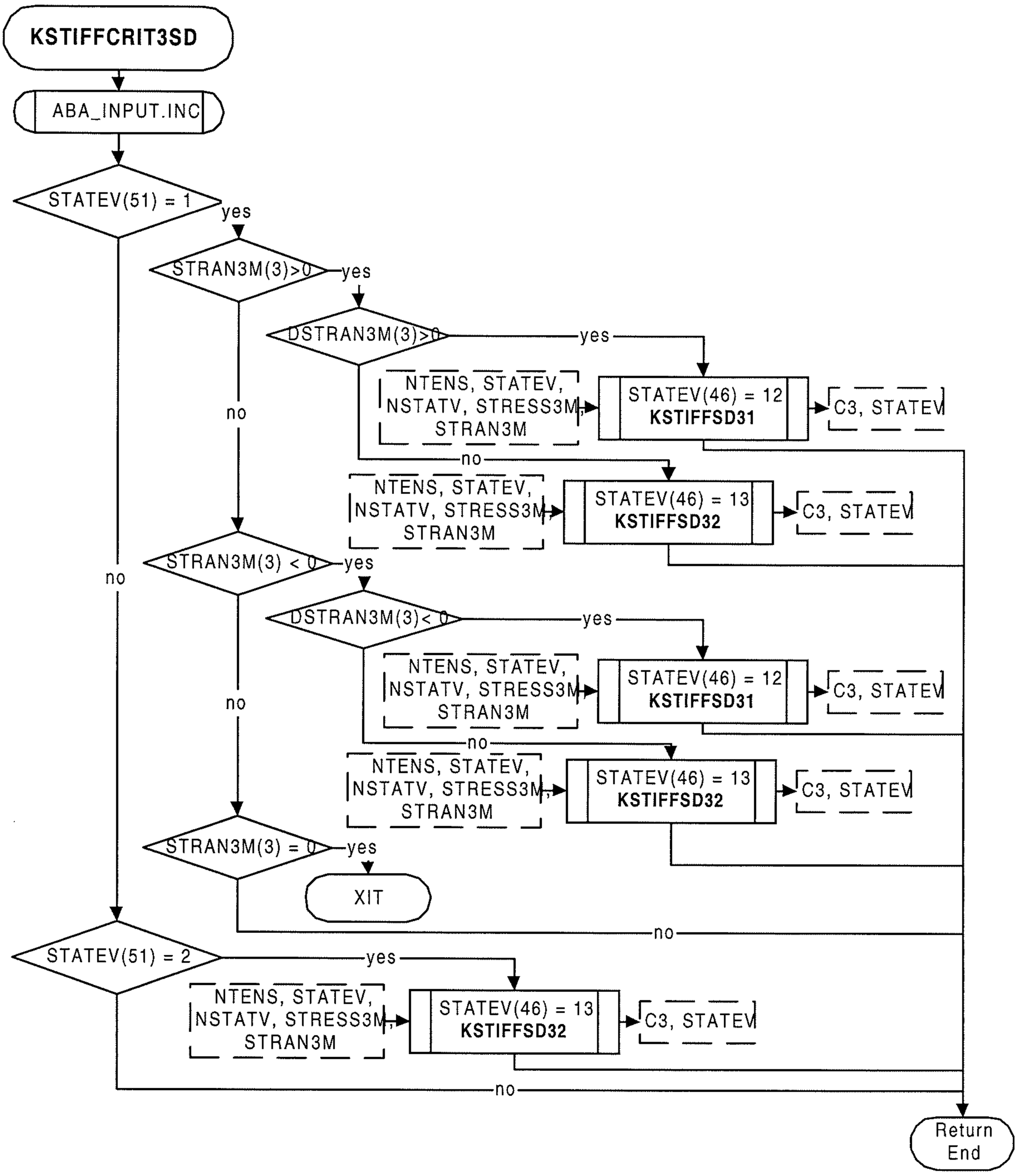

Fig 7.5.4-9 Flow diagram of the subroutine KSTIFFCRIT3SD

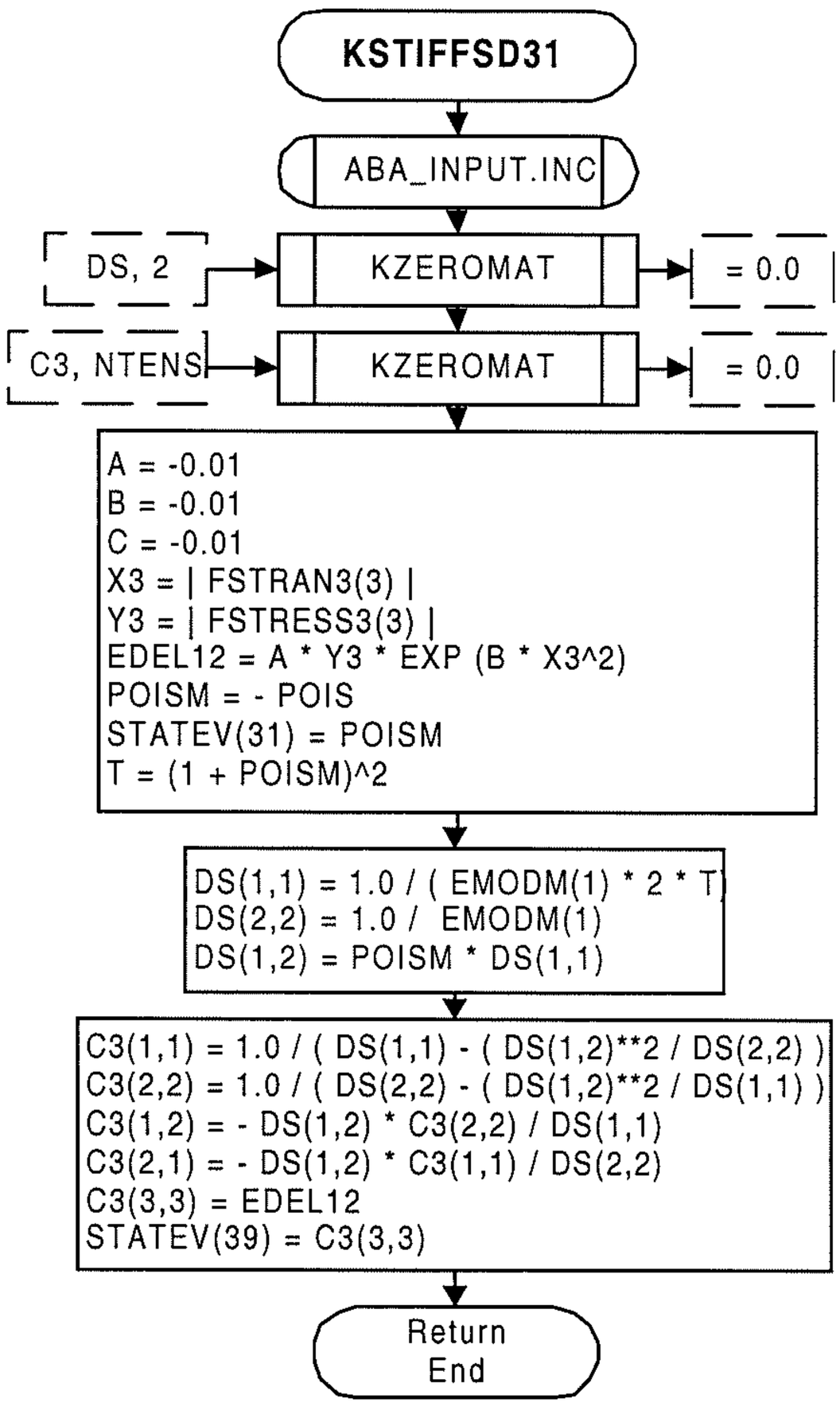

Fig 7.5.4-10
Flow diagram of the subroutine KSTIFFSD31

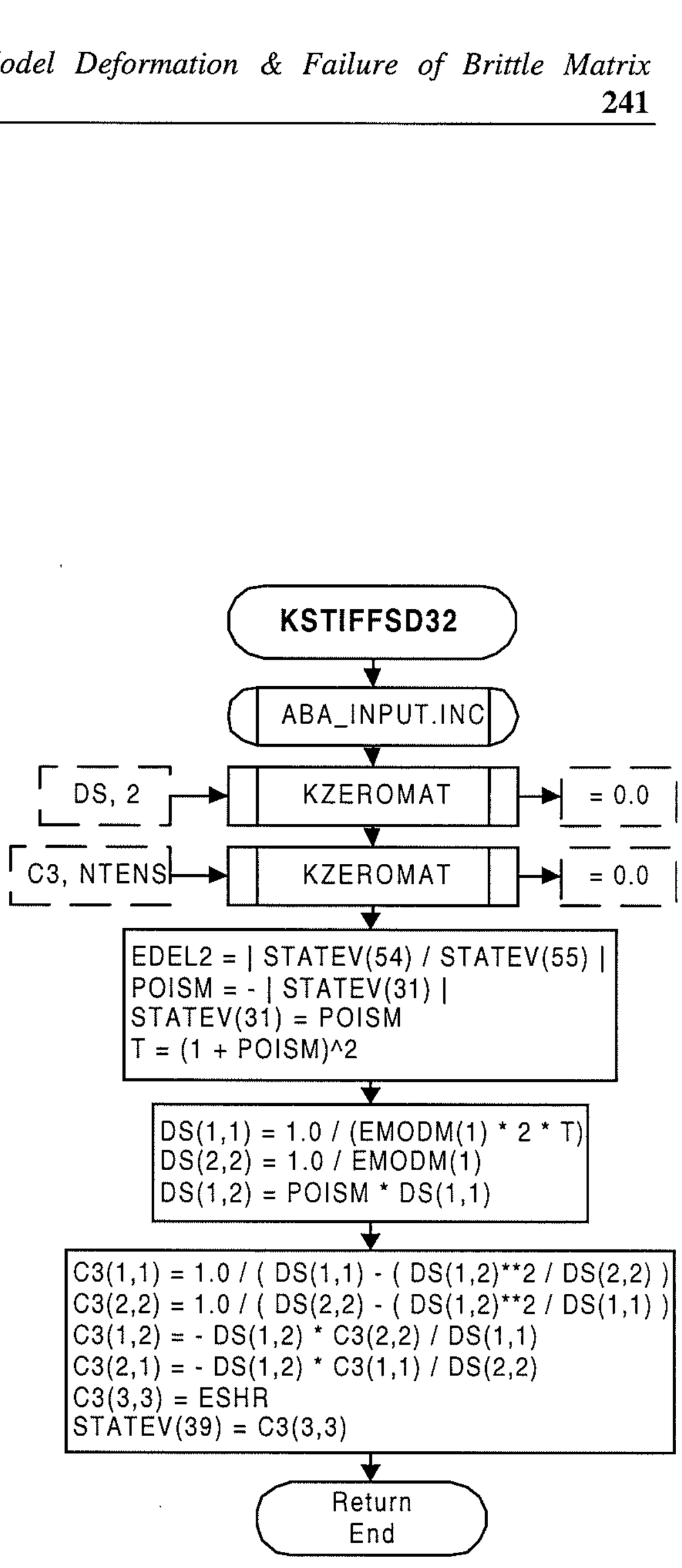

Fig 7.5.4-11
Flow diagram of the subroutine KSTIFFSD32

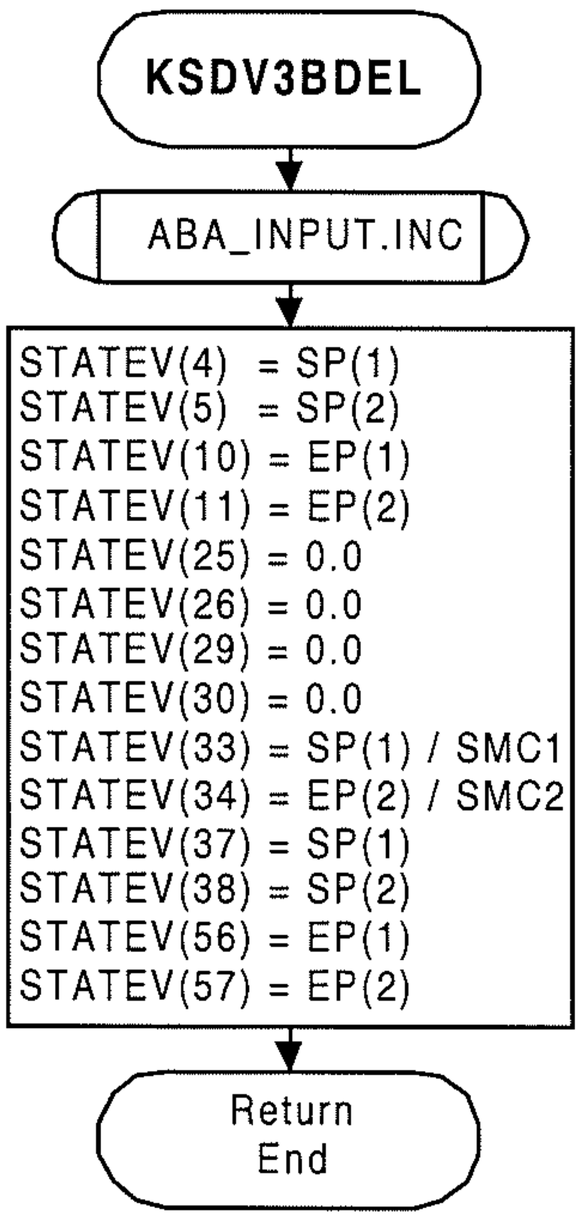

Fig 7.5.4-12 Flow diagram of the subroutine KSDV3BDEL

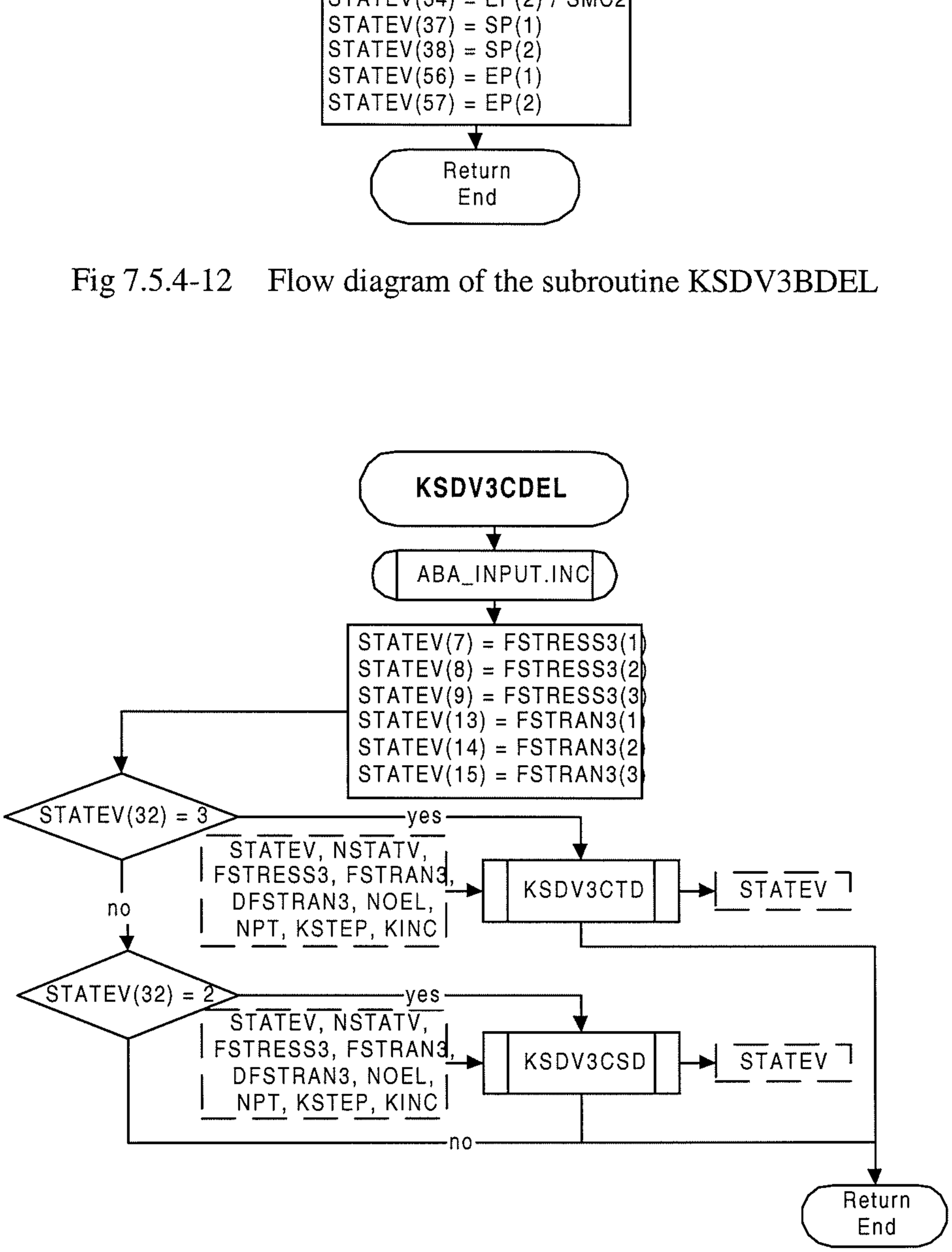

Fig 7.5.4-13 Flow diagram of the subroutine KSDV3CDEL

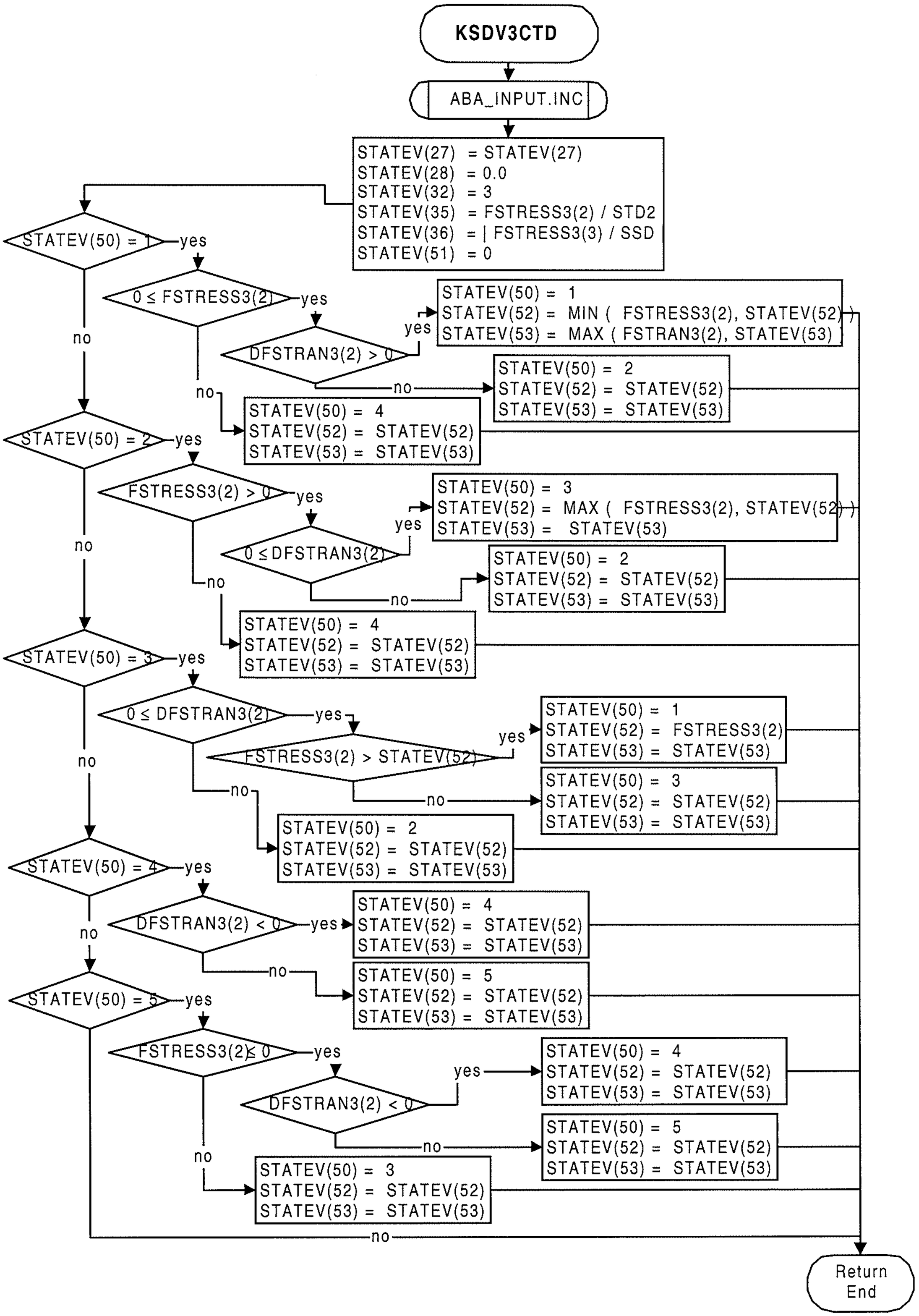

Fig 7.5.4-14 Flow diagram of the subroutine KSDV3CTD

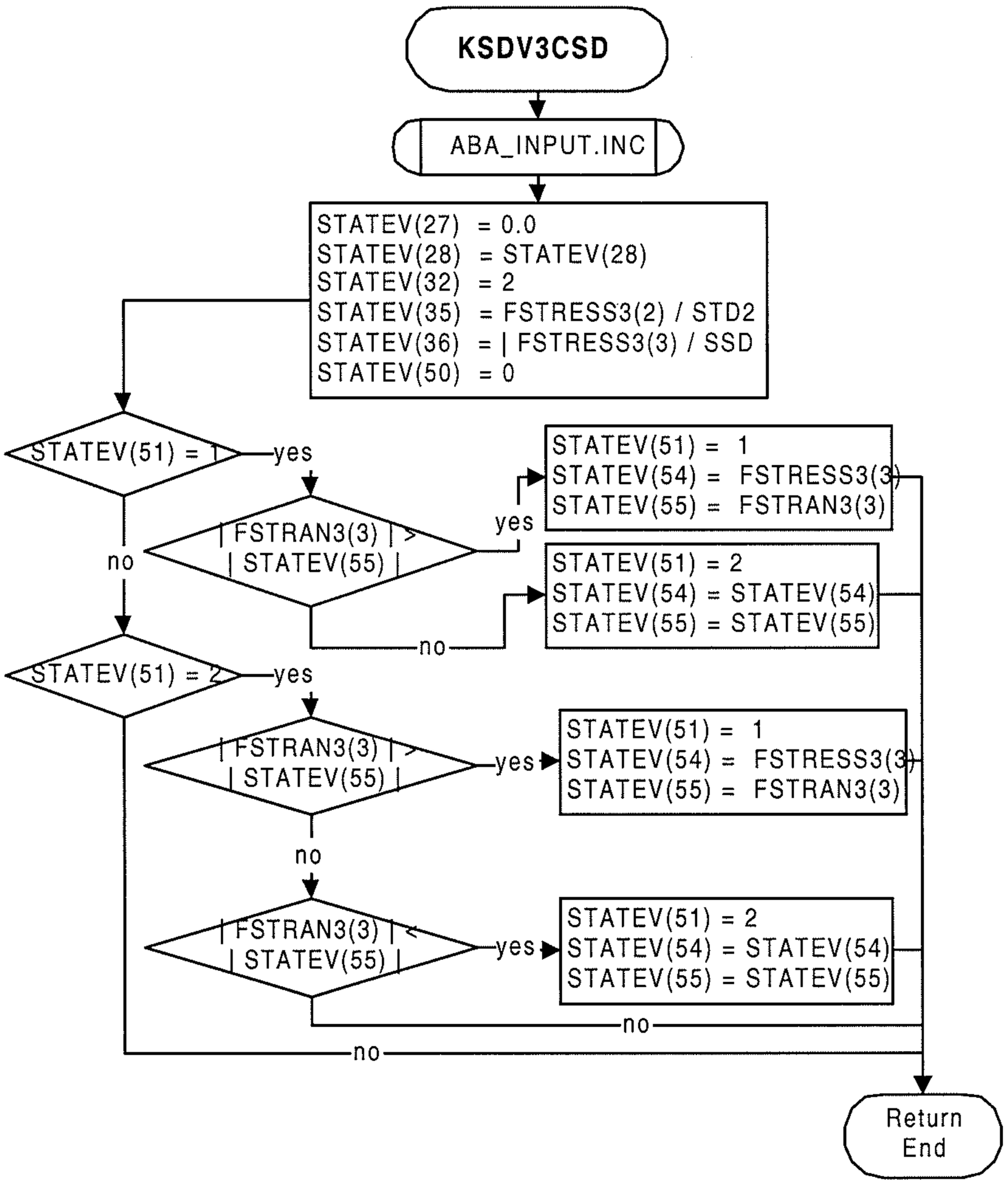

Fig 7.5.4-15 Flow diagram of the subroutine KSDV3CSD

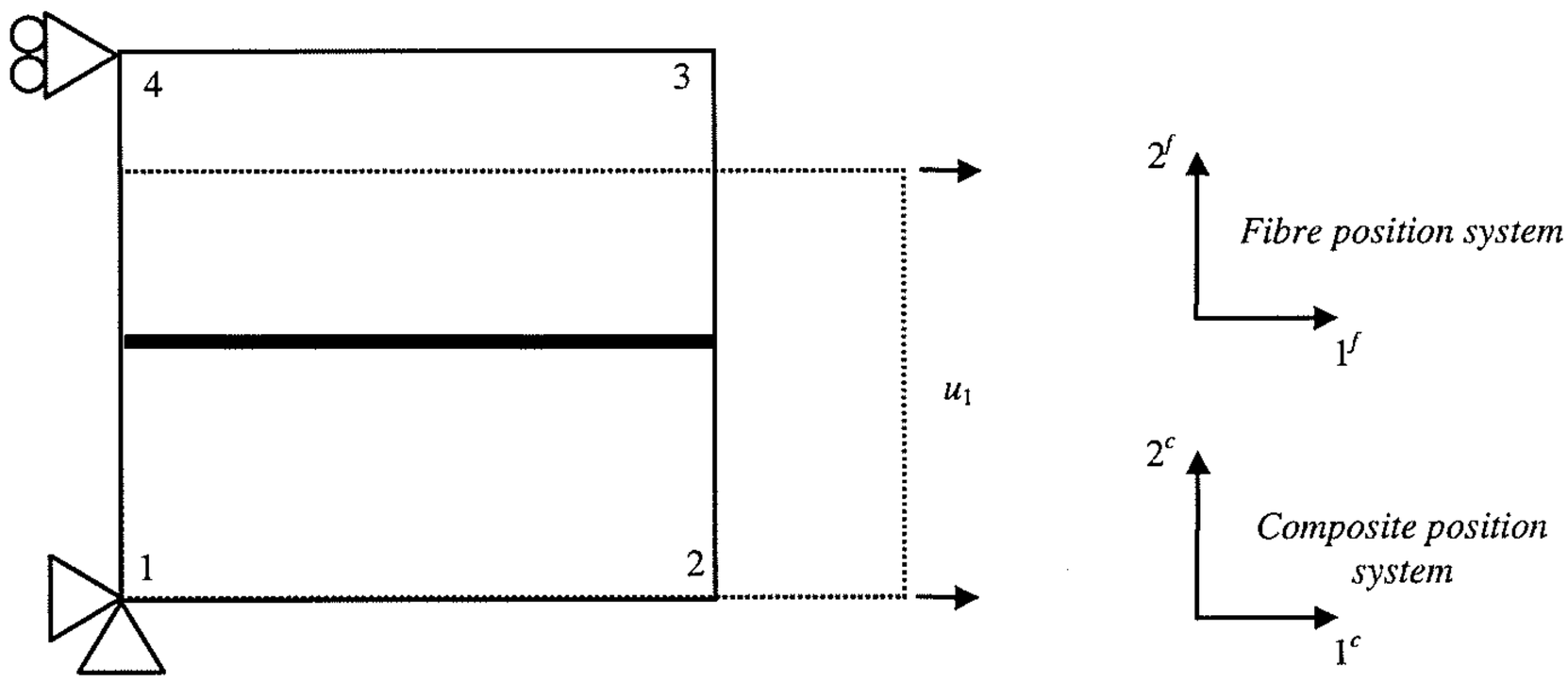

(a) Case Studies 1 & 2

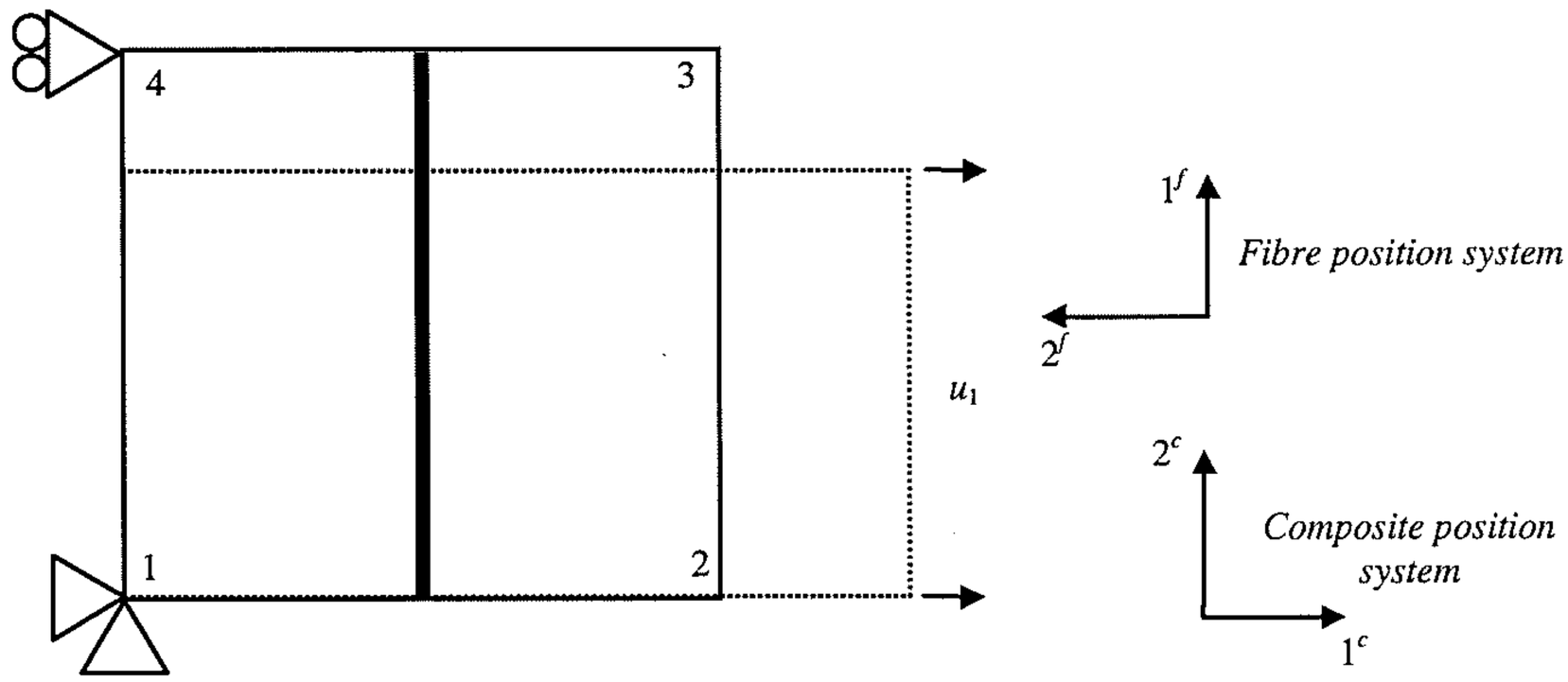

(b) Case Studies 3 & 4

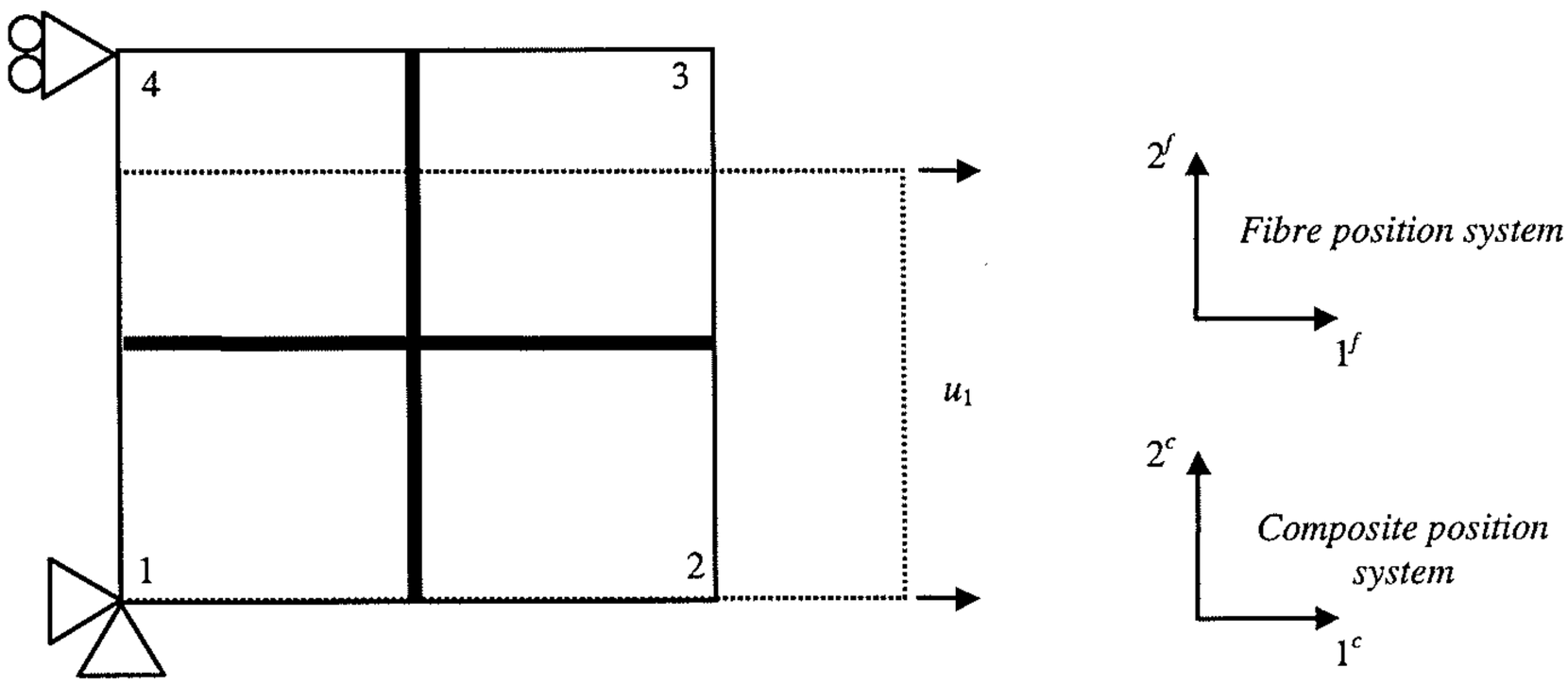

(c) Case Studies 5 & 6

Fig 7.6.1.1-1 Schematic diagrams of the benchmark problems for the pre-damage states.

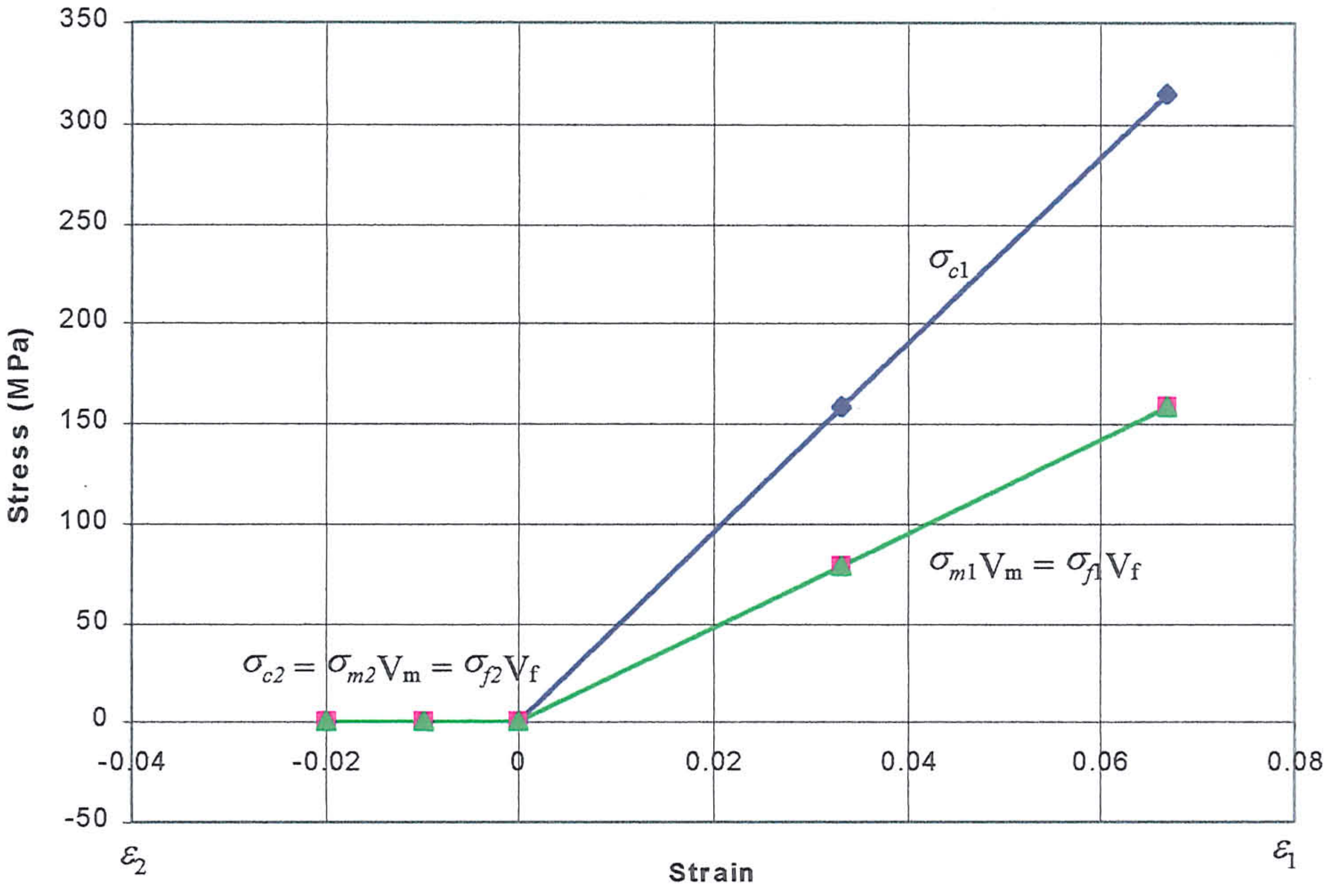

Fig 7.6.1.3-1 Stress-strain relations by UMAT for Load Case 1

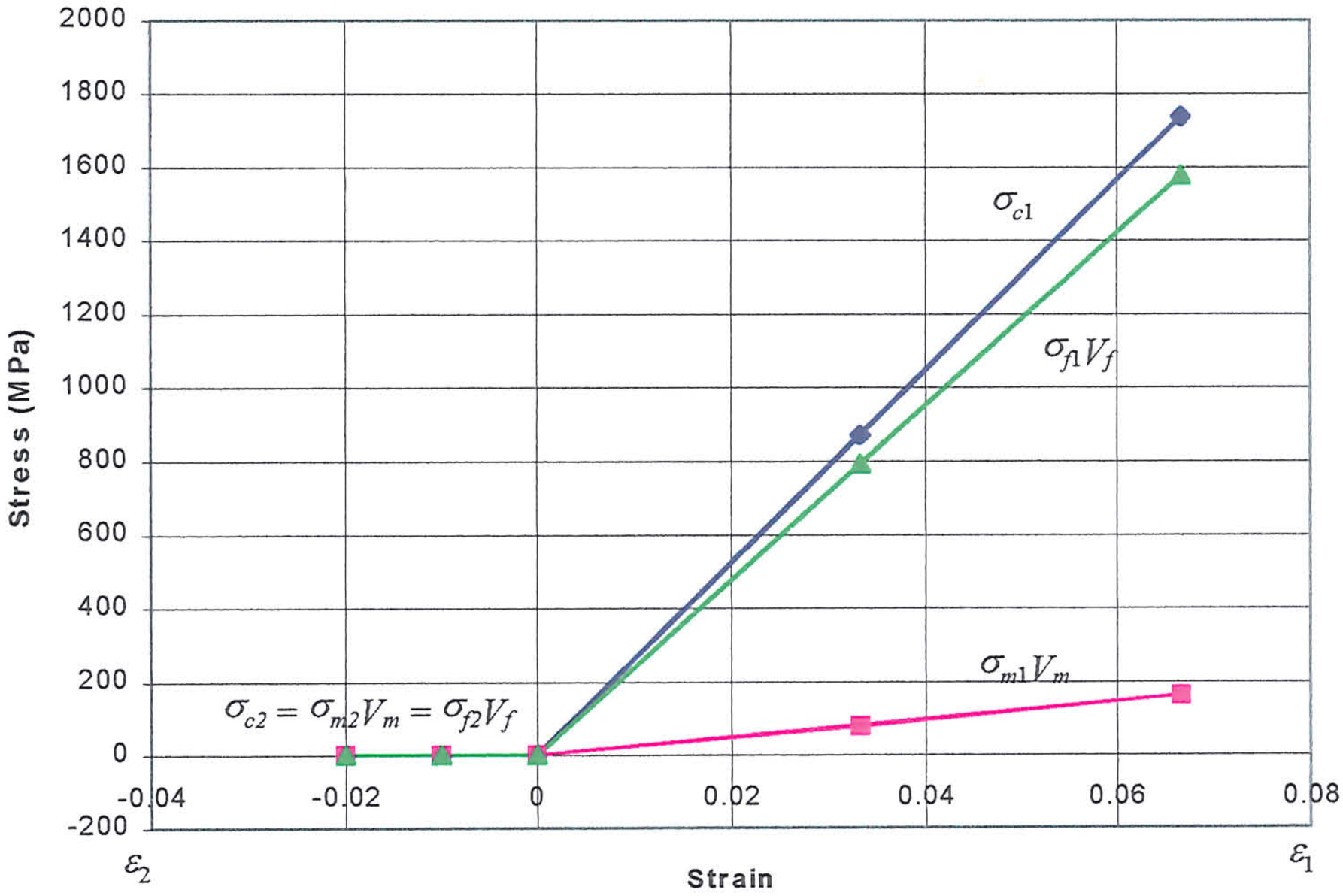

Fig 7.6.1.3-2 Stress-strain relations by UMAT for Load Case 2

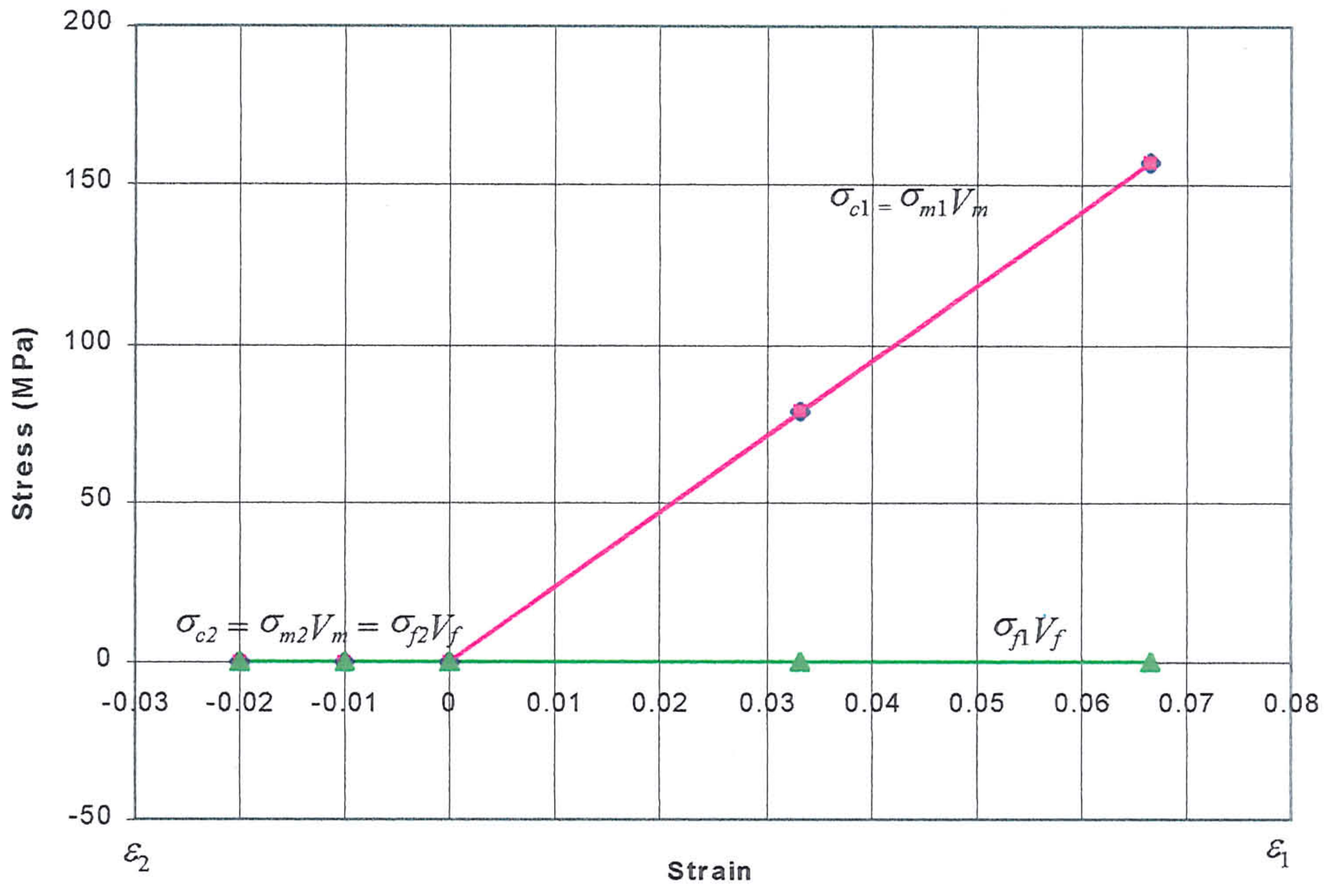

Fig 7.6.1.3-3a Stress-strain relations by UMAT for Load Case (3a)

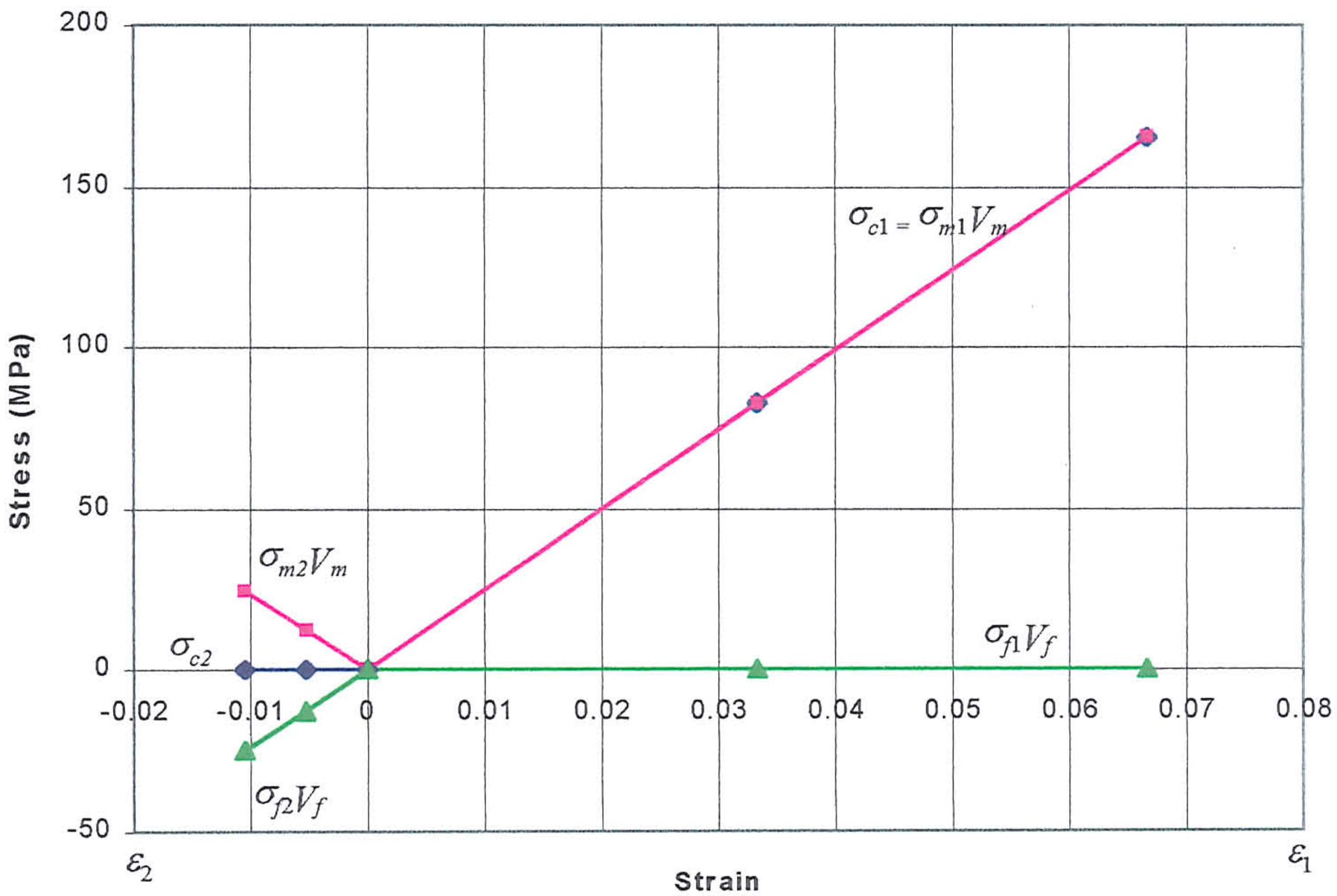

Fig 7.6.1.3-3b Stress-strain relations by UMAT for Load Case (3b)

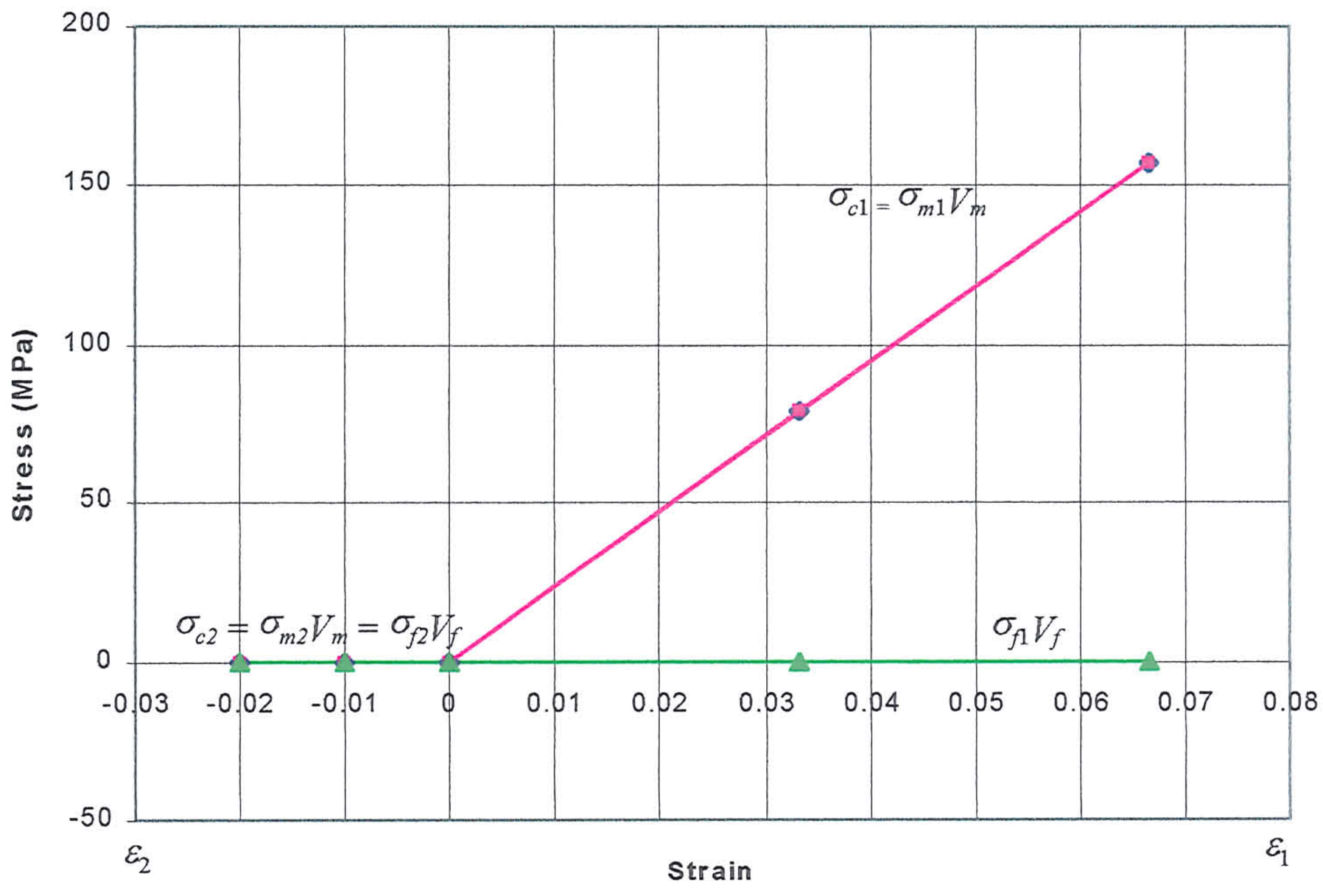

Fig 7.6.1.3-4a Stress-strain relations by UMAT for Load Case (4a)

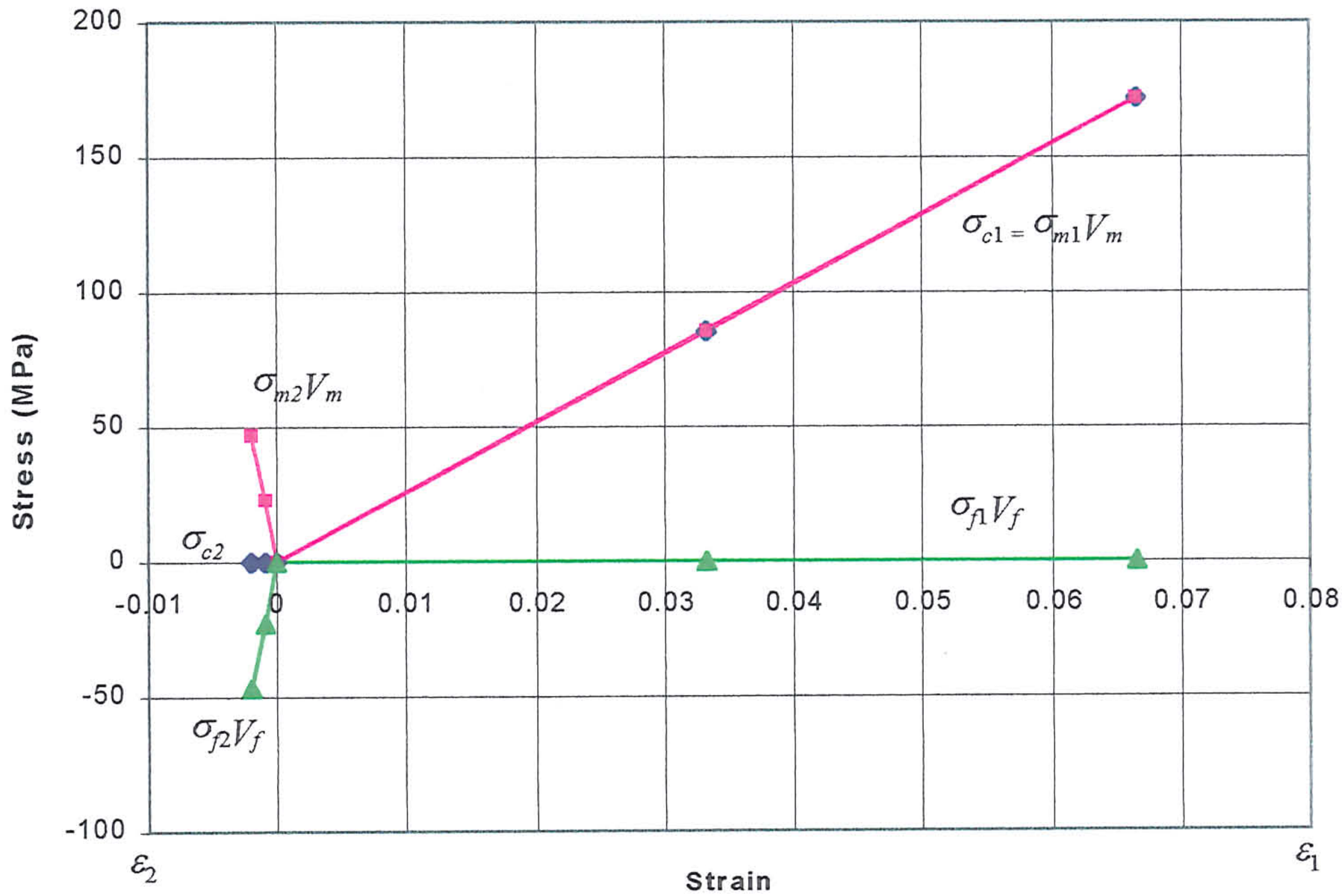

Fig 7.6.1.3-4b Stress-strain relations by UMAT for Load Case (4b)

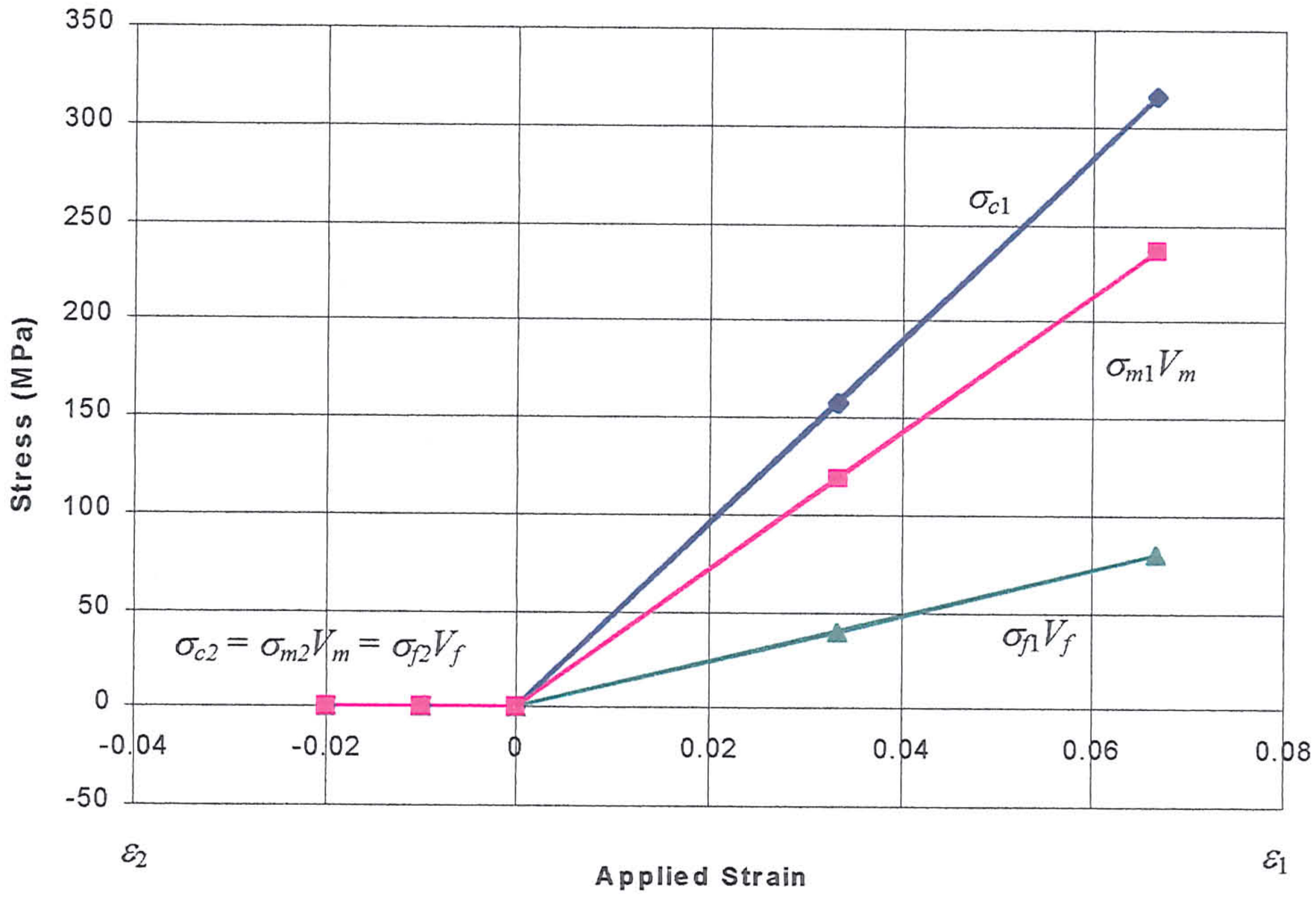

Fig 7.6.1.3-5a Stress-strain relations by UMAT for Load Case (5a)

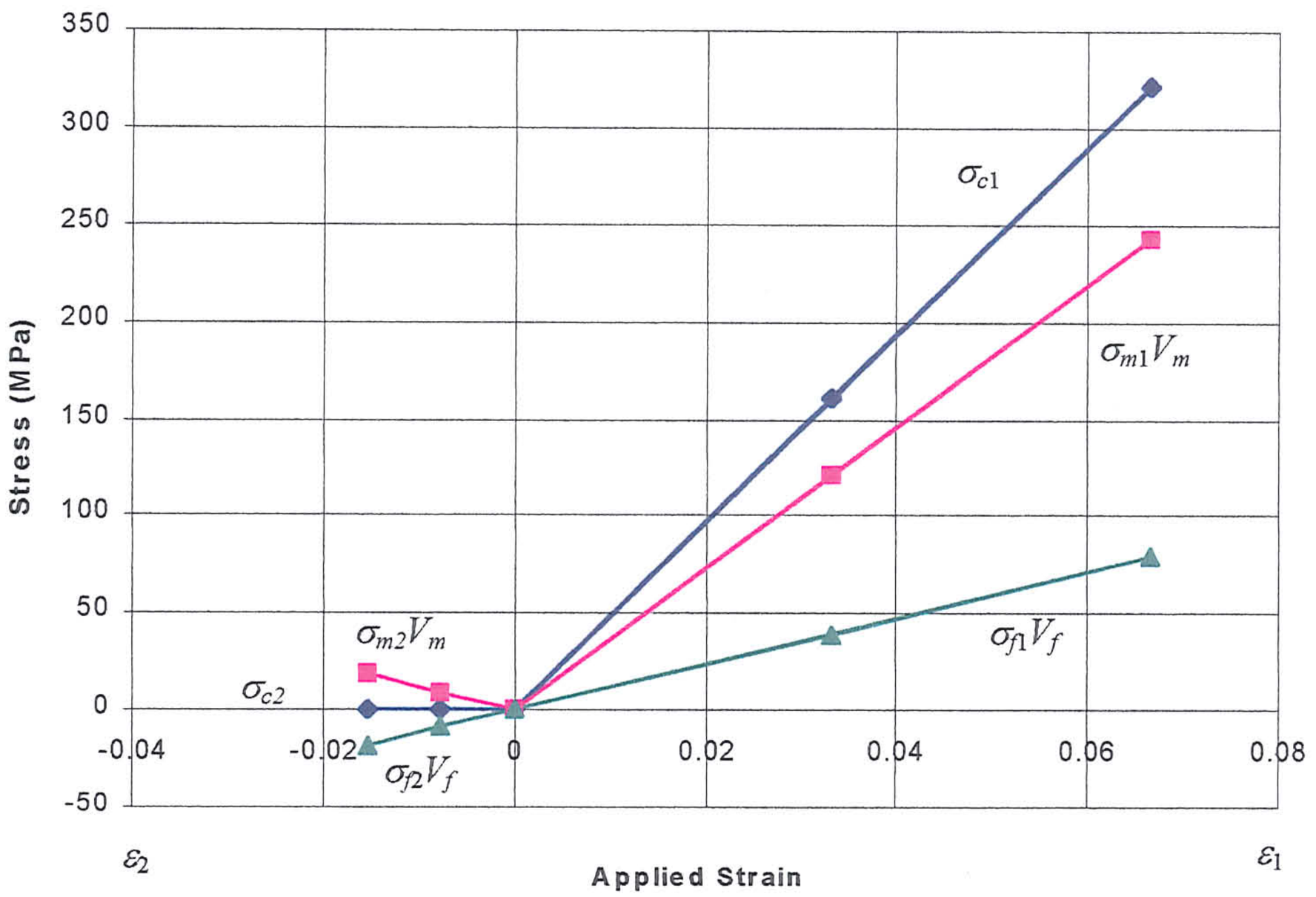

Fig 7.6.1.3-5b Stress-strain relations by UMAT for Load Case (5b)

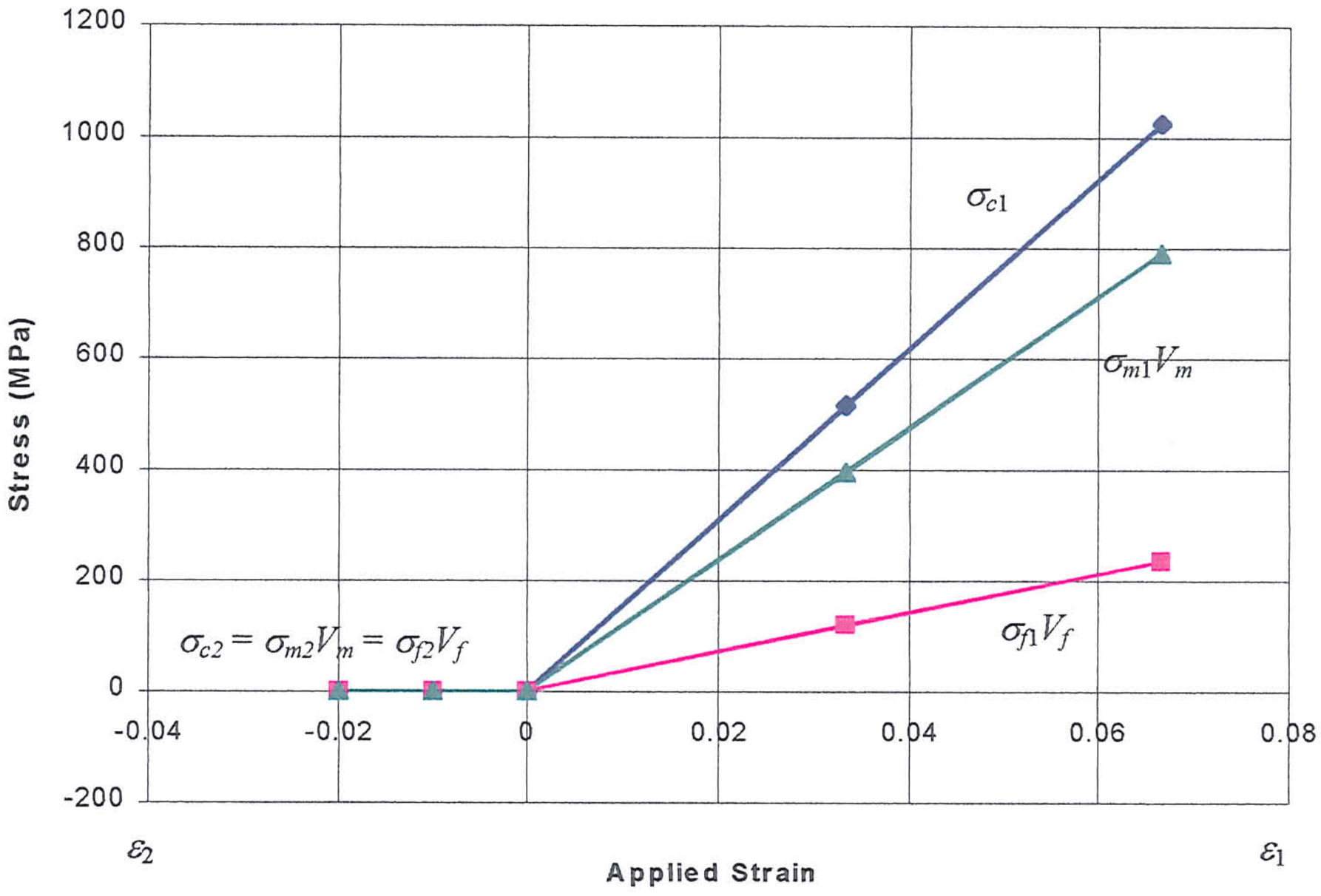

Fig 7.6.1.3-6a Stress-strain relations by UMAT for Load Case (6a)

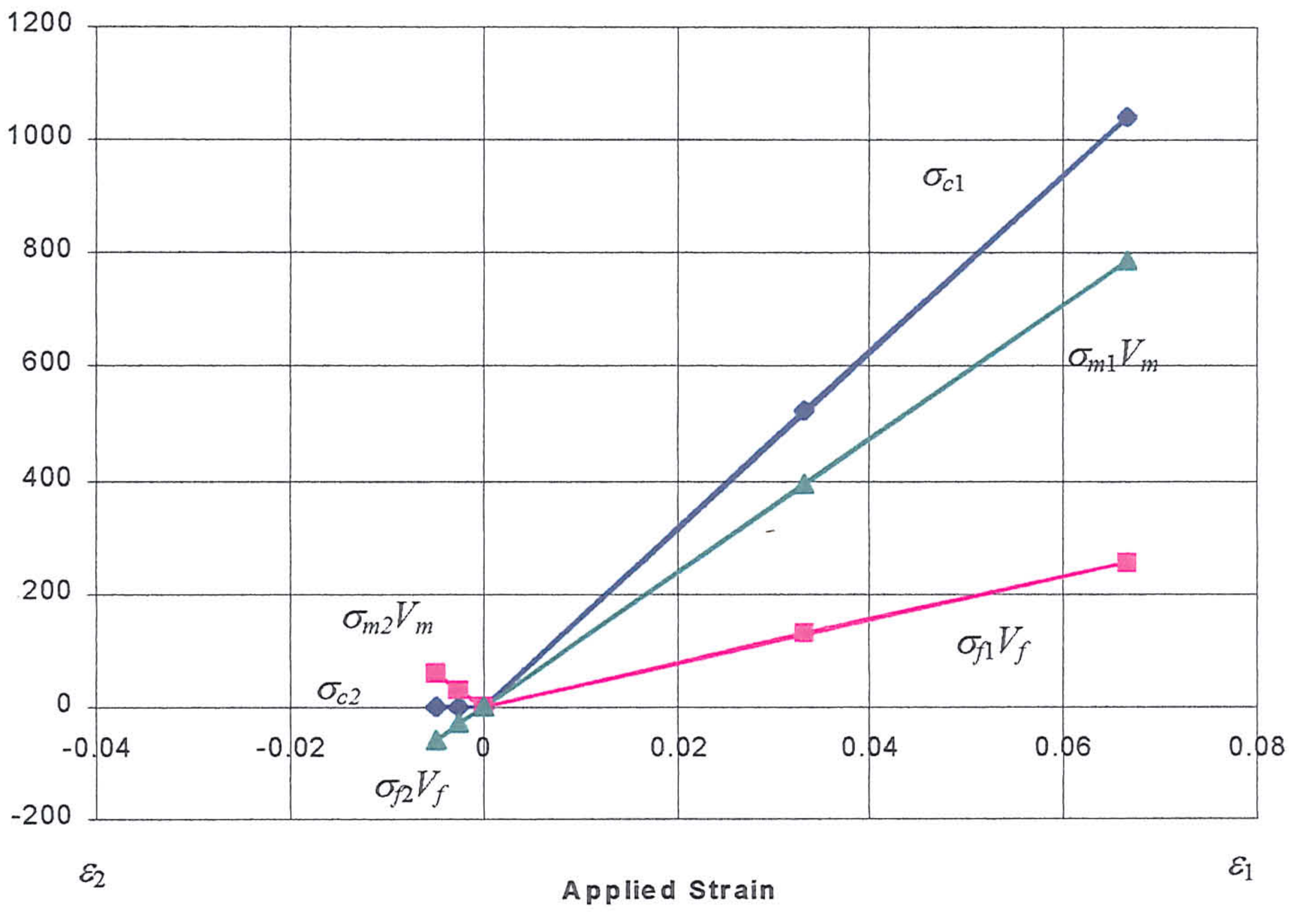

Fig 7.6.1.3-6b Stress-strain relations by UMAT for Load Case (6b)

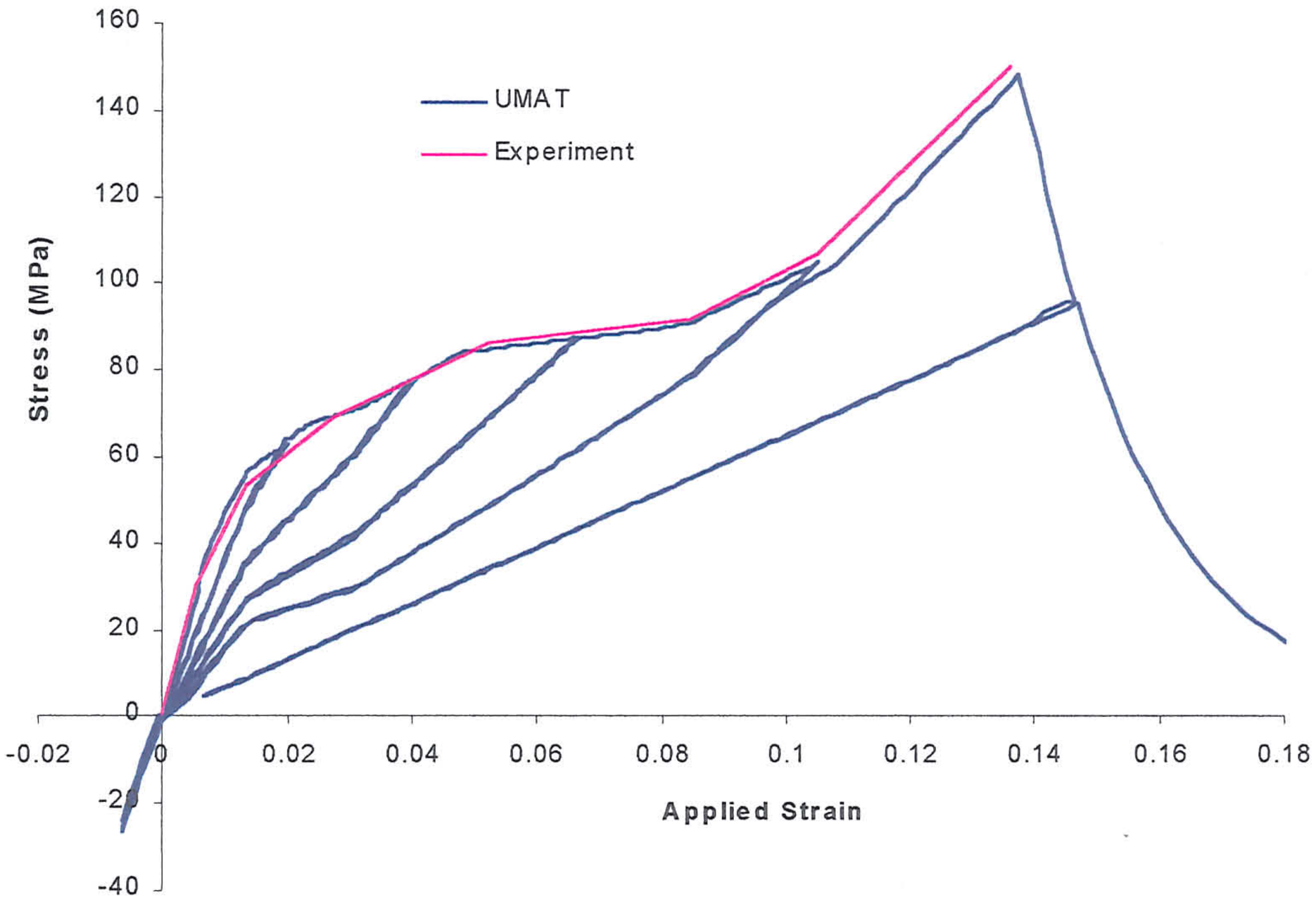

(a)

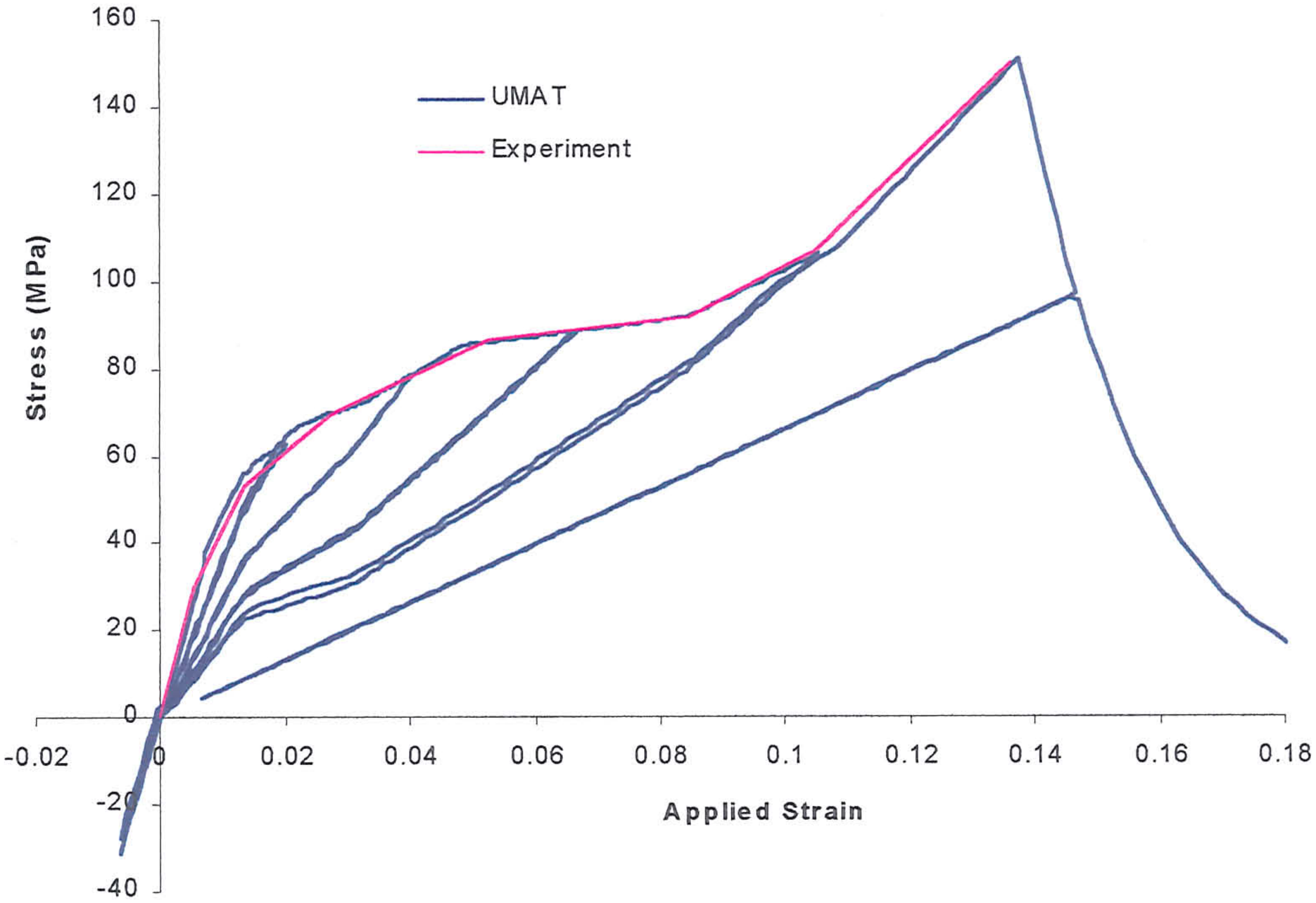

(b)

Fig. 7.6.2.2-1 The numerical stress-strain response of the composite when the compressive modulus of the fibres was (a) zero and (b) finite.

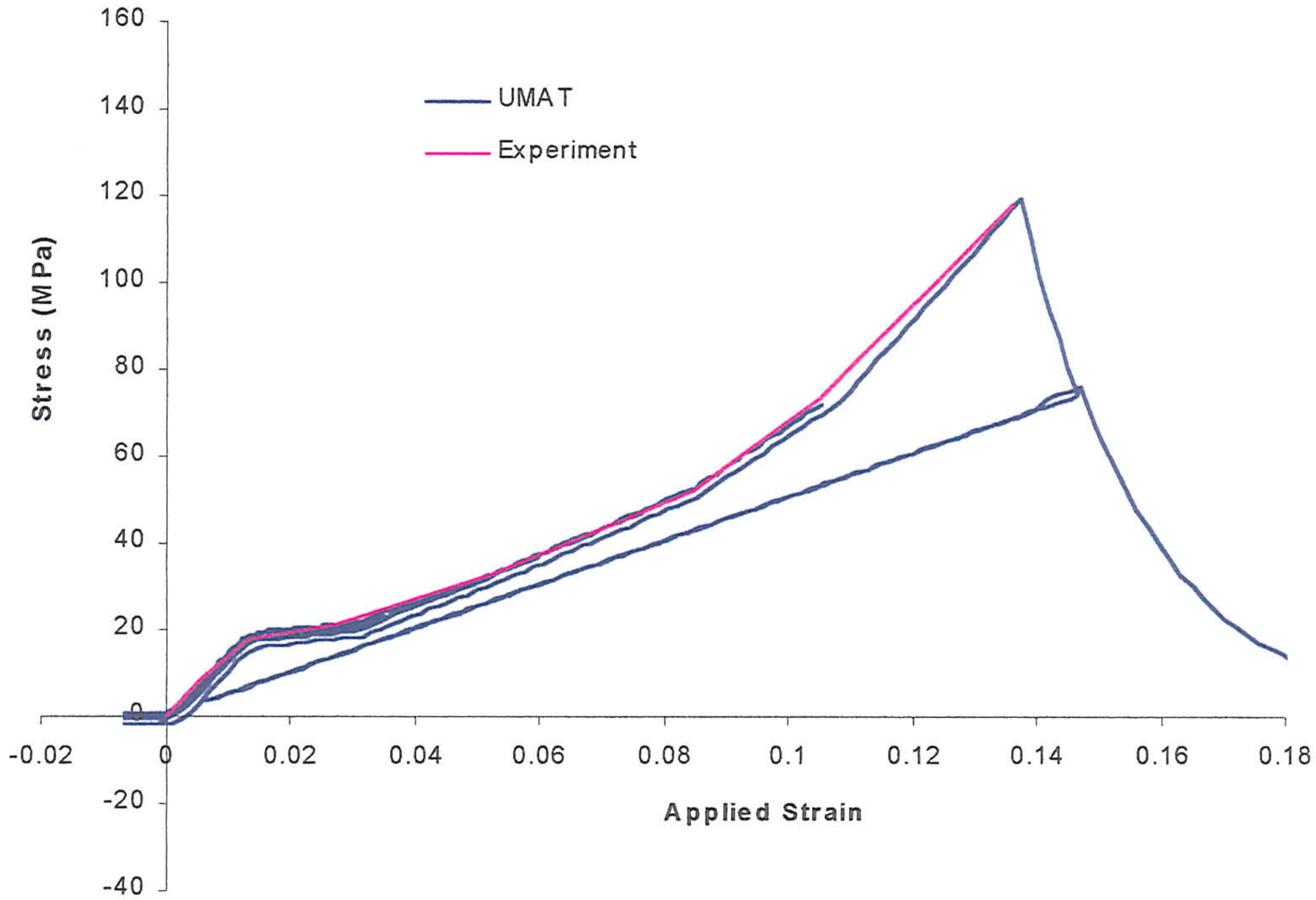

(a)

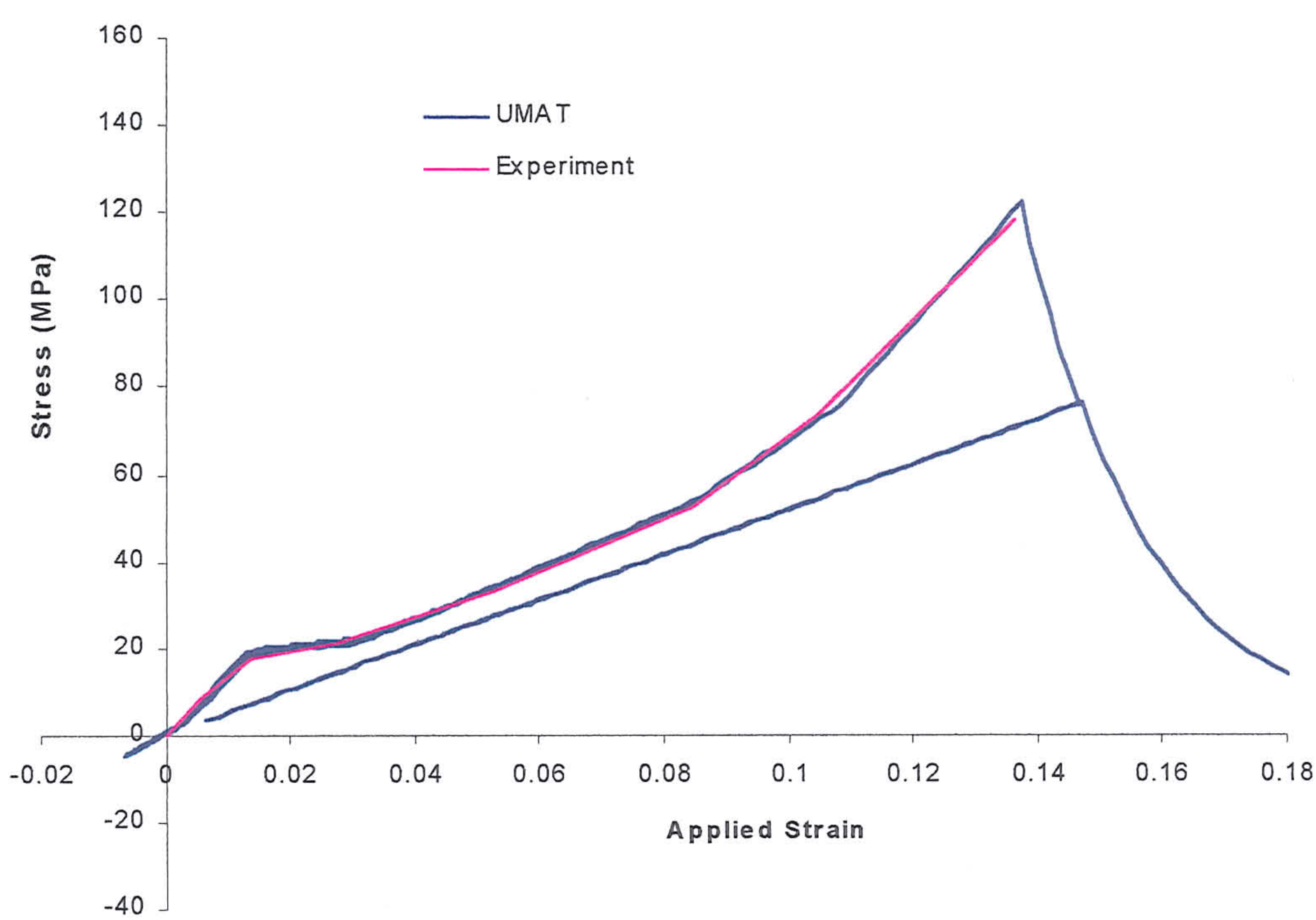

(b)

Fig. 7.6.2.2-2 The numerical stress-strain relations of the volume fraction of fibres when the compressive modulus of the fibres is (a) zero and (b) finite.

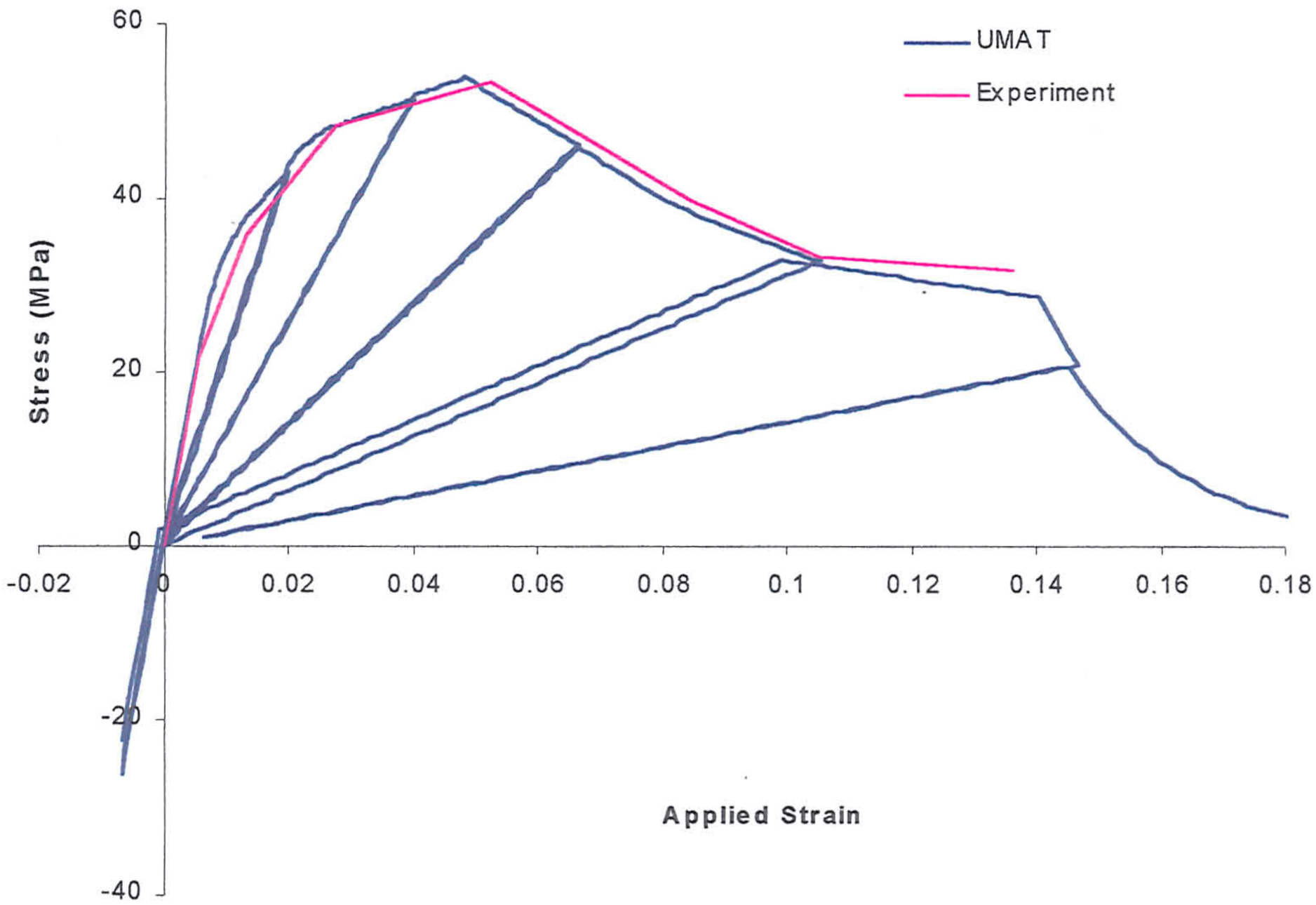

Fig. 7.6.2.2-3 The numerical stress-strain relations of the volume fraction of matrix when the compressive modulus of the fibres is zero and finite.

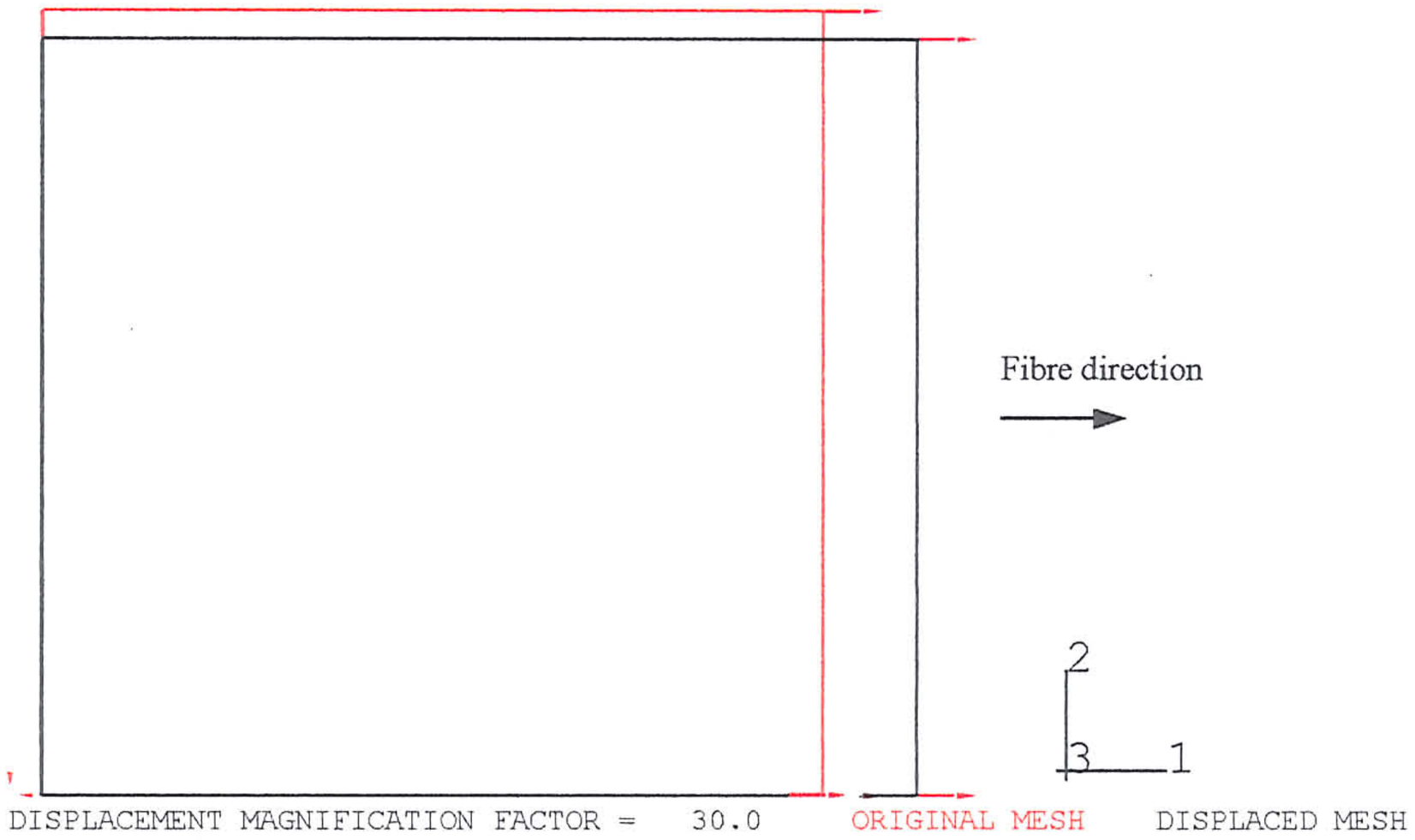

(a)

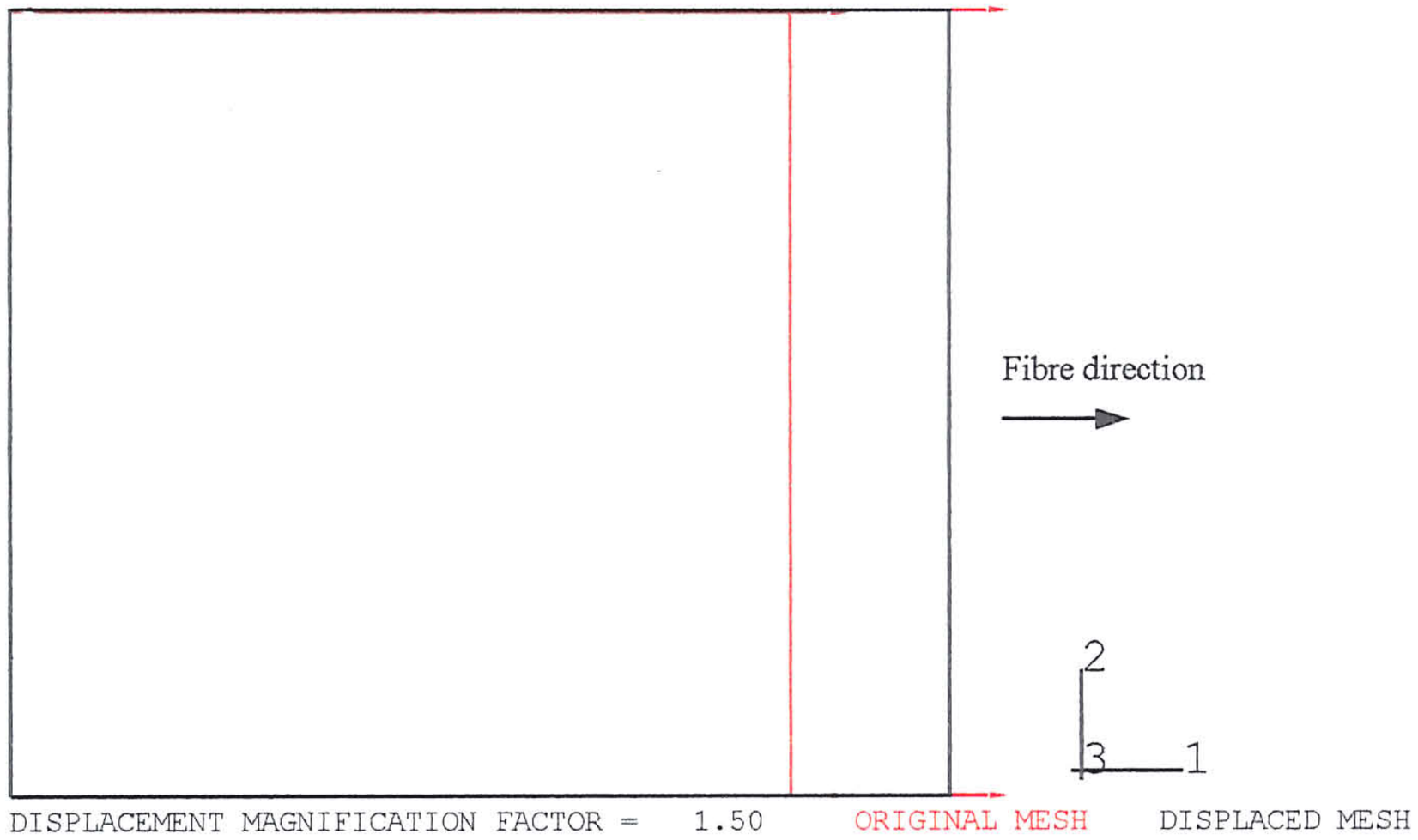

(b)

Fig. 7.6.2.2-4 Deformed meshes of the composite (a) before matrix cracking and (b) after matrix cracking.

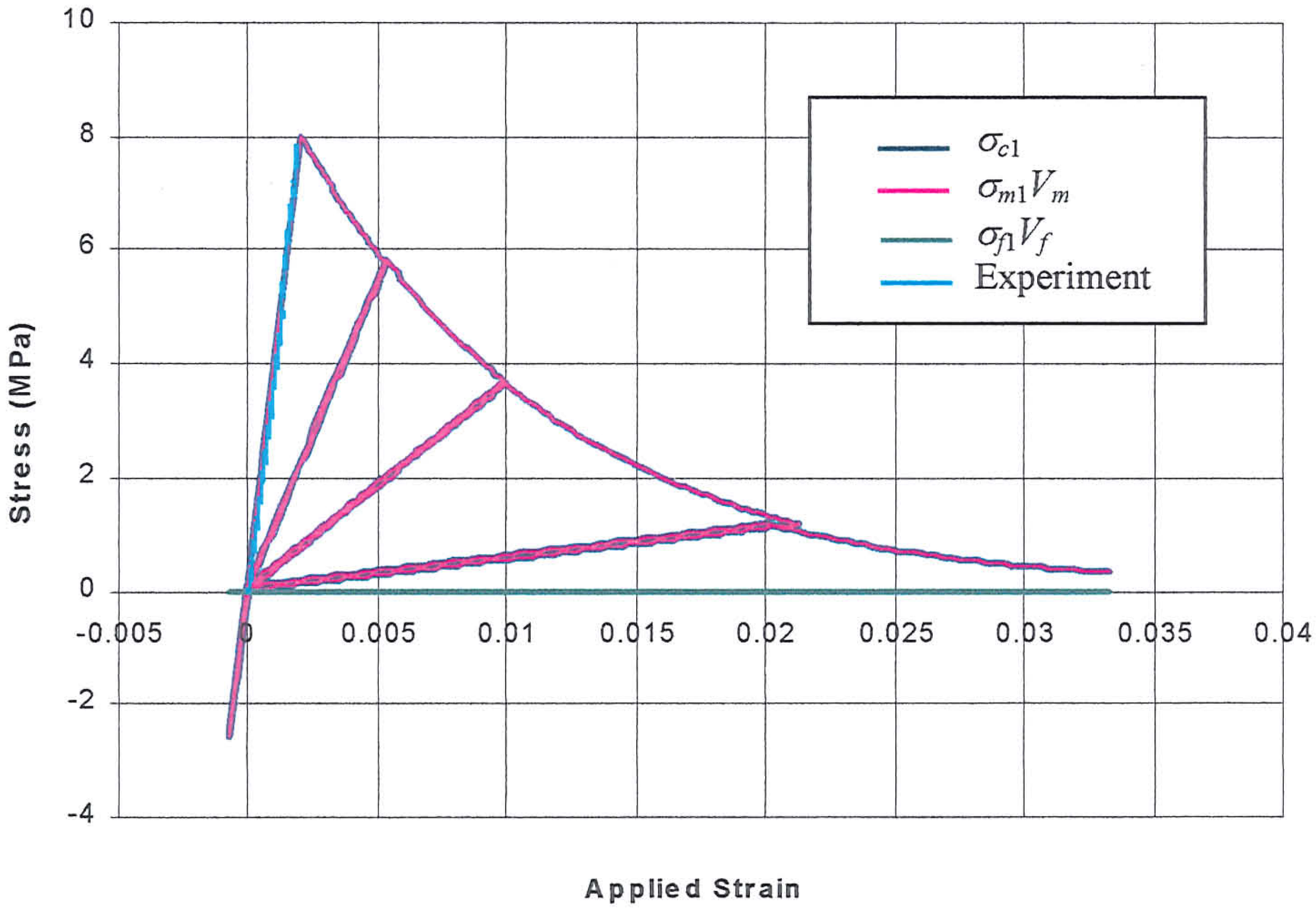

Fig. 7.6.3.2-1a Stress-strain relations of the composite and volume fraction of matrix and fibre during tensile delamination (without compressive fibre modulus)

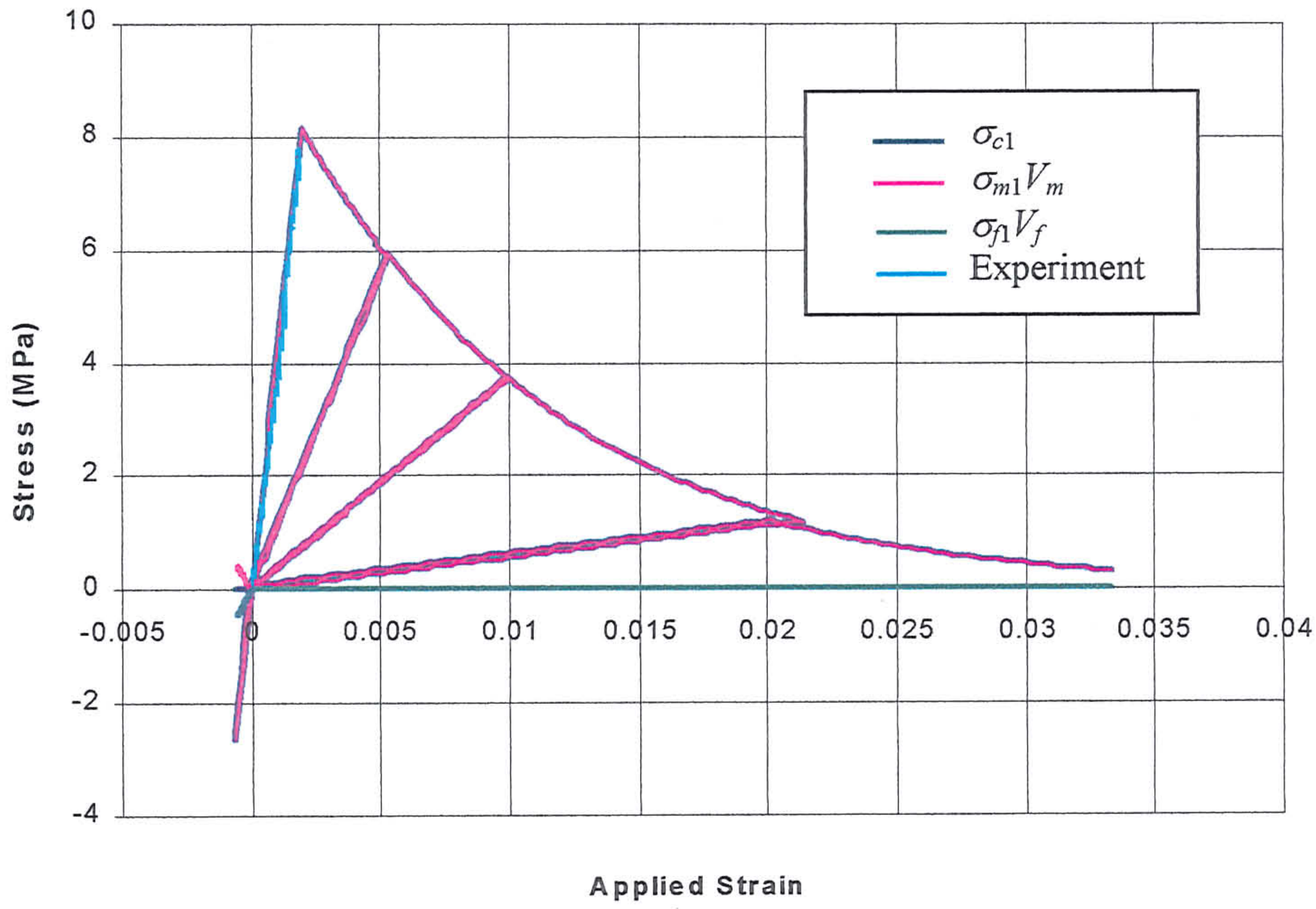

Fig. 7.6.3.2-1b Stress-strain relations of the composite and volume fraction of matrix and fibre during tensile delamination (with compressive fibre modulus)

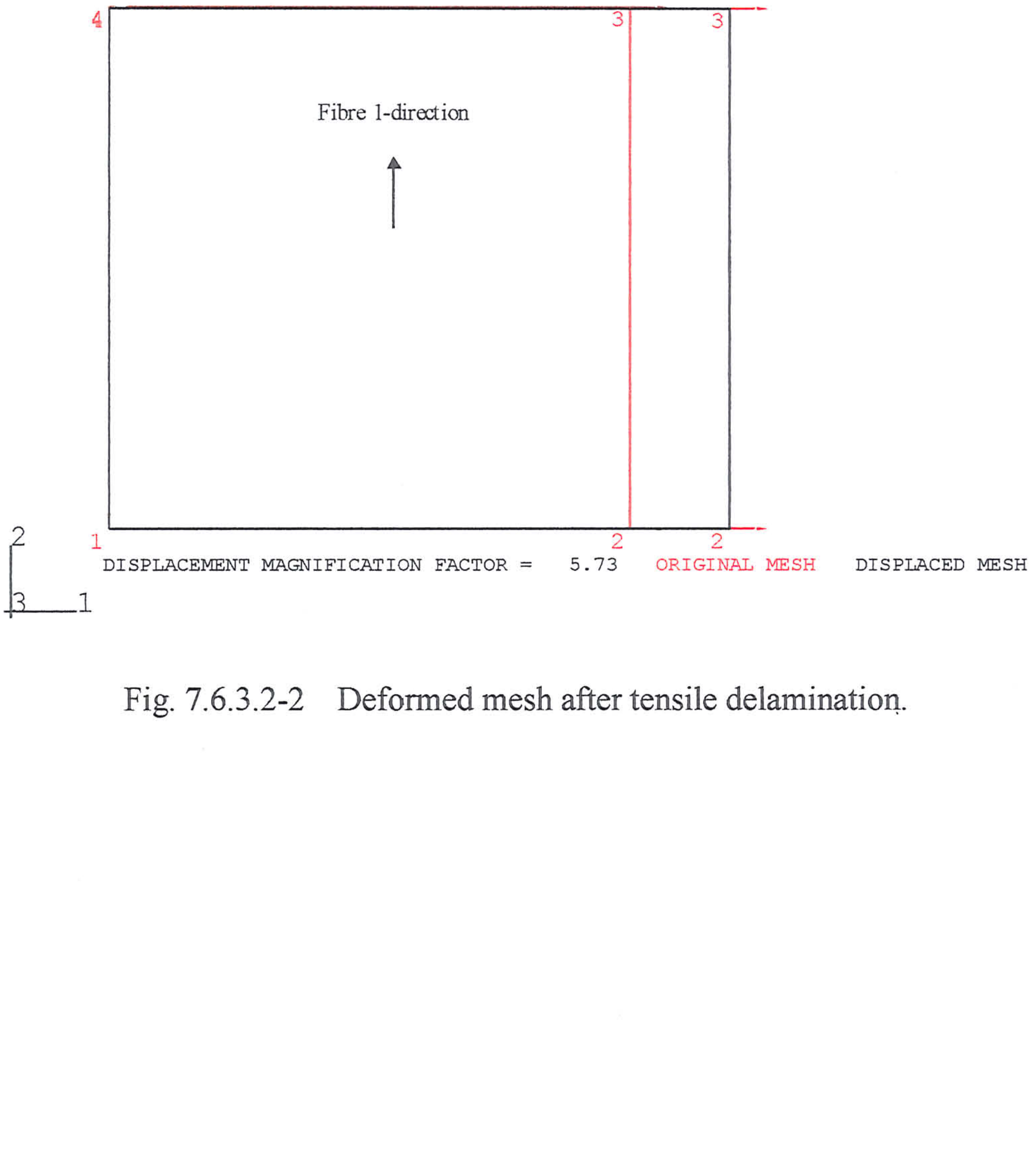

Fig. 7.6.3.2-2 Deformed mesh after tensile delamination.

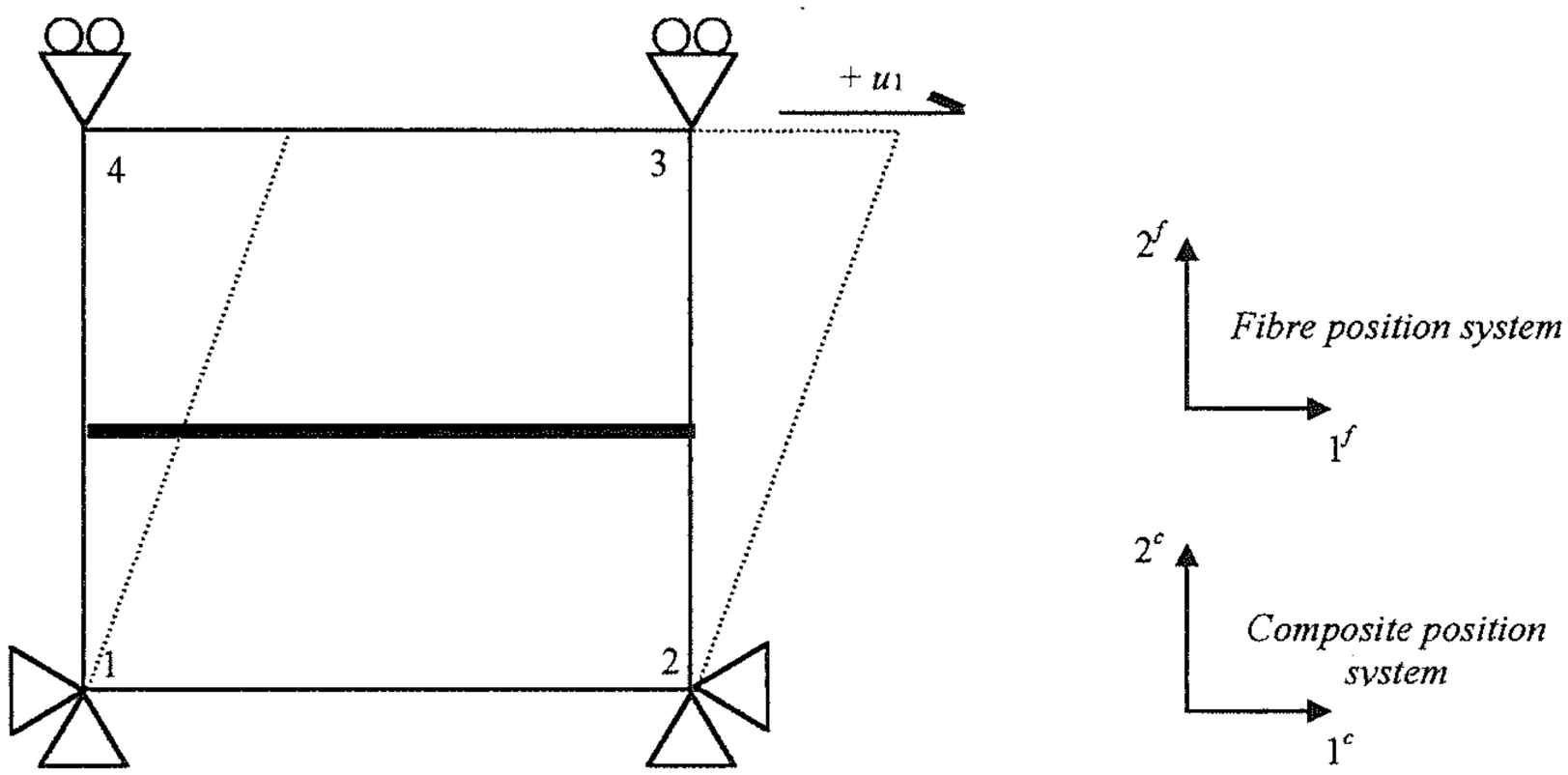

(a) Positive cyclic shear

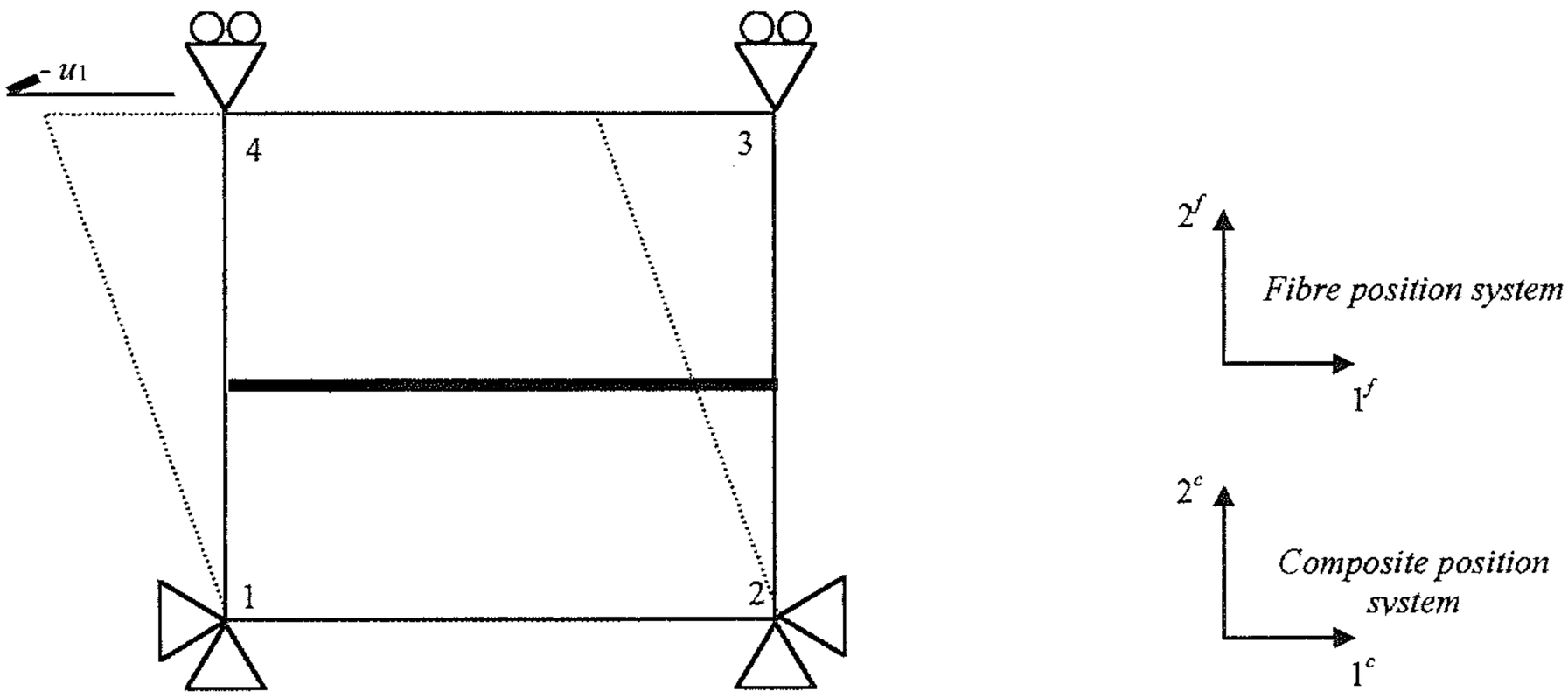

(b) Negative cyclic shear

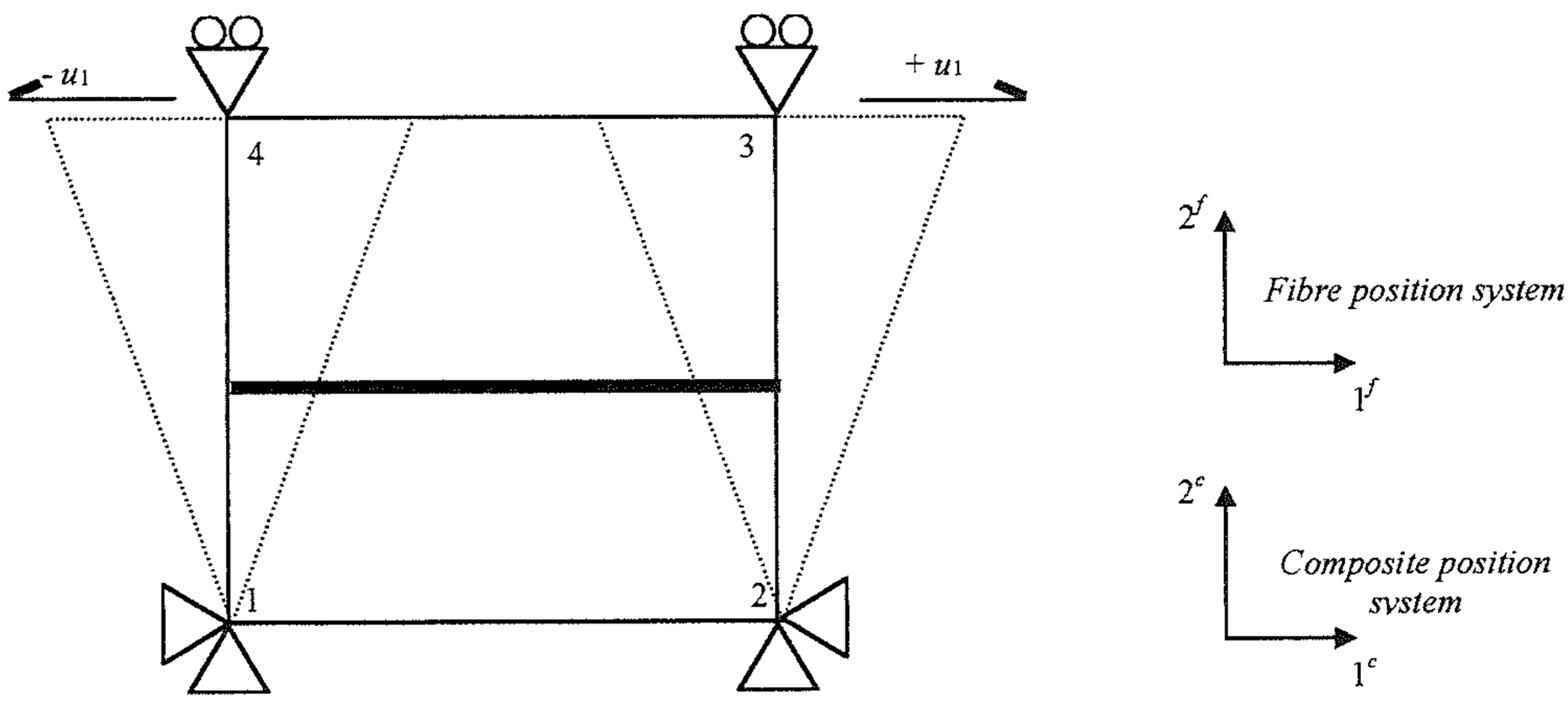

(c) Positive and negative cyclic shear

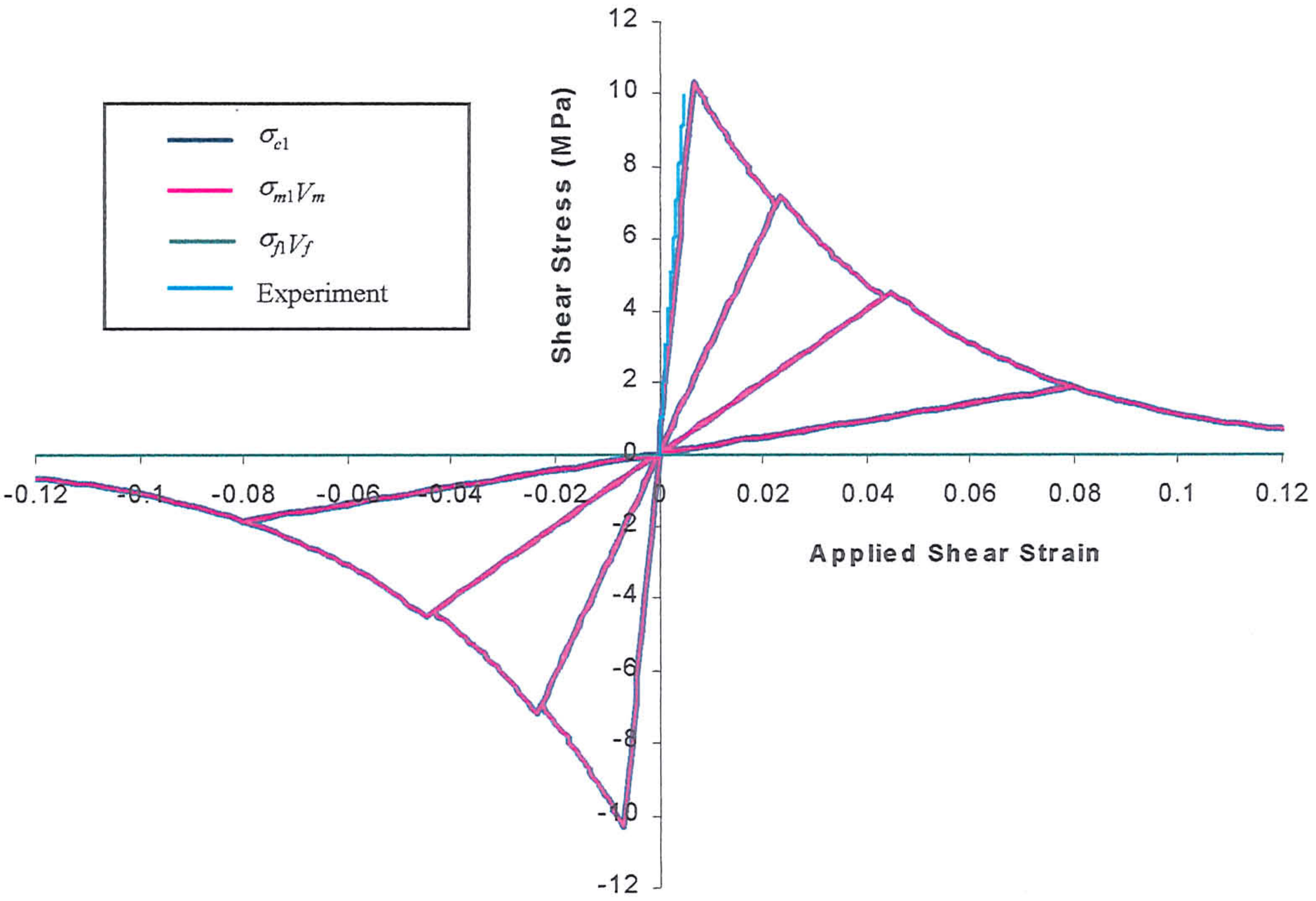

Fig. 7.6.4.2-1 The numerical shear stress-strain curves of the composite and volume fraction of matrix and fibre during shear delamination.

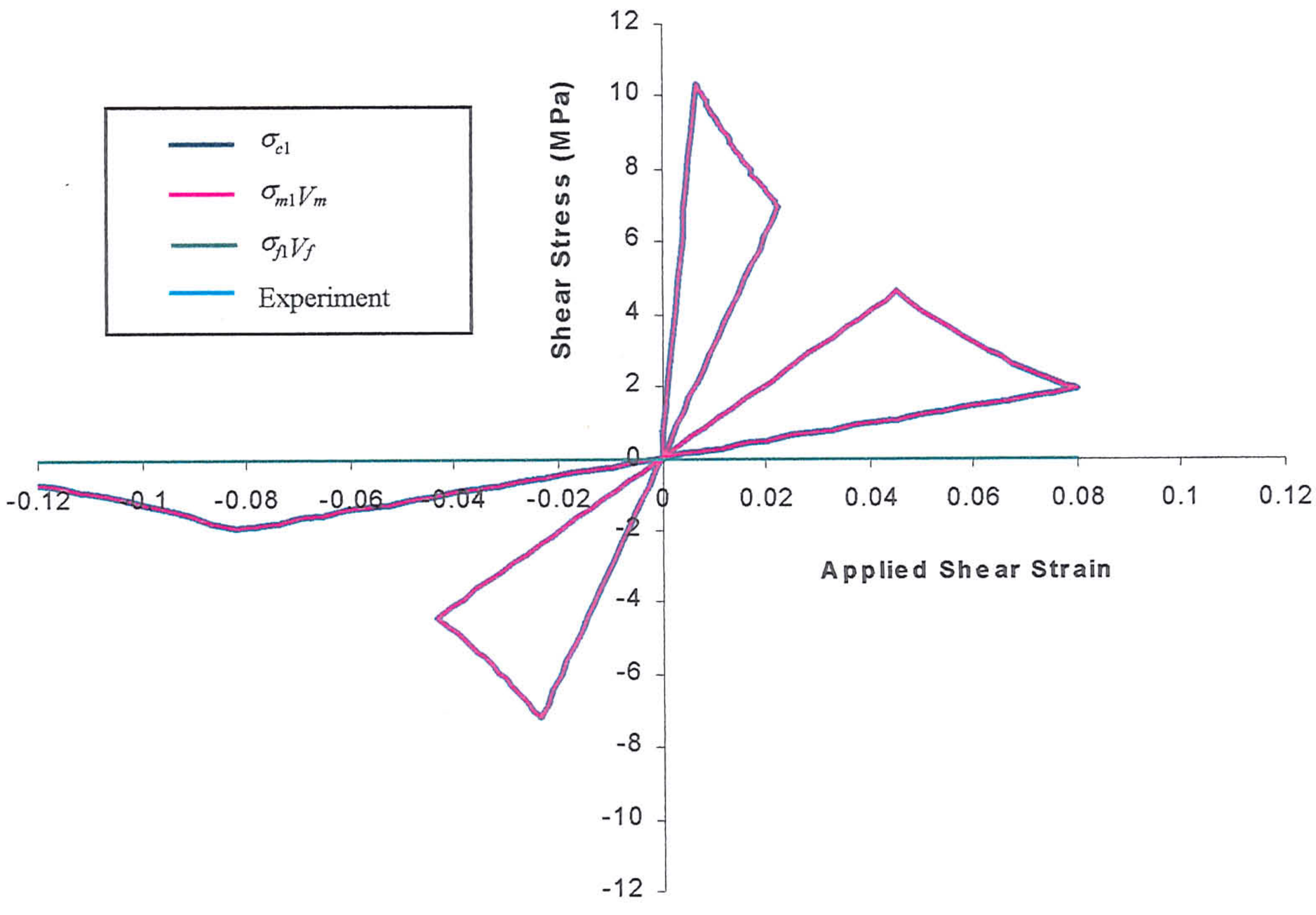

Fig. 7.6.4.2-2 The numerical shear stress-shear strain curves of the composite and volume fraction of matrix and fibre transiting between a positive and

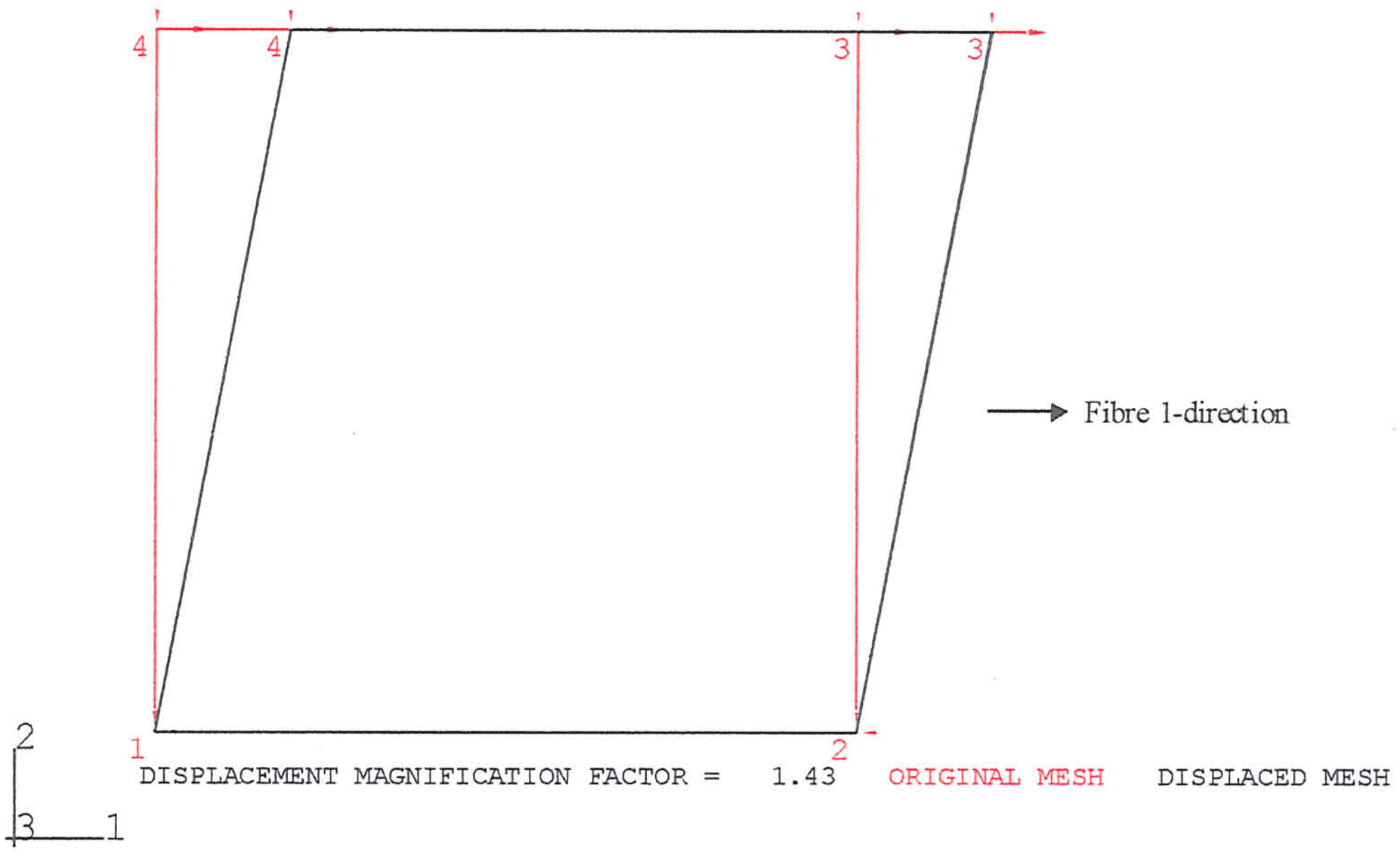

Fig. 7.6.4.2-3 The deformed mesh of the composite in simple shear

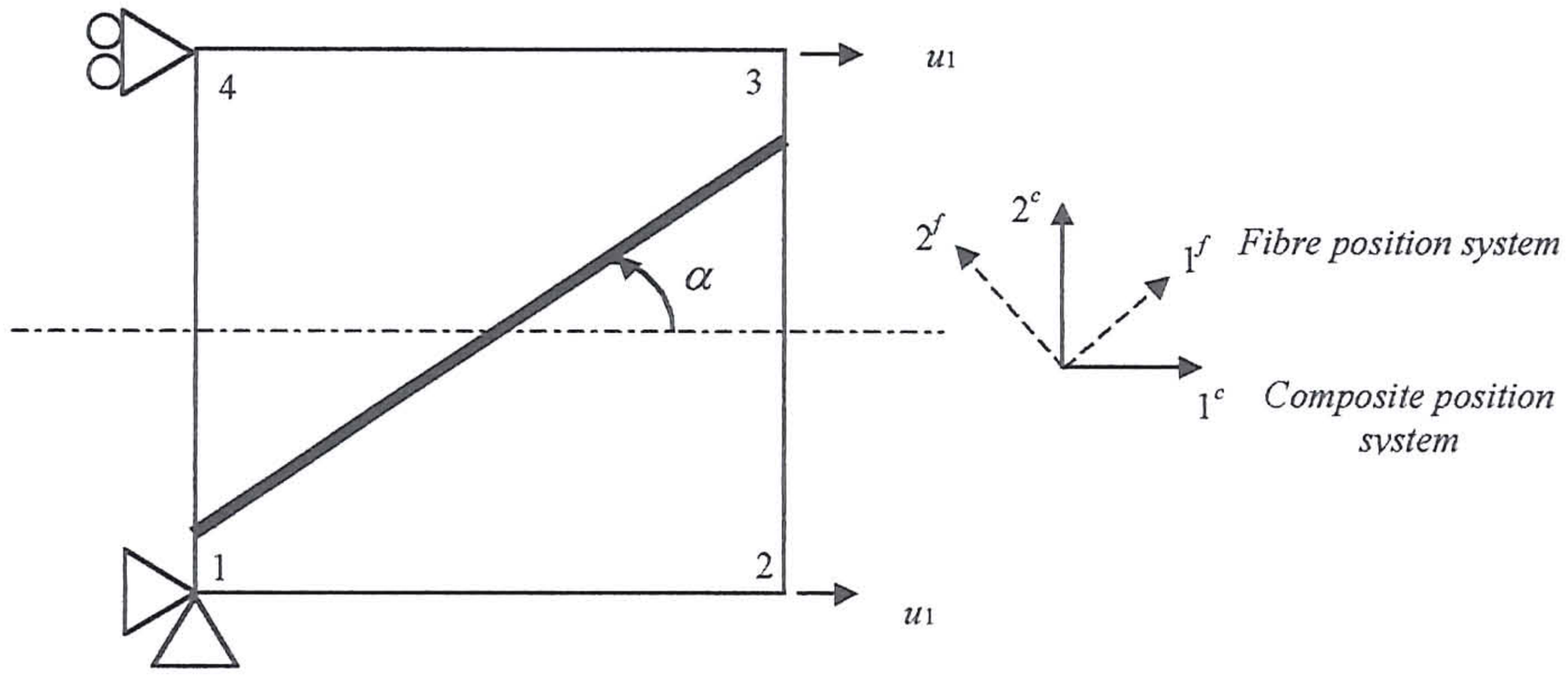

Fig. 7.6.5.1-1 Schematic diagrams of the one-dimensional composites, boundary conditions and position systems used to benchmark the maximum stress criterion in the subroutine UMAT.

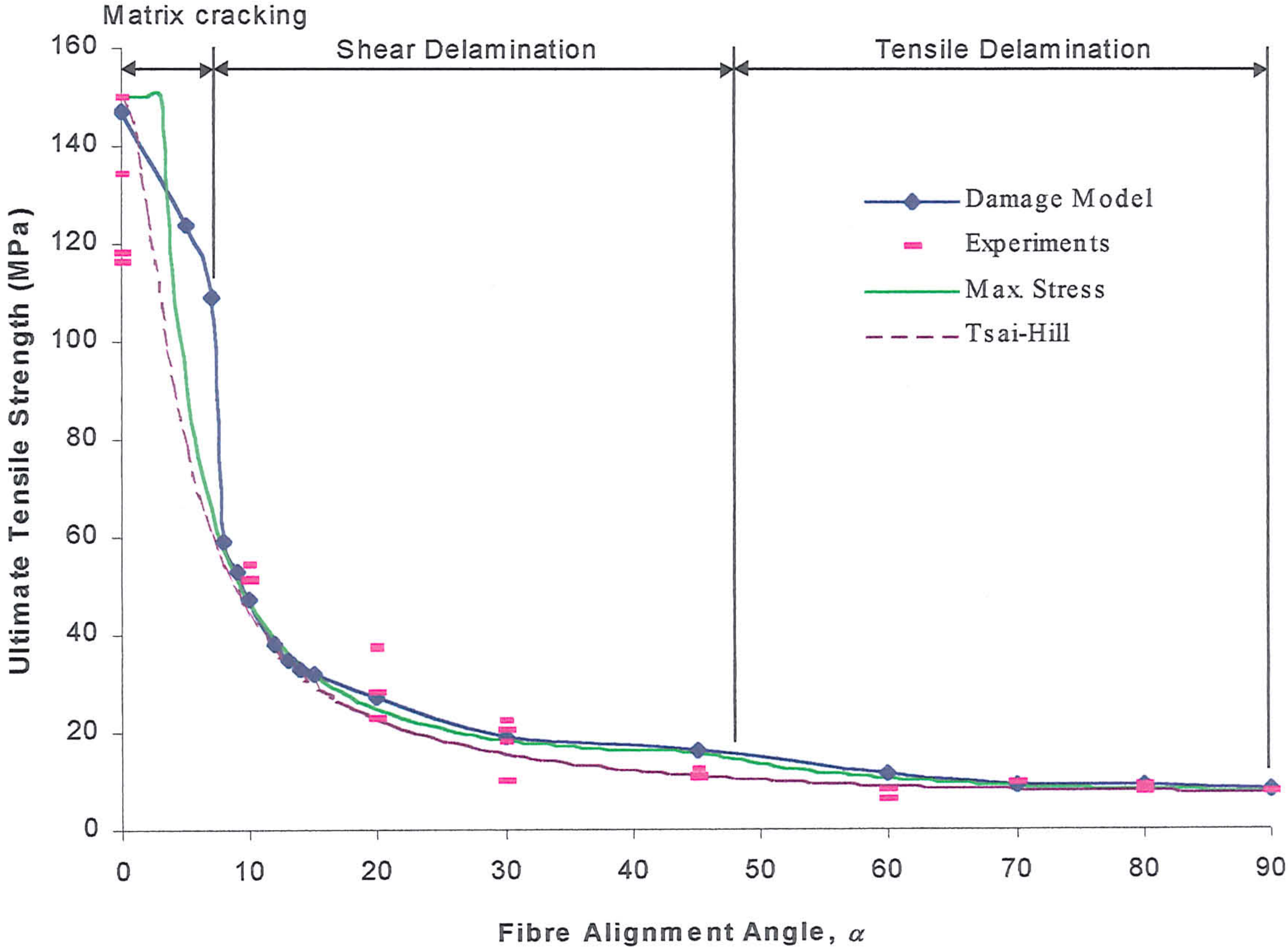

Fig. 7.6.5.2-1 Benchmarking of the ultimate tensile strengths of the one-dimensional polyester composite in uniaxial tension plotted with respect to fibre

CHAPTER 8:

Computational Analysis

8.1 Introduction

In Chapter 5, sub-structures representing idealised structural parts of an aero-engine exhaust diffuser unit were tested experimentally. The test specimens included rectangular, T-shaped and wedge-shaped bars (see Fig. 5.3-1 to 3). The experimental programme established the force-deflection response and the damage mechanisms. However, reliance on experiments for design and analysis is slow and cost ineffective. The alternative is to design and analyse sub-structures computationally. In this chapter, the computational model developed in Chapter 7 is used to model the behaviour of the sub-structures tested in Chapter 5.

8.2 Composites with Misaligned Fibres

As a preliminary to sub-structure modelling, the analysis of the deformation and failure of composites with misaligned one and two-dimensional fibre reinforcements in uniaxial tension is considered. The composites tested in Sect 4.3 provide the data for the analysis.

8.2.1 Uniaxial Tension Tests of 1-D Composites

8.2.1.1 Mesh and Model Descriptions

The meshes of the one-dimensional composite coupon specimens are shown in Fig. 8.2.1.1-1. The meshes comprised between 240 and 720 first-order plane stress quadrilateral solid elements CPS4 with an aspect ratio approximately 0.125 times the specimen width. Mesh (a), (b), (c) and (d) represent composites with fibre alignment angles $\alpha = 0°$, 10°, 20° and 30°, while mesh (e) modelled misalignments between $\alpha =$ 45° to 90°. The figure also shows the position systems, boundary conditions and the fibre orientation α. The boundary conditions are indicated using red arrows.

delamination in the normal elements were given as 50.0MPa, 7.79MPa and 9.96MPa, while the failure stresses in the weakened elements were lower. The perturbation allowed matrix cracking and delamination to developed from one site rather than occurring simultaneously across the full gauge length. Uniaxial tension was modelled by displacing the node set RIGHT in the composite 1-direction.

8.2.1.2 Results & Analyses

The deformed meshes are shown in Fig. 8.2.1.2-1. The distorted or elongated elements indicate the damaged regions.

The predicted tensile stress-strain responses for the full range of the fibre alignments are shown in Figs 8.2.1.2-2 to 10. The material constants used to model fibre failure, matrix crack saturation, shear delamination and tensile delamination in eqns (7.4.4.1.11 & 12), eqn (7.4.4.3.2) and eqn (7.4.4.2.2) are given in Table 8.2.1.2-1. The figures also show contour plots of the damage zones at different stress levels. The state dependent variables (hereafter SDV) 50, 51 and 30 indicate the various deformation modes during tensile delamination, shear delamination and matrix cracking, respectively, whereas SDV 32 symbolises the global damage state variable which indicates the damage mechanisms in the composite according to the nomenclature in Table 7.5.1-3. For fibre alignments between 90° and 45° the composite failed by tensile delamination while at 30° the composite failed by shear delamination. As the fibre misalignment decreased, a mixture of shear delamination and matrix cracking was predicted at α = 20° and 10°, and finally for aligned fibres the composite failed by matrix cracking followed by fibre failure. The predicted damage agrees with observations from experiments (see Sect 4.3.2). At α = 20° and 10°, the numerical and experimental results show that the transition from shear delamination to matrix cracking occurs by simultaneous shear delamination and matrix cracking.

The damage plots in Figs 8.2.1.2-2 to 6 demonstrate the development of a clear tensile delamination plane from the perturbation parallel to the fibres. As the misalignment reduces from 90° to 45°, the orientation of the failure plane in the composite rotates in agreement with experimental observations. The damage plots show that the stress-strain response of the misaligned composites unload when more than half the cross-sectional area of the composite parallel to the fibre has undergone tensile

α	**Fibre Failure** eqn (7.4.4.1.11)	**Matrix Crack Saturation** eqn (7.4.4.1.12)	**Shear Delamination** eqn (7.4.4.3.2)	**Tensile Delamination** eqn (7.4.4.2.2)
	a	***a***	***a***	***a***
0°	50	50	-	-
10°	50	50	1	-
20°	50	50	20	-
30°	50	50	20	-
45°	-	-	-	50
60°	-	-	-	20
70°	-	-	-	50
80°	-	-	-	50
90°	-	-	-	50

Note: Magnitude of constants b and c in all these equations is 0.01.

Table 8.2.1.2-1 The material constants of the misaligned one-dimensional.

Figs 8.2.1.2-7 to 10 show the development of shear delamination and matrix cracking for misalignments between 30° and 0°. The orientation of the failure plane is not obvious. To clarify the failure plane, the maximum principal strain direction in the composite (or the matrix) is plotted in Fig. 8.2.1.2-11 using blue arrows superimposed on the deformed meshes, while the normal to the fibre axis is indicated with '**n**'. The figure also show the predictions for $\alpha = 45°$ to 90°. During matrix cracking or tensile delamination, the maximum principal strain direction of the composite is normal to the failure plane while the maximum principal strain direction during shear delamination is inclined at 45° to the direction of shear. This is demonstrated in the maximum principal strain plots in Fig 8.2.1.2-11, which verified that the orientation of the failure plane in the aligned and misaligned one-dimensional composites is correctly predicted. For fibre alignments between 30° and 10°, the results show that failure is caused mainly by shear delamination.

The predicted Young's modulus of the one-dimensional composite is plotted as a function of the fibre alignment angle α in Fig 8.2.1.2-12. Agreement with the experimental data is demonstrated. The Young's modulus of the composite is almost constant at small fibre misalignment angles ($\alpha \leq 10°$) but decreases as the fibre

is due to the assumption that the fibres are weakly bonded to the matrix and only transmit axial load.

8.2.2 Uniaxial Tension Tests of 2-D Composites

8.2.2.1 Mesh and Model Descriptions

The two-dimensionally reinforced composite coupons described in Fig. 4.3.1-6 were modelled using the meshes shown in Fig 8.2.1.1-1. For fibre alignment angles $\alpha =$ 0° and 20°, mesh (c) was used. For $\alpha = 10°$, 30° and 45°, meshes (b), (d) and (e) were used. The meshes were uniaxially tensioned by displacing the node set RIGHT in the composite 1-direction. The average strain was determined over the gauge length used in the one-dimensional experiments. The mesh of the two-dimensional composites and the boundary conditions used are shown in Fig. 8.2.2.1-1. The stress to initiate matrix cracking was 24MPa.

8.2.2.2 Results & Analyses

The deformed meshes are shown in Fig 8.2.2.2-1. The predicted stress-strain response of the two-dimensional composites is shown in Figs 8.2.2.2-2 to 6, and these include damage plots at various stress levels. In addition, the predicted Young's moduli are compared with the experimental data in Fig 8.2.2.2-7. The results confirm that the stress-strain response of the composite is correctly modelled for different fibre alignments. The agreement with experimental data indicates that the decrease in composite modulus is caused by the fibre alignment.

Fibre Alignment Angle (Deg)	Angle of Matrix Crack Plane Normal w.r.t. Loading axis	
	Damage Model	**Experiment**
0°	0°	0°
10°	26°	25°
20°	20°	20°
30°	12°	10°
45°	0°	0°

Table 8.2.2.2-1 The angles between the normal to the matrix crack plane and the tensile axis for misaligned two-dimensional composites.

The local maximum principal strain directions of the composite shown in Fig 8.2.2.2-8 indicate the normal to the matrix cracks. The predicted orientations of the crack plane normal with respect to the loading axis are presented in Table 8.2.2.2-1 as a function of fibre alignment angle. The predictions indicate that the matrix cracks are not orthogonal to the fibres. Significantly, the predicted orientations of the matrix cracks agree well with the experimental data, which confirms that matrix cracking occurs normal to the maximum principal stress direction of the matrix as oppose to normal to the fibre axis as assumed by Hull & Clyne (1996).

8.3 Sub-Structure Analyses

In this section, the sub-structures with one and two-dimensional reinforcements tested in Chapter 5 are analysed computationally. The test configurations, which include rectangular, T and wedge-shaped sub-structures, loaded in three-point bending are shown in Figs 5.1-1 to 3. The problems are symmetric allowing meshes representing a symmetric half of the test specimens to be used to model the sub-structures.

8.3.1 Rectangular Bars

8.3.1.1 Mesh and Model Descriptions

Meshes representing the rectangular composite bars are shown in Fig 8.3.1.1-1. The meshes are based on second-order quadrilateral solid elements, and use four levels of mesh refinement: 4x10, 8x20, 12x30 and 16x40. The aspect ratio of the elements was maintained at 2.5. The one-dimensionally reinforced composite bar had a fibre volume fraction of 0.182 and a matrix crack initiation stress of 55MPa. In the two-dimensional composite bar, the volume fraction of fibres was 0.364 and the matrix crack initiation stress was 24.2MPa.

8.3.1.2 Results and Analysis

The deformed mesh of the one-dimensional composite is shown in Fig 8.3.1.2-1. The matrix cracking zone at an applied deflection of 2.62mm is shown in Fig 8.3.1.2-2 and the predicted force-deflection responses are shown in Fig 8.3.1.2-3. The results show that deformation of the rectangular bar during three-point bending is correctly modelled, and that the solution is only weakly dependent on mesh refinement unless

Figs 8.3.1.2-4 and 5 show the predicted force-deflection response and matrix cracking zone at the initiation of matrix cracking, matrix softening and the final applied deflections of the one- and two-dimensional composite bars. The material constants used to model fibre failure and matrix cracking saturation are given in Table 8.3.1.2-1. The predicted stiffness, matrix cracking load and maximum load of the composite bars are compared with the experimental data in Table 8.3.1.2-2. The results demonstrate that the force-deflection response and matrix cracking load of the composite bars are correctly predicted. The analysis also correctly indicates the damaged and final load borne by the composite bars. The damage plots in Fig 8.3.1.2-4 and 5 show that the extent of the matrix cracking zone of the two-dimensional composite is greater than the one-dimensional composite at the same deflection, as the two-dimensional composite has a lower matrix cracking stress.

Description	**1-D Composite bar**			**2-D Composite bar**		
	a	*b*	*c*	*a*	*b*	*c*
Fibre Failure Eqn (7.4.4.1.11)	50	0.01	0.01	20	0.01	0.01
Matrix crack saturation Eqn (7.4.4.1.12)	50	0.01	0.01	1	0.01	0.01

Table 8.3.1.2-1 The material constants modelling rectangular composite bars in three-point bending.

	1-D Reinforcement			**2-D Reinforcement**		
	Damage Model	**Experiment**	**Error**	**Damage Model**	**Experiment**	**Error**
Stiffness (KN/m)	429	371*	+15.5%	388	323*	20.1%
Matrix Cracking Load (N)	223	202	+10.4%	136	177+	23.2%
Maximum Load (N)	629	578	+8.8%	557	556	+1.8%

Legends: '*' indicates the effect of slip during the initial stage of bending is excluded.
'+' indicates the point where the force-deflection curve becomes non-linear w.r.t. the origin.

Table 8.3.1.2-2 Comparison of the stiffness, matrix cracking load and maximum load of the rectangular bars obtained computationally and experimentally.

The maximum principal strain direction of the matrix is plotted in Fig. 8.3.1.2-6.

At the loading plane, the matrix crack plane is shown normal to the tensile surface of

inclined. The crack planes obtained from experiment (see Fig. 5.4.1-3) show similar changes in the orientation of the matrix cracks. This demonstrates the model's ability to correctly predict changes in the matrix crack orientation

8.3.2 Wedge-Shaped Bars

8.3.2.1 Mesh and Model Descriptions

Symmetric halves of the one and two-dimensionally reinforced wedge-shaped sub-structures are shown in Fig 8.3.2.1-1. The figure gives the dimensions of the sub-structures, and the position systems used to define the boundary conditions and mechanical properties. The meshes comprised 96 and 168 second-order quadrilateral plane-stress solid elements. At the thickest section of the sub-structures, the fibre volume fractions were 0.0528 & 0.120, while in the thinner section the volume fractions were 0.117 & 0.218. In the tapered section, the fibre volume fraction was assumed to vary linearly between these limits. Figs 8.3.2.1-2 and 3 show the detail of the fibre alignment of the composites. To load the sub-structures, a deflection of 6mm was applied.

Matrix cracking was taken to occur at stress of 50.0MPa in the one-dimensionally reinforced sub-structure and at 27.4MPa in the two-dimensionally reinforced sub-structure. The shear and tensile delamination strength of the one and two-dimensional composites as a function of fibre area fraction was derived by an interpolation procedure. The shear and tensile delamination strength trends estimated are shown in Fig 8.3.2.1-4. The shear and tensile delamination strengths used in the one and two-dimensionally reinforced sub-structure are shown in Figs 8.3.2.1-5 & 6.

8.3.2.2 Results and Analysis

The deformed meshes shown in Fig 8.3.2.2-1 demonstrate that the boundary conditions used were correctly applied. The predicted force-deflection curves are plotted in Fig 8.3.2.2-2 and 3. The material constants modelling fibre failure, matrix crack saturation, and tensile and shear delamination are given in Table 8.3.2.2-1. The predicted stiffness, matrix cracking load and maximum load of the sub-structures are shown in Table 8.3.2.2-2. In comparison with the experimental results, the computational analyses show:

1. Good agreement in the force-deflection behaviour of the one and two-dimensionally

2. Matrix cracking initiation and final failure of the sub-structures were correctly predicted.
3. Delamination has little influence on the force-deflection behaviour of wedge-shaped sub-structures.

Description	**1-D Composite bar**			**2-D Composite bar**		
	a	*b*	*c*	*a*	*b*	*c*
Fibre Failure Eqn (7.4.4.1.11)	1.0	0.01	0.01	0.1	0.01	0.01
Matrix crack saturation Eqn (7.4.4.1.12)	2.5 & 2.0	0.01	0.01	0.1	0.01	0.01
Tensile Delamination Eqn (7.4.4.2.2)	2	0.01	0.01	0.1	0.01	0.01
Shear Delamination Eqn (7.4.4.3.2)	0.1	0.01	0.01	0.1	0.01	0.01

Table 8.3.2.2-1 The material constants modelling the wedge-shaped polyester bar in three-point bending.

	1-D Reinforcement			**2-D Reinforcement**		
	Damage Model	**Experiment**	**Error**	**Damage Model**	**Experiment**	**Error**
Stiffness (KN/m)	326	318	+2.5%	179	185	3.2%
Matrix Cracking Load (N)	469	564	-16.6%	179	280	36.1%
Maximum Load (N)	1020	1008	+1.2%	518	500	+3.6%

Table 8.3.2.2-2 Comparison of the stiffness, matrix cracking load and maximum load of the wedge-shaped sub-structures obtained computationally and experimentally.

The damage mechanisms at different load levels are shown in Figs 8.3.2.2-2 & 3. Blue indicates no damage, green indicates matrix cracking, while the orange & red colours indicate shear and tensile delamination respectively. Matrix cracking initiates in the fillet where the highest tensile stress is located. As the applied deflection is increased, further matrix cracking is predicted to occur in the tapered and thick sections. The orientations of the crack planes are indicated in Fig 8.3.2.2-4, and the predictions agree well with the experimental observations shown in Fig 5.4.3-2 & 3.

The analyses also predicts shear delamination in the fillet of the one and two-

deflection of 3.87mm. The analyses indicate the tendency for delamination at low shear and tensile delamination stresses. In the experiments by McCafferty (1994) and Gibson (1993), delamination was observed in the fillets of wedge-shaped SiC/SiC composite bars during three-point bending. A micrograph of the matrix cracked and delaminated SiC/SiC wedge-shaped sub-structure is shown in Fig 8.3.2.2-5.

The reason for shear delamination is shown in Fig 8.3.2.2-6. The matrix shear stress contour of 9.5MPa is plotted in the composite and fibre position systems. In both position systems, the shear band (in red) passes through the fillet. Since the shear delamination stress in the tapered section is greater than the fillet, shear delamination initiates in the fillet. The analysis also shows that the tapered section near the fillet is vulnerable to tensile delamination as illustrated by the contour of stress normal to the fibre plotted in Fig 8.3.2.2-7.

8.3.3 T-Shaped Bars

8.3.3.1 Mesh and Model Descriptions

A mesh representing a symmetric half of the composite bar is shown in Fig 8.3.3.1-1. The mesh consists of 119 plane-stress second-order quadrilateral solid elements, and comprised a matrix core and fibre reinforced sections. In the fibre reinforced sections, the fibres are aligned parallel to the edge of the elements and the fibre alignment angles are given in Fig 8.3.3.1-1.

The one-dimensionally reinforced T-bar was modelled with a fibre volume fraction of 0.142. This was determined using optical microscopy. The stresses to initiate matrix cracking, shear and tensile delamination were 50.6MPa, 13MPa and 16MPa. In the two-dimensionally reinforced T-bar, the fibre volume fraction was 0.284 and the matrix cracking stress, and shear and tensile delamination stresses were 20.3MPa, 5.2MPa and 5.6MPa. The matrix core was treated as linear elastic and cracking initiated at a stress of 50MPa. After which, the matrix was unloaded rapidly by softening the matrix stress-strain curve. The T-bar with the one and two-dimensional reinforcements were subject to displacements of 2mm and 2.25mm.

8.3.3.2 Results & Analysis

The deformed meshes shown in Figs 8.3.3.2-1 confirm that the boundary conditions imposed are correct. The predicted force-deflection responses of the T-bars

suppressing and not suppressing delamination. The material constants modelling the deformation are given in Table 8.3.3.2-1. The stiffness, matrix cracking load and maximum load are compared with the experimental data in Table 8.3.3.2-2.

Description	**1-D Composite bar**			**2-D Composite bar**		
	a	*b*	*c*	*a*	*b*	*c*
Fibre Failure Eqn (7.4.4.1.11)	1.0	0.01	0.01	1.0	0.01	0.01
Matrix crack saturation Eqn (7.4.4.1.12)	5.0	0.01	0.01	3.4	0.01	0.01
Tensile Delamination Eqn (7.4.4.2.2)	0.5	0.01	0.01	0.01	0.01	0.01
Shear Delamination Eqn (7.4.4.3.2)	6.8	0.01	0.01	0.92	0.01	0.01

Table 8.3.3.2-1 The material constants for the T sub-structure.

	1-D Reinforcement			**2-D Reinforcement**		
	Damage Model	**Experiment**	**Error**	**Damage Model**	**Experiment**	**Error**
Stiffness (KN/m)	409	404	+1.2%	387	369	+4.8%
Matrix Cracking Load (N)	225	271	-17.0%	116	169	-31.3%
Maximum Load (N)	416	299	+39.1%	264	236	11.8%

Table 8.3.3.2-2 Comparison of the stiffness, matrix cracking load and maximum load of the T sub-structures obtained computationally and experimentally.

The nature of the damage developed in the T sub-structures is shown in Figs 8.3.3.2-2(b) & 3(b). For the one-dimensionally reinforced T sub-structure, matrix cracking and shear delamination developed in the fillet where the maximum matrix principal stress and the maximum matrix shear stress defined with respect to the fibre axis occurred. The maximum principal stress plot in Fig 8.3.3.2-4 and the maximum shear stress plot in Fig 8.3.3.2-5 of the matrix showed this. In addition, the predicted damage sites agree with experiment. From the data file of the computational analysis, the printed damage warnings indicated that matrix cracking initiated before shear delamination. When further load was applied, the shear delamination plane developed along the curved surface of the matrix core. Subsequently, the matrix core cracked, due to the stress re-distribution associated with the shear delamination. This in turn caused

final damage plot demonstrates that the sudden load drop observed in the force-deflection curve at an applied deflection of ~2mm is caused by extensive cracking in the matrix core. The predicted evolution of damage is in agreement with the experimental observations

For the two-dimensionally reinforced T sub-structure, the damage initiation sequence and locations are predicted to be the same as the one-dimensional reinforcement. Shear delamination adjacent to the matrix core develops parallel to the curvature of the matrix core. However, unlike the one-dimensionally reinforced sub-structure, the core does not crack and shear and tensile delamination initiates in the region surrounding the core ligament, at an approximately constant applied load. The damage evolution described by the computational analysis agrees well with the experimental observations for two-dimensionally reinforced T sub-structures described in Sect 5.4.2.

To summarise, the results demonstrate four important capabilities of the model:

1. The model is able to represent the response of the T sub-structures before damage; the error in the stiffness being less than 5%.
2. The model is able to predict the applied load and location at which matrix cracking starts. The load at which the sub-structure's response became non-linear agrees with the experimental data.
3. The model can model the damage behaviour of the T sub-structure. The results show that both matrix cracking and delamination can reduce the stiffness of the sub-structures. However, the significant loss in stiffness is largely due to delamination while matrix cracking plays a less significant role.
4. The model is able to model complex damage evolution of the T sub-structure.

8.4 Discussion

8.4.1 The Computational Model

The results of the misaligned brittle matrix composites and sub-structures have demonstrated four important abilities of the computational model. Firstly, the model can model the behaviour of the composite before damage. The Young's modulus of the offaxis one and two-dimensionally reinforced composites and the stiffness of a wide

Secondly, the model is able to model the initiation of matrix cracking, shear delamination and tensile delamination, and the orientation of the crack or delamination plane. This confirms the advantages of using intersecting failure criteria developed at a constituent level compared to failure criteria applied at a composite level, i.e. Tsai-Hill theory or maximum stress theory. In the current work the matrix crack plane is allowed to form normal to the maximum principal stress direction of the matrix and not orthogonal to the fibre axis. In addition, the delamination plane during shear or tensile delamination is allowed to develop parallel to the fibres.

Thirdly, the computational model is able to predict delamination failure. The tensile stress-strain response of the misaligned one-dimensional composites begins to unload when more than half the composite cross-sectional area parallel to the fibres undergoes tensile delamination. In the case of shear delamination, softening initiates when the entire cross-sectional area of the composite suffers shear delamination.

Arguably, the computational model can predict composite failure when the fibres break. However, this is limited to tension applied parallel to the fibre axis. A difficulty associated with predicting failure of misaligned fibres arises from the stress concentration introduced in the fibres at the matrix crack plane as shown in Fig 8.4.1-1. When the matrix cracks, the fibres in the crack plane align with the maximum tensile stress direction of the composite. Consequently, the fibres experience localised bending, which results in stress concentration in the fibres, and the premature failure of a misaligned composite as indicated in Figs 8.3.2.2-2 to 6. In addition, the localised bends in the fibres may affect slip at the fibre-matrix interface hence the overall stress-strain behaviour of the composite. This may explain why the predicted damage response of the misaligned two-dimensional composites in tension showed problems agreeing with the experimentally measured responses at fibre alignments of $\alpha = 10°$ and 45°.

Fourthly, the computational model is able to model damage evolution and the mechanical behaviour of damaged composites. The predicted force-deflection curve of the sub-structures shows agreement with experiment data. In addition, the predicted matrix crack zone and delamination plane agrees with experimental observations. Significantly, the ability to model damage evolution and behaviour has been demonstrated in situations where damage interaction is present. This is possible because the non-interacting damage criteria used are uniquely applied to the integration points.

single composite element can exhibit multiple damage mechanisms hence model damage interaction.

Arguably, the presence of damage interaction suggests the use of interactive damage criteria, e.g. Tsai (1966) and Hoffman (1967). However, these criteria are developed at a composite level and lack a physical base. This is due to their curve-fitting nature. In comparison, the current approach to using non-interactive damage criteria at a constituent level captures the influence of stress-redistribution, which is the mechanism controlling damage interaction. In this respect, the current approach is considered superior to using interactive damage criteria.

Stress redistribution in the matrix is treated to be damage-elastic while the fibre is non-linear elastic. These simple assumptions are used to provide the simplest damage formulation for modelling stress redistribution during unloading and reloading. However, cyclic experiments by Aveston, Copper & Kelly (1971) and McCafferty (1994) have shown that inelasticity and hysteresis are present, which depend on the extent of debonding and frictional sliding at the fibre-matrix interface. It is possible that neglecting these interfacial effects contributed to the mildly higher load predicted for the T-shaped sub-structures.

Alternatively, the mild overestimate may be caused by the mesh and mechanical properties of the T-shaped substructures. It is assumed that the substructures are symmetric and contain homogeneously positioned fibres. Cox *et al* (1994) have argued that heterogeneous positioning of the fibres can influence the average moduli and strength. In the substructure specimens, some non-symmetric features in the fillets and heterogeneous fibre positioning are observed. As such, these experimental factors could have caused the experimental load to be mildly lower than the computational predictions.

Finally, the computational model is motivated towards solving problems with proportional loading. The first step in developing any model must be to deal with the physis of proportional loading before addressing non-proportional loading. Experiments have shown that some damage interaction exists. To determine the mechanics of damage interaction, non-proportional loading tests may be explored as a means to advance the computational model. The data obtained could be used to establish and verify a mechanistic law governing stress-redistribution.

8.4.2 The Sub-Structures

First, the predicted force-deflection response confirmed that the non-linearity in the force-deflection behaviour was caused by damage developed in the sub-structures. Matrix cracking was shown to be the damage mechanism causing the rectangular and wedge sub-structures to fail, while shear delamination caused the failure of T sub-structure.

Secondly, the sub-structures with two-dimensional reinforcement are more prone to matrix cracking, shear, or tensile delamination, compared with the one-dimensionally reinforced case. This is caused by the weak interfaces of the transverse fibres.

Finally, a matrix core in the fillet of the T sub-structure can delay delamination initiation and provide higher load bearing capability. McCafferty (1994) analysed the T sub-structure with two-dimensional reinforcement and observed that tensile delamination initiate in the fillet as shown in Fig 8.4.2-1. The T sub-structure used however did not contain a matrix core. In the current analyses where a matrix core is present in the fillet, matrix cracking was shown to initiate before delamination. Since the stress for matrix cracking is higher than the delamination stress, a greater load is borne by the T sub-structure with a matrix core before failure.

8.5 Conclusions

Computational analyses of composites and substructures using the simple computational model developed in Chapter 7 were performed. In comparison to experimental data, the computational model has demonstrated the ability to model damage initiation, orientation, development, interaction and mechanical behaviour. In addition, the computational model is able to identify the damage mechanism and location of the final failure in the composite substructures. To improve the computational model, factors such as frictional sliding at the fibre-matrix interface, fibre bending at matrix cracks and non-proportional loading could be explored. However, the existing computational model shows promise for the analysis of engineering components and structures.

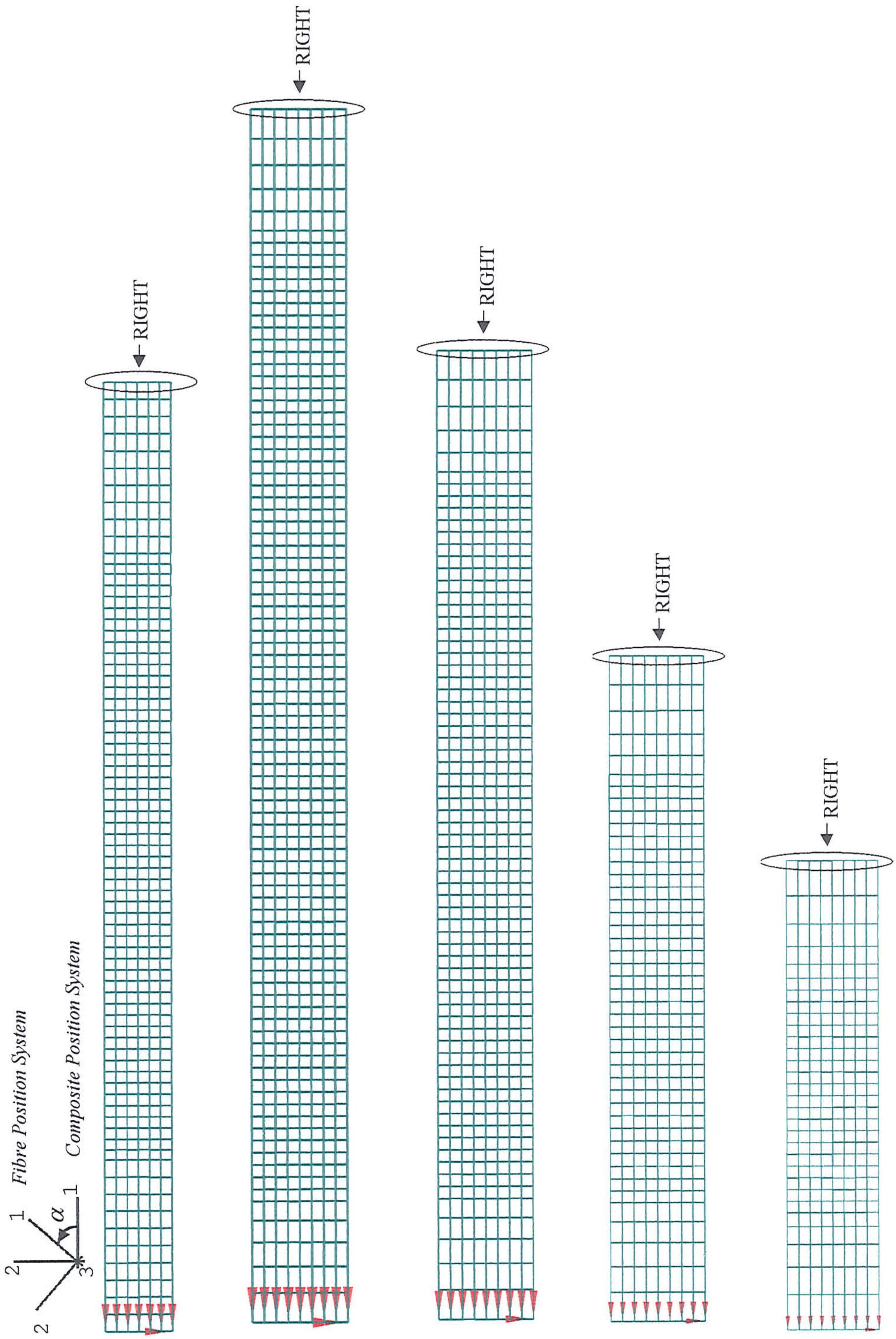

(a) (b) (c) (d) (e)

Fig 8.2.1.1-1 The undeformed mesh of the one-dimensional composite with fibre

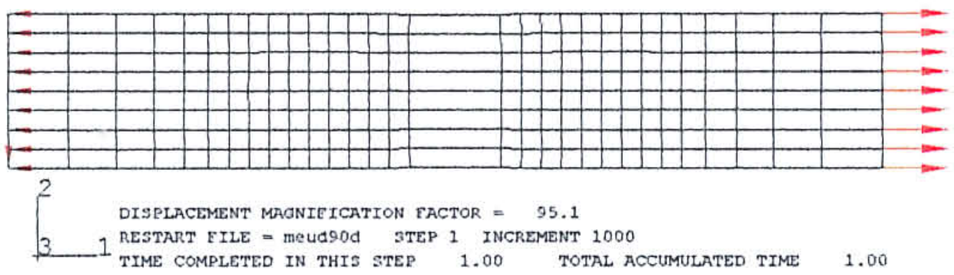

$\alpha = 90°$

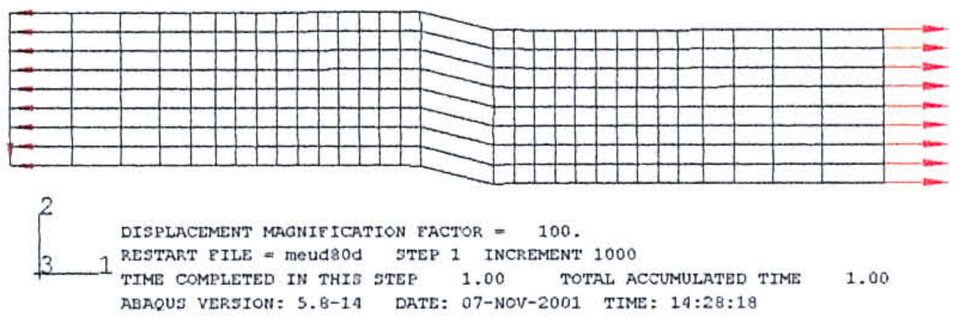

$\alpha = 80°$

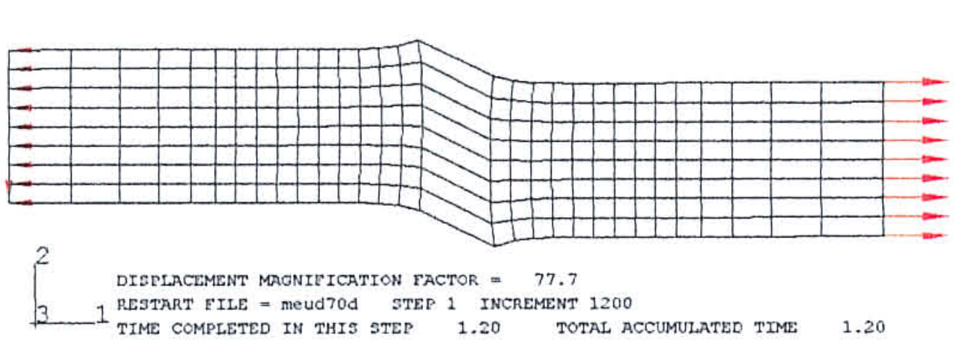

$\alpha = 70°$

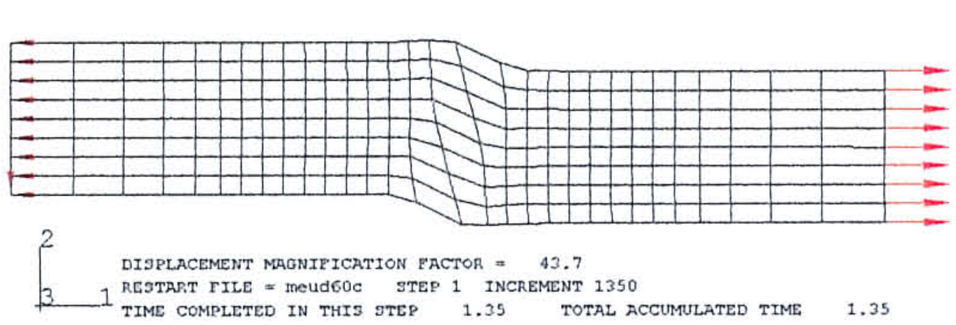

$\alpha = 60°$

$\alpha = 45°$

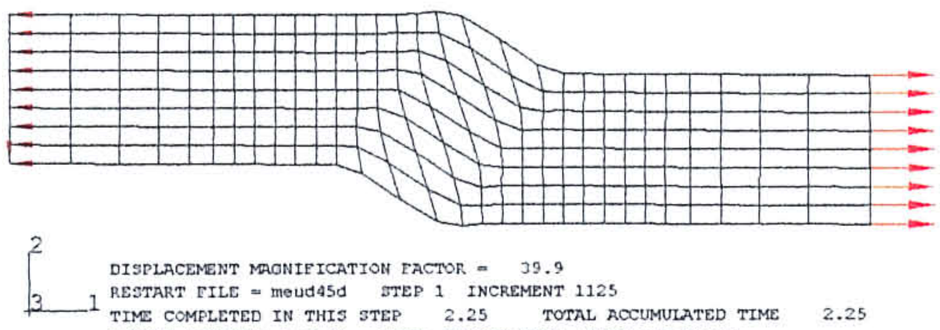

$\alpha = 30°$

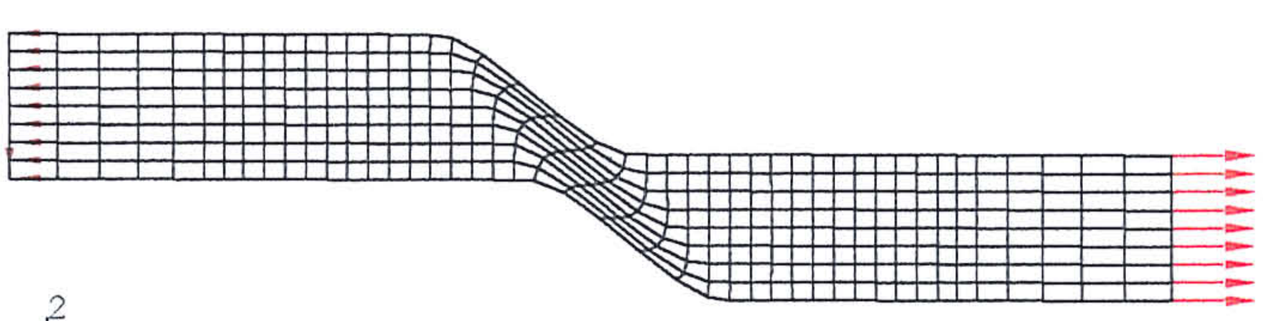

$\alpha = 20°$

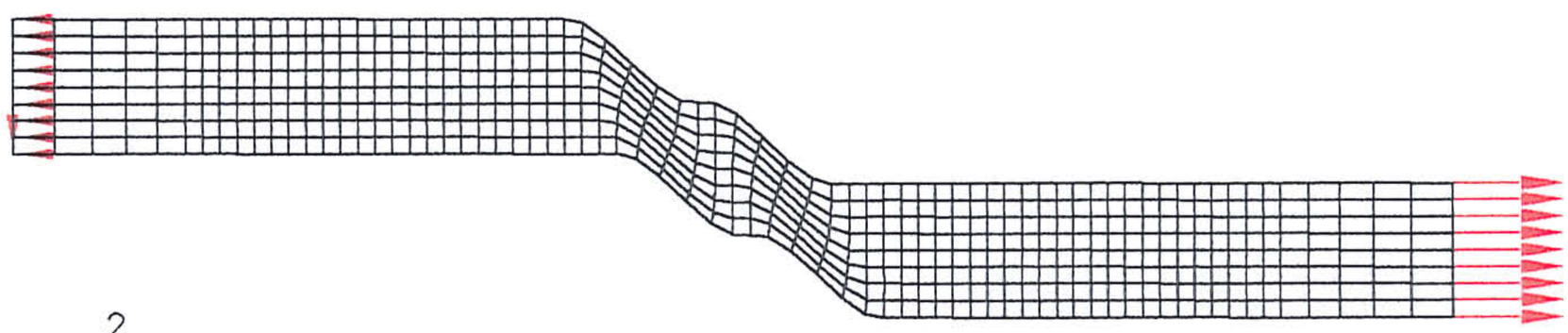

$\alpha = 10°$

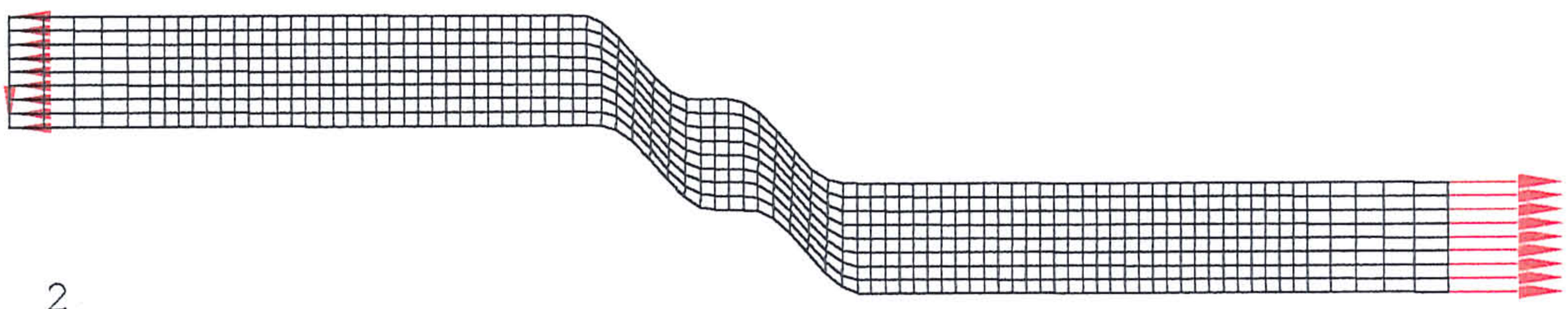

$\alpha = 0°$

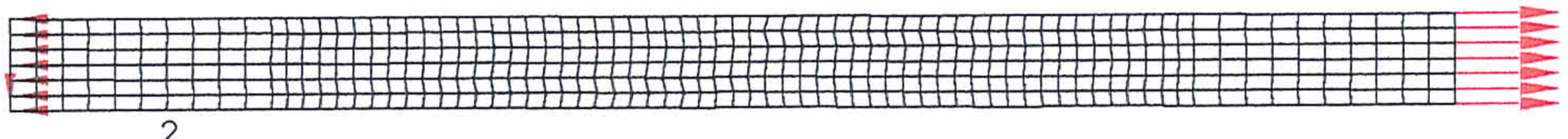

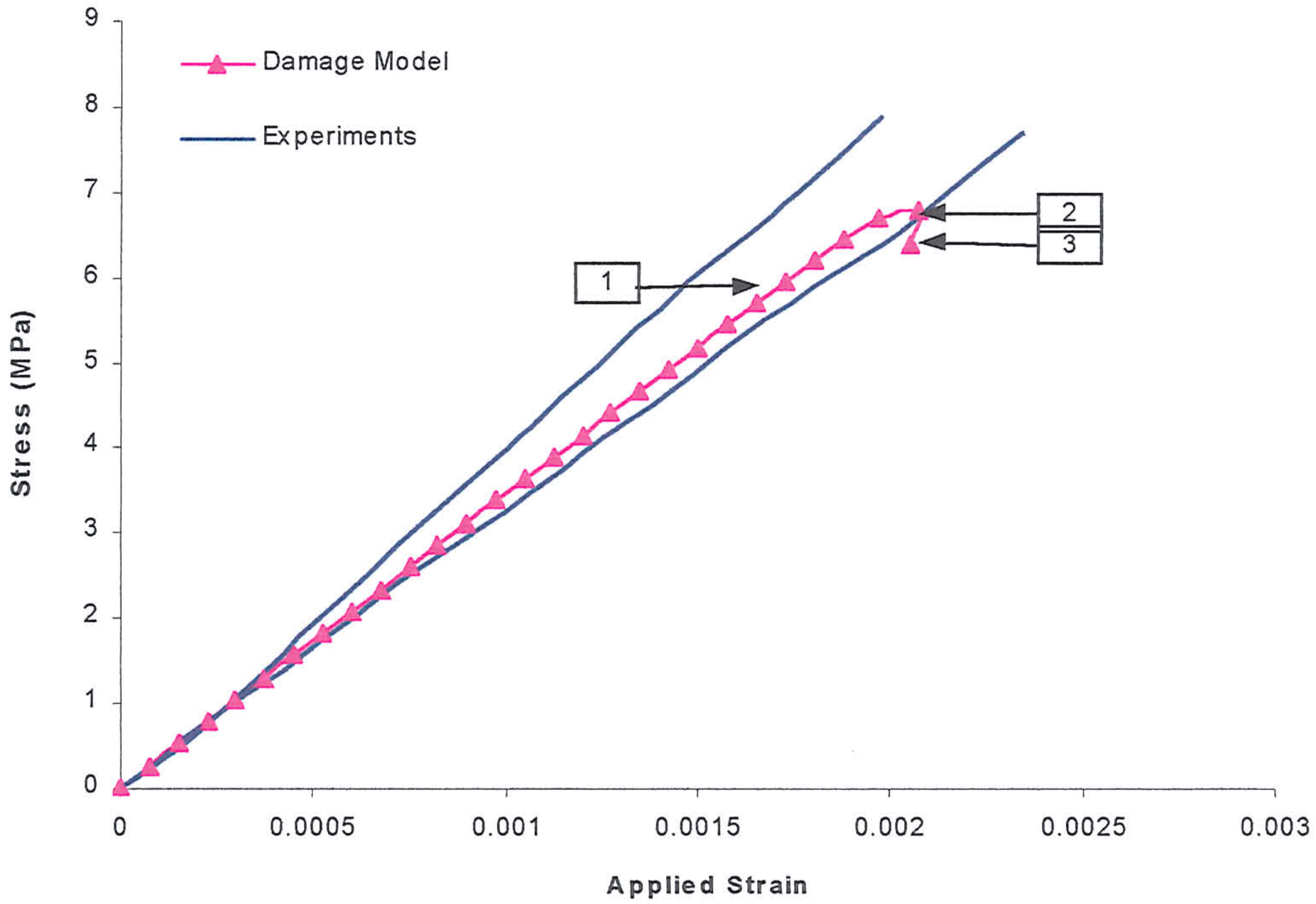

(a)

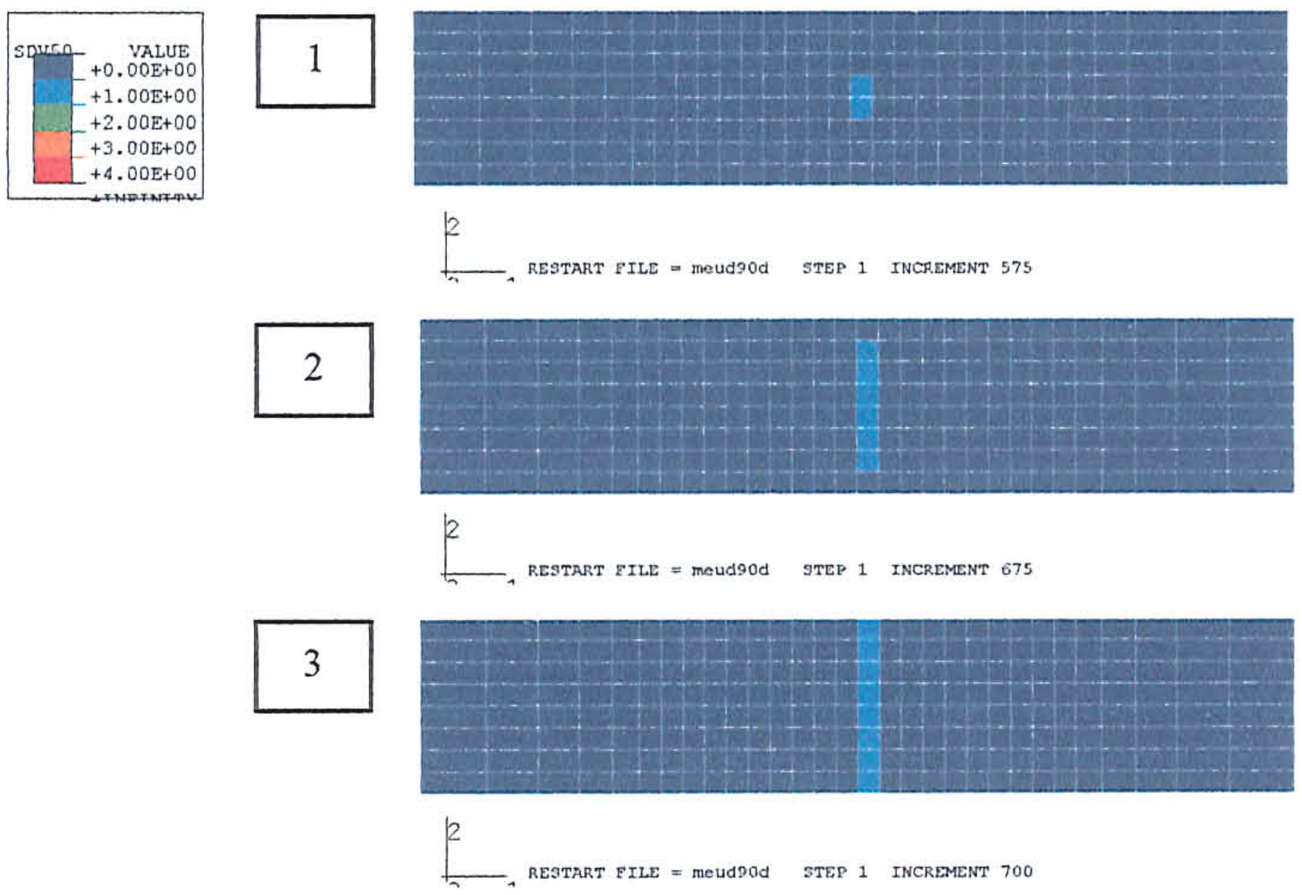

(b)

Fig 8.2.1.2-2 A comparison of the predicted and experimental tensile stress-strain response and tensile delamination zone, of a misaligned one-dimensional composite ($\alpha = 90°$).

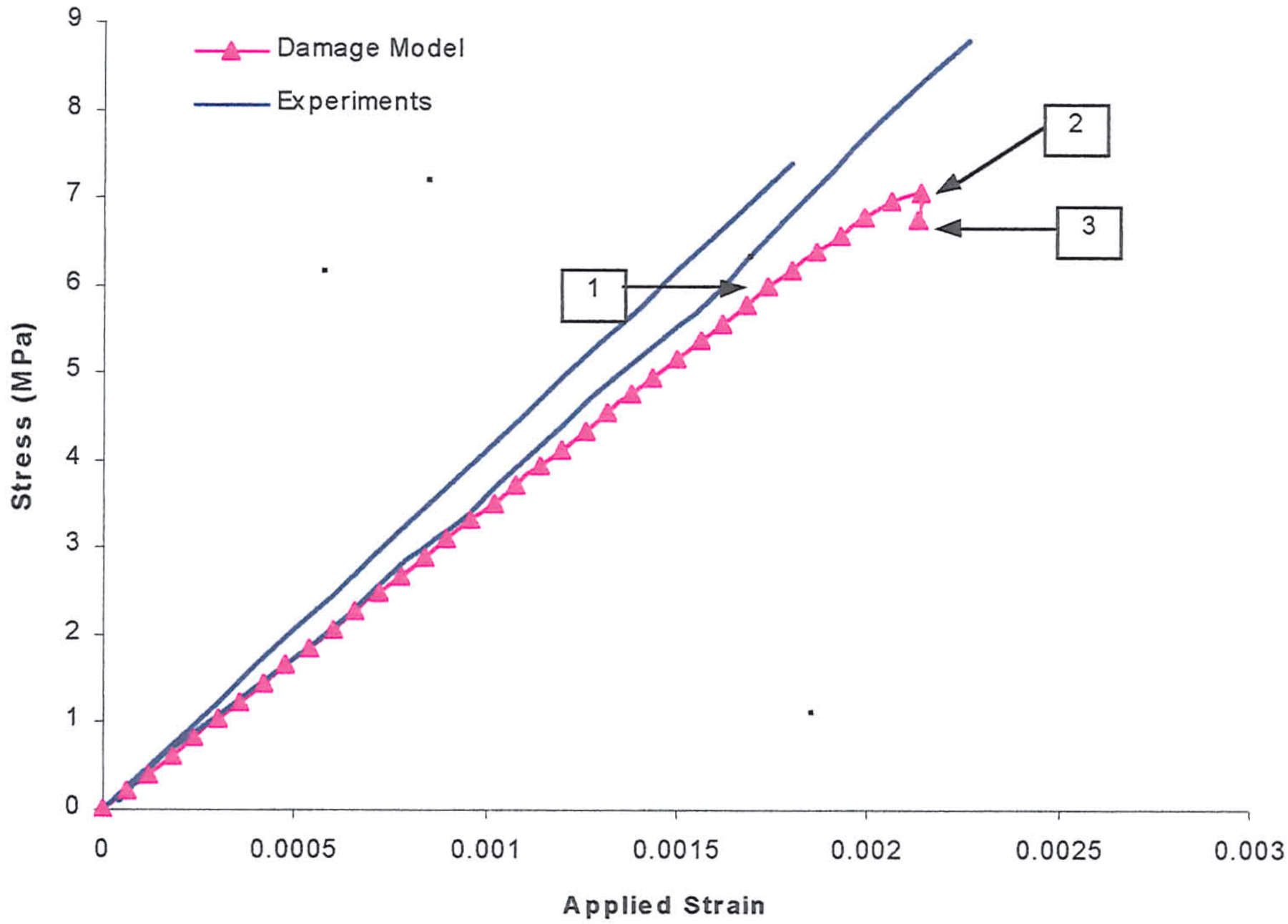

(a)

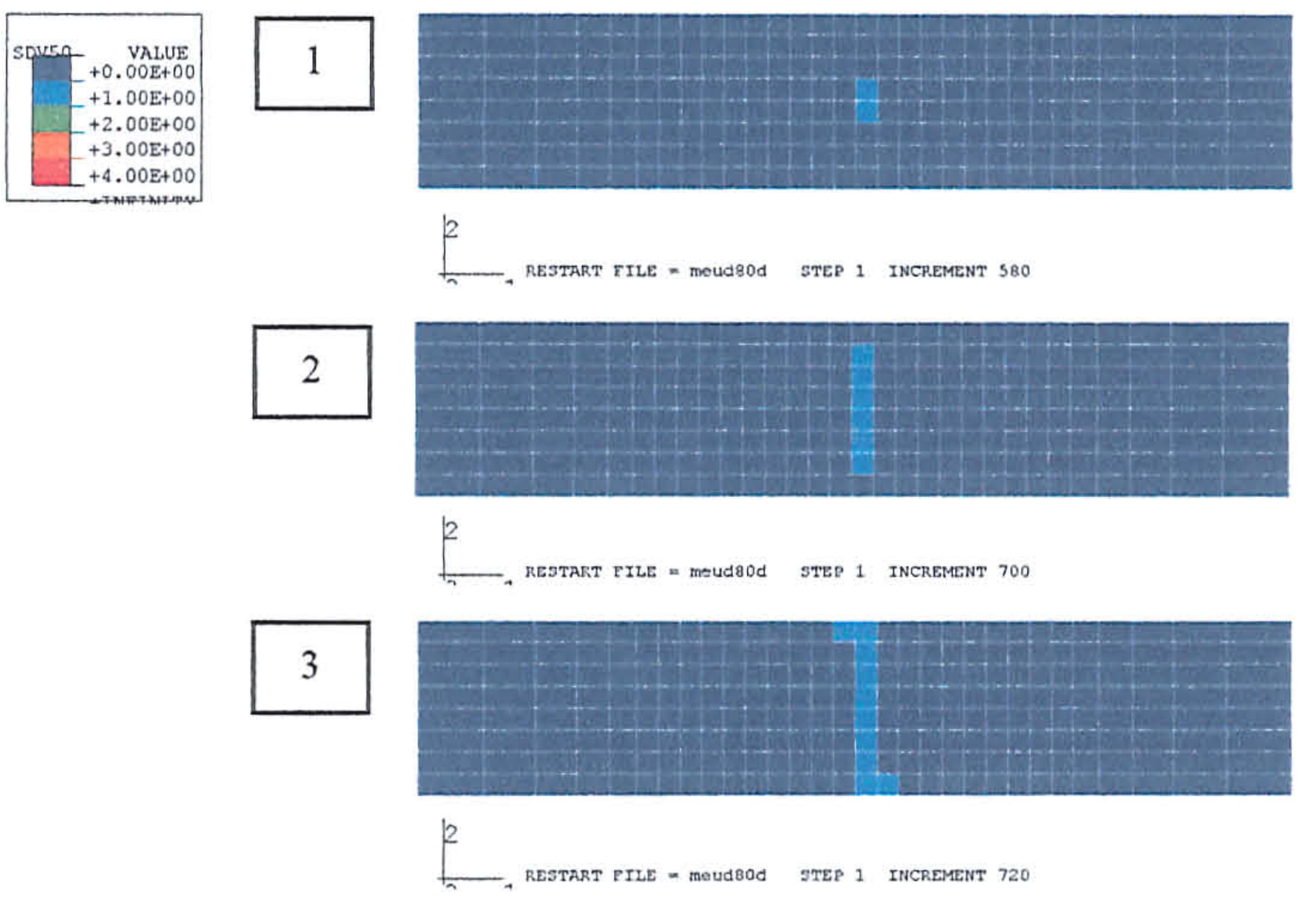

(b)

Fig 8.2.1.2-3 A comparison of the predicted and experimental tensile stress-strain response and tensile delamination zone, of a misaligned one-dimensional composite ($\alpha = 80°$).

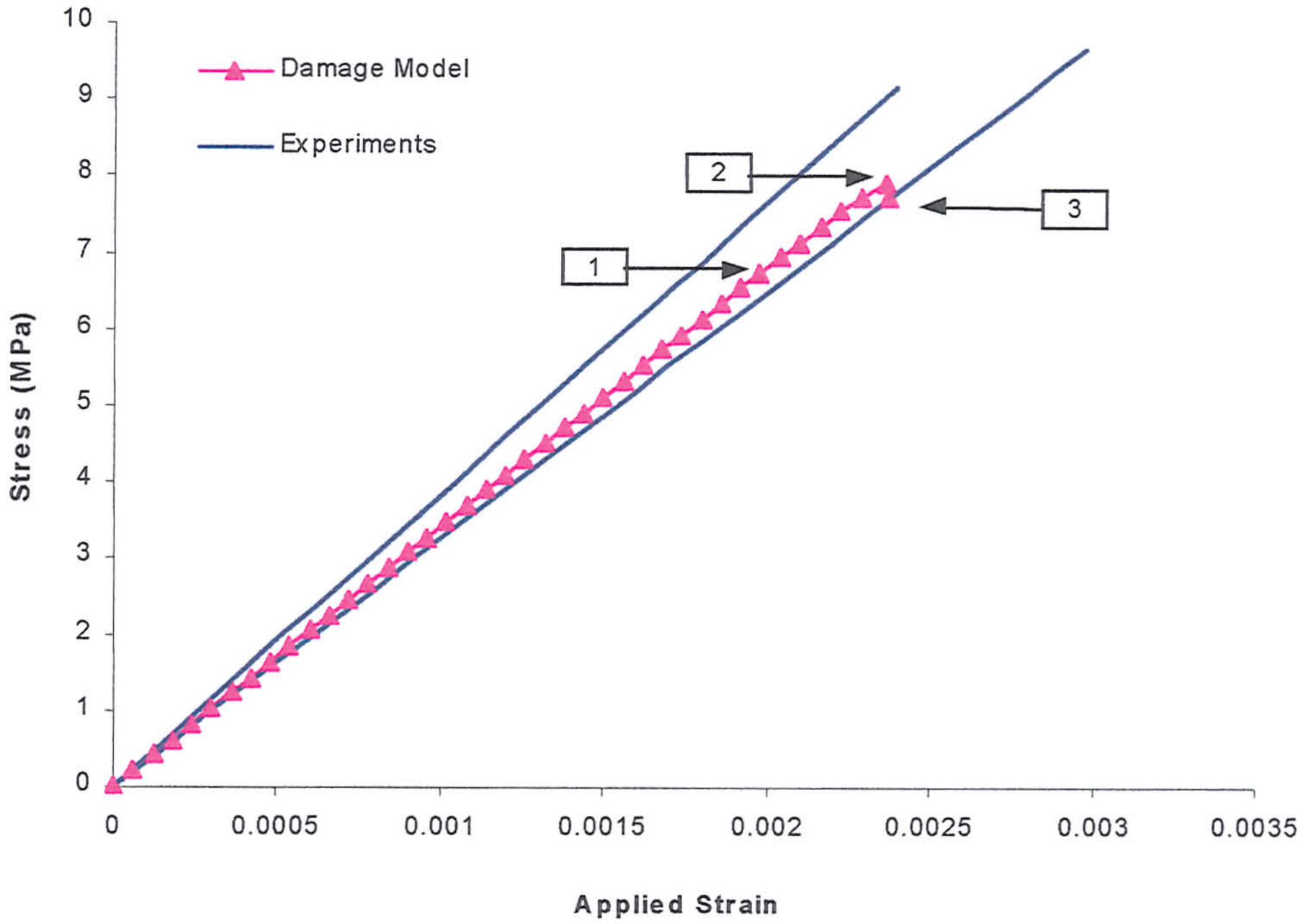

(a)

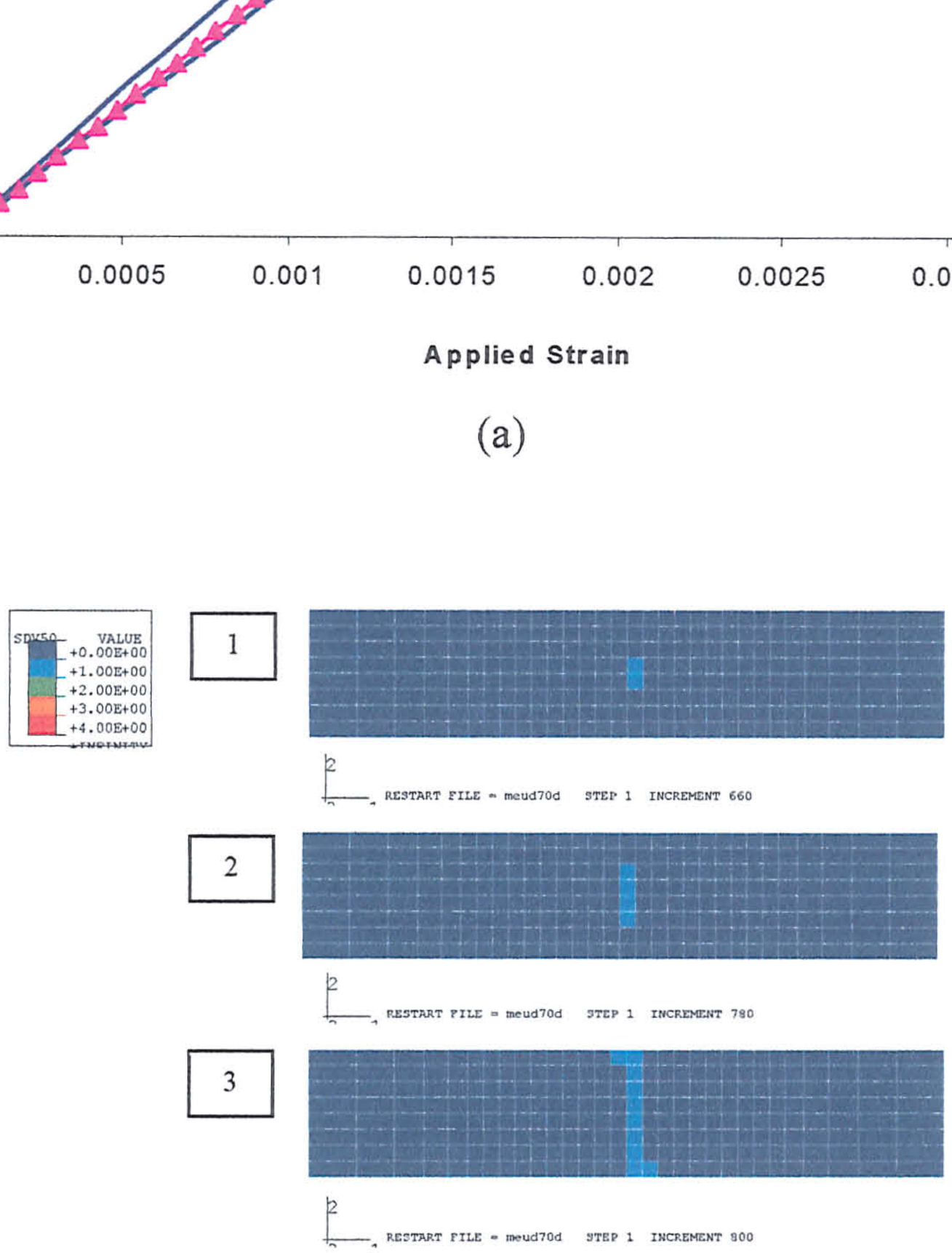

(b)

Fig 8.2.1.2-4 A comparison of the predicted and experimental tensile stress-strain response and tensile delamination zone, of a misaligned one-dimensional composite ($\alpha = 70°$).

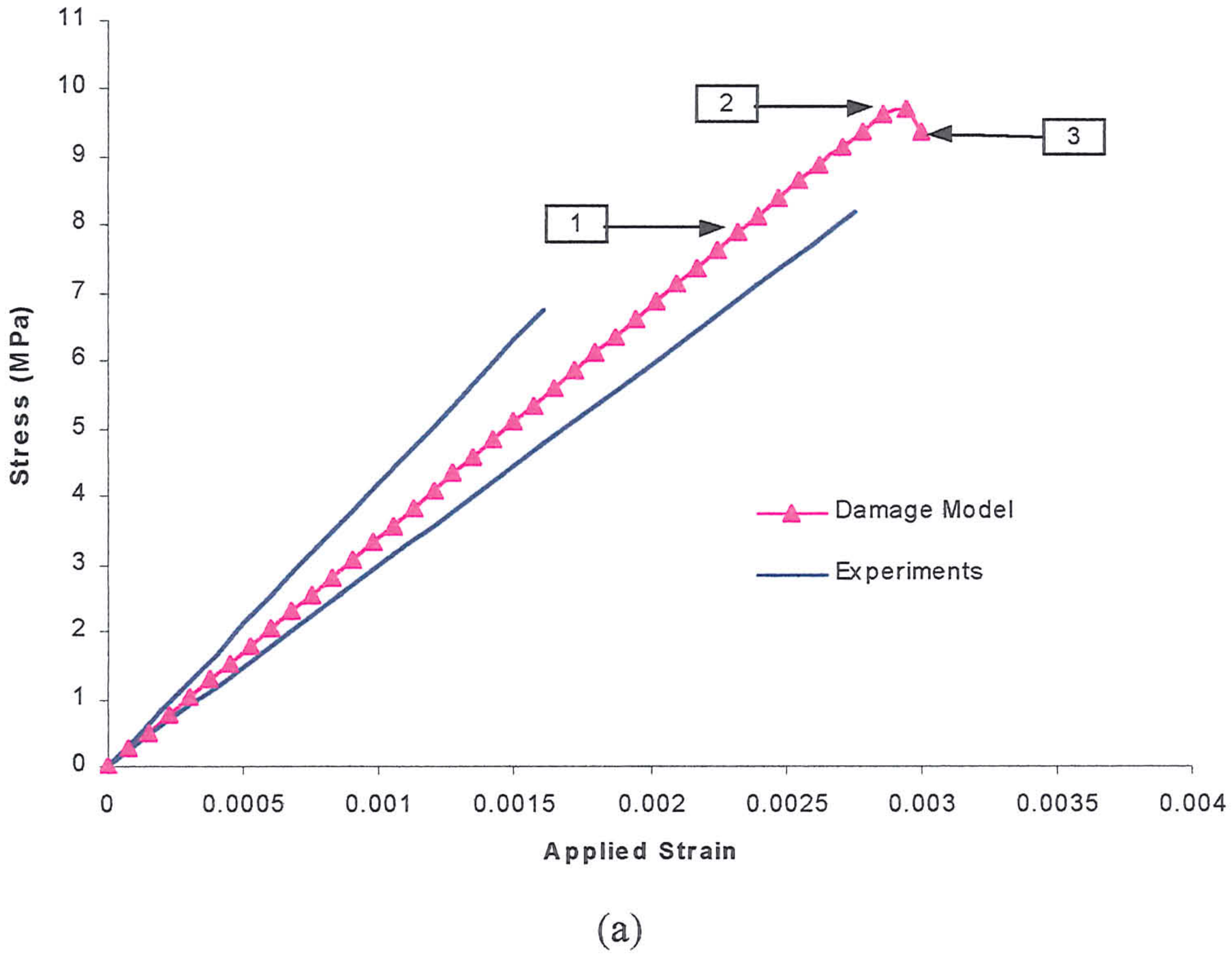

(a)

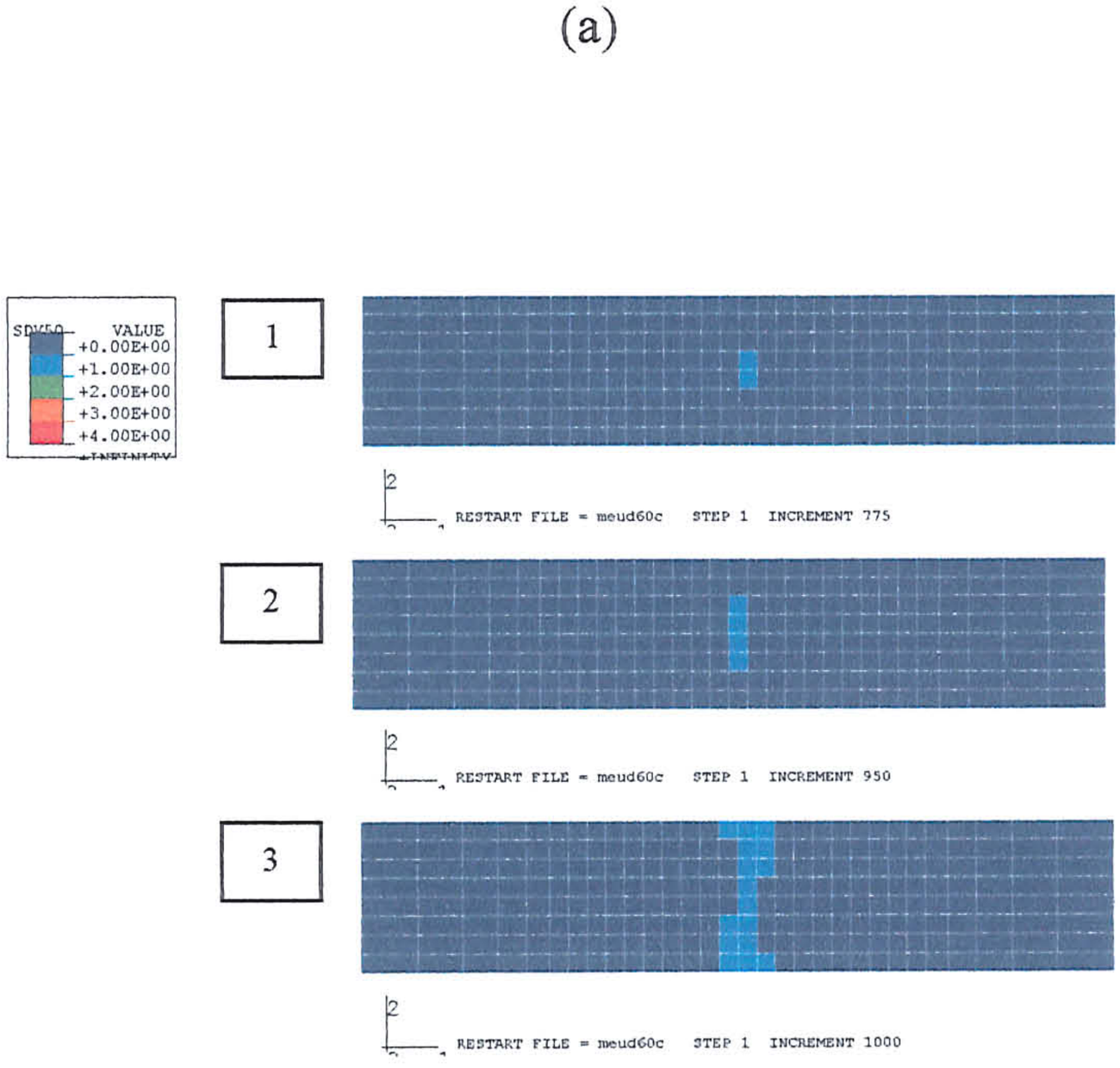

(b)

Fig 8.2.1.2-5 A comparison of the predicted and experimental tensile stress-strain response and tensile delamination zone, of a misaligned one-dimensional composite ($\alpha = 60°$).

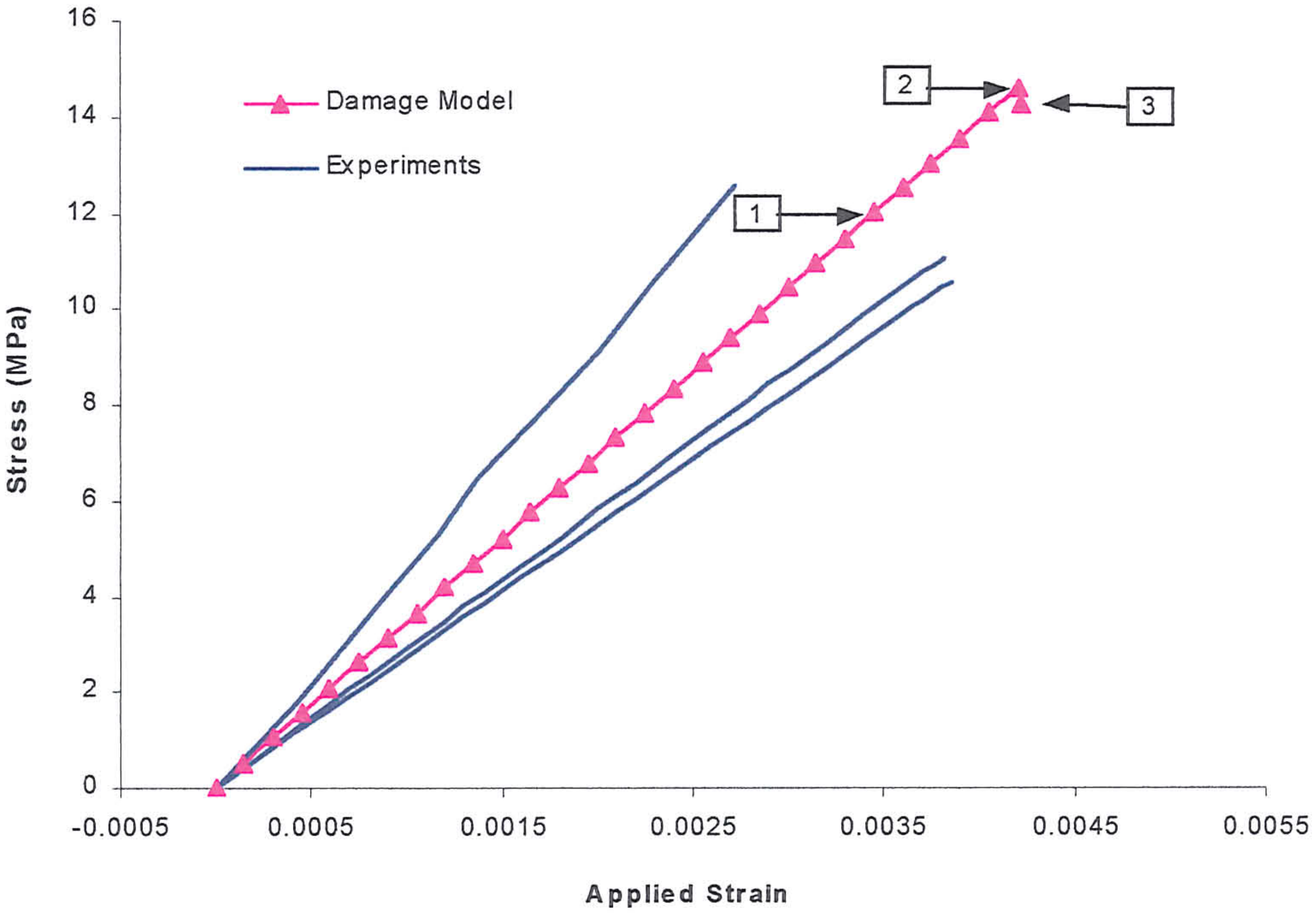

(a)

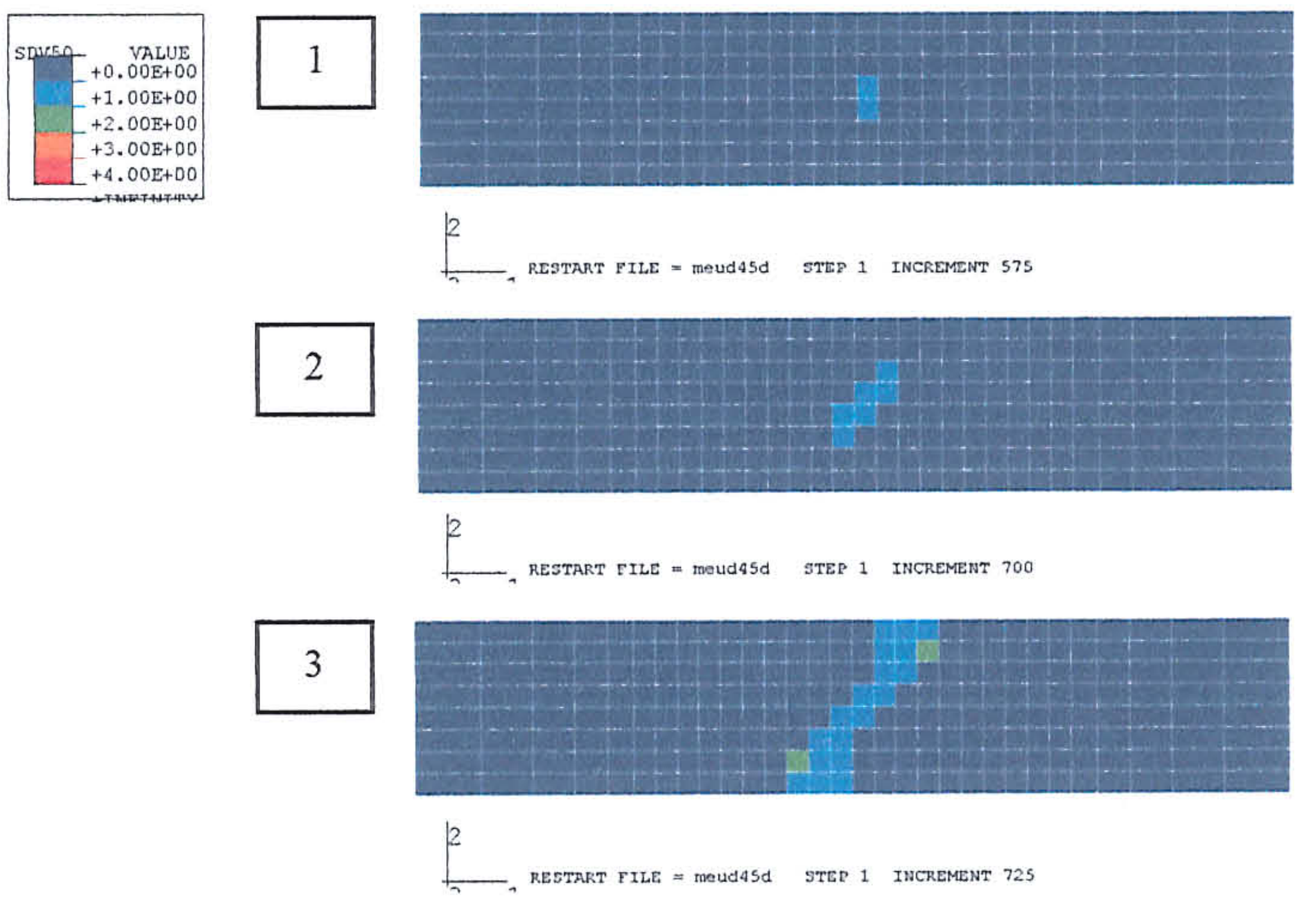

(b)

Fig 8.2.1.2-6 A comparison of the predicted and experimental tensile stress-strain response and tensile delamination zone, of a misaligned one-dimensional composite ($\alpha = 45°$).

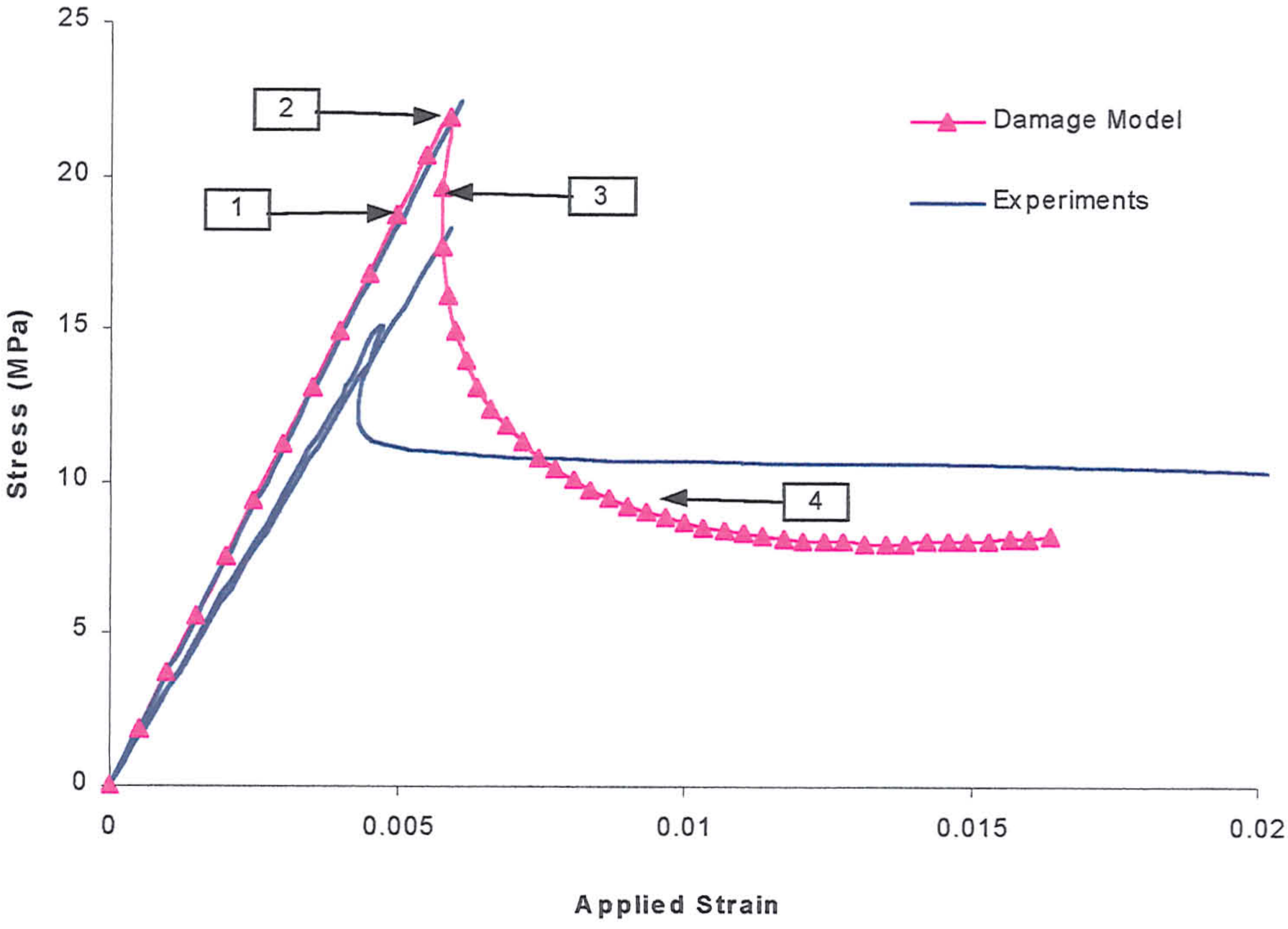

(a)

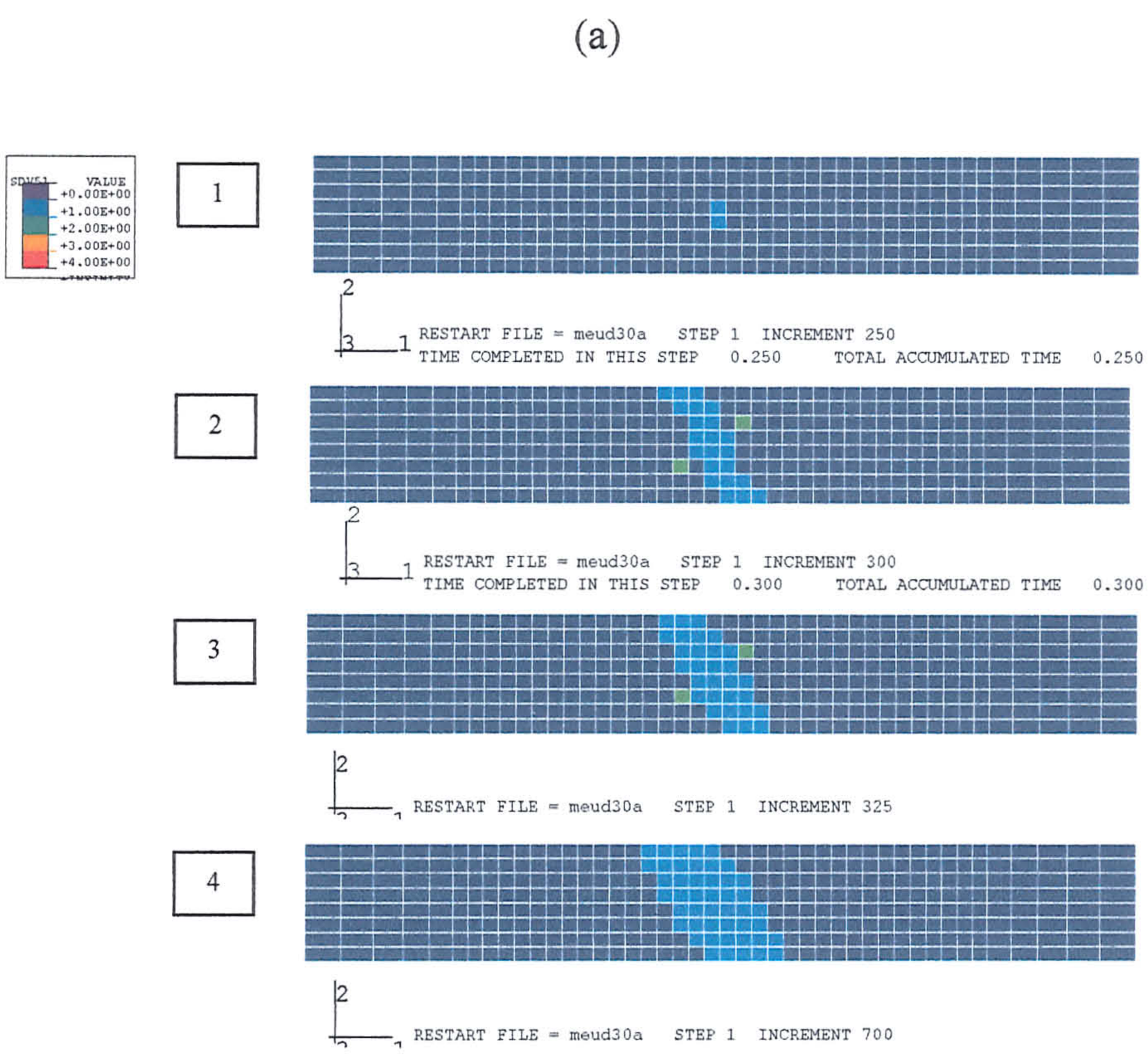

(b)

Fig 8.2.1.2-7 A comparison of the predicted and experimental tensile stress-strain response and shear delamination zone, of a misaligned one-dimensional

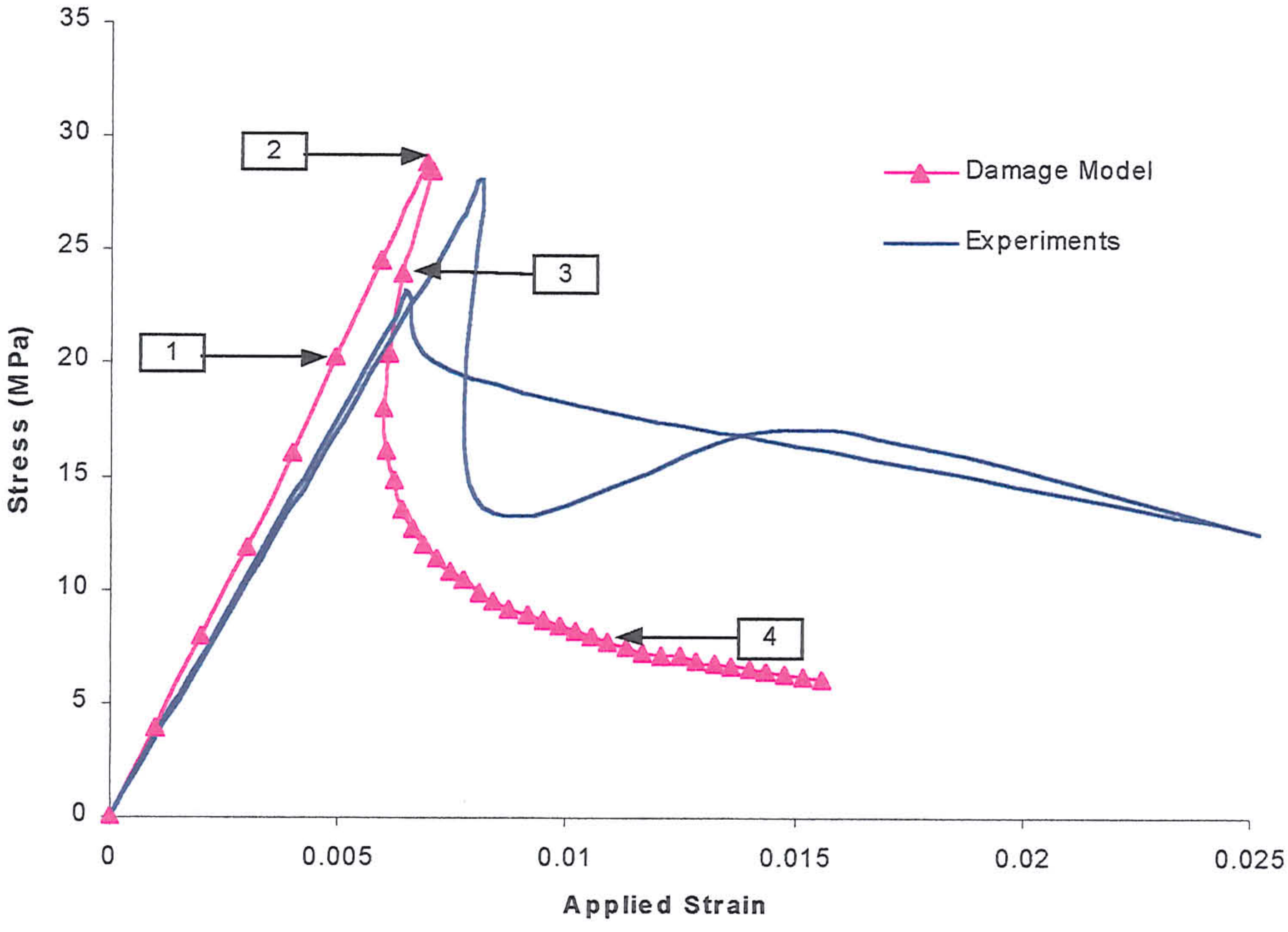

(a)

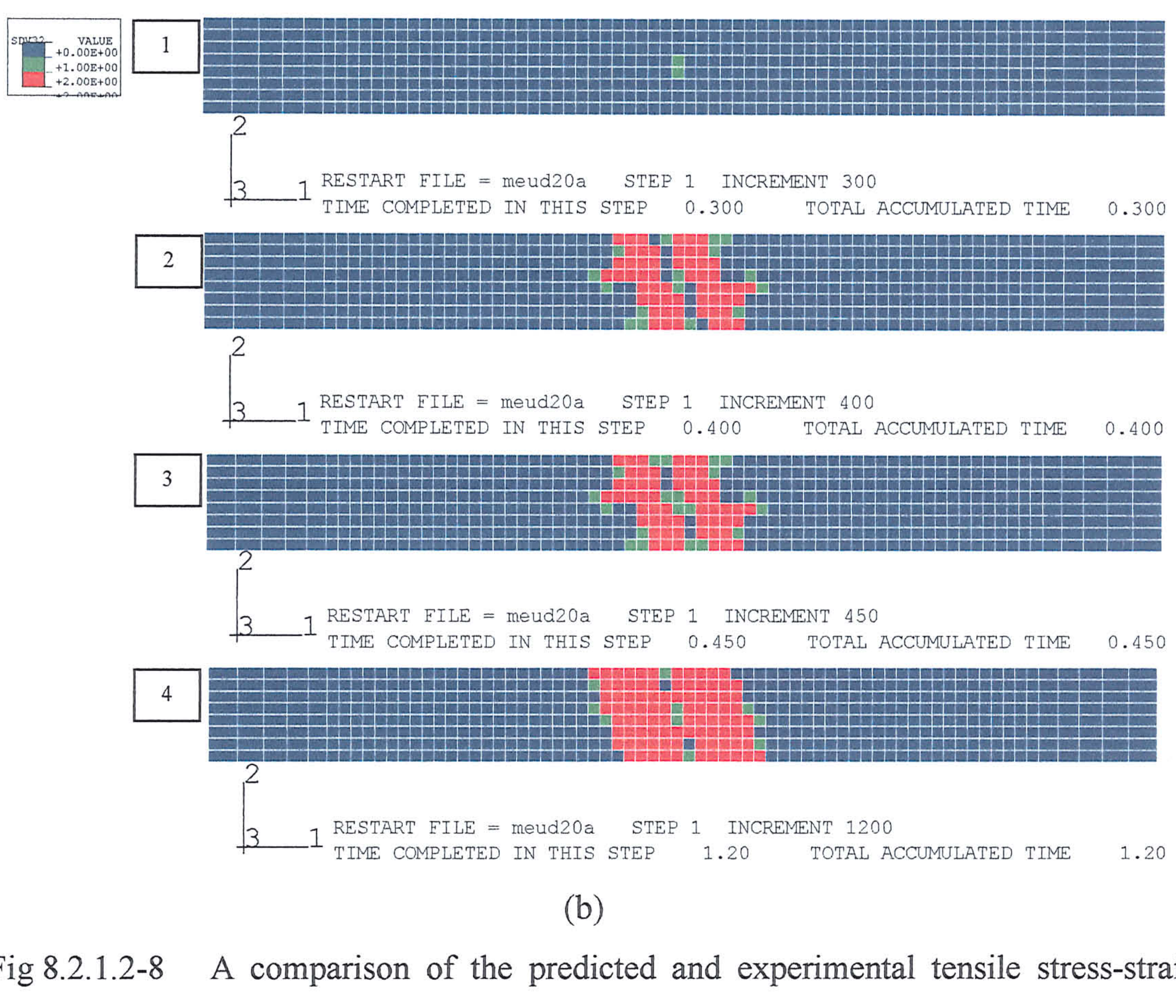

(b)

Fig 8.2.1.2-8 A comparison of the predicted and experimental tensile stress-strain response and shear delamination and matrix cracking zone, of a

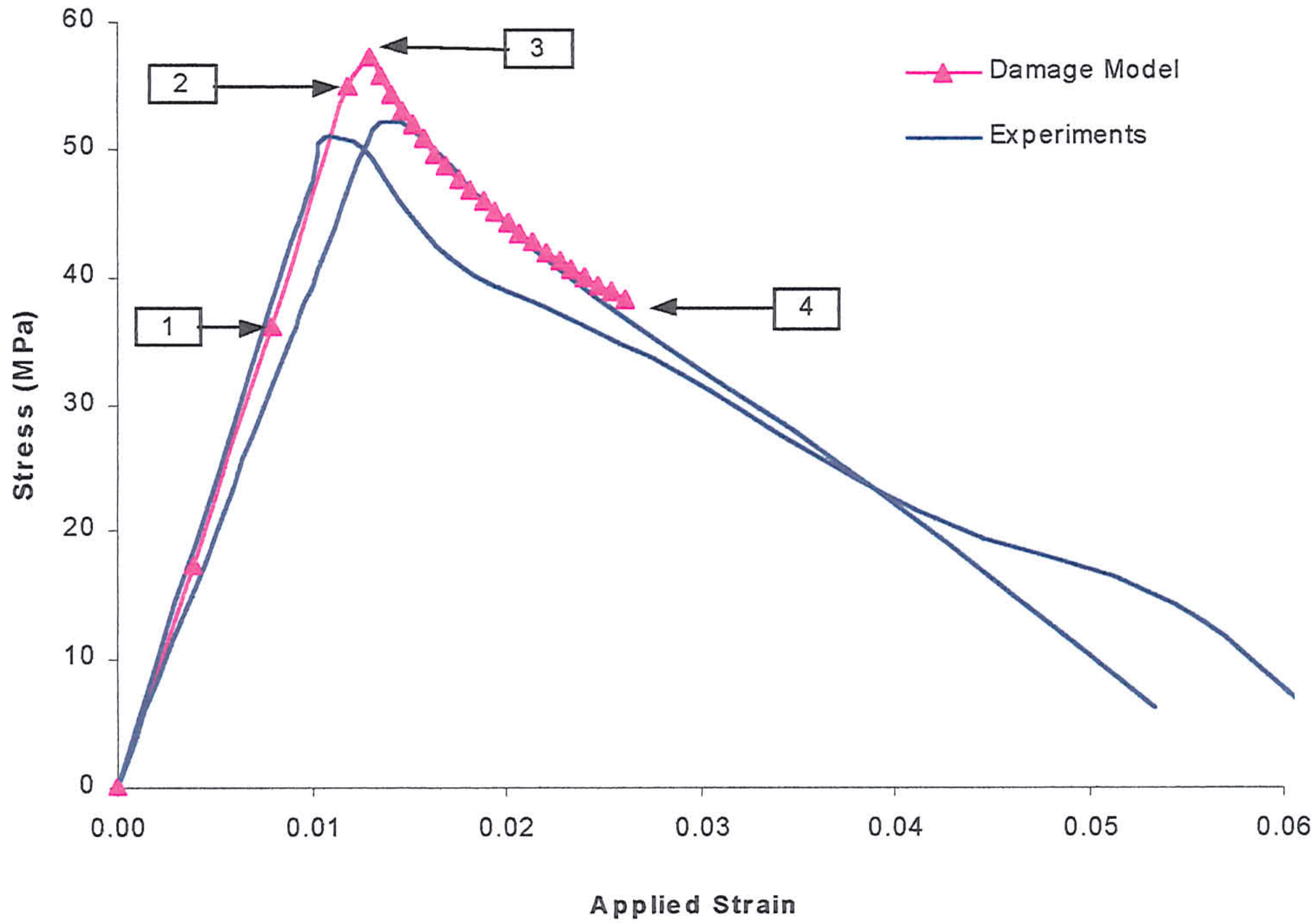

(a)

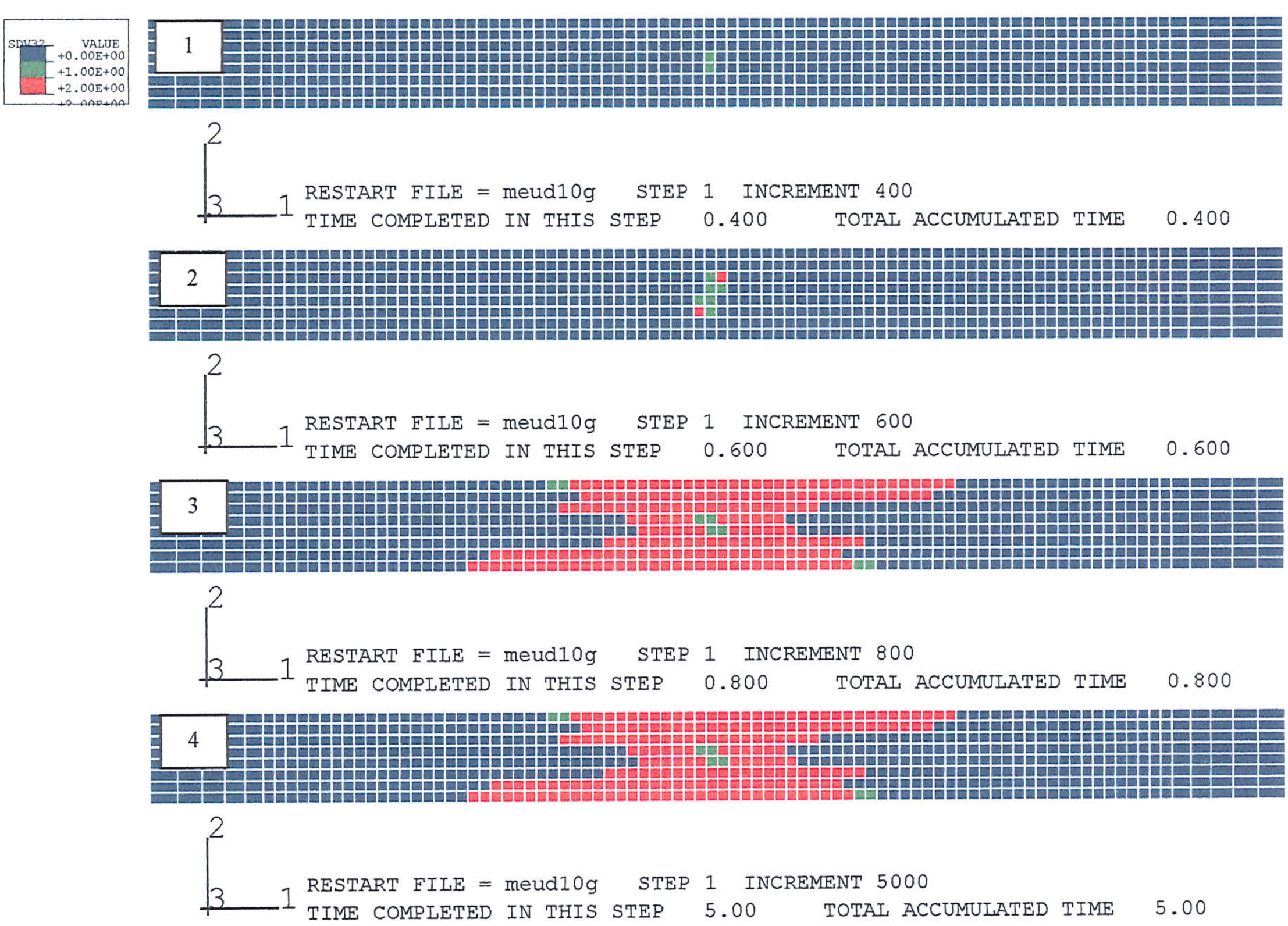

(b)

Fig 8.2.1.2-9 A comparison of the predicted and experimental tensile stress-strain

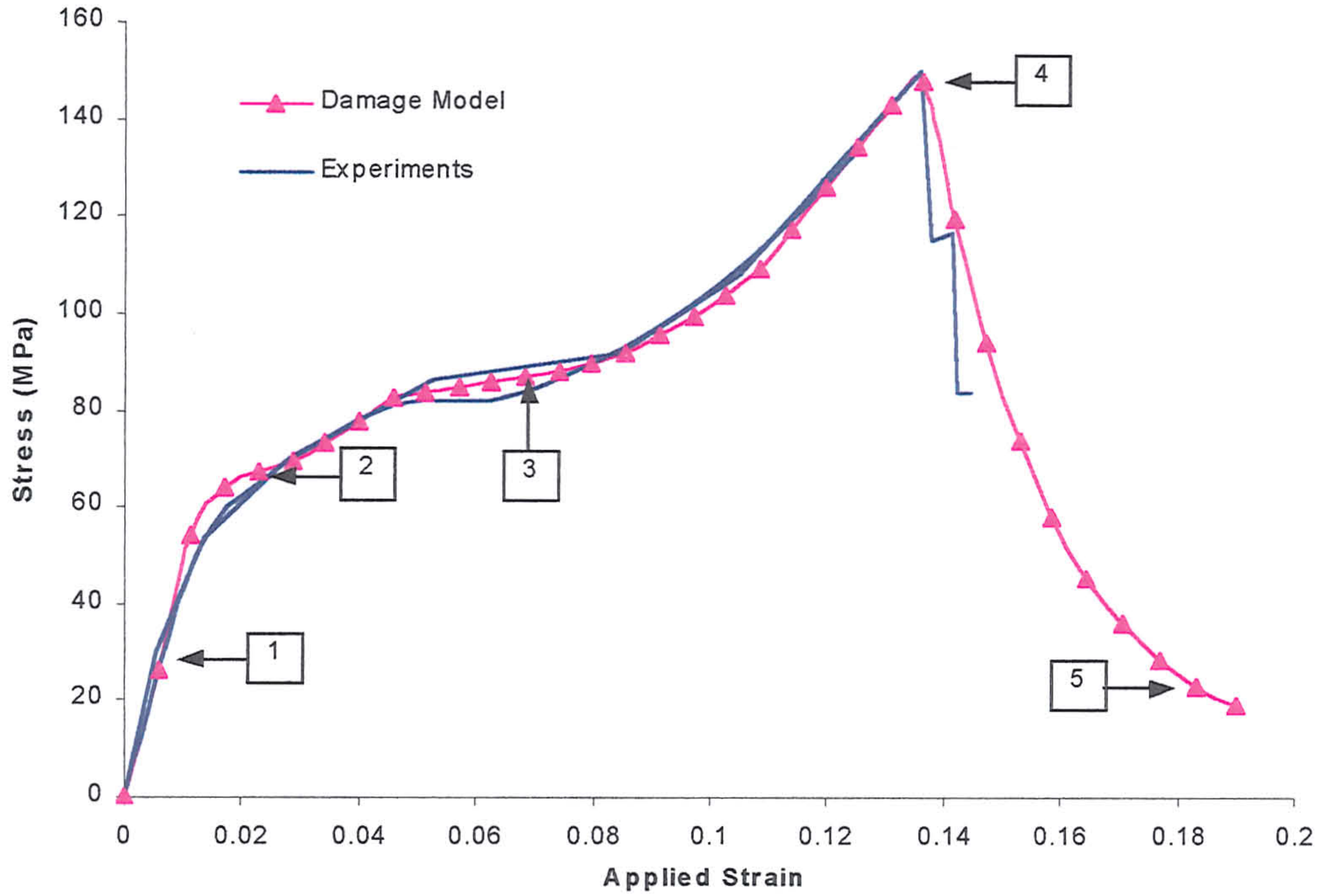

(a)

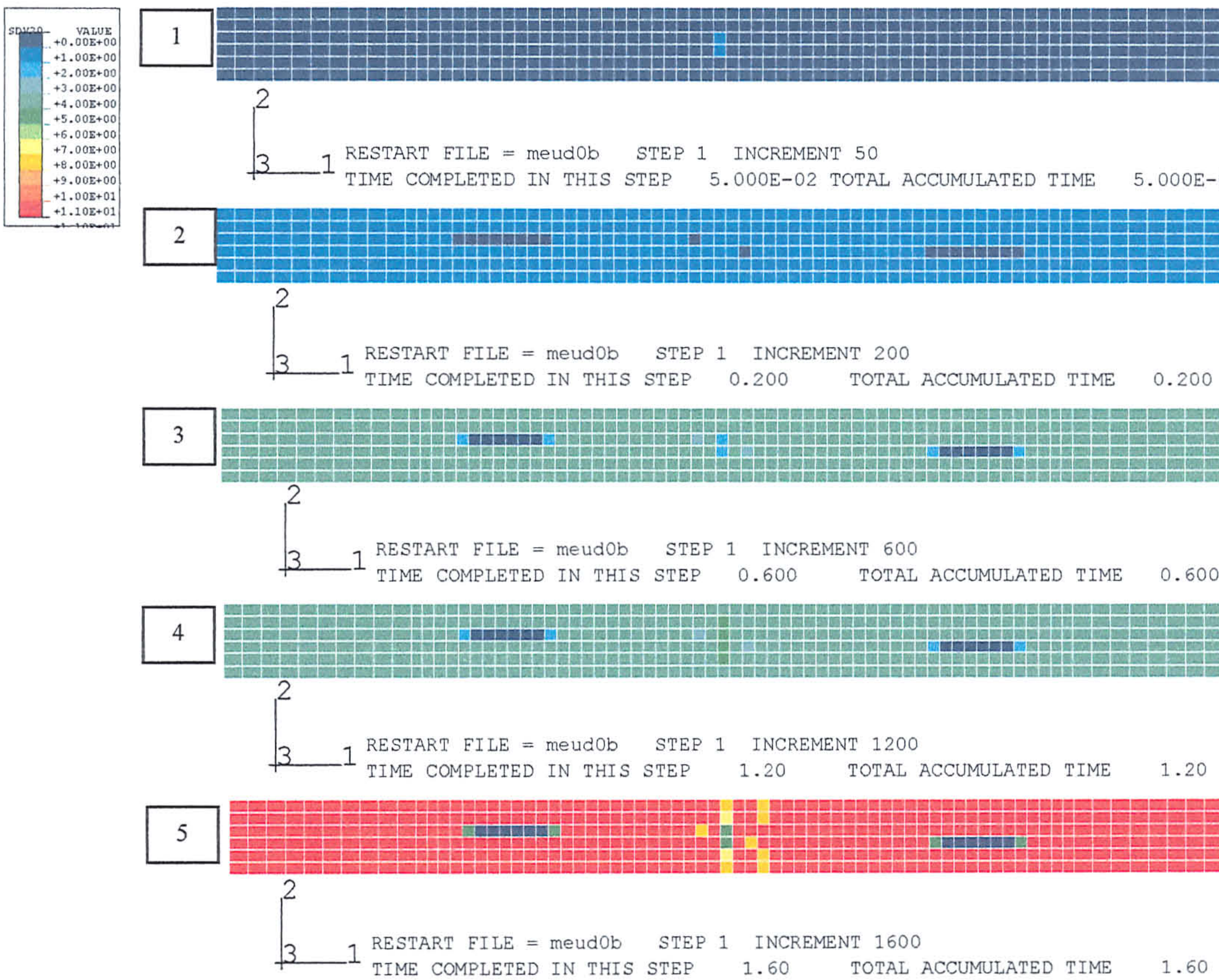

(b)

Fig 8.2.1.2-10 A comparison of the predicted and experimental tensile stress-strain

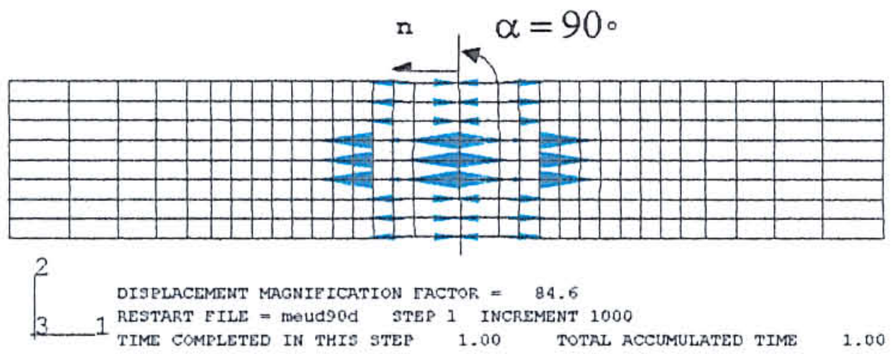

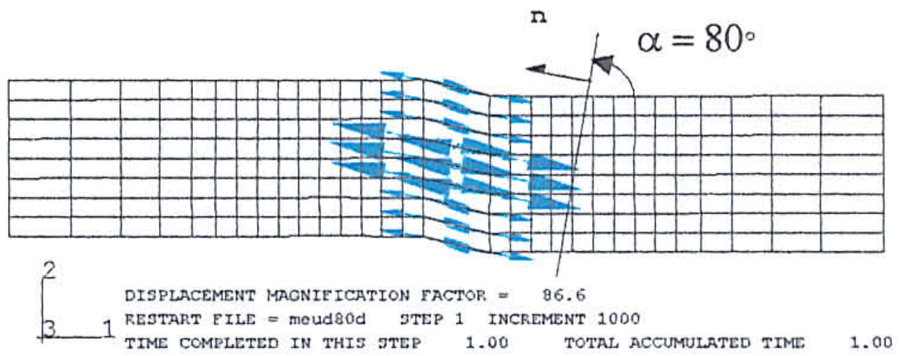

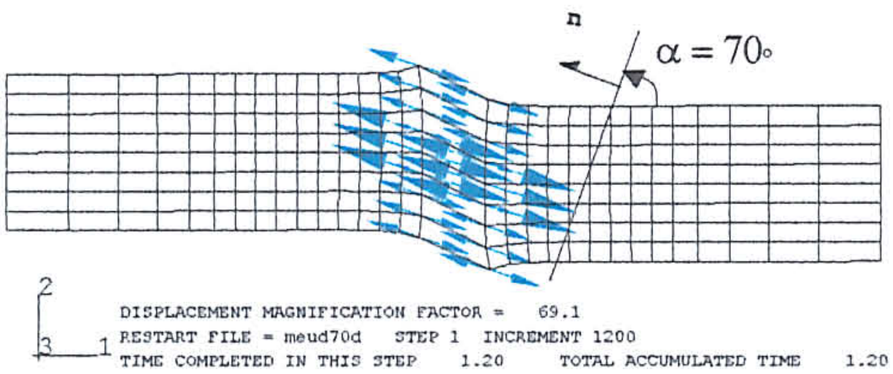

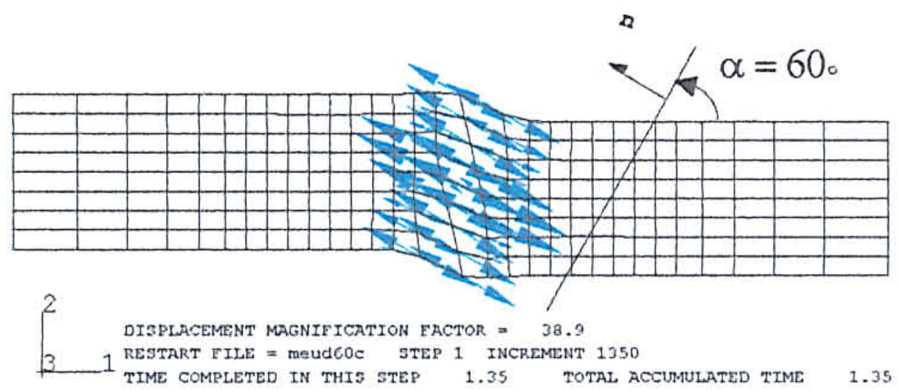

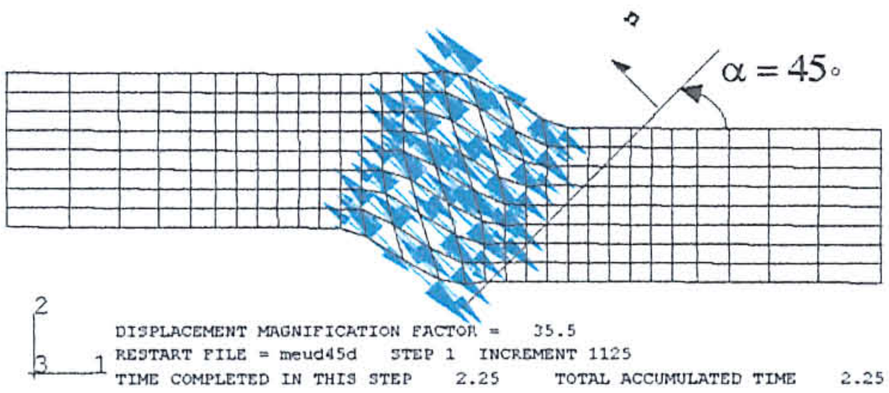

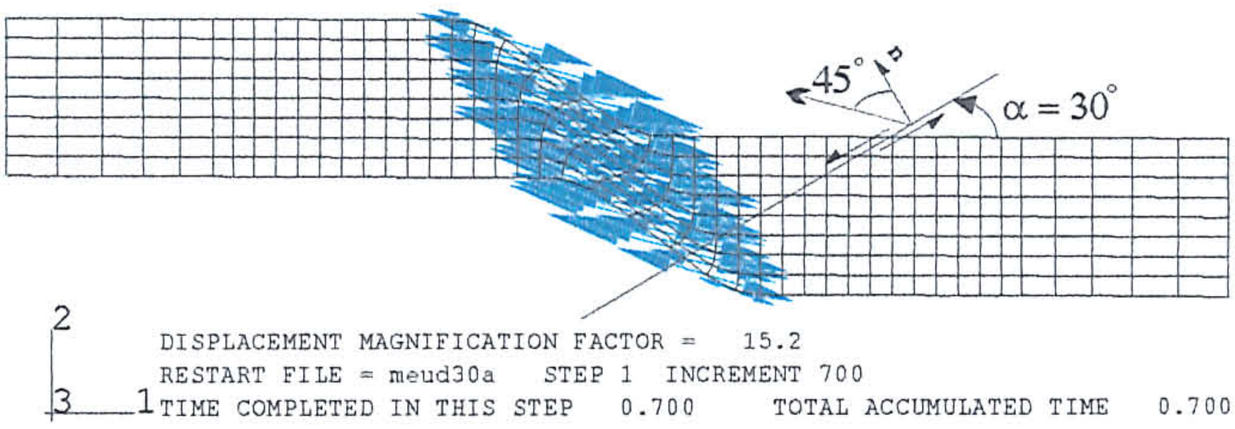

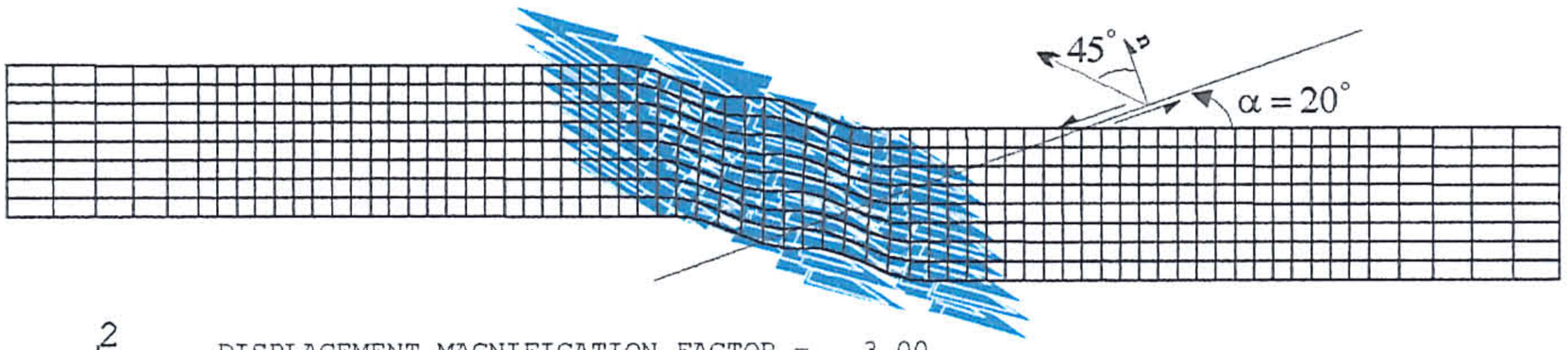

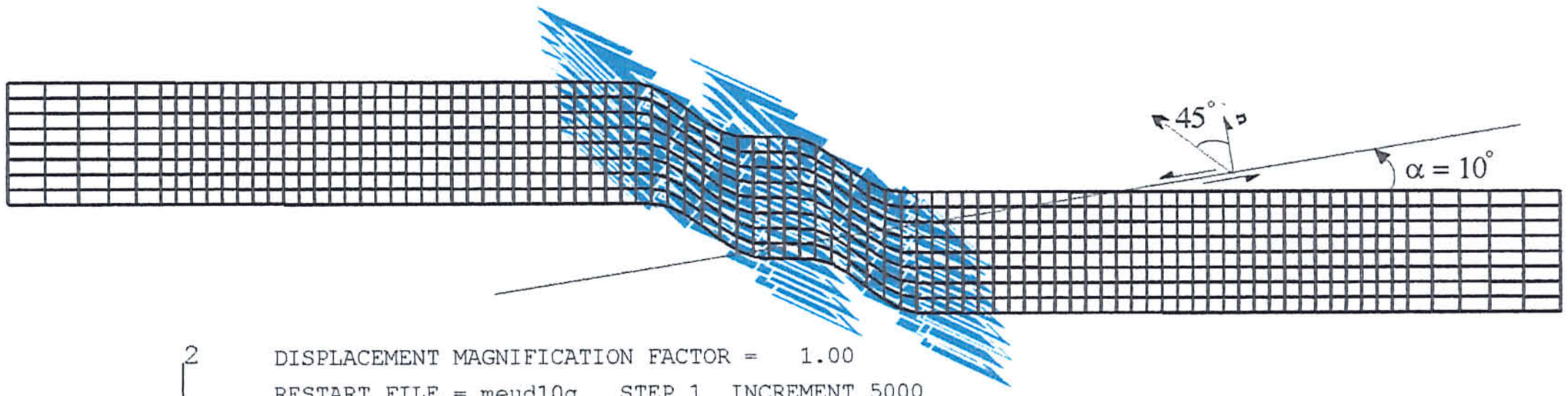

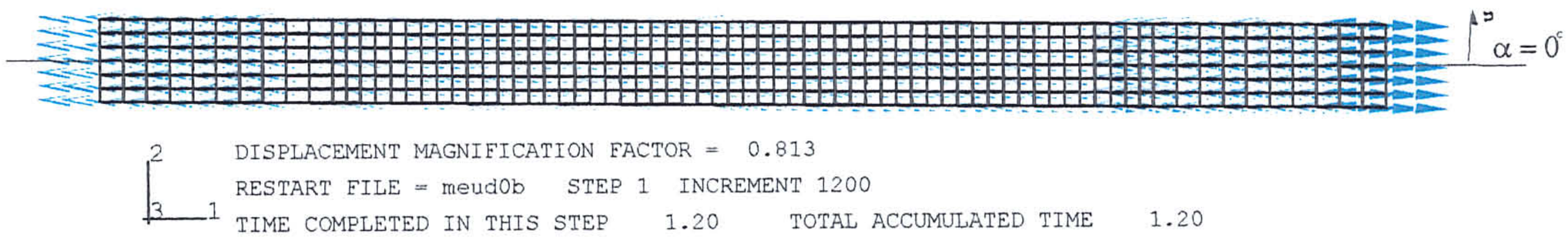

Fig 8.2.1.2-11 The maximum principle strain directions of the damaged one-

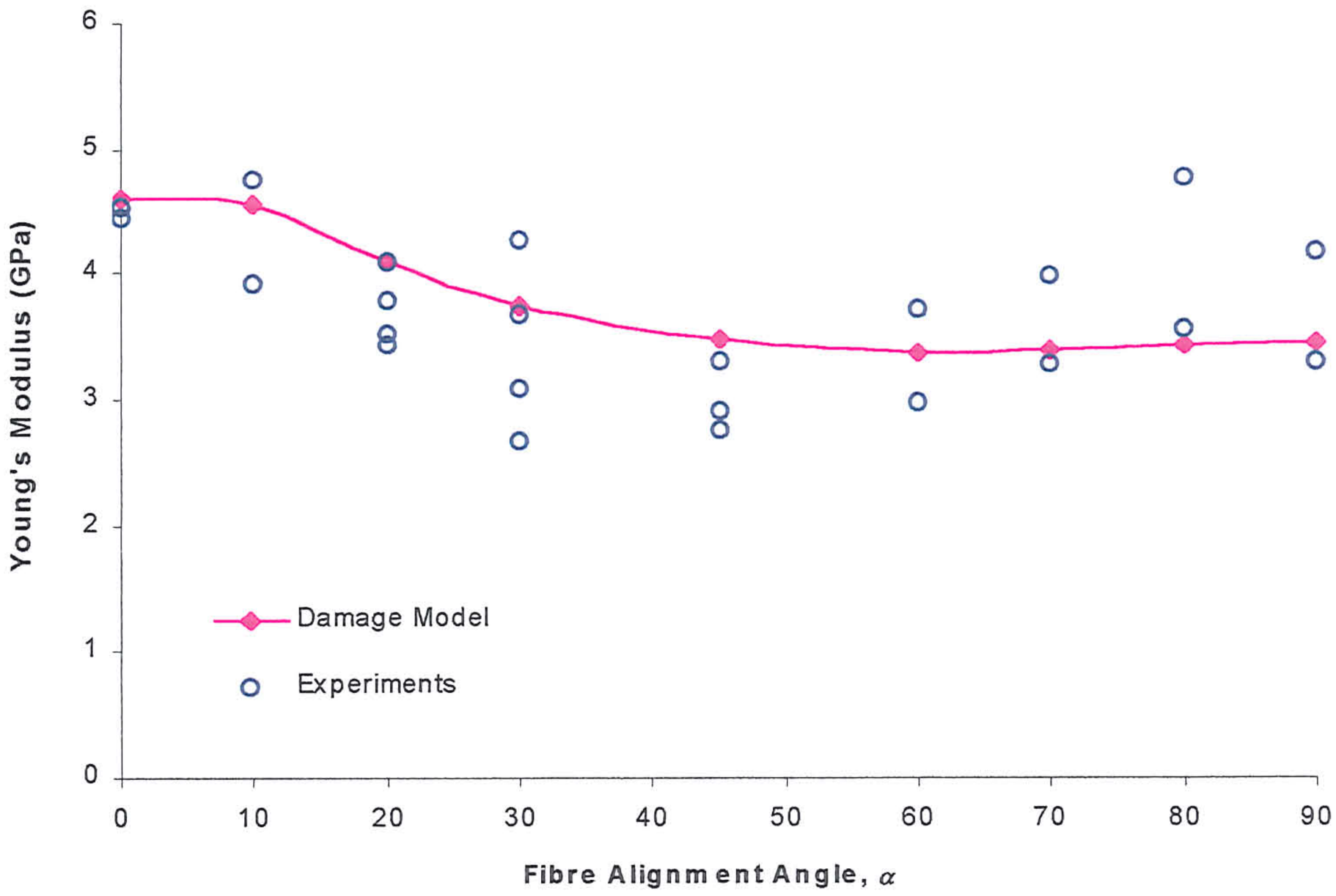

Fig 8.2.1.2-12 Comparison of the experimental and computationally modelled Young's modulus of the one-dimensional polyester composite.

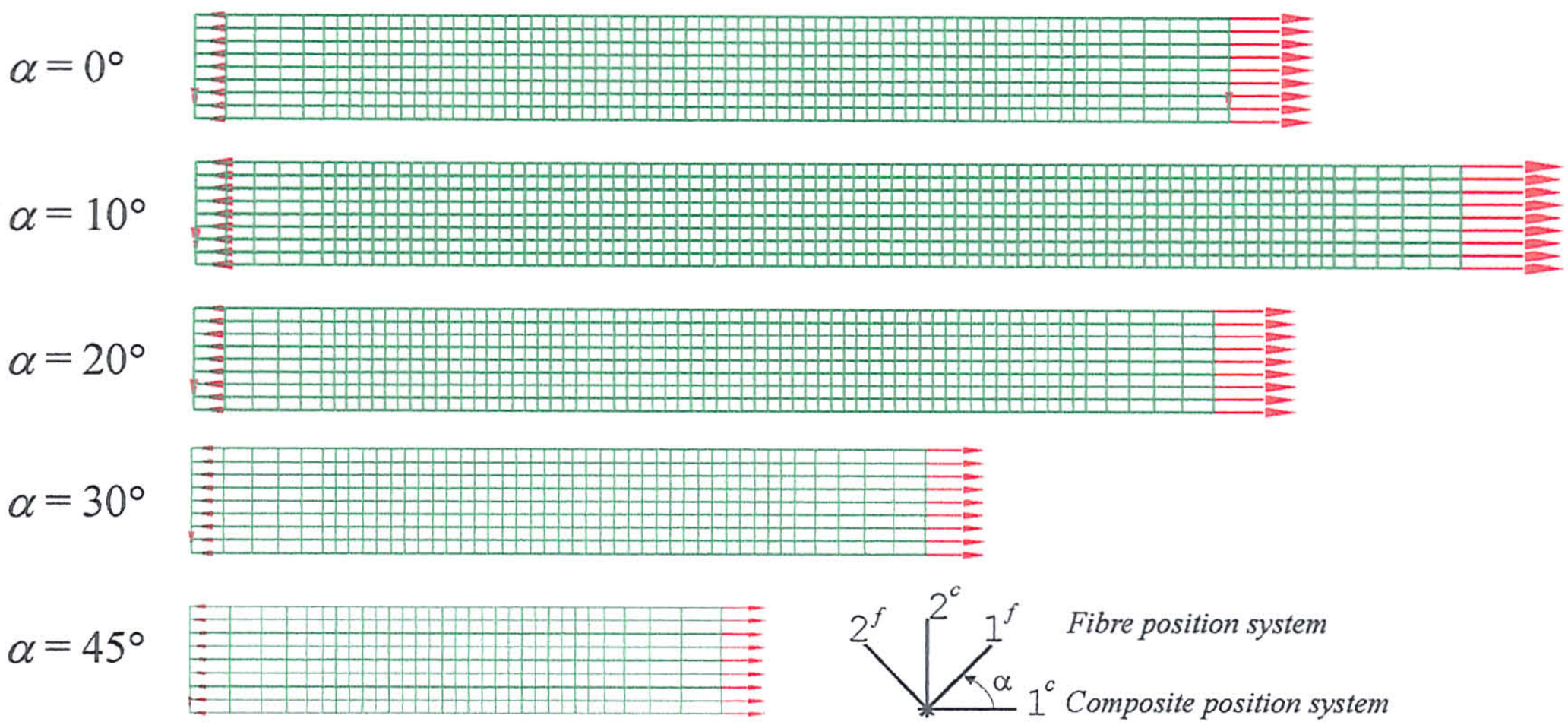

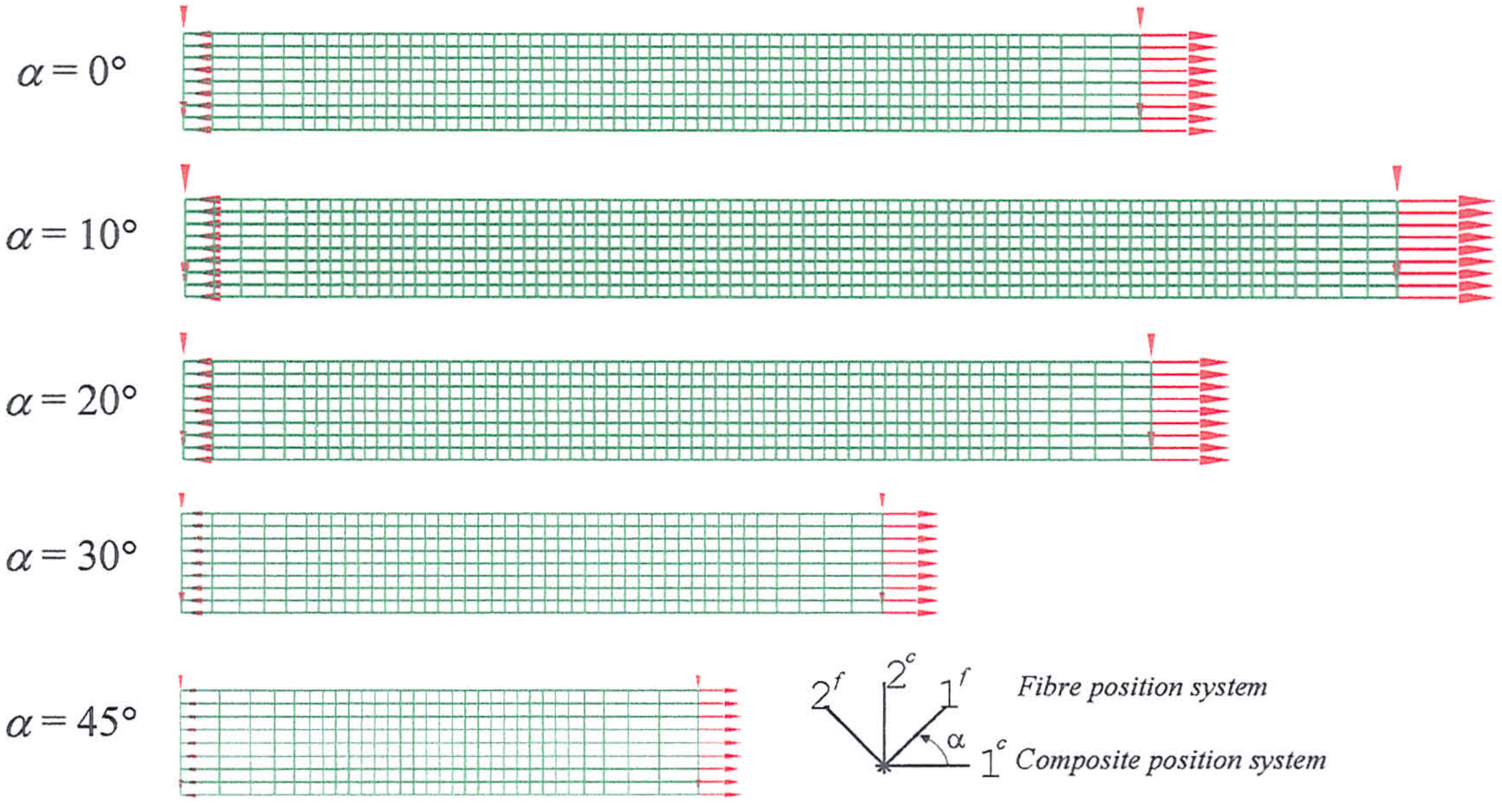

(b)

Fig 8.2.2.1-1 Schematic diagrams of the two-dimensional composite meshes and the boundary conditions: (a) without transverse constraint and (b) with transverse constraint.

$\alpha = 0°$

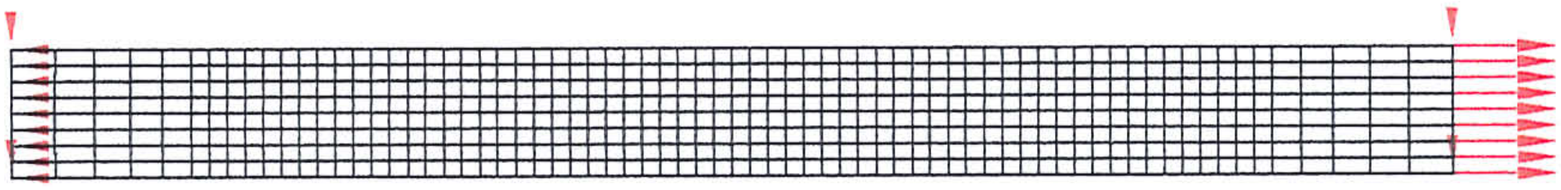

DISPLACEMENT MAGNIFICATION FACTOR = 0.893
RESTART FILE = mew0b1 STEP 1 INCREMENT 1400
TIME COMPLETED IN THIS STEP 1.40 TOTAL ACCUMULATED TIME 1.40

$\alpha = 10°$

DISPLACEMENT MAGNIFICATION FACTOR = 0.975
RESTART FILE = mew10b1 STEP 1 INCREMENT 1400
TIME COMPLETED IN THIS STEP 1.40 TOTAL ACCUMULATED TIME 1.40

$\alpha = 20°$

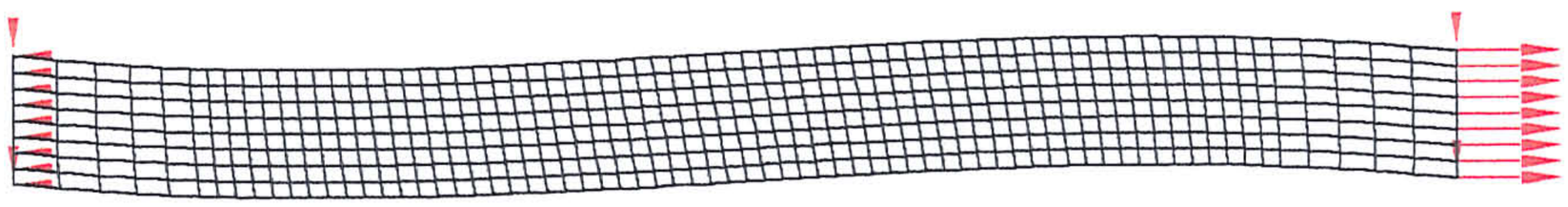

DISPLACEMENT MAGNIFICATION FACTOR = 0.707
RESTART FILE = mew20b1 STEP 1 INCREMENT 1500
TIME COMPLETED IN THIS STEP 1.50 TOTAL ACCUMULATED TIME 1.50

$\alpha = 30°$

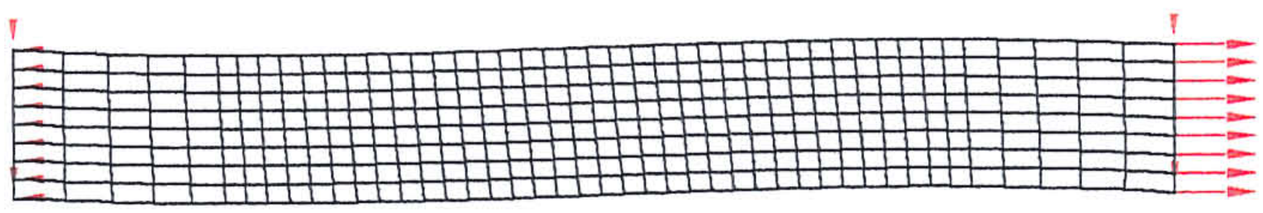

DISPLACEMENT MAGNIFICATION FACTOR = 0.667
RESTART FILE = mew30b1 STEP 1 INCREMENT 1100
TIME COMPLETED IN THIS STEP 1.10 TOTAL ACCUMULATED TIME 1.10

$\alpha = 45°$

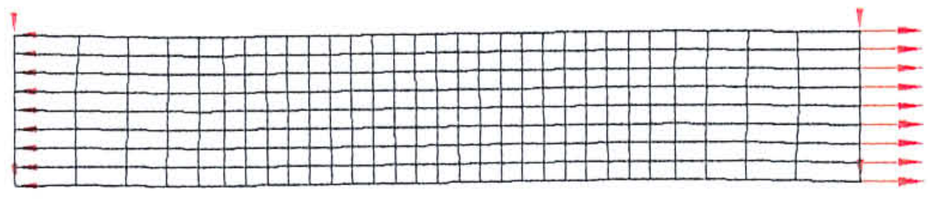

DISPLACEMENT MAGNIFICATION FACTOR = 2.53
RESTART FILE = mew45b1 STEP 1 INCREMENT 10600

Fig 8.2.2.2-1 Deformed mesh of the misaligned two-dimensionally reinforced composite with transverse constraint.

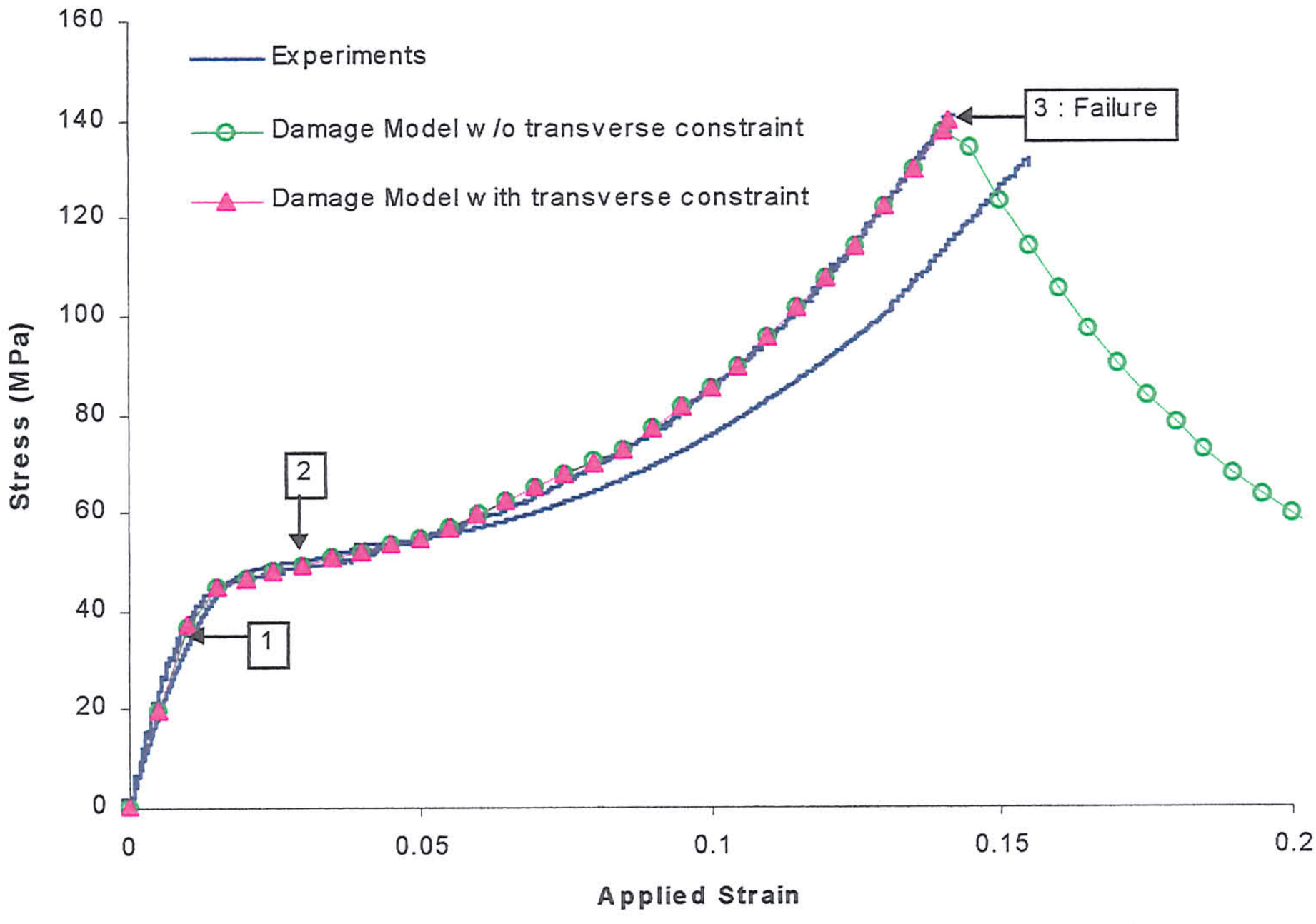

(a)

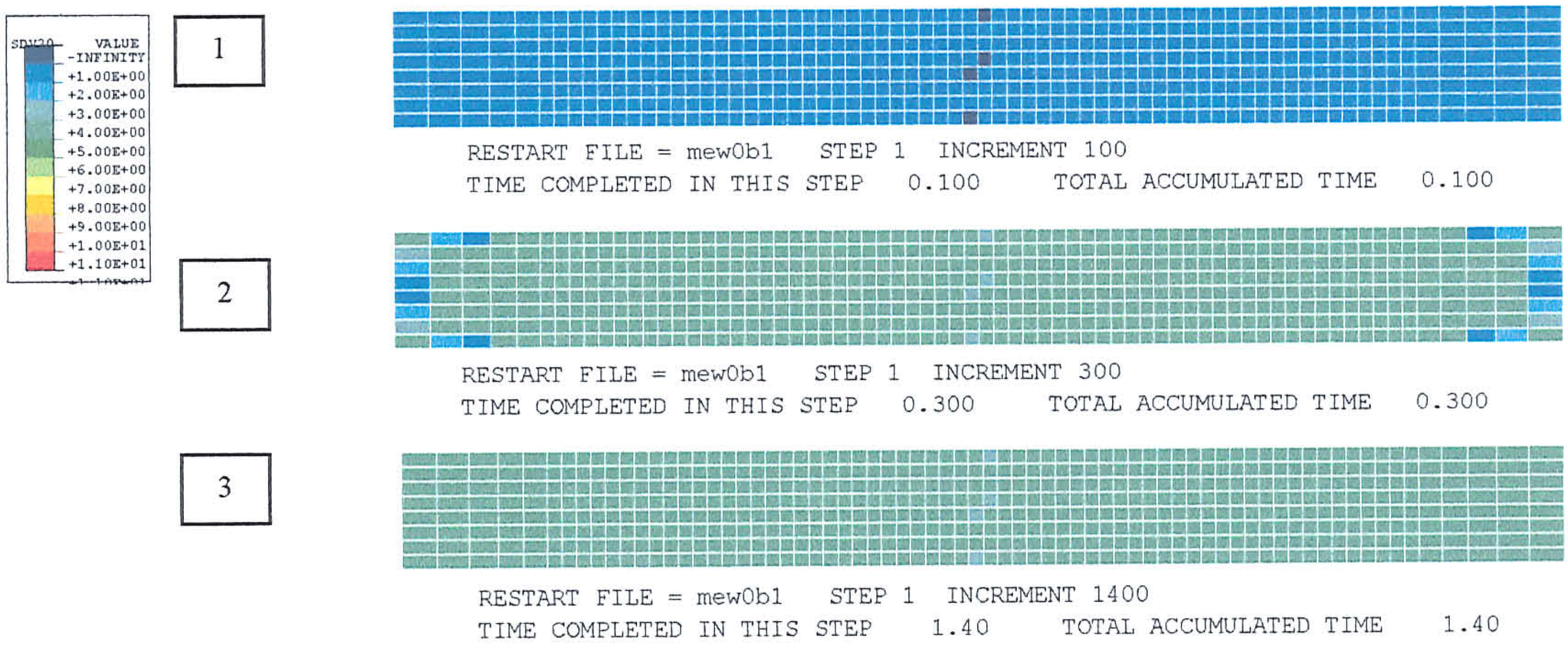

(b)

Fig 8.2.2.2-2 A comparison of the predicted and experimental tensile stress-strain response and matrix cracking zone, of an aligned two-dimensional

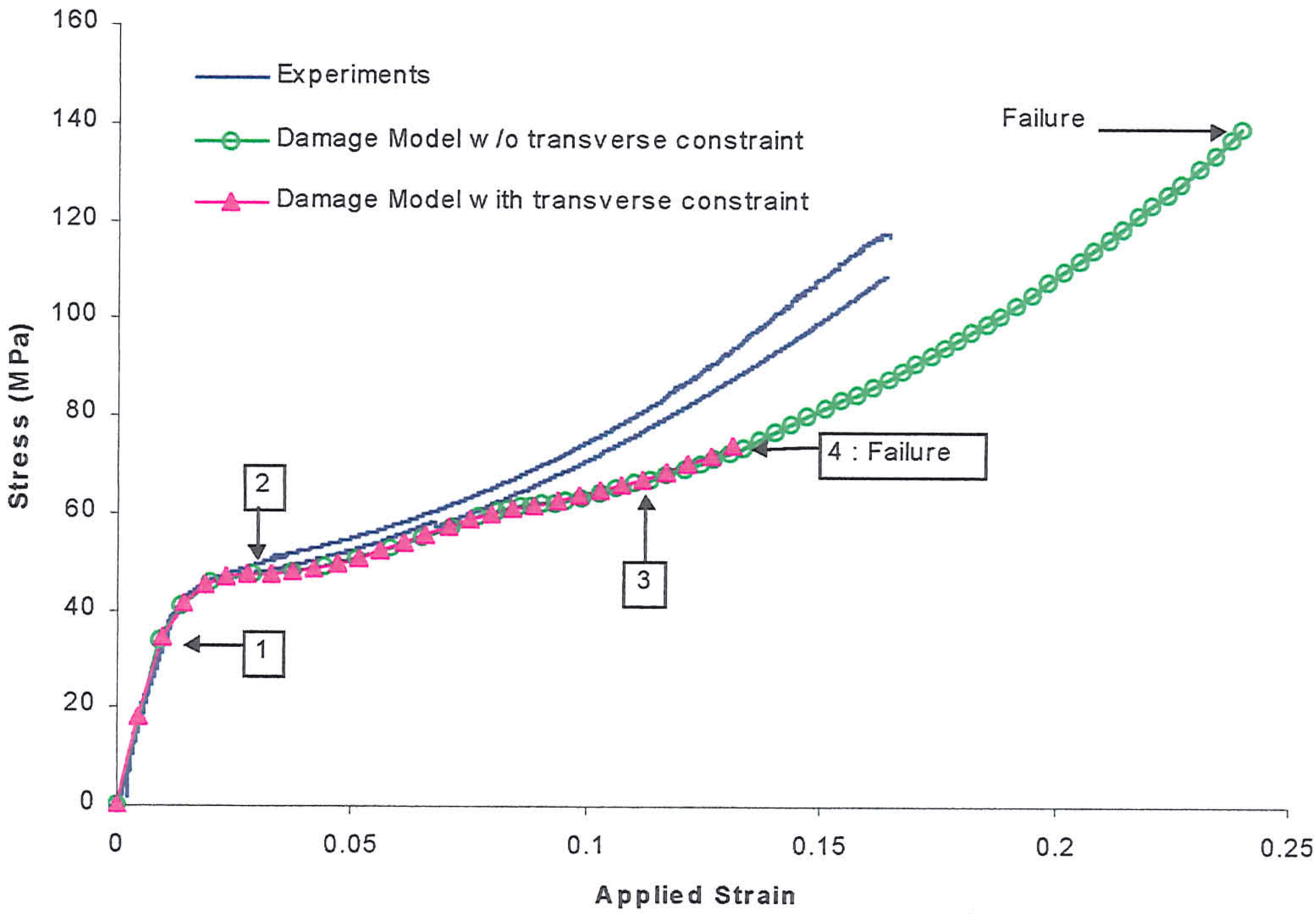

(a)

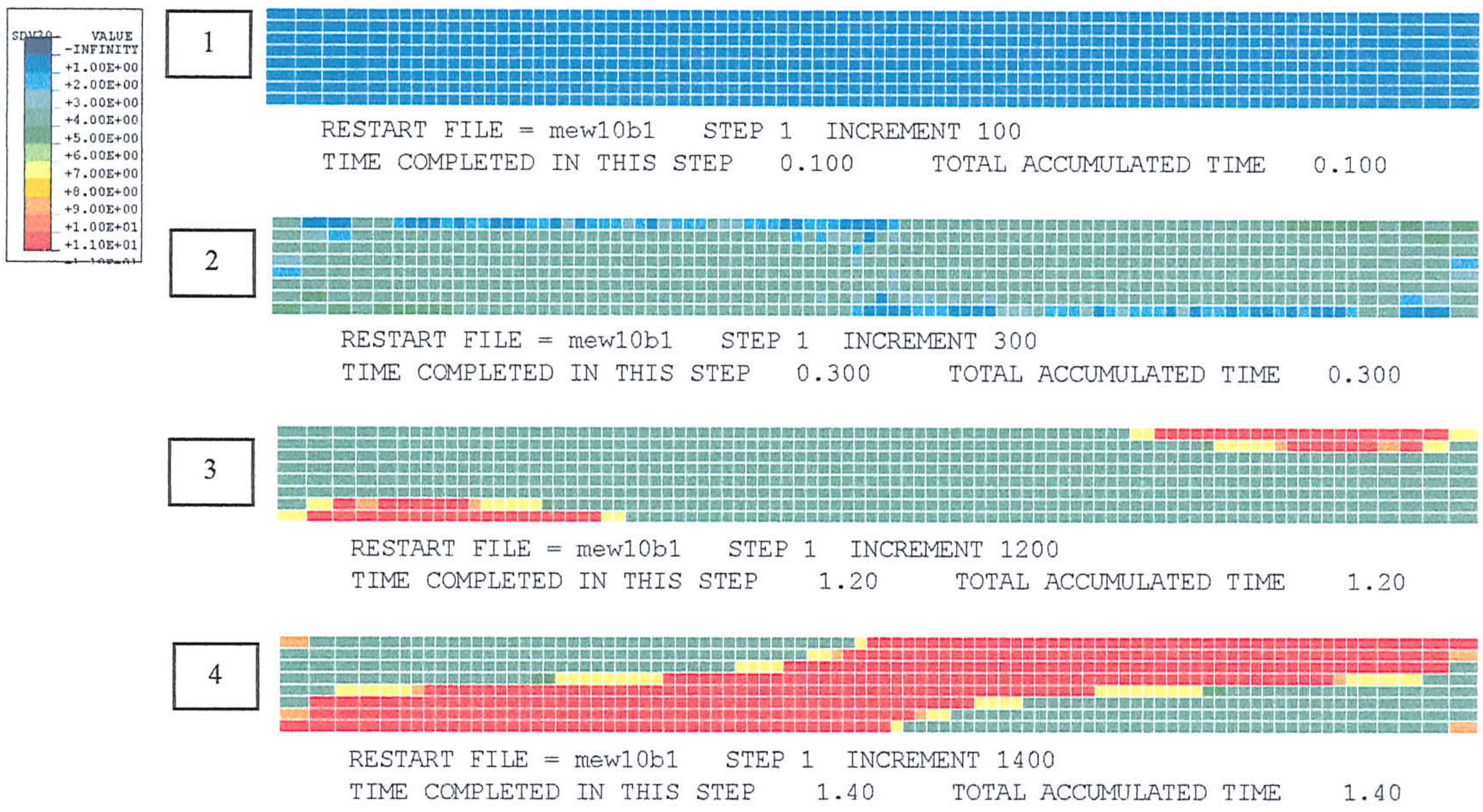

(b)

Fig 8.2.2.2-3 A comparison of the predicted and experimental tensile stress-strain response and matrix cracking zone of a misaligned two-dimensional

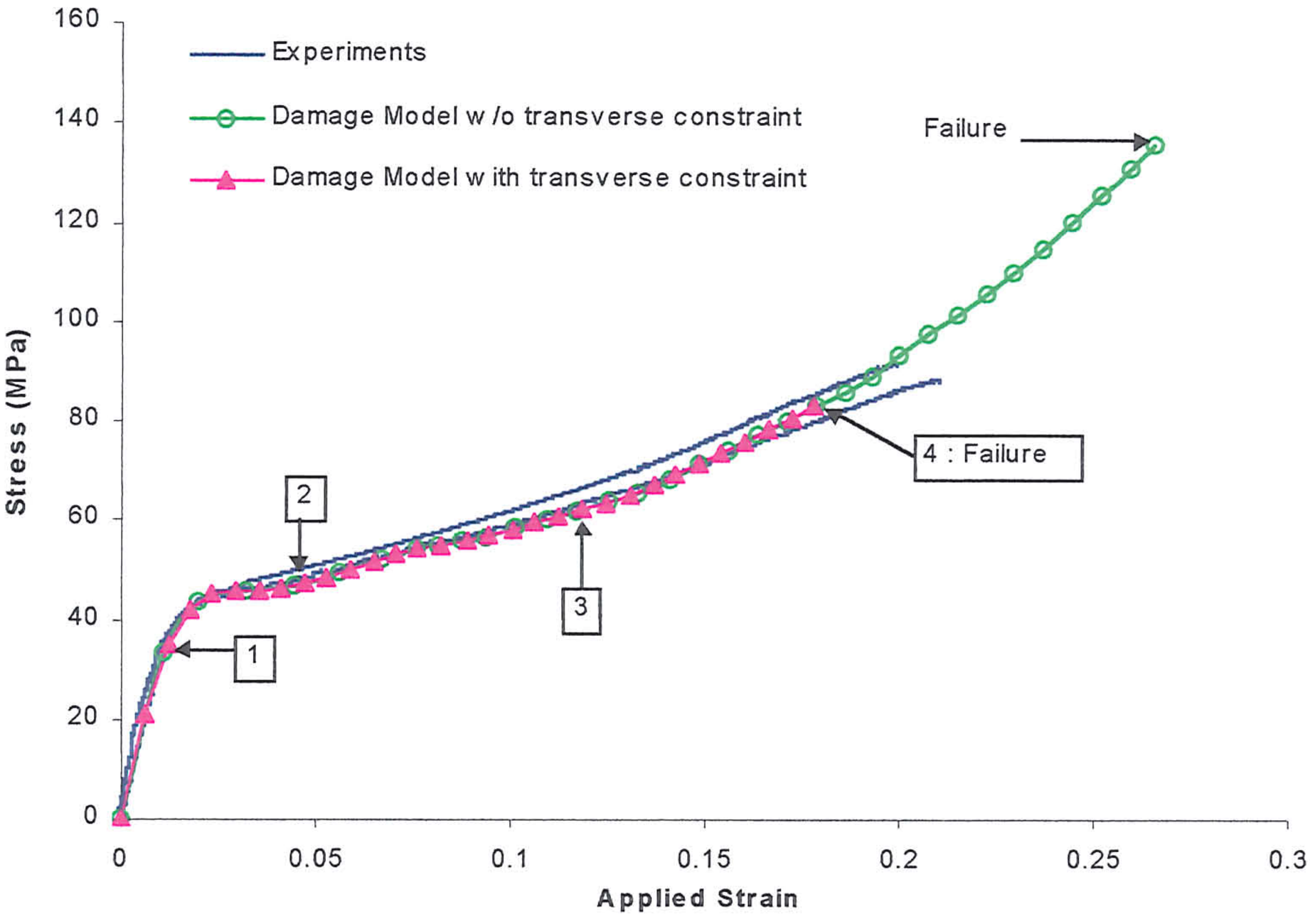

(a)

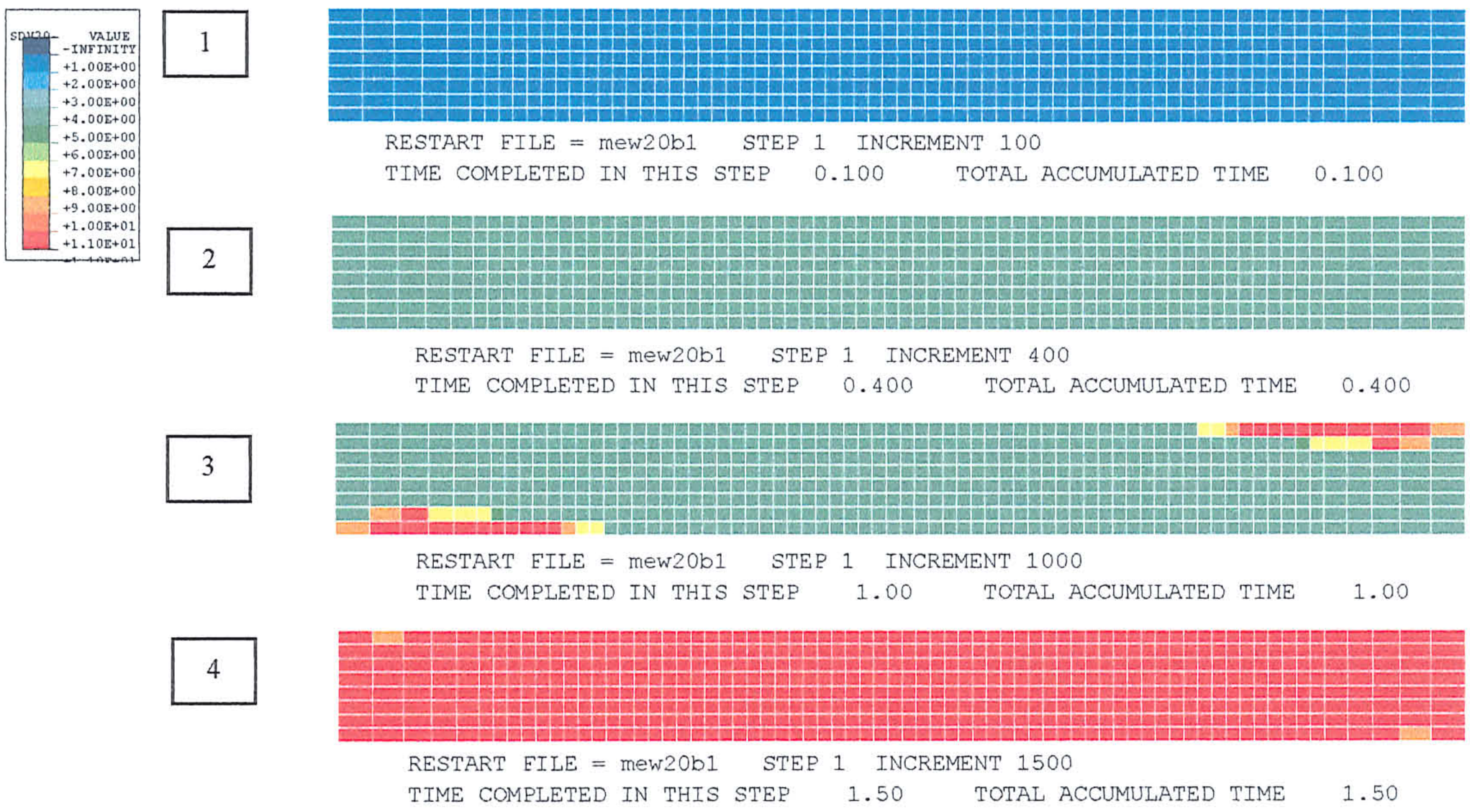

(b)

Fig 8.2.2.2-4 A comparison of the predicted and experimental tensile stress-strain response and matrix cracking zone of a misaligned two-dimensional

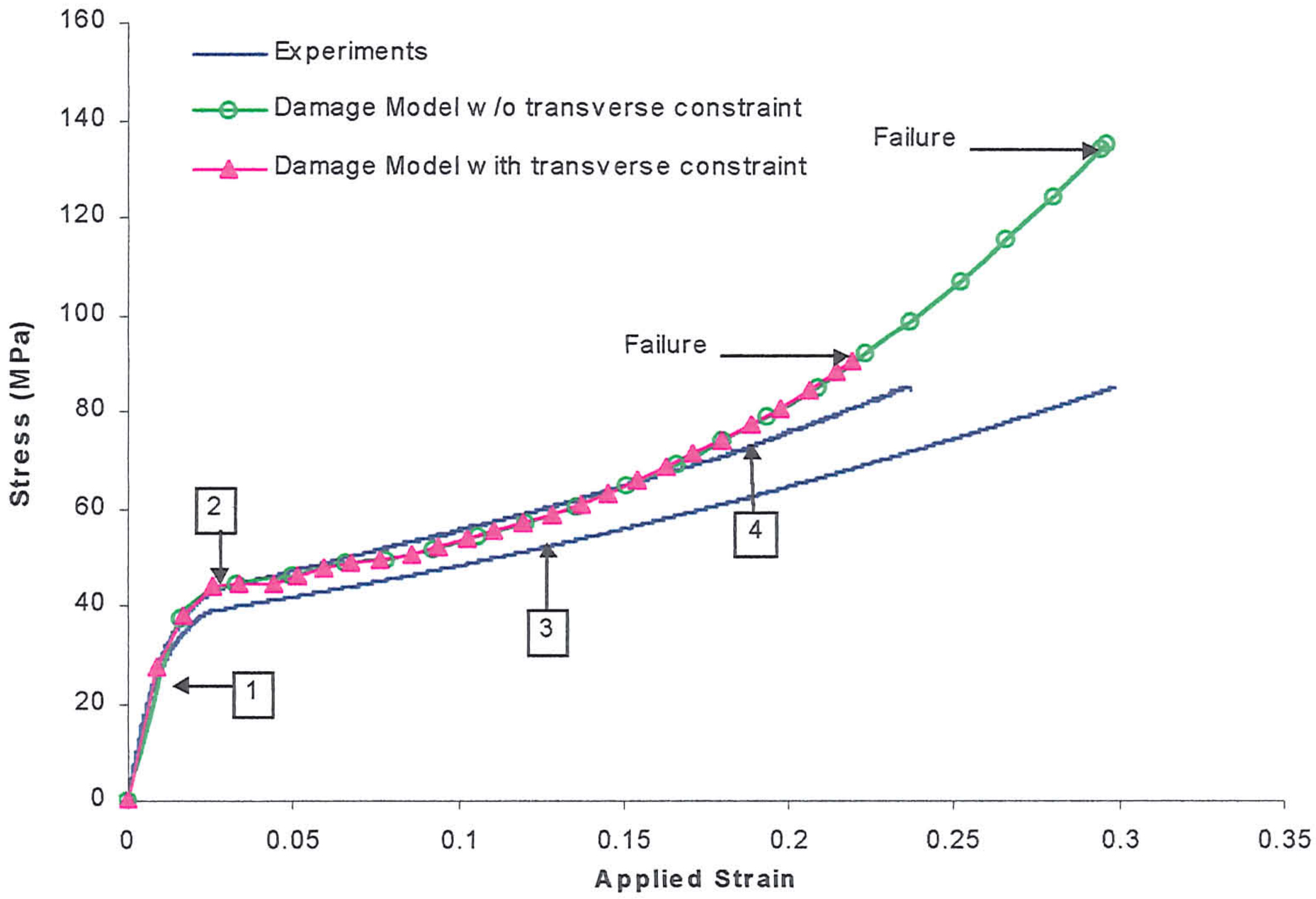

(a)

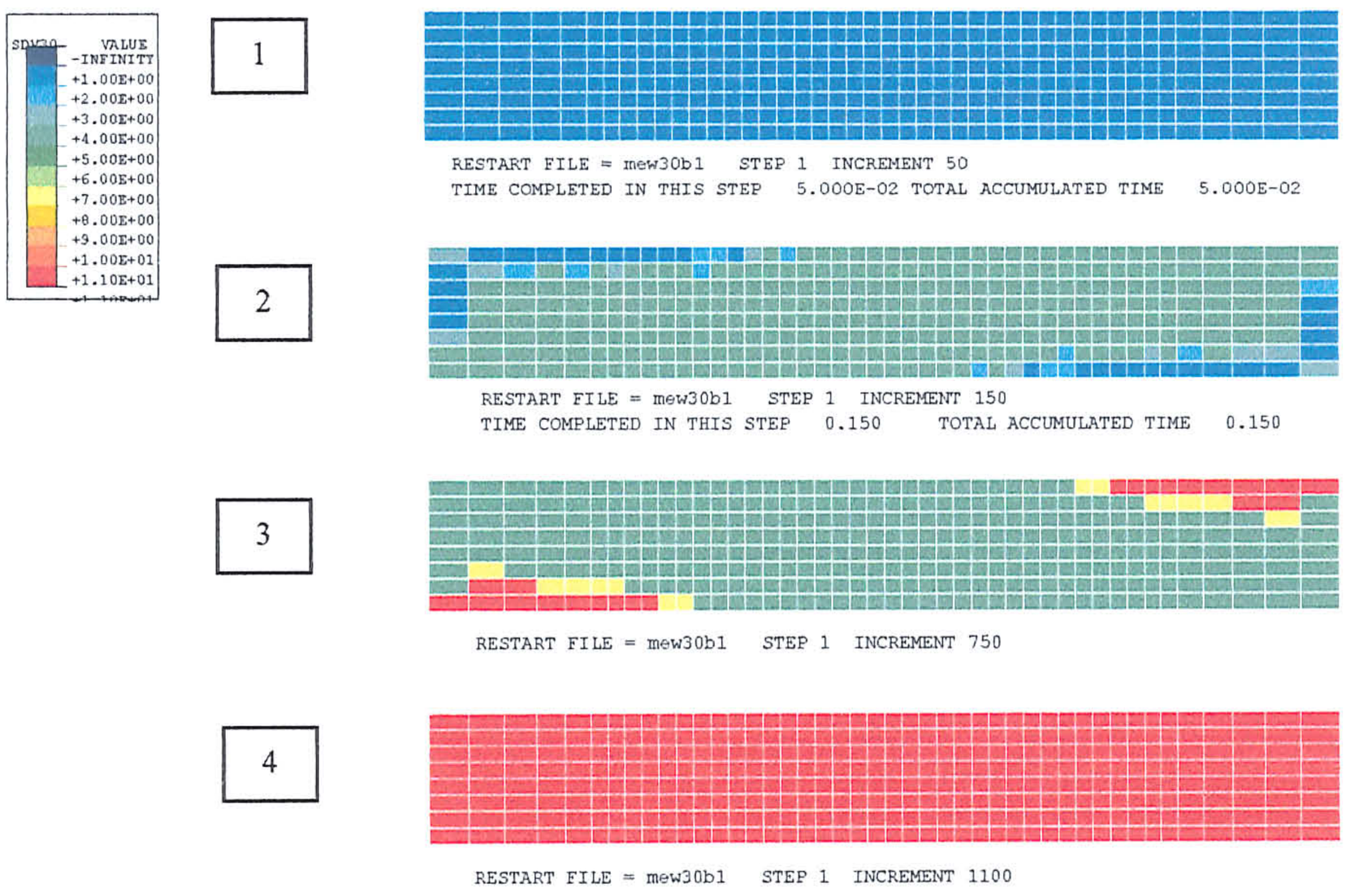

(b)

Fig 8.2.2.2-5 A comparison of the predicted and experimental tensile stress-strain response and matrix cracking zone of a misaligned two-dimensional

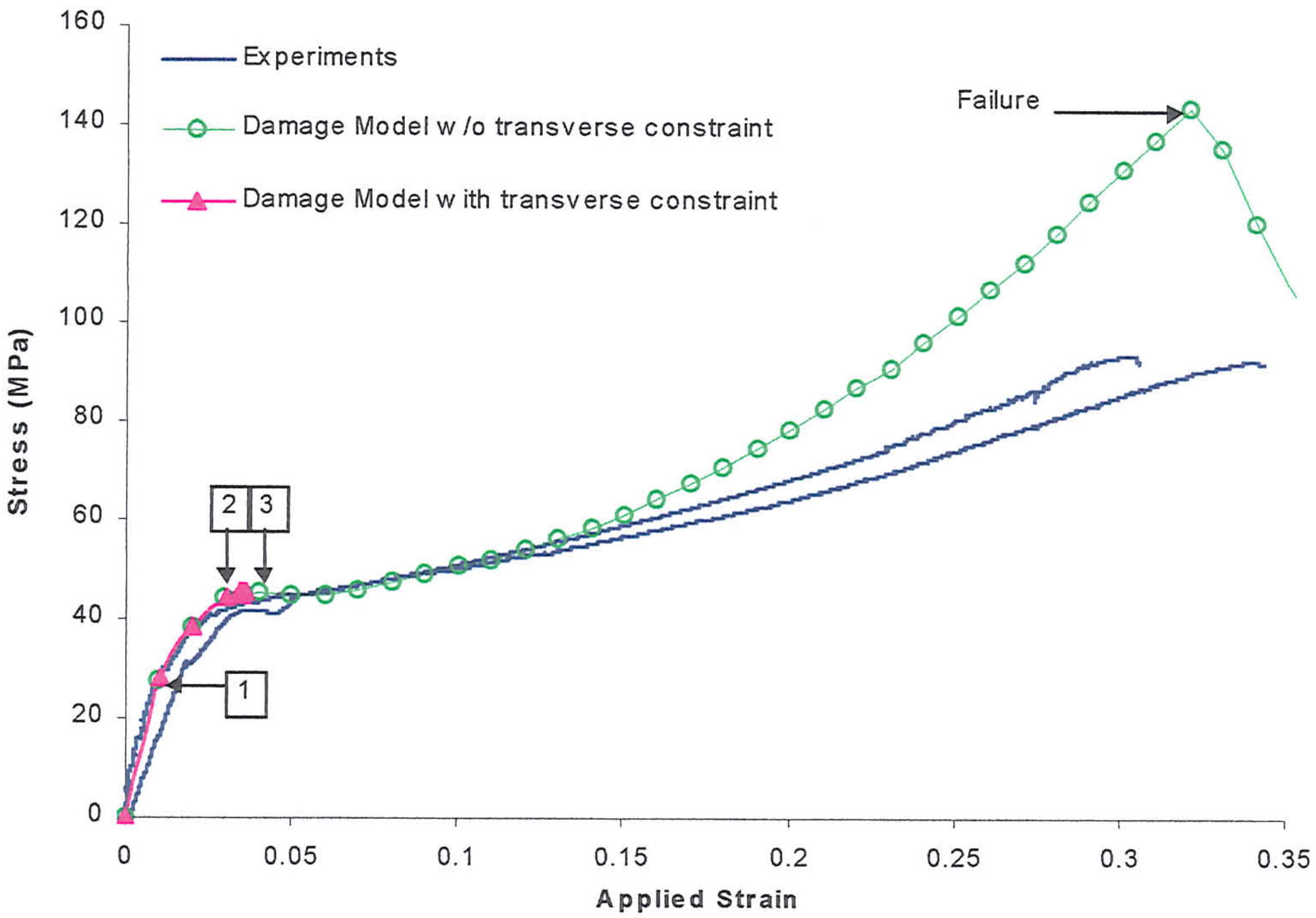

(a)

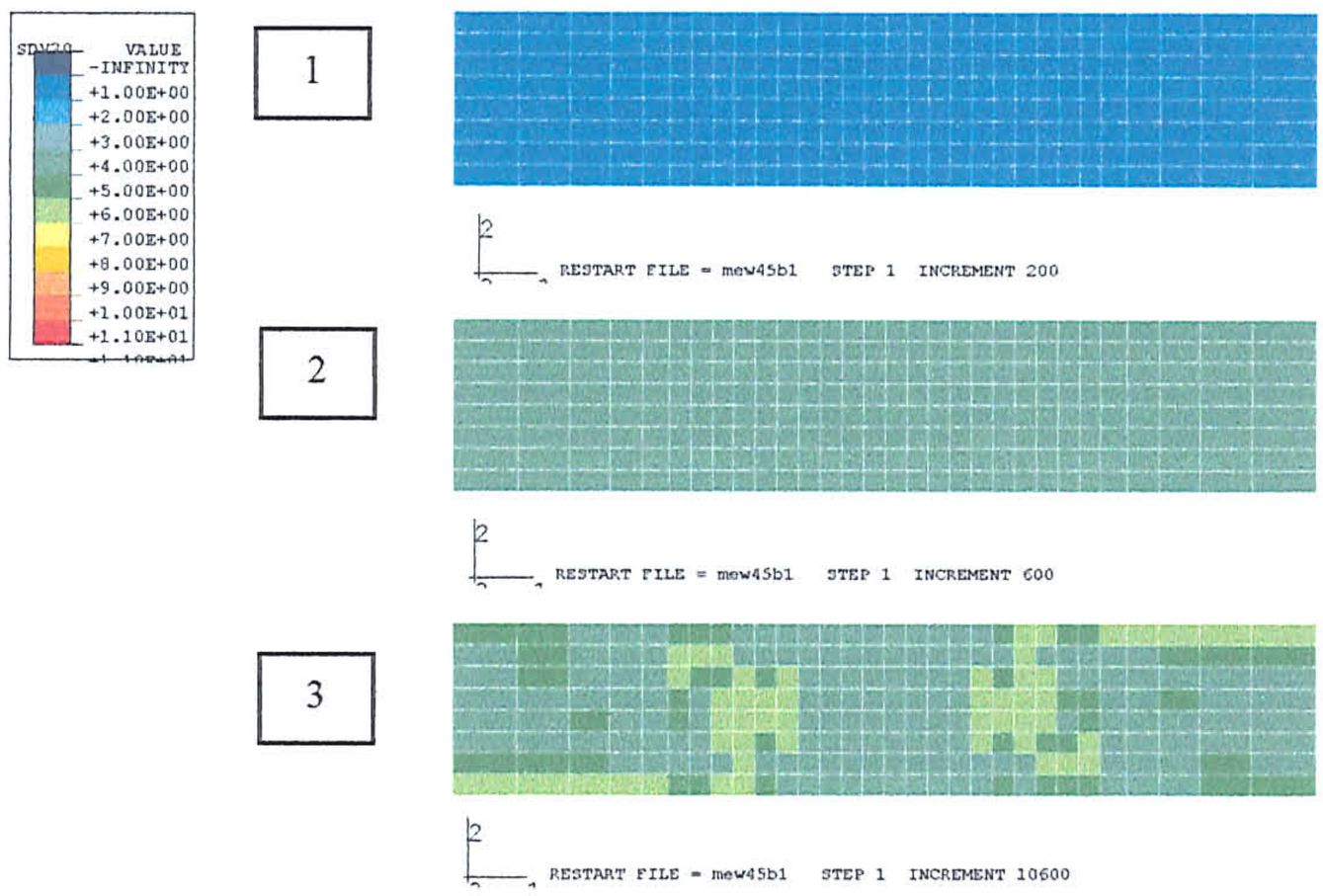

(b)

Fig 8.2.2.2-6 A comparison of the predicted and experimental tensile stress-strain response and matrix cracking zone, of a misaligned two-dimensional

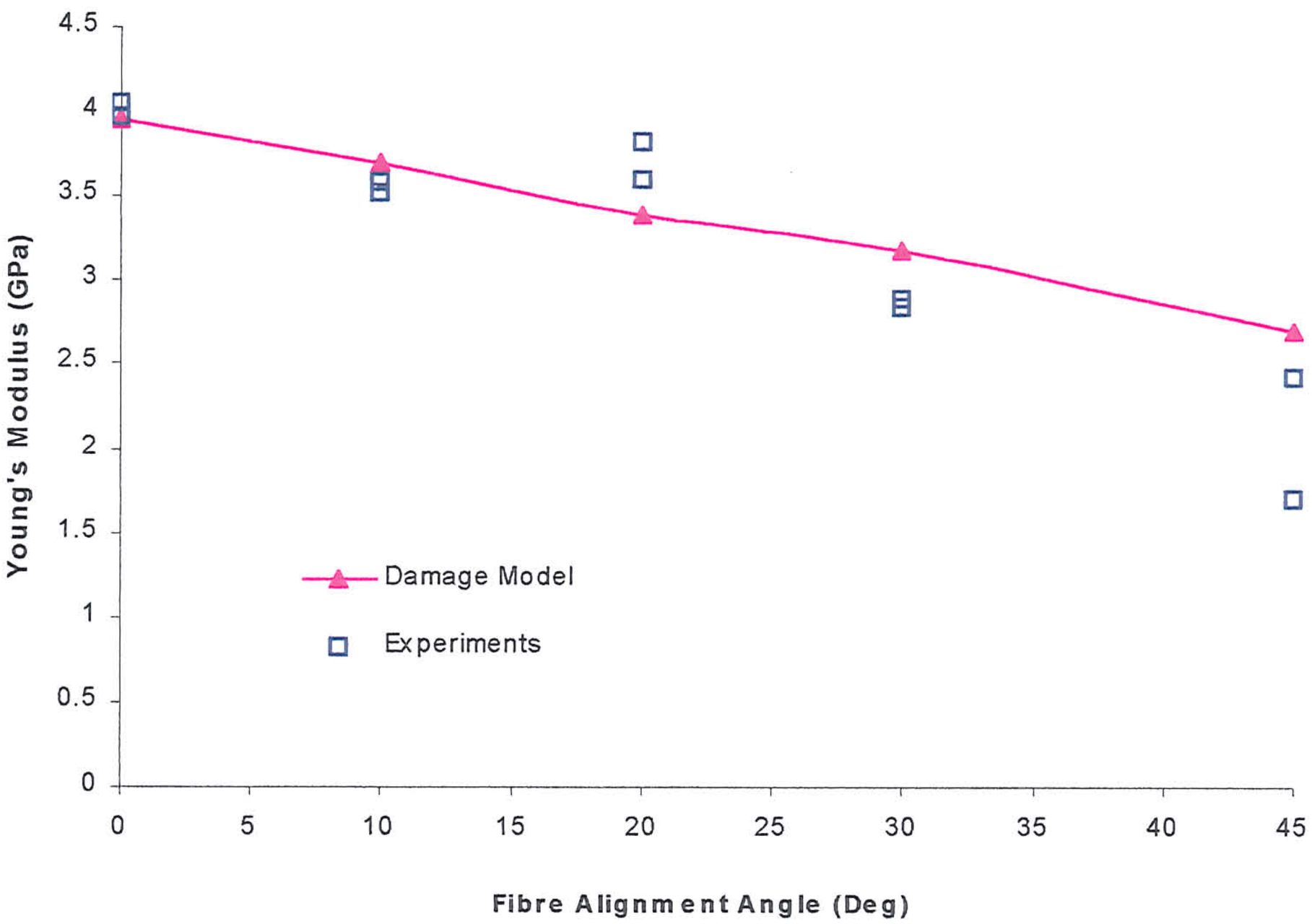

Fig 8.2.2.2-7 A comparison of the experimental and computationally modelled Young's modulus of the two-dimensional polyester composite.

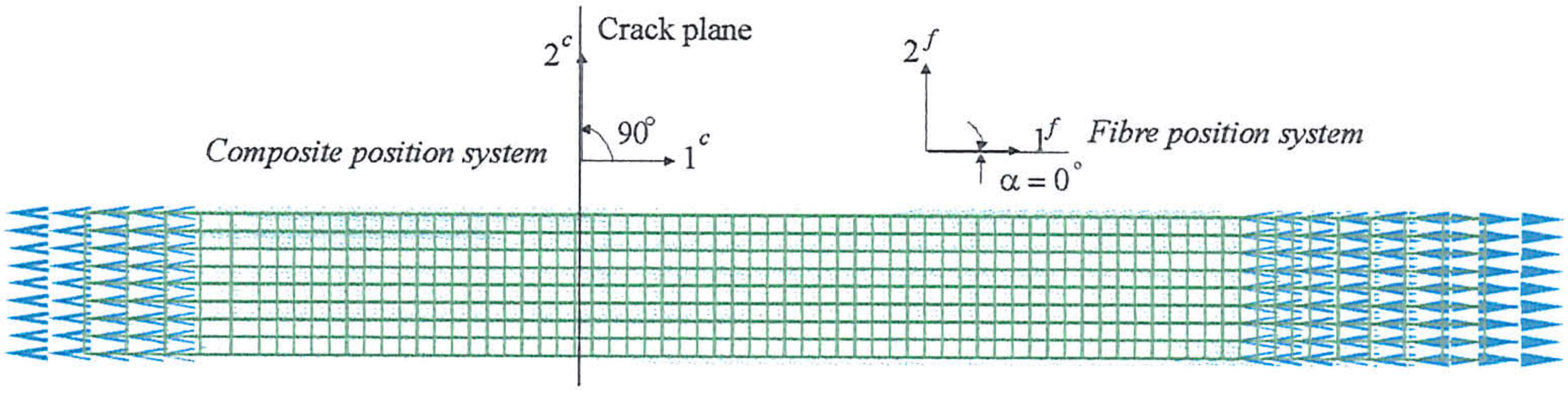


```
RESTART FILE = mew0b1    STEP 1  INCREMENT 1500
TIME COMPLETED IN THIS STEP     1.41      TOTAL ACCUMULATED TIME     1.41
```

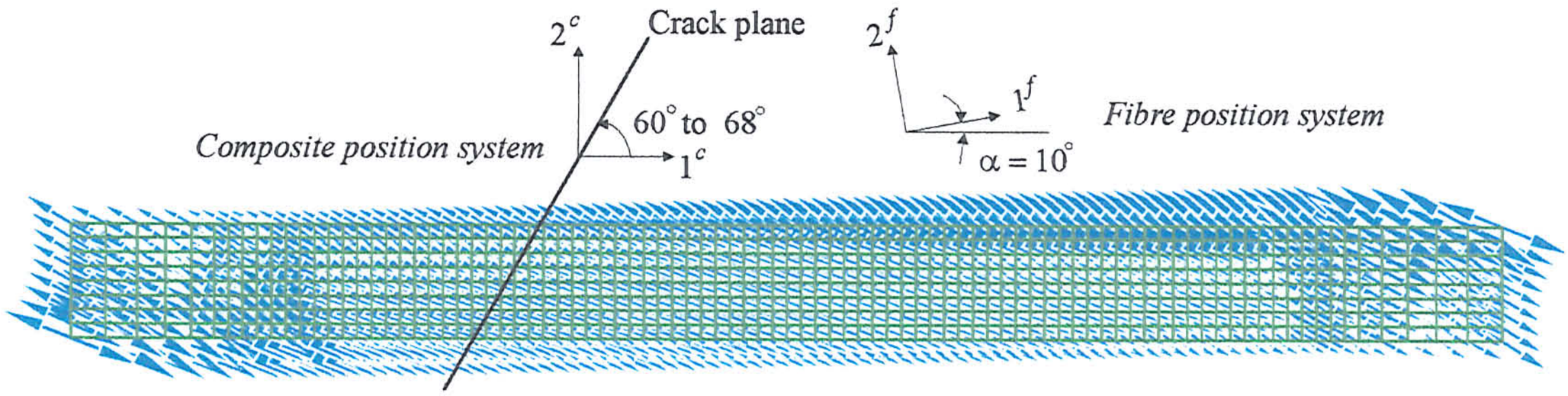


```
RESTART FILE = mew10b1    STEP 1  INCREMENT 1400
TIME COMPLETED IN THIS STEP     1.40      TOTAL ACCUMULATED TIME     1.40
```

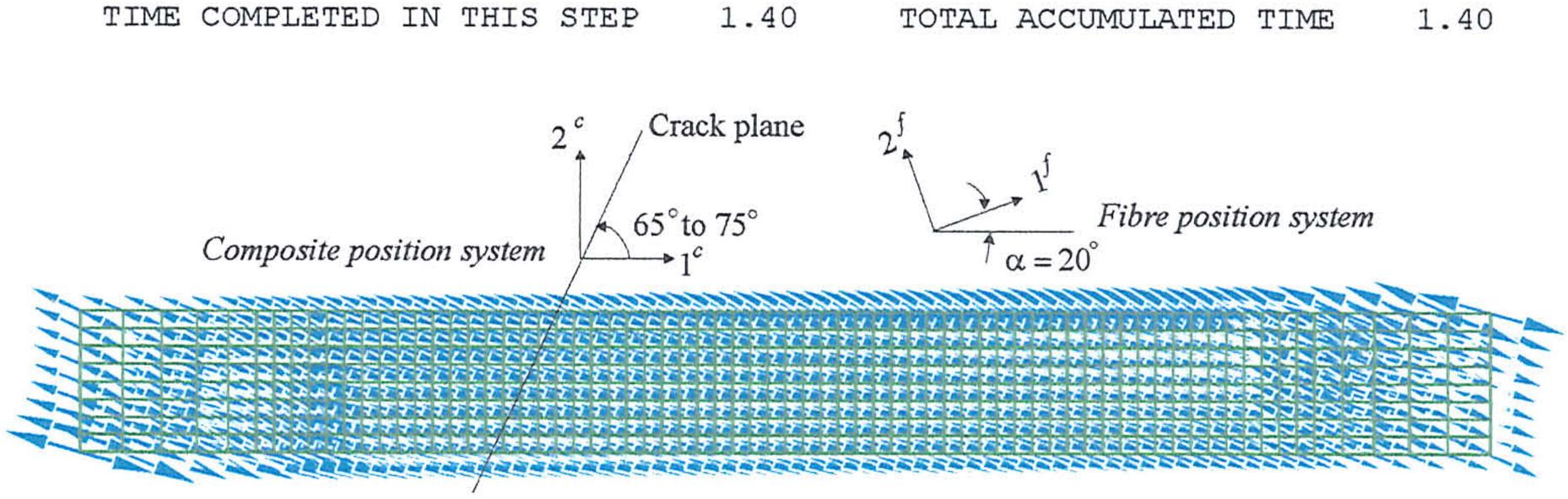


```
RESTART FILE = mew20b1    STEP 1  INCREMENT 1500
TIME COMPLETED IN THIS STEP     1.50      TOTAL ACCUMULATED TIME     1.50
```

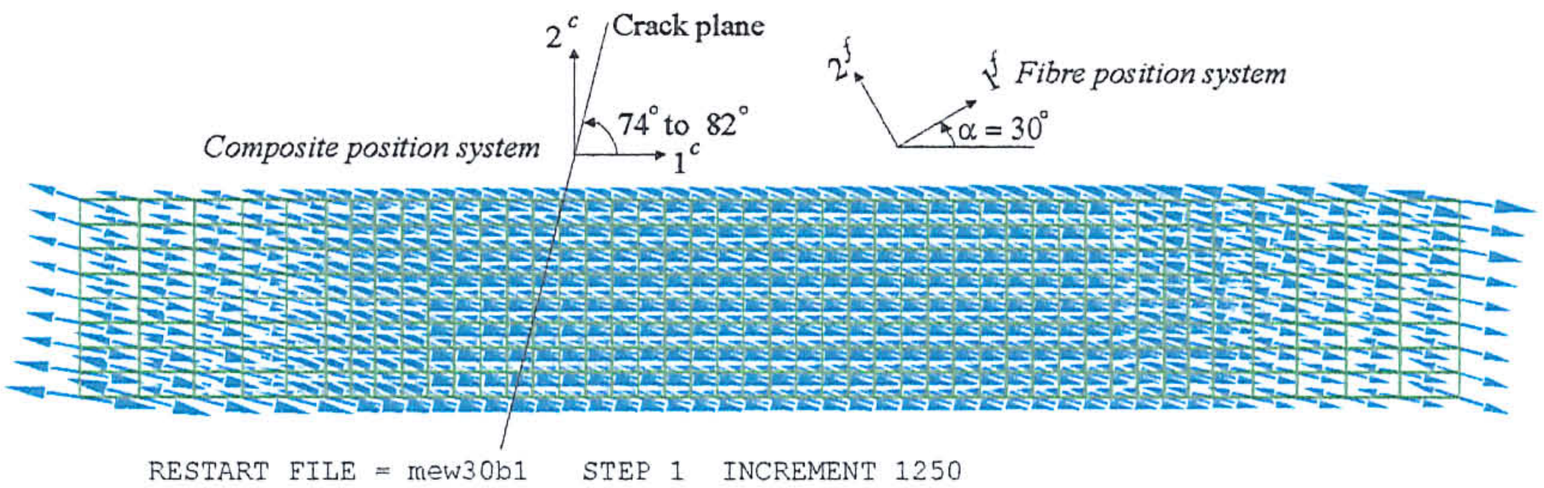


```
RESTART FILE = mew30b1    STEP 1  INCREMENT 1250
TIME COMPLETED IN THIS STEP     1.25      TOTAL ACCUMULATED TIME     1.25
```

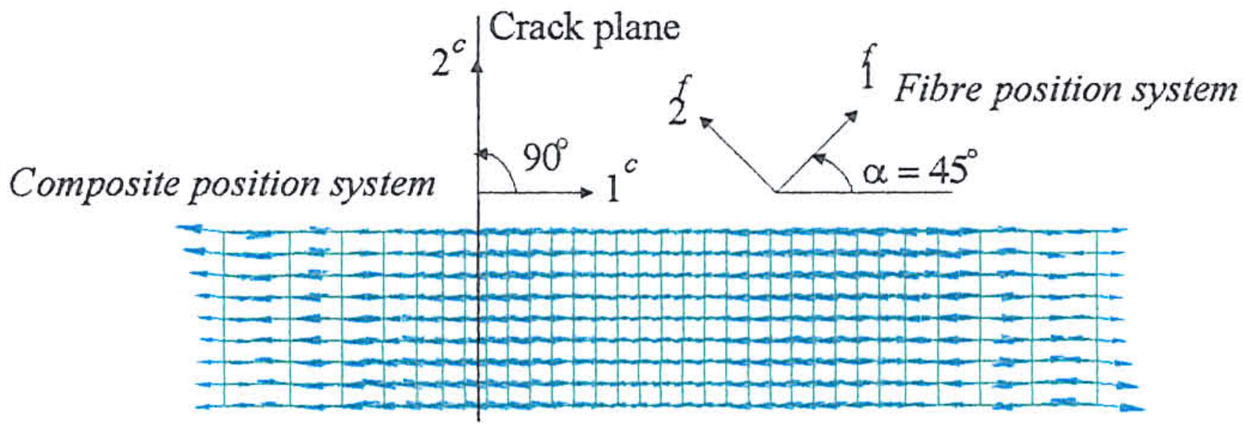


```
RESTART FILE = mew45b1    STEP 1  INCREMENT
TIME COMPLETED IN THIS STEP     1.99      TOTAL ACCUMULATED TIME
```

Fig. 8.2.2.2-8 The maximum principal strain directions of the damaged two-

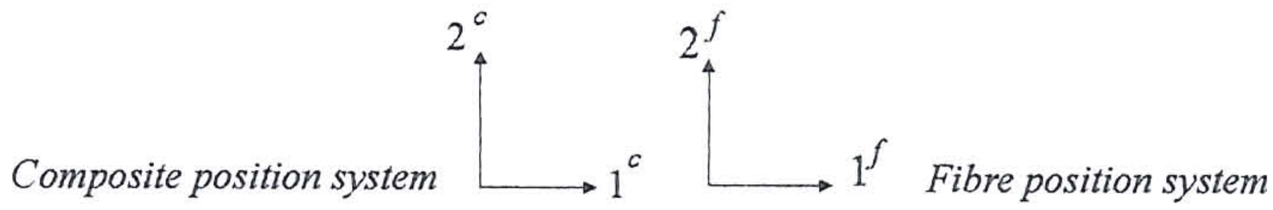

(a)

(b)

(c)

(d)

Fig 8.3.1.1-1 The meshes and boundary conditions of the rectangular polyester composite bar during three-point bending: (a) 4x10, (b) 8x20, (c) 12x30 and (d) 16x40 elements along the bar's thickness and half span

(a)

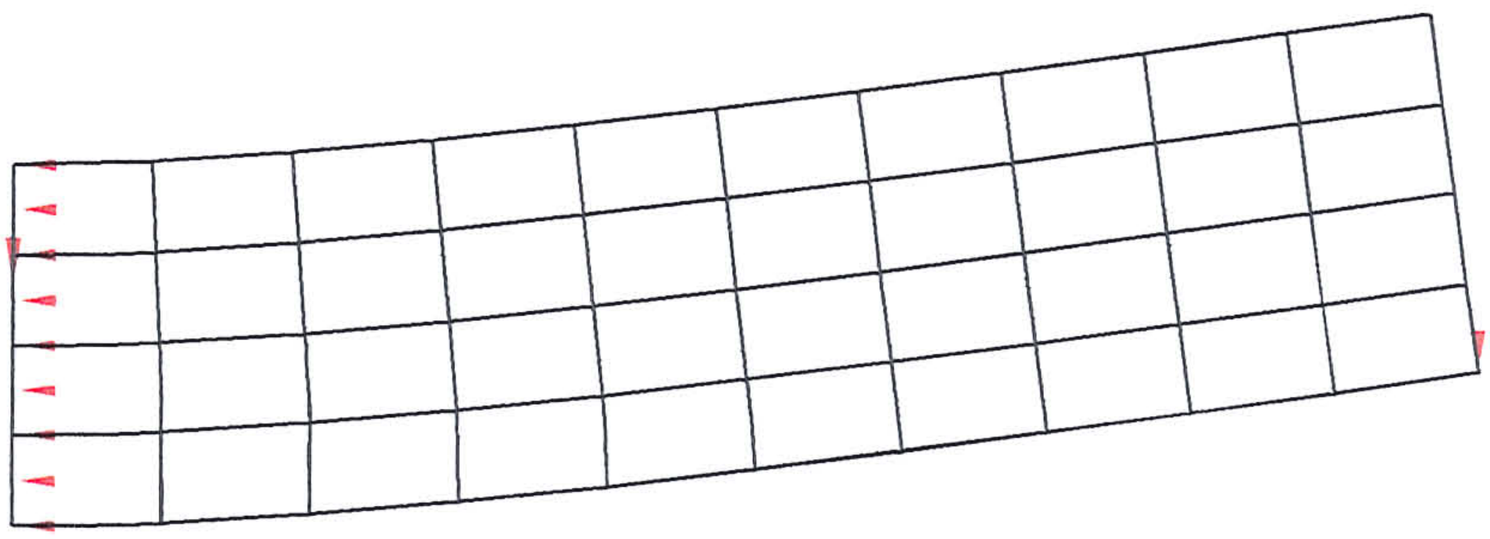

(b)

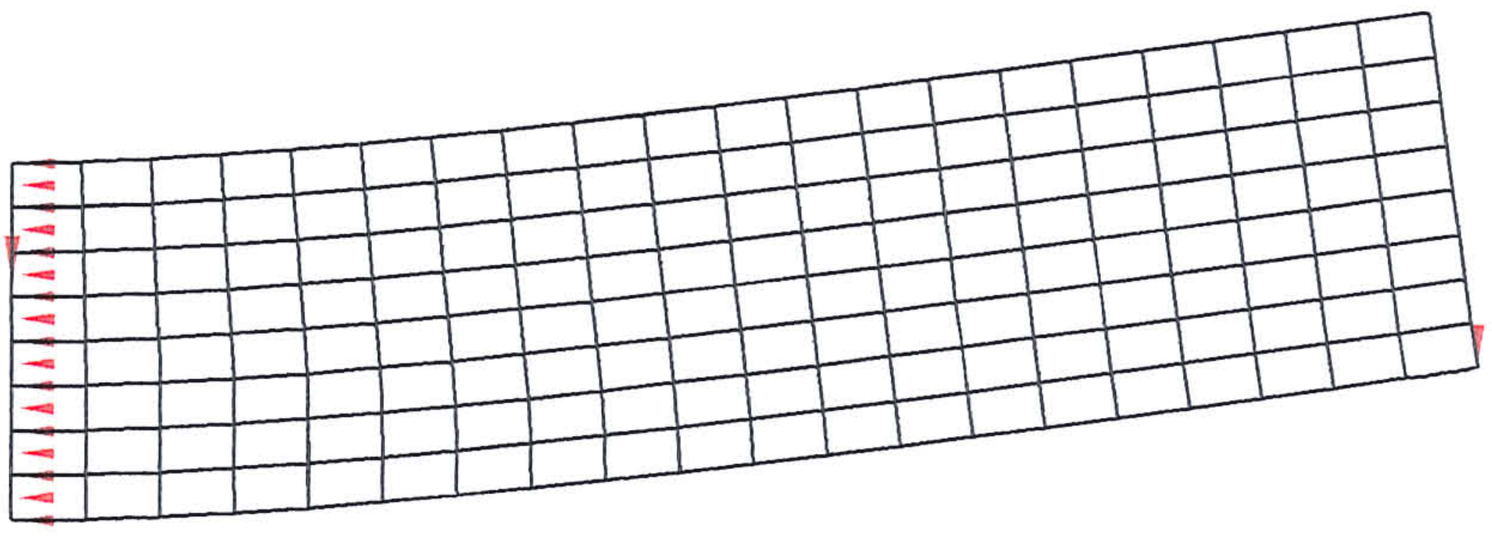

(c)

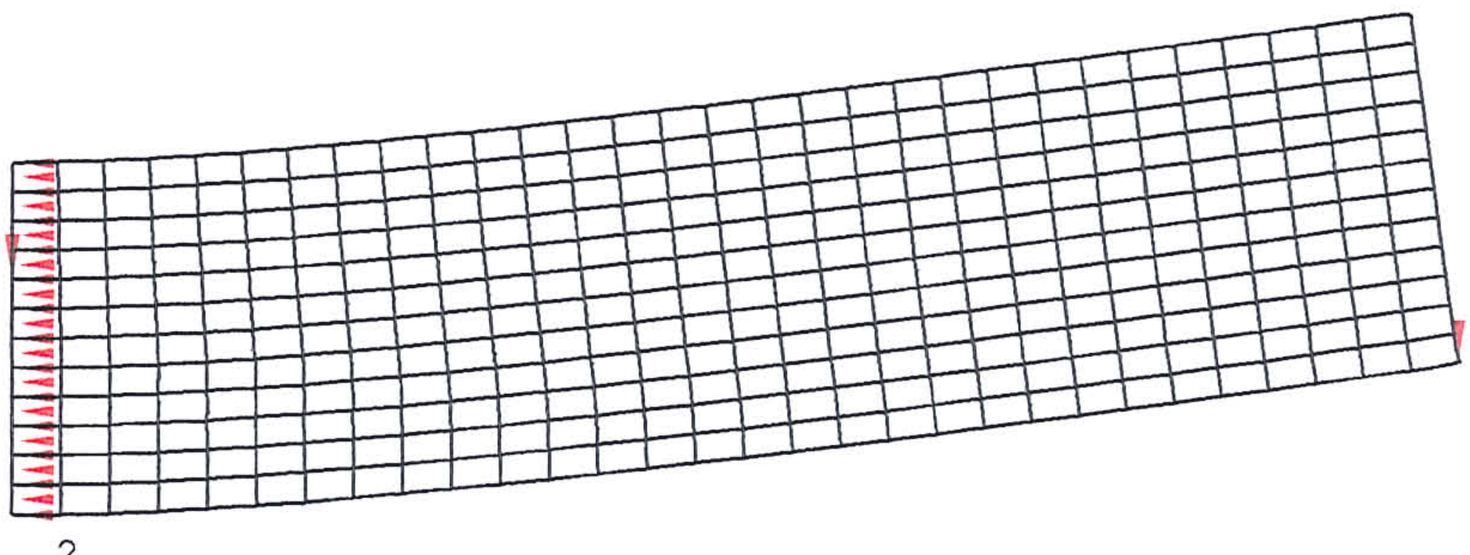

(d)

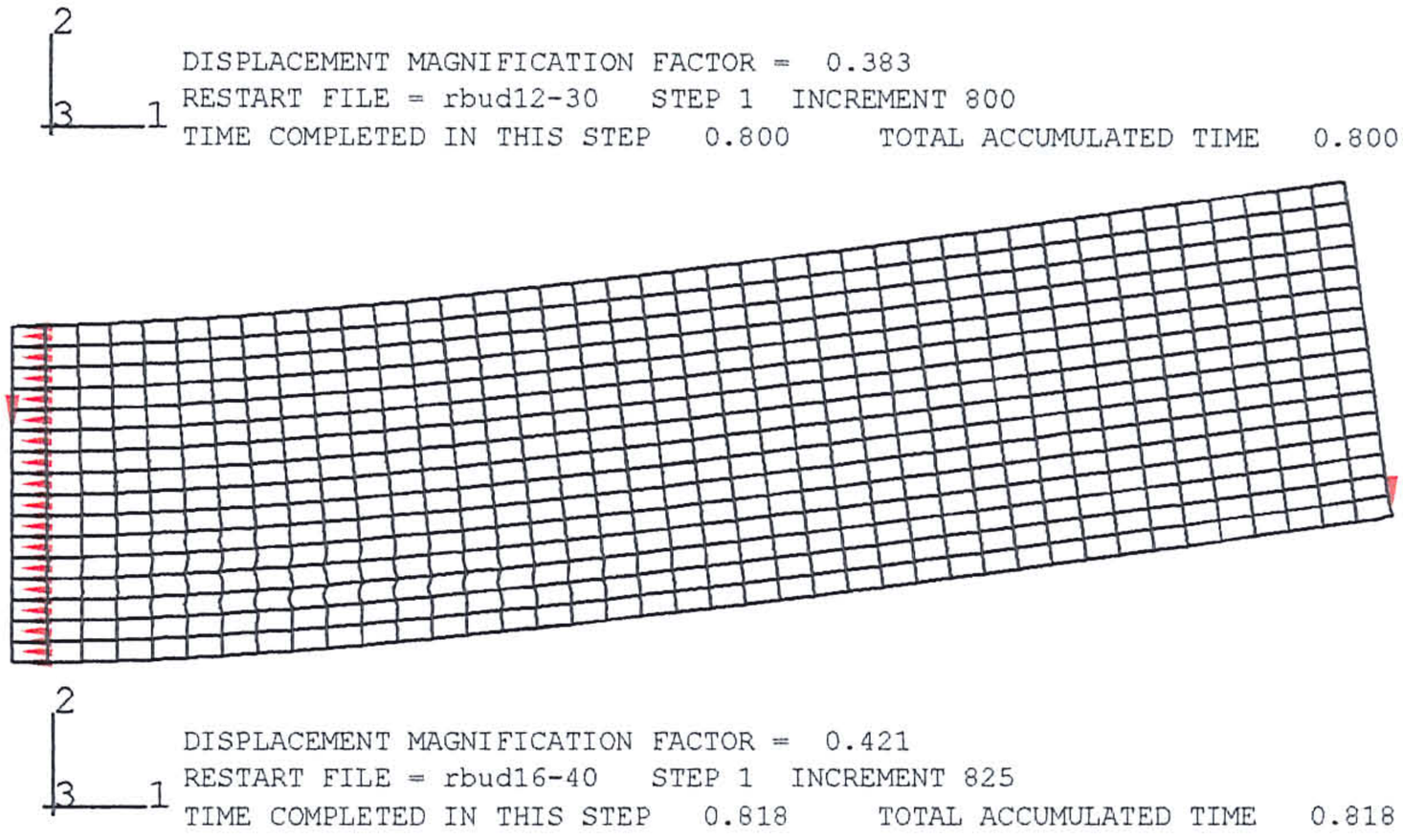

Fig 8.3.1.2-1 The deformed meshes of the one-dimensional polyester composite bar at the applied deflection of 2.62mm with (a) 4x10, (b) 8x20, (c) 12x30

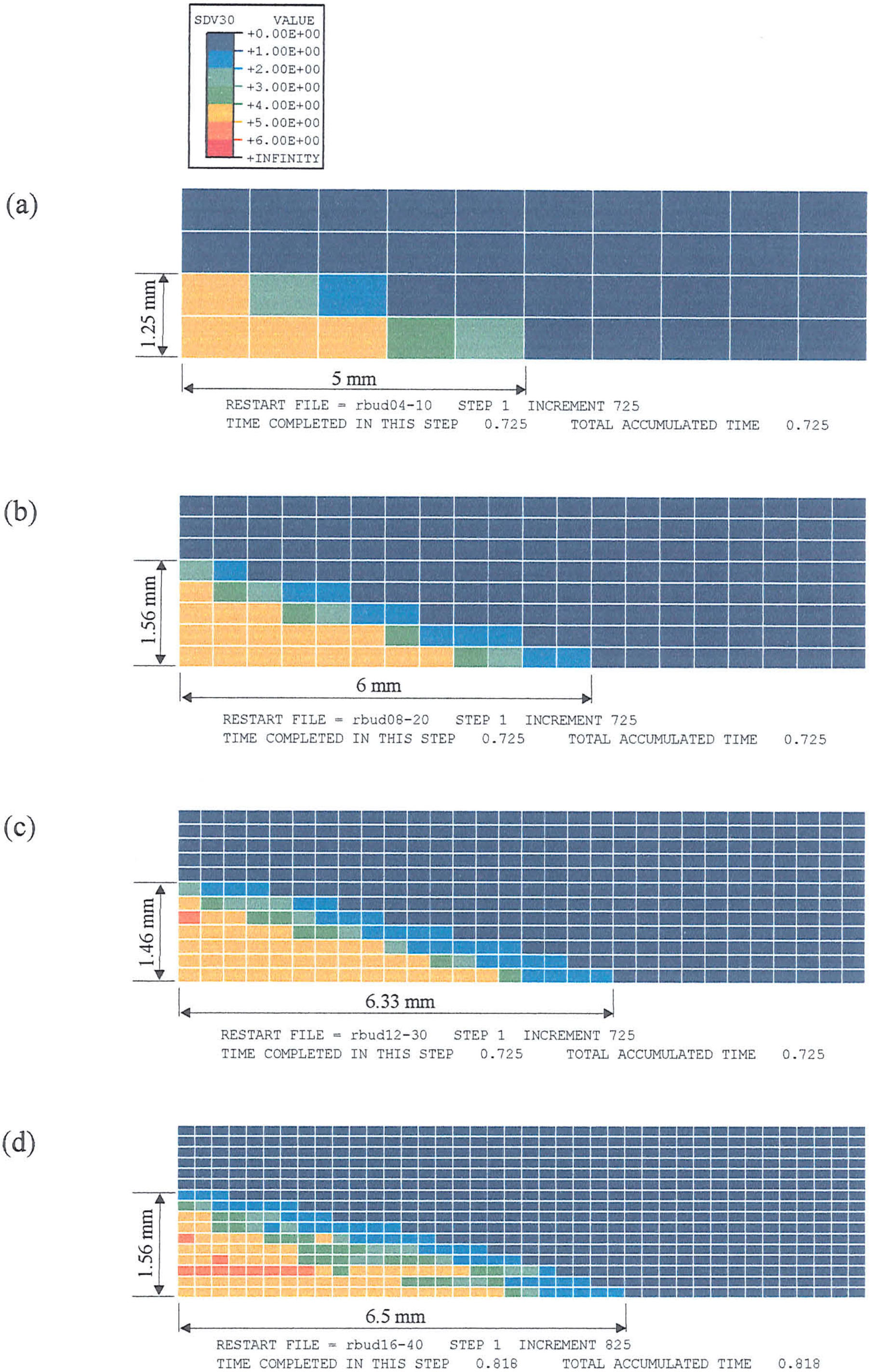

Fig 8.3.1.2-2 The matrix cracking zone of one-dimensional polyester composite bar at an applied deflection of 2.62mm with mesh refinements (a) 4x10, (b)

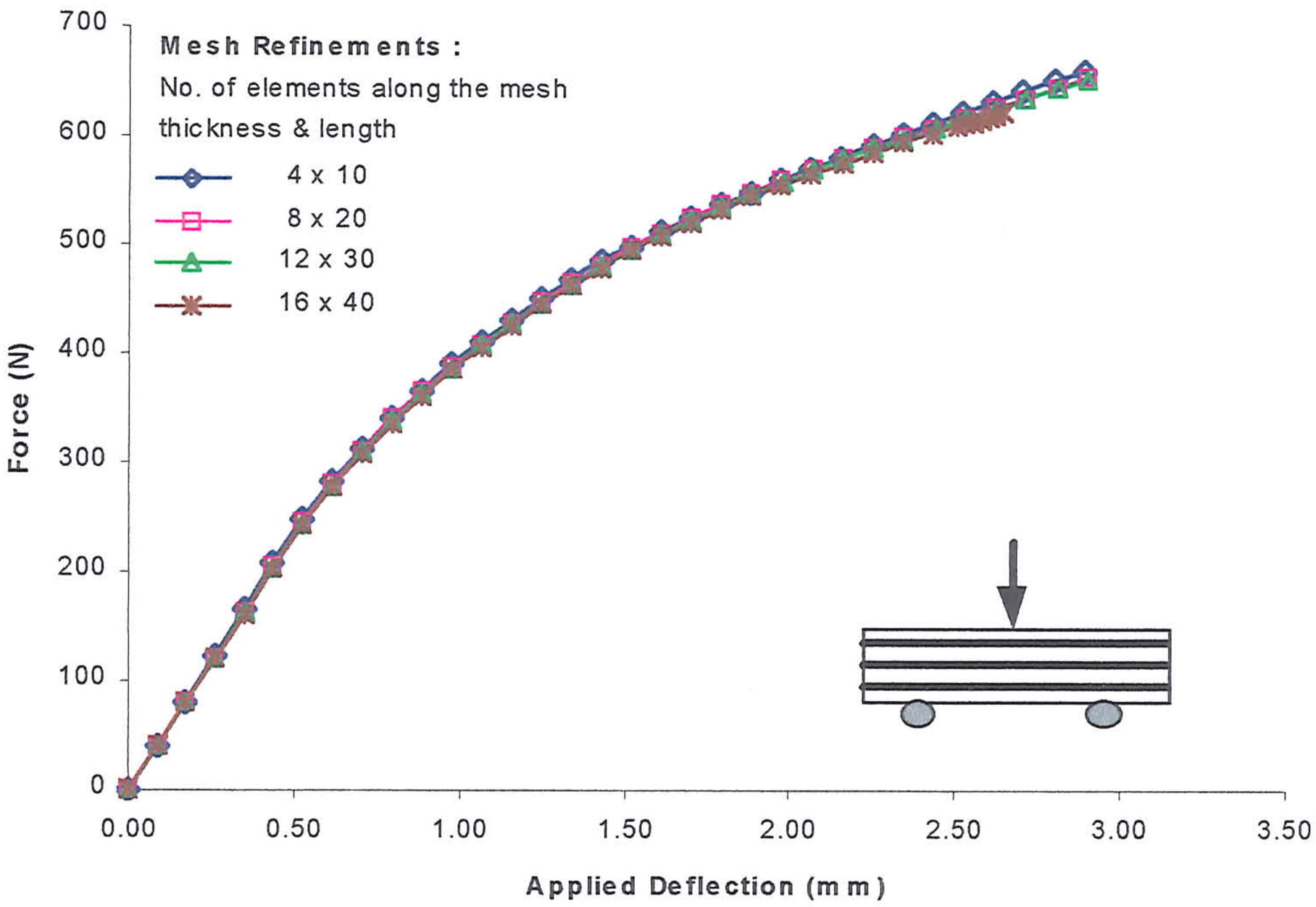

Fig 8.3.1.2-3 The predicted force-deflection response of the one-dimensional polyester composite bar at different levels of mesh refinement.

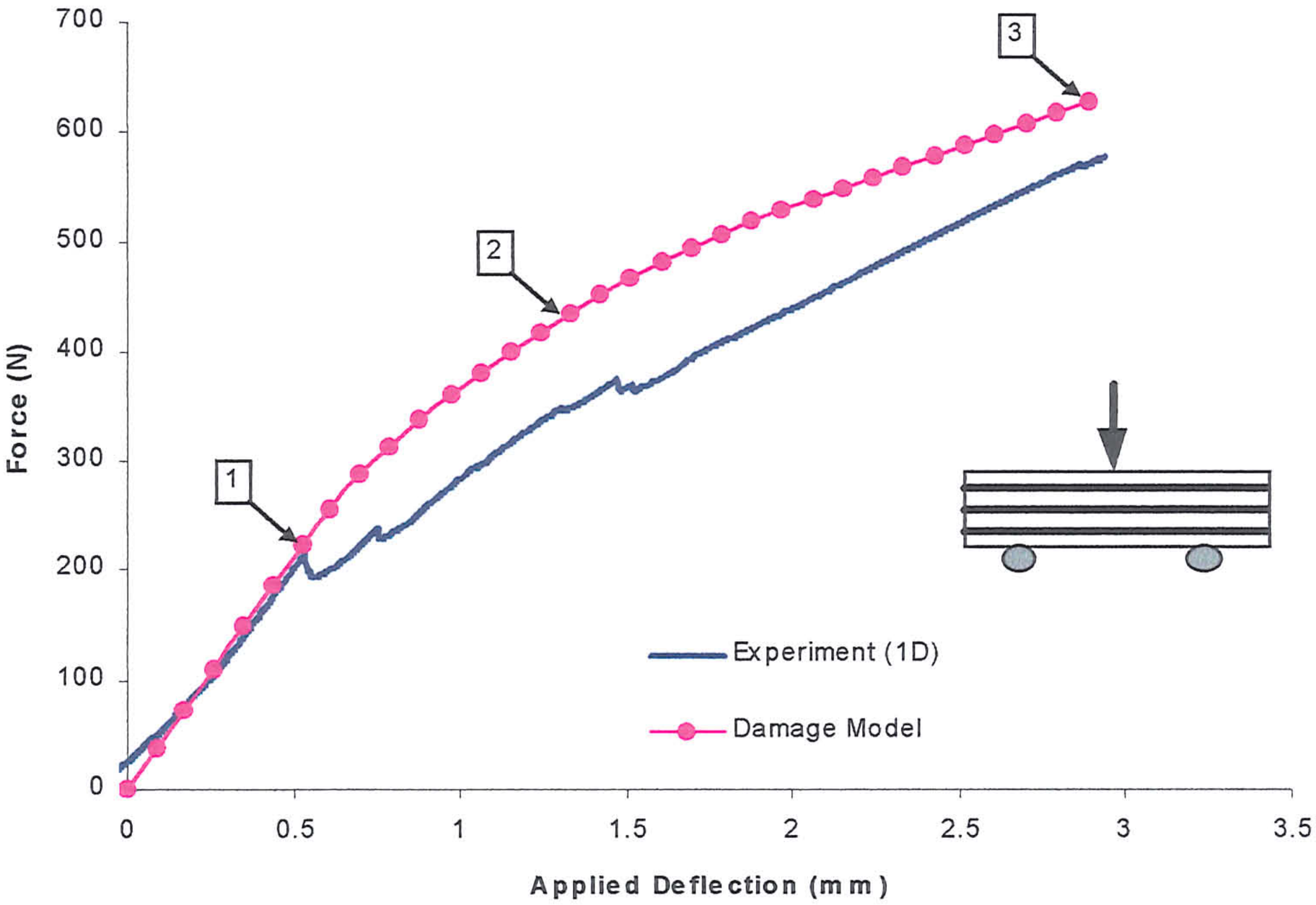

(a)

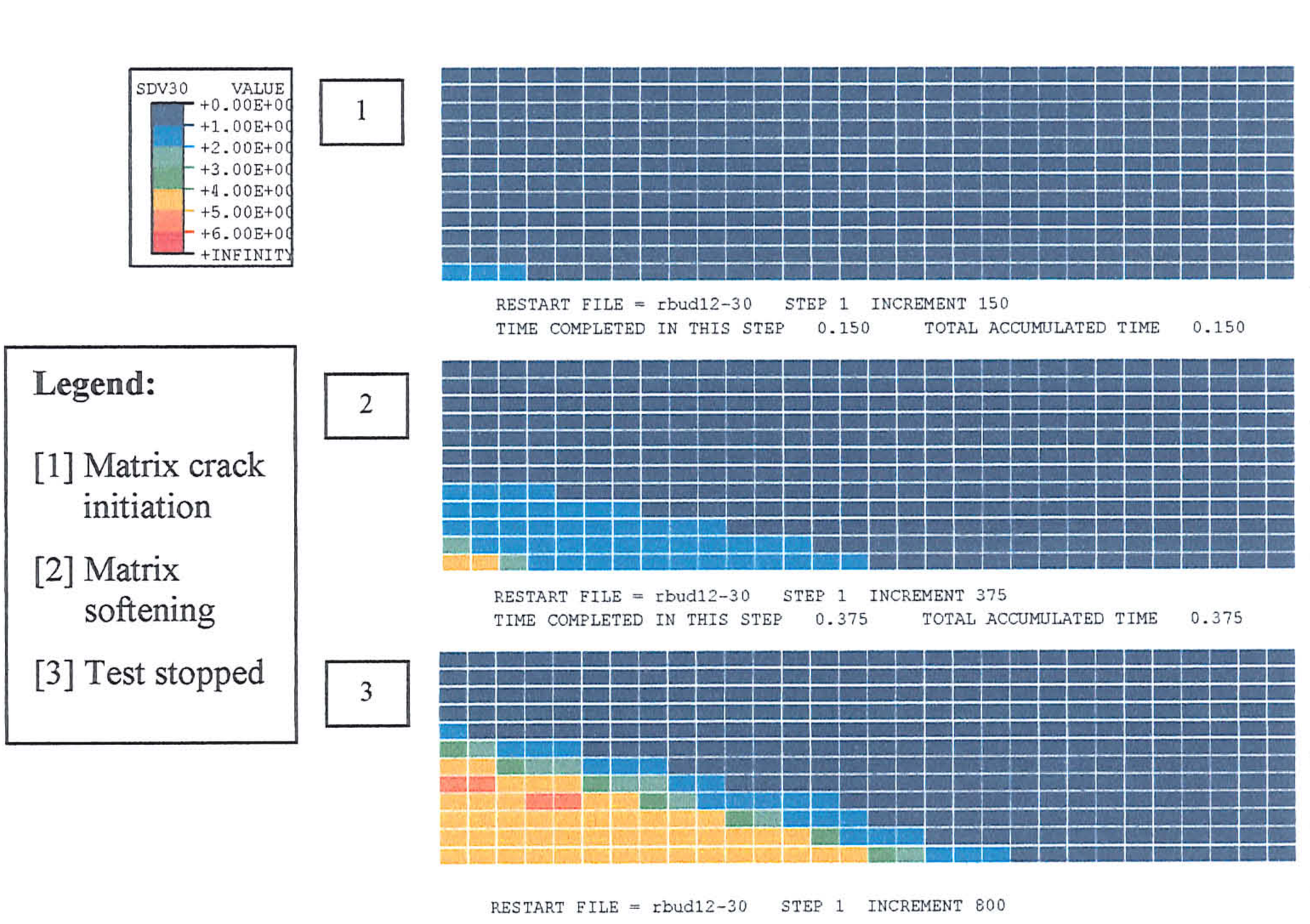

(b)

Fig 8.3.1.2-4 The (a) numerical and experimental force-deflection responses and (b) the matrix cracking zone at the initiation of matrix cracking, matrix

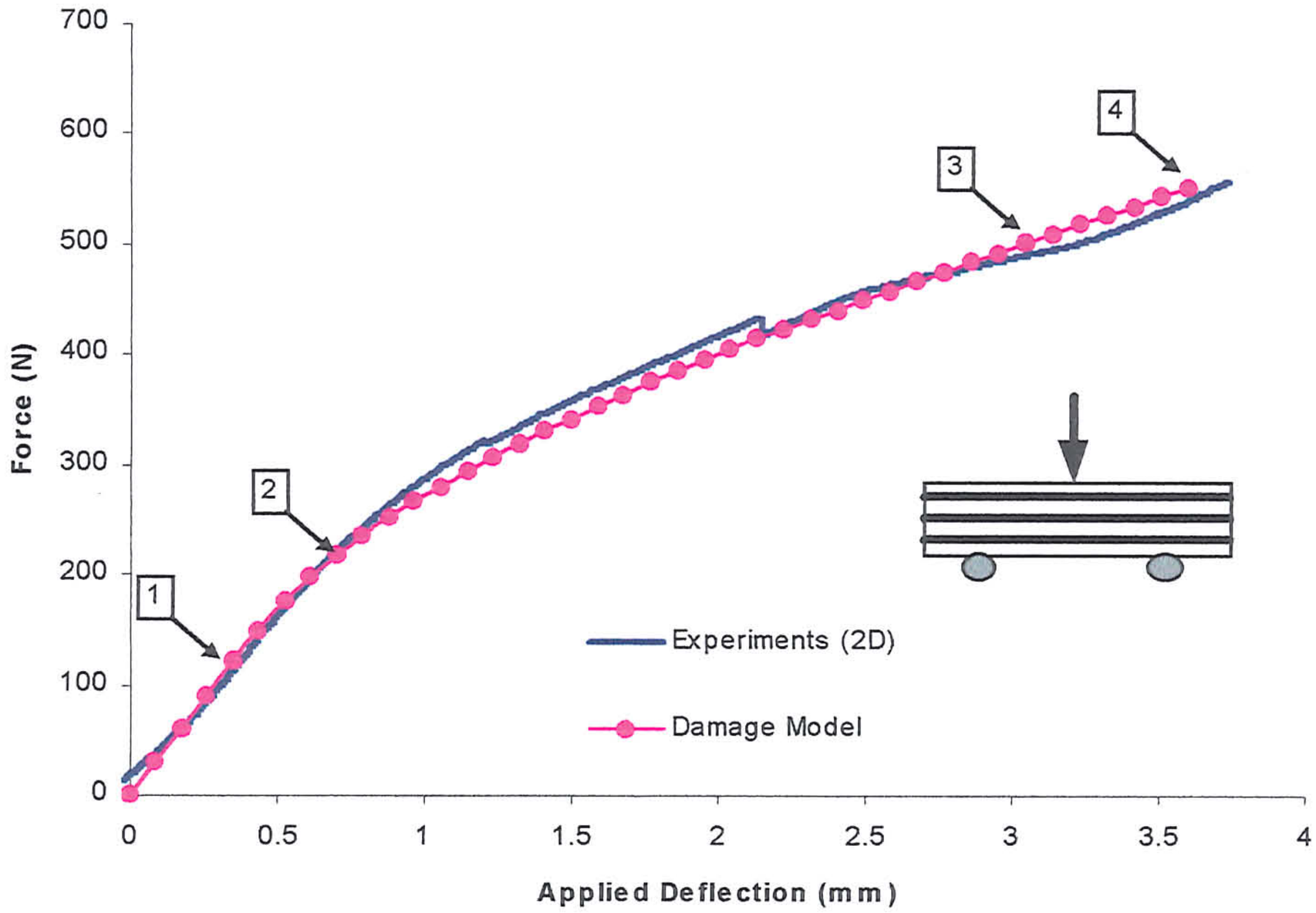

(a)

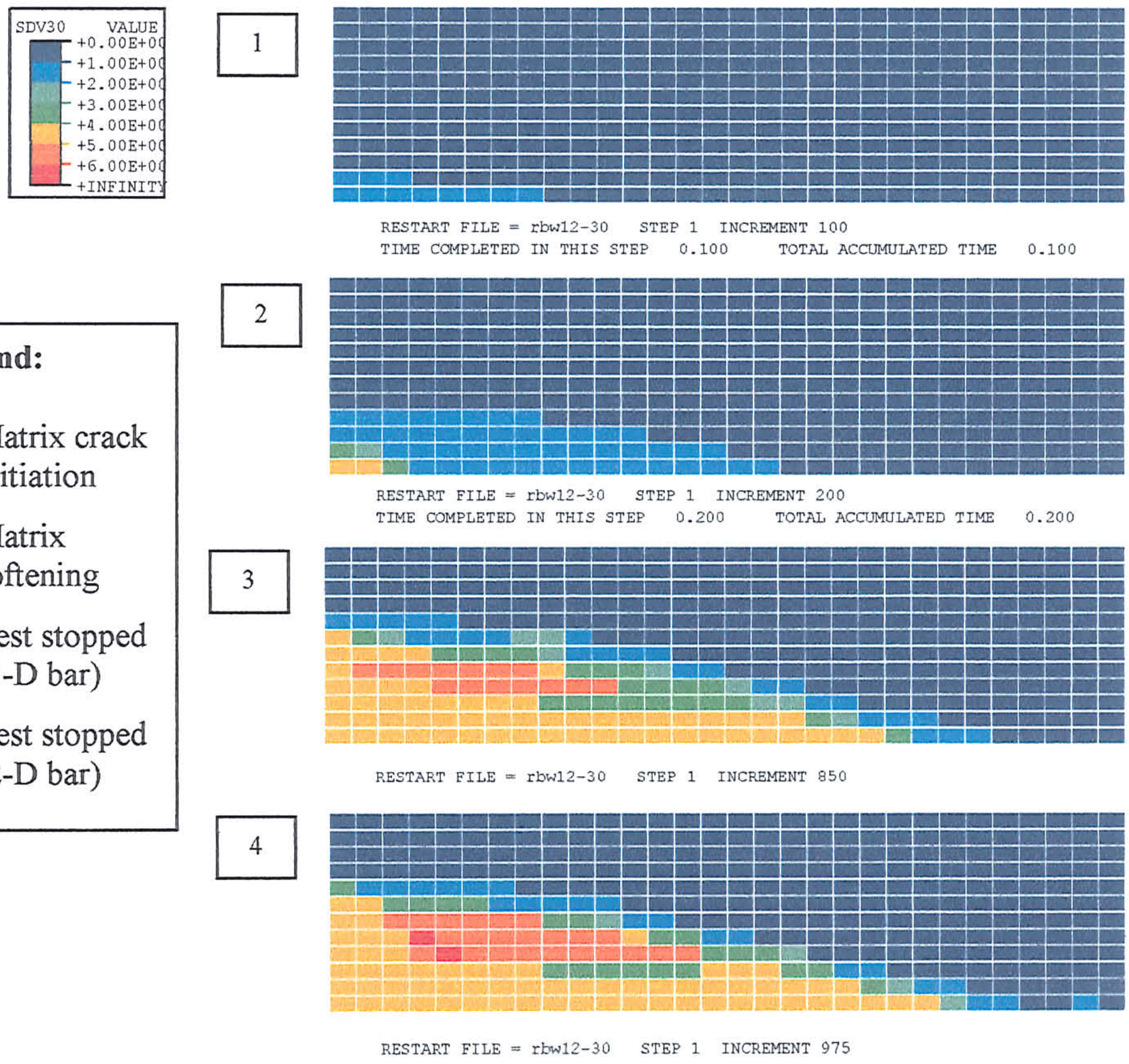

Legend:

[1] Matrix crack initiation

[2] Matrix softening

[3] Test stopped (1-D bar)

[4] Test stopped (2-D bar)

(b)

Fig 8.3.1.2-5 The (a) numerical and experimental force-deflection responses and (b) the matrix cracking zone at the initiation of matrix cracking, matrix

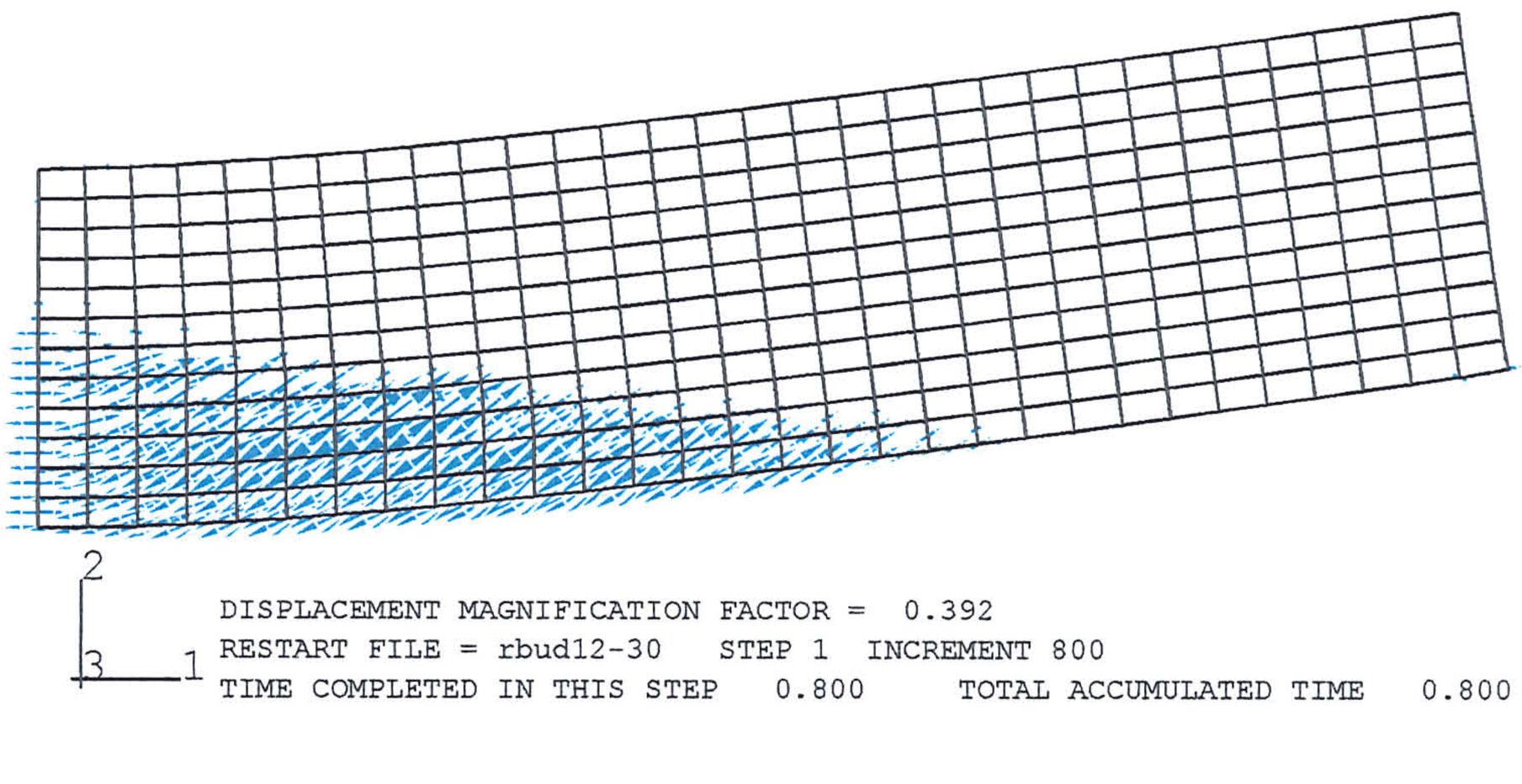

Fig 8.3.1.2-6 Vector plot of the maximum principal strain directions of the one-dimensional composite bar.

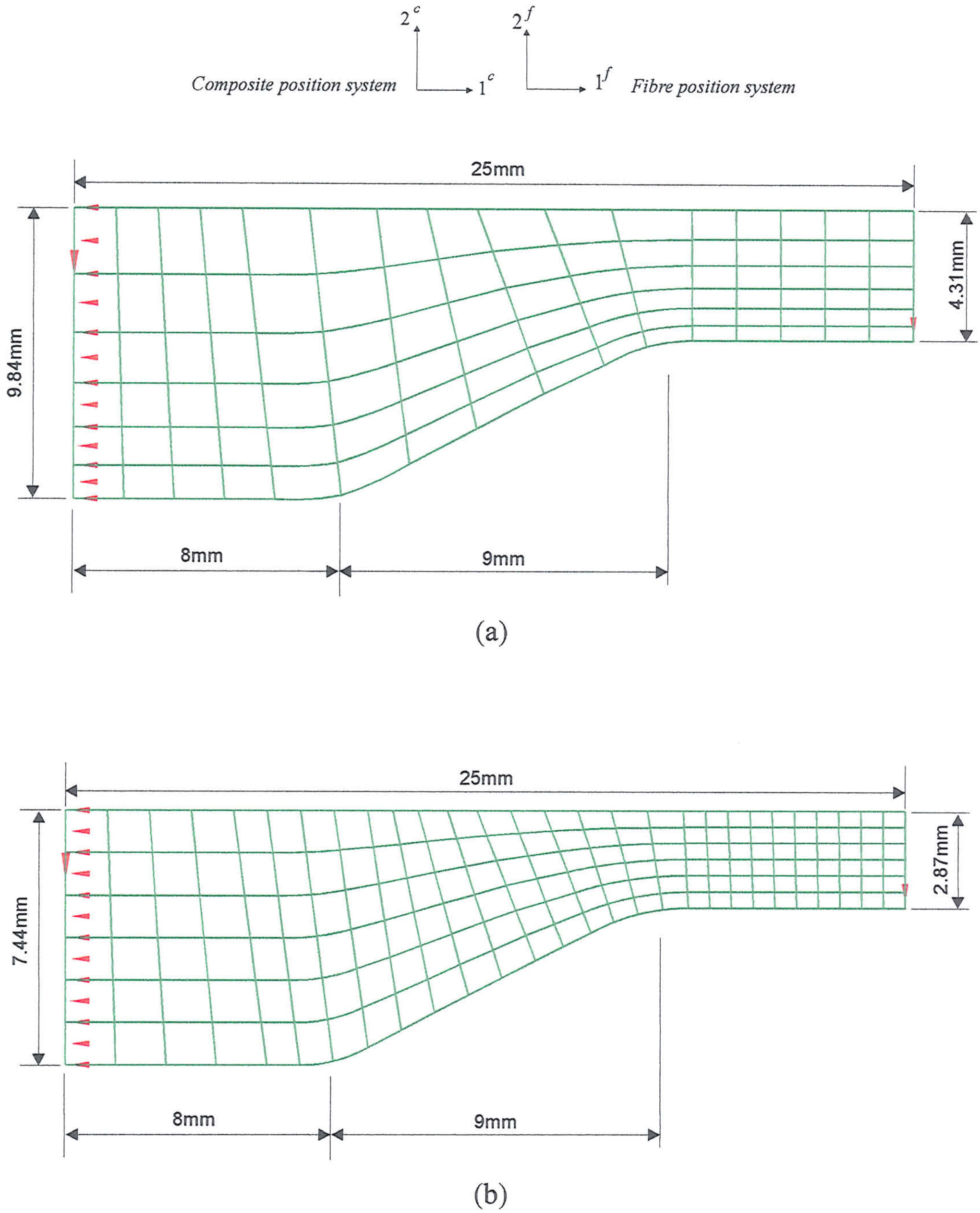

Fig 8.3.2.1-1 The mesh of the wedge-shaped polyester composite bar with (a) one-dimensional and (b) two-dimensional reinforcement, and the boundary conditions modelling three-point bending.

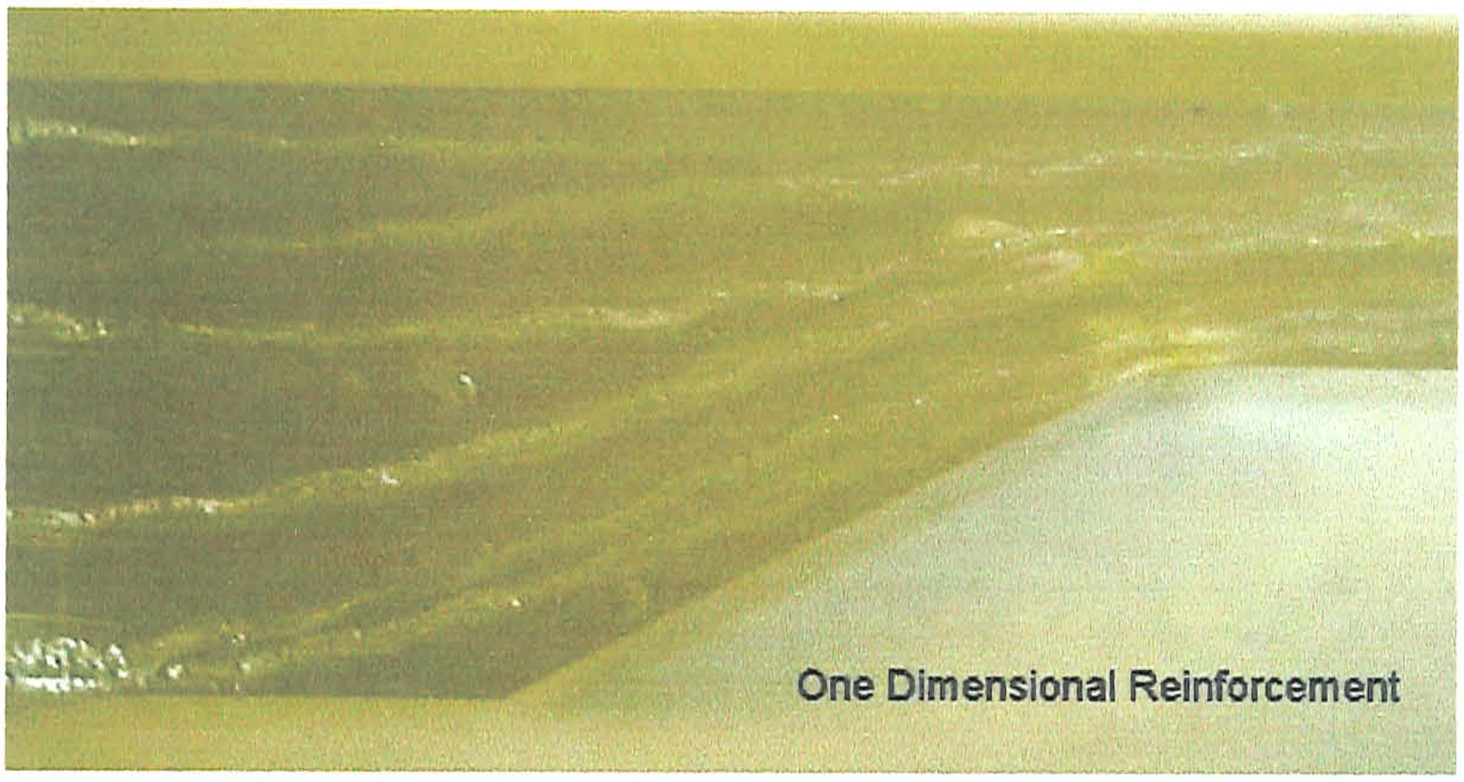

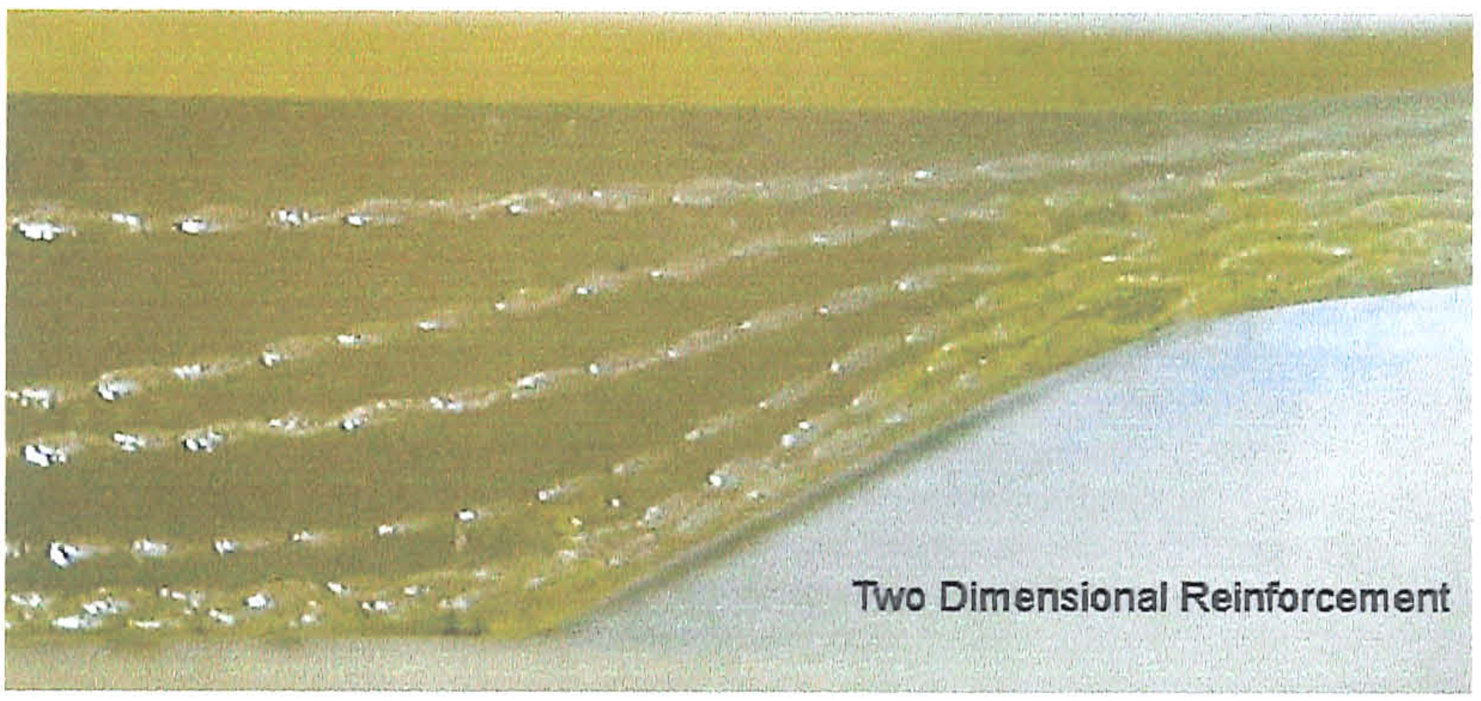

Fig 8.3.2.1-2 The fibre alignments of the wedge-shaped test specimens in Chapter 5.

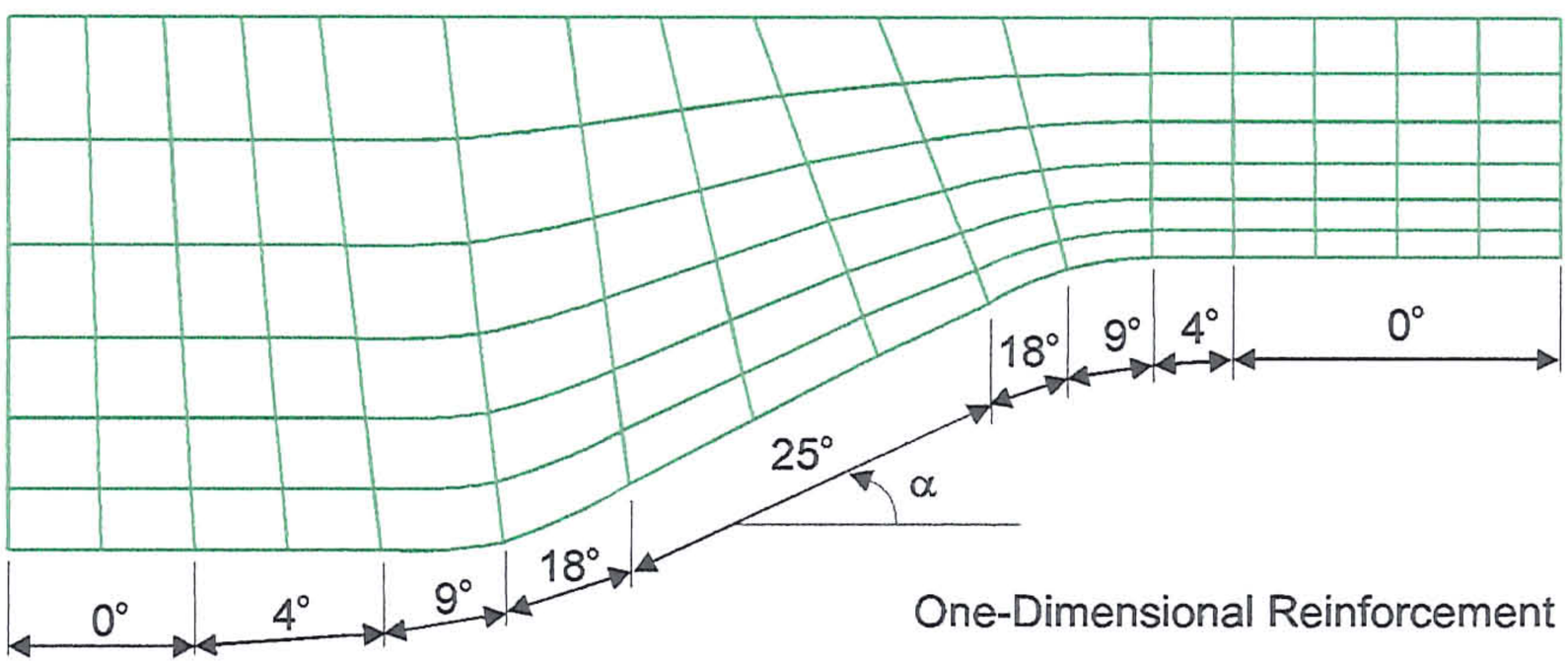

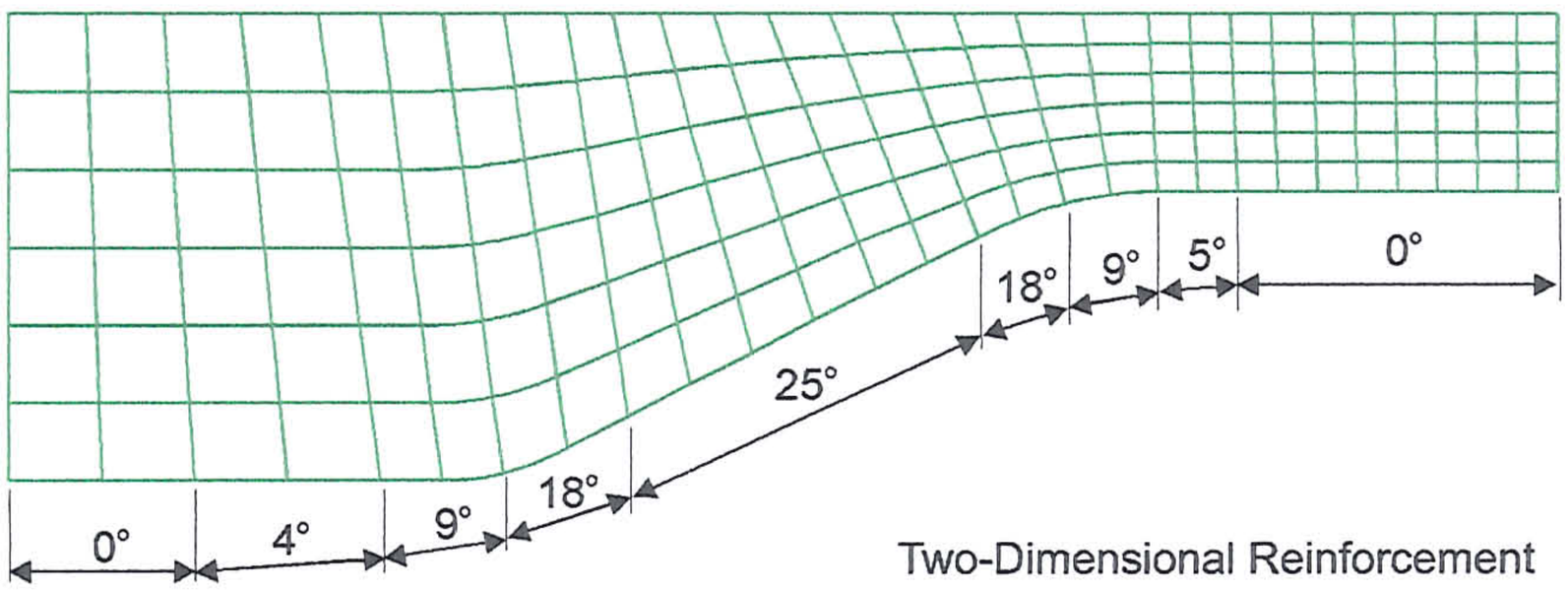

Fig 8.3.2.1-3 The fibre alignment angle α used to model fibres in the the wedge-

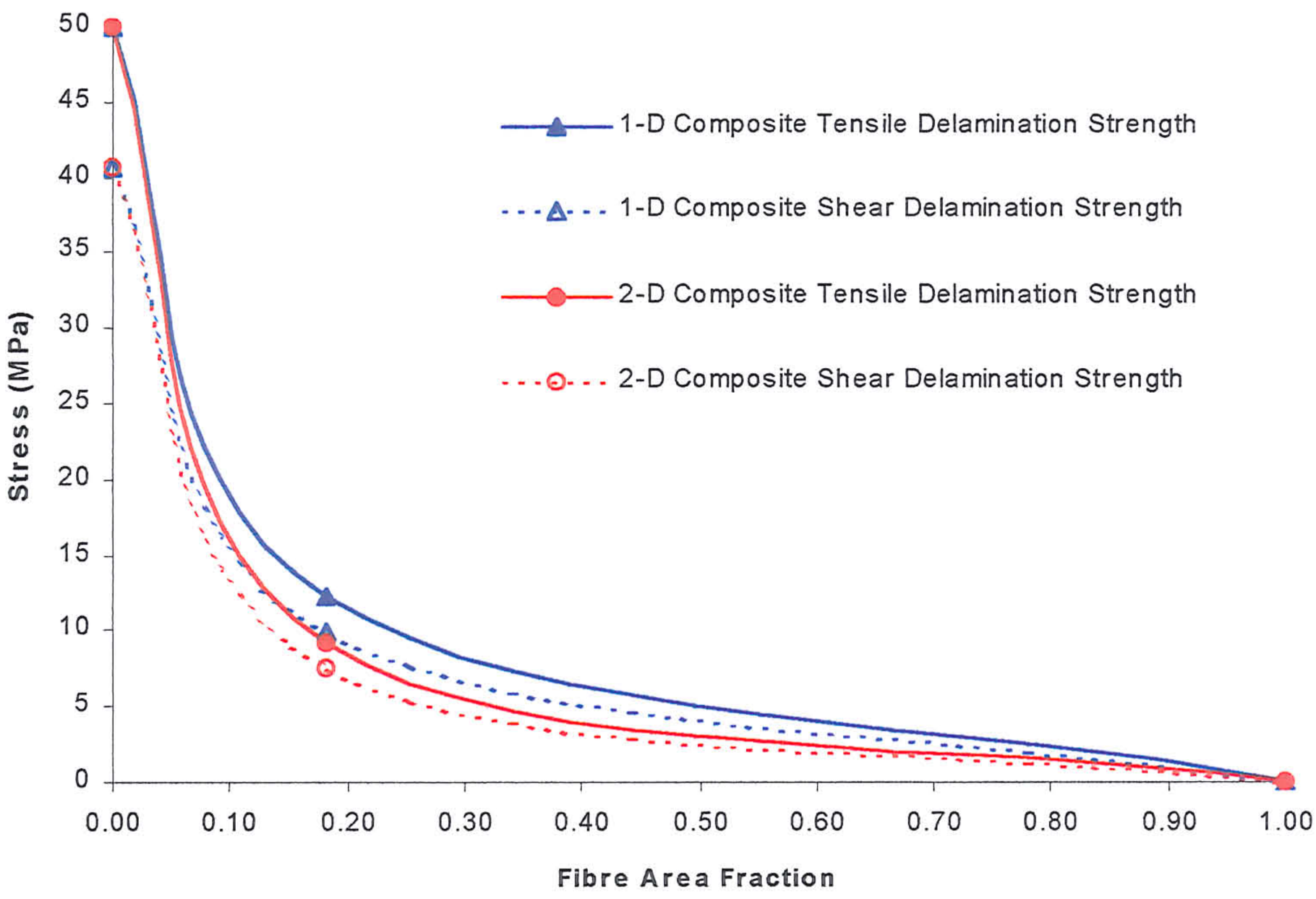

Fig 8.3.2.1-4 Plots of the tensile and shear delamination strength of the one and two-dimensional polyester composite as a function of the fibre area fraction.

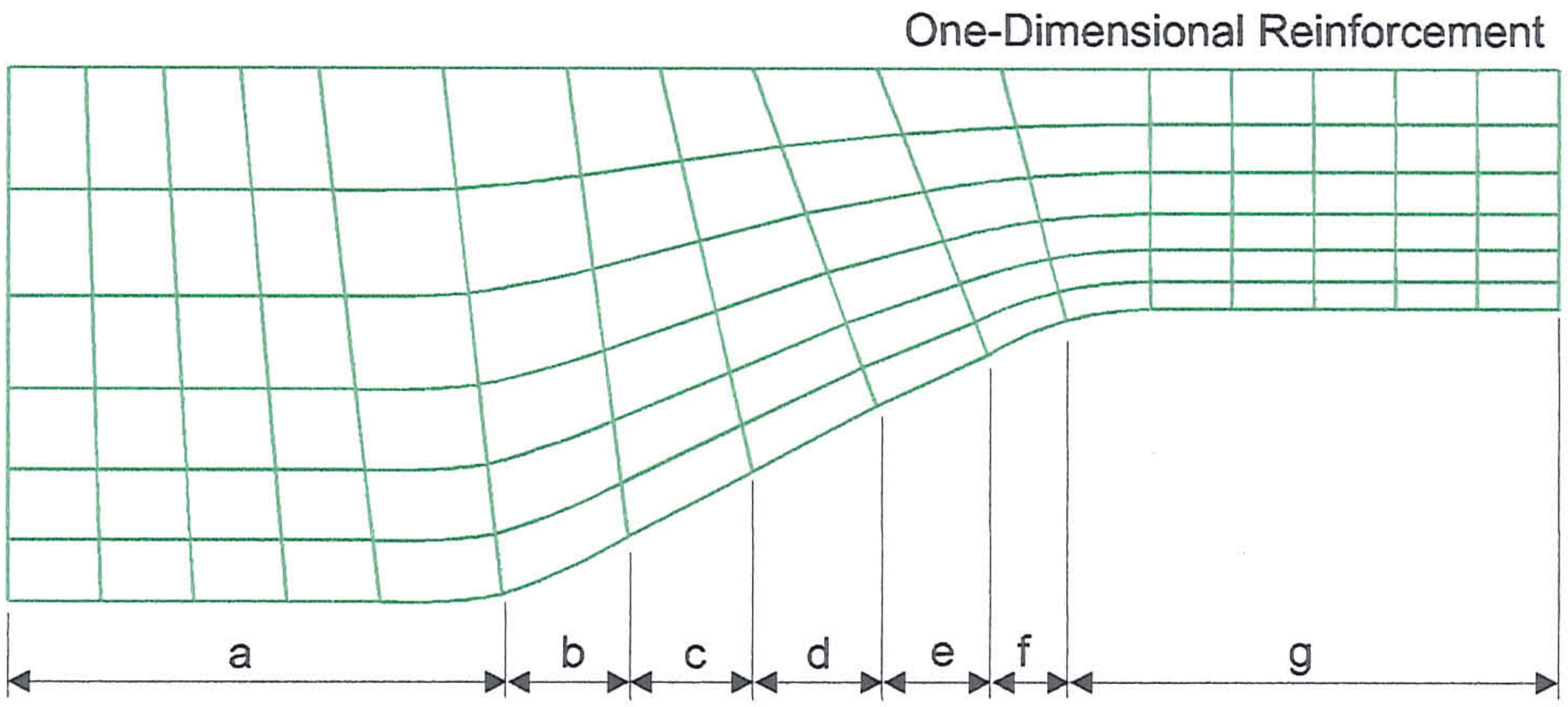

Section	Fibre Volume Fraction	Shear Delamination Stress (MPa)	Tensile Delamination Stress (MPa)
a	0.0528	28.5	35.1
b	0.0545	28.1	34.5
c	0.0623	26.2	32.1
d	0.0728	23.8	29.2
e	0.0876	20.7	25.5
f	0.1098	17.2	20.8
g	0.1172	15.9	19.7

Fig 8.3.2.1-5 The fibre volume fraction and the tensile and shear delamination strength used to model the different sections of the one-dimensionally reinforced wedge-shaped sub-structure.

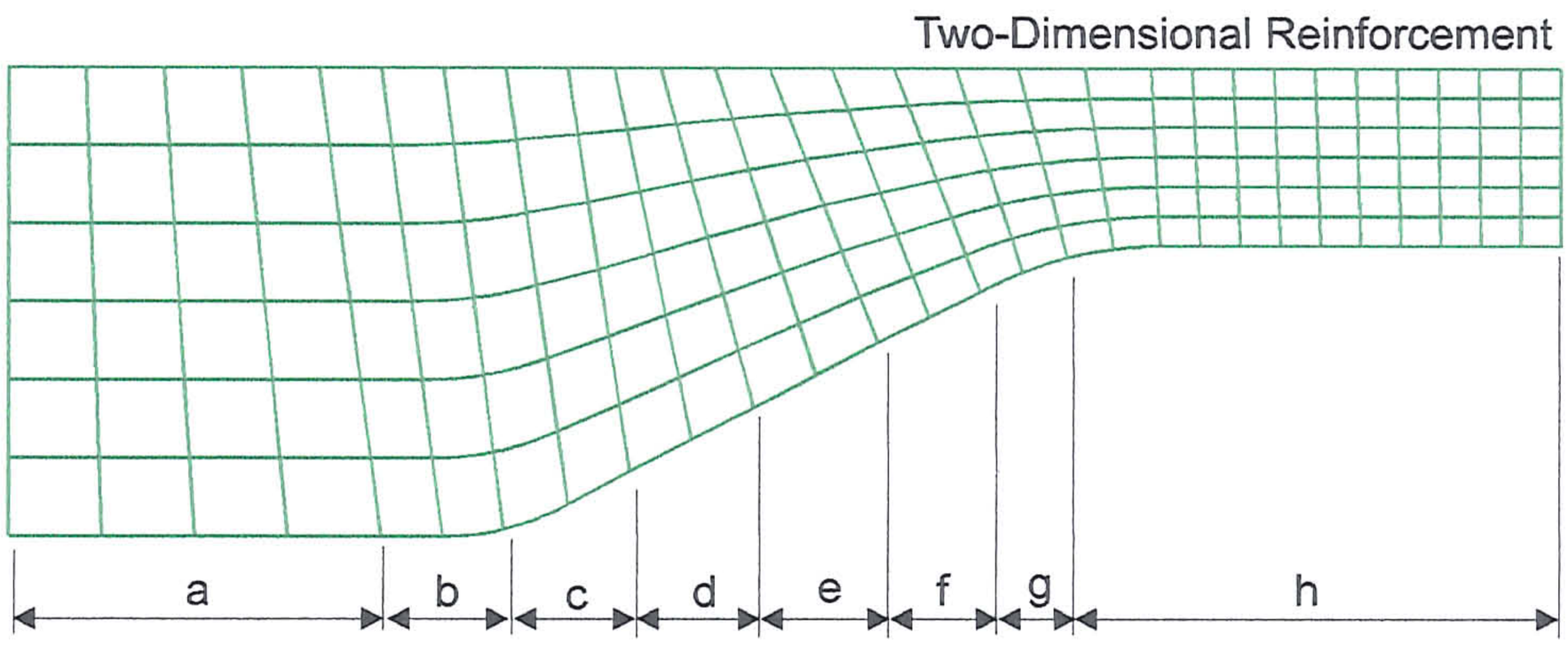

Section	Fibre Volume Fraction	Shear Delamination Stress (MPa)	Tensile Delamination Stress (MPa)
a	0.121	21.2	32.3
b	0.125	25.7	31.6
c	0.146	23.4	28.7
d	0.175	20.2	24.5
e	0.218	15.8	20.3
f	0.249	13.2	16.2
g	0.291	10.7	13.1
h	0.317	9.5	11.6

Fig 8.3.2.1-6 The fibre volume fraction and the tensile and shear delamination strength used to model the different sections of the two-dimensionally reinforced wedge-shaped sub-structure.

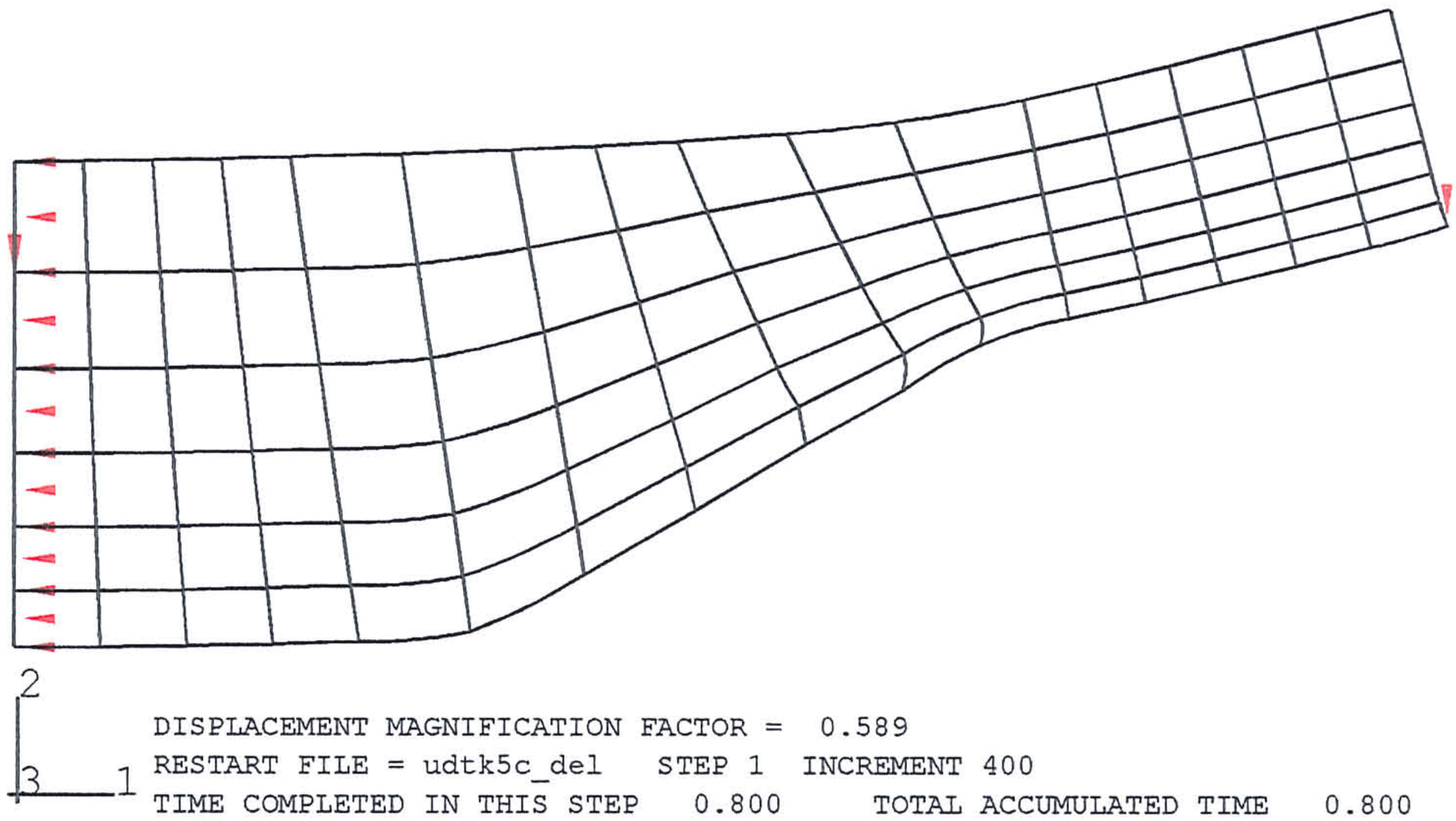

(a)

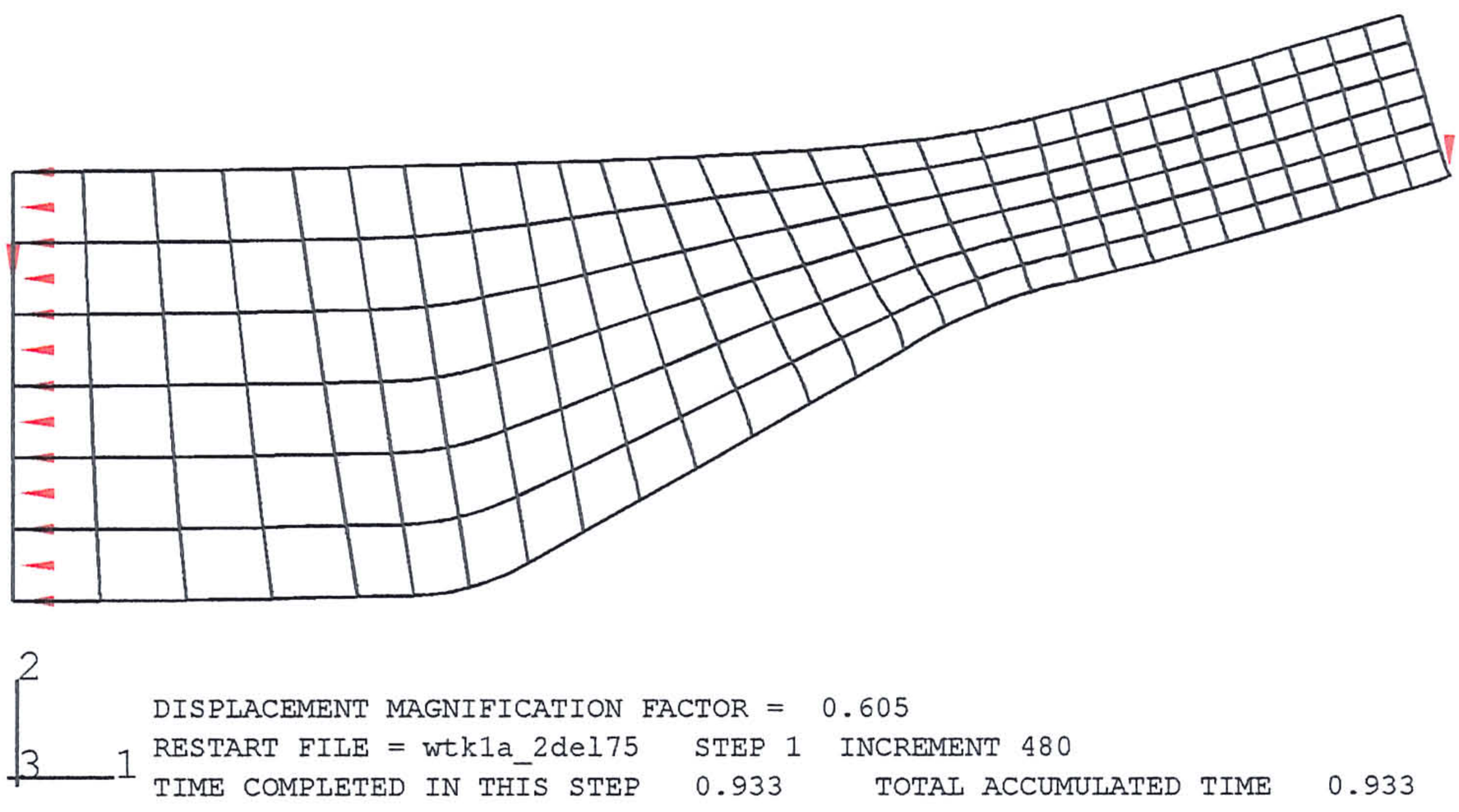

(b)

Fig 8.3.2.2-1 The deformed mesh of the wedge-shaped polyester composite bar with (a) one-dimensional and (b) two-dimensional reinforcement.

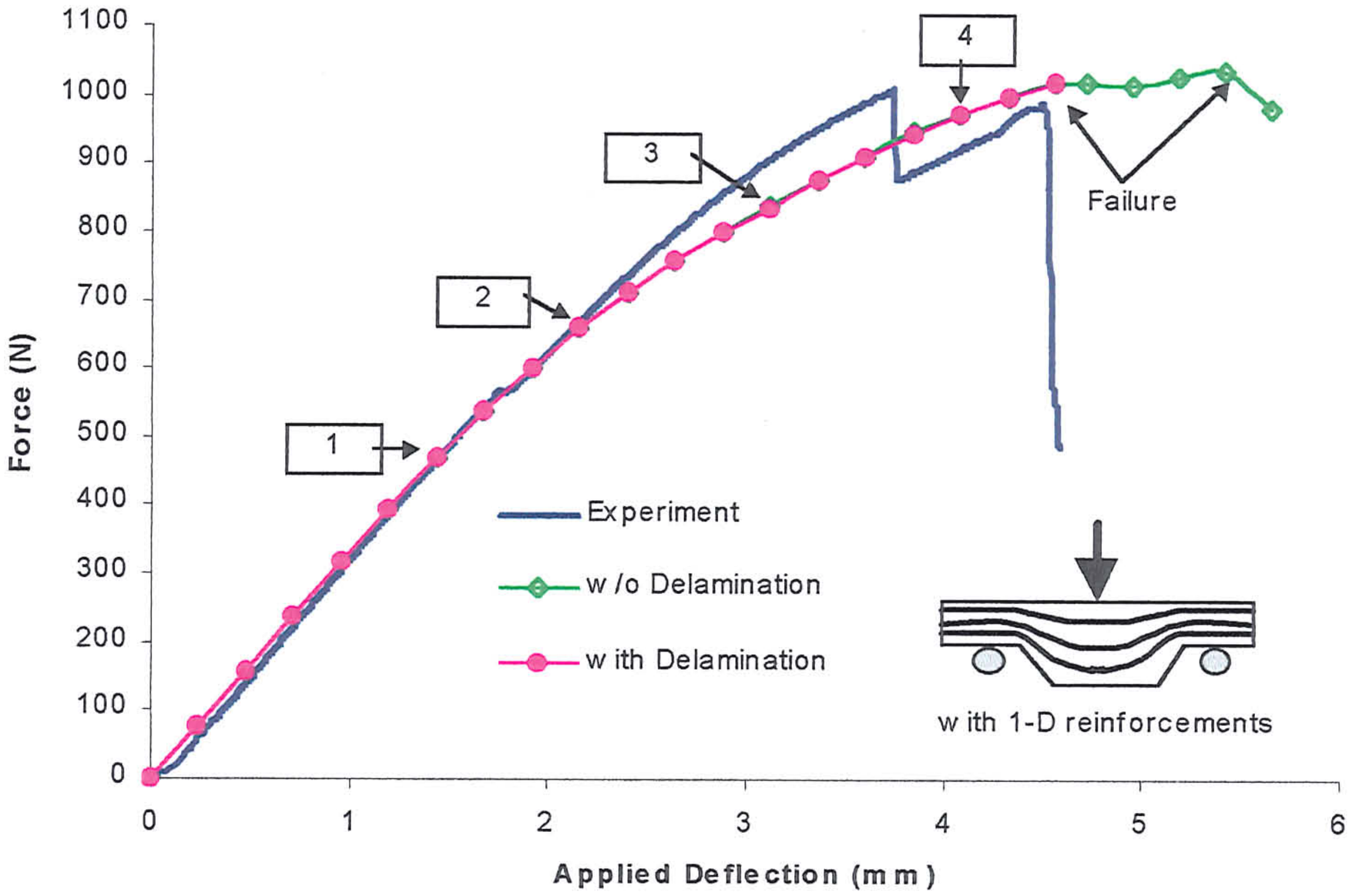

(a)

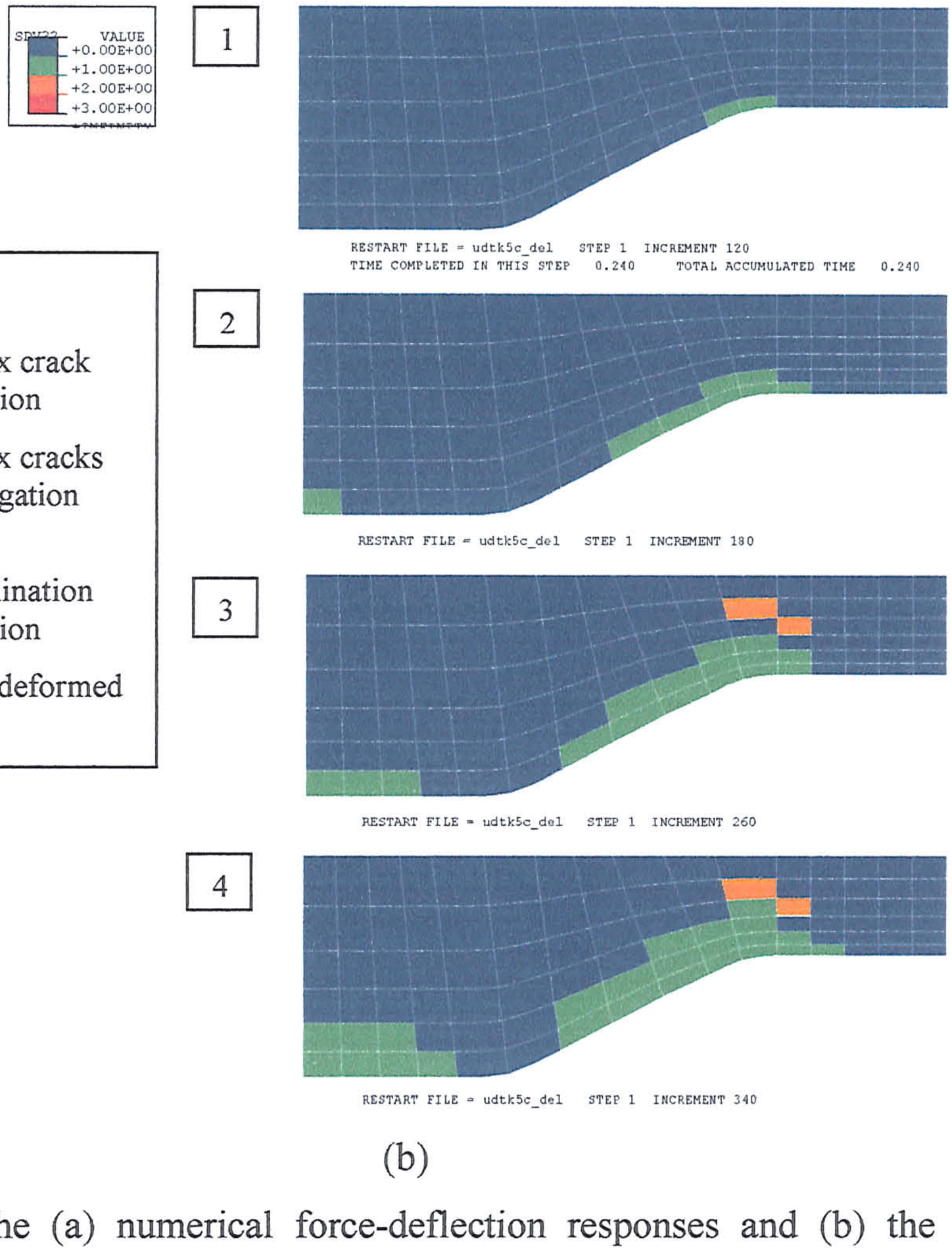

(b)

Fig 8.3.2.2-2 The (a) numerical force-deflection responses and (b) the predicted

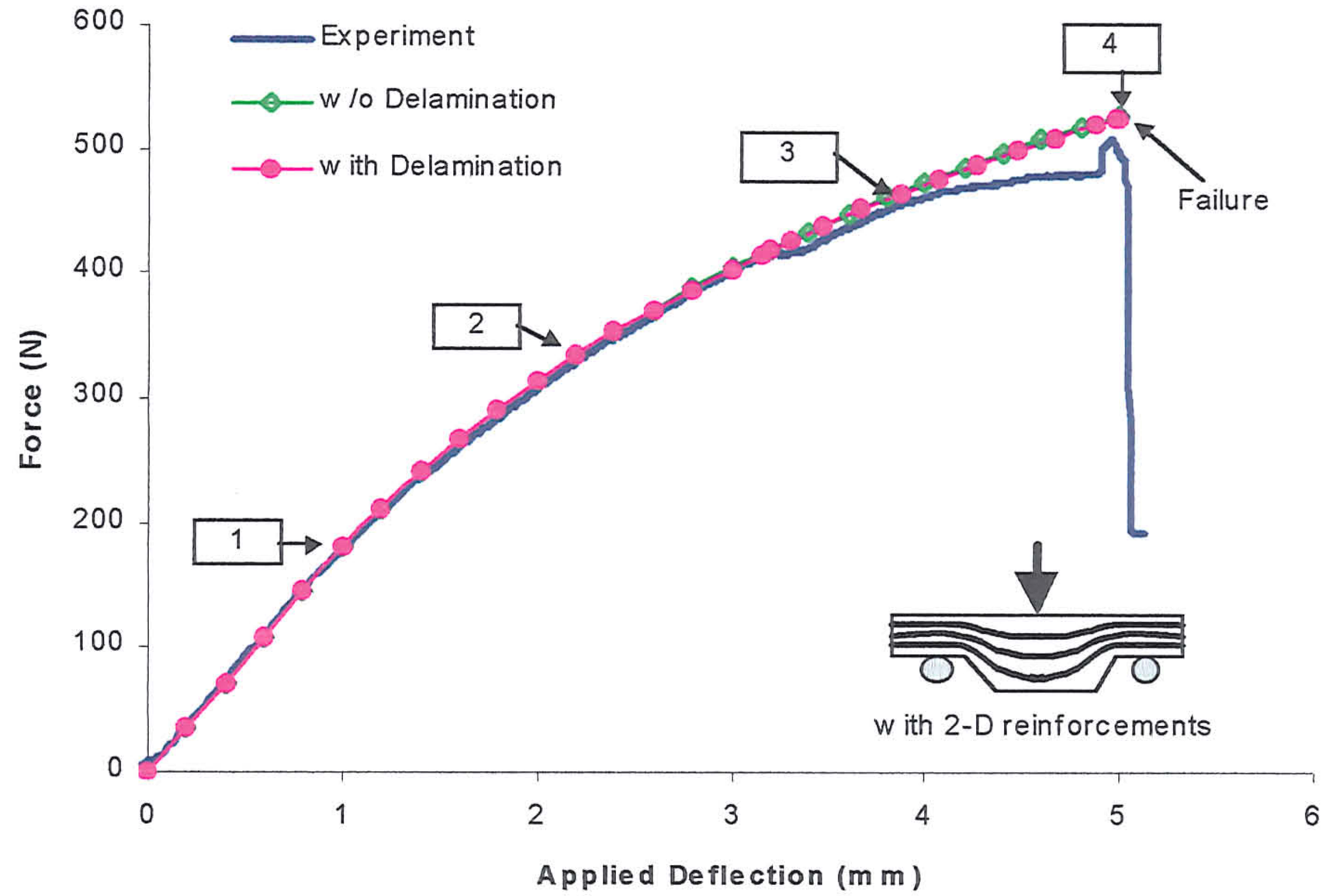

(a)

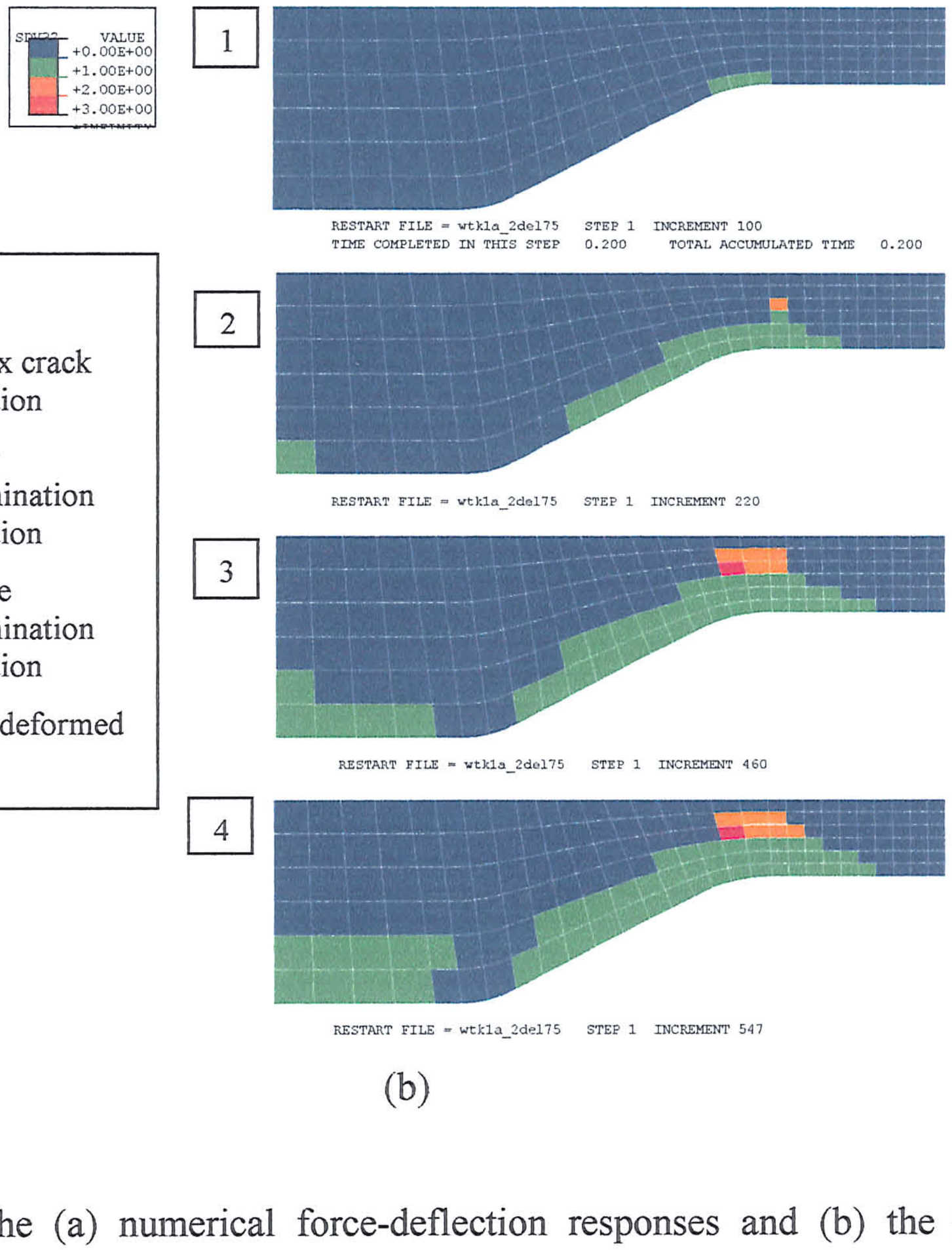

Legend:

[1] Matrix crack initiation

[2] Shear delamination initiation

[3]Tensile delamination initiation

[4] Final deformed state

(b)

Fig 8.3.2.2-3 The (a) numerical force-deflection responses and (b) the predicted

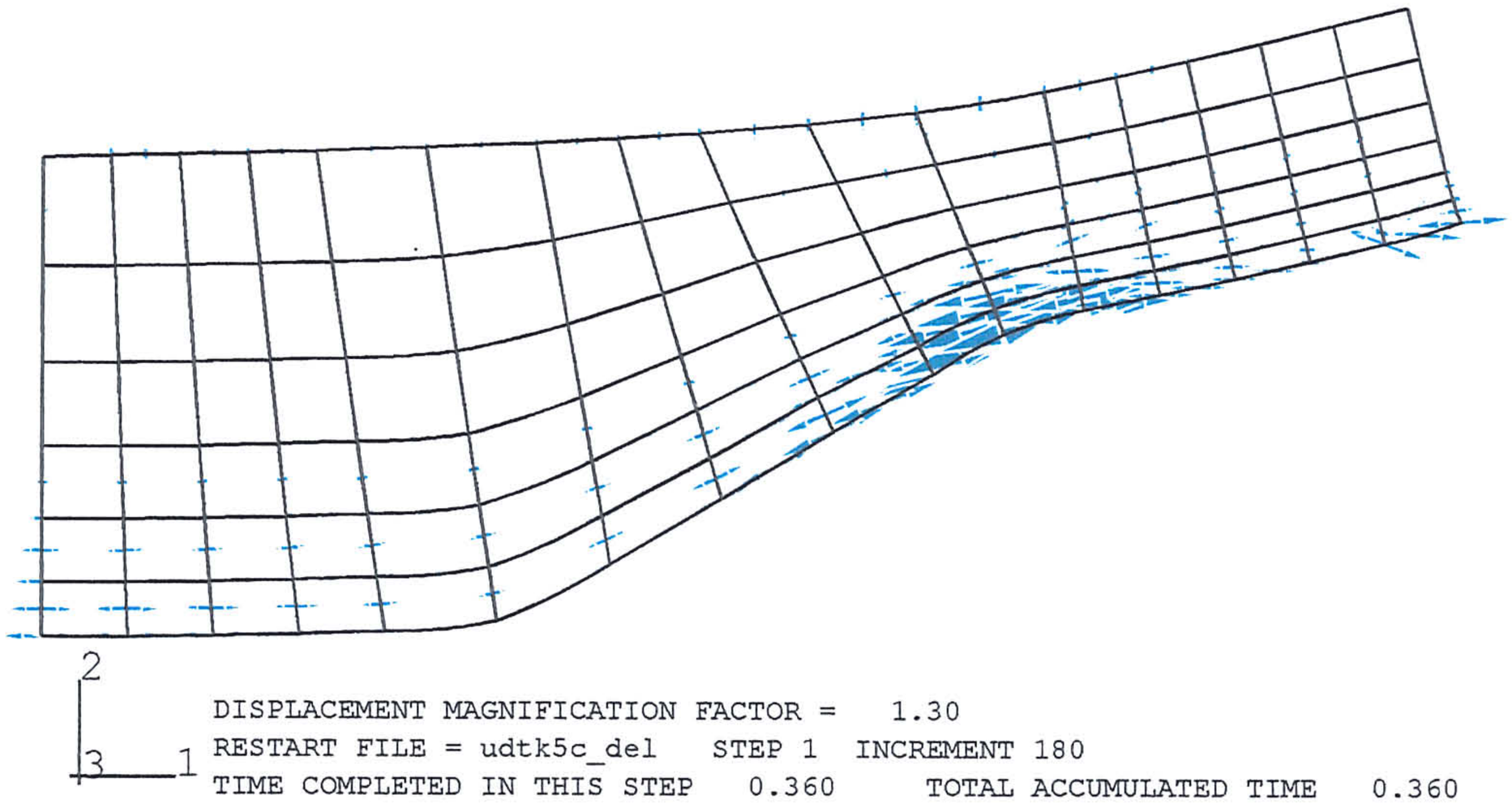

(a)

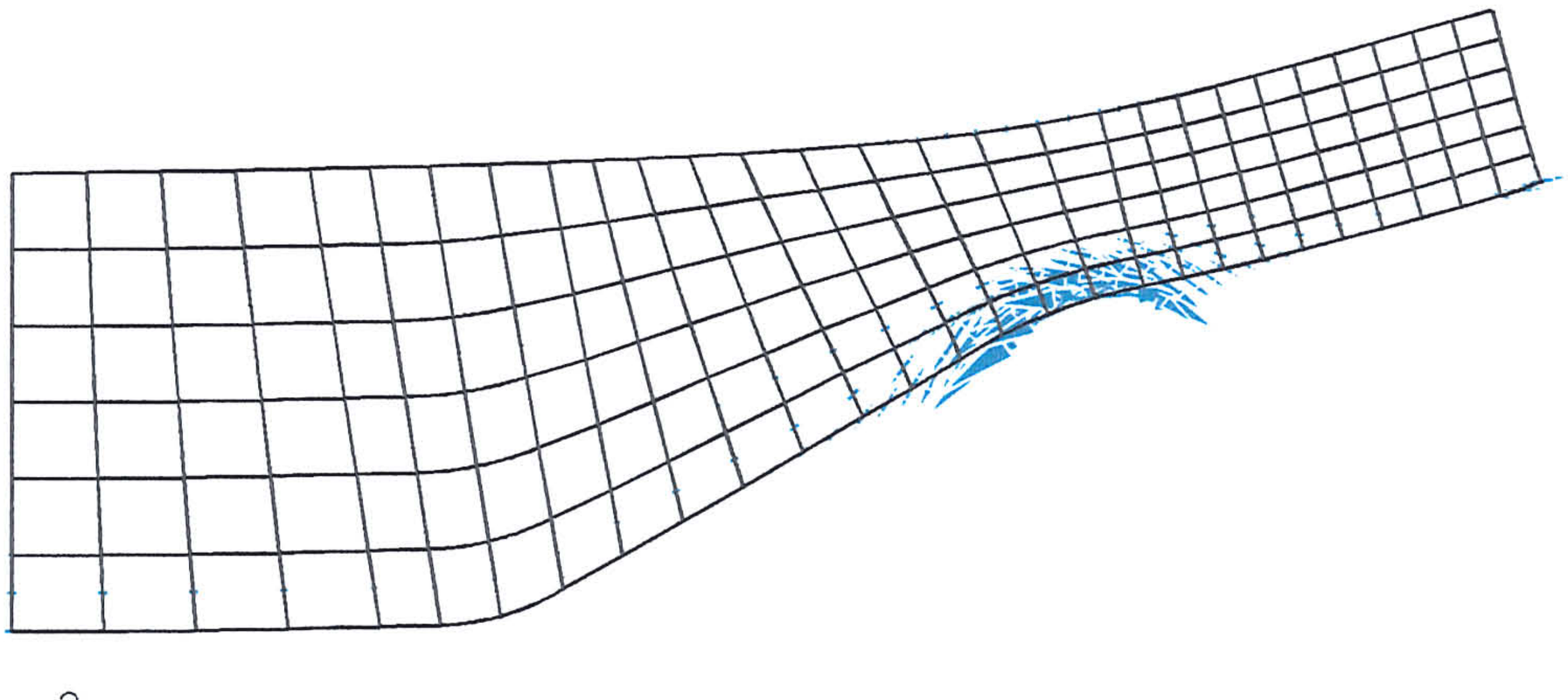

(b)

Fig 8.3.2.2-4 Vector plot of the maximum principal strain direction of the one and two-dimensional wedge-shaped polyester composite bar

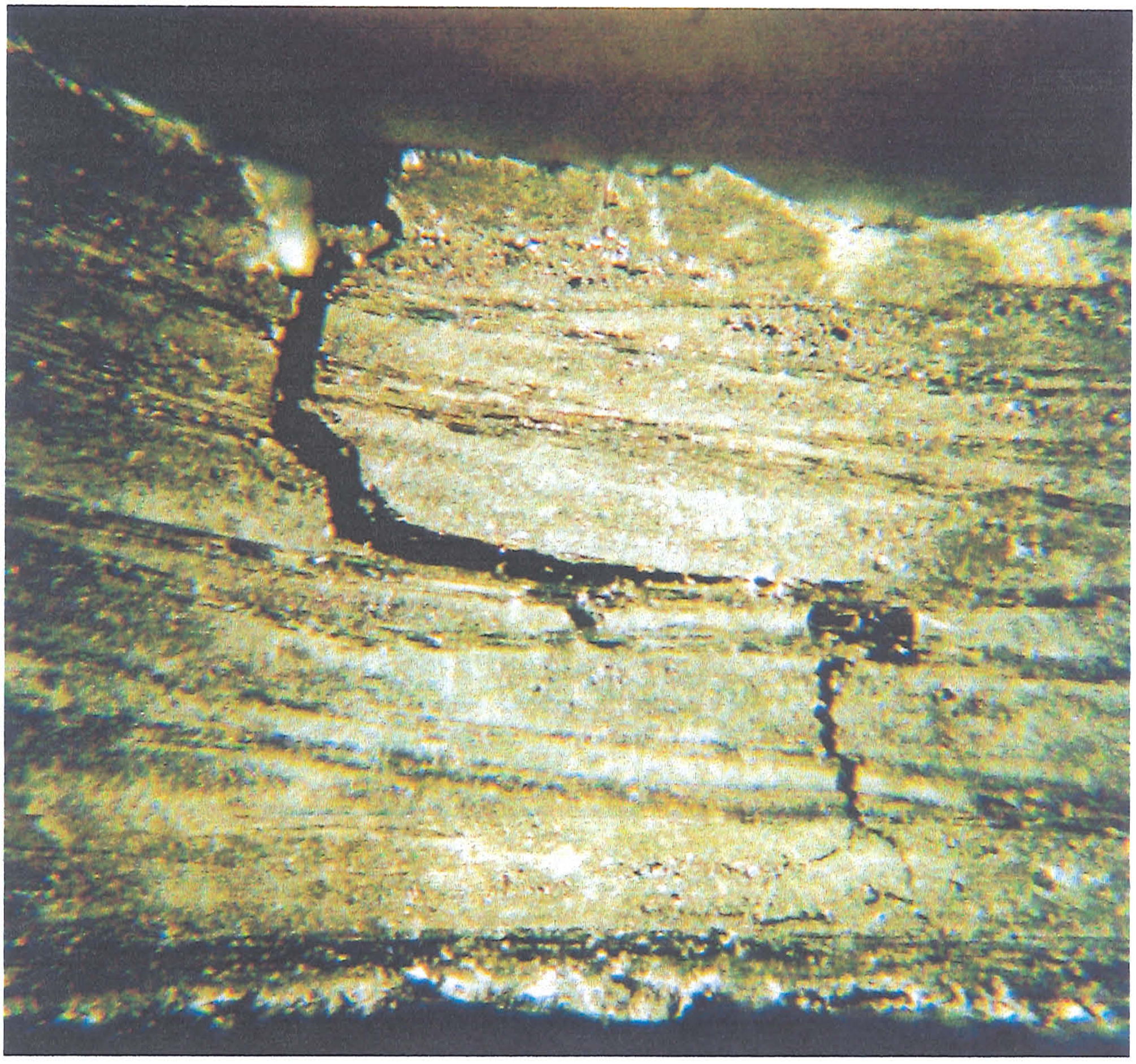

Fig 8.3.2.2-5 Micrograph of the matrix cracks and delamination in the wedge-shaped SiC/SiC sub-structure tested by McCafferty (1994).

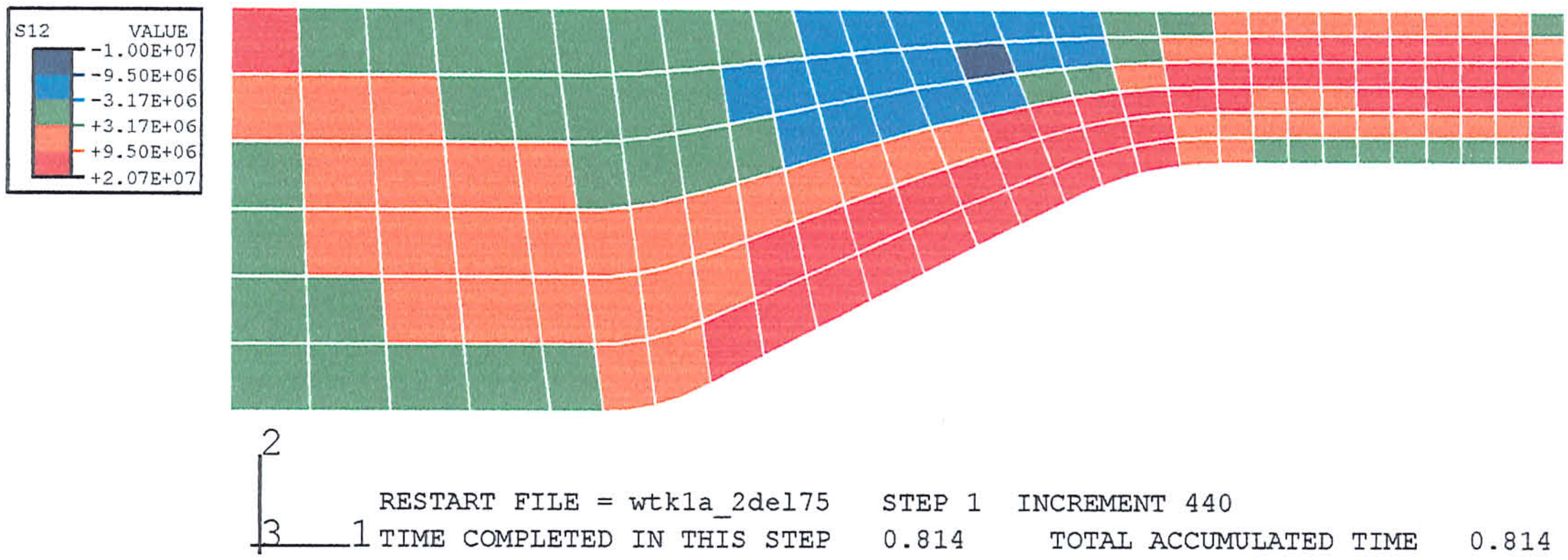

(a)

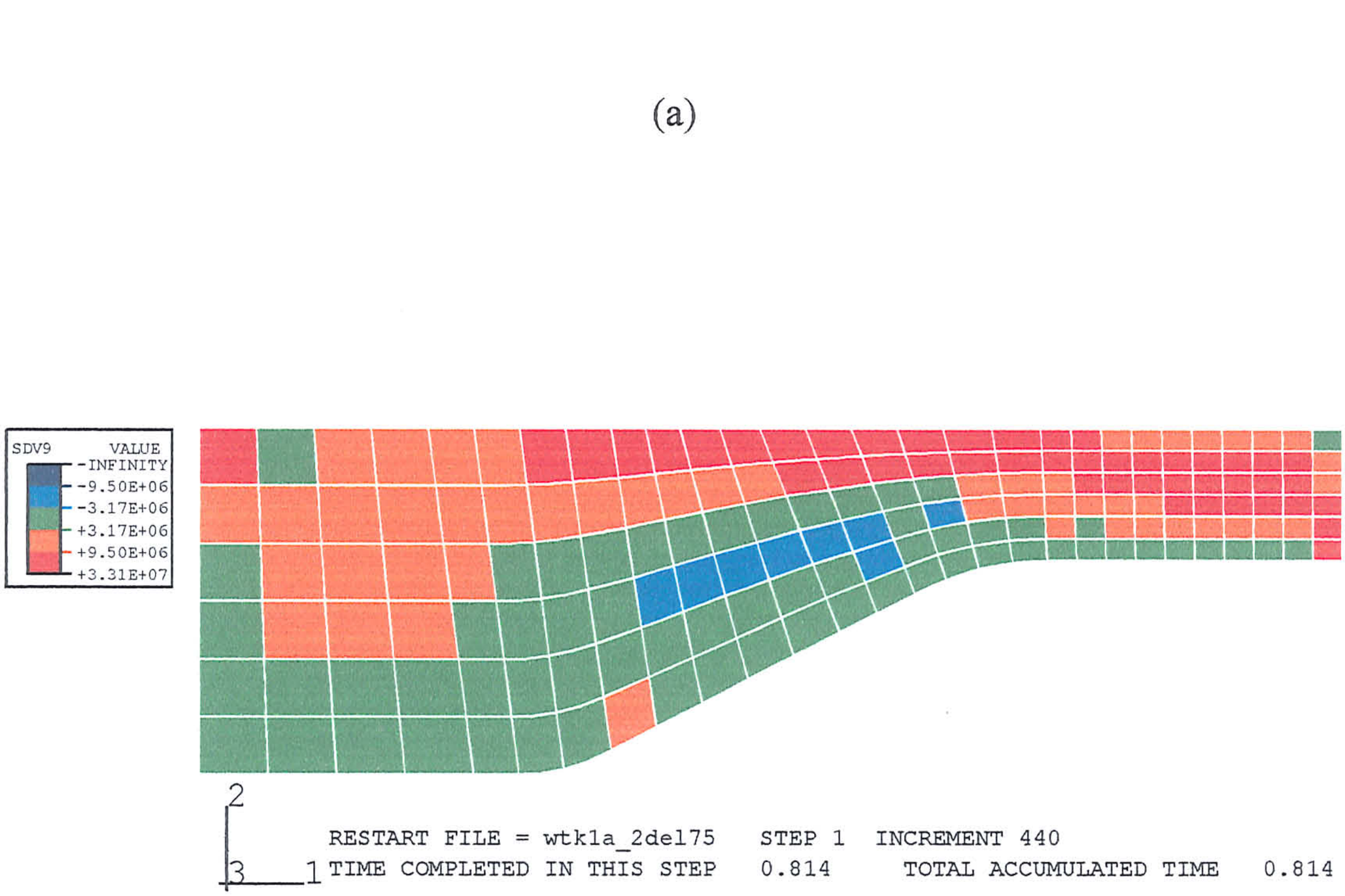

(b)

Fig 8.3.2.2-6 The shear band (red) of the wedge-shaped composite bar plotted in the (a) composite and (b) fibre position system.

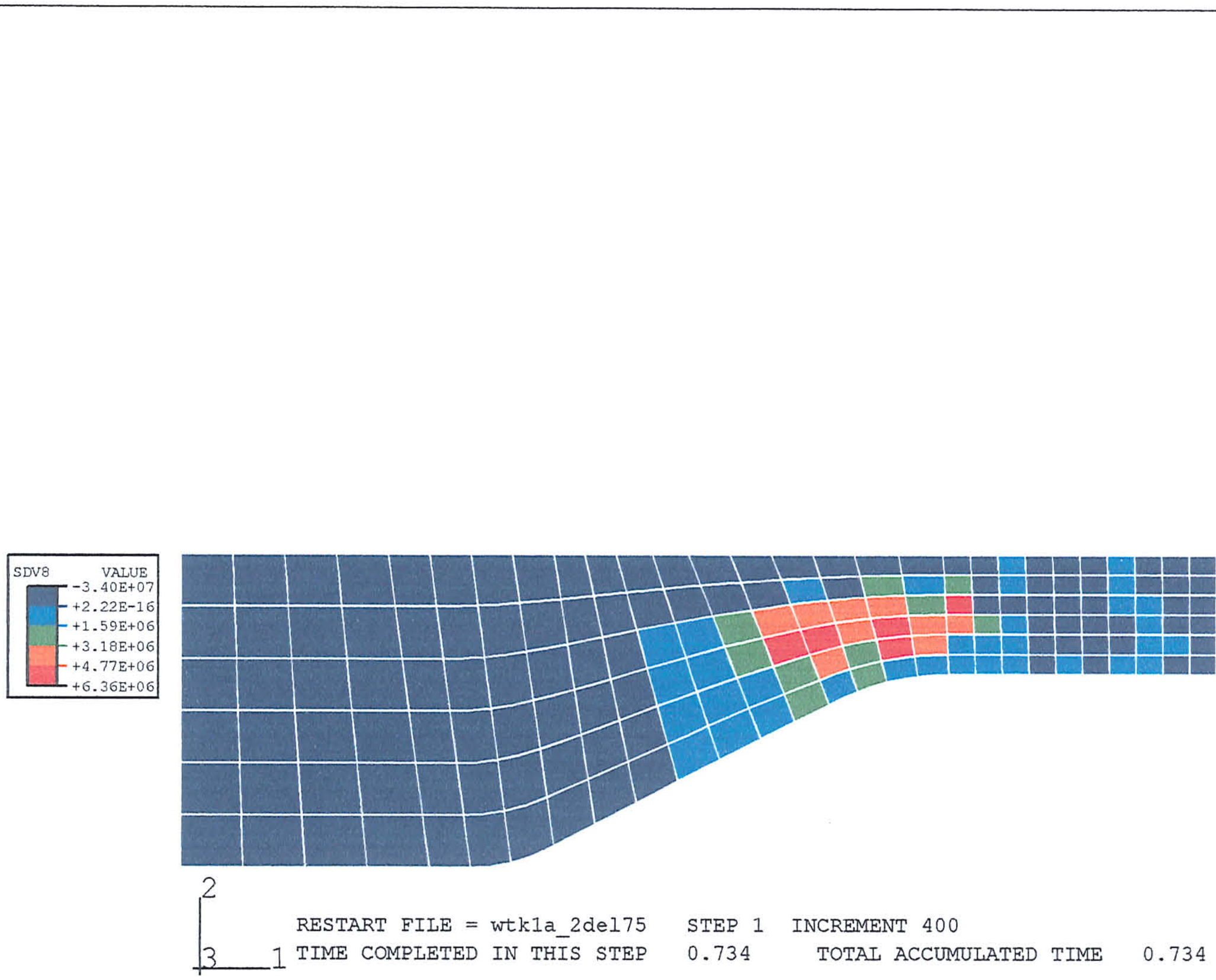

Fig 8.3.2.2-7 Contour plot of the stress normal to the fibre alignment during three-point bending of the two-dimensional reinforced wedge-shaped polyester composite bar.

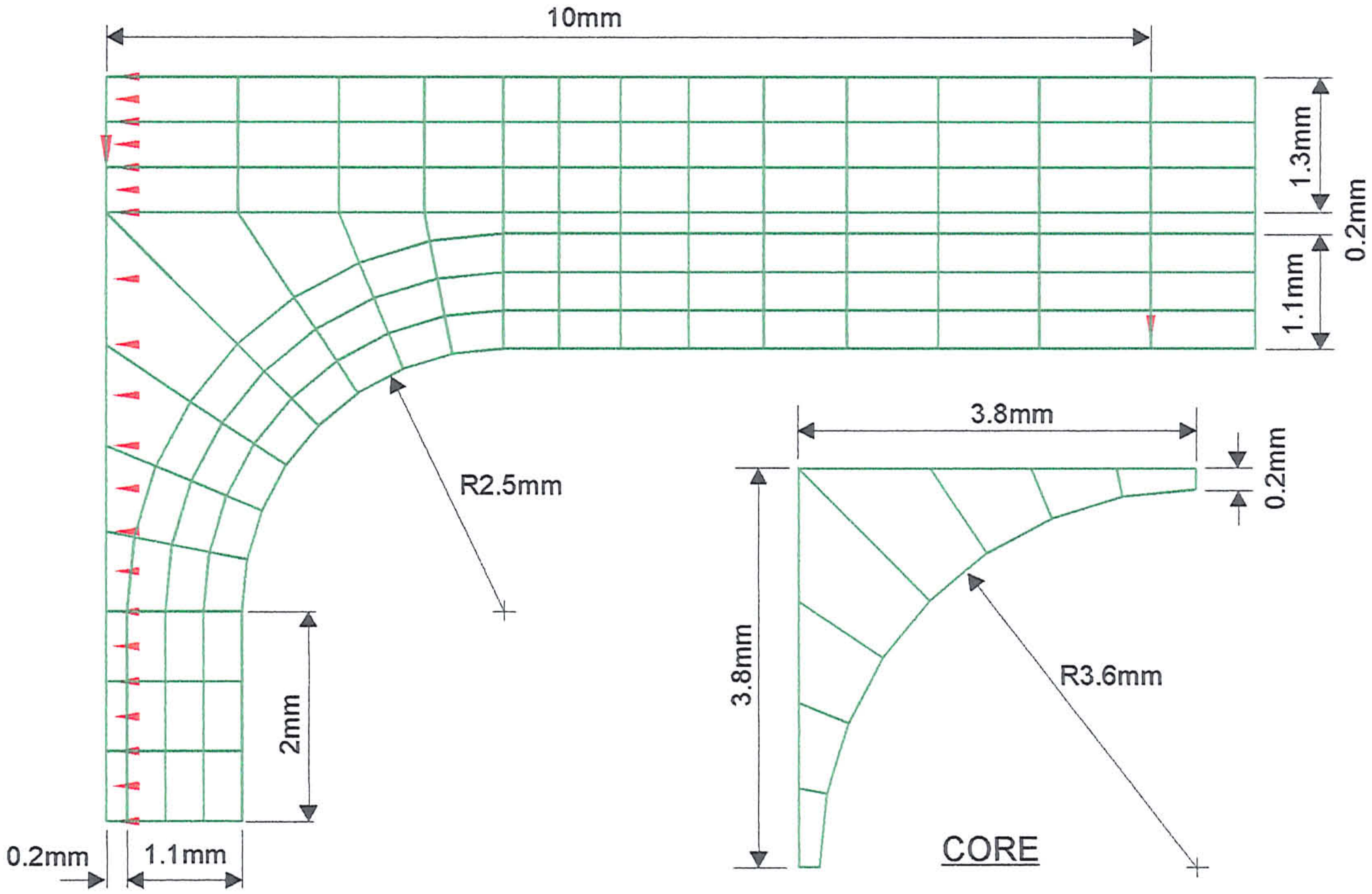

Fig 8.3.3.1-1 The half-sectioned mesh of the T-shaped bars with one and two-dimensional reinforcement.

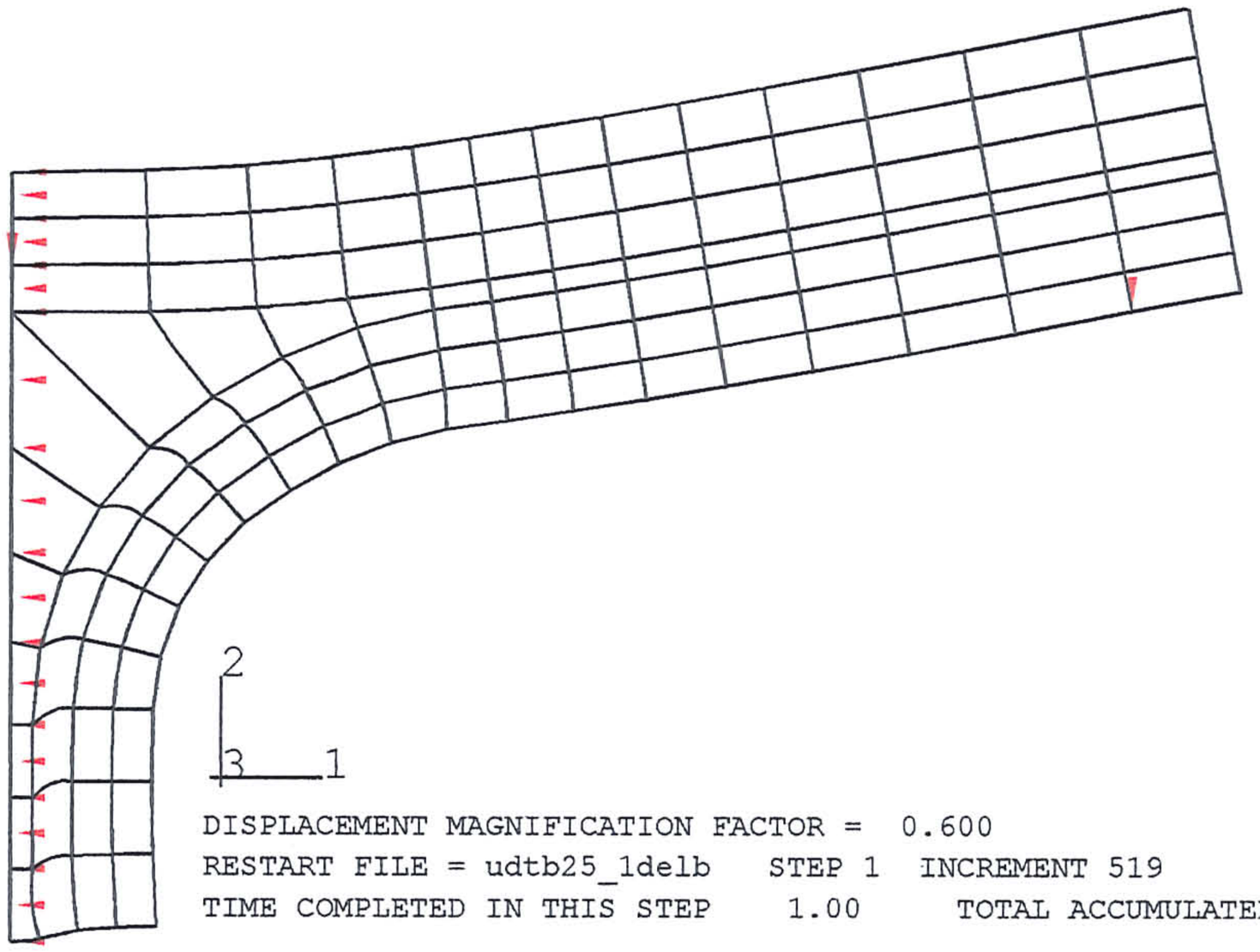

(a)

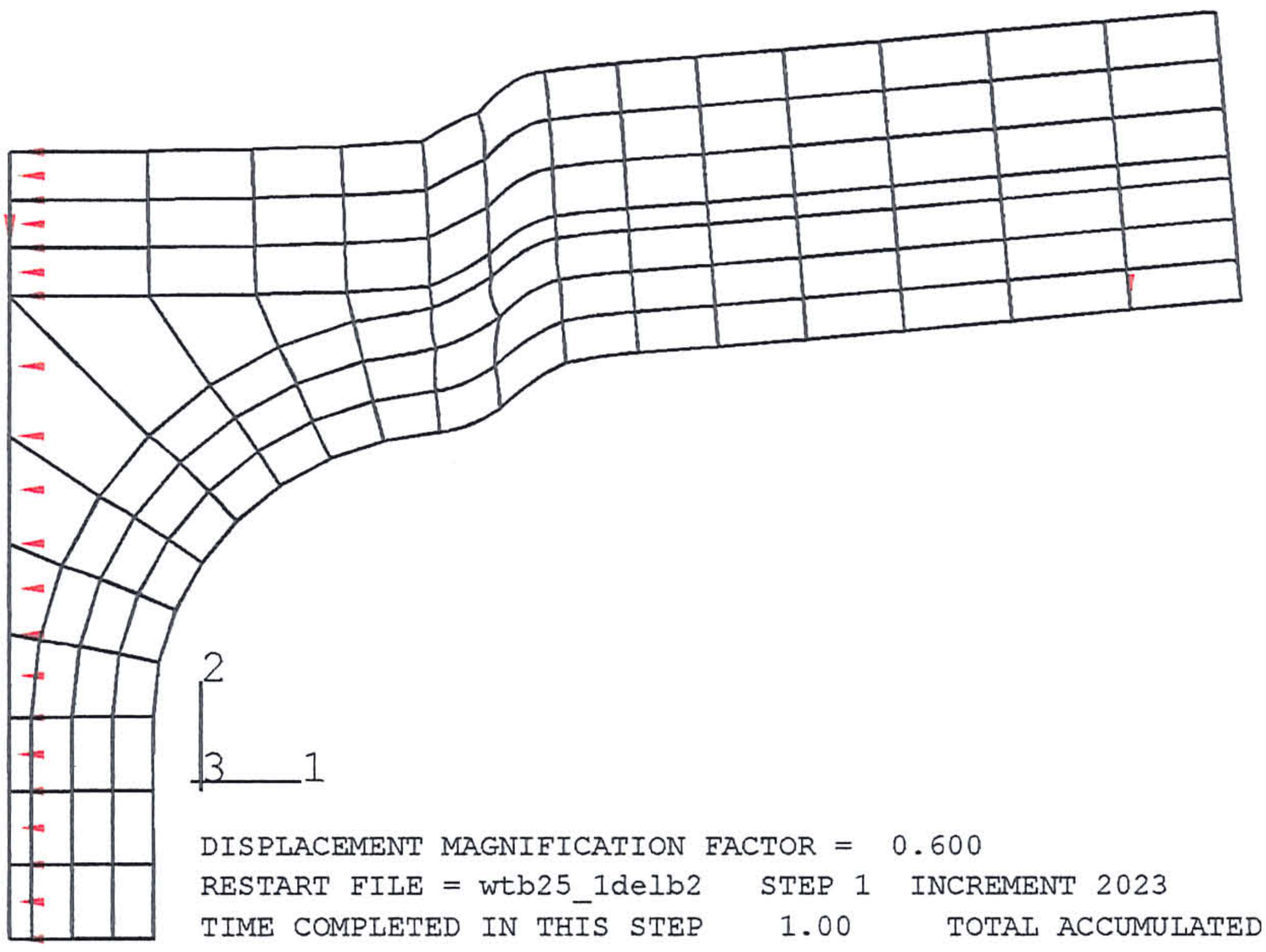

(b)

Fig 8.3.3.2-1 Deformed mesh of the T-shaped bar modelled with (a) one and (b) two-

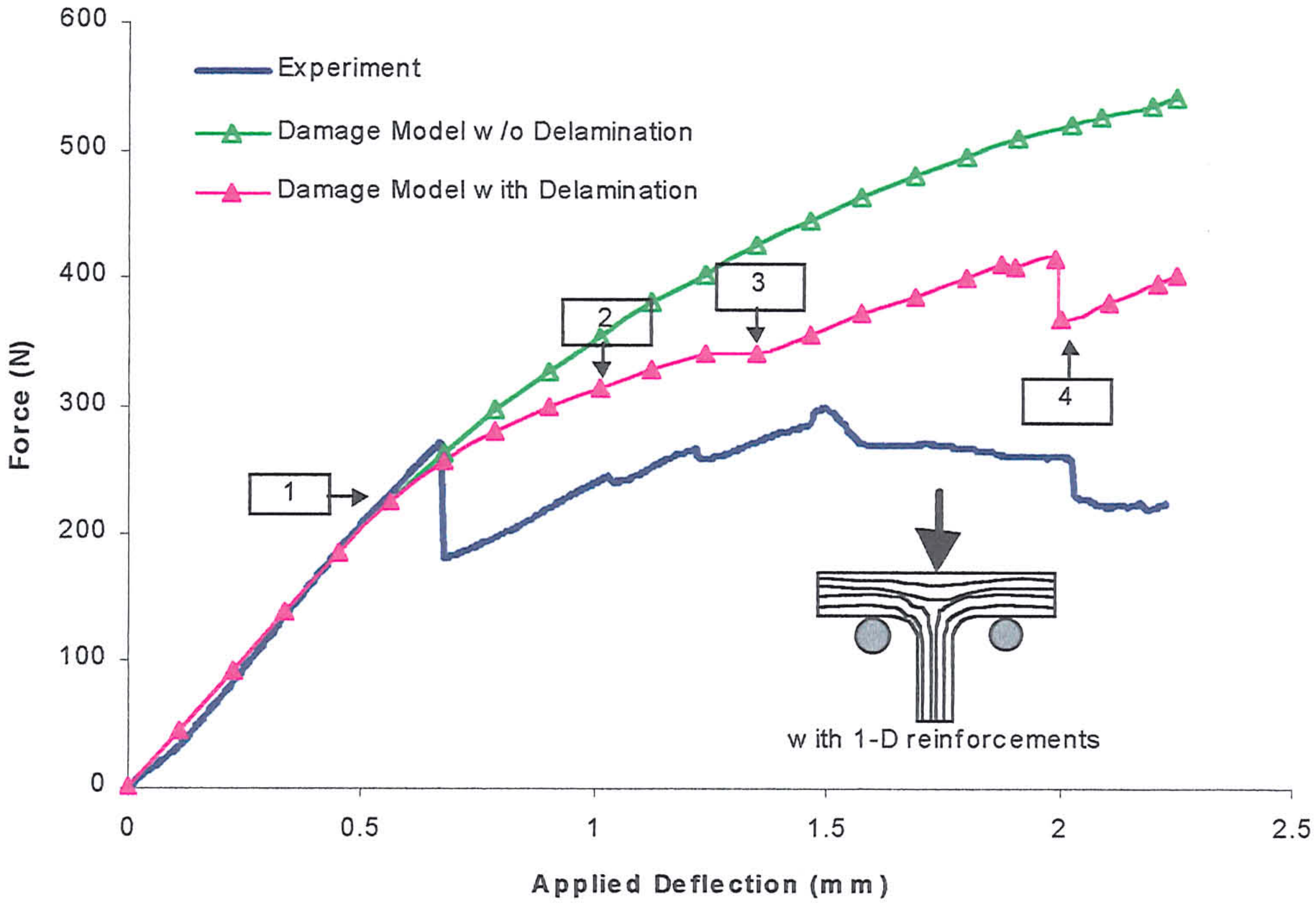

(a)

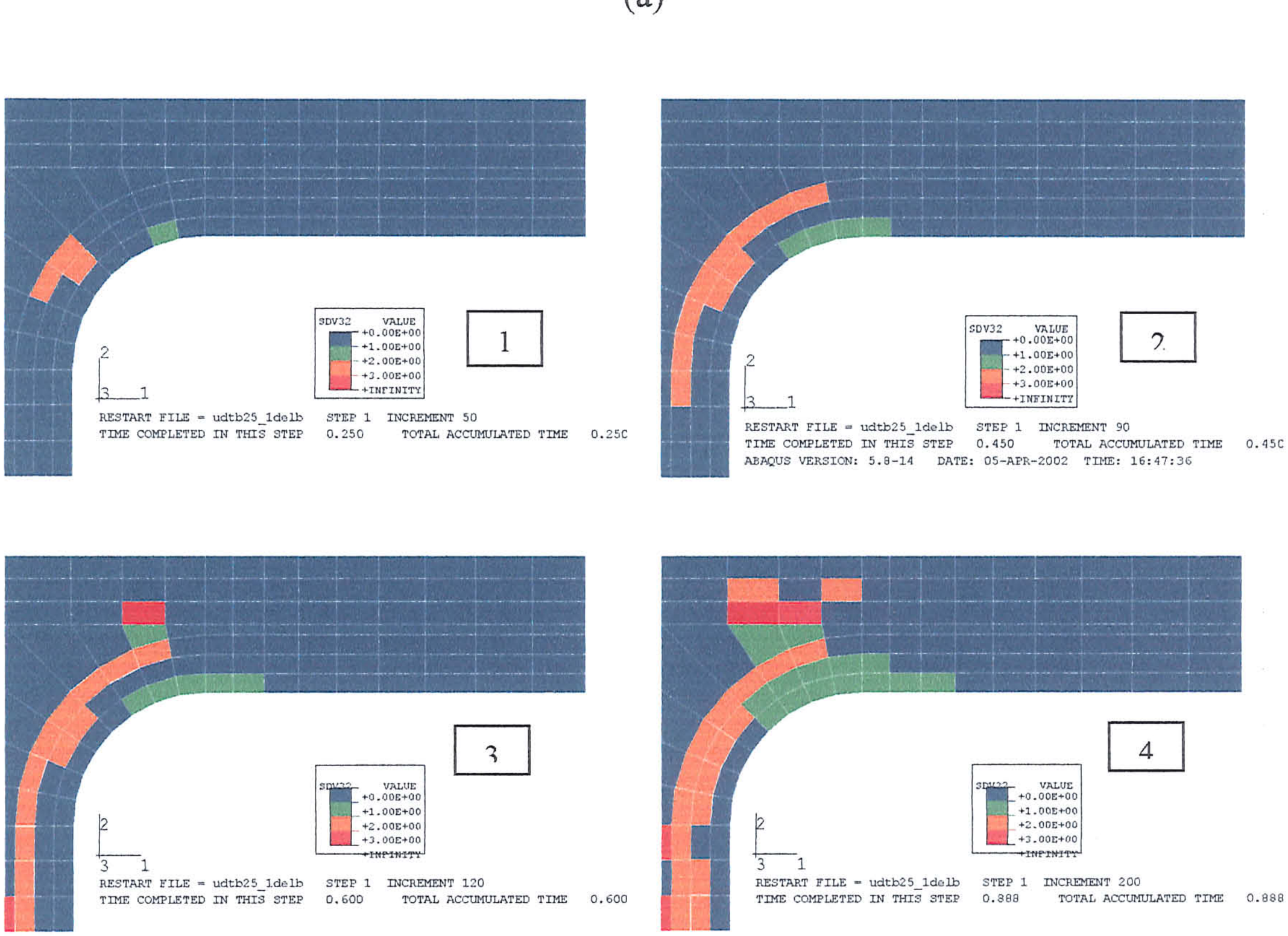

(b)

Fig 8.3.3.2-2 The predicted (a) force-deflection responses and (b) developed damage

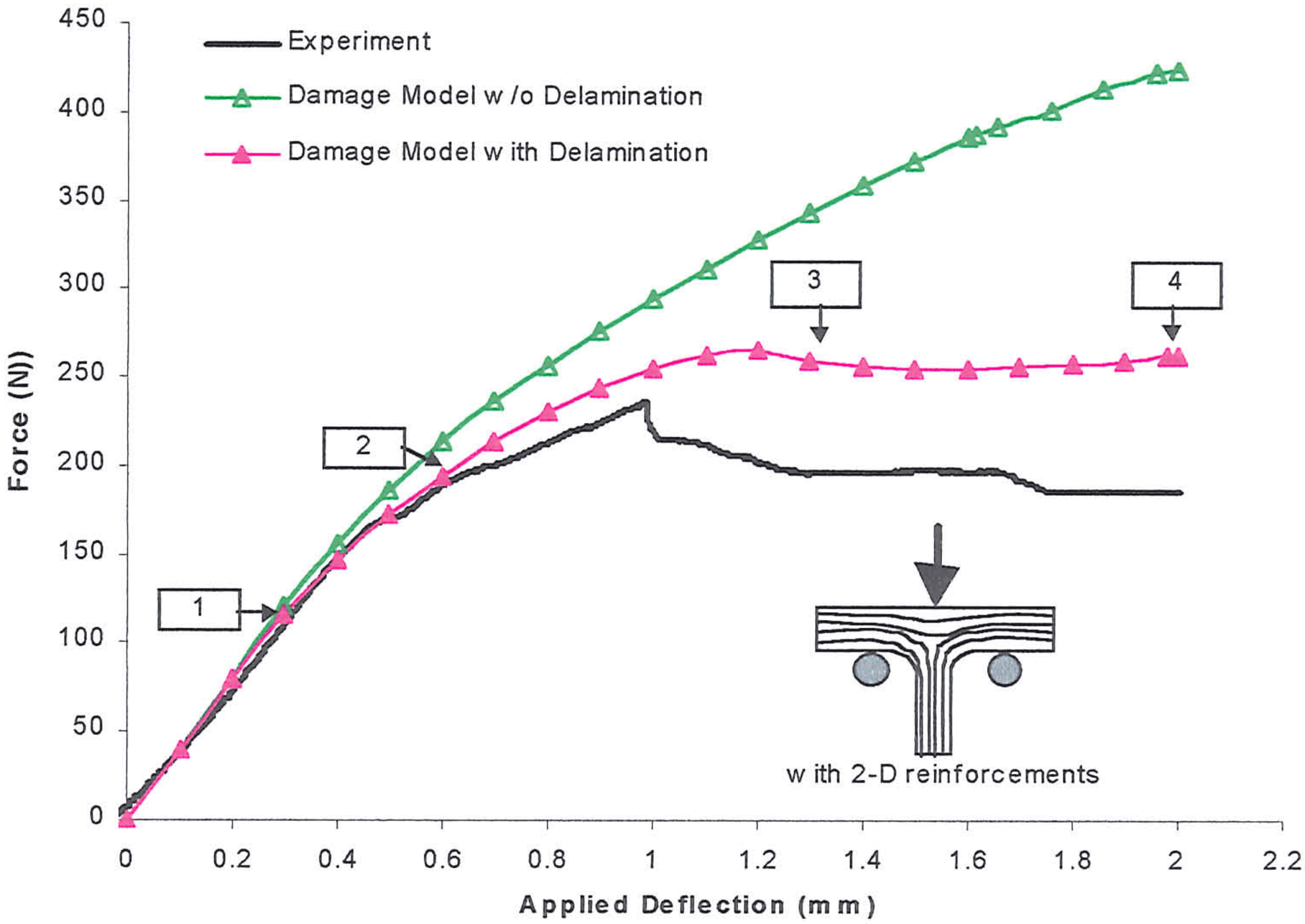

(a)

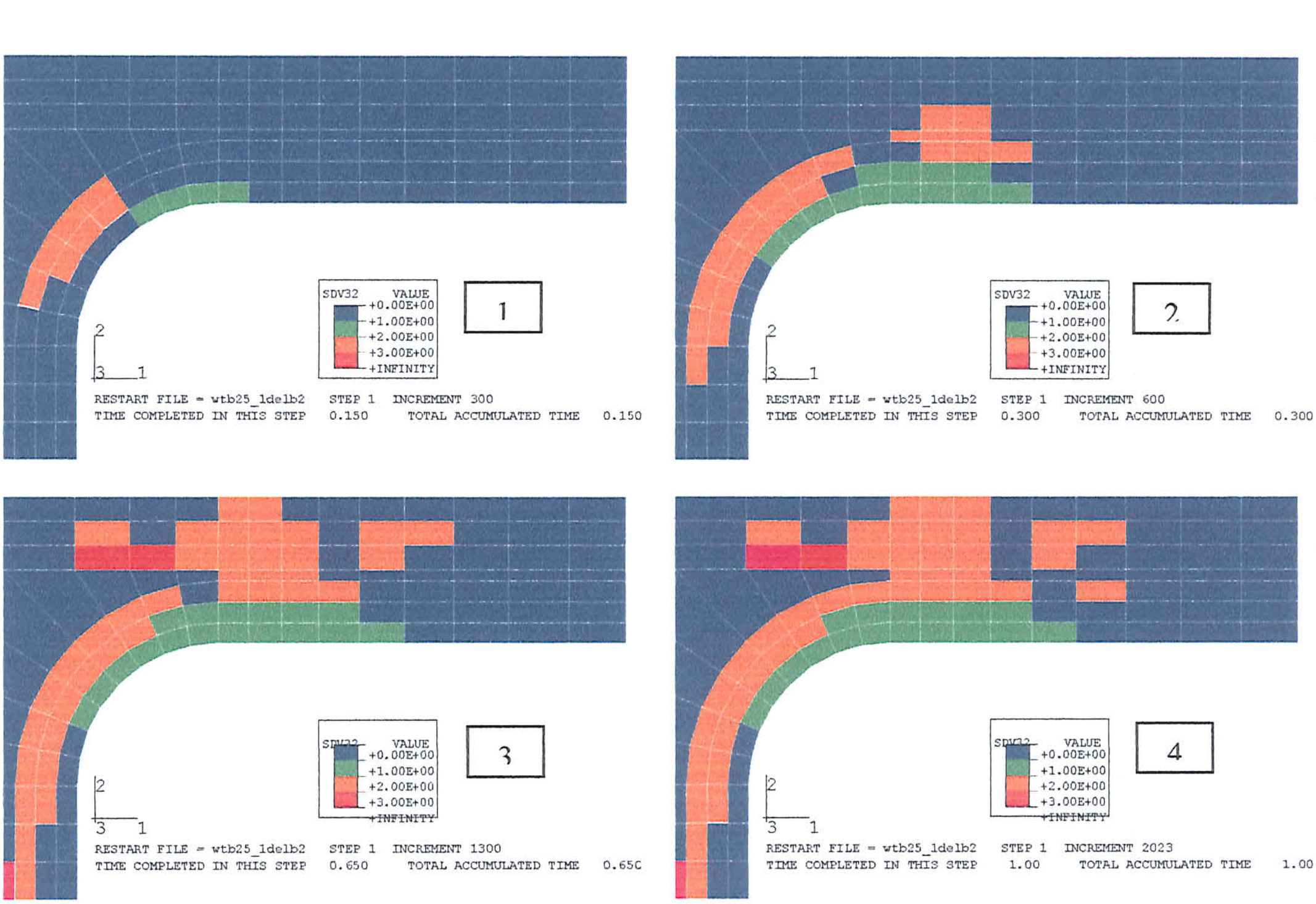

(b)

Fig 8.2.3.2.3 The predicted (a) force-deflection responses and (b) developed damage

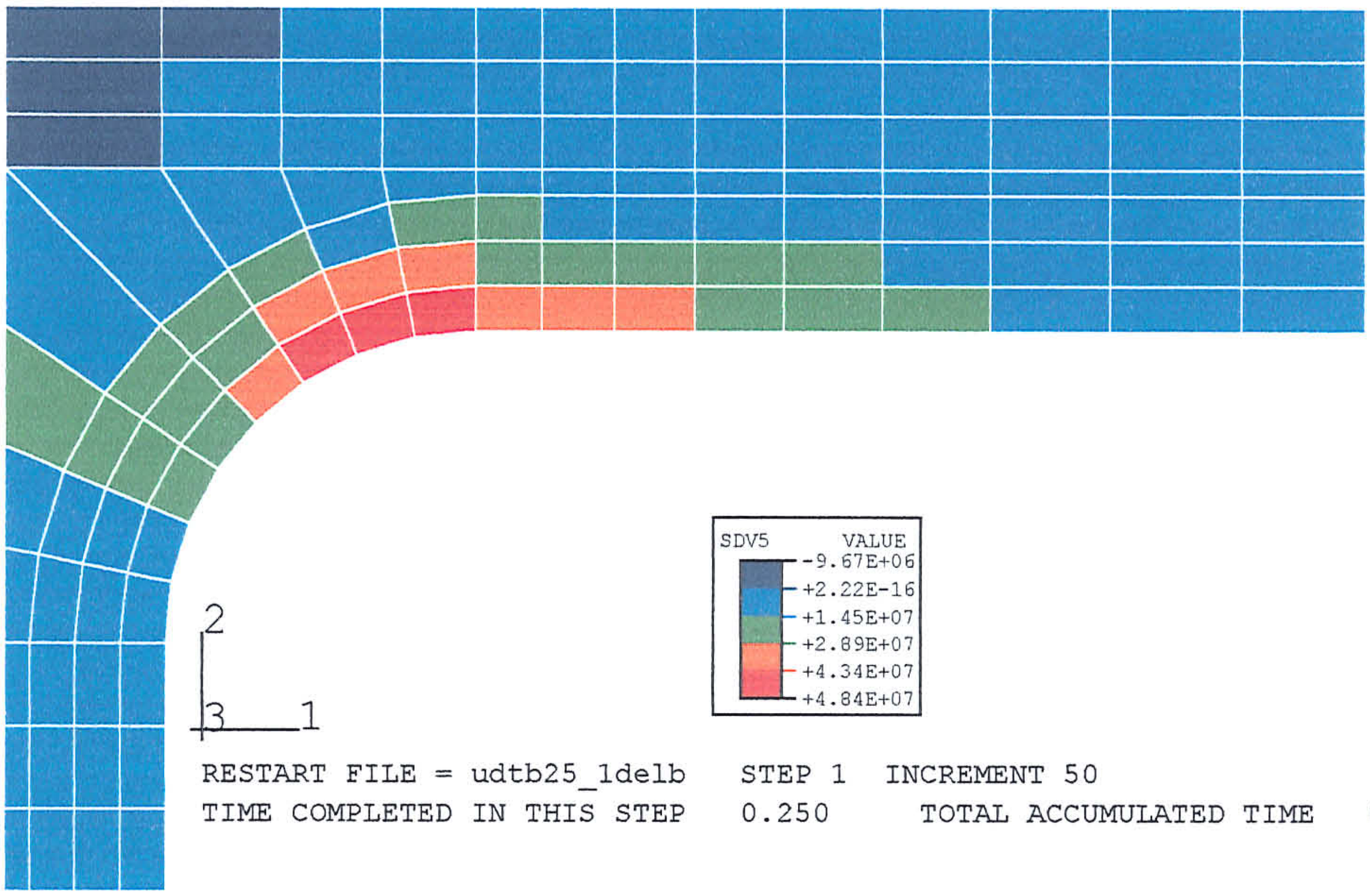

Figs 8.3.3.2-4 Contour plot of the matrix maximum principal stress after matrix cracking initiation.

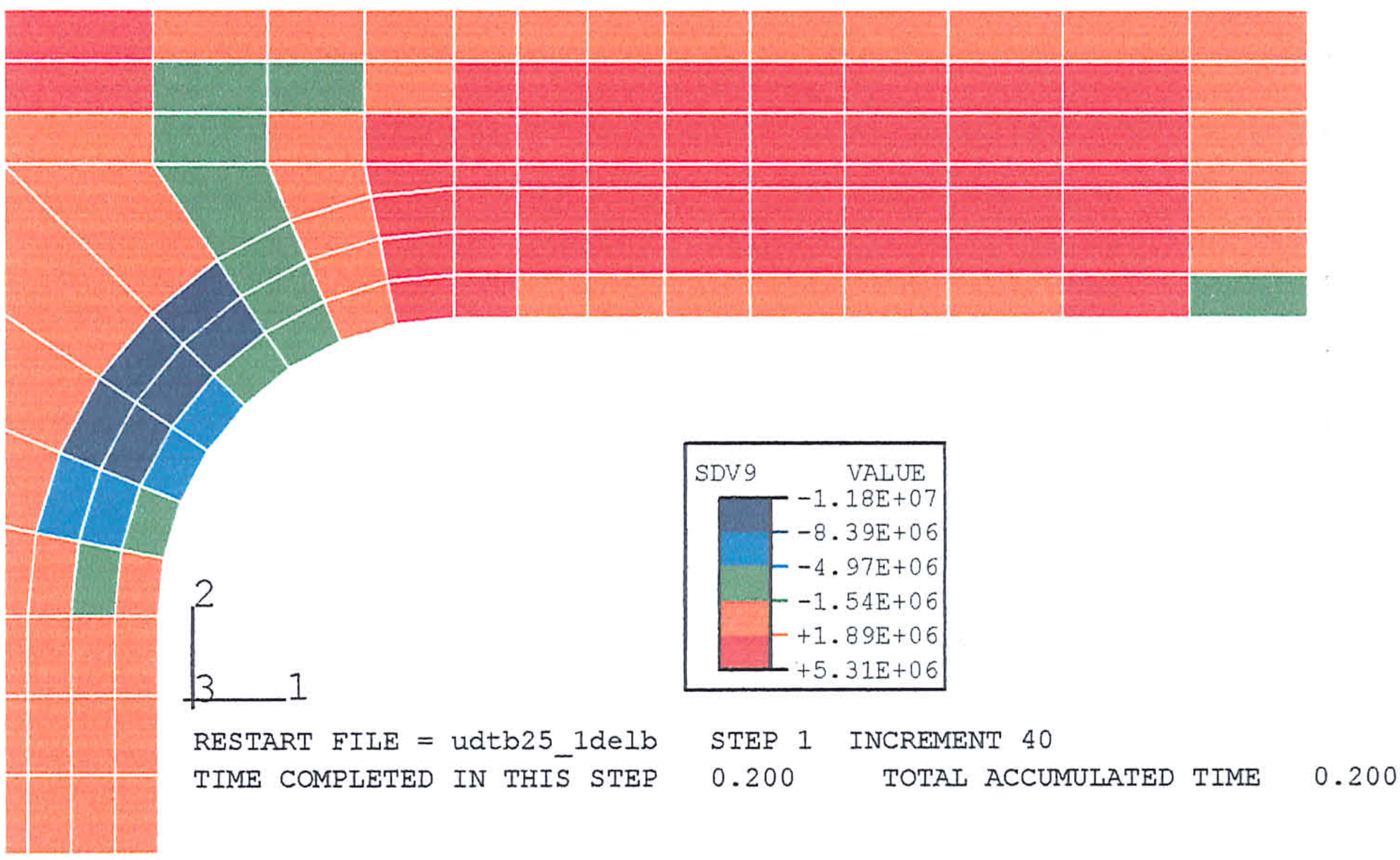

Figs 8.3.3.2-5 Contour plot of the matrix shear stress in the fibre position system before damage initiation.

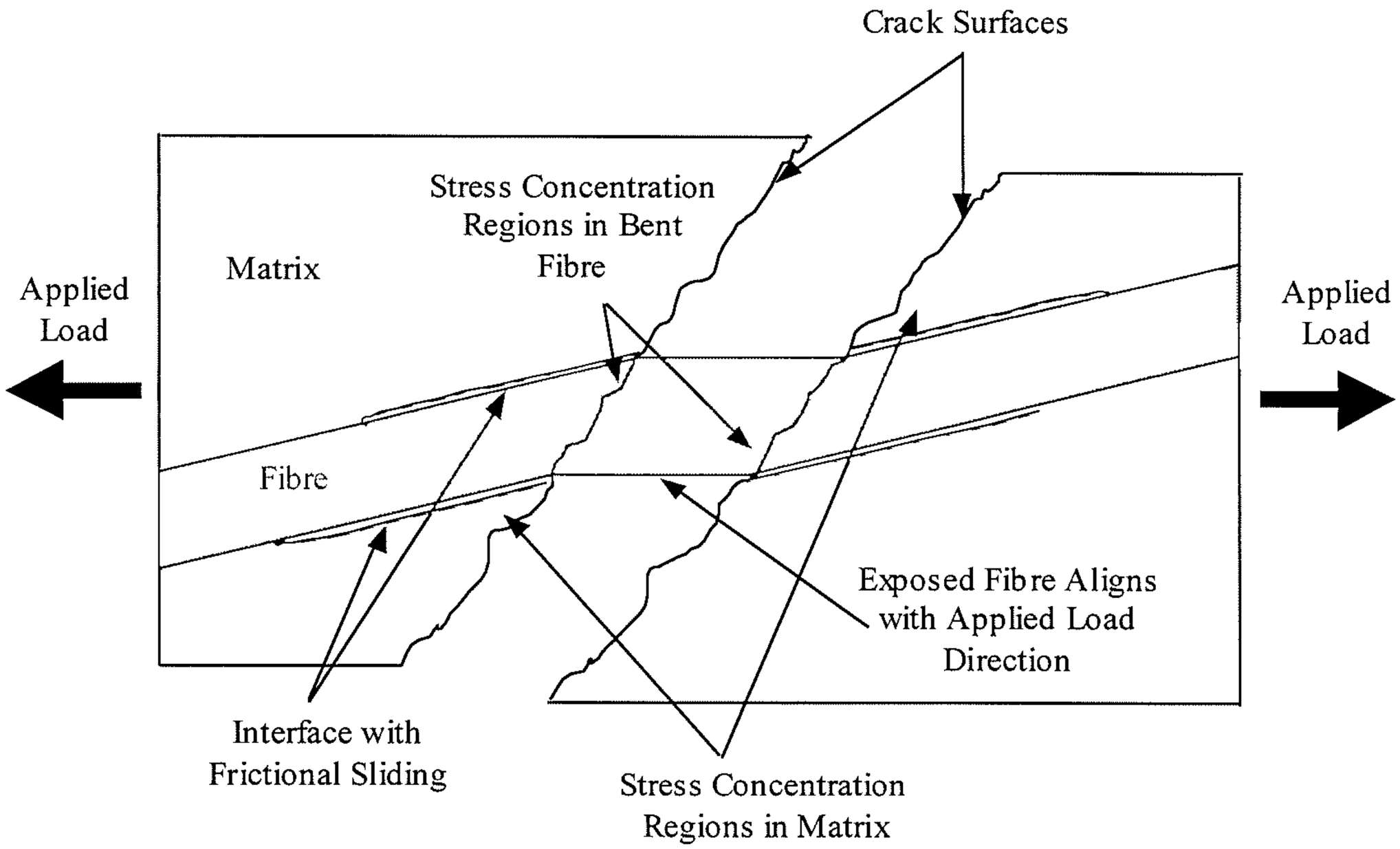

Fig 8.4.1-1 Localized fibre bending at the matrix crack plane of a composite with misaligned fibres.

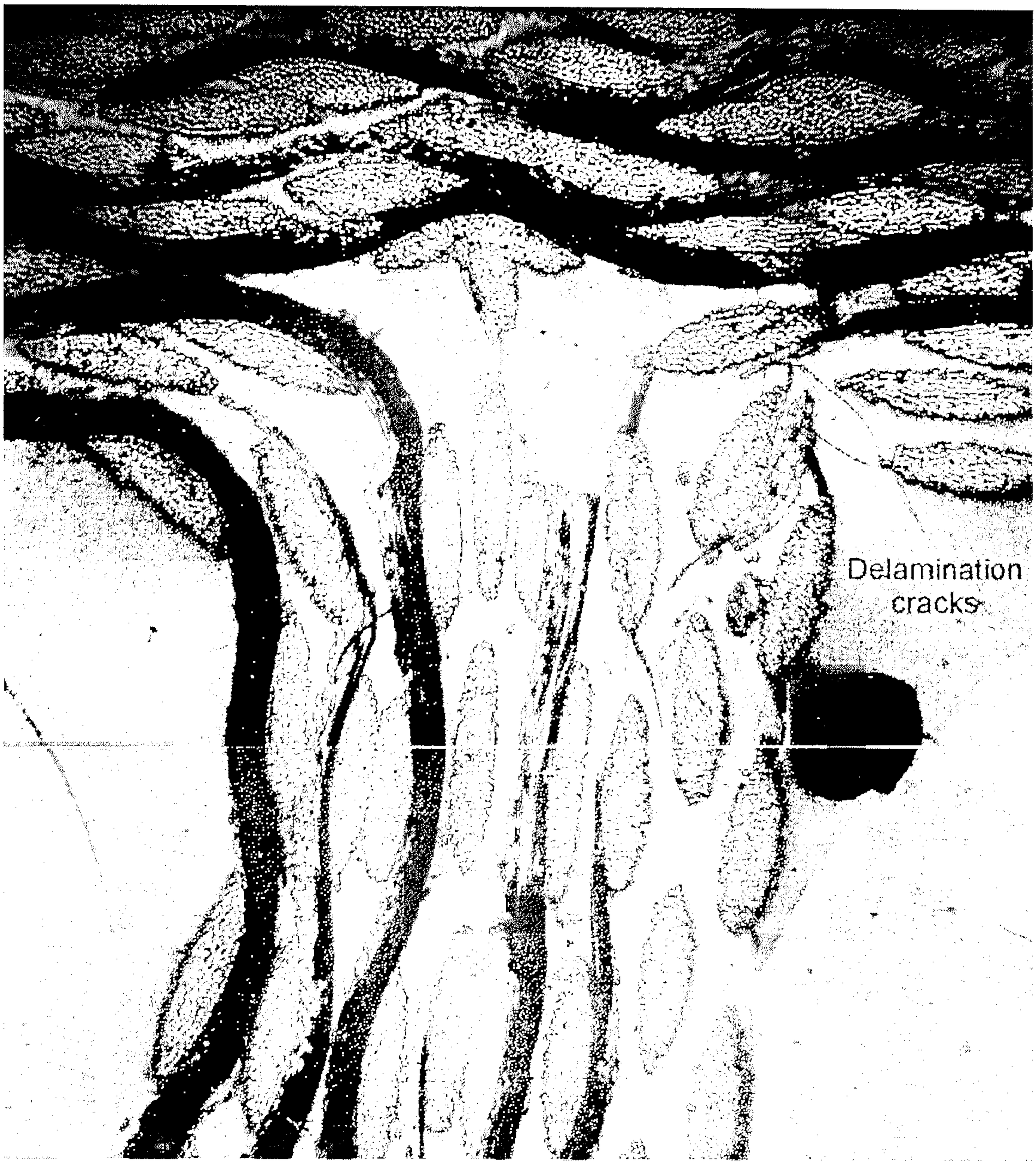

Fig 8.4.2-1 Micrograph of the tensile delaminated polyester/polyester T sub-structure three-point bent by McCafferty (1994).

CHAPTER 9

Modelling Imperfect Interfaces

9.1 Introduction

The development of composites has introduced structural integrity problems which depends on the properties of the interface between the phases. The hypothesis is that interfaces may posses a range of properties between perfectly bonded and completely unbonded. Intermediate states maybe formalised by considering an interface with a periodic array of cracks. As the area fraction of cracks changes from zero to one, the behaviour of the interface changes from being perfectly bonded to being de-cohered. The formality of representing an imperfect interface as one containing a periodic array of interfacial cracks can be rationalised in two ways. Firstly, it is reasonable to regard this as a physical model of an interface, which is strongly bonded in some sites and weakly bonded in others. Alternatively, at a larger size scale, it is possible to smear the specific cracks into a continuum description of an interface, which can have a range of strengths. With this hypothesis, the work initially examines the properties of interface containing an infinite periodic arrays of cracks, as a preface to modelling interface properties due to imperfection as a continuum.

The *line-spring* concept first developed by (Rice & Levy, 1972) will be extended to model the properties of imperfect interfaces at a continuum level. Line springs are a computationally efficient tool for modelling complicated three-dimensional fracture mechanics problems. The technique allows a three dimensional surface crack to be represented by one-dimensional line-springs with traction-displacement relations corresponding to the stiffness contribution of the crack. Comparison with the full three dimensional solutions such as Raju & Newman (1979) shows the stress intensity factor K_I obtained by line-springs to be within 3.5% of the full three-dimensional solution over the range of maximum relative crack depths to plate thickness of 0.2 to 0.6. The study demonstrates that the line-springs is an effective compromise between cost and a full three-dimension description of crack problems. In developing line-springs for modelling

provide data on interfacial stress concentrations, stress intensity factors $K_{n,}$ and strain energy release rates $\mathcal{G}$ of elastic interface cracks. Secondly, its application to composites is intended to provide a quantitative description of losses in stiffness due to imperfectly bonded interfaces.

9.2 An Imperfect Interface Model

9.2.1 The Model

The analysis is based on the hypothesis that interfacial imperfection can be represented as an infinite periodic array of co-linear cracks located on the interface between a matrix and a substrate as shown in Fig. 9.2.1-1. For simplicity, the substrate is assumed to be rigid while the matrix is deformable. The length of the cracks is denoted by a and the separation of the crack tips is W-a, where W is the width of a representative unit cell of an infinite interface (shaded). The area fraction of the cracked interface, β, (which is a measure of interface damage) is defined as the ratio of the crack length a to the cell width W.

9.2.2 Mesh Design and Boundary Conditions

Finite element meshes of the representative unit cell with crack area fractions β = 0.25, 0.50, 0.75 and 0.90 are presented in Fig 9.2.2-1. The unit cell comprised 500 to 1200 second-order isoparametric plane strain solid quadrilateral elements while the rigid substrate was modelled by fully restraining the interface nodes. The interfacial length of the matrix cell is denoted L and its width W. The aspect ratio W/L of all the meshes was 1/3. The smallest elements at the crack tip were approximately $3\text{x}10^{-4}$ W.

The meshes were subjected to a series of load cases representing tension, shear, and mixed-mode loading by displacing the nodes at the top of the meshes at angles θ = 0°, 30°, 45°, 60°, 80° & 90° to the global 2 axis. Periodic boundary conditions were imposed by enforcing identical but undefined displacements on the transverse sides of the matrix cell. The matrix is treated as elastic with Young's modulus E set at 3.0E11 and Poisson's ratios set at v = 0.49.

9.2.3 Numerical Results

The elastically deformed unit cells for $\beta = 0.25$, 0.50, 0.75 and 0.90 during mode I and II displacement loading are given in Fig 9.2.3-1 for $v = 0.49$. The deformed meshes demonstrate that the imperfect unit cells dilated by void growth under mode I and mixed-mode loadings, while no dilation occurred in pure mode II loading. The total reaction force and stiffness of the unit cells when subjected to a pure mode I and pure mode II displacement of 200 units are given in Table 9.2.3-1. To normalise the numerically determined stiffnesses, the stiffness of the matrix for a perfectly bonded interface was used. In mode I, the normalising stiffness was obtained by multiplying the matrix bulk modulus $B = E/3(1 - 2v)$ with the aspect ratio of the unit cells (W/L). In mode II, the normalising stiffness was obtained by multiplying the matrix shear modulus $G = E/2(1 - v)$ with W/L. The normalised stiffnesses are plotted in Fig 9.2.3-2 as a function of crack area fraction β. The figure shows that the normalised mode I stiffness of the interface decreases as β increases while the normalised mode II stiffness is unaffected by β, accept when β approaches 1. The the normalised mode I stiffness of the interface as a function of β can be approximated as:

$$\frac{k_{1'1'}}{k_{o\mathrm{I}}} = -8.3865\beta^5 + 17.433\beta^4 - 10.642\beta^3 + 1.0644\beta^2 - 0.4683\beta + 1 \qquad (9.2.3\text{-}1)$$

where $k_{o\mathrm{I}}$ is the mode I stiffness of the perfect interface.

Cracks Area Fraction β	Mode I			Mode II		
	Reaction Force	Stiffness	*Normalised Stiffness	Reaction Force	Stiffness	+Normalised Stiffness
0	342×10^{12}	1.71×10^{12}	1.03	6.70×10^{12}	33.6×10^{9}	1.00
0.25	281×10^{12}	1.41×10^{12}	0.84	6.68×10^{12}	33.4×10^{9}	1.00
0.50	176×10^{12}	0.882×10^{12}	0.53	6.76×10^{12}	33.8×10^{9}	1.01
0.75	94.5×10^{12}	0.472×10^{12}	0.28	6.54×10^{12}	32.7×10^{9}	0.98
0.90	56.0×10^{12}	0.280×10^{12}	0.17	6.10×10^{12}	30.5×10^{9}	0.91
1.0	0	0	0	0	0	0

* The normalising mode I stiffness $k_{o\mathrm{I}} = 1.67 \times 10^{12}$.
\+ The normalising mode II stiffness $k_{o\mathrm{II}} = 33.6 \times 10^{9}$.

Table 9.2.3-1 The mode I and mode II reaction forces and stiffnesses of the unit cell models for an applied displacement of 200 units.

$$A_v = \frac{\pi a b}{2} \qquad (9.2.3\text{-}2)$$

in which a and b denote the crack surface distances on the principal axes of the void as shown in Fig 9.2.3-3. In Table 9.2.3-2, the void area as a function of crack area fraction during mode I loading is given.

Cracks Area Fraction β	Unit Cell Model			Interface Model		Error
	a	b	A_v (unit^2)	$u_{1'(i)}$	A_v (unit^2)	%
0.25	125	182	35.7 x 10^3	32.6	32.6 x 10^3	-10.09
0.50	250	247.3	97.1 x 10^3	95.5	95.5 x 10^3	-1.43
0.75	375	244.2	143.8 x 10^3	144.4	144.4 x 10^3	+0.32
0.90	450	229.3	162.1 x 10^3	167.2	167 x 10^3	+3.16

Table 9.2.3-2 The void area of the unit cell model and the interface model for mode I loading of an applied displacement of 200 units

9.3 The Interfacial Element

The one-dimensional spring-like element (JOINT2D) implemented in ABAQUS/Standard (HKS, 1998a) was used to develop the interface element. To validate its use, it is necessary to benchmark the interfacial element stiffness as a function of the crack area fraction. A simplified interface model of the unit cell models of Sect. 9.2.1 was developed for benchmarking and is shown in Fig. 9.3-1. The undamaged matrix was represented using a first-order plane-strain continuum element with a aspect ratio (W/L) of 1/3, while the damage interface was represented using two zero length interfacial elements pinned to a rigid surface. The mechanical properties and boundary conditions are defined in Sect. 9.2. The local $1'$ & $2'$ position system of the interfacial element and the global 1-2 position system of the model are also shown in Fig 9.3-1.

The interfacial element is conceptually similar to the *elastic line-spring* introduced by Rice & Levy (1972). This requires the introduction of a stiffness as a function of the crack area fraction β. The elastic in-plane force-displacement relations of the interfacial element are modelled through the expression:

$$\begin{Bmatrix} V \end{Bmatrix} = \begin{bmatrix} k_{1'1'} & 0 \end{bmatrix} \begin{Bmatrix} u_{1'} \end{Bmatrix} \qquad (9.3.1)$$

Here, V denotes the axial load in the local $1'$ direction and H denotes the normal load in the local $1'$-$2'$ plane. The symbols $k_{1'1'}$ and $k_{2'2'}$ denote the corresponding axial and transverse stiffnesses of the interfacial element while symbols $u_{1'(i)}$ and $u_{2'(i)}$ denotes the displacement components of the interface element in the local position system.

The total displacement u_{Total} of the interface model shown in Fig. 9.3-1 is given as:

$$u_{Total} = u_{(i)} + u_{(m)} \tag{9.3.2}$$

in which $u_{(m)}$ denotes the remote displacement of the matrix for a perfectly bonded interface. The remote displacement components of the matrix are determined by considering a simple homogeneous state of stress in the matrix cell, i.e.:

$$u_{1'(m)} = \frac{F_{1'}}{B} \times \frac{L}{W} \qquad u_{2'(m)} = \frac{F_{2'}}{G} \times \frac{L}{W} \tag{9.3.3}$$

in which $F_{1'}$ and $F_{2'}$ are the remote loads in the local $1'$ & $2'$ position system.

To benchmark the elastic interfacial elements, the simplified interface model shown in Fig 9.3-1 was subjected to a remote pure mode I and pure mode II displacement of 200units. The deformed meshes are shown in Fig 9.3-2. The stiffnesses of the interface element used in the benchmark are given in Table 9.3-1. The stiffnesses were determined using eqns (9.3.1 to 3). The predicted reaction forces and stiffnesses of the simplified interface model are given in Table 9.3-2. The corresponding normalised stiffnesses of the imperfect interface model are compared with the unit cell models in Fig. 9.3-3. In addition, a comparison of the void area predicted by the interface model and unit cell model is given in Table 9.2.3-2. The results show good agreement between the estimates from the interface model and the unit cell model, which establishes the interfacial element as an acceptable representation of the imperfect interface under elastic deformation.

Cracks Area Fraction β	$k_{1'1'(i)}$	$k_{2'2'(i)}$
0	1×10^{20}	1×10^{20}
0.25	4.47×10^{12}	3.57×10^{12}
0.50	0.932×10^{12}	2.17×10^{12}
0.75	0.330×10^{12}	0.640×10^{12}
0.90	0.168×10^{12}	0.167×10^{12}
1.0	1×10^{-20}	1×10^{-20}

Cracks Area Fraction (β)	Mode I			Mode II		
	Reaction Force	Stiffness	Normalised Stiffness	Reaction Force	Stiffness	Normalised Stiffness
0	342×10^{12}	1.71×10^{12}	1.03	6.71×10^{12}	3.36×10^{10}	1.00
0.25	287×10^{12}	1.44×10^{12}	0.86	6.68×10^{12}	3.34×10^{10}	1.00
0.50	179×10^{12}	0.894×10^{12}	0.54	6.66×10^{12}	3.33×10^{10}	0.99
0.75	95.2×10^{12}	0.476×10^{12}	0.29	6.54×10^{12}	3.27×10^{10}	0.97
0.90	56.2×10^{12}	0.281×10^{12}	0.17	6.10×10^{12}	3.05×10^{10}	0.91
1.0	0	0	0	0	0	0

* The normalising mode I stiffness $k_{oI} = 1.67 \times 10^{12}$.
\+ The normalising mode II stiffness $k_{oII} = 33.6 \times 10^{9}$.

Table 9.3-2 The mode I and mode II reaction forces and stiffnesses of the interface model for an applied displacement of 200 units.

9.4 The Fibre Problem

9.4.1 General

In fibre-reinforced composites, the mechanical properties of the composite normal to the fibre axis depend on the integrity of the fibre-matrix interface. The interfacial element developed in Sect. 9.3 has the potential to quantify the degradation in mechanical properties and its use is explored in this section.

A unit cell model of the composite is schematically shown in Fig. 9.4.1-1. The model approximates the infinite medium solution for an embedded inclusion developed by Goodier (1933). The fibre can be modelled as a rigid cylindrical inclusion embedded in a deformable matrix that is infinite and the imperfect interface can be represented by an array of periodic cracks. The figure shows the cylindrical position system used following Goodier (1933). The cylindrical co-ordinates (r, ω) are located at the centre of the fibre and the direction of the remotely applied tensile stress σ_∞ under plane strain condition is at $\omega = 0$.

9.4.2 Stress Concentration Fields

9.4.2.1 Perfect Interface

Goodier (1933) has analysed the stress fields near a rigid cylindrical inclusion

Fig. 9.4.1-1). Subject to a remotely applied uniaxial tensile stress σ_∞ at $\omega = 0$, the stress field in the matrix is given by:

$$\sigma_{rr} = 2G\left[-\frac{A}{r^2} + \left(3\frac{B}{r^4} - 2\frac{C}{r^2}\right)\cos 2\omega\right] + \frac{\sigma_\infty}{2}(1 + \cos 2\omega)$$

$$\sigma_{\omega\omega} = 2G\left[\frac{A}{r^2} - \left(3\frac{B}{r^4}\right)\cos 2\omega\right] + \frac{\sigma_\infty}{2}(1 - \cos 2\omega) \qquad (9.4.2.1.1)$$

$$\sigma_{r\omega} = 2G\left(-3\frac{B}{r^4} + 2\frac{C}{r^2}\right)\sin 2\omega - \frac{\sigma_\infty}{2}(\sin 2\omega)$$

where v denote Poisson's ratio and G is the elastic shear modulus. The constants A, B, C are defined as:

$$A = -\frac{\sigma_\infty R^2}{4G}(1 - 2v)$$

$$B = -\frac{\sigma_\infty R^4}{4G(3 - 4v)} \qquad (9.4.2.1.2)$$

$$C = -\frac{\sigma_\omega R^2}{2G}(3 - 4v)$$

in which R is the radius of the rigid inclusion. On the interface ($r = R$), the maximum radial and hoop stresses occur in the direction of the applied stress where $\omega = 0$. For incompressible deformation, i.e. $v = 0.5$, the maximum radial and hoop stresses at $\omega = 0$ reduce to:

$$\sigma_{rr} = \sigma_{\omega\omega} = 1.5\sigma_\infty \qquad (9.4.2.1.3)$$

The maximum shear stress at the interface is equal magnitude to the applied stress at $\omega = \pm 45°$.

9.4.2.2 Imperfect Interface

A finite element mesh of a symmetric half of the rigid inclusion problem is illustrated in Fig. 9.4.2.2-1. The ratio of the fibre radius R to the dimension of the matrix cell is 0.028 and the unit fibre volume fraction is 0.641E-3. The matrix consists of approximately 4100 first-order plane-strain continuum elements and the interface 64 interfacial elements.

For remote uniaxial tension, the deformed mesh for $v = 0.49$ with a perfect interface is shown in Fig 9.4.2.2-2. The corresponding finite element solution of the stress concentrations of the matrix near the rigid inclusion and at the interface are

stress concentrations agree well with Goodier's solution. The corresponding stress concentrations for different crack area fraction β undergoing near incompressible deformation (v = 0.49) are presented in Fig. 9.4.2.2-3 to Fig. 9.4.2.2-4. As the level of imperfection β increased from zero to 1.00, only small changes in stress concentrations are observed for all the stress components. In addition, the maximum hoop stress concentration is shown to be interpolated from $\omega = 0°$ to 90°.

9.4.3 The Interface Stress Intensity Factors K & Strain Energy Release Rates $\mathcal{G}$

To determine the stress intensity factors K and the strain energy release rates $\mathcal{G}$ associated with cracks on the interface of a rigid cylindrical fibre, the fracture modes of interfacial cracks under periodic conditions (see Sect 9.2) are examined. This can be achieved by considering the displacements between the free and rigid surfaces near the crack tip. The plots of the displacement ratios u_x/u_y as a function of the normalised distance from the crack tip x and crack length a are presented in Fig. 9.4.3-1. The sign conventions following Westergaard are shown in Fig. 9.4.3-2, in which x and y are the local right hand Cartesian system, r is the radial distance from the crack tip and the symbol θ denotes a positive anticlockwise angle from the local x-axis. The interfacial crack is shown to be mixed-mode when remotely tensioned or sheared.

For mixed-mode fracture, the displacement ratios u_x/u_y can define the crack tip stress intensity factor ratios K_{II}/K_I, which define the mixity of the crack tip singularity through Westergaard's equation of the crack tip displacement fields for mode I:

$$u_x = \frac{K_I}{2G}\sqrt{\frac{r}{2\pi}}\cos\left(\frac{\theta}{2}\right)\left[\kappa - 1 + 2\sin^2\left(\frac{\theta}{2}\right)\right]$$
$$u_y = \frac{K_I}{2G}\sqrt{\frac{r}{2\pi}}\sin\left(\frac{\theta}{2}\right)\left[\kappa + 1 - 2\cos^2\left(\frac{\theta}{2}\right)\right] \qquad (9.4.3.1)$$

and for mode II:

$$u_x = \frac{K_{II}}{2G}\sqrt{\frac{r}{2\pi}}\sin\left(\frac{\theta}{2}\right)\left[\kappa + 1 + 2\cos^2\left(\frac{\theta}{2}\right)\right]$$
$$u_y = -\frac{K_{II}}{2G}\sqrt{\frac{r}{2\pi}}\cos\left(\frac{\theta}{2}\right)\left[\kappa - 1 - 2\sin^2\left(\frac{\theta}{2}\right)\right] \qquad (9.4.3.2)$$

where for plane strain $\kappa = 3 - 4\nu$ and for plane stress $\kappa = (3 - \nu) / (1 + \nu)$. By substituting $\theta = 180°$ into (9.4.3-1) and (9.4.3-2),

$$\frac{u_1}{u_2} = \frac{K_{II}}{K_I} \qquad (9.4.3.3)$$

The ratio K_I/K_{II} is plotted in Fig. 9.4.3-3 as a function of the crack area fraction β.

Rice (1968) defined the energy release rates of linear elastic cracks through a path-independent contour integral J which is identical to the strain energy release rate, $\mathcal{G}$ introduced by Irwin (1956 & 1957). For cracks under mixed mode I & II loading, the strain energy release rate expressed in terms of stress intensity factors are related to J and $\mathcal{G}$ by:

$$J = \mathcal{G} = \frac{K_I^2}{E'} + \frac{K_{II}^2}{E'} \qquad (9.4.3.4)$$

Here $E' = E$ in plane stress and $E' = E/(1 - \nu^2)$ in plane strain. The $\mathcal{G}$ values of the interfacial cracks were determined using the domain integral method of Shih, Li & Needleman (1986) which is implemented in *ABAQUS* and are presented in Table 3.4.2-1 and Table 3.4.2-2 as a function of α. Substituting (9.4.3.3) into (9.4.3.4) establishes the corresponding K_I & K_{II} components. These are normalised by:

$$K_o(t) = \sigma\sqrt{\pi a} \qquad \text{or} \qquad K_o(s) = \tau\sqrt{\pi a} \qquad (9.4.3.5)$$

The former is the stress intensity factor due to the remotely applied tensile stress σ (mode I loading) while the latter is caused by the remote applied shear stress τ (mode II loading). The normalised stress intensity factors are plotted in Fig. 9.4.3-4 and Fig. 9.4.3-5.

The stress intensity factors for interfacial cracks are given as:

$$\begin{Bmatrix} K_I \\ K_{II} \end{Bmatrix} = \sqrt{\pi a} \begin{bmatrix} K_I/K_o(t) & K_I/K_o(s) \\ K_{II}/K_o(t) & K_{II}/K_o(s) \end{bmatrix} \begin{Bmatrix} \sigma_i \\ \tau_i \end{Bmatrix} \qquad (9.4.3.6)$$

where σ_i and τ_i are the local interfacial stress components. These interfacial K_n values are normalised by $K_o(t)$ and are plotted in Fig. 9.4.3-6 for the different applied strain. Substituting eqn (9.4.3.6) for eqn (9.4.3.4), the energy release rate along the imperfect fibre-matrix interface is determined. These are normalised by $\mathcal{G}_0 = K_0^2 / E'$ and are presented in Fig. 9.4.3-7.

$_2$ = 0.0067

β	$\mathcal{G}_I$	u_x / u_y	K_I	K_{II}	K_I / K_{II}	$K_o(t)$	$K_I / K_o(t)$	$K_{II} / K_o(t)$
0.25	0.4158E12	-0.0325	0.4186E12	-13.61E9	-30.769	0.7876E12	0.5317	-0.0173
0.50	0.3842E12	-0.0357	0.4039E12	-14.42E9	-28.002	0.6990E12	0.5778	-0.0206
0.75	0.2641E12	-0.0505	0.3401E12	-17.17E9	-19.802	0.4586E12	0.7415	-0.0374
0.90	0.2504E12	-0.0309	0.3244E12	-10.03E9	-33.363	0.2976E12	1.090	-0.0337

$_2$ = 0.0667

β	$\mathcal{G}_I$	u_x / u_y	K_I	K_{II}	K_I / K_{II}	$K_o(t)$	$K_I / K_o(t)$	$K_{II} / K_o(t)$
0.25	41.58E12	-0.0325	4.186E12	-0.1361E12	-30.769	7.876E12	0.5317	-0.0173
0.50	38.42E12	-0.0357	4.039E12	-0.1442E12	-28.002	6.990E12	0.5778	-0.0206
0.75	26.41E12	-0.0505	3.401E12	-0.1717E12	-19.802	4.586E12	0.7415	-0.0374
0.90	25.04E12	-0.0309	3.244E12	-0.1003E12	-33.363	2.976E12	1.090	-0.0337

$_2$ = 0.6667

β	$\mathcal{G}_I$	u_x / u_y	K_I	K_{II}	K_I / K_{II}	$K_o(t)$	$K_I / K_o(t)$	$K_{II} / K_o(t)$
0.25	415.8E12	-0.0325	41.86E12	-1.361E12	-30.769	78.76E12	0.5317	-0.0173
0.50	384.2E12	-0.0357	40.39E12	-1.442E12	-28.002	69.90E12	0.5778	-0.0206
0.75	264.1E12	-0.0505	34.01E12	-1.717E12	-19.802	45.86E12	0.7415	-0.0374
0.90	250.4E12	-0.0309	32.44E12	-1.003E12	-33.363	29.76E12	1.090	-0.0337

.4.3-1 Results of the interfacial cracks strain energy release rate G_I, crack tip displacement ratio u_x / u_y, stress intensity factors K_I & K_{II} and the stress intensity factor for a crack in an infinite body $K_o(t)$, during remote tension.

$E_2 = 0.0067$

β	$\mathcal{G}_{II}$	u_x / u_y	K_I	K_{II}	K_I / K_{II}	$K_o(s)$	$K_I / K_o(s)$	$K_{II} / K_o(s)$
0.25	0.236E9	38.508	0.244E9	9.398E9	0.0260	18.73E9	-0.0130	0.502
0.50	0.306E9	-10.093	-1.207E9	12.18E9	-0.0991	26.80E9	-0.0450	0.454
0.75	0.649E9	-7.412	-2.496E9	18.50E9	-0.1349	31.77E9	-0.0786	0.582
0.90	2.974E9	34.494	-0.965E9	33.30E9	0.0290	32.43E9	-0.0298	1.027

$E_2 = 0.0667$

β	$\mathcal{G}_{II}$	u_x / u_y	K_I	K_{II}	K_I / K_{II}	$K_o(s)$	$K_I / K_o(s)$	$K_{II} / K_o(s)$
0.25	23.6E9	38.508	2.44E9	93.98E9	0.0260	187.3E9	-0.0130	0.502
0.50	30.6E9	-10.093	-12.07E9	121.8E9	-0.0991	268.0E9	-0.0450	0.454
0.75	64.9E9	-7.412	-24.96E9	185.0E9	-0.1349	317.7E9	-0.0786	0.582
0.90	297.4E9	34.494	-9.65E9	333.0E9	0.0290	324.3E9	-0.0298	1.027

$E_2 = 0.6667$

β	$\mathcal{G}_{II}$	u_x / u_y	K_I	K_{II}	K_I / K_{II}	$K_o(s)$	$K_I / K_o(s)$	$K_{II} / K_o(s)$
0.25	2.36E12	38.508	24.4E9	0.9398E12	0.0260	1.873E12	-0.0130	0.502
0.50	3.06E12	-10.093	-120.7E9	1.218E12	-0.0991	2.680E12	-0.0450	0.454
0.75	6.49E12	-7.412	-249.6E9	1.850E12	-0.1349	3.177E12	-0.0786	0.582
0.90	29.74E12	34.494	-96.5E9	3.330E12	0.0290	3.243E12	-0.0298	1.027

4.3-2 Results of the interfacial cracks strain energy release rate G_{II}, crack tip displacement ratio u_x / u_y, stress intensity factors K_I & K_{II} and the stress intensity factor for a crack in an infinite body $K_o(t)$, during remote shear.

9.5 A Finite Fibre Problem

9.5.1 General

In this section, the analysis of a finite fibre embedded in an elastic matrix is considered. The fibre is treated as either rigid or elastic, with a fibre volume fraction of 0.185 matching the experimental material described in Chapter 4. Also, the bonding at the fibre-matrix interface is allowed to degrade by introducing interfacial imperfections.

9.5.2 Mesh & Model Descriptions

The finite element mesh of the rigid and elastic fibre problem is shown in Figs 9.5.2-1 and 2. The rigid fibre was modelled by restraining the interface nodes while the elastic fibre was modelled using 268 second-order plane strain quadrilateral elements. The elastic matrix was modelled using 1024 second-order plane strain quadrilateral elements and 65 interface elements were used to represent the fibre-matrix interface. The properties of the fibre were identical to be the matrix which are described in Sect 9.2.2. To model the degradation of the fibre-matrix interface, the stiffnesses of the interface element for the crack area fractions $\beta = 0$, 0.25, 0.50, 0.75, 0.90 and 1.00 were used. To introduce periodic boundary condition, the sides of the meshes were restrained to have identical translation. A uniaxial stretch was applied by displacing the top nodes of the matrix by 200 units.

9.5.3 Stress Concentration Fields

The deformed meshes of the rigid fibre problem are shown in Fig 9.5.3-1, and the stress concentrations in the matrix adjacent to the interface and at the interface are plotted as a function of the angular co-ordinate ω in Figs 9.5.3-2 & 3. The predicted stress concentrations for a perfect interface agrees with Goodier's solution (see (9.4.2.1.1)). The maximum stress concentrations are insensitive to interfacial imperfections until the crack area fraction β is greater than 0.9. For bonded fibre-matrix interfaces, the maximum stress concentration in the matrix adjacent to the interface and at interface occurs at $\omega = 0°$. However, when the interfaces becomes unbonded, the maximum stress concentration in the matrix was interpolated to $\omega = \pm 70.3°$. This

unbonded matrix, the maximum stress concentration was approximately twice the bonded matrix.

The deformed mesh of the elastic fibre problem is shown in Fig 9.5.3-4. The stress concentrations of the matrix and the interface are plotted as a function of the angular co-ordinate ω in Figs 9.5.3-5 and 6. Like the rigid fibre problem, the stresses at the fibre-matrix interface are insensitive to imperfections unitil the crack area fraction β approaches 1. No stress concentrations exist at the fibre-matrix interface when the interface is bonded as a homogeneous stress and strain field is recovered. However when the interface becomes unbonded, the matrix adjacent to the interface has a hoop stress concentration of 2.84 in the angular range +76° to +90° and -76° to -90°. The stress state in the deformable fibre and deformable matrix with bonded and unbonded interfaces is contour plotted in Fig 9.5.3-7.

9.5.4 Stiffness

The stiffnesses of the unit cell model for the rigid fibre and elastic fibre problem are presented in Table 9.5.4-1 and 2 with respect to interfacial damage β. For plane strain condition, the composite stiffness E_c is defined as:

$$E_c = \frac{\sigma}{\varepsilon}\left(1-\nu^2\right) \qquad (9.5.4\text{-}1)$$

in which σ and ε are the remote stress and strain and ν is the Poisson's ratio of the matrix. The stiffnesses for the rigid fibre and elastic fibre problem are normalised by the stiffness E_c at $\beta = 0$, the Young's modulus of the matrix (E_m = 3.00E11), and $V_m E_m$ (1 - ν^2) and are plotted in Figs 9.5.4-1 and 2 as a function of the interfacial damage β.

For both the rigid and elastic fibre problem, the stiffness of the composite is significantly reduced when the interfacial damage approached 1. For the rigid fibre problem, the composite stiffness with unbonded fibres is 0.4 times the bonded fibres. When no modulus mismatch is present, the stiffness of the composite with unbonded fibres is 0.64 times the bonded fibres. In both problems, interpenetration of the fibre and matrix surfaces is shown to have little effect on the composite stiffness.

Crack Area Fraction β	σ	E_c	$E_c / E_{c\,(\beta=1)}$	E_c / E_m	$E_c / V_m E_m (1 - \nu^2)$
0	3.616×10^{10}	4.809×10^{11}	1.00	1.60	2.59
0.25	3.609×10^{10}	4.800×10^{11}	1.00	1.60	2.58
0.50	3.593×10^{10}	4.778×10^{11}	0.99	1.59	2.57
0.75	3.551×10^{10}	4.722×10^{11}	0.98	1.57	2.54
0.90	3.465×10^{10}	4.607×10^{11}	0.96	1.54	2.48
1.00	1.427×10^{10}	1.898×10^{11}	0.39	0.63	1.02
*1.00	1.449×10^{10}	1.943×10^{11}	0.40	0.65	1.05

* indicate that interpenetration at the fibre-matrix interface does not exist

Table 9.5.4-1 Stiffness of a composite reinforced with rigid cylindrical fibres, determined as a function of interfacial imperfection.

Crack Area Fraction β	σ	E_c	$E_c / E_{c\,(\beta=1)}$	E_c / E_m	$E_c / V_m E_m (1 - \nu^2)$
0	2.256×10^{10}	3.000×10^{11}	1.00	1.00	1.61
0.25	2.255×10^{10}	2.999×10^{11}	1.00	1.00	1.61
0.50	2.252×10^{10}	2.995×10^{11}	1.00	1.00	1.61
0.75	2.245×10^{10}	2.986×10^{11}	1.00	1.00	1.61
0.90	2.233×10^{10}	2.969×10^{11}	0.99	0.99	1.60
1.00	1.427×10^{10}	1.898×10^{11}	0.63	0.63	1.02
*1.00	1.449×10^{10}	1.927×10^{11}	0.64	0.64	1.04

* indicate that interpenetration at the fibre-matrix interface does not exist

Table 9.5.4-2 Stiffness of a composite reinforced with deformable cylindrical fibres, determined as a function of interfacial imperfection.

For composites with weakly bonded fibre-matrix interfaces, the numerical results show that the composite stiffness in plane strain conditions depends solely on the matrix, i.e.:

$$E_c = V_m E_m \left(1 - \nu_m^2\right) \qquad (9.5.4\text{-}2)$$

For very stiff fibre composites the error from eqn (9.5.4-2) is of the order of 5%, and for a composite with no modulus mismatch the error is of the order of 4%. The stiffness predicted by eqn (9.5.4-2) is less than the upper bound stiffness estimated by Voigt. This can be shown by following the minimum potential energy theorem analysis given in eqns (3.2.4 to 10) for plane strain conditions and using the boundary conditions:

i.e. $$\frac{E_c(1-\nu_c)}{(1+\nu_c)(1-2\nu_c)} \le \frac{V_m E_m(1-\nu_m)}{(1+\nu_m)(1-2\nu_m)} \qquad (9.5.4\text{-}4)$$

Assuming that the Poisson's ratio of the composite ν_c is identical with the Poisson's ratio of matrix ν_m, the composite stiffness E_c satisfying both equilibrium and compatibility conditions must be greater than Voigt's estimate, is:

$$E_c \le \left(E_{c(Voigt)} = E_m V_m\right) \qquad (9.5.4\text{-}5)$$

Comparing eqn (9.5.4-2) with the Voigt's estimate in eqn (9.5.4-5), the inequality defined in eqn (9.5.4-4) is satisfied. This implies that the stiffness given in eqn (9.5.4-2) is admissible for plane strain condition. For plane stress condition, the transverse stiffness given in eqn (9.5.4-2) simply reduces to:

$$E_c = V_m E_m \qquad (9.5.4\text{-}6)$$

For the polyester composite described in Chapter 4, the average transverse modulus measured was 3.45GPa, and the transverse modulus predicted for plane strain and plane stress conditions is 3.19GPa and 3.50GPa. Given that errors are only –7.5% and +1.58%, eqns (9.5.4-2 and 5) are verified for a unidirectional fibre composite having no modulus mismatch. The results also validate the computational model developed in Chapter 7 for the transverse deformation of a uni-directional fibre reinforced composite.

9.6 Conclusion

The use of interfacial elements have shown to be cost effective way to modelling the interfacial response due to periodic imperfections at the interface of an elastic cylindrical fibre and a elastic matrix. The interface element is able to derive the stress concentrations, mixed-mode stress intensity fields and the crack energy release rate of periodically cracked interfaces. For composites with very weakly bonded fibre-matrix interface, the composite stiffness normal to the fibre direction in plane strain and plane stress condition can be approximated as $E_m V_m(1-\nu^2)$ and $E_m V_m$, which validates the assumption used to developed the computational model developed in Chapter 7. The hoop stress concentration developed in the weakly bonded matrix show the possibility of pre-mature matrix cracking, which explains the lower matrix cracking stress observed in brittle matrix composites with woven fibres as opposed to the higher matrix cracking

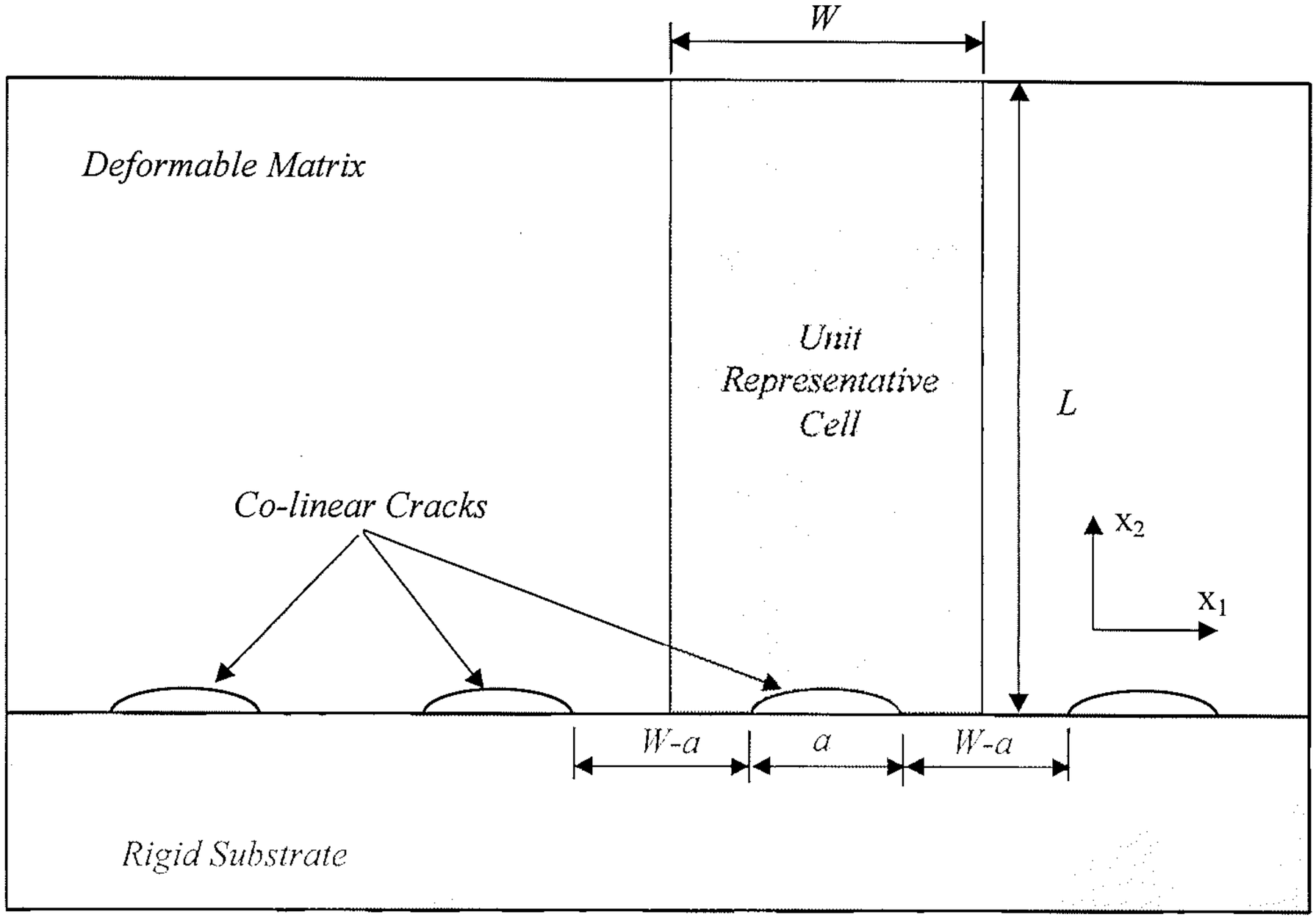

Fig 9.2.1-1 Representation of an imperfect bimaterial interface using an infinite periodic array of co-linear cracks.

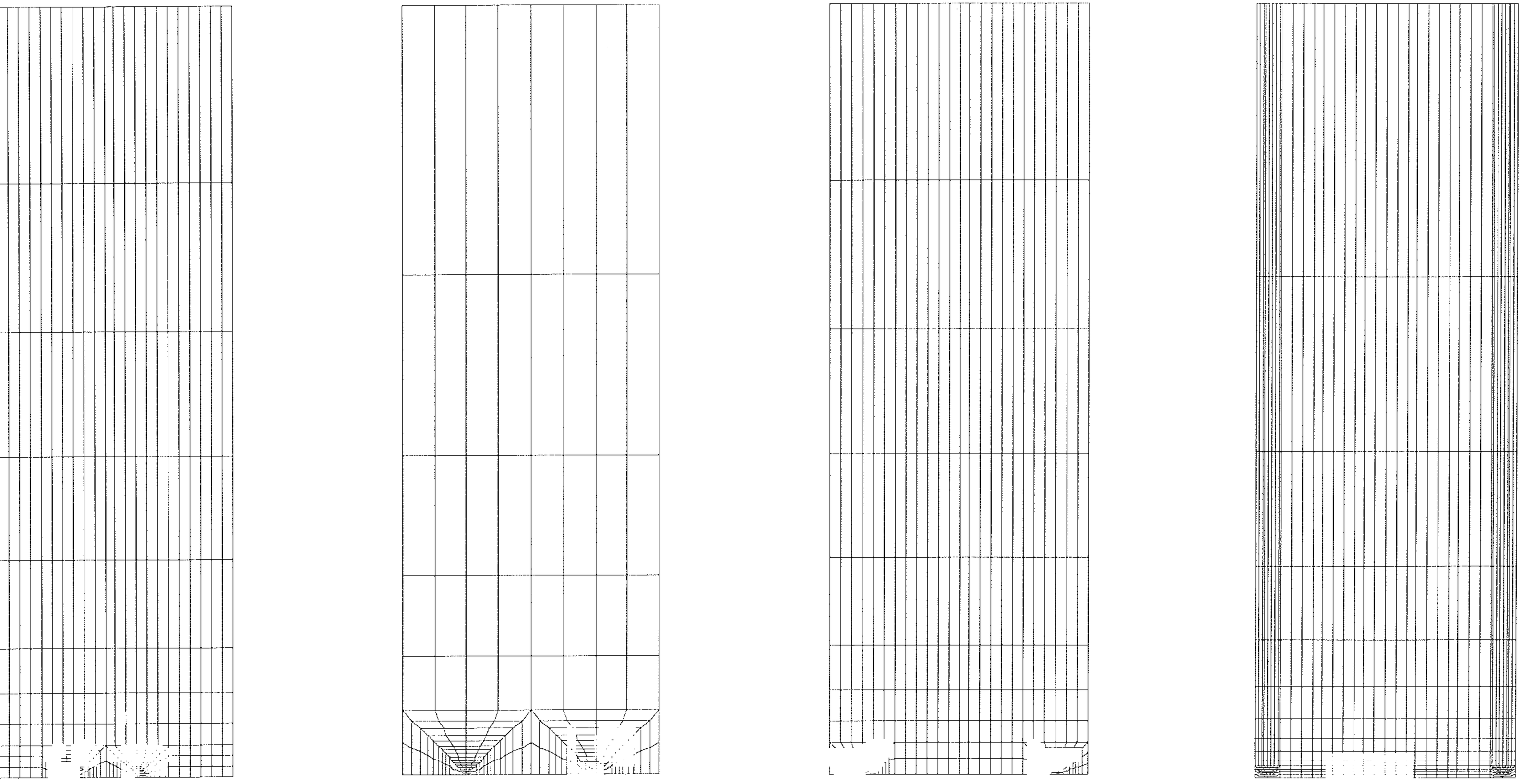

(a) (b) (c) (d)

2-1 The finite element mesh of the deforming matrix with crack area fraction of (a) β=0.25, (b) β=0.50, (c) β=75 and (d) β=0.90

β	**Mode I**	**Mode II**
0.25	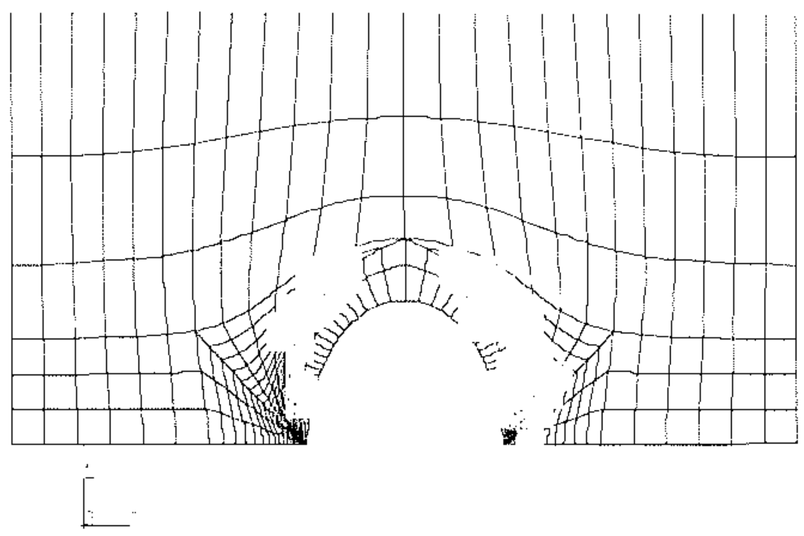	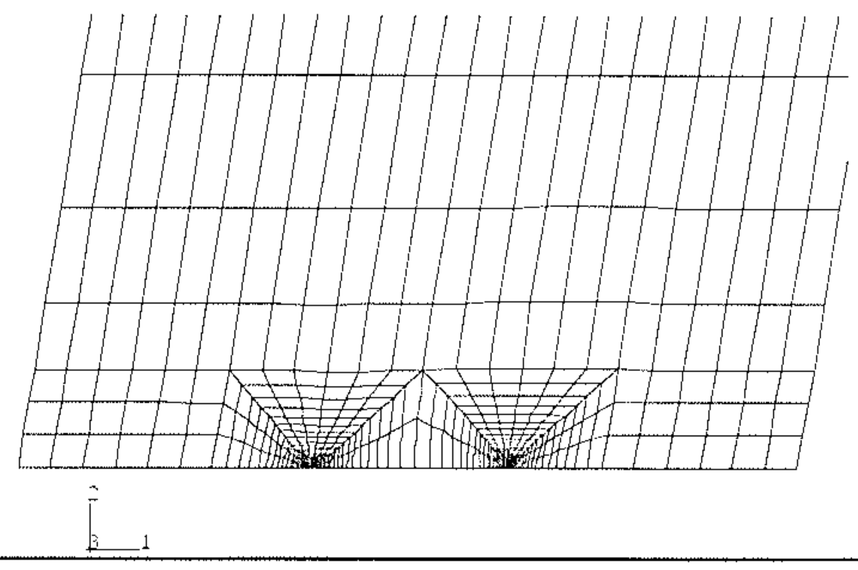
0.50	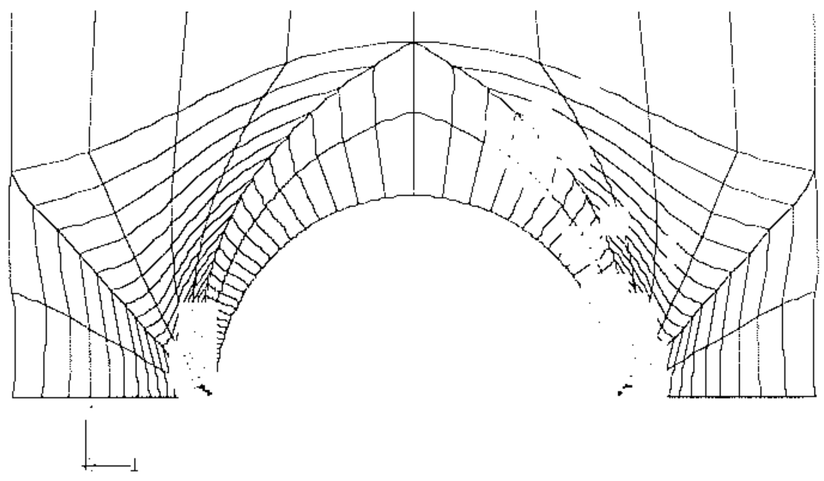	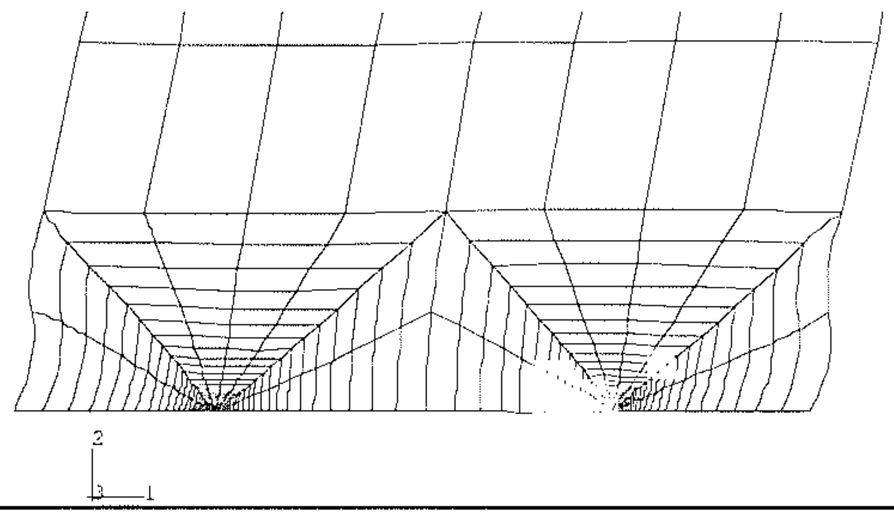
0.75	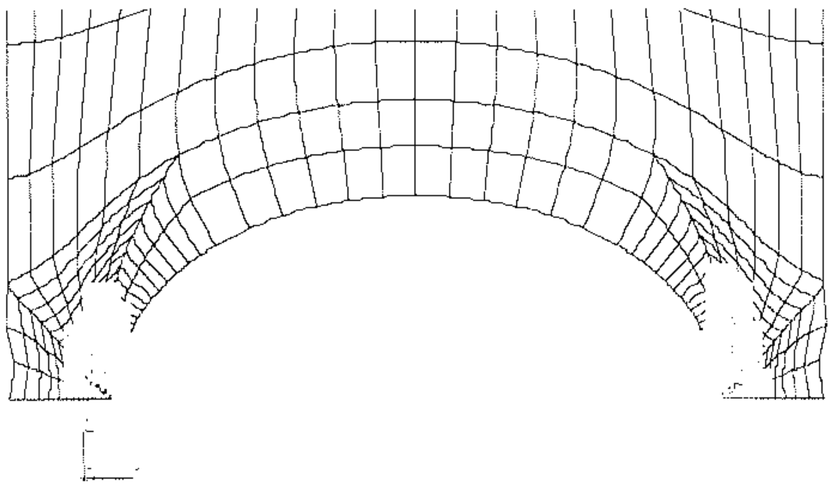	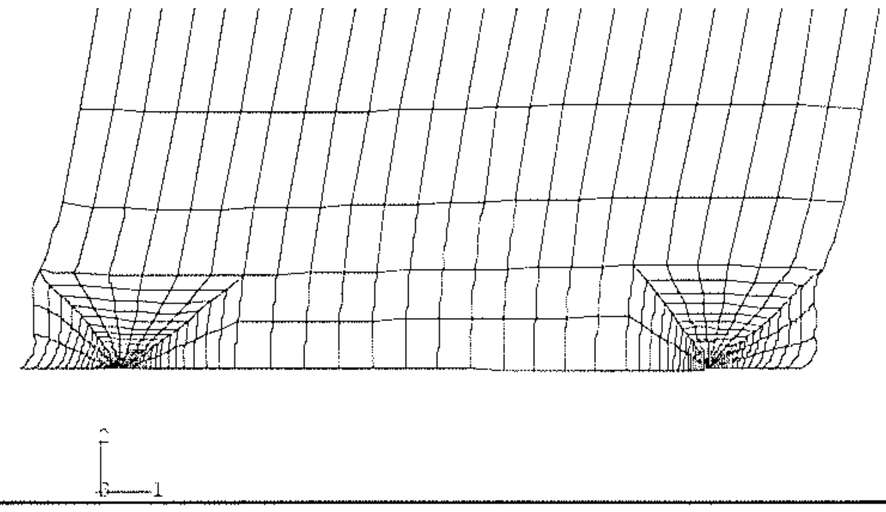
0.90	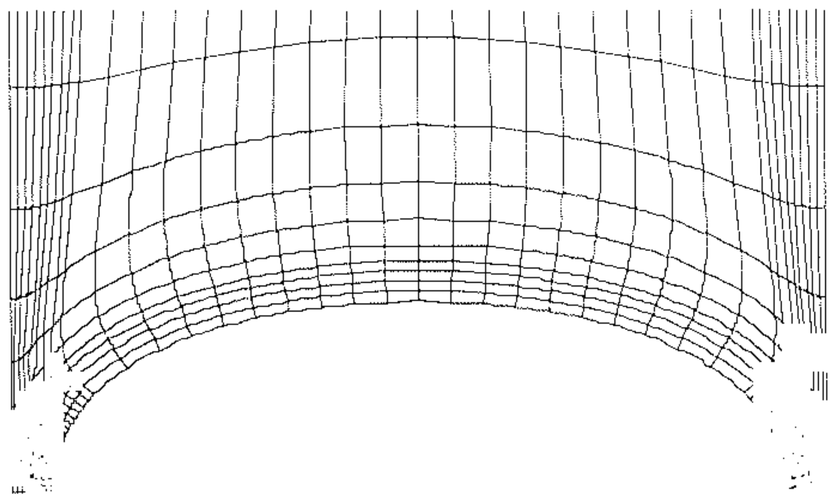	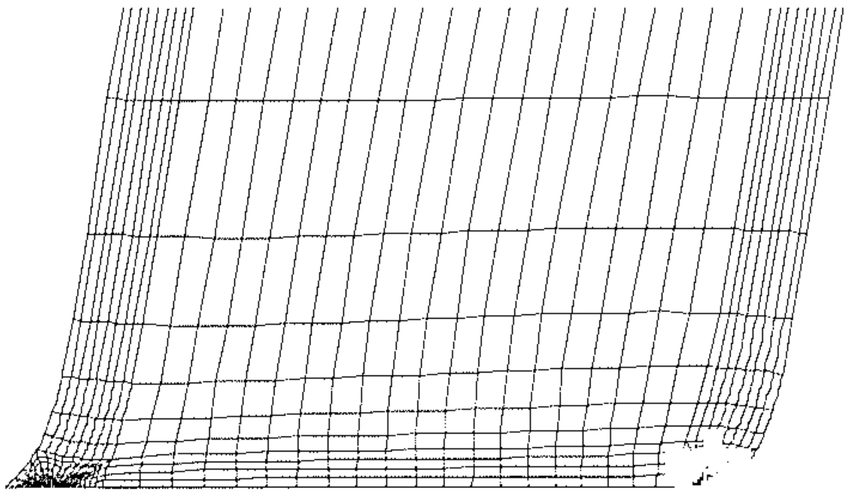

Fig 9.2.3-1 The elastically deformed mesh for $\beta = 0.25$, 0.50, 0.75 and 0.90 with $\nu =$ 0.49 during mode I and mode II displacement loading.

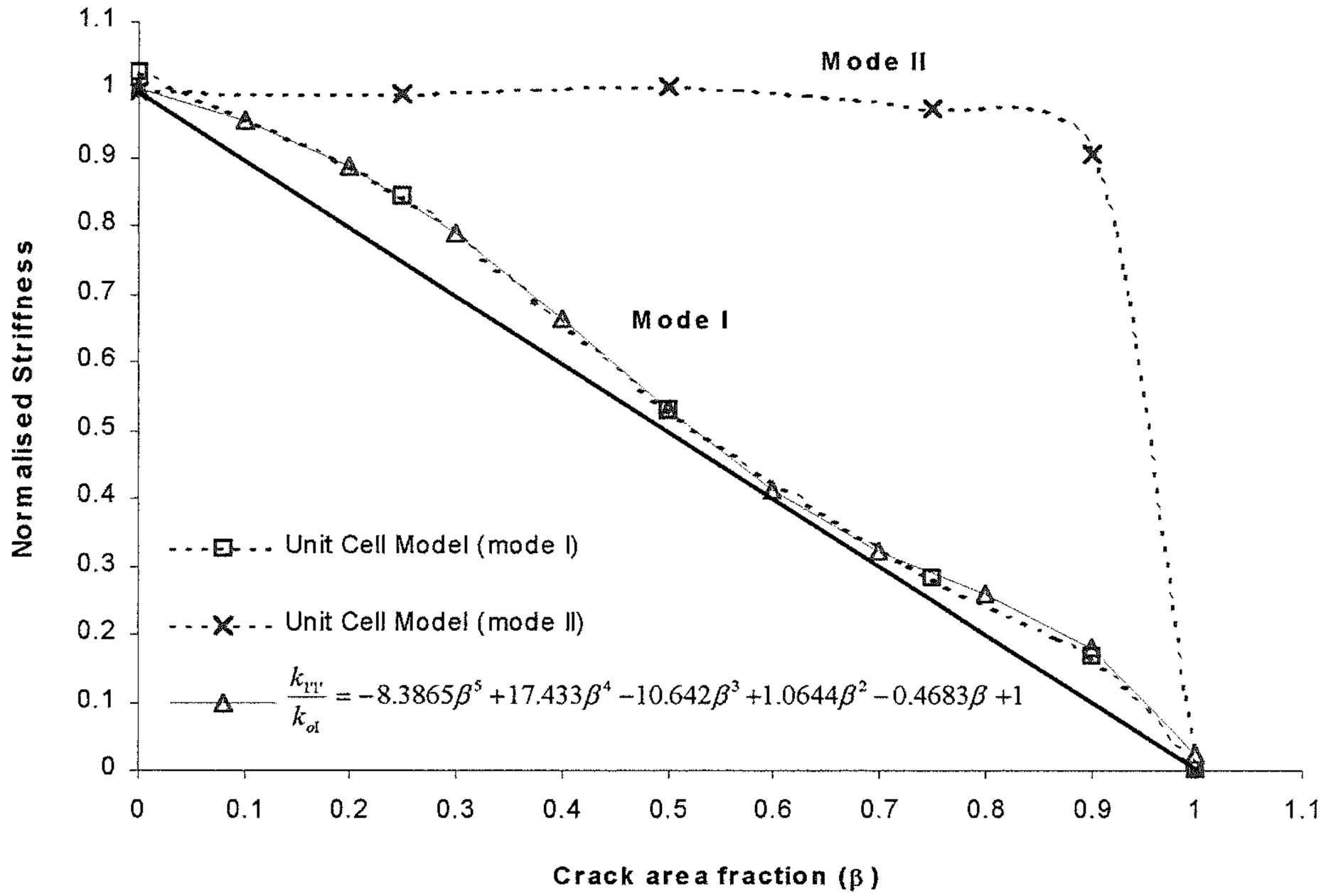

The normalising mode I stiffness $k_{oI} = 1.67 \times 10^{12}$.
The normalising mode II stiffness $k_{oII} = 33.6 \times 10^{9}$.

Fig 9.2.3-2 The normalised stiffness components of an imperfect interface as a function of crack area fraction β.

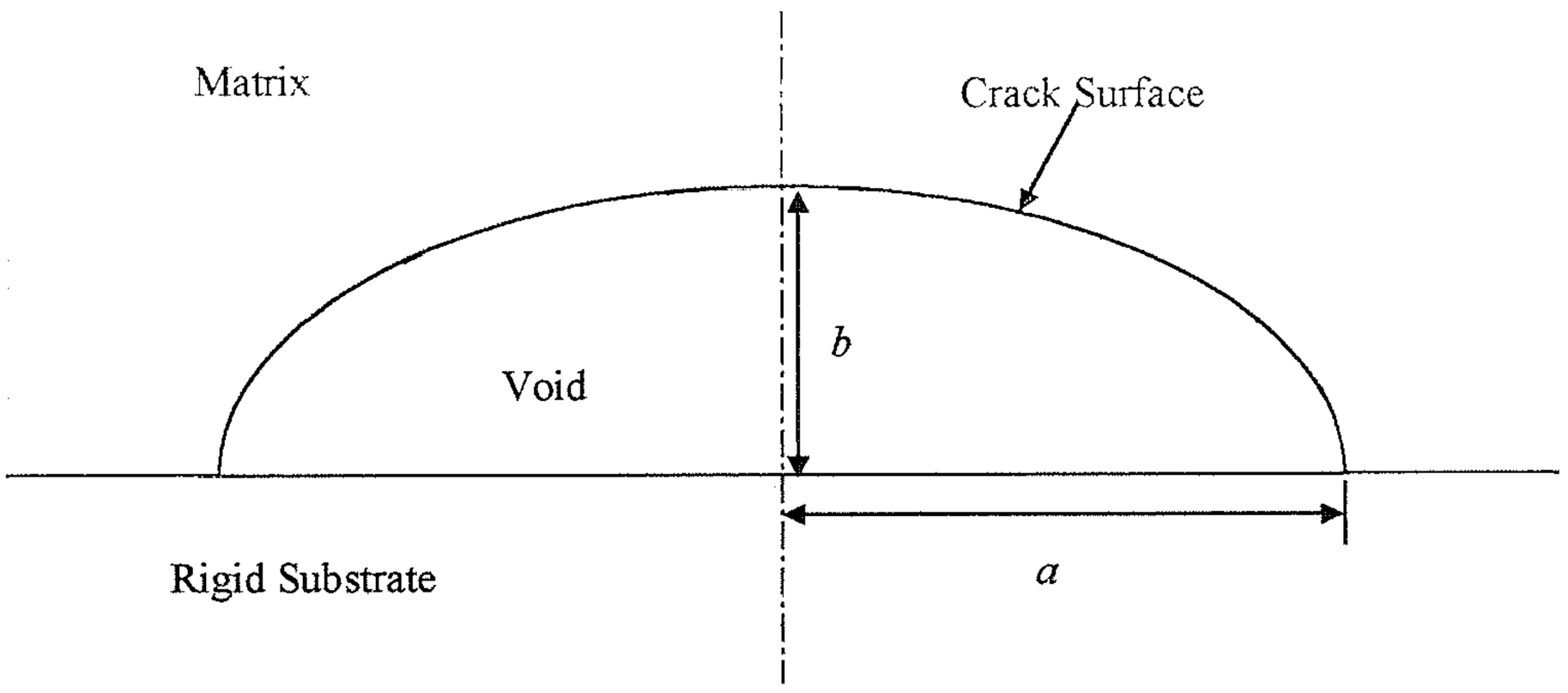

Fig 9.2.3-3 The distances of the principal axes of the void.

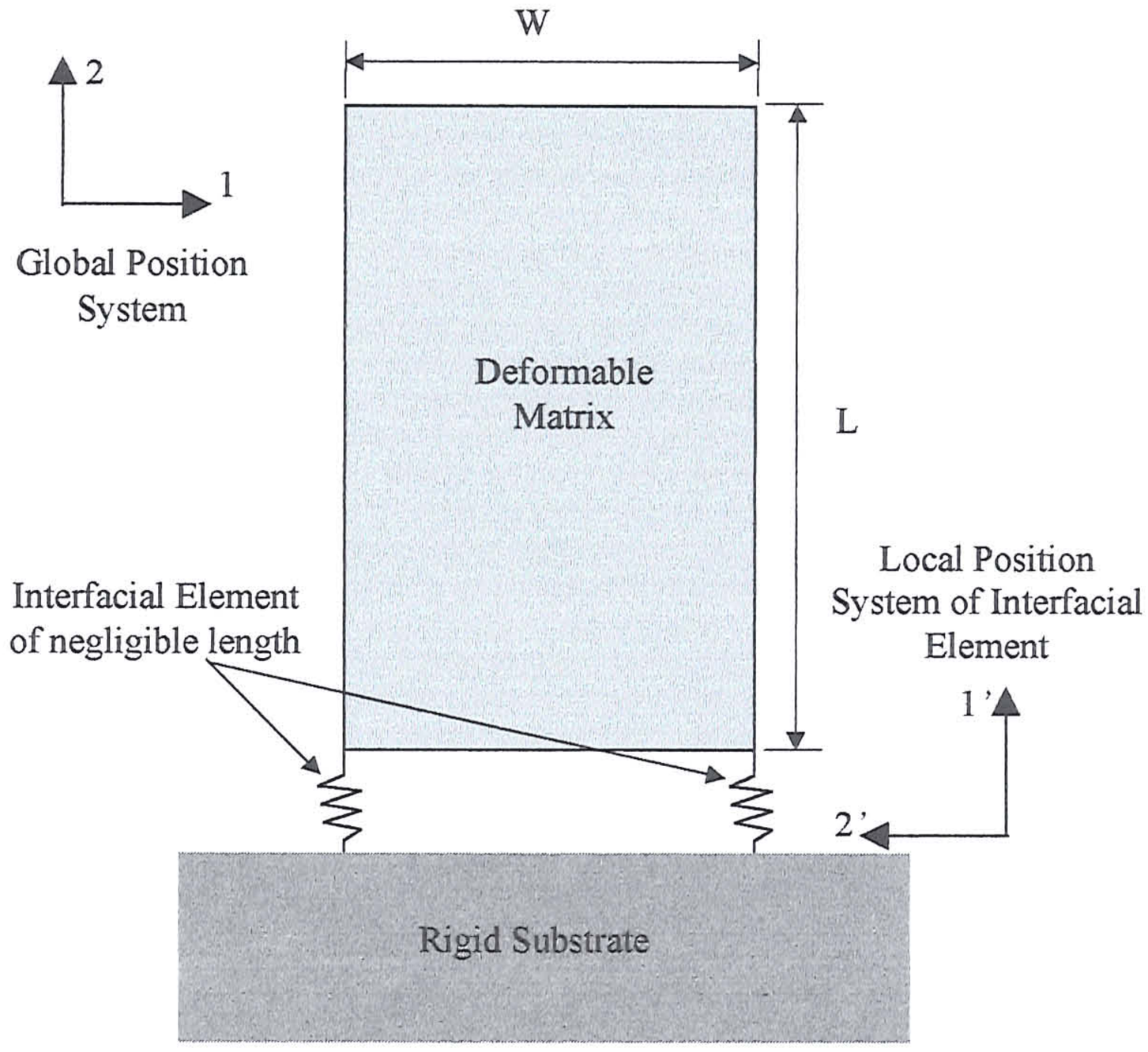

Fig. 9.3-1 Schematic diagram of the interface model used to benchmark the stiffness and yield criterion of the interfacial element.

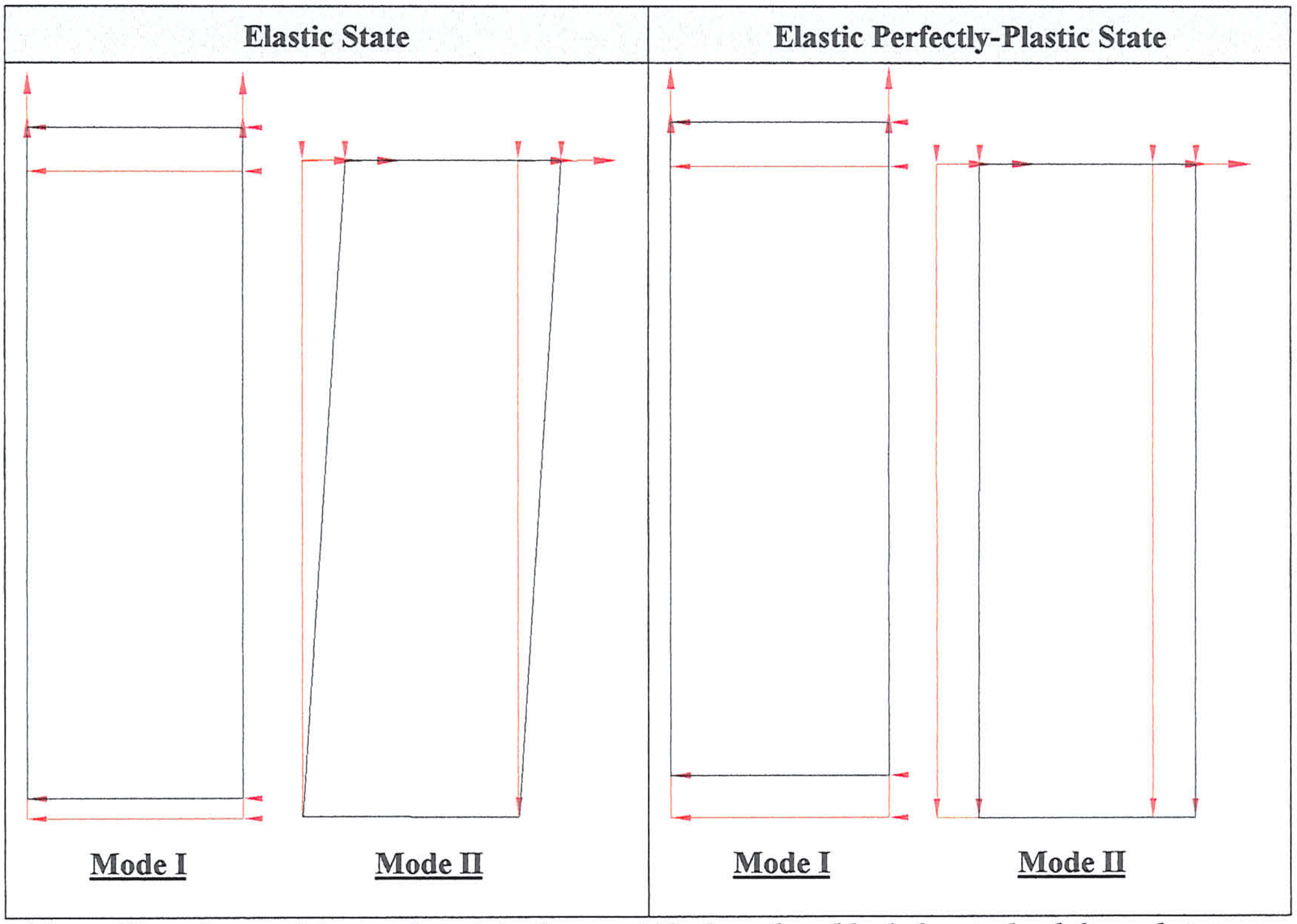

Note : The colour red denote the original state while the colour black denote the deformed state.

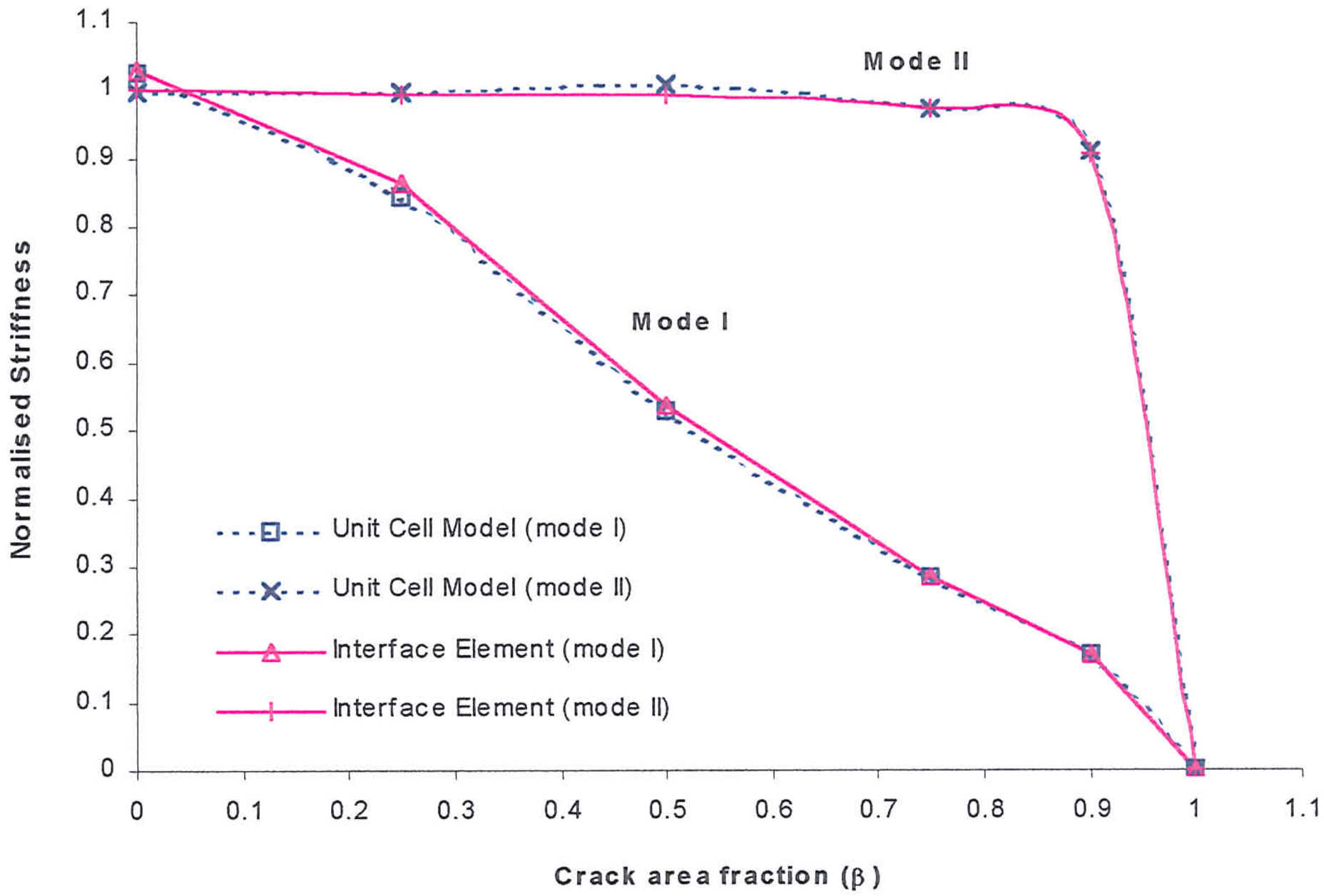

The normalising mode I stiffness $k_{oI} = 1.67 \times 10^{12}$.
The normalising mode II stiffness $k_{oII} = 33.6 \times 10^{9}$.

Fig. 9.3-3 The normalised stiffnesses predicted by the unit cell models and the interface model plotted as a function of crack area fraction β.

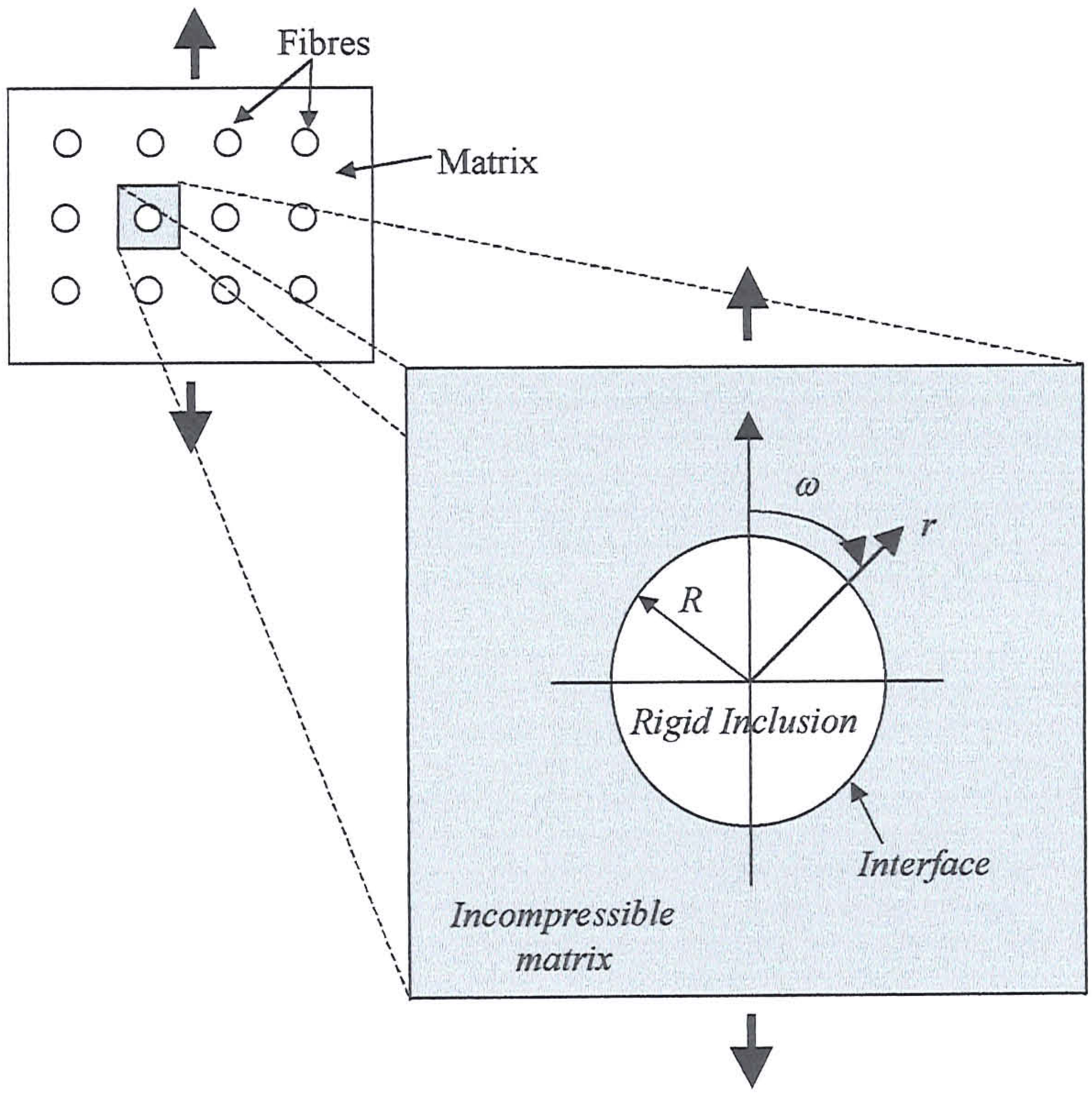

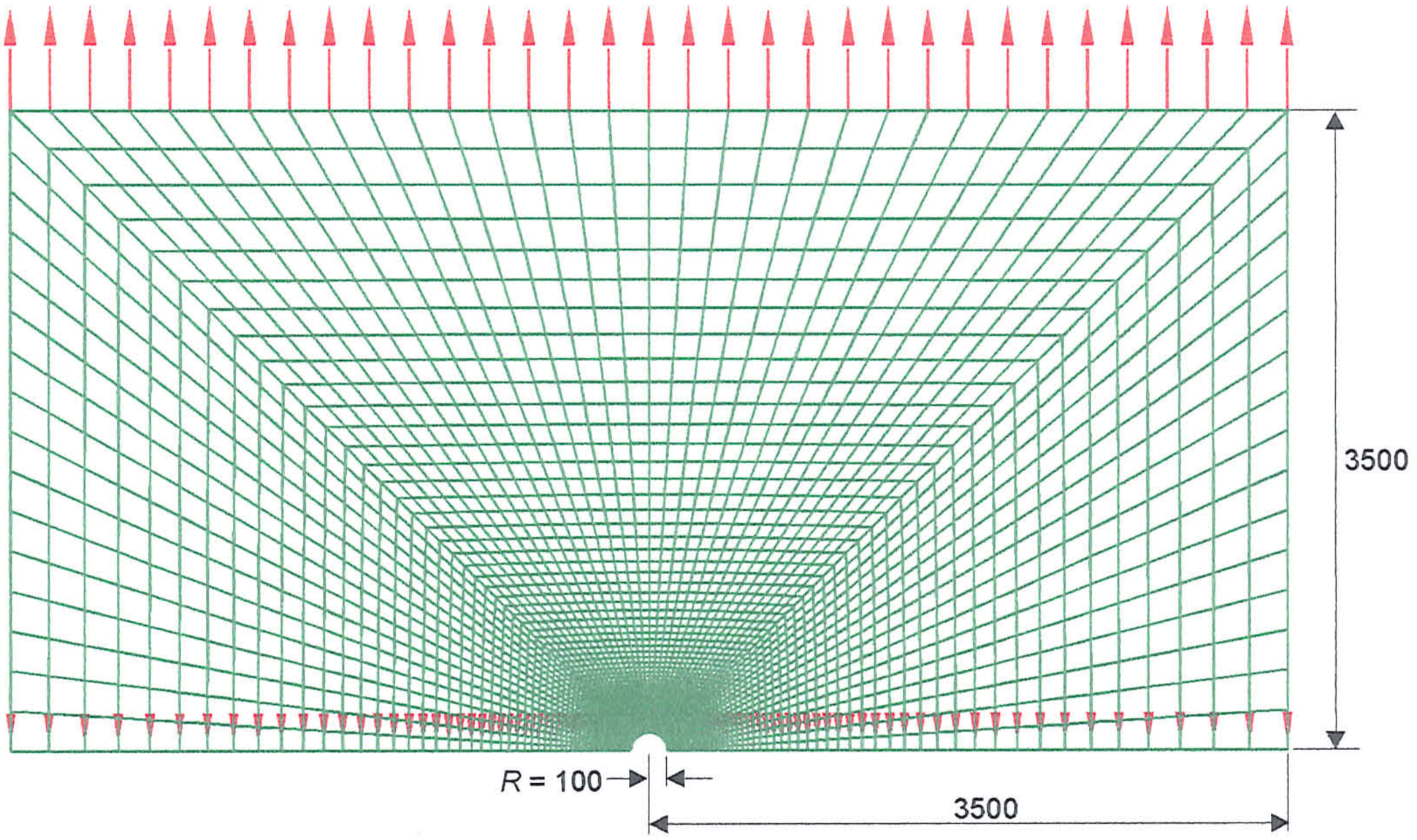

Fig 9.4.2.2-1 Schematic of the unit cell model of a rigid cylindrical fibre embedded in a deformable matrix.

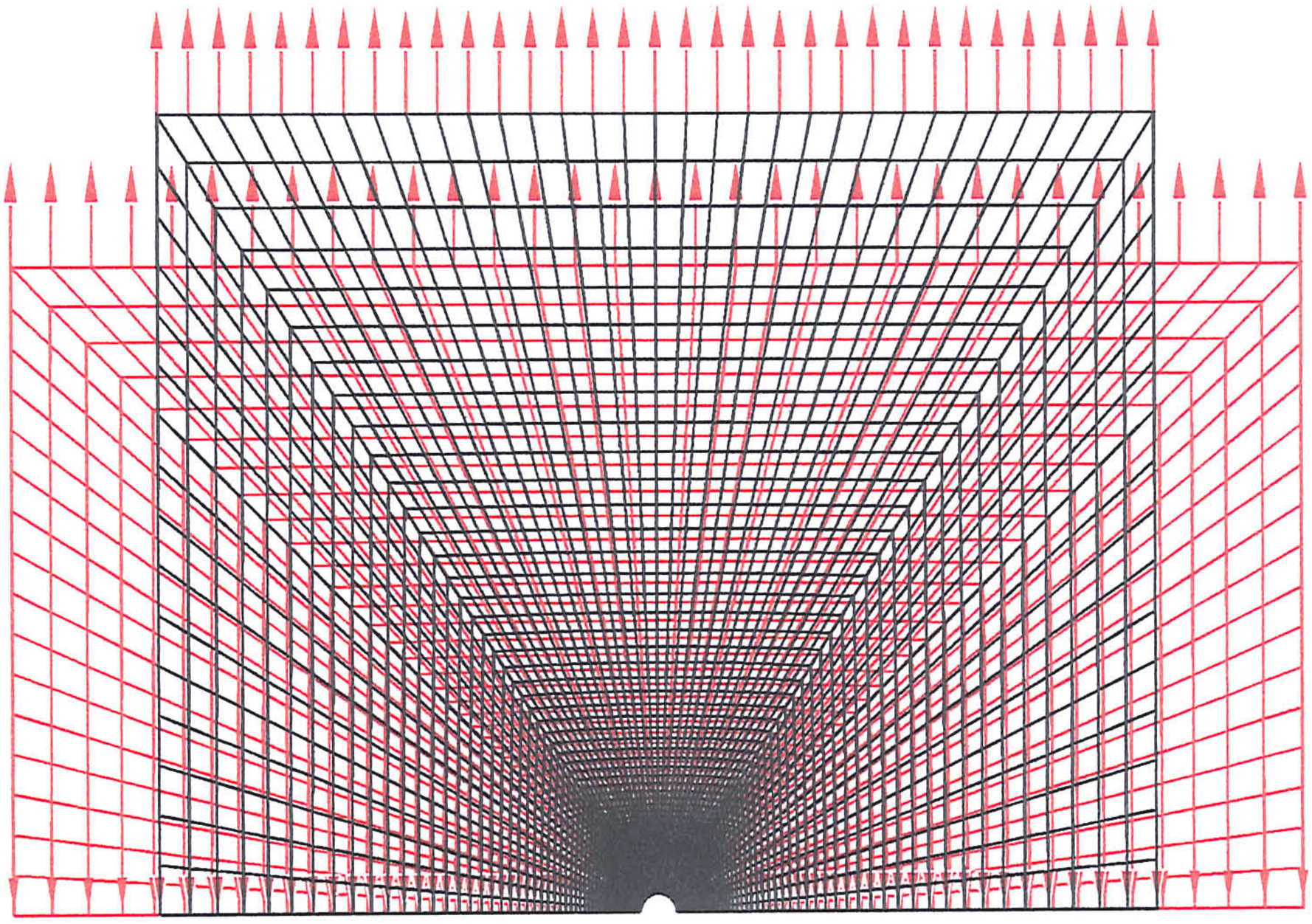

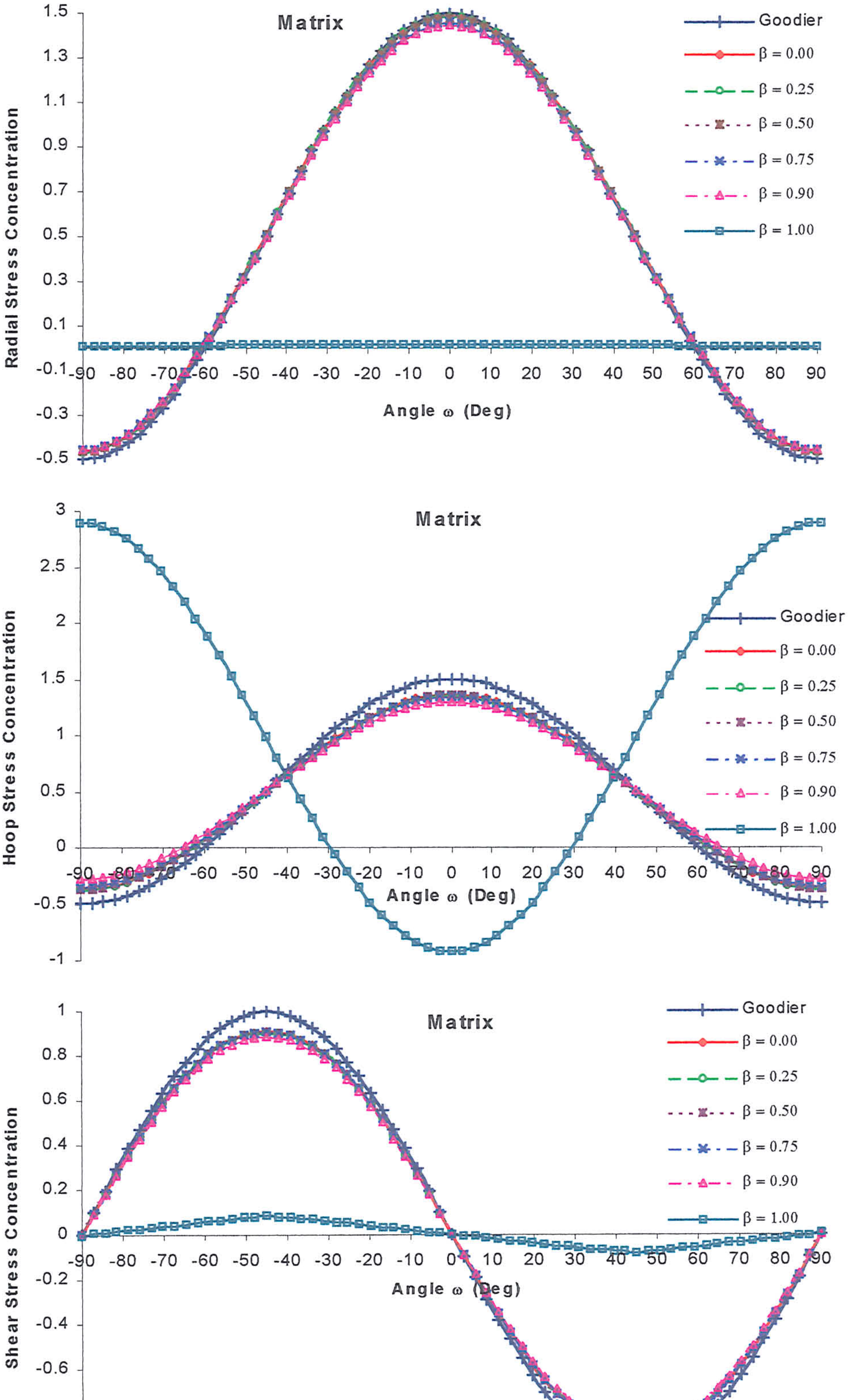

Fig 9.4.2.2-3 The radial, hoop and shear stress concentrations in the elastic matrix for different crack area fraction β plotted as a function of angular orientation

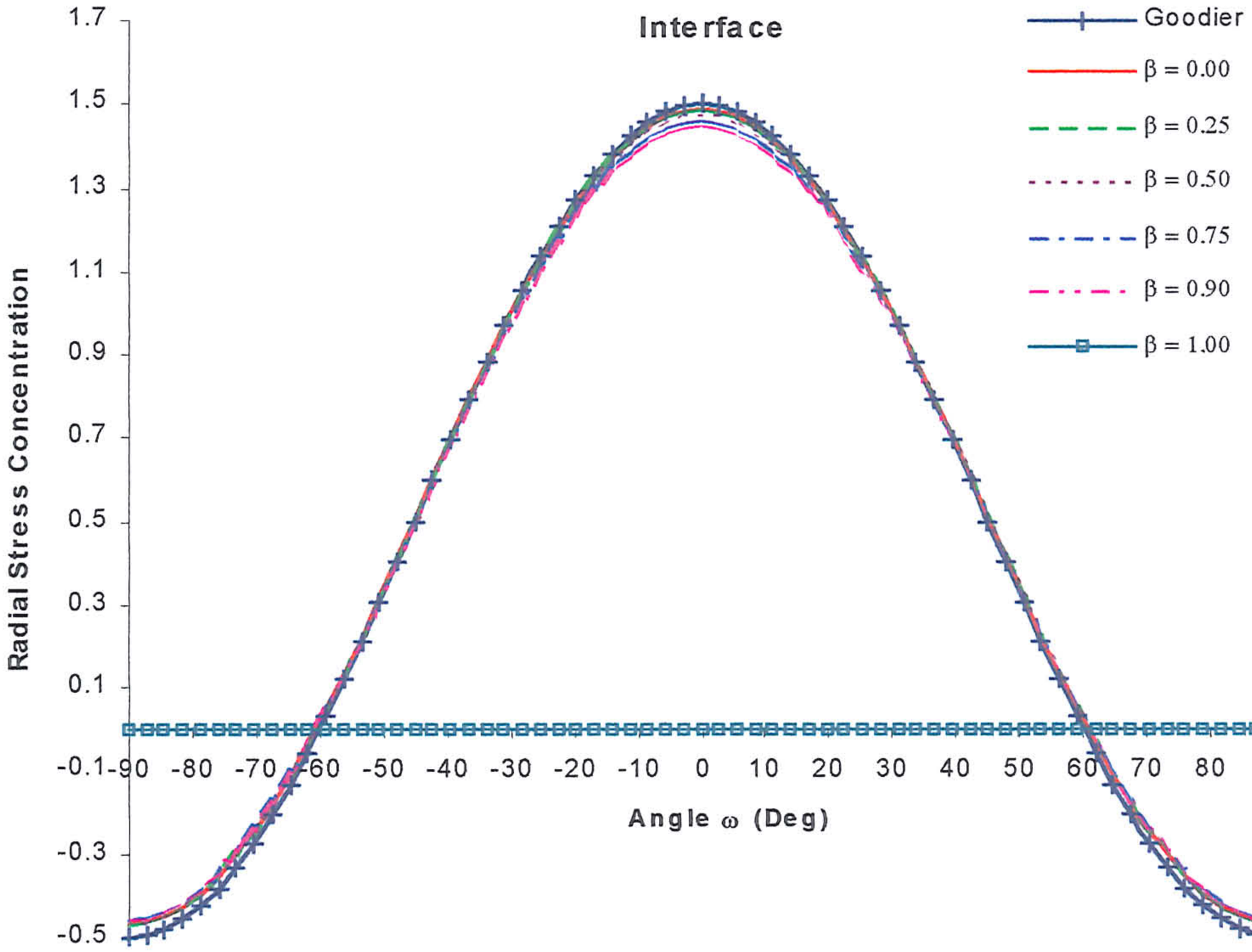

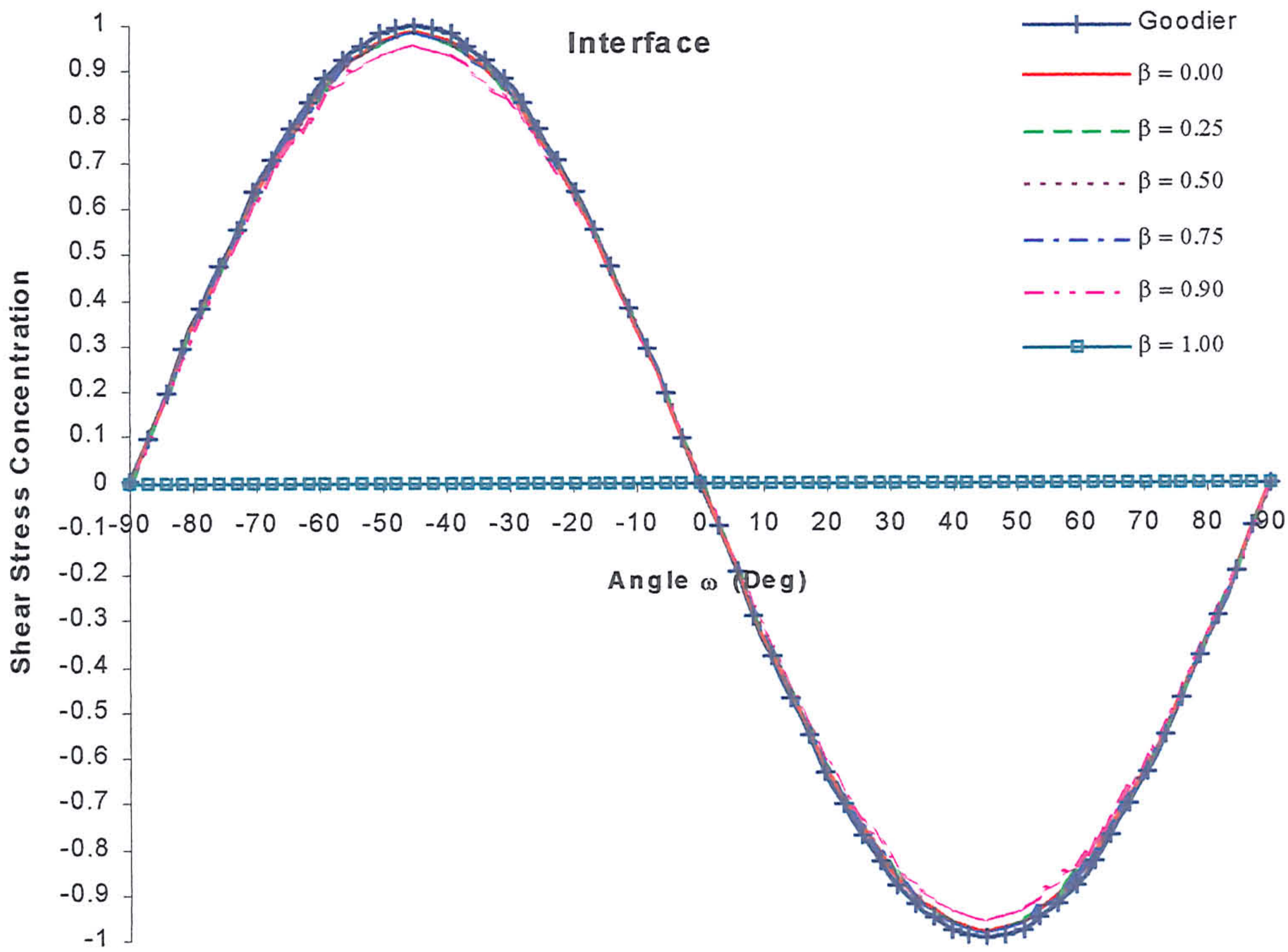

Fig 9.4.2.2-4 The radial and shear stress concentrations of an interface with different

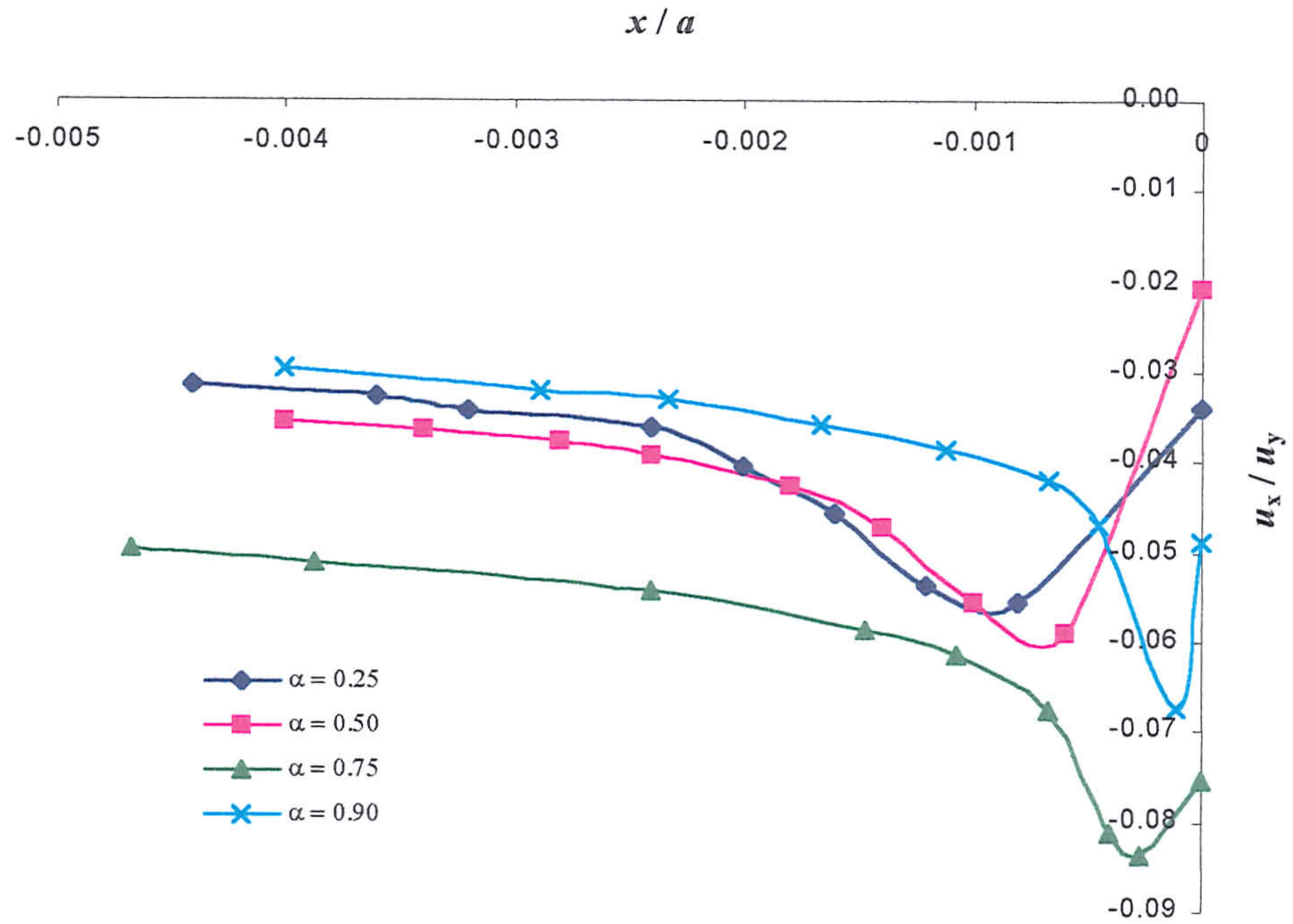

(a)

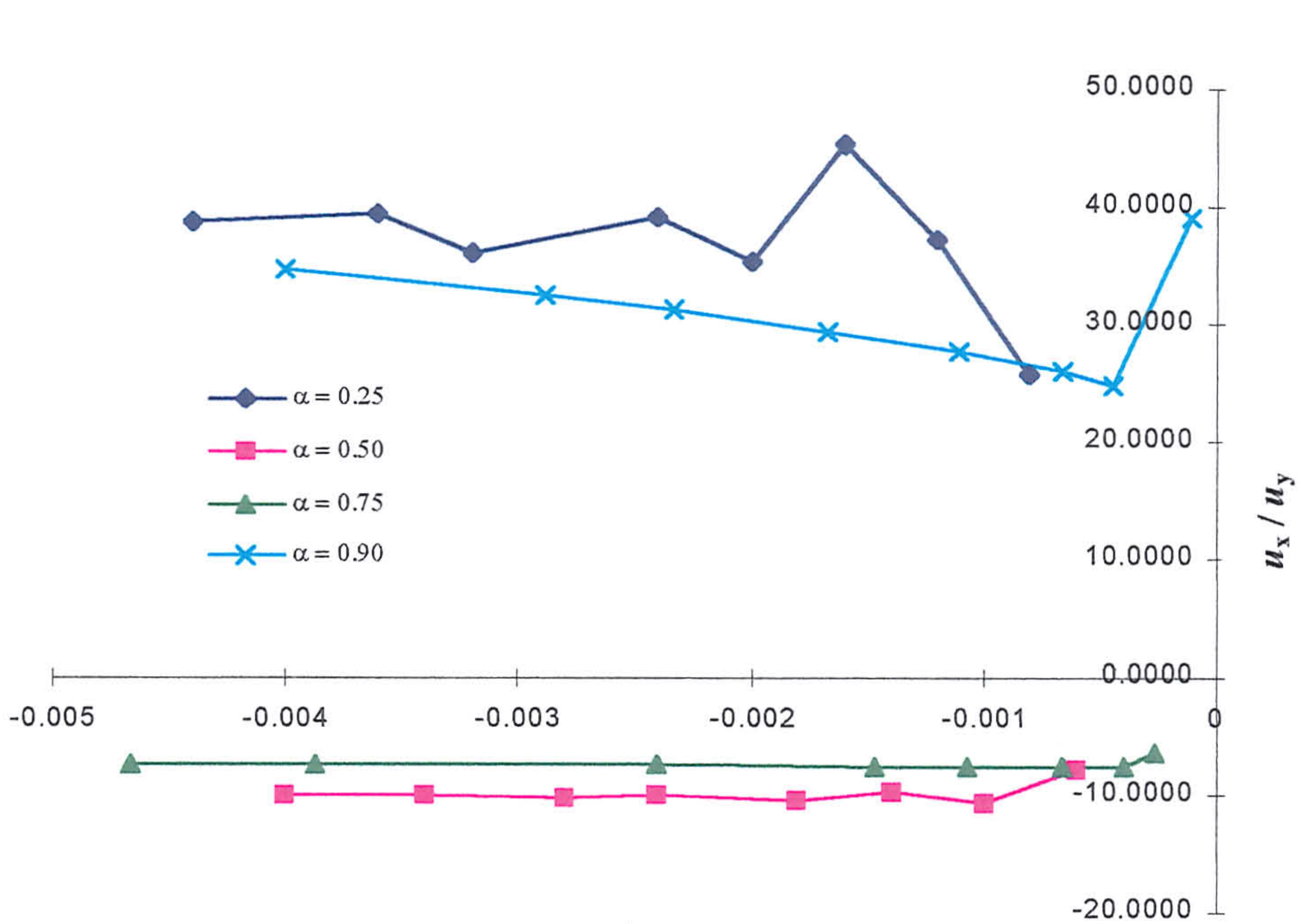

(b)

Fig 9.4.3-1 The crack tip displacement ratios u_x/u_y of co-linear cracks between a rigid substrate and elastic matrix in remote (a) tension and (b) shear,

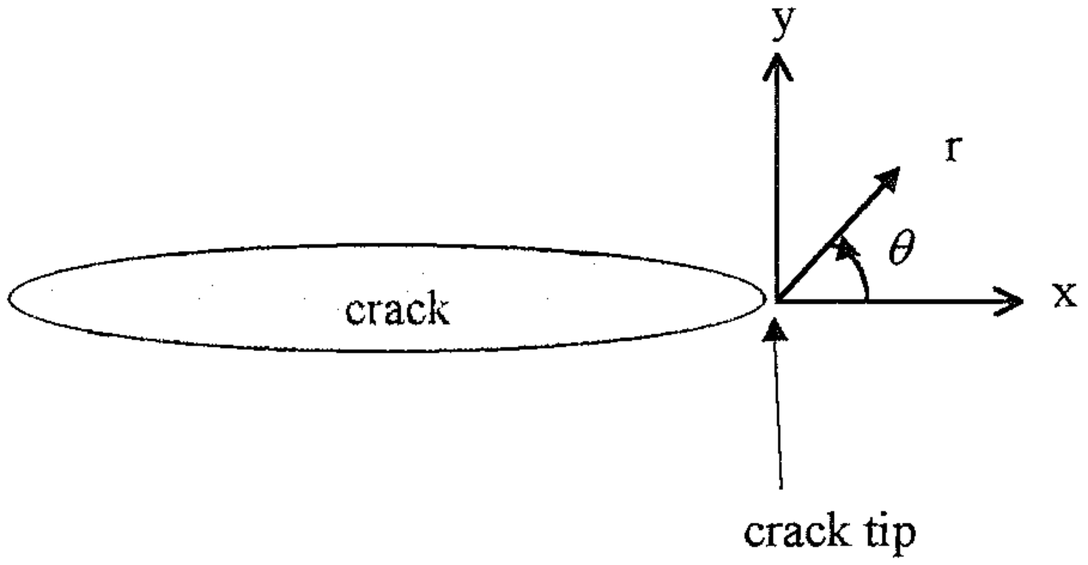

Fig. 9.4.3-2 Westergaard's crack tip sign conventions

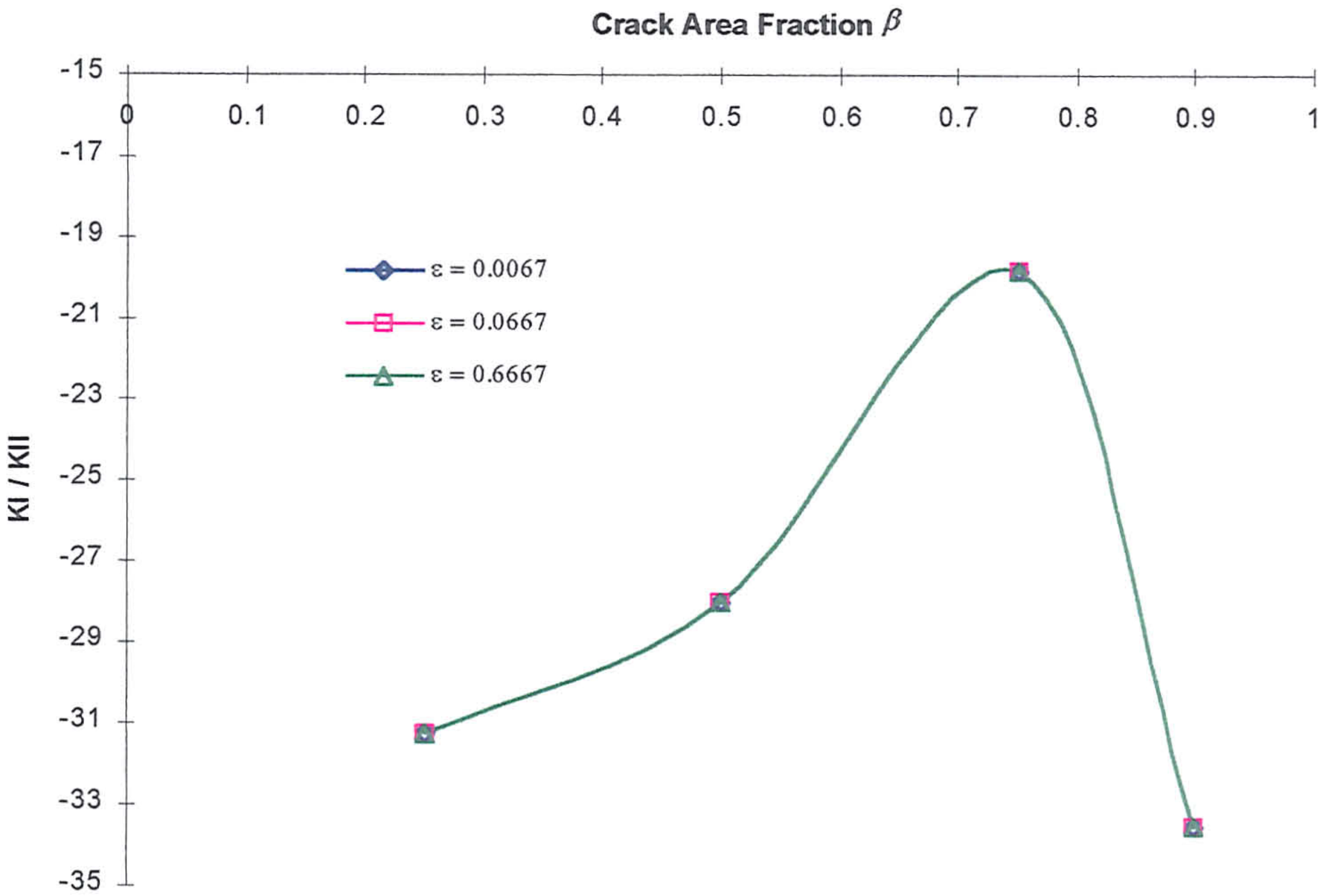

(a)

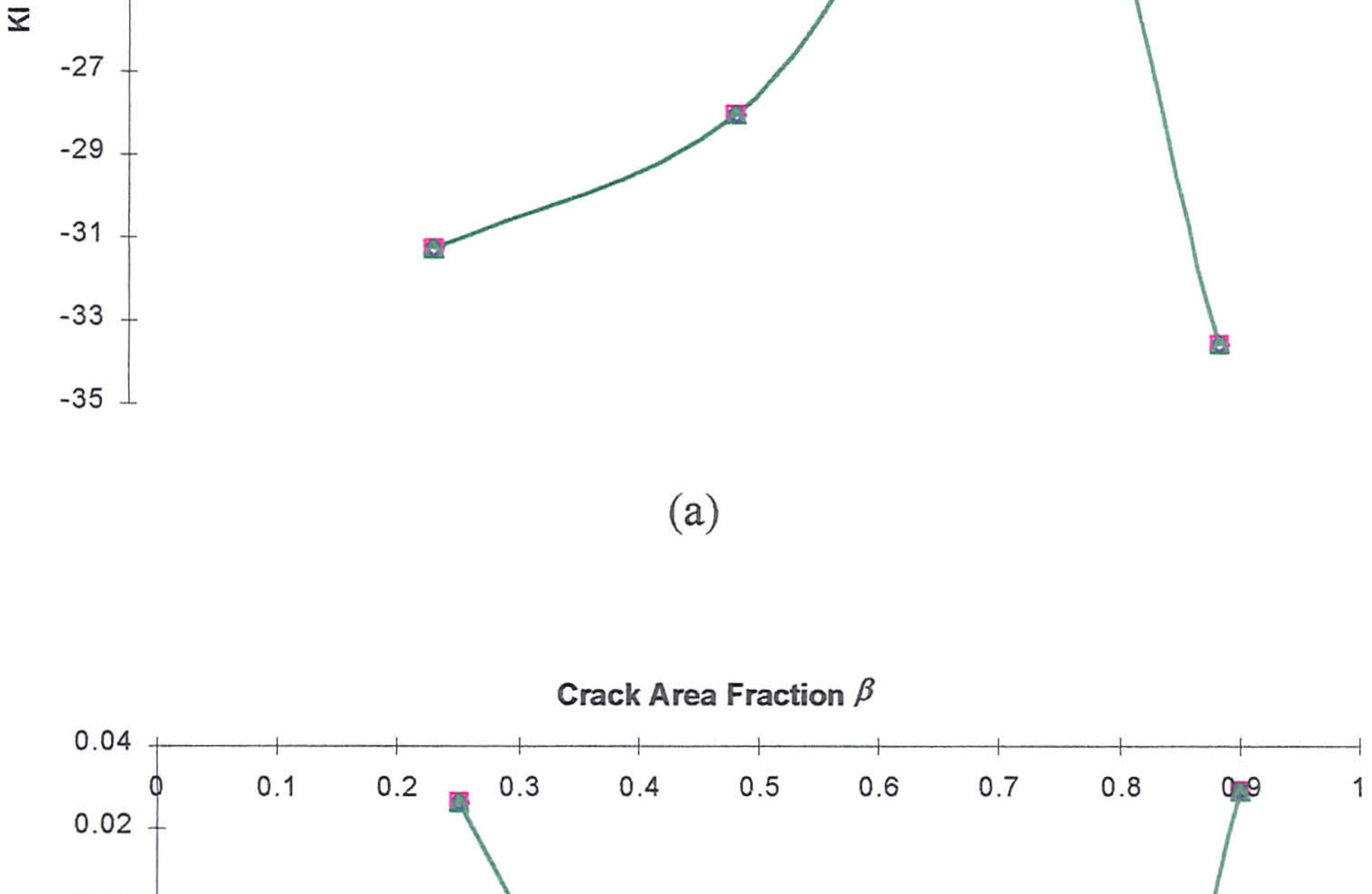

(b)

Fig. 9.4.3-3 The interfacial stress intensity ratio K_I/K_{II} plotted as a function of crack area fraction β in remote (a) tension and (b) shear for the applied strain

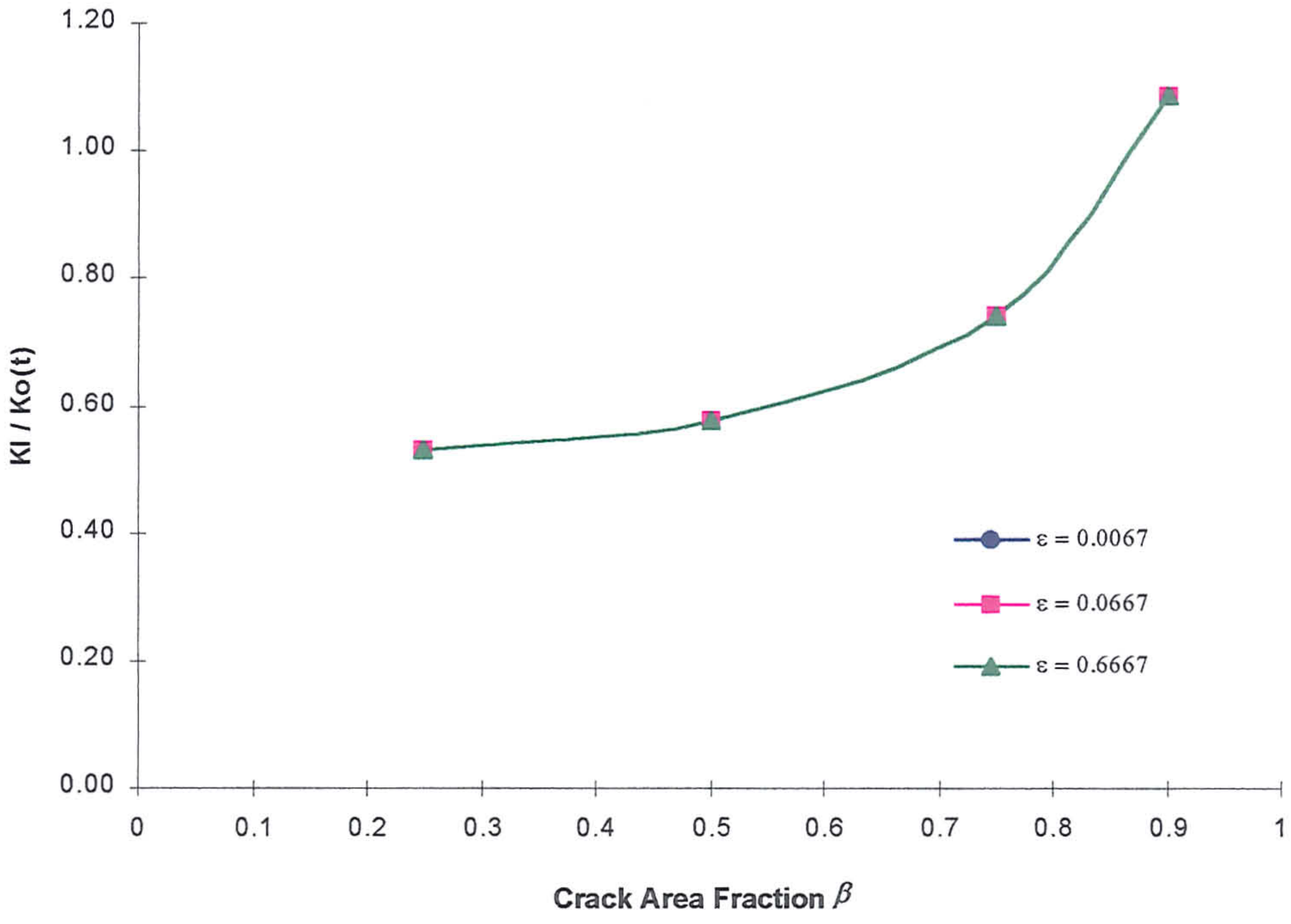

(a)

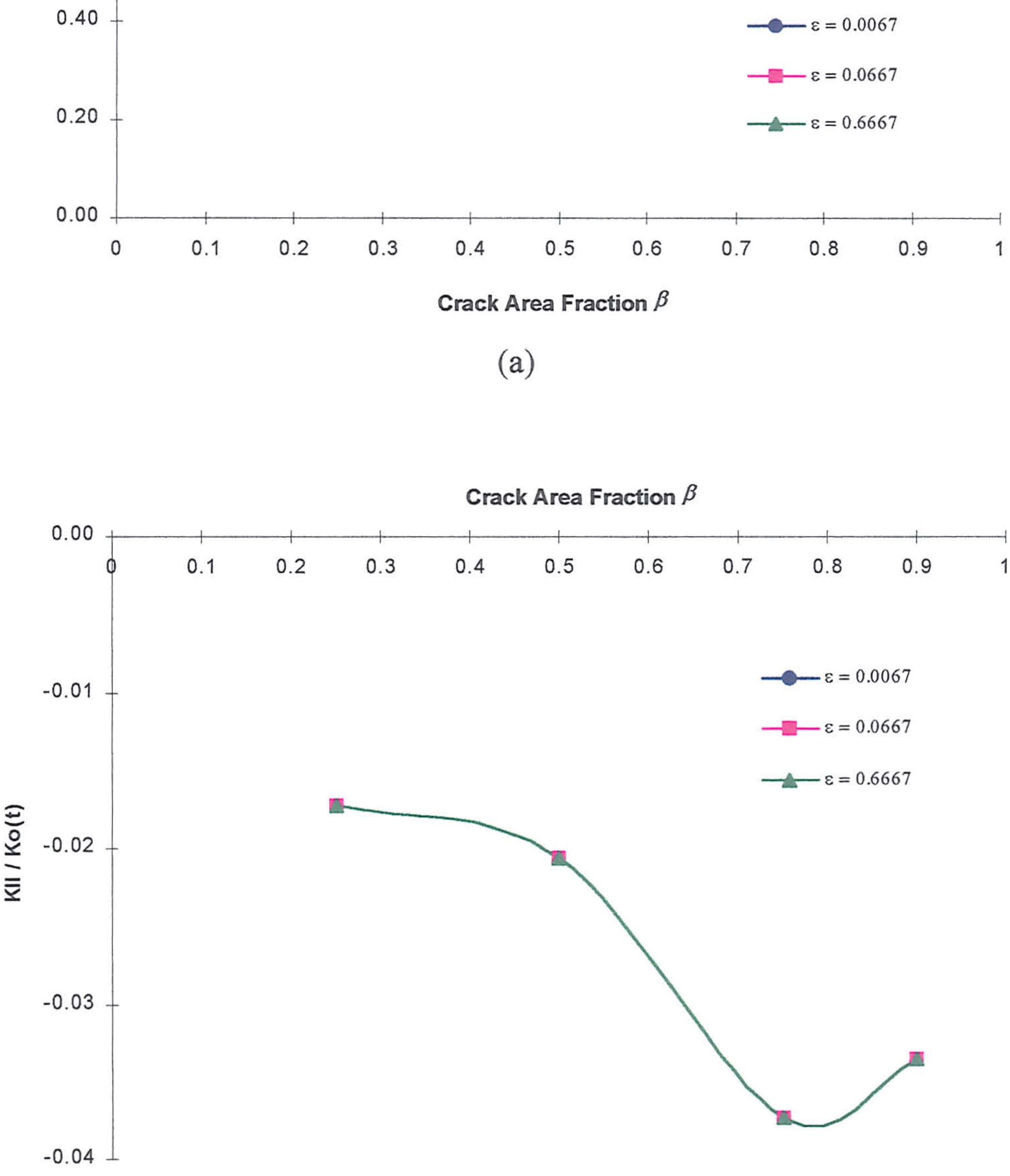

(b)

Fig. 9.4.3-4 Components of the normalised stress intensity factor of a co-linear crack in tension plotted as a function of β for different applied strain of ε : (a)

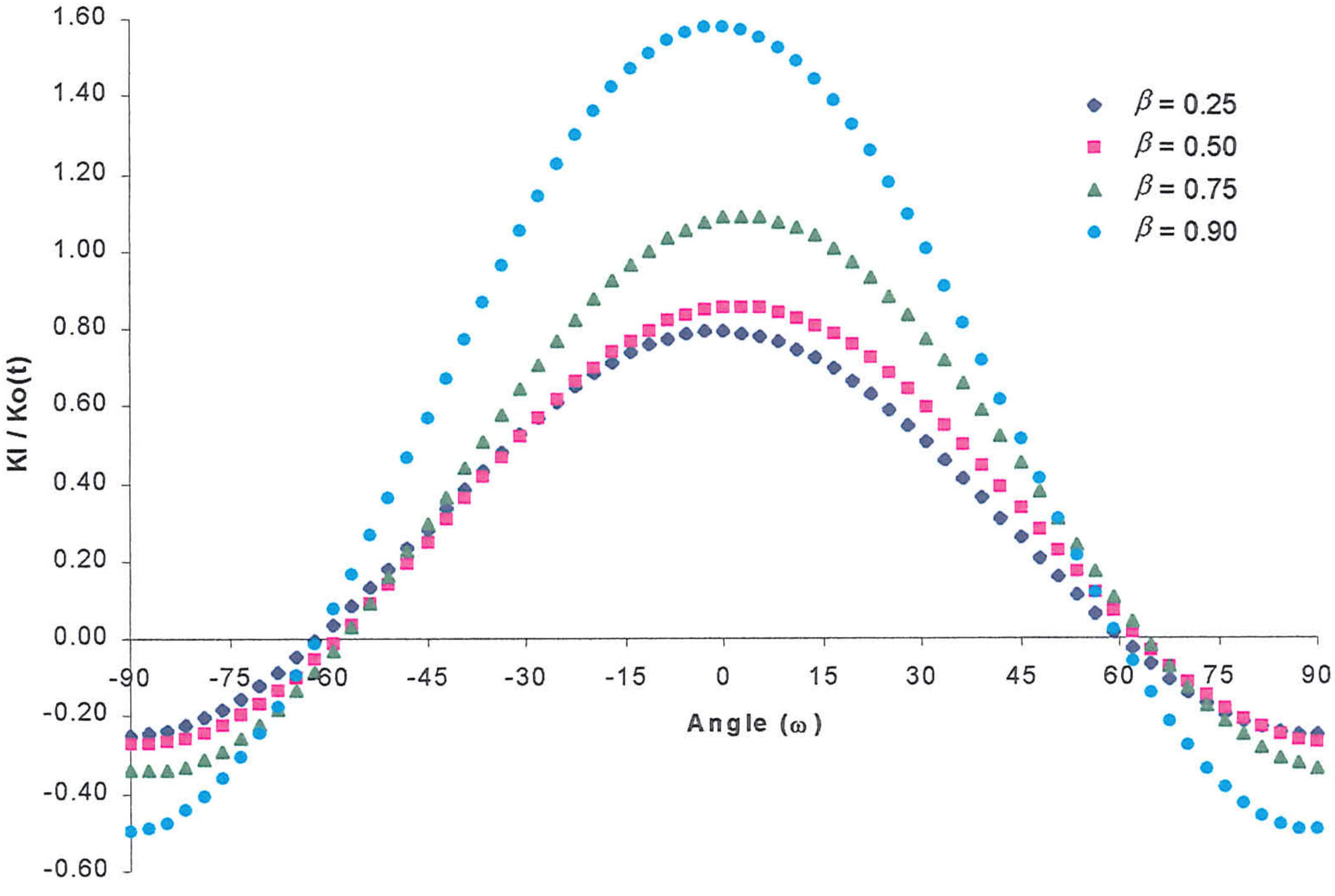

(a)

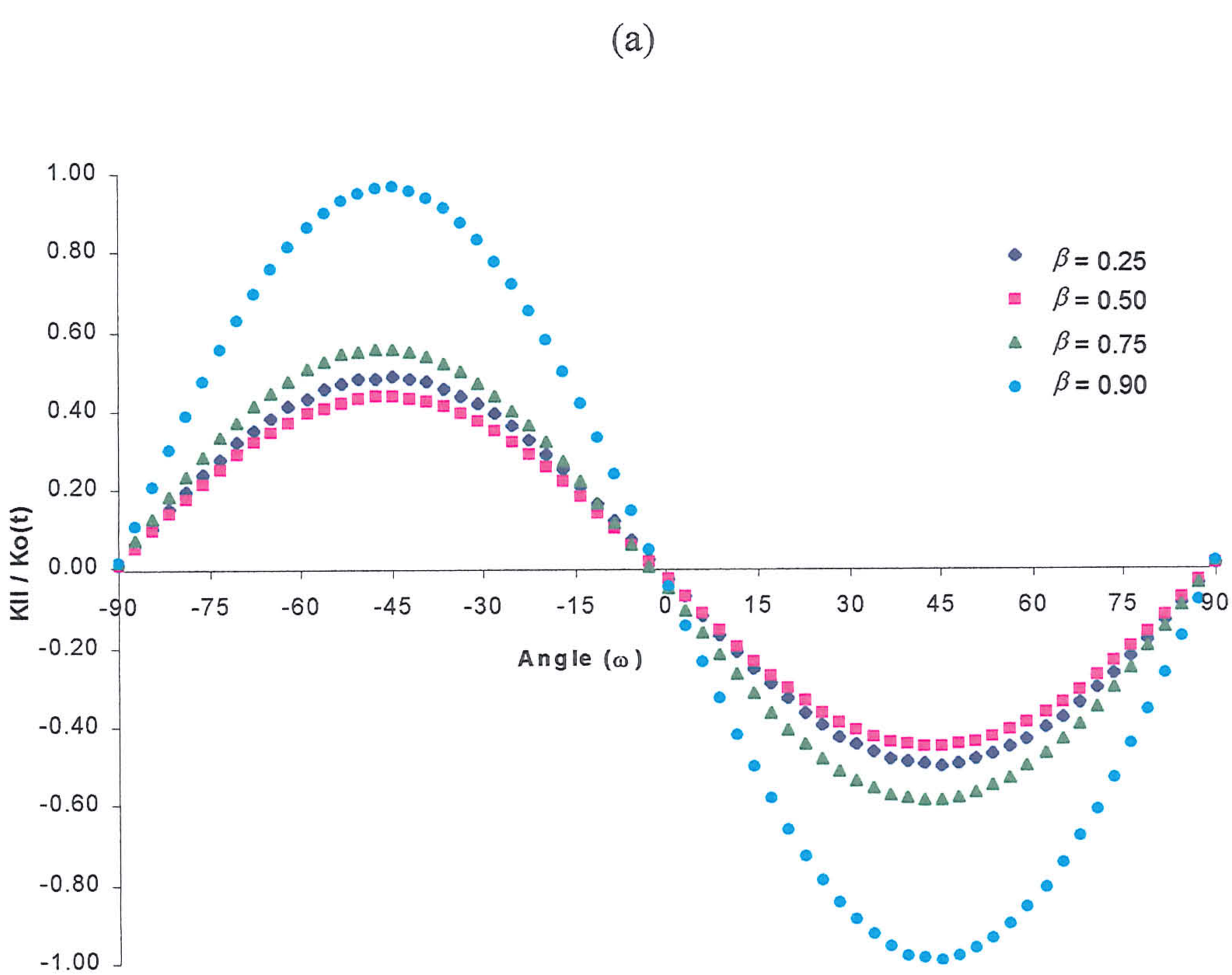

(b)

Fig. 9.4.3-6 Normalised K_n fields along the damaged interface of a rigid inclusion and an elastic matrix with periodic boundary conditions when remotely

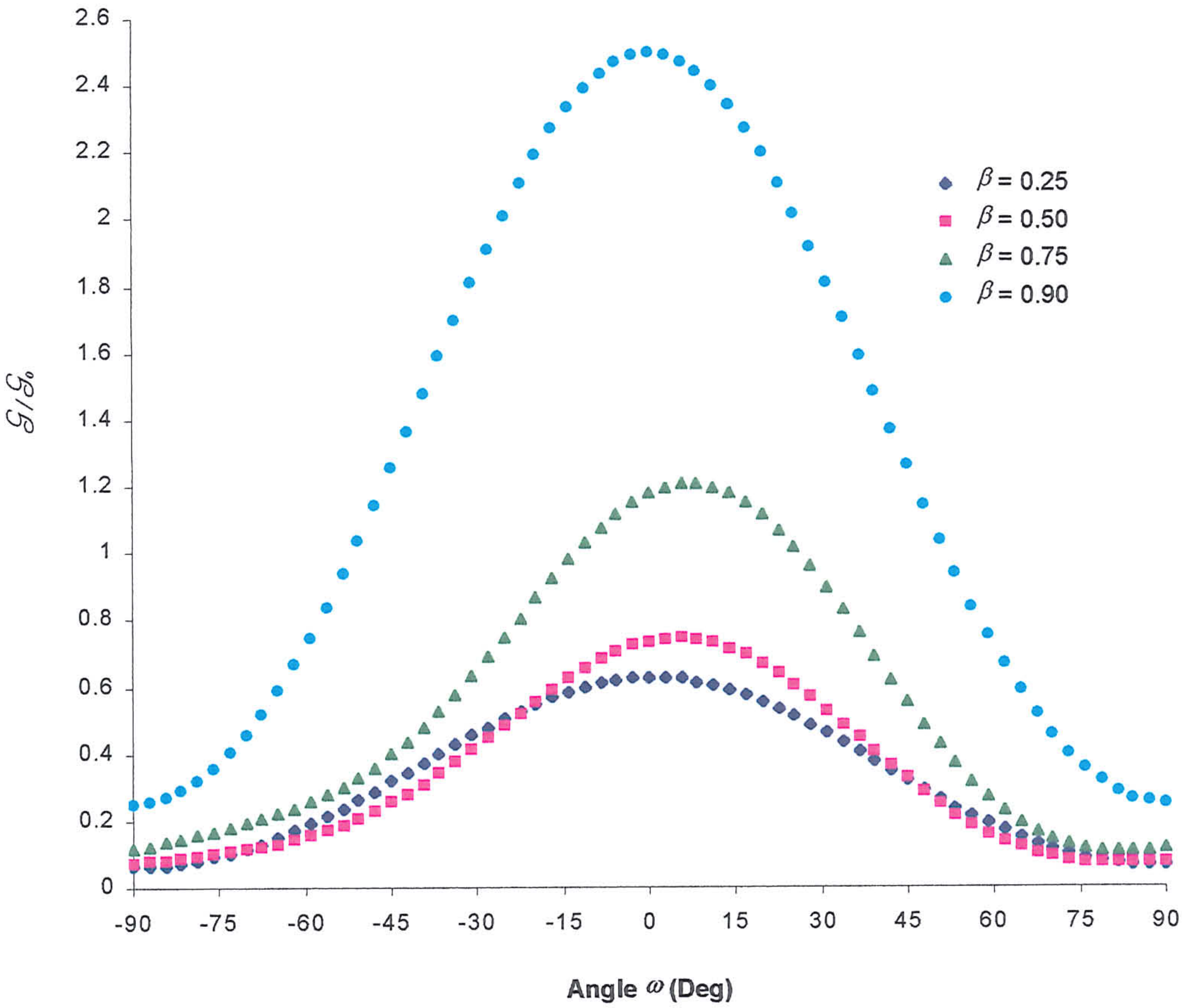

Fig. 9.4.3-7 Normalised strain energy release rate along the interface of a rigid inclusion and elastic matrix when remotely tension for crack area fraction $\beta = 0.25$, 0.50, 0.75 and 0.90.

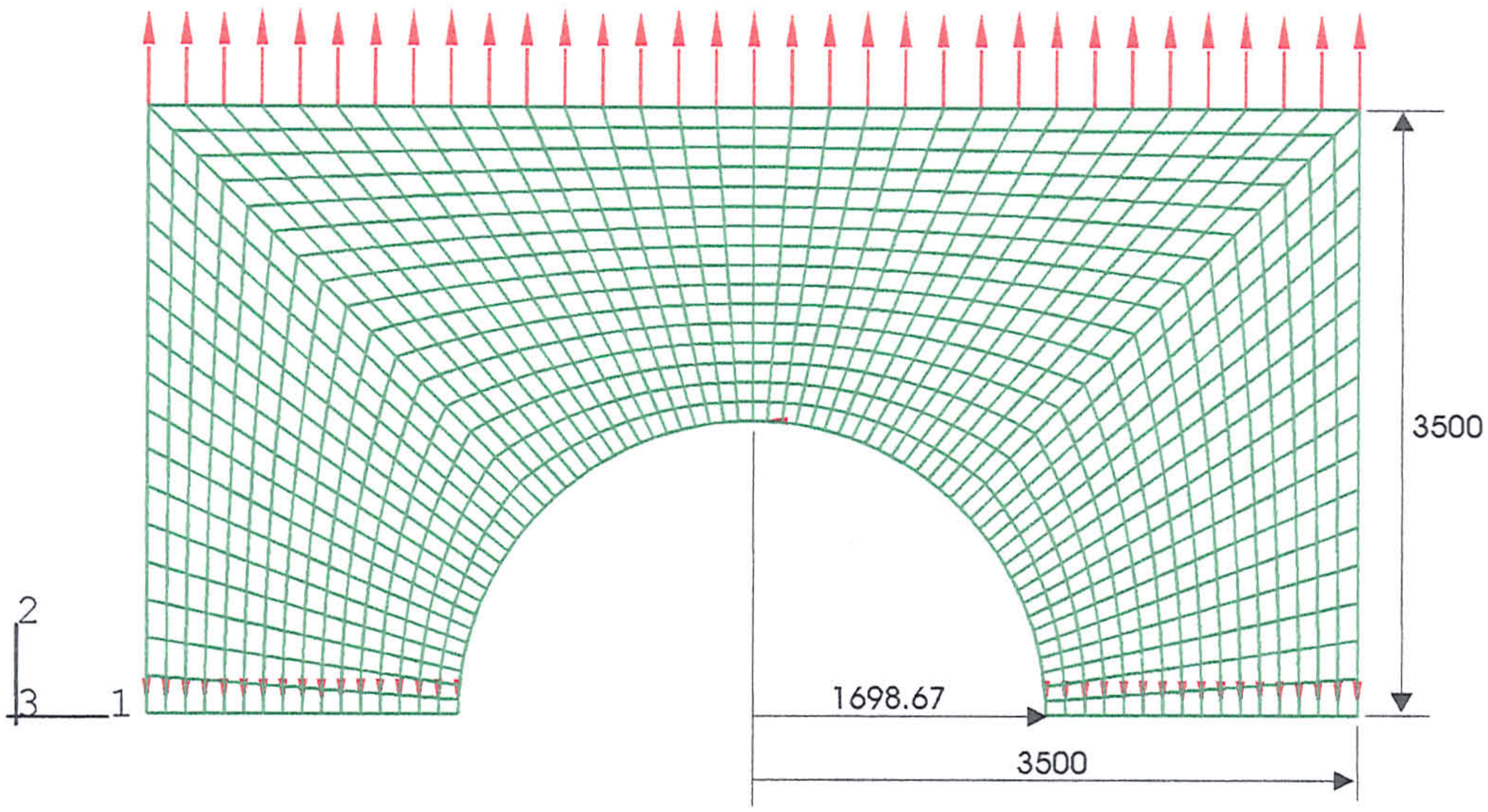

Fig 9.5.2-1 Schematic half of the unit cell model of a rigid cylindrical fibre embedded in a deformable finite matrix.

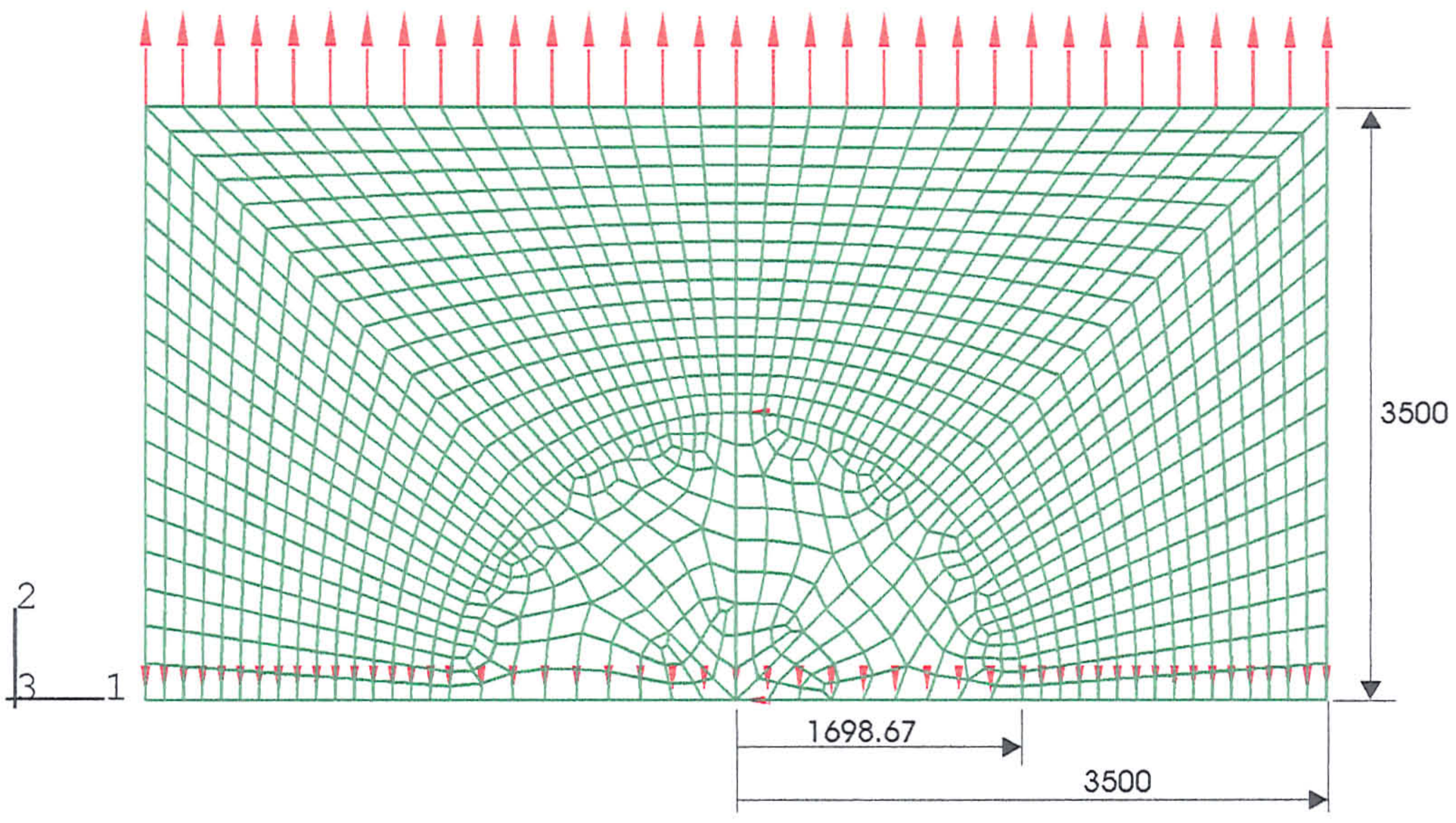

Fig 9.5.2-2 Schematic half of the unit cell model of a deformable cylindrical fibre embedded in a deformable finite matrix.

(a) $\beta = 0$

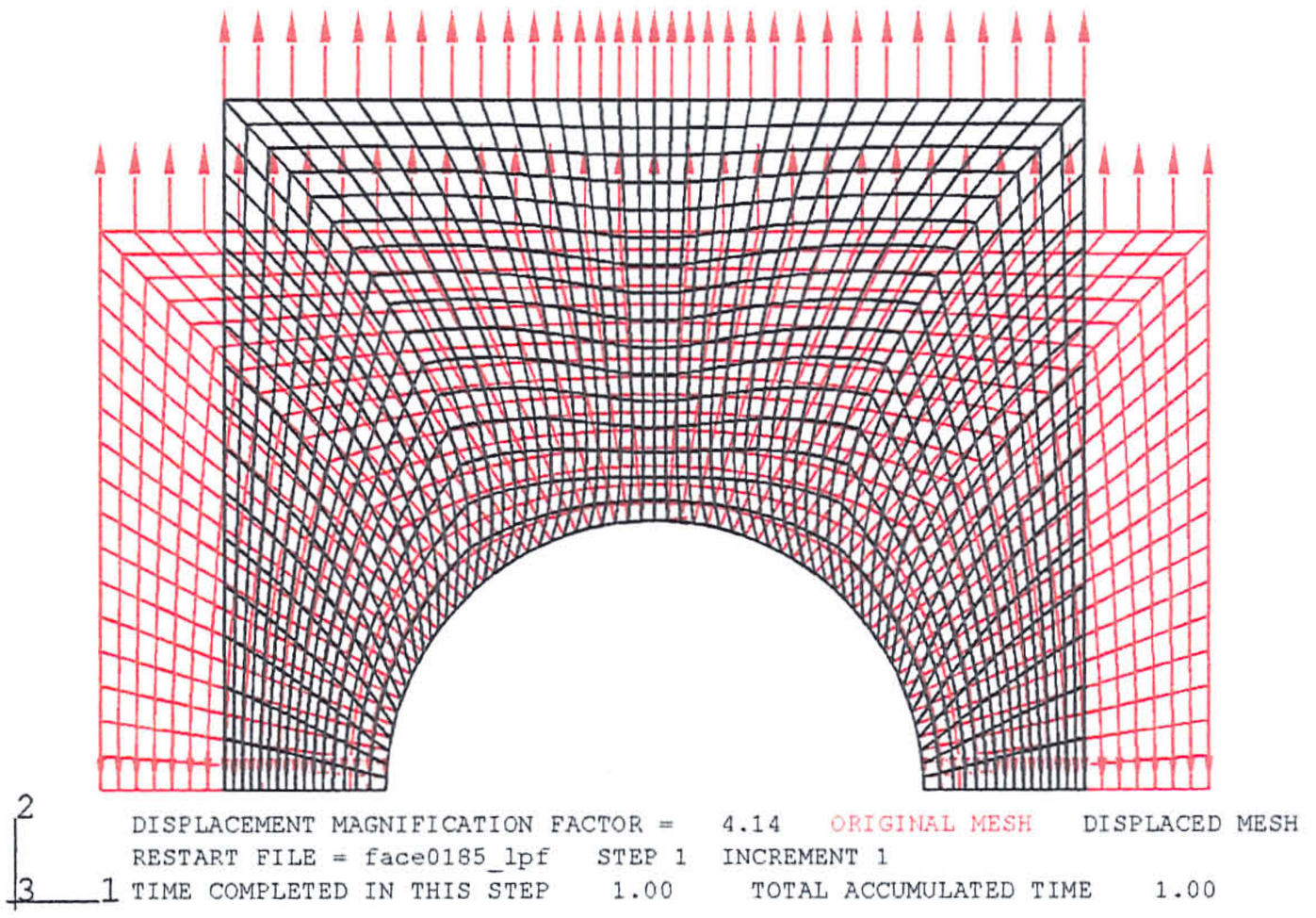

(b) $\beta = 1.00$

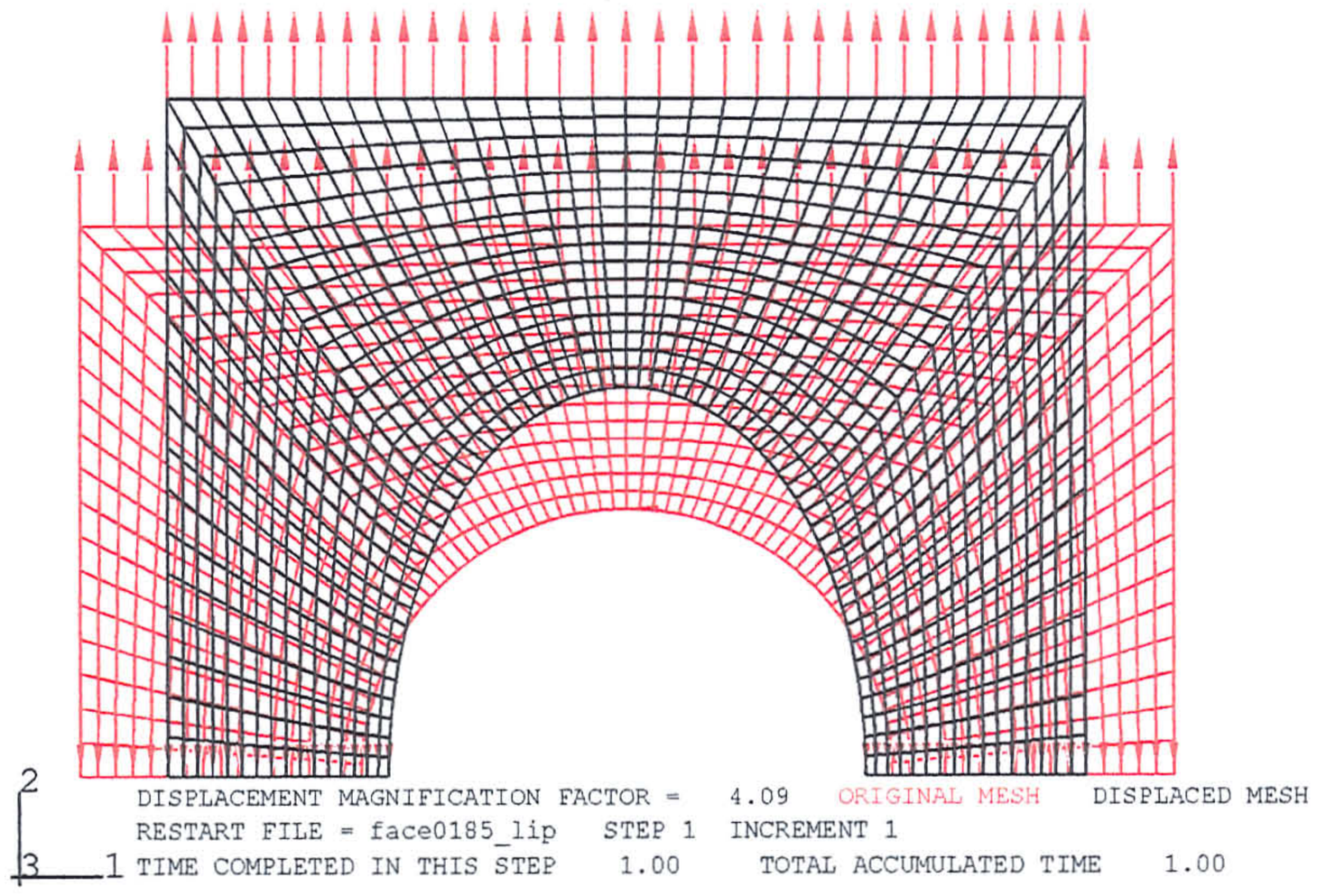

(c) $^*\beta = 1.00$ with no interpenetration

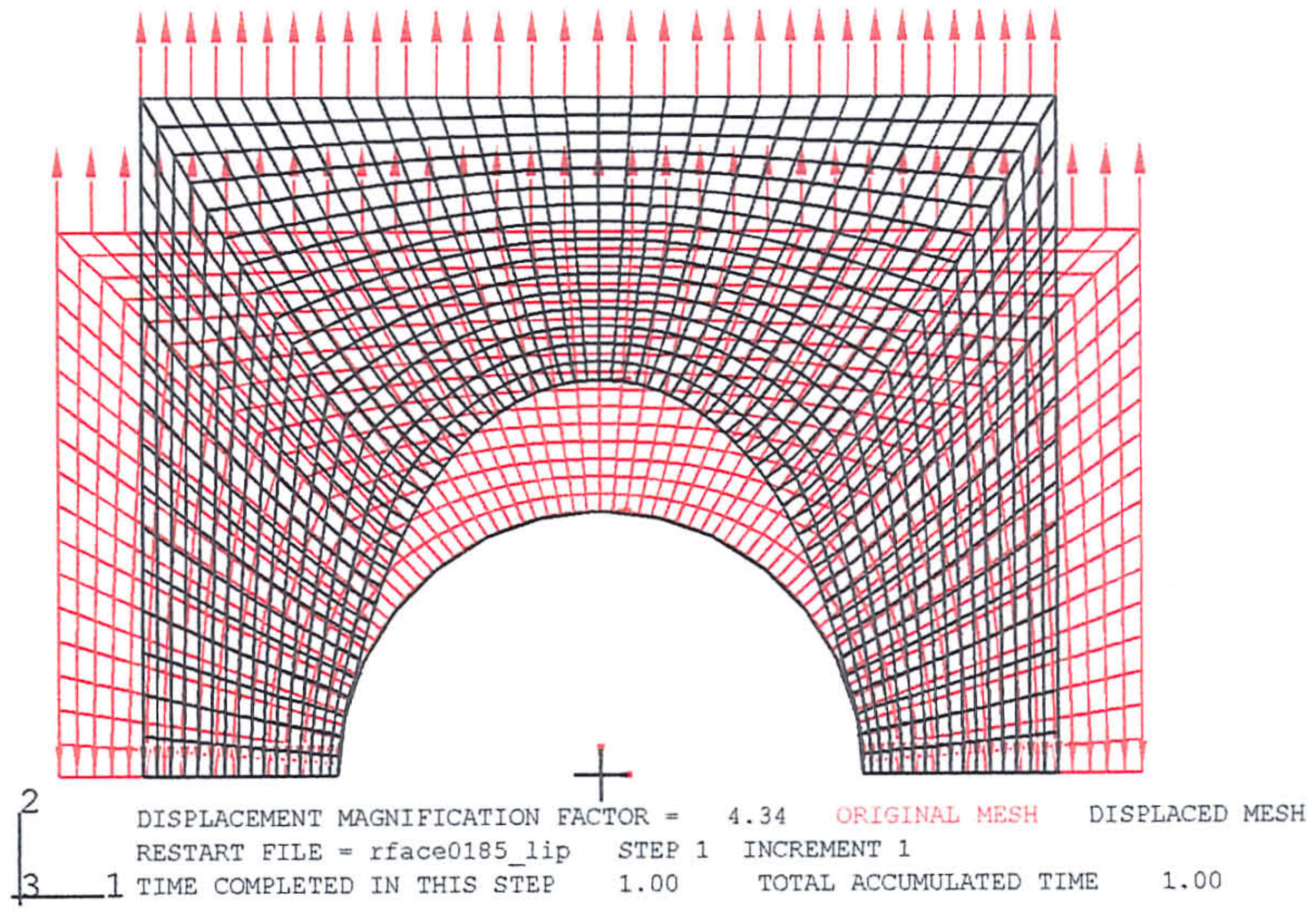

Fig 9.5.2.2 The deformed mesh of the unit cell model of a finite rigid fibre

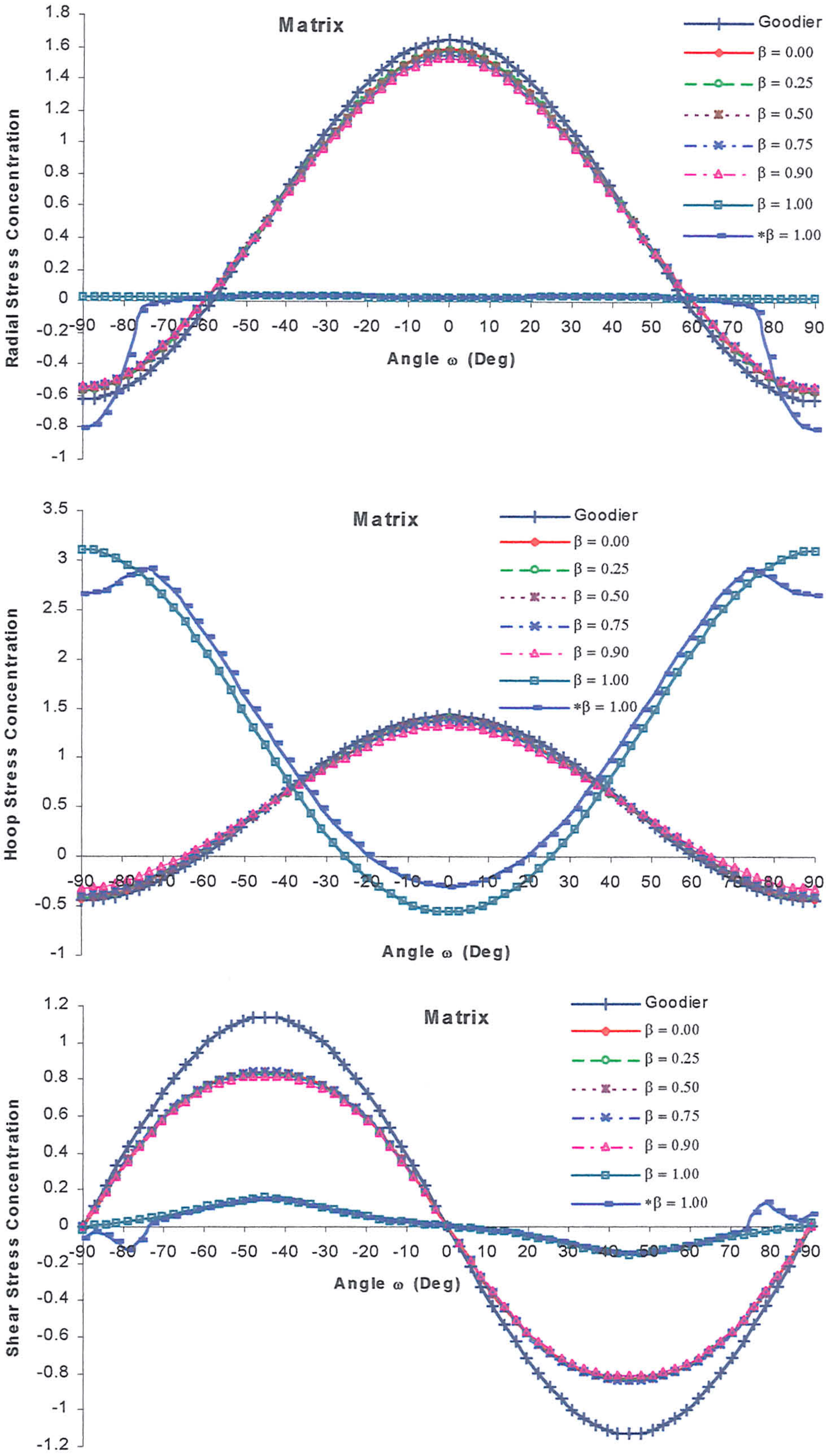

Fig 9.5.3-2 The radial, hoop and shear stress concentrations of the matrix near a finite rigid fibre, plotted as a function of angular orientation ω, for

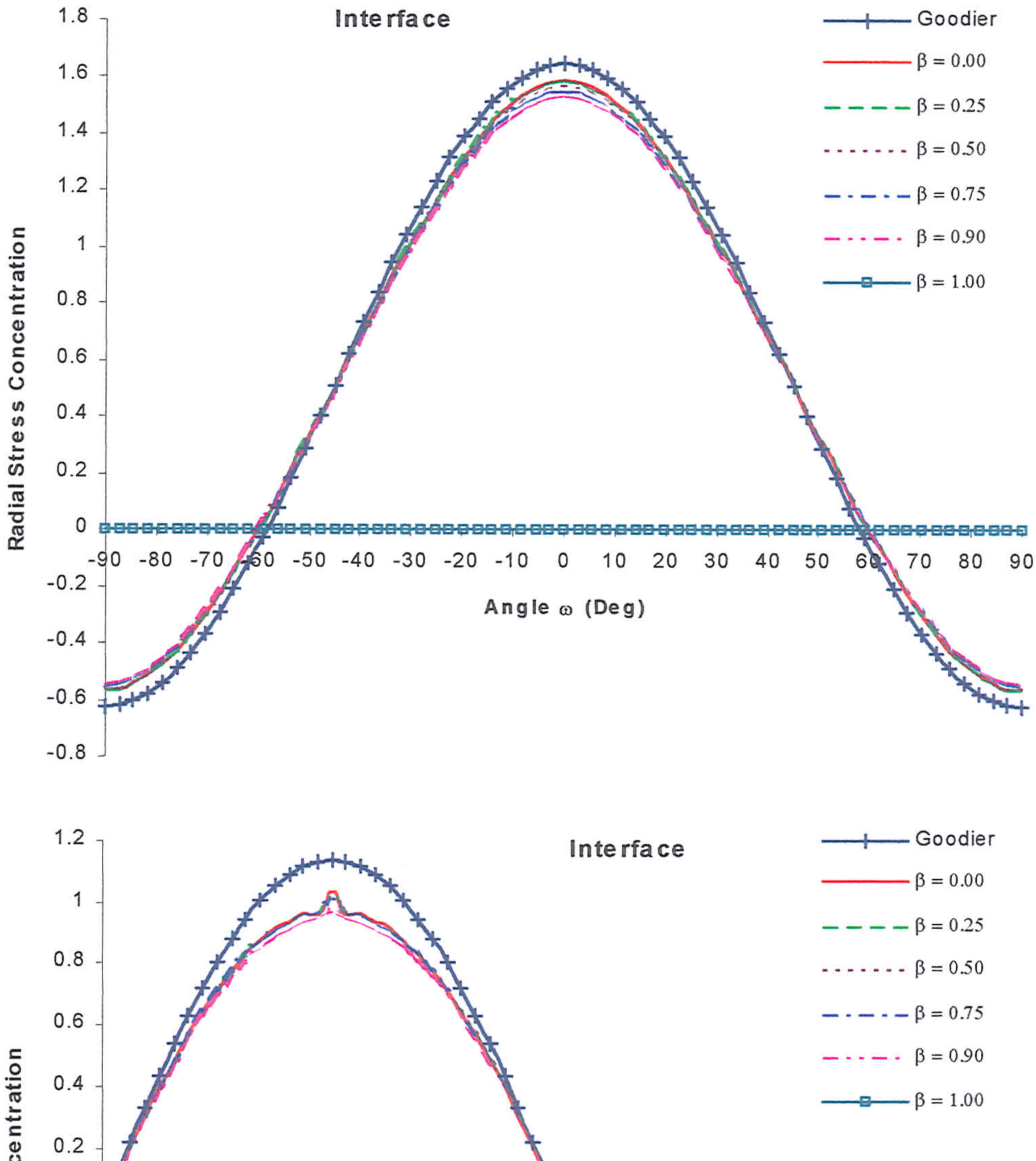

Fig 9.5.3-3 The radial and shear stress concentrations of a rigid interface with different crack area fraction β plotted as a function of the angular

(a) $\beta = 0$

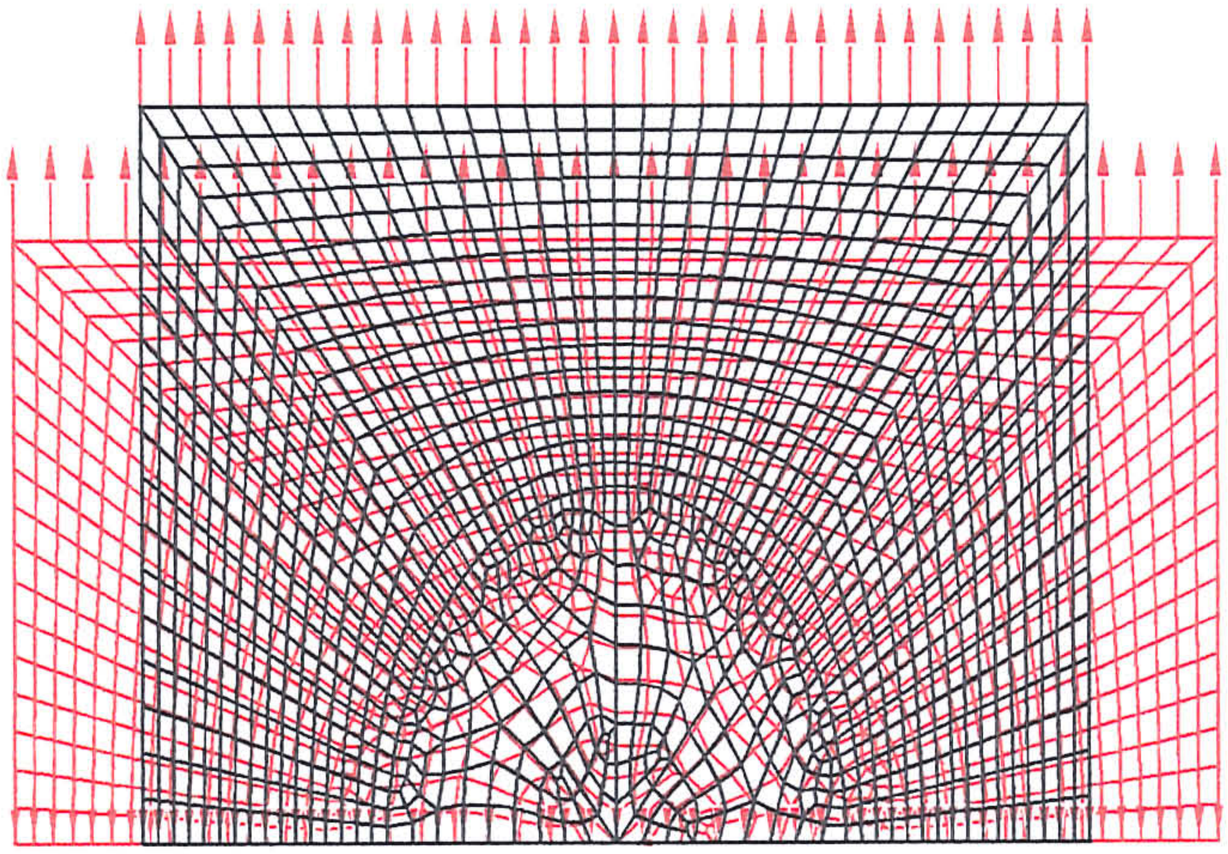

(b) $\beta = 1.00$

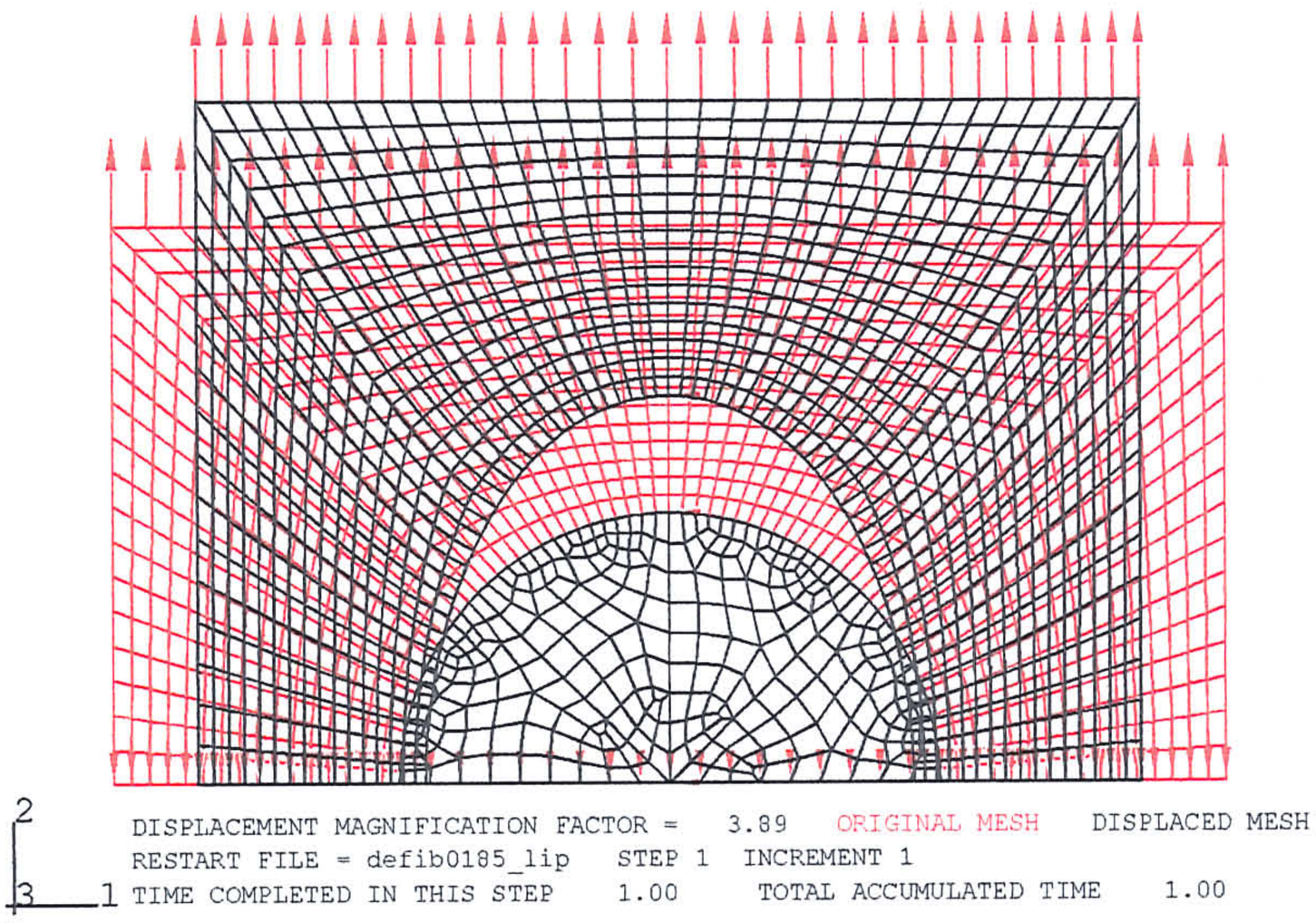

(c) $*\beta = 1.00$ with no interpenetration

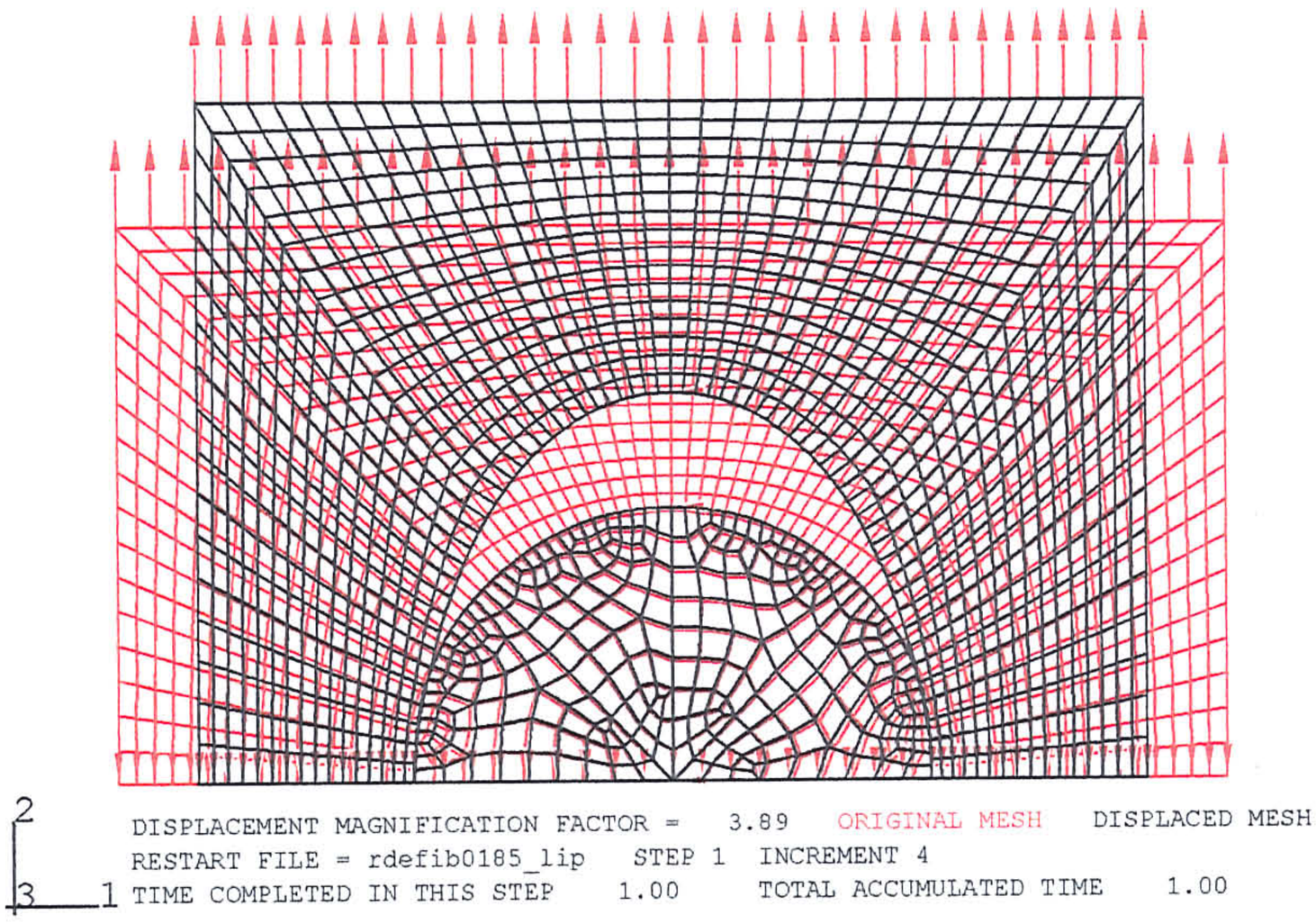

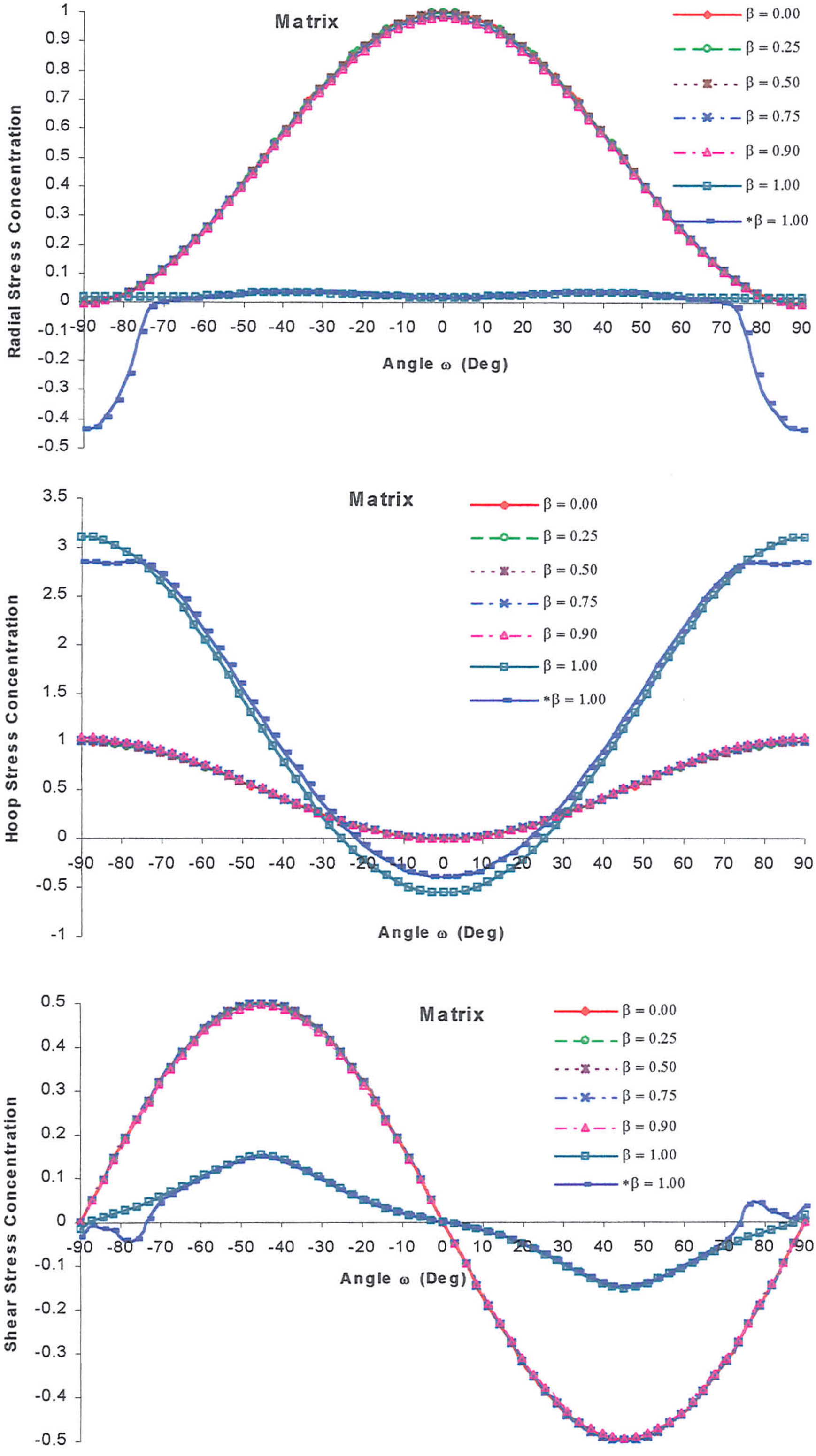

Fig 9.5.3-5 The radial, hoop and shear stress concentrations of the matrix near a

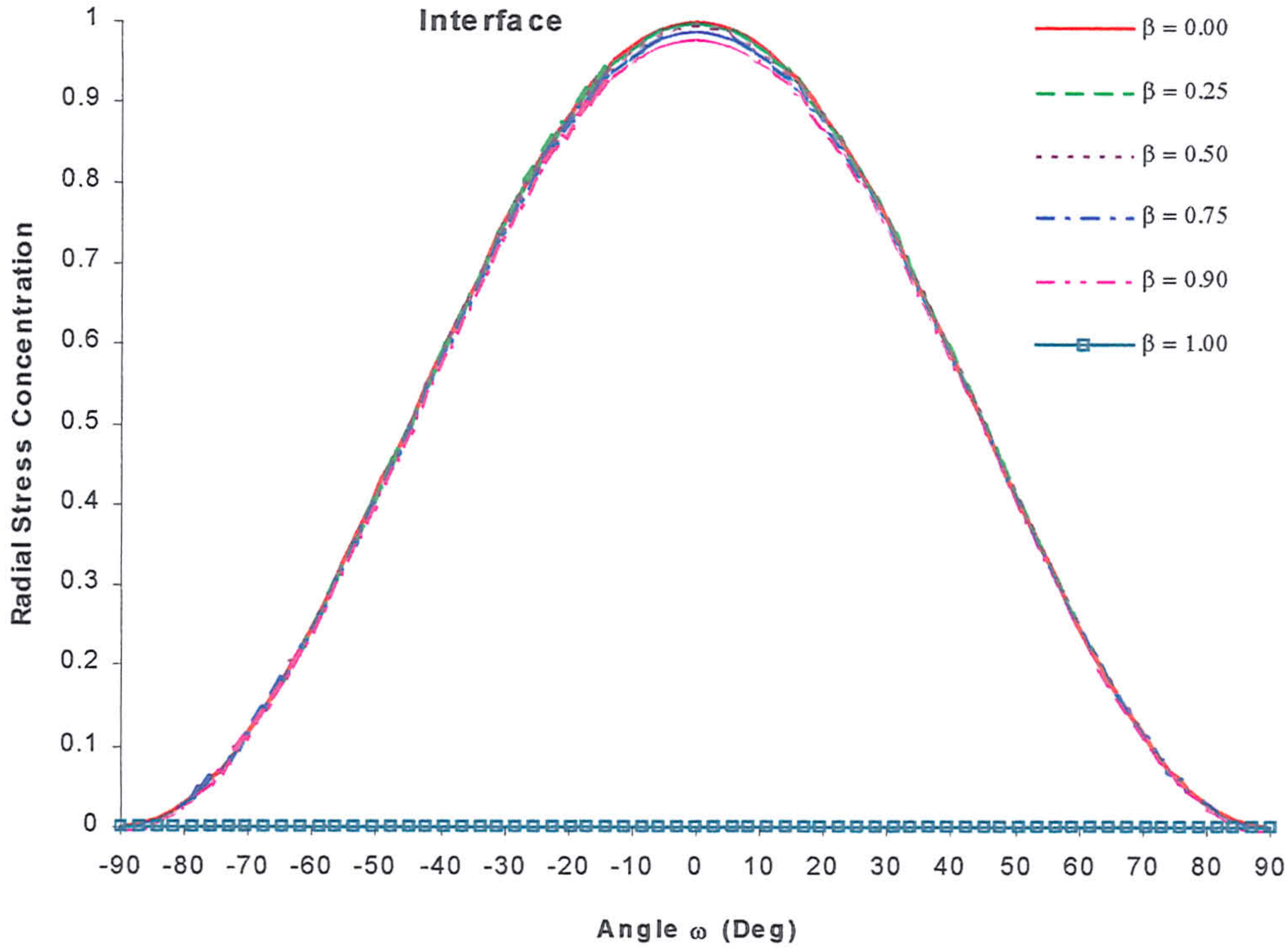

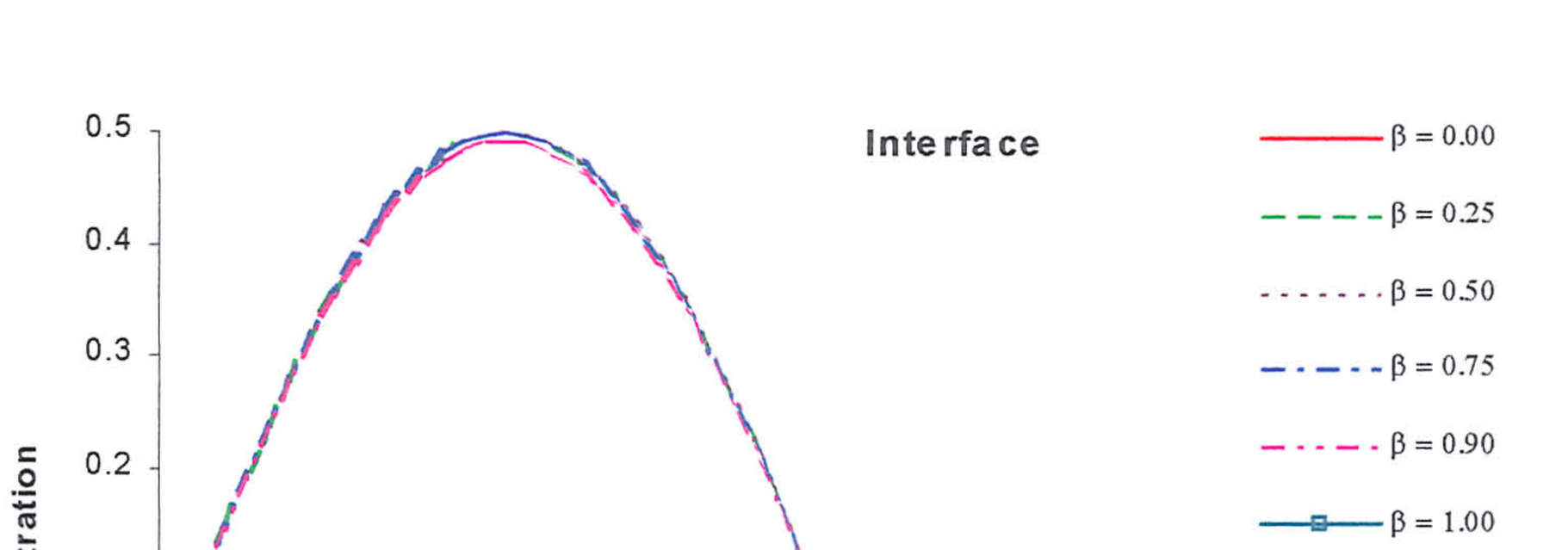

Fig 9.5.3-6 The radial and shear stress concentrations of an interface of a deformable fibre and matrix with different crack area fraction β plotted as a function

Perfectly Bonded Interface **Unbonded Interface**

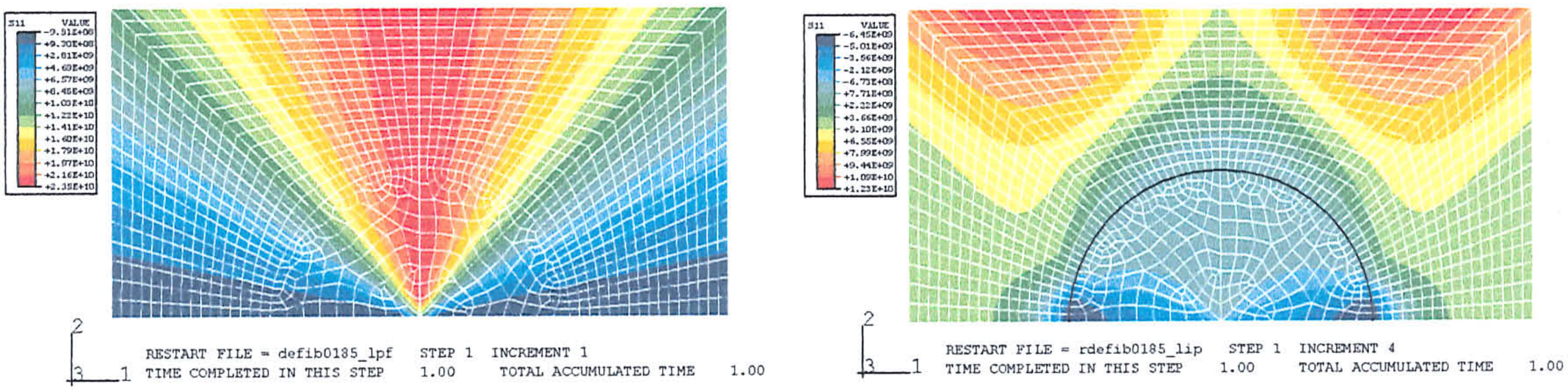

Radial Stress Component

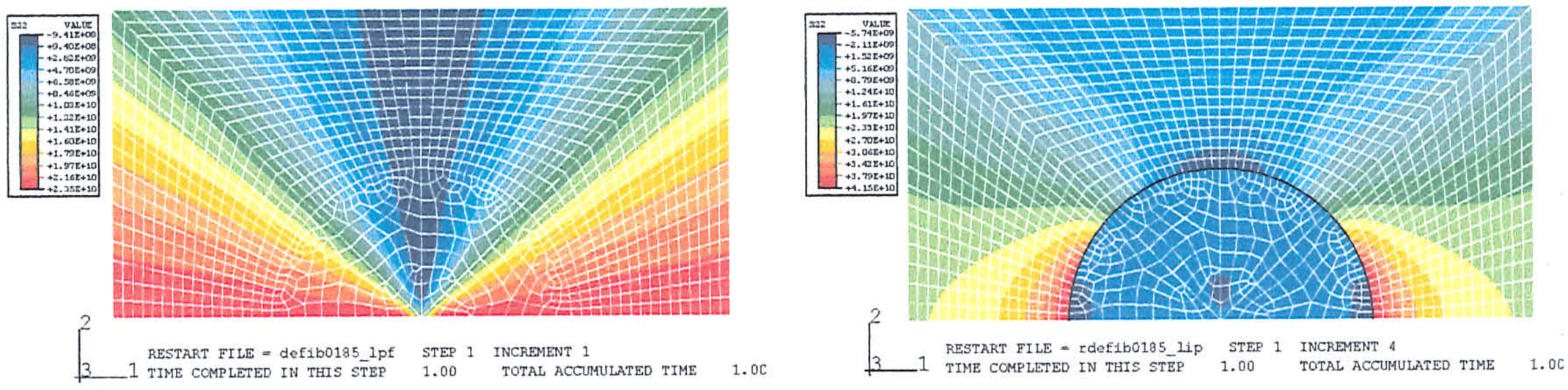

Hoop Stress Component

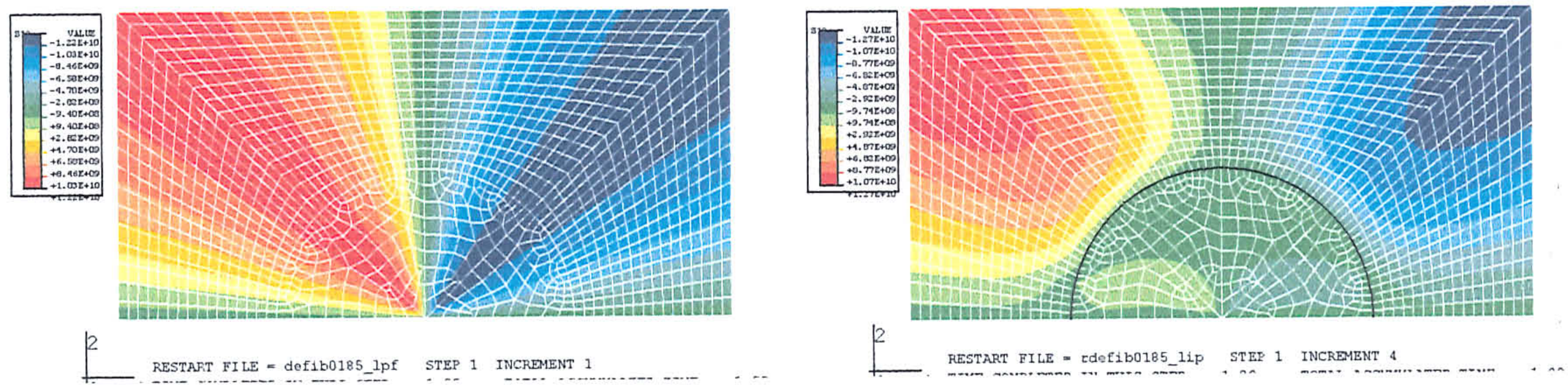

Shear Stress Component

Fig 9.5.3-7 Contour plots of the radial, hoop and shear stresses in the finite deformable fibre and matrix during uniaxial tension.

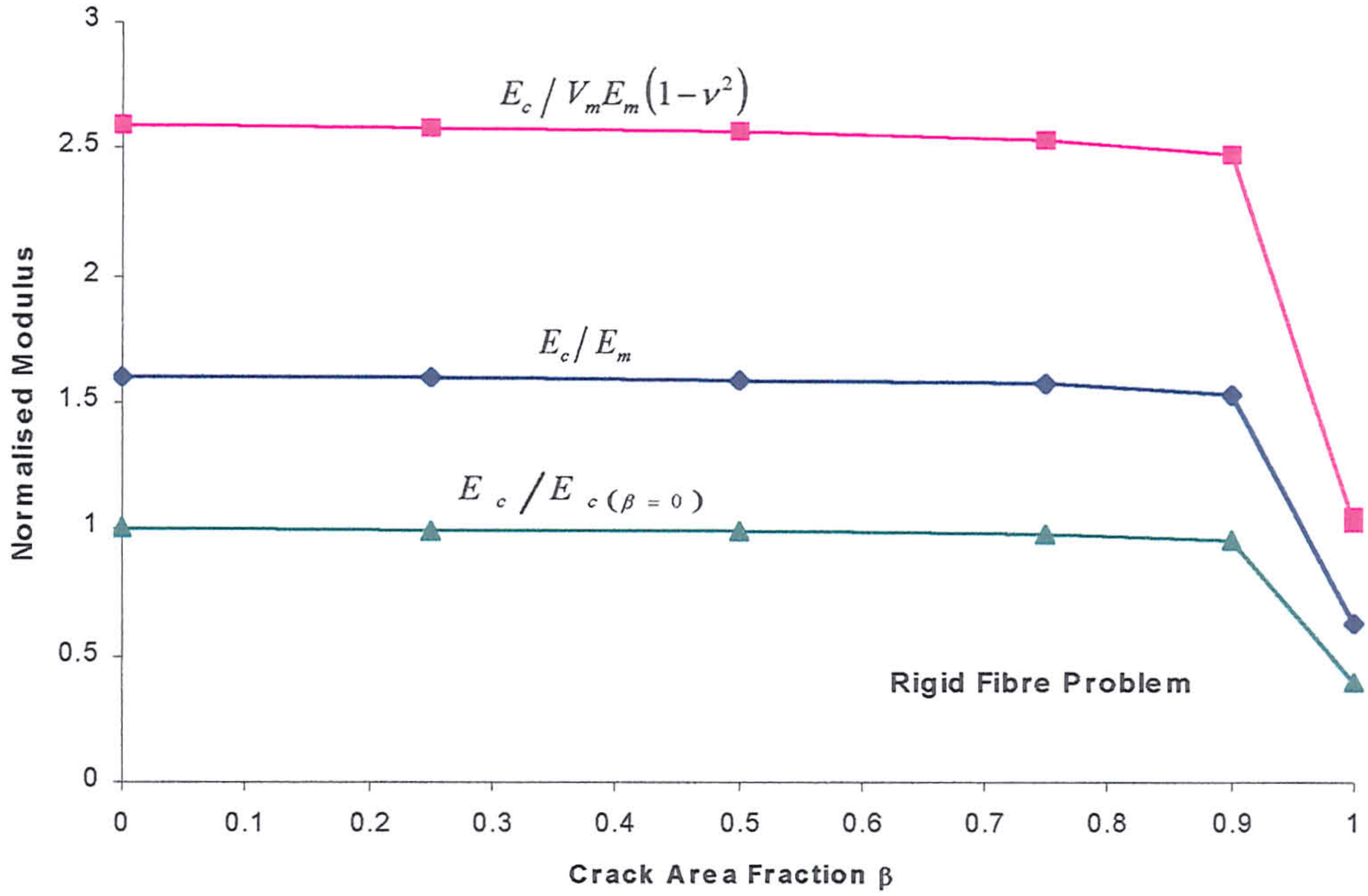

Figs 9.5.4-1 Normalised plot of the transverse modulus of a composite embedded with unidirectional rigid cylindrical fibres.

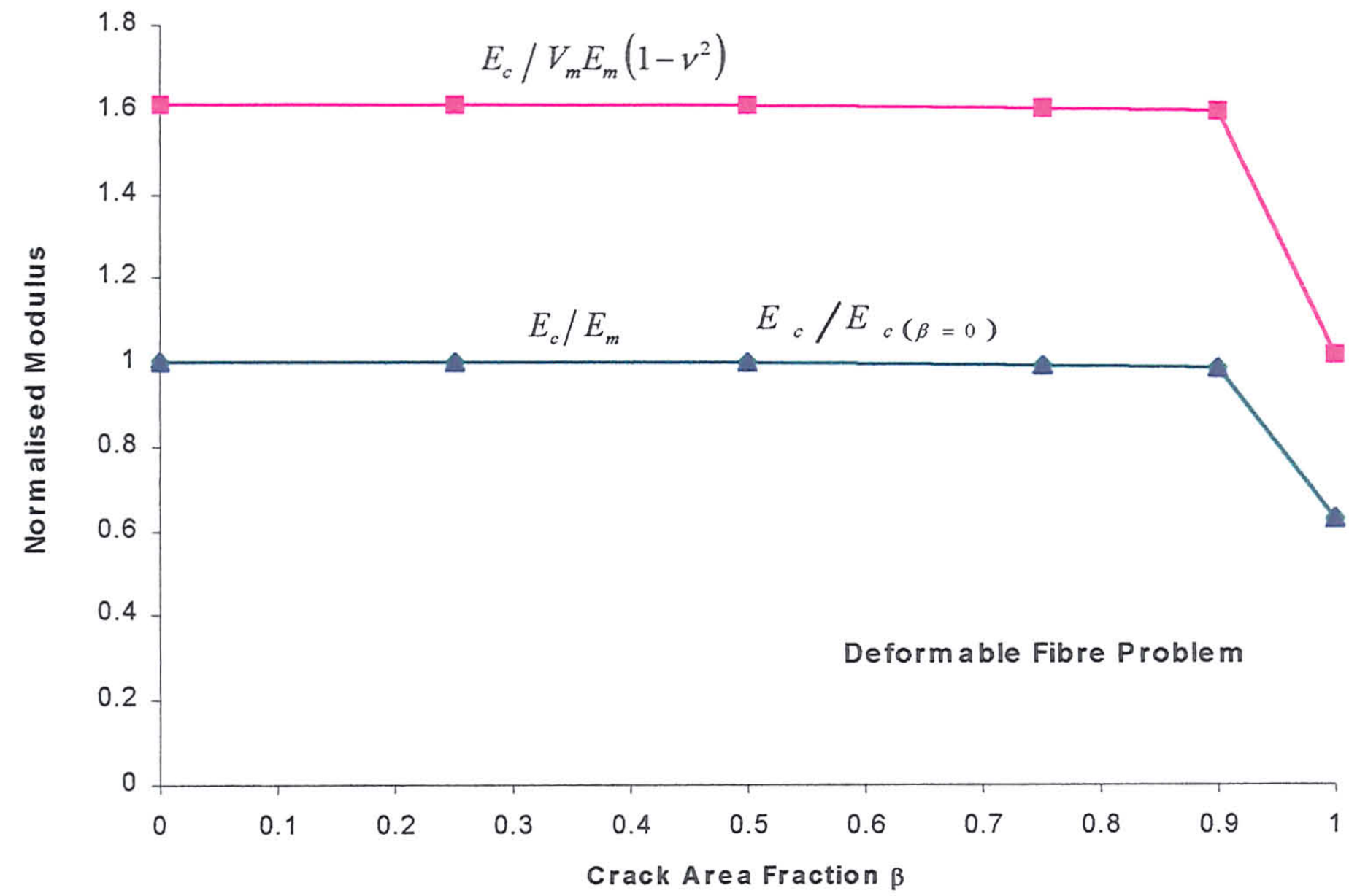

Figs 9.5.4-2 Normalised plot of the transverse modulus of a composite embedded with unidirectional elastic cylindrical fibres, with no modulus mismatch

CHAPTER 10

Conclusions

The thesis describes a micromechanics-based continuum damage mechanics approach to model the mechanical behaviour of brittle matrix composites. The aim was to develop a computational tool for the design and analysis of engineering components made of brittle matrix composites with continuous fibres.

To develop the damage mechanics model, the micromechanics of the deformation and failure of brittle matrix composites were established by mechanical testing polyester/polyester composite systems with unidirectional and a balanced 0°-90° woven fibre architectures. The polymer system was considered because it exhibits low elastic mismatch between the fibres and matrix, and shows similar non-dimensionalised stress–strain response to a SiC/SiC composite proposed for the exhaust diffuser unit of the Rolls-Royce EJ200 aero-engine. The polymer system was cheap to manufacture and the lead-time was shorter than the SiC/SiC composite. Specimens are translucent which allowed damage in the composite to be easily observed optically.

In specimens with aligned and misaligned unidirectional fibres, uniaxial tension tests demonstrated that matrix micro-cracking, delamination and fibre failure caused anisotropic non-linear deformation and fracture. Matrix micro-cracking did not necessarily form normal to the fibre direction as assumed by Hull & Clyne (1996). Instead, the micro-crack normal was inclined at an angle to the fibres when the applied load was greater than 10° off-axis to the fibre direction. When the angle between the applied load and the fibre direction was greater than 30°, delamination developed parallel to the fibres. When matrix micro-cracking was in transition to delamination, both matrix micro-cracking and delamination were shown to occur simultaneously.

In test specimen reinforced with woven fibres, off-axis uniaxial tension tests revealed that matrix micro-cracking caused the composite to deform non-linearly and the composite failed when the fibres failed. The normal to the matrix cracks was shown inclined at an angle to the fibres during off-axis load, with the exception for the fibre

direction, the crack initiation stress of the matrix was lower than the matrix cracking stress of the composite reinforced with unidirectional fibres. The reduction in matrix strength implied that the weakly bonded interface of the orthogonal fibres influenced the matrix crack initiation stresses.

To provide experimental data to verify the damage mechanics model, a range of idealised structures of the exhaust diffuser unit of the Rolls-Royce EJ200 aero-engine have also been manufactured and tested in bending. The sub-structural specimens included a simple rectangular bar, a bar with a thickened cross-section, and a T-shaped structure. These sub-structures showed the full range of damage mechanisms, which often simultaneously occurred in brittle matrix composite engineering structures.

It is advantageous to model damage at a constituent level as opposed to the composite level, since the anisotropic non-linear deformation and fracture of brittle matrix composites are caused by damage in the matrix and fibres. The damage mechanics approach developed in the thesis modelled the constitutive relation of the composite by decomposing the composite compliance into terms attributable to the fibre and matrix. This approach is valid over sizes scales large compared to the spacing of the fibres and the dimensions of the damage, and has been shown to satisfy both the equilibrium and compatibility conditions of a composite through the computational study of the distributive fibre representation scheme. The matrix has been allowed to sustain damage in the form of matrix micro-cracking, shear delamination and tensile delamination, and the matrix compliance has been modelled as transversely-isotropic damage-elastic. The fibres were allowed to break in the fibre direction, and were treated as weakly bonded to the matrix in which the fibre compliance have been modelled as one-dimensionally elastic until failure. The initiation of damage in the matrix and fibre failure were modelled using maximum stress theory, in which matrix micro-cracking was taken to occur normal to the maximum principal stress direction of the matrix, and shear or tensile delamination occurred parallel to the fibres. The model requires the evolution of matrix micro-cracking to be modelled using experimental data of the damaged stress-strain response of the matrix. Delamination failure was modelled by rapidly decaying the matrix stiffness to reduce the load bearing capacity of the composite. During compression, the matrix stiffness was identical to the undamaged state with the exception that the fibres were assumed not to transmit compressive loads.

plane stress and integrated into the ABAQUS/Standard displacement based finite-element solver, through a user-defined subroutine.

Uniaxial tension test specimens containing aligned and misaligned fibres and the idealised structures of the diffuser unit of the Rolls Royce EJ200 aero-engine have been analysed. The computational and experimental results show that the damage mechanics model was able to correctly predict the damage mechanisms, failure processes and non-linear deformation of brittle matrix composites. In particular, the damage mechanics model was able to model competing and co-existing damage mechanisms, as demonstrated by the agreement between the experimental and computational force-deflection responses and damage zones of the composite sub-structural components. The computational model identified the factors that determined the integrity of the idealised structures as follows:

1. Matrix micro-cracking caused the initial loss in stiffness in the sub-structures.
2. In the rectangular and wedged-shaped structures, the subsequent loss in stiffness was determined by the level of multiple matrix cracking, whereas the T-shaped sub-structure stiffness was largely dependent on the extent of shear delamination.
3. The structures containing woven fibres were more prone to damage compared to the structures reinforced with unidirectional fibres. The weak bonding at the fibre-matrix interface caused the lower cracking stress. As such, the stiffness of the sub-structures with woven fibres during multiple matrix cracking has been shown less stiff than the same structure reinforced with unidirectional fibres.
4. In the T shaped structure, the formation of a core of matrix centrally located in the fillet can delay the initiation of delamination and increase the load bearing capability to the structure. This is because the shear strength of the matrix was greater than the shear strength of the composites, which was weakened by the fibre-matrix interface.

A reason for the success of the damage mechanics model was that the criteria modelling matrix cracking, shear delamination and tensile delamination initiation have a physical base. Matrix cracks were allowed to form normal to the maximum principal stress direction of the matrix and not orthogonal to the fibre axis, and the orientation of shear and tensile delamination were necessarily fixed by the orientation of the fibres. The other reason attributing to the success was that the criteria modelling damage were implemented at a constituent level and not at a composite level. This establishes an

advantage over macroscopic failure criteria, which do not provide information on the physical nature of damage or failure.

The success of the damage mechanics model supports the technique used to obtain the experimental matrix stress-strain response during multiple matrix cracking. The technique is based upon the micromechanics of composites developed by Aveston, Cooper & Kelly (1971), which allows the average matrix response to be obtained by subtracting the response of the volume fraction of fibres from the composite response. An advantage of using the experimental matrix data is that the nature of the atomic bonds and the effects of stress concentration, fibre distribution, crack size, crack distribution and crack interaction in the matrix were considered. As such, the prediction of matrix crack initiation would be better than the predictions given by the energy balance theories and stress intensity theories reviewed in Sect 3.4, which do no comprehensively consider the factors influencing matrix crack initiation. The other advantage is that damage is treated as a fourth order tensor and the evolution of multiple matrix cracking modelled through the experimental matrix stress-strain response did not violate any thermodynamic laws.

The effect of imperfect fibre-matrix interfaces on the mechanical properties of composites has been studied. Interface elements, which could represent the stiffness of imperfect interfaces, were developed to do this. For composites reinforced with cylindrical fibres, the stress concentration fields at the fibre-matrix interface were shown sensitive to imperfections only when the fibre-matrix interface was imperfect. For an imperfect interface, i.e. unbonded fibre-matrix interface, a maximum hoop stress concentration factor of 2.84 was reported in the matrix adjacent to the fibre-matrix interface at the angular co-ordinate of $+76^o \le \omega \le +90^o$ and $-76^o \le \omega \le -90^o$. These stress concentration regions indicated the possibility of pre-mature and also explain the lower matrix micro-cracking stress observed in the polyester/polyester composite reinforced with woven fibres. Another important finding from the computational study was that the presence of interfacial perfection reduced the stiffness. The transverse stiffness of composites with weakly bonded interface was approximated to be $E_m V_m$ in plane stress. Significantly, this approximation is similar to the stiffness used in the damage mechanics model. As such, a numerical validation for treating the fibre as a one-dimensional load bearing component in the damage mechanics model was

References:

ASTM D4255/D4255M-83 (1997), Standard Guide for Testing In-Plane Shear Properties of Composite Laminates, *Annual Book of ASTM Standards*, Vol. 15.03, p190-199.

ASTM E8M-88 (1988), Standard Test Methods for Tension Testing Metallic Materials, *Annual Book of ASTM Standards*, Vol. 3.01, p137-151.

Aveston, J., Cooper, G.A. and Kelly, A. (1971), Single and Multiple Fracture, *Conference Proceedings of the National Physical Laboratory: The Properties of Fibre Composites* (IPC Science and Technology Pres, Surrey, England), p15-26.

Aveston J. and Kelly A. (1973), Theory of Multiple Fracture of Fibrous Composites, *Journal of Materials Science*, **8**, p352-362.

Baaklini G.Y. & Batt R.T. (1991), In-situ X-ray Monitoring of Damage Accumulation in SiC/RSBN Tensile Specimens, *Ceram. Eng. Sci. Proc.*, **12** (7-8), p1599-1615.

Beyerle D.S., Spearing S.M. & Evans A.G. (1992), Damage Mechanisms and the Mechanical Properties of Laminate 0/90 Ceramic.Matrix Composite, *J. Am. Ceram. Soc.*, **75** [12], p3321-3330.

Bhatt R.T. & Phililps R.E. (1990), Laminate Behaviour of SiC Fiber Reinforced Reaction-Bonded Silicon Nitride Matrix Composites, *CCM Research Report 92-34*, University of Delaware.

Brender, B.A., *et al* (1984), Electron Microscopy of Ceramic Fibre-Ceramic Matrix Composites, Comparison with Processing and Behavior, *Ceram. Eng. Sci. Proc.*, 5 (7-8), p513-529.

Brennan, J.J. & Prewo, K.M. (1982), Silicon Carbide Fibre Reinforced Glass-Ceramic Composites Exhibiting High Strength and Toughness, *J. Mater. Sci.*, 17(8), p2371-2382.

BS EN ISO 527-5: 1997, Plastics-Determination of Tensile Properties—Part 5: Test Condition for Unidirectional Fibre-Reinforced Plastic Composites, British Standard, p1-9.

Butler E. (1992), Private Communication, Rolls Royce Plc, PO Box 31, Moor Lane, Derby.

Budiansky, B., Hutchinson, J.W. & Lambropolous (1983), Continuum Theory of Dilatant Tranformation Toughening in Ceramics, *Int. J. Solids Struct.*, 19[4], p337-55.

Budiansky B., Hutchinson J.W. and Evans A.G. (1986), Matrix Fracture in Fiber-Reinforced Ceramics, *J. Mech. Phys. Solids*, Vol. 34, No. 2, p167-189.

Burr, Hild & Leckie (1997), Continuum Description of Damage in Ceramic-Matrix Composites, *Eur. J. Mech. A/Solids*, 16, no. 1, p53-78.

Cao H.C., Bischoff E., Sbaizero O., Ruhle M., Evans A.G. Mashall D.B. & Brennan J. (1990), Effect of Interfaces on the Properties of Fibre-reinforced Ceramics, *J. Am. Ceram. Soc.*, **73** [6], p1691-1699.

Cao H. & Thouless M.D. (1990), Tensile Test of Ceramic-Matrix Composites: Theory and Experiment, *J. Am. Ceram. Soc.*, **73** (7), p2091-2094.

Chaboche, J.L. (1979), Le concept de contrainte effective appliqué à l'élasticté et à la viscoplasticité en présence d'un endom-magement anisotrope, Coll. Euromech 115, Grenoble, (CNRS, 1982).

Chaboche, J.L. (1981), Continuous Damage Mechanics – A Tool to Describe Phenomena Before Crack Initiation, *Nuclear Engineering and Design*, 64, p233-247.

Chaboche, J.L. (1982), Mechanical Behaviour of Anisotropic Solids, *Colloques internationaux du CNRS*, (ed. Boehler, J.P.), Martinus Nijhoff, p737-760

Chaboche, J.L. (1987), Continuum Damage Mechanics: Present State and Future Trends, *Nuclear Engineering and Design*, 105, p19-33.

Chen W.F & Saleb A.F (1994), Constitutive Equations for Engineering Materials Vol. 1: Elasticity and Modelling, Elsevier.

Chia J.Y.H & Hancock J.W (2000), Finite Element and Experimental Modelling of One-Dimensional SiC/SiC Composites, *7th Annual International Conference on Composites Engineering ICCE/7*, Juliy 2-8, Denver, Colorado, p127-128.

Chia J. & Hancock J.W (2002), Finite Element Modelling Damage in Brittle Matrix Composites, *Key Engineering Materials*, Vol. 227, p55-60.

Colemen B.D. (1958), On the Strength of Classical Fibres and Bundles, *J. Mech, Phys. Solids*, **7** (1), p60-70.

Cook, J. & Gordon, J.E. (1964), A Mechanism for the Control of Crack Propagation in All-Brittle Systems, *Proc. Roy. Soc. London*, **A282**, p508-520.

Cordebios, J.P. & Sidoroff, F. (1981), Damage Induced Elastic Anisotropy, *Colloques internationaux du CNRS*, (ed. Boehler, J.P.), Martinus Nijhoff, p761-744.

Cox B.N, Carter W.C and Fleck N.A (1994), A Binary Model of Textile Composites – I. Formulation, *Acta Mettall. Mater.*, Vol. 42, No. 10, p3463-3479.

Curtin W.A. (1991), Theory of Mechanical Properties of Ceramic Matrix Composites, , *J. Am. Ceram. Soc.*, **74** (11), p2837-2845.

Danchaivijit, S. & Shetty, D.K. (1993), Matrix Cracking in Ceramic-Matrix

Daniel H. E. (1945), The Statistical Theory of the Strength of Bundles of Threads, *Proc. R. Soc.*, **A183**, p405.

Davidge R.W. & Briggs A. (1989), The Tensile Failure of Brittle Matrix Composites Reinfroced with Unidirectional Continuous Fibres, *J. Mater. Sci.*, **24**, p2815-2819.

Davison, L & Stevens, A.L. (1973), Themomechanical Constitution of Spalling Elastic Bodies, *J. Appl. Phys.*, Vol. 44, No. 2, February.

Eckold, G.C. (1998), Failure Criteria for Use in the Design Environment, *Compos. Sci & Technol.*, **58**(7), p1095-1105.

Edge, E.C. (1998), Stress Based Grant-Sanders Method for Predicting Failure of Composite Laminates, *Compos. Sci & Technol.*, **58**(7), p1033-1044.

Ellis T.M.R. (1993) *FORTRAN 77 Programming with an Introduction to the Fortran 90 Standard*, Second Edition, Addison Wesley Publishing Company.

Evans, A.G. (1990), Perspective on the Development of High-Toughness Ceramics, *J.Am. Ceram. Soc.*, **73**[2], p187-206.

Gibson R. (1993), *MSc Thesis*, University of Glasgow.

Goda Koichi (1999) The Role of Interfacial Debonding in Increasing the Strength and Reliability of Unidirectional Fibrous Composites, *Composite Sci. & Techno.*, **59**, 1871-1879

Goodier (1933), Concentration of Stress Around Spherical and Cylindrical Inclusions and Flaws, *ASME Applied Mechanics Magazine*, 55, p39-44

Gotsis P.K, Chamis C.C & Minnetyan L. (1998), Prediction of Composite Laminate Fracture: Micromechanics and Progressive Fracture, *Compos. Sci. Technol.*,**58**(7), p1137-1149.

Grande D.H., Mandell J.F., Hong K.C.C (1988) Fibre-Matrix Bond Strength Studies of Glass Ceramic, and Metal Matrix Composites. *J of Mat. Sci.*, **23**, 311-328.

Hale, D.K. & Kelly, A. (1972), Strength of Fibrous Composite Materials, *Annual Review of Material Science*, 2R, ed. Huggin, A. *et al*, p405-462.

Hart-Smith L.J. (1993), Should Fibre Composite Failure Modes be Interacted or Superimposed, *Composites*, Vol. 24, No. 1, p53-55.

Hart-Smith L.J. (1993), An Inherent Fallacy in Composite Interaction Failure Curves, *Composites*, Vol. 24, No. 6, p523-524.

Hart-Smith, L.J. (1998), Prediction of a Generalised Maximum-Shear-Stress Failure Criterion for Certain Fibrous Composite Laminates, *Compos. Sci & Technol.*, **58**(7), p1179-1208.

Hayhurst, D.R. & Leckie, F.A (1973), The Effect of Creep Constitutive and Damage Relationships Upon the Rupture Time of a Solid Circular Torsion Bar, *J. Mech. Phys. Solids.*, Vol. 21, p431-446.

Heuer, A.H. (1987), Transformation Toughening in ZrO_2-Containing Ceramics, *J.Am. Ceram. Soc.*, **70**[10], p689-698.

Hibbitt, Karlsson & Sorensen (1998a) *ABAQUS/Standard*, Ver 5.8, *Theory Manual*.

Hibbitt, Karlsson & Sorensen (1998b) *ABAQUS/Standard Example*, Ver 5.8, *Problems Manual Vol. I & II.*

Hinton & Soden (1998), Predicting Failure in Composite Laminates: The Background of the Exercise, *Compos. Sci. Technol.*,**58**(7), p1001-1010.

Hill R. (1950), *The Mathematical Theory of Plasticity*, Oxford University Press: London.

Hoffman, O. (1967), The Brittle Strength of Orthotropic Materials, *J. Comp. Mat.*, April, p200-206.

Hull & Clyne (1996), *An Introduction to Composite Materials*, 2ed, Cambridge Solid State Science Series (Cambridge University Press).

Jamet J.F. *et al* (1984), Characterization of Mechanical Behaviour and Fractographic Observations on Compglas SiC/LAS Composites, *Ceram. Eng. Sci. Proc.*, 5 (7-8), p625-642.

Jones, R.M. (1999), *Mechanics of Composite Materials*, 2ed, (Taylor & Francis).

Ju, J.W. (1989), On Energy-Based Coupled Elastoplastic Damage Theories: Constitutive Modelling and Computational Aspects, *Int. J. Solids Structures*, Vol. 25, No. 7, p803-833.

Karandikar P.G. & Chou T.W (1993), Characterization and Modeling of Microcracking and the Elastic Moduli Changes Nicalon-CAS Composites, *Comp. Sci. Tech.*, 46 (3), p253-263.

Kim R.Y. & Pagano N.J. (1991), Crack initiation in Unidirectional Brittle-Matrix Composites, *J. Am. Ceram. Soc.*, **74** [5], p1082-1090.

Kimber A.C. and Keer J.G. (1982), On the Theorectical Average Crack Spacing in Brittle Matrix Composites containing Continuous Aligned Fibres, *Journal of Material Science Letters*, 1, p353-354.

Lawn B.R. & Wilshaw T.R. (1975), *Fracture of Brittle Solids*, Cambridge Univ. Press.

Lemaitre, J. (1992), A *Course on Damage Mechanics*, 2nd Edition., Springer-Verlag.

Levitt, S.R (1972), High-strength Graphite Fibre/Lithium Aluminosilicate Composites,

Lewis, D. III (1995), Continuous Fiber-Reinforced Ceramic Matrix Composites: A Historical Overview, *Handbook on Continuous Fiber-Reinforced Ceramic Matrix Composites*, ed. Leham, R.L., El-Rahaiby, S.K., Wachtman, J.B. Jr., (AMPTIAC), p1-34.

Lubliner, J. (1972), On the Thermodynamic Foundations of Non-Linear Solid Mechanics, *Int. J. Non-Linear Mechanics*, Vol. 7, p237-254.

Kachanov, L.M. (1958), Izv. Acad. Nauk SSR, otd. Tekh. Nauk, (in Russian), No. 8, p26-31.

Krajcinovic, D. & Fonseka, G.U. (1981), The Continuous Damage Theory of Brittle Materials, *Journal of Applied. Mechanics*, Dec, Vol. 48, p809-815.

Krajcinovic, D. (1985), Continuous Damage Mechanics Revisited: Basic Concepts and Definitions, *Journal of Applied. Mechanics*, Dec, Vol. 52, p829-834.

Krajcinovic, D. & Mastilovic, S. (1995), Some Fundamental Issues of Damage Mechanics, *Mechanics of Materials*, Vol. 21, p217-230.

Leckie, F.A & Hayhurst, D.R. (1974), Creep Rupture of Structures, *Proc. R.Soc. Lond. A*, **340**, p323-347.

Lemaitre, J. & Chaboche, J.L. (1978), *J. Mécanique Appliquée*, Vol. 2, No.3, p317-365.

Lemaitre, J. 1984, How To Use Damage Mechanics, *Nuclear Engineering and Design*, 80, 233-245.

Lemaitre, J. (1992), A *Course on Damage Mechanics*, 2nd Edition., Springer-Verlag.

Lubliner, J. (1972), On the Thermodynamic Foundations of Non-Linear Solid Mechanics, *Int. J. Non-Linear Mechanics*, Vol. 7, p237-254.

Marquis D. & Lemaitre, J. (1988), Constitutive Equations for the Coupling Between Elasto-Plasticity Damage and Aging, *Revue Phys. Appl.*, **23**, p615-624

Marshall D.B., Cox B.N. & Evans A.G. (1985), The Mechanics of Matrix Cracking in Brittle Matrix Composites, *Acta metall.*, Vol. 33, No. 11, p2013-2021.

Marshall, D.B. (1986), Strength Characteristics of Transformation-Toughened Zirconia, *J.Am. Ceram. Soc.*, **69**[3], p173-180.

Marshall, D.B. & Ritter, J.E. (1987), Reliability of Advanced Structural Ceramics and Ceramic Matrix Composites – A Review, *Ceramic Bulletin*, Vol. 66, No. 2, p309-317.

Matzenmiller, A., Lubliner, J. & Taylor, R.L. (1995), A Constitutive Model for the Anisotropic Damage in Fibre-Composites, *Mech. Mater.*, 20, p125-152.

McCartney L.N. (1987), Mechanics of Matrix Cracking in Brittle-Matrix Fibre-Reinfroced Composites, *Pro.R. Soc. Lond. A*, **409**, p329-350.

McCartney, L.N. (1998), Predicting Transverse Crack Formation in Cross-Ply Laminate, *Compos. Sci & Technol.*, **58**(7), p1069-1081.

McClintock F.A. and Argon A.S. (1966), Mechanical Behaviour of Materials, Addison-Wesley Publishing Company, Inc, Reading, Massachusetts, USA.

McMeeking, R.M. & Evans, A.G (1982), Mechanics of Transformation-Toughening in Brittle Materials, *J.Am. Ceram. Soc.*, **65**[5], p242-247.

Mukherjee A., Rao H.S. (1995) FE-Modelling of the Toughening Mechanism in Whisker Reinforced Ceramic-Matrix-Composites, *Computational Material Science*, **4**, 249-262.

Murakami, S. (1983), Notion of Continuum Damage Mechanics and its Application to Anisotropic Creep Damage Theory, *Journal of Engineering Materials and Technology*, April, Vol. 105, p99-105.

Needleman A. (1990) An Analysis of Decohesion Along an Imperfect Interface. *Inter. J of Fracture.*, **42**, 21-40

Phillips D.V. & Zienkiewicz O.C. (1976) Finite Element Non-Linear Analysis of Concrete Structures. *Proc. Instn Civ. Engrs*, Part 2, **61**, Mar., 59-88.

Prewo K.M. (1986), Tension and Flexural Strength of Silicon Carbide Fibre-Reinforced Glass-Ceramics, *J. Mater. Sci.*, **21** (10), p3590-3600.

Prewo, K.M. and Brennan, J.J. (1980), High Strength Silicon Carbide Fibre-Reinforced Composites, *J. Mater. Sci.*, 15(2), p463-468.

Prewo, K.M. and Brennan, J.J. (1982), Silicon Carbide Yarn Reinforced Glass Matrix Composites, *J. Mater. Sci.*, 17(4), p1201-1206.

Puck, A. and Schürmann, H. (1998), Failure Analysis of FRP Laminates by Means of Physically Based Phenomenological Models, *Compos. Sci & Technol.*, **58**(7), p1045-1067.

Rabotnov, Y.N. (1968), Creep Rupture, *Proc. XII Internat. Cong. Appl. Mech.*, (Standford-Springer, 1969).

Raju I.S. & Newman J.C. Jr. (1979), Stress Intensity Factors for a Wide Range of Semi-Elliptical Surface Cracks In Finite-Thickness Plates, *Engineering Fracture Mechanics*, Vol. 11, p817-829.

Rice J.R. & Levy N. (1972), The Part-Through Surface Crack in an Elastic Plate, ASME *Journal of Applied Mechanics*, Vol. 39, p 185-194.

Rice, R.W. (1981b), Mechanisms of Toughening in Ceramic Matrix Composites, *Ceram. Eng. Sci. Proc.*, 2 (7-8), p661-701.

Rice, R.W, *et al* (1982), Refractory Ceramic-Fibre Composites: Progress, Needs and Opportunities, *Ceram. Eng. Sci. Proc.*, 3(9-10), p698-713.

Richlen, S. (1995), Application of Fiber-Reinforced Ceramic Matrix Composites, ed. Leham, R.L., El-Rahaiby, S.K., Wachtman, J.B. Jr., (AMPTIAC), p1-34.

Rosen B.W. (1970), Thermo-Mechanical Properties of Fibrous Composites, *Proc. R. Soc. A319*, p79.

Rotem, A. (1998), Prediction of Laminate Failure with Rotem Failure Criterion, *Compos. Sci & Technol.*, **58**(7), p1083-1094.

Sambell, R.A.J. *et al* (1972), Carbon Fibre Composites with Ceramic and Glass Matrices, *J. Mater. Sci.*, 7(6), p676-681.

Scott Bader (1998), Crystic Polyester Handbook, Scott Bader Company Ltd, Wollaston, Wellingborough, Northhamptonshire, NN29 7RL.

Schlumberger (1987), 3531 D, F and G Data Acquisition System Operation Manual, Schlumberger Technologies, Instrumentation Division, Victoria Road, Farnborough, Hampshire GU14 7PW.

Shetty D.K. (1995), Overview of Design Methodology for Ceramic Matrix Composites, *Handbook on Continous Fibre-Reinforced Ceramic Matrix Composites*, ed. by Lehman R.L., El-Rahaiby S.K. & Wachtman J.B. Jr., AMPTIAC.

Shih C.F., Li C.W. & Needleman A. (1986), Energy Release Rate Along a Three-Dimensional Crack Front in a Thermo-Mechanical Field, *International Journal of Fracture*, p79-102.

Sih G.C (1973), *Handbook of Stress Intensity Factors*, Lehigh University, Bethlehem.

Sneddon I.N. & Lowengrub M. (1969), *Crack Problems in the Classical Theory of Elasticity*, Wiley, New York.

Sun, C.T. and Tao, J.X. (1998), Prediction of Failure Envelopes and Stress/Strain Behaviour of Composite Laminates, *Compos. Sci & Technol.*, 1998, **58**(7), p1125-1136.

Talreja, R (1994), *Damage Mechanics of Composite Materials*, Elsevier, Amsterdam,.

Talreja, R (1985), A Continuum Mechanics Characterization of Damage in Composite Materials, *Proc. Roy. Soc. London*, **A399**, p195-216.

Tsai, S.W. (1966), Strength Theories of Filamentary Structures, in *Fundamental Aspects of Fiber Reinforced Plastic Composites*, Conference Proceedings, ed. Schwartz, R.T. and Schwartz, H.S., Dayton, Ohio, 24-26 May 1996 (Wiley

Tsai, S.W. and Wu, E.M. (1971), A General Theory of Strength for Anisotropic Materials, *J. Compos. Mater.*, **5**, p58-80.

Tinklepaugh, J.R. (1965), Ceramic-Metal Fibre Composite Systems, *Proceedings of the 12th Sagamore Army Materials Research Conference on Strengthening Metals and Ceramics* (New York: Plenum Press), p1-33.

Tsai, S.W. (1966), Strength Theories of Filamentary Structures, in *Fundamental Aspects of Fiber Reinforced Plastic Composites*, Conference Proceedings, ed. Schwartz, R.T. and Schwartz, H.S., Dayton, Ohio, 24-26 May 1996 (Wiley Interscience, New York, 1968), p3-11.

Voyiadjis, G.Z. & Kattan, P.I. (1999), *Advances in Damage Mechanics: Metals and Metal Matrix Composites*, Elsevier Science Ltd, Oxford, ISBN: 0 08 043601 3.

Wang S.W. & Parvizi-Maljidi A. (1992), Experimental Characcterisation of the Tensile Behaviour of Nicalon Fiber-Reinforced Calcium Aluminosilicate Composite, *J. Mater. Sci.*, **27** (20), p5483-5496.

Weibull W. (1951), A Statistical Distribution Function of Wide Applicability, *J. Appli. Mech.*, 18, p293-305.

Westergaard, H.M. (1939), Bearing Pressures and Cracks, *Journal of Applied Mechanics*, Vol. 6, p49-53.

Wolfe, W.E. and Butalia, T.S. (1998), A Strain Energy Based Failure Criterion for Non-Linear Analysis of Composite Laminates Subjected to Biaxial Loading, *Compos. Sci & Technol.*, **58**(7), p1107-1124.

Yazdani, S. & Schreyer, H.L. (1988), An Anisotropic Damage Model with Dilation of Concrete, *Mechanics of Material*, 7, p231-244.

Zienkiewicz O.C. *et al.* (1972) Finite Element Methods in the Analysis of Reactor Vessels. *Nucl. Engng & Des.*, **20**, No. 2, 507-541.